EFFECT OF DEFECTS ON STRUCTURE, ELECTRONIC AND MAGNETIC PROPERTIES OF 2D HETEROSTRUCTURE MATERIAL GRAPHENE/HEXAGONAL-BORON NITRIDE

A THESIS SUBMITTED TO THE

CENTRAL DEPARTMENT OF PHYSICS

INSTITUTE OF SCIENCE AND TECHNOLOGY

TRIBHUVAN UNIVERSITY

NEPAL

FOR THE AWARD OF

DOCTOR OF PHILOSOPHY

IN PHYSICS

BY

HARI KRISHNA NEUPANE

AUGUST 2022

EFFECT OF DEFECTS ON STRUCTURE, ELECTRONIC AND MAGNETIC PROPERTIES OF 2D HETEROSTRUCTURE MATERIAL GRAPHENE/HEXAGONAL-BORON NITRIDE

A THESIS SUBMITTED TO THE

CENTRAL DEPARTMENT OF PHYSICS

INSTITUTE OF SCIENCE AND TECHNOLOGY

TRIBHUVAN UNIVERSITY

NEPAL

FOR THE AWARD OF

DOCTOR OF PHILOSOPHY

IN PHYSICS

BY

HARI KRISHNA NEUPANE

AUGUST 2022

DECLARATION

Thesis entitled **"Effect of Defects on Structure, Electronic and Magnetic Properties of 2D Heterostructure Material Graphene/Hexagonal-Boron Nitride"** which is being submitted to the Central Department of Physics, Institute of Science and Technology (IOST), Tribhuvan University, Kirtipur, Kathmandu Nepal for the award of the degree of Doctor of Philosophy (Ph.D.) is a research work carried out by me under the supervision of Prof. Dr. Narayan Prasad Adhikari of Central Department of Physics, Tribhuvan University, Kirtipur, Kathmandu Nepal.

This research is original and has not been submitted earlier in part or full in this or any other form to any university or institute, here or elsewhere, for the award of any degree.

Hari Krishna Neupane

RECOMMENDATION

This is to recommend that **Mr. Hari Krishna Neupane** has carried out research entitled **"Effect of Defects on Structure, Electronic and Magnetic Properties of 2D Heterostructure Material Graphene/Hexagonal-Boron Nitride"** for the award of Doctor of Philosophy (Ph.D.) in **Physics** under my supervision. To my knowledge, this work has not been submitted for any other degree.

He has fulfilled all the requirements laid down by the Institute of Science and Technology (IOST), Tribhuvan University, Kirtipur for the submission of the thesis for the award of Ph.D. degree.

. . . . . .

Dr. Narayan Prasad Adhikari
Supervisor
(Professor)
Central Department of Physics
Tribhuvan University
Kirtipur, Kathmandu, Nepal

[August 2022]

LETTER OF APPROVAL

[Date: 03/08/2022]

On the recommendation of **Prof. Dr. Narayan Prasad Adhikari**, this Ph.D. thesis submitted by **Mr. Hari Krishna Neupane**, entitled **"Effect of Defects on Structure, Electronic and Magnetic Properties of 2D Heterostructure Material Graphene/ Hexagonal-Boron Nitride"** is forwarded by Central Department of Research Committee (CDRC) to the Dean, IOST, T. U..

. . . . . .

Dr. Om Prakash Niraula
Professor
Head
Central Department of Physics
Tribhuvan University
Kirtipur, Kathmandu
Nepal

ACKNOWLEDGEMENTS

I would like to express my wholehearted gratitude to my respected supervisor, Prof. Dr. Narayan Prasad Adhikari for his artful guidance, regular supervision and perpetual help throughout the entire span of my Ph.D. research work. His words of suggestion and encouragement had helped to me bring out a fruitful analysis of this work.

I would like to acknowledge Prof. Dr. Om Prakash Niraula, Head of Central Department of Physics for his valuable help to complete this work. Also, I am thankful to all members of the Central Department of Physics. My sincere reverence goes to Prof. Dr. Binil Aryal, Dean, IOST, TU for his consolation and motivation during the work. Also, I would like to express my deep thanks to Prof. Dr. Raju Khanal, Prof. Dr. Narayan Chapagain, Prof. Dr. Rajendra Parajuli, Prof. Dr. Leela Pradhan Joshi, Asso. Prof. Dr. Gopi Chandra Kaphle and Asso. Prof. Dr. Nurapati Pantha for their valuable suggestion, cooperation and encouragement.

I am grateful to Dr. Saran Lamichhane, Dr. Rajendra Prasad Koirala, Dr. Manoj Kumar Chaudary, Dr. Shyam Prakash Khanal and Mr. Pitamber Shrestha, for their academic help and moral support during my difficuly days of journey. Also, I would like to acknowledge Prof. Argya Taraphdar and his team for fruitful academic discussion at IIT Kharagpur India. Additionally, I am grateful to my labmates Mr. Jhulan Pourel, Mrs. Bidhya Thapa, Mr. Prakash Khatri and Mr. Narayan Prasad Gautam for their help during this journey. I am also thankful to my friends, Dinesh Kumar Chaudary, Yogesh Maharjan, Indra Bahadur Bhandari, Devendra Raj Upadhaya, Ram Krishna Tiwari, Arjun Dhungana, Sangeeta Maharjan, Anil Khadka, Sajan Shrestha, Narayan Panthi, Umakanta lal Karna, Arun Kumar Shaha, Khagendra Pokharel, Bipin Bhattarai, Bal Bikram Khatri, Birendra Yadav and other colleagues with whom I spent significant hours during the period of my Ph.D. work.

My acknowledge also goes to University Grants Commission for its partial financial support to my Ph.D. research work. I am equally thankful to Amrit Campus family. Finally, I want to dedicate this thesis to my parents who scarify their happiness to grow our family. Also, I would like to express my thanks to my family members; Mrs. Jamuna Adhikari (Neupane), Mr. Kumar Neupane and Prince Sadhil Neupane for their constant support in different dimensions. At last, I want to acknowledge to all my relatives, friends and well wishers for their inspiration in each and every step of my life.

Hari Krishna Neupane
August 2022

ABSTRACT

Two dimensional (2D) monolayer (ML) and heterostructure (HS) materials have attracted much attention in the field of modern technological applications because of their use in spintonic, electronic, optoelectronic, sensors and memory devices. To gauge the task played by the crystalline defects in HS is also of compelling by reason of their peculiar properties. The structural, electronic, magnetic and transport properties of ML, HS and vacancy defects in HS have been the subject of instense research due to their applications in many technological purpose. Therefore, in the present work, we have explored the structural, electronic, magnetic and transport properties of 2D materials graphene (G) and hexagonal boron nitride (h-BN) ML, G/h-BN HS, and different possible vacancy defects of boron (B), nitrogen (N) and carbon (C) atoms in G/h-BN HS using spin-polarized density functional theory (DFT) incorporating van der Waals (vdWs) interactions (DFT-D2) approach under computational tools Quantum ESPRESSO (QE) and BoltzTraP (BTP) software packages. QE is used for the study of structural, electronic and magnetic properties, and BTP is used for the study of transport properties of considered materials.

To study the structural properties, firstly we have replicated the optimized and relaxed structures of graphene, h-BN, G/h-BN HS, 1B vacancy defect in G/h-BN (G/h-BN_1B), 1N vacancy defect in G/h-BN (G/h-BN_1N), nearest neighbour 1B and 1N vacancy defects in G/h-BN (G/h-BN_nBN), alternate zone of 1B and 1N vacancy defects in G/h-BN (G/h-BN_aBN), 1C vacancy defect in G/h-BN (G/h-BN_1C) and 2C vacancy defects in G/h-BN (G/h-BN_2C) materials, then studied the stability of these materials based on their binding energy. They are found to be stable materials. The interlayer distance of the consistuents of HS are estimated and found that vdWs force exists between them. Hence, the pristine and vacancy defected HS are appellated stable 2D vdWs HS materials.

In order to understand the electronic properties of the material, we have performed electronic band structure calculations. Our findings show that graphene and h-BN are zero band gap (0 eV) and wide band gap (4.98 eV) materials respectively. They are fairly acceptable with experimentally reported values. By the conscientious probe, we found that G/h-BN, and B and N sites vacancy defected G/h-BN materials open small band gap at K-point in band structure, which are corresponding with the reported value, and hence they have semimetallic properties. On the other hand, band states of G/h-BN_2C appear around the Fermi energy level, thus it has metallic properties but G/h-BN_1C has small band gap of value 0.40 eV at K-point in its band structure, hence it is labeled

n-type semiconductor.

Furthermore, magnetic properties of materials are explored by the analysis of their density of states (DOS) and projected density of states (PDOS) calculations. Our calculations suggest that graphene and h-BN are non-magnetic materials, and pristine G/h-BN HS and vacancy defected all HS have magnetic properties. It has been found that vacancy defected HS have higher value of magnetic moment than that of pristine HS. Thus, the study of defected materials is of great interest from magnetic point of view.

Transport properties of our designed ML, HS and vacancy defects in HS materials are regarded based on Boltzmann transport equations (BTE) within constant relaxation time approximation (RTA). For transport properties, we have calculated Seebeck coefficient (S), electrical conductivity (σ), electronic contribution of thermal conductivity (K) and thermoelectric power factor (P) by virtue of the effect of temperature at constant energy (Fermi), and chemical potential (energy) at constant temperature respectively. The values of S and P are obtained at different temperatures by taking constant energy, and are supported by the effect of chemical potential on S and P at constant temperature. The computed values of S and P obtained from the materials we studied, agree with the reported values of previous studies. Therefore, they are assuring aspirant for use in the fields of thermoelectricity.

LIST OF ACRONYMS AND ABBREVIATIONS

BFGS	Broyden Fletcher Goldfrab Shanno
BOA	Born Oppenheimer Approximation
BTE	Boltzmann Transport Equation
BTP	BoltzTraP
BZ	Brillouin Zone
CPN	Charge Neutrality Point
CVD	Chemical Vapour Deposition
DFPT	Density Functional Perturbation Theory
DFT	Density Functional Theory
DOS	Density of States
ESPRESSO	opEn-Source Package for Research in Electronic Structure, Simulation, and Optimization
eV	electron Volts
FET	Field Effect Transistor
G	Graphene
GGA	Generalized Gradient Approximation
GPL	General Public License
h-BN	hexagonal-Boron Nitride
HEG	Homogenous Electron Gas
HF	Hartree Fock
HK	Hohenberg Kohn
HS	Heterostructure
IPPS	In-Plane Pressure Sensor
KS	Kohn Sham
LDA	Local Density Approximation
LED	Light Emitting Diode
LHS	Left Hand Side
ML	Monolayer
MDFT	Modern Density Functional Theory
MP	Monkhorst Pack
MV	Marzarri Vanderbilt

nscf	non selfconsistent field
ntype	number of type
PBE	Perdew Burke Ernzerhof
PDOS	Projected Density of States
PPs	pseudopotentials
PW	Plane Wave
QE	Quantum ESPRESSO
QHE	Quantum Hall Effect
QMC	Quantum Monte-Carlo
QTT	Quantum Tunneling Transistor
RRKJ	Rappe Rabe Kaxiras Joannopoulos
RTA	Relaxation Time Approximation
scf	self-consistent field
SDFT	Spin-polarized Density Functional Theory
SWE	Schrodinger Wave Equation
TDOS	Total Density of states
TE	Thermoelectric
TF	Thomas Fermi
TPS	Tunneling Pressure Sensor
USPPs	Ultra-Soft Pseudo-Potentials
vdWs	van der Waals
XC	Exchange Correlation

LIST OF SYMBOLS

k_{B}	Boltzmann constant
K	Electronic contribution of thermal conductivity
S	Seebeck coefficient
P	Thermoelectric power factor
σ	Electrical conductivity
Ψ	Wave function
$n(r)$	Electron density
0D	Zero dimensional
1D	One dimensional
2D	Two dimensional
3D	Three dimensional
E_f	Fermi energy
E_g	Bandgap energy
μ_B	Bohr magneton
m^*	Effective mass
P_m	Maximum thermoelectric power factor
S_m	Maximum Seebeck coefficient
μ	Chemical potential
τ	Relaxation time
Å	Degree Angstrom
H	Hamiltonian
Ry	Rydberg
E_{corr}	Correlation energy
E_0	Ground state energy
μ_T	Total magnetic moment

LIST OF TABLES

LIST OF FIGURES

TABLE OF CONTENTS

Page No.

CHAPTER 1

1. INTRODUCTION

1.1 General Consideration

Scientific discoveries have been made in all areas of condensed matter and material physics in the decade (Brinkman, 1986). They are important for technological advancing which enhance the understanding of basis physics of materials. The technological revolution would be impossible without the continuing increase in our scientific understanding of materials. The technological impact of advancing is best example in the areas of condensed matter and material physics based on the electronic, magnetic, transport and optical properties of materials (Singh, 2006; Mansoori, 2005). Technology based on electronic, magnetic, transport and optical properties of materials is accelerating the information age through revolutions in computing, communications and electronics (Mansoori, 2005; Liang et al., 2020). Electronic components and electronic devices are becomming rapidly available in the world, which empowered the information age, are radically changing how we live, interact and accomplish business (Liang et al., 2020). Therefore, materials are used in the fields of device applications based on their electronic, magnetic, transport and optical properties.

Conductor and semiconductor materials give an outstanding exhibit of the powerful interplay between and inter-dependence of science and technology. Materials theory researches highlights on predicting, modelling, and designing of materials what people encounter in their daily life. The main basis of understanding materials depends on the knowledge of their electronic structural properties. The study of materials and their properties has been ongoing for as long as the existence of human being. Materials have played an integral role in forming the current society. Materials research area rely on all branches of science and technology in today's world, which has helped to make better connection between them. The properties and interactions of different materials are different, hence regorous investigations on the materials are essential before using in the field of devices. Most of the electronic, optoelectronic, spintonic and memory devices are fabricated by using the monolayer of graphene (G), molybedenum disulphide

(MoS_2), hexagonal-boron nitride (h-BN), heterostructure of graphene/h-BN (G/h-BN), graphene/MoS_2 (G/MoS_2) materials (Castro et al., 2007; Radisavljevic et al., 2012; Phuc et al., 2018; Yu et al., 2013; Roy et al., 2013). Thus, the monolayer and heterostructure materials have intriguing properties, and hence they are used in academic as well as industrial sectors.

1.2 Nanomaterials

Materials with physical size dimension in the range 1 nm (1 nm = 10^{-9} m) to 100 nm are called nanomaterials. Nanomaterials created large surface area, lower density and have great chemical and physical stability at molecular/atomic level. They have substantial applications in the fields of nanotechnology (Pankhurst et al., 2003; M. Berger, 2009). The development of nanotechnology is based on the physical properties and materials dimensions of nanomaterials. Nanomaterials have particular optical, magnetic, electrical and transport properties. Hence, they have conceivable applications in the fields of medical and industrial areas, Optical, electronic, sensing and thermoelectric devices (Pankhurst et al., 2003; Thanh et al., 2014). Basically, nanomaterials are nanostructured and nanoparticle materials. Nanostructured assign to concise dimension's materials which are assembled of grains in the nanometer size range. On the other hand, nanoparticles (dimension length < 100 nm) have zero-dimension (0D), one-dimension (1D), two-dimension (2D) and three-dimension (3D) such as carbon quantum dot, graphene quantum dot, metal nanoparticle are 0D; wires, rods and nanofibers are 1D; thin-films, thin-plates etc. are 2D; and bulk powders dispersion of nanoparticles, bundles of nanowires, nanotubes and multinanolayers are 3D of nanoparticles materials (M. Berger, 2009). In the present work, we have used two dimensional nanomaterials/nanoparticles, which are described as follows.

1.3 Two Dimensional (2D) Materials

Two dimensional materials are a classification of nanomaterials, made of single layer crystalline materials of atoms or compounds (Rao et al., 2009). Not every compound or atom can be made a 2D structure. This is due to the fact that melting temperature decreases with decreasing in thickness of thin films so that most materials only survive our ambient conditions by natural passivation of their surfaces. This means, for a material to be able to sustainably survive as a 2D material, it needs to have a high enough melting point to survive at a useable temperature and be unreactive with the natural ambient environment, when reduced to a 2D structure. These materials exhibit unique structural, mechanical and optoelectronic properties that have a broad set of practical

applications (Wang, Ma, & Sun, 2017), if said materials can be sustainably made. These properties are much stronger than the same materials bulk counterpart. 2D materials are mostly made through the process known as exfoliation. The process of exfoliation is the repeated peeling of layers from a 3D material to produce 2D mateials. This was first performed in 2004 by Novosolov and co-authors (Novoselov et al., 2004) on graphite to produce graphene, hence graphene is now used to produce other 2D materials. Graphene has been developed since 2004, and became more sustainable for mass production of other 2D materials. Moreover, hexagonal boron nitride (h-BN) is a 2D material which is structurally similar with grapphene (Goriachko et al., 2007; Wang, Ma, & Sun, 2017). In the present work, we will be concerned about the properties of graphene (G), hexagonal boron nitride (h-BN), and their pristine and vacancy defected heterostructure (HS) materials because these type of materials exhibit the properties that make them capable of surviving as 2D materials (Novoselov et al., 2004; Ooi et al., 2005).

1.3.1 Graphene and Hexagonal-Boron Nitride (h-BN) Materials

Carbon is the p-block element in the periodic table having atomic number 6 and atomic mass 12 with electronic configuration $1s^2 2s^2 2p^4$. Carbon has the possibility of making a lot of different inorganic and organic compounds because of its 4 valence electrons in its outermost shell. Carbon has only two naturally occuring crystal structures namely: graphite and diamond. Graphite is the stock of graphene pilled on the top of each other which is black whereas diamond is the network of carbon atom arranged in tetrahedron one after another and is clear. Graphene is made of carbon and is considered as a basic building block of graphite (Novoselov et al., 2004).

Graphene is a single layer of sp^2-bonded carbon atoms compact into benzene ring with hexagonal structure (Novoselov et al., 2004). It is a 2D crystalline material. Graphene is only one atom-thick and is very thin. It is most strongest and is still flexible. Graphene can be wrapped up into 0D fullerenes, rolled into 1D nanotubes and stacked into 3D graphite as shown in figure (1). The fullerenes C_{60} (Neto et al., 2006) is a graphene ball looks like a football, consists of some pentagons and some hexagons. The 1D nanotubes are rolled-up cylinder of graphene and graphite is the stack of graphene layer one above other. Graphene has been studied theoretically for many years but it was confined for the first time in 2004 (Novoselov et al., 20 04). Before graphene was isolated, it was commonly believed that two dimensional (2D) compounds are unstable and could not exist, but graphene is strong and completely stable. It is super-strong, super-tensile and highly-transparent (Tran et al., 2019). In, 2010, the Noble prize in physics was awarded for two physicists Andre Geim and Konstantin Novoselov at the

University of Manchester, England for their "groundbreaking experiments regarding the two dimensional material graphene" (Cooper et al., 2012).

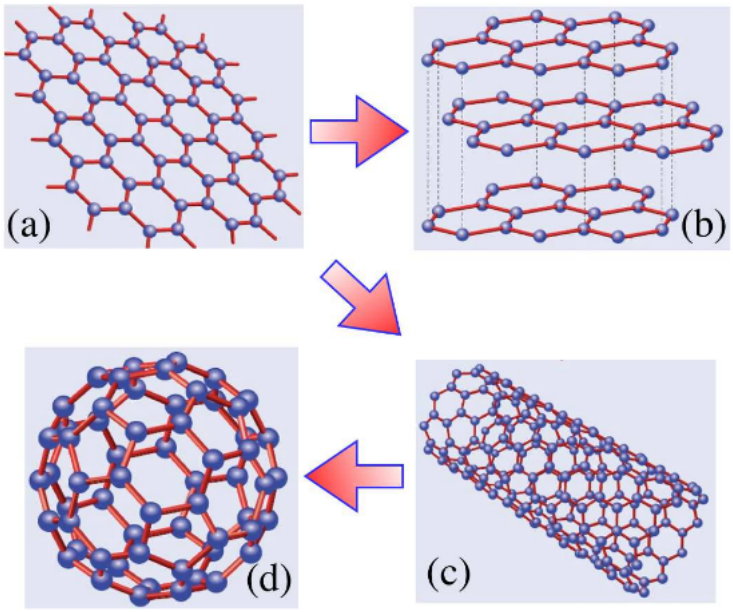

Figure 1: Various form of carbon, showing graphene is the building block of all graphite materials: (a) 2D layer of carbon i.e. graphene, (b) stacked of graphene i.e. 3D graphite, (c) rolled-up cylinder of graphene i.e. 1D carbon nanotubes, and (d) wrapped-up graphene i.e. 0D fullerenes (C_{60}) (Tetlow et al., 2014).

The hexagonal lattice of graphene can be treated as two interleaving triangular lattices, where each carbon atom is separated by 3 neighbouring carbons by a distance of 1.42 A^0, with area 0.052 nm^2 and density of graphene is 0.77 mg/m^3 (Gibertini et al., 2010). Figure (2) shows that, each carbon atom in two sublattices A and B has nearest neighbour in three different directions.

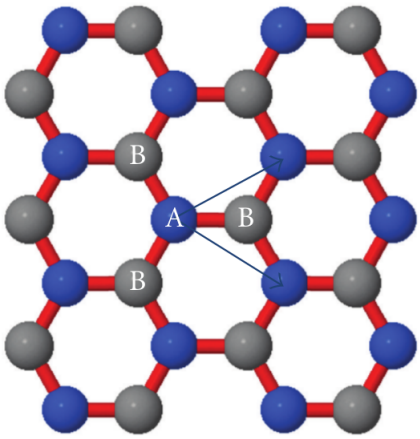

Figure 2: Triangular sublattice of graphene, where each atom in one sublattice has 3 nearest neighbour in another sublattice (Cooper et al., 2012).

Graphene carries heat extremely well and is best thermal conductor with the value of

conductivity about 5000 W/mK at room temperature (Balandin et al., 2008), which is 10 times to the value of copper. Because of its super-thermal conduction property, it can be considered as an exquisite material for thermal management. Since, high thermal conductivity is beneficial for more compact circuits, because it facilitates the diffusion of heat to the contact. Further, the charge carrier in a graphene has shown remarkably high intrinsic mobility with zero effective mass (Neto et al., 2006; Geim & Novoselov, 2007), so it can travel thousands inter-atomic distances without scattering. It is basically relativistic particles and is explained by Dirac-like equation. Value of electrical conductivity is about $10^6\ \Omega^{-1}cm^{-1}$, which is 1000 times more than that of copper (Geim, 2009). Because of the terrific conductive and thermal properties of graphene, scientists are very excited about the possibility of using graphene as a replacement of sillicon and microchips. Other most important properties of graphene are fractional Quantum hall effect (QHE) at room temperature (Neto et al., 2006; Novoselov et al., 2005), tunable band gap (Liu & Shen, 2009), high elasticity (Gomeznavarro et al., 2008) etc.

More experimental and theoretical works are undertaken regarding optical, electronic and magnetic properties of graphene (Valimukhametova et al., 2020; Mikhailov, 2011; Neupane, et al., 2020). Nowadays, scientists are very excited towards it because of its excellent mechanical, thermal, electrical and other unique properties. So, graphene is regarded as rising star of material science and condensed mattter physics. It has many potential applications such as it can be used to enhance the strength of other materials. It is useful in microelectroincs, transparent electrodes, super-capacitors, super-small transister, energy storage devices and many more (Novoselov et al., 2004; Castro et al., 2007).

Hexagonal-boron nitride (h-BN) is a structurally similar material with graphene but has diffrent physical and chemical properties (Goriachko et al., 2007; Wang et al., 2017). It is formed by the arrangement of boron (B) and nitrogen (N) atoms alternately to form honeycomb lattice structure as shown in figure (3).

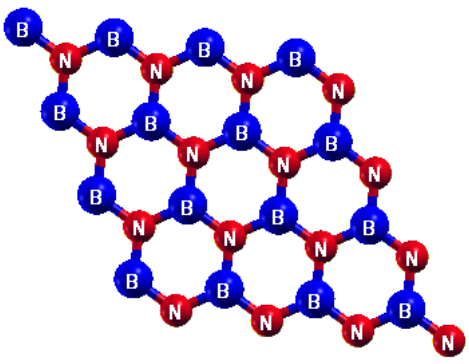

Figure 3: Supercell structure of h-BN, where B and N atoms are alternately arranged to form honeycomb lattice structure.

h-BN has not formed dangling bonds on the surface. The bond length of B-N atoms is 1.45 Å, in monolayer h-BN structure (Lynch & Drickamer, 1966), which is formed by sp^2 hybridization. On the other hand, B and N atoms are bonded by covalent bonds in each layer of layered structures, and adjoining layers of h-BN are connected by weak van der Waals (vdWs) forces (Lynch & Drickamer, 1966; Jin et al., 2009; Nag et al., 2010). It has attracting physical and mechanical properties such as Young's modulus nearly 270 Nm^{-2}, thermal conductivity 300 $Wm^{-1}K^{-1}$ at room temperature, and tensile strength 41 MPa (Zhi et al., 2009; Zhou et al., 2014; Zhou et al., 2007) because of its wide band gap (5.80 eV) and large optical phonon mode (Watanabe et al., 2004). Due to these properties, it has a growing interest for electronic and optoelectronic devices (Geim & Novoselov, 2007; Zhang et al., 2016; Wang et al., 2014; Wang et al., 2012; Song et al., 2010; Tran et al., 2016). Therefore, various theoretical and experimental research groups have explored the h-BN for its more novel properties. The non-magnetic nature of h-BN restrict its practical applications in extensively awarding field of devices applications. So that, researchers (Liu, et al., 2005; Peng, et al., 2005; Si & Xue, 2007) found that defects in h-BN have unprompted spin magnetization due to this defected h-BN presents exemplary half-metallic magnetism in a arry of states. Magnetic materials are more useful in medical, nanoelectronic devices, and industrial applications (Makarova et al., 2019; Peng et al., 2016). In summary, 2D materials graphene and h-BN has great attracting properties, due to this they are useful materials in field of technological a pplications. Hence, in the present work we have used graphene, h-BN, heterostructure of graphene and h-BN (G/h-BN), and B, N and C sites vacancy defects in G/h-BN materials for the investigations of their additional physical properties.

1.3.2 Graphene/Hexagonal-Boron Nitride (G/h-BN) Heterostructure Material

The monolayers of 2D material are used to form Heterostructure (HS) materials where each monolayers are being by van der Waals (vdWs) interactions. These structures are important as they allow the combination of the extreme properties of individual 2D materials to make a combination of new materials with combined novel properties (Ramasubramaniam et al., 2011; Ilyasov et al., 2014). These structures are theorised to revolutionise many aspects of everyday technology, in particular electronics, opto-electronic and spintonic devices, with graphene based hetereostructures allowing the creation of efficient, high mobility transistors, allowing the production of even smaller circuitry (Wang et al., 2017; Yu et al., 2013; Liang et al., 2020).

In the present work, we consider graphene/h-BN (G/h-BN) heterostructure (HS) material which is formed by direct stacking components of graphene and h-BN monolayers. It has very impressive physical and chemical properties like physical strength, high electrical

and thermal conductivities, high temperature stability, high sensitivity and mechanical strength, low noise effect, which are different than its consistuents (Liu et al., 2011; Li et al., 2015; Wang et al., 2015; Lin et al., 2014; Okada et al., 2014; Beniwal et al., 2017). Electronic and magnetic properties of G/h-BN are distinct than graphene and h-BN monolayers. These properties are described by the analysis of their; band structure, density of states (DOS), and projected (partial) density of states (PDOS) calculations (Gao et al., 2015; Zhang et al., 2015). The electronic and magnetic properties of materials are great attracted properties in solid state physics because materials are used in the field of device applications based on these properties. In the present work, we have created vdWs G/h-BN HS material through graphene and h-BN with a small value of lattice mismatch (1.4 %) as shown in figure (4), this is approximate with noted values (Ramasubramaniam et al., 2011; Quhe et al., 2012; Slotman et al., 2015).

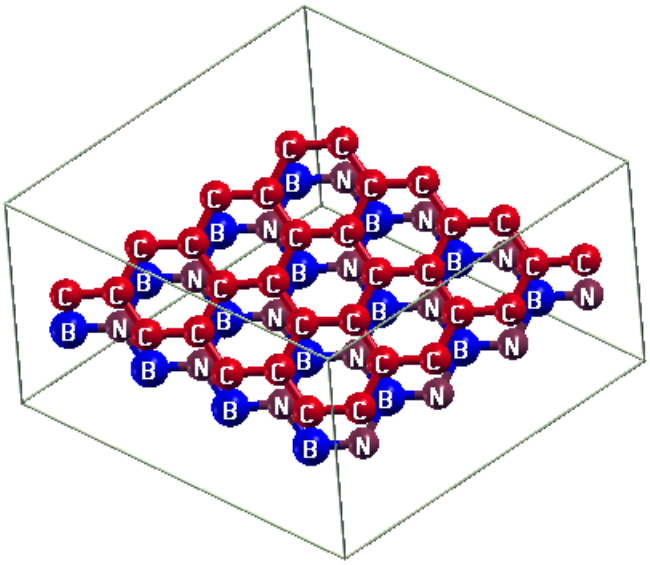

Figure 4: HS of G/h-BN, where vertically stacking configuration of G/h-BN is formed by graphene and h-BN monolayers with considerable value (1.4 %) of lattice mismatch (Neupane, et al., 2021).

Defects in 2D materials obtained remarkable properties than the pristine form (Hou et al., 2012; Neupane, et al., 2020, 2021). Hence, we have created the vacancy defects in G/h-BN vdWs heterostrucure, which are described as follows.

1.4 Defects in 2D Heterostructure Materials

Imperfection is an important property of crystal structure in solid state physics. They are formed due to the presence of chemical impurities, vacant lattice sites or impurity atom/s present in structures. The conductivity, colour, luminescence, atomic diffusion, mechan-

ical and plastic properties of many materials arise by impurities or imperfections (Kittel, 2005). Missing of atoms or ions from the lattice surface is called lattice vacancy (Kittel, 2005). The presence of defects in the lattice structure are the propitious access to adjust and stunt the properties of materials. Thus, defects impact the properties of materials in solids (Kittel, 2005). The vacancy defects in 2D materials (monolayer (ML) and heterostructure (HS)) can bear unique properties. They are convenient in technological applications (Kittel, 2005; Yazyev & Helm, 2007; Neupane, et al., 2020, 2021). In particular, understanding the electronic, magnetic and transport properties of graphene and graphene based materials add an opportunity for the researchers. The vacancy defects in graphene and graphene based 2D materials like graphene/h-BN, graphene/MoS2 etc. HS have attracted in various experimental and theoretical studies (Yazyev & Louie, 2010; Hashimoto et al., 2004; Krasheninnikov & Banhart, 2007; Crespi et al., 1996; Kim et al., 2011; Singh & Kroll, 2009; Faccio et al., 2010). The non-magnetic materials can be changed into mangetic materials by the presence of vacancy defects (Neupane, et al., 2020, 2021), such as vacancy defects in graphene induces local magnetic mo-ments due to the formation of dangling bond around the vacant sites (Yazyev & Louie, 2010; Hashimoto et al., 2004; Krasheninnikov & Banhart, 2007; Neupane, et al., 2020; Robertson et al., 2013; Fedorov et al., 2012). Magnetic materials are useful in modern technological devices. They are used in the fields of medical, nanoelectronic devices and several industrial applications (Makarova et al., 2019; Peng et al., 2016). Thus, defects engineering need to construct high-speed functional devices. Hence, defects in 2D heterostructures have compelling role in the performance of devices (Huang et al., 2020; Hu et al., 2018; Han et al., 2021).

1.5 Applications of 2D Materials

2D Materials have many applications that can significantly improve modern life and technology (Wang et al., 2017; Yu et al., 2013; Liang et al., 2020). This is due to their unique extreme properties. 2D materials can be made light and strong, which allows it to use in applications such as the construction of vehicles like Aircraft. They can be made very flexible allowing for the construction of flexible electronics. 2D materials such as graphene have electrons with an exceptionally large mobility, means that when used in the construction of computer components such as CPU's, may lead to a significant increase in computational speeds. When these materials are used to make heterostructures, the number of unique useful materials that can exist and exhibit these extreme properties increases significantly. This is due to the stacking effects allowing the combination of properties to make customised materials. Combining these materials allows to make smaller scale electronic devices like transistors by using both n-and

p-type semiconductors of 2D materials.

1.6 Rationale of the Study

Graphene is an atom-thick two dimensional (2D) honeycomb lattice. It has a array of particular electronic and physical properties. As a carbon material, it is cheap, widely distributed and abundant in nature. Its remarkable properties such as physical strength, surface area, conductivity etc. delve into multiple possible applications (Novoselov et al., 2005; Schedin et al., 2007). Graphene with its high sensitivity towards external charge, magnetic field a nd m echanical s train, h as c ontrollably t unable b and s tructure (zero band gap energy) which deserves its application for industrial sectors like electronic, spintronics (Han et al., 2014), chemical and gas sensors (Basu & Bhattacharyya, 2012). Because of tunable graphene bands and well developed experimental techniques at nano level, doped graphene including other carbon nanomaterials are becoming interesting areas for material scientists (Chan et al., 2008). Similar like graphene, hexagonal boron nitride (h-BN) has adorable temperature stability, mechanical strength, and thermal conductivity properties. Hence, it has budding applications in the fields of electronic, spintonic and optoelectronic devices (Rubio et al., 1994; Chopra et al., 1995; Henck et al., 2017).

Heterostructures (HS) are constructed by joining distinct monolayer constituents. They can tune new properties than their individual counterparts. The vertical stacking configuration of the graphene/hexagonal-boron nitride (G/h-BN) heterostructure open very impressive perspective because of its imploring physical properties (Liu et al., 2011; Li et al., 2015; Wang et al., 2015; Lin et al., 2014; Okada et al., 2014; Beniwal et al., 2017). Structural, electronic, magnetic, optical and transport properties of materials have great admiring properties in solid state physics because materials are used in the devices based on these properties. G/h-BN has electro-optical, magnetic (paramag-netic behaviour at low temperature), electronic and transport properties (Wang, Ma, & Sun, 2017). It is used in field effect transistor (FET), quantum tunneling transistor (QTT), thermoelectric devices, light emitting diode (LED), solar cell, in-plane pressure sensor (IPPS), tunneling pressure sensor (TPS) etc. Hence, G/h-BN has wide potential application and practical significance (Wang, Ma, & Sun, 2017; Neupane, et al., 2021).

Defects are intrinsic properties in the crystaline structure. The presence of defects (vacancy/impurity) in the materials will access on the localization of electron and phonon waves in 2D materials, which can bear novel properties (Zhao & Zeng, 2016; Neupane, et al., 2022). Vacancy defects (boron (B), nitrogen (N) and carbon (C) sites) in G/h-BN heterostructure (HS) material obtain high-performance functional devices (Huang et al., 2020; Hu et al., 2018; Han et al., 2021). Therefore, defects in G/h-BN

HS have persuasive role in the performance of electronic, spintonic and opto-electronic devices (Neupane, et al., 2021, 2022). To the best of our knowledge, investigation of structural, electronic, magnetic, and transport properties of 2D van der Waals (vdWs) G/h-BN HS with B, N, and C sites vacancy defects have not been reported in literature. Hence, in present work we study the effect of B, N, and C sites vacancy defects in G/h-BN HS through first-principles calculations by employing computational tools Quantum ESPRESSO (QE)and BoltzTraP (BTP) packages.

1.7 Objectives of the Study

Studying the effect of vacancy defects on 2D HS material graphene/hexagonal-boron nitride (G/h-BN) is the focus of this research work. Several studies about structural, electroinc, magnetic, and transport properties on heterostructure materials have been conducted. however, effect of defects on structural, electronic, magnetic, and transport properties of 2D HS material G/h-BN at boron (B), nitrogen (N), and carbon (C) sites is yet to be performed. Therefore, we have explored the structural, electronic, magnetic and transport properties of G/h-BN HS at B, N and C sites vacancy defects by First-principles calculations using computational tool Quantum EXPRESSO (QE) and BoltzTraP (BTP) packages.

General Objective

Study of structural, electronic, magnetic and transport properties of vacancy defected 2D G/h-BN heterostructure materials.

Specific Objectives

- To study the structural properties of 2D G/h-BN heterostructure material by removing 1B atom, 1N atom, nearest neighbour 1B atom and 1N atom, and 1B atom and 1N atom of alternate zone from the surface of h-BN of G/h-BN, and 1C atom and 2C atoms respectively from the surface of graphene of G/h-BN.
- To study the electronic and magnetic properties caused by B, N and C sites vacancy defects on 2D G/h-BN heterostructure material.
- To study the transport properties of B, N and C sites vacancy defects on 2D G/h-BN heterostructure material.

1.8 Organization of the Thesis

The structure of this thesis is organized as follows:

(i) In chapter 2, we have discussed the available literatures related to the present work. The chapter is named as "Literature Review", which aims to prepare the required background and justify the objectives of the current work.

(ii) We have presented the theoretical background, necessary formulas and algorithm that we have used during the entire work in Chapter 3 "Materials and Methods". Basic introduction of density functional theory (DFT) with some special features including the systems under study are discussed in the chapter.

(iii) The main findings of this work are presented and discussed in the chapter 4 entitled "Results and discussion". Section 4.1 introduces the background for the whole chapter. We have analyzed the structural properties through the calculations of total ground state energy and binding energy of pristine and vacancy defects heterostructure materials in section 4.2. Electronic properties of all considered materials are investigated by the analysis of their band structure in section 4.3. In section 4.4, we have investigated the magnetic properties of studied materials by analyzing their density of states (DOS) and projected density of states (PDOS) calculations. Additionally, we have studied the transport properties of considered materials on the basis of their Seebeck coefficient, thermoelectric power factor, electrical conductivity, and electronic contribution of thermal conductivity in section 4.5.

(iv) We briefly summarized the conclusions with possible extensions of the work in future in chapter 5. Finally, the summary is presented in chapter 6 followed by the references.

CHAPTER 2

2. LITERATURE REVIEW

2.1 General Consideration

In this chapter, we briefly discussed some literatures relevant to the present work. We have reviewed the literatures related to two dimensional (2D) materials especially graphene, hexagonal-boron nitride (h-BN) and their heterostructure (HS) G/h-BN, that are focused on their structure preparation, properties and applications. They are given as follows.

2.2 Graphene

Two dimensional (2D) material graphene has attracted tremendous interest due to their atom-thickness structure and excellent physical properties. Before 2004, theoretical and experimental scientists convinced that 2D graphene crystal could not be stable at finite temperature. Geim and Novoselov in 2004, prepared in atom-thickness structure of single layer of carbon (Novoselov et al., 2004), then accomplished series of studies and found that honeycomb (hexagonal) structure of graphene was stable at finite temperature (Tang et al., 2009; Geng et al., 2010; Geim, 2011; Chen et al., 2012). After 2004, graphene was constructed by various physical and chemical methods such as; Berger et al. (Berger et al., 2006) and Sutter et al. (Sutter et al., 2008) created the structure of graphene by metal catalysis method, Geim and Novoselov (Geim & Novoselov, 2007) created the structure of graphene by mechanical peeling method, Kim et al. (Kim et al., 2009) created the structure of graphene by chemical vapour deposition (CVD) method, Biel et al. (Biel et al., 2009) created the structure of graphene by low thermal expansion method, Jiao et al. (Jiao et al., 2009) created the structure of graphene by nanotubes cutting method and Yu et al. (Yu et al., 2011) created the structure of graphene by epitaxial growth method. Later, Wang et al. (Wang & Yu, 2016) explained in brief about the growth of graphene as a substrates in the materials.

Because of the increasing area of interest and method of investigations, the subjects related to graphene and graphene based 2D materials have attracted scientific a nd industrial communities especially since 2004. The popularity could be understood on the basis of their applications in moderen technological devices (Wang et al., 2017; Neupane, et al., 2020, 2021). Magnetic properties of graphene was studied by Novoselov et al. and Zhang et al. in 2005 (Novoselov et al., 2005; Zhang et al., 2005). They found that graphene has quantum hall effect at room temperature but has aberrant properties below 4 K temperature. The electronic properties of graphene was explored by Partoens and Peeters in 2006 (Partoens & Peeters, 2006), they investigated that graphene is a zero band gap material having band gap energy 0 eV because band states of valence band and conduction band are touched in the brillouin zone (BZ) at a high symmetric K-point on the Fermi energy level where Dirac point (cone) is formed at K-point of Fermi energy level. Avouris et al. (Avouris et al., 2007) noted that the effective mass of electron of graphene at Dirac point has zero value, hence electron in graphene is a massless Dirac fermion. The Castro et al., Zhou et al., and Mattausch and Pankaatov (Castro et al., 2007; Zhou et al., 2007; Mattausch & Pankratov, 2007) obtained the results that band gap of graphene and graphene based materials have controlled by altering the interconnection between graphene and substrate materials even in the presence of electric field. Also, transmission properties of graphene was studied by Geim and Novoselov (Geim & Novoselov, 2007), and found that it has bipolar field effect. In 2007, Tombros et al. (Tombros et al., 2007) examined the electron spin of graphene and determined graphene has pseudo-magnetic field. They also committed that electron spin and current are identified in the graphene at room temperature. Optical properties of graphene was observed by Ni et al. (Ni et al., 2007) and found monolayer of graphene is colourless material, but optical behaviour of graphene has occured in the defected system (Ni et al., 2007; Nair et al., 2008; Kuzmenko et al., 2008). In 2008, Chen et al. and Lherbier et al., and in 2009, Pereira et al. probed the electrical properties of graphene and determined that mobility of graphene based on SiO_2 material has equiv-alent value with of field effect transistor (FET). Hence, graphene has best conductivity as compared with other known 2D materials at room temperature (Chen et al., 2008; Lherbier et al., 2008; Pereira et al., 2009). Mechanical properties of graphene were studied by Lee et al. and Gomez-Navarro et al. in 2008, they determined, graphene is a unique nanomaterial and it has outstanding mechanical properties (Lee et al., 2008; Gomeznavarro et al., 2008). Thus, graphene has great scopes in the fields of device applications.

In 2009, Neto (Neto et al., 2009) predicted that graphene has magnificent electrical conductivity (up to 10^6 $(\Omega m)^{-1}$), that is the possibility of electron crossing through graphene barrier is approximatly 100 percentage, which is due to its distinctive band

arrangement of the Dirac point. Similarly, Kim et al. (Kim et al., 2009) found thermal conductivity of graphene, which was high within the range (3000-6000) W/mK and decreases as the temperature increases. Thus, thermal conductivity of graphene depends upon its temperature. Moreover, Wang et al., Sepioni et al., and Gomez-Santos and Stauber (Wang et al., 2009; Sepioni et al., 2010; Gomezsantos & Stauber, 2011) analyzed the magnetic properties of various form of graphene, they found that oxidized graphene was existed at ferromagnetism at room temperature while normal graphene has diamagnetic properties at room temperature and it has paramagnetic behaviour on low temperature. But, defected graphene has shown the condition of paramagnetism.

Kaloni et al. and Pantha et al. (Kaloni et al., 2014; Pantha et al., 2015) investigated the electronic and magnetic properties of multilayer graphene and impurity dopped with graphene at different concentrations through first-principles calcualtions, they found the distinct electronic and magnetic properties than that of pristine graphene sheet. Hence, graphene has potential applications in the field of electronic devices. Ne-upane and Adhikari (Neupane, et al., 2020, 2021) explored the structural, electronic and magnetic properties of C sites vacancy on graphene using spin-polarized DFT method. They predicted that defected graphene sheet have metallic and magnetic properties. It means properties of material were affected by the presence of defects on it surface. From the study of above literatures, we concluded that graphene has great attraction in indus-trial as well as academic sectors due to it remarkable optical, mechanical, electrical, thermal and magnetic properties. Therefore, it is an essential 2D material in the fields of modern technological devices.

2.3 Hexagonal-Boron Nitride (h-BN)

The monolayer (ML) structure of hexagonal boron nitride (h-BN) was studied by various theoretical and expermental groups of scientists since 1995, and they came to an end that it is an essential component in the field of electronic, spintonic and optoelectronic devices. Nagashima et al. (Nagashima et al., 1995) used multilayers advancement on a array of metal surfaces to acquire h-BN crystals. Novoselov et al. (Novoselov et al., 2005) constructed 2D h-BN by using micromechanical peeling method. Later, theoretical and experimental groups prepared h-BN by considering various methods such as; Pacile et al. (Pacile et al., 2008) used mechanical separation method, Han et al. and Zhi et al. (Han et al., 2008; Zhi et al., 2009) used solvent stripping method, Song et al. and Nag et al. (Song et al., 2010; Nag et al., 2010) used chemical vapour deposition (CVD) method, and Lin et al. (Lin et al., 2011) used aqueous solvent thermal synthesis method.

Wu et al. (Wu, Liu, et al., 2005) and Wu et al. (Wu, Peng, et al., 2005) explored the mag-

netic properties of h-BN material, they found that magnetic properties were developed in h-BN by the presence of impurity or vacancy defect in it. In 2007, Goriachko et al. (Goriachko et al., 2007) examined the lattice structure of h-BN and found that structures of h-BN and graphene are similar but have different physical and chemical properties. Zhou et al. (Zhou et al., 2007) investigated the thermal conductivity and tensile strength of h-BN and found that it has high thermal conductivity and high compressive strength. Geim and Novoselov (Geim & Novoselov, 2007) studied the optical properties of h-BN, they predicted that h-BN has excellent photoluminescence property. Magnetic properties of B and N sites vacancy defects in h-BN material was also examined by Si et al. (Si & Xue, 2007) and found that they have spontaneous spin magnetization. Barone et al. (Barone & Peralta, 2008) studied the electro-magnetic properties of h-BN and then obtained the results, h-BN has wide band gap and non-magnetic properites. Also, properties of wide band gap h-BN has changed into semimetallic properties by the influence of applied external electric field. Topsakal et al. (Topsakal et al., 2009) analyzed the band structure of h-BN by using local density approximation (LDA) and GW methods, they predicted that wide band gap h-BN material has direct band gap at high symmetric K-point in band structure. Gao et al. (Gao et al., 2009) measured the absorption spectrum of infrared, visible and ultraviolet light in h-BN surface in 2009. They found that infrared and visible light are transmitted through h-BN surface but strong absorption spectra was formed in h-BN surface due to the presence of ultraviolet light. Hence, optical properties of h-BN was measured only due to the effect of ultraviolet light. The mechanical and thermal properties of h-BN were observed by Boldrin et al. in 2011, Andrew et al. in 2012, Jo et al. in 2013, Zhou et al. in 2014, and Chen et al. in 2015 respectively, they found that h-BN has high value of Young's modulus (270 N/m) and thermal conductivity (up to 400 W/mK) at room temperature (Boldrin et al., 2011; Andrew et al., 2012; Jo et al., 2013; Zhou et al., 2014; Chen et al., 2015). Thus, h-BN has good mechanical and thermal properties, so it is employed in the area of technological advancement.

In addition, Cassabo et al. in 2016 (Cassabois et al., 2016), studied the intervalley scattering in h-BN. They embelished the various rearrangement dynamics of the phonon models. They suggested that virtual excitonic or real electronic states are presented in the structural defects. Henck et al. in 2017 (Henck et al., 2017), experimentally explored the band structure in bulk h-BN, and found that the valence band maxima are detected around the K-points at 2.5 eV below the Fermi level.This, verify the residual p-type nature of h-BN. Schuster et al. in 2018 (Schuster et al., 2018), observed the lowest indirect exciton state in the bulk of h-BN through experimental and computational works. They obtained that noticeable pointed forms of small pocket with a dispersion band width of approximately 100 meV, also obtained date approved with previously reported work. In

2018, Sponza et al. (Sponza et al., 2018) also examined the electronic band structure and excitonic dispersion of h-BN in single layer and three bulk polymorphs configurations through ab initio many body perturbation theory. They found that electronic band gaps are changed direct to indirect from single layer to bulk systems. According to above discussed literatures, we gather the informations regarding to 2D h-BN material. Hence, based on the physical and chemical properties, h-BN can be used in the modern technological devices.

2.4 Heterostructure of Graphene and h-BN (G/h-BN)

Graphene and graphene based 2D heterostructure (HS) materials like G/h-BN, G/MoS_2, G/h-BN/G etc. have substantial appeal in the fields of spintonic, electronic, optoelectronic and memory devices being their outstanding physical properties (Geim & Novoselov, 2007; Zhang et al., 2016; Wang et al., 2014; Wang et al., 2012; Song et al., 2010; Tran et al., 2016). Nevertheless, the absence of intrinsic band gap and non-magnetic identity of graphene (Geim & Novoselov, 2007) curb its prac-tical applications in extensively advancing field of carbon-based materials because high speed nanoelectronic and optoelectronic devices require reasonable band gap of material. Thus, the various theoretical and experimental researchers created the convincing band gap of graphene based materials using several techniques (Elias et al., 2009; Liu & Shen, 2009; Oh et al., 2010; Zhang et al., 2009). Among them, the heterostructure of graphene sheet with similar structural material h-BN (i.e. G/h-BN) having small value of lattice mismatch was commonly used in the fields of modern technolocical devices. Therefore, in the present work, we have taken G/h-BN heterostructure material with small lattice mismatch of value 1.4 %, this is closely agreement with the reported values (Ramasubramaniam et al., 2011; Quhe et al., 2012; Slotman et al., 2015).

In 2000, Oshima et al. (Oshima et al., 2000) constructed G/h-BN HS, then studied the influences of graphene sheet with h-BN on its electronic structure. They observed the slightly changed band structure of in HS than the band structure of single graphene sheet. Okada and Oshiyama, in 2001 (Okada & Oshiyama, 2001) explored the magnetic properties of G/h-BN material, and found that it has little bit electron ferromagnetic and antiferromagnetic properties. Many computatioanl and experimental research works were done by various scientists since 2001 to 2010. Dean et al. 2010 (Dean et al., 2010) and Mayorov et al. in 2011 (Mayorov et al., 2011), studied the electrical properties of G/h-BN, and found that weak van der Waals (vdWs) force existed between the layers of components. h-BN reduced the transport properties of graphene in HS, and hence mobility of graphene on BN substrate is determined up to 10^5 cm^2/Vs. Decker et al. and Xue et al. in 2011 (Decker et al., 2011; Xue et al., 2011), also analyzed the band

structure of G/h-BN, they determined the small band gap energy at a symmetric K-point on Fermi energy level, which changed the electronic properties of monolayer graphene superlattice. Natalia Berseneva et al. in 2011 (Berseneva et al., 2011), explored the magnetic properties of G/h-BN composites material using DFT theory. They found that half-spin magnetic moment was produced in HS material. In 2012, Yankowitz et al. (Yankowitz et al., 2012) studied the electronic properties of G/h-BN material by DFT method, Fermi velocity, states of local density, superlattice features of local charge density, and electronic band gap of G/h-BN has changed as compared to pristine graphene supercell structure. These properties tuned electronic properties of G/h-BN in the fields of device applications. Furthermore, Quhe et al. in 2012 (Quhe et al., 2012), also observed the band structure of G/h-BN HS using DFT method of calcualtions and noted that small band gap can be opened at Fermi level, and Yokomizo and Nakamura in 2013 (Yokomizo & Nakamura, 2013), studied the Seebeck coefficeint of the graphene/h-BN superlattices using first-principles calculations based on the DFT, and found to be finite energy band gap. Ilyasov et al. in 2014 (Ilyasov et al., 2014), investigated the electronic, magnetic and transport properties of graphene on h-BN by the effect of electric field based on DFT-D2 approach. They investigated that established magnetic moments, band gap, and carrier mobility in the system can be changed due to the impact of transverse electric field. Hence, they predicted that examined material can be used in spintronic devices.

In addition, Wang et al. in 2016 (Wang et al., 2016), measured the Dirac cone of G/h-BN HS, and found that G/h-BN has 100 meV to 160 meV energy gaps, it was reflected that G/h-BN has semimetallic properties. Wang et al. and Yang et al. in 2016 (Wang et al., 2016; Yang et al., 2016), examined the optical properties of G/h-BN experi-mentally, and found that no impact on the optical properties of it than of graphene and h-BN. In 2016, D'Souza and Mukherjee (D'Souza & Mukherjee, 2016a) studied the thermoelectric properties of graphene based heterostructure materials by studying their Seebeck coefficient, electrical conductivity and thermal conductivity using Boltzmann transport theory (BTT) based on first-principles calculations. They found that considered systems are good thermal materials and can be used in the field of thermoelectric de-vices. Aggoune et al. in 2020 (Aggoune et al., 2020), explored the structural, electronic, and optical properties of periodic G/h-BN vdWs HS material through density functional and many-body perturbation theory. It was found that interaction of graphene with h-BN open small band gap (few hundred meV) in graphene. The size of band gap and optical excitations are influenced by its stacking configurations. From the band structure calculations, it has semimetallic properties. The conduction band edge of semimetal has slightly lower than that of the valence band and has small band gap. Narrow band gap semiconductors, band edges are close but do not overlap (Saunders, 1973).

From all above discussion regarding to the related available literatures of the present work, we conclude that literatures consist of study of structural, electronic, magnetic, optical and transport properties of graphene, h-BN and HS of graphene/h-BN materials using fist-principles calcualtions based on DFT method with van der Waals interaction DFT-D2 approach. But, we could not find the study of structural, electronic, magnetic and transport properties of boron (B), nitrogen (N) and carbon (C) atoms vacancy defects in G/h-BN HS material in the literatures yet. Therefore, we focused our attention to study the structural, electronic, magnetic and transport properties properties of vacancy defected G/h-BN materials using first-principles calculations using DFT with DFT-D2 method through computational tools Quantum ESPRESSO and BoltzTraP packages.

2.5 Research Gap

From the review of relevant literatures, it has been observed that many experimental and theoretical works were been carried out to understand the physical properties of 2D materials especially; monolayers (ML) of graphene and h-BN, and heterostructure (HS) of these constituents (i.e. G/h-BN HS) (Geim & Novoselov, 2007; Elias et al., 2009; Liu & Shen, 2009; Oh et al., 2010; Zhang et al., 2009). As well, computational works were been carried out to understand the structural, optical, electronic, magnetic and transport properties of graphene, h-BN and G/h-BN HS materials by different groups using DFT based first-principles calculations (Aggoune et al., 2020; Dean et al., 2010; Mayorov et al., 2011). 2D (ML, HS and vacancy defects in HS) materials have attracted in the field of modern technological applications like spintonic, electronic, optoelectronic, sensors and memory devices. To evaluate the task entertained by the crystalline defects in HS is also of deciding by reason of their distinct properties. The structural, electronic, magnetic and transport properties of 2D ML, HS and vacancy defected HS materials have been the subject of instense research due to their applications in many technological purpose. In this context, the investigation of structural, electronic, magnetic and transport properties of vacancy defected G/h-BN HS is relevant to get more insight about the uses in the areas of electronic, spintonic and optoelectronic devices. Based on the reported literatures we found that study of structural, electronic, magnetic and transport properties of boron (B), nitrogen (N) and carbon (C) sites vacancy defects in 2D van der Waals (vdWs) G/h-BN heterostructure material are not incorporated. Therefore, in the present work, we explored the effect of B, N and C sites vacancy atoms on structural, electronic, magnetic and transport properties of G/h-BN HS material through first-principles calculations by spin-polarized density functional theory (DFT) with vdWs interactions DFT-D2 method under computational tools Quantum ESPRESSO and BoltzTraP packages.

CHAPTER 3

3. MATERIALS AND METHODS

3.1 General Consideration

In this chapter, we have described the methodology used to accomplish the objectives of the present work. For this, we begin our explanation from the theoretical background and then move into the system considered for the present work. Thus, we started our discussion from Hamiltonian of many body system and its corresponding Schrodinger equations in which nuclei is assumed to be frozen as compared to electronic motion. We have also discussed about certain approximation to solve many body Schrodinger equation, they are; Born Oppenheimer approximation (BOA) (Born & Oppenheimer, 1927), the Hartree's self consistent field approximation (Hartree, 1928) and Hartree-Fock (HF) approximation (Fock, 1930). We discussed their limitations also. In addition, we have explaned Thomas Fermi (TF) method (Fermi, 1927) and we briefly described the density functional theory (DFT). More importantly, we heighlighted how DFT overcome such limitations and led to the Kohn-Sham (KS) equations (Kohn & Sham, 1965). In DFT, electron density is a basis variable so functional of electron density instead of wave functions in many particle (body) system is superior in many perspectives. Based on electron density, Schrodinger wave equation of many particle system is solved by using local density approximation (LDA) and generalized gradient approximation (GGA). The effect of dispersion interactions in DFT calculations can be achieved either for the long-ranged interactions into the exchange-correlation functional or by using new-functional which incorporate the non-local electronic interactions. In normal DFT, an additional term $\frac{-c}{r^6}$ (where c is a constant term and r is the inter-particle distance) is added which describes the asymptotic behaviour of interactions in between the particles at larger separation. This model called Grimme model of DFT-D2 which is well tested with high accuracy in different applications (Grimme, 2004). So, total energy is the sum of KS-DFT energy and dispersion energy that is; $E_{total} = E_{KS-DFT} + E_{dispersion}$. The KS-DFT energy with approximated exchange-correlation (XC) functional and $E_{dispersion}$ is the empirical dispersion energy term in DFT-D2 gives total dispersion due to all pairs of

particles (Grimme, 2004). This chapter follows the following organization.

In section 3.2, we have discussed about many body Schrodinger wave equation. Electrons and nuclei are treated as interacting many body particles by using Schrodinger equation. The accurate solution of Schrodinger wave equation for many nuclei system is difficult to obtain, hence we require certain apporximations. Among them, Born Oppenheimer approximation (BOA) is considered to be the simplest. BOA separates nuclear and electronic equations including external potentials wherever necessary. The interaction of many-body problem can be converted into non-interacting single particle problem in both the wave function and density functional theory (DFT) methods of calculations. The introduction of single particle approximation is given in section 3.3, and single particle approximation based on wave function approaches are described in section 3.4. The exact solution of many body Schrodinger wave equation are not determined by single body approximation based on wave function approach. To reduce the limitations of non-interacting single particle approximation according to wave function approach, density functional theroy (DFT) method was introduced based on electron density as a basic variables which is discussed in section 3.5. DFT method is solved based on mathematical model of approximation known as Kohn-Sham (KS) formalism. Exchange-correlation functional term is used in KS potential, which is complex term and requires approximations. They are called local density approximation (LDA) and generalized gradient approximation (GGA). Exchange-correlation functional along with LDA and GGA approximations are explained in section 3.6. The DFT method along with LDA and GGA works well for the materials having chemical bonding. But, for van der Waals interactions, we need to adopt some hybrid functional in standard GGA functionals. Hence, we discussed London dispersion interactions in section 3.7. The basis sets and pseudopotential used in the present works are discussed in section 3.8. The details about the simulation and software used in our work are explained in section 3.9, where we have explained the calculation tools and simulations software packages. Computational details of the present work are given in section 3.10.

3.2 Many Body Schrodinger Wave Equation

Materials are made up of atoms, which contains electrons and nuclei (Kittel, 2005). In metals, valence electrons are loosely bound to their individual atoms. They are free to move throughout the volume at solid and behaves almost like gas molecules called as electron gas. The positive ions at the lattice sites produce attractive potential to the free electrons and so, they are confined within the boundary of solid and are not allowed to leak from there. Therefore, interior of the metals behaves like a potential energy box. In free electron gas model, the movement of electron in a material is equivalent movement

of free electron gas inside a potential energy box. The gas of free and non-interacting electrons subject to Pauli exclusion principle is called free electron Fermi gas (Kittel, 2005). A simple demonstration of many body (particle) system (i.e. conductors and semiconductors) is shown in figure (5).

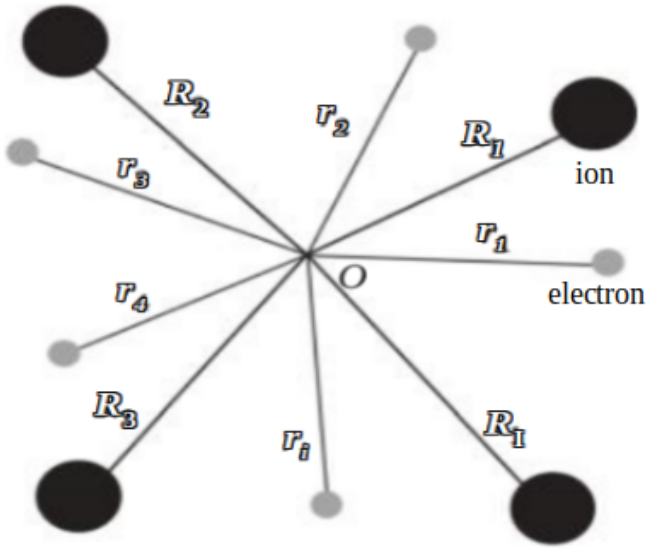

Figure 5: Filled and dots circles respectively denote ions and electrons, and O denotes the origin.

Classical mechanics can not explain the behaviour of electrons; therefore, one should use Quantum mechanical approach for the correct description of materials. For this, a quantum mechanical many body problem consisting of Schrodinger equation for interacting electron and nuclei should be solved (Parr et al., 1989). Many properties of the interacting systems such as atoms, molecules and solids can be understood by determining the eigen functions of the Hamiltonian:

$$\hat{H} = \hat{T} + \hat{V} \tag{3.1}$$

The solids consist up of mutually interacting electrons and the nuclei, and in general the dynamics of these particles cannot be treated separately. The Schrodinger equation of system having N electrons and M nuclei can be written as:

$$\hat{H}_{tot}\ \psi(x_1, x_2, ...x_N, \mathbf{R}_1, \mathbf{R}_2, ..., \mathbf{R}_M) = \hat{E}_{tot}\psi(x_1, x_2, ...x_N, \mathbf{R}_1, \mathbf{R}_2, ..., \mathbf{R}_M) \tag{3.2}$$

where, coordinates x_i represent both the position coordinates $\mathbf{r}_i$ and the spin co-ordinates s_i of the N electrons, and the coordinates $\mathbf{R}_I$ represents the position coordinates of the M atomic nuclei in the system. For such system the Hamiltonian operator $\hat{H}_{tot}$ is given

by:

$$\hat{H}_{tot} = -\sum_{i=1}^{N} \frac{\hbar^2}{2m_e}\nabla_i^2 - \sum_{I=1}^{M} \frac{\hbar^2}{2M_I}\nabla_I^2 - \sum_{i=1}^{N}\sum_{I=1}^{M} \frac{Z_I e^2}{|\mathbf{r}_i - \mathbf{R}_I|} + \sum_{j>i}^{N}\sum_{i=1}^{N} \frac{e^2}{|\mathbf{r}_i - \mathbf{r}_j|} + \sum_{J>I}^{M}\sum_{I=1}^{M} \frac{Z_I Z_J e^2}{|\mathbf{R}_I - \mathbf{R}_J|} \tag{3.3}$$

where indices i, j mention to electrons; I, J mention to nuclei; m_e indicates to the mass of electron; M_I and Z_I are denoted to the masses and atomic numbers of the nuclei respectively. The first and second terms in equation (3.3) correspond to the kinetic energies of electrons and nuclei respectively. The third, fourth and fifth terms respectively indicate the electron-nucleus, electron-electron, and nucleus-nucleus coulomb interaction energies. The accurate solution of the Schrodinger equation (3.2) for many nuclei system is difficult to obtain, hence we require certain approximations. Among them, Born Oppenheimer approximation (BOA) (Born & Oppenheimer, 1927) was considered to be the simplest.

3.2.1 Born-Oppenheimer Approximation (BOA)

Born-Oppenheimer approximation (BOA) (Born & Oppenheimer, 1927), also called adiabatic approximation, is the simplest approximation used for dealing with atoms, molecules of many body systems. This approximation separates the whole atomic system into two sub-systems: electrons system and another nuclei system.

Even for simplest nuclei, the weight of proton (lightest nucleus) is approximately 1836 times that of an electron. This implies that in comparison to electrons, nuclei is taken to be stationary. Then, the electronic wave function depends only on the position of the nuclei and is independent upon their momenta. Thus, the total wave function can be written as (Born & Oppenheimer, 1927):

$$\psi_{tot}(x : \mathbf{R}) = \psi_e(x; \mathbf{R})\, \psi_N(\mathbf{R}) \tag{3.4}$$

where, $\psi_e(x; \mathbf{R})$ and $\psi_N(\mathbf{R})$ are electronic and nuclear wave function respectively. Here, the electronic wave function depends parametrically on the nuclear coordinates, which is also called the zeroth order BOA. Also, the kinetic energy of nuclei is negligible as compared to that of electrons and the nuclei-nuclei interacting energy is a constant. Therefore, constant term can be dropped from Hamiltonian because it doesn't change the nature of wave function. Then, under BOA, total Hamiltonian (3.3) reduces to:

$$\hat{H}_{tot} = -\sum_{i=1}^{N} \frac{\hbar^2}{2m_e}\nabla_i^2 - \sum_{i=1}^{N}\sum_{I=1}^{M} \frac{Z_I e^2}{|\mathbf{r}_i - \mathbf{R}_I|} + \sum_{j>i}^{N}\sum_{i=1}^{N} \frac{e^2}{|\mathbf{r}_i - \mathbf{r}_j|} \tag{3.5}$$

The Hamiltonian (3.5) is completely determined by the number of electrons N, the atomic positions $\mathbf{R}_I$ and charges Z_I of the nuclei. A result of applying the Born Oppenheimer approximation to Hamiltonian of equation (3.3) is the removal of the nuclear coordinates from many particle wave functions as given in equation (3.5). The total energy of the electronic system is given as:

$$\hat{E}_{tot} =< H_{tot} >=< T > + < V_{ee} > + < V_{ext} > \tag{3.6}$$

where, the expectation values are taken with respect to ψ_e. It does not indicate that the energy is independent of nuclear coordinates, rather the interaction between the electrons and nuclei is only included as an interaction with the external potential:

$$V_{ext}(\mathbf{r}) = \sum_I \frac{Z_I}{|\mathbf{r} - \mathbf{R}_I|} \tag{3.7}$$

The electronic coordinates in (3.5) are coupled and variables cannot be separated. Thus, it is not possible to get the exact solution in such cases. So, we use single particle approximation based on wave function approach and DFT method.

3.3 Single Particle Approximation

Although, BOA (Born & Oppenheimer, 1927) reduces the complexity of the Schrodinger wave equation by separating it into the electronic and nuclear parts of Hamiltonian. The solutions are still complicated due to unknown electron-electron interactions. This problem can be further resolved by replacing interacting electrons into a system of non-interacting electrons where every electron moves under the influence of effective potential created by nuclei and the remaining electrons. This leads to a single particle picture and also called independent electron/particle approximation. There are mainly two approaches for using independent particle approximation instead of many body problem. They are called wave function method and density functional theory method.

3.4 Wave Function Approach

In order to solve the many body Schrodinger wave equation by single particle approximation based on wave function approach, we can use Hartree (Hartree, 1928) and Hartree-Fock (Fock, 1930) approximations. They are described as following.

3.4.1 Hartree's Self-Consistent Field Approximation

This is a simplest approach to solve Schrodinger equation by self-consistent field approximation method which assumes that, in an atom with N-electrons, each electron moves independently in the central field generated by the nucleus as well as resting $(N-1)$ electrons. And, the motion of individual electron is driven by a one particle Schrodinger equation (Hartree, 1928). Using Hartree's central field approximation, the Schrodinger wave equation for the N electrons system is given by (Hartree, 1928):

$$\hat{H}\psi_H(\mathbf{r_1}, \mathbf{r_2}, ..., \mathbf{r_N}) = E_H\psi_H(\mathbf{r_1}, \mathbf{r_2}, ..., \mathbf{r_N}) \tag{3.8}$$

where, $\hat{H}$ is Hamiltonian of the system given by equation (3.5), E_H is Hartree's energy and ψ_H is total wave function of the N electrons which can simply be written as the product of one electron wave functions (Hartree, 1928):

$$\psi_H(\mathbf{r_1}, \mathbf{r_2}, ..., \mathbf{r_N}) = \phi_1(\mathbf{r_1})\ \phi_2(\mathbf{r_2}).....\phi_N(\mathbf{r_N}) \tag{3.9}$$

The minimization of total energy

$$\text{E}= \langle\psi_H|\hat{H}|\psi_H\rangle\ = \langle\psi_H| - \tfrac{1}{2}\sum_i^N \nabla_i^2 + \tfrac{1}{2}\sum_{i\neq j}^N \tfrac{1}{|\mathbf{r_i}-\mathbf{r_j}|} - \sum_i^N\sum_I^M \tfrac{Z_I}{|\mathbf{r_i}-\mathbf{R_I}|}|\psi_H\rangle \tag{3.10}$$

subject to normalization condition

$$\int \psi^*\psi\ d^3\mathbf{r} = 1 \tag{3.11}$$

gives a set of N-coupled integro-differential equation:

$$\left(-\frac{1}{2}\nabla_i^2 + V_{ext} + V_{SC}\right)\phi_i(\mathbf{r_i}) = \lambda_i\phi_i(r_i) \qquad (i = 1, ..., N;\ \epsilon \rightarrow \lambda_i) \tag{3.12}$$

where,

$$V_{ext} = \sum_i\sum_I \frac{Z_I}{|\mathbf{r}_i - \mathbf{R}_I|} \tag{3.13}$$

and

$$V_{SC} = V_H = \sum_{j\neq i}\int d\tau_j \frac{|\phi_j(\mathbf{r_j})|^2}{|\mathbf{r_i} - \mathbf{r_j}|} \tag{3.14}$$

N equations (3.12) are called Hartree equations. They are solved in self-consistent manner. This method fails to satisfy the anti-symmetricity of fermionic wave function because wave function of N electrons is taken only the simple product of one electron

wave functions as in (3.9). In addition, though this method takes into account the interaction of an electron with other electrons and nuclei on an average by considering coulomb interactions, it fails to explain the exchange and correlation terms.

3.4.2 Hartree-Fock (HF) Approximation

To overcome the limitations of Hartree's method, Fock corrected this method by taking into account of spin direction of electrons and maintained anti-symmetric wave function by expressing approximate wave-function in the Slater determinantal form as shown in equation (3.15) (Fock, 1930; Slater, 1937):

$$\psi_{HF} = \frac{1}{\sqrt{N!}} \begin{vmatrix} \phi_1(\mathbf{r_1}, s_1) & \phi_2(\mathbf{r_1}, s_2) & \dots & \phi_N(\mathbf{r_1}, s_N) \\ \phi_2(\mathbf{r_2}, s_1) & \phi_2(\mathbf{r_2}, s_2) & \dots & \phi_N(\mathbf{r_2}, s_N) \\ \vdots & \vdots & \cdot & \vdots \\ \phi_N(\mathbf{r_N}, s_1) & \phi_2(\mathbf{r_N}, s_2) & \dots & \phi_N(\mathbf{r_N}, s_N) \end{vmatrix} \tag{3.15}$$

Here,
$\frac{1}{\sqrt{N!}}$ = normalizing factor,
Φ_i = ith single electron spin-orbital,
r_i = position coordinate of ith electron,
s_i = spin coordinate of ith electron.
By using (3.15) instead of (3.9), we again get N-equations:

$$\left[-\frac{1}{2}\nabla^2_{\mathbf{r}} - \sum_{i=1}^{N}\sum_{I=1}^{M} \frac{Z_I}{|\mathbf{r_i} - \mathbf{R_I}|} + \sum_{j\neq i} \int d\mathbf{r}' \phi_j^*(\mathbf{r}') \frac{1}{|\mathbf{r} - \mathbf{r}'|} \phi_j(\mathbf{r}') \right] \phi_i(\mathbf{r})$$
$$- \sum_{j\neq i} \left[\int d\mathbf{r}' \phi_j^*(\mathbf{r}') \frac{1}{|\mathbf{r} - \mathbf{r}'|} \phi_i(r') s_i s_j \right] \phi_j(\mathbf{r}) = \epsilon_i \phi_i(\mathbf{r}) \tag{3.16}$$

These N coupled equations are called HF self consistent equations. The third term in LHS of (3.16) is called Coulomb potential/integral (J) which is similar to Hartree potential (V_H) as introduced earlier in (3.14). It arises due to interaction between interpenetrating charge distributions. The last term of LHS is a purely quantum phenomena arised due to anti-symmetric nature of wave function for fermions, called exchange potential (K). The integration of equation (3.16) performed over only the spin variables implies that only the occupied spin-orbitals with parallel spins contribute to exchange potential (K).

The integro-differential form is a main difficulty in HF equations to solve. As the number of electrons in the system increase, the Slater determinant increases in dimensions, thereby making the calculations demanding. Although, HF wave function satisfies anti-symmetric nature of fermionic particles, as required by the Pauli exclusion principle, and

also takes into account of correlation effect of electrons with parallel spins, the motion of electrons with opposite spins is yet to be understood. As a result, the energy obtained from HF method differs from exact energy eigen value obtained from BO approximation by solving Schrodinger equation. In order to deal with such problems, number of methods have been developed, among them DFT method is the most popular one, for the study of ground-state properties of a many body system (Dirac, 1930; Capelle, 2006).

3.5 Density Functional Theory (DFT)

DFT is a most popular and greatly accepted quantum mechanical approach applicable for matter to explore the electronic structure of atoms, molecules, and the condensed phases (Koch & Holthausen, 2015; Capelle, 2006). DFT assumes the ground state density $n_0(r)$ as a single variable to describe many body interacting particles. The functional of electron density can describe all the ground state and excited state electronic properties of solids, molecules and other finite systems. The electronic density contains details information of many body wave functions and reduces the degree of freedom. For an example, a single DFT based Schrodinger equation solves N-electron system, instead of 3N degree of freedom in case of wave functions method. The fundamental concept of DFT was first introduced by Thomas and Fermi in 1927 (Thomas, 1927; Fermi, 1928). Later, the exchange and correlation terms were introduced by Dirac (Dirac, 1930) and the approximation is named as Thomas-Fermi-Dirac (TFD) known as DFT approximation. However, it has been in widely used after the breakthrough of Hohenberg-Kohn theorems (Hohenberg & Kohn, 1964b) and Kohn-Sham approach (Kohn & Sham, 1965).

The most eccentric feature of DFT is that, it takes into account the electron correlation arises due to interaction between the electrons of the parallel as well as antiparallel spins. The correlation energy (E_{corr}) is defined as the difference between the exact ground state energy (E_0), obtained from BOA in non-relativistic approach and the ground state energy is given by HF method (E_{HF}) in infinite basis set limits (Koch & Holthausen, 2015):

$$E_{corr} = E_0 - E_{HF} \tag{3.17}$$

Representing various parameters such as energy, potential, etc. as a functional of ground state density $n_0(\mathbf{r})$. $n_0(\mathbf{r})$ is very convenient for one. It is used to deal with the many body interacting systems which is the underlying principle of DFT. Thus, $n_0(\mathbf{r})$ determines all information of the many body wave functions for ground state and all excited states.

According to the definition, electron density $n(\mathbf{r})$ represents the probability of finding an electron in a certain volume element d$\mathbf{r}$. It can be obtained by the integration of wave function over all spin and space coordinates except the first one as below (Koch &

Holthausen, 2015):

$$n(\mathbf{r}) = N \sum_{s_1} ... \sum_{s_N} \int ... \int |\psi(\mathbf{r}_1, s_1, \mathbf{r}_2, s_2, ..., \mathbf{r}_N, s_N)|^2 ds_1 d\mathbf{r}_2 .... d\mathbf{r}_N \tag{3.18}$$

Electrons are identical and are not distinguished. The probability of finding any electron in $d\mathbf{r}$ is equal to N times the probability of finding one electron. It is called probability density, $n(\mathbf{r})$ which is referred to as electron density. It has to be positive for all $\mathbf{r}$, zero at infinity, and do integration gives total number of electrons N. Mathematically:

$$n(\mathbf{r}) \geq 0 \tag{3.19}$$

$$n(\mathbf{r} \rightarrow \infty) = 0 \tag{3.20}$$

$$\int n(\mathbf{r}) d\mathbf{r} = N \tag{3.21}$$

The wave function of N-electron system requires $3N$ spatial coordinates whereas electron density needs only 3-spatial coordinates for any system with any number of electrons. With the application of DFT, the computational cost and the time can be reduced to huge extent.

The DFT can be extended to deal with large number of systems including spin-polarized systems, multicomponent systems such as nuclei and hole droplets (Capelle, 2006). In 1965, Hohenberg and Kohn published a paper on inhomogeneous electron gas which served as a basis for the modern formulation of DFT (Hohenberg & Kohn, 1964a). It gave validity to DFT as a fundamental theory. Further, Kohn along with Sham, introduced the concept of atomic orbitals and effective potential in 1965 (Kohn & Sham, 1965) and made DFT applicable to computation. All of these revolutions were possible only after Thomas and Fermi gave the path through their theory in 1927 (Fermi, 1927).

3.5.1 Thomas-Fermi (TF) Model

Thomas-Fermi (TF) model (Fermi, 1927) is considered as the root of modern DFT. It considered electrons as non-interacting inhomogeneous gas and is based on the semi-classical approach in which the kinetic energy of the system of electrons is approximated as the explicit functional of density. The Thomas-Fermi equation can be expressed

as (Fermi, 1927; Thomas, 1927):

$$\frac{5}{3}\frac{3}{10}(3\pi^2)^{2/3}[\rho(\mathbf{r})]^{\frac{2}{3}} + v_{ext}(\mathbf{r}) + \int \frac{\rho(\mathbf{r}')}{|\mathbf{r}-\mathbf{r}'|}dr' - \mu = 0 \tag{3.22}$$

The ground state density is obtained by solving this equation (Fermi, 1927; Thomas, 1927). Here, μ is Lagrange multiplier, it is analogus to chemical potential. Though, this theory is a step forward towards DFT, it has certain limitations too. It does not incorporate the actual shell structure of atoms and binding of molecules. Only after 37 years, Hohenberg and Kohn (Hohenberg & Kohn, 1964a) gave more reliable theoretical basis for modern DFT.

3.5.2 Hohenberg-Kohn (HK) Theorems

Hohenberg-Kohn theorems are regarded as the heart of DFT (Hohenberg & Kohn, 1964a). These theorems were published in 1964 and proved the exactness and feasibility of using n($\mathbf{r}$) instead of ψ (Dreizler & Gross, 2012). A system of N interacting electrons, total Hamiltonian is given by the sum of kinetic energy (T), electron-electron interaction energy (V_{ee}), and electron-nuclei interaction energy (V_{ext}) as:

$$H = T + V_{ee} + V_{ext} \tag{3.23}$$

In equation (3.23), kinetic energy (T) and electron-electron interaction energy (V_{ee}) are system independent. They are same for all systems but external potential is given by:

$$V_{ext} = \sum_{i=1}^{N}\sum_{I=1}^{M}\frac{Z_I}{|\mathbf{r}_i - \mathbf{R}_I|} = \sum_{i=1}^{N} V_{ext}(\mathbf{r}_i) \tag{3.24}$$

where, $V_{ext}(\mathbf{r}_i) = \sum_{I=1}^{M}\frac{Z_I}{|\mathbf{r}_i - \mathbf{R}_I|}$ is system dependent external potential on the i^{th} electron due to M^{th} nuclei present in the system. Hohenberg-Kohn (HK) theorems are two types. They are described as follows.

First Hohenberg-Kohn (HK) Theorem

It states that "the ground state density n($\mathbf{r}$) of a bound system of interacting electrons in some external potential $\upsilon(\mathbf{r})$ uniquely determines this potential". Thus, $v(\mathbf{r})$ gives Hamiltonian $\hat{H}$, and n($\mathbf{r}$) find out N and $v(\mathbf{r})$. Hence, n($\mathbf{r}$) determines all the properties of ground state of the system. We prove this theorem for non-degenerate ground state system. It also can be further generalized to degenerate ground state as well.

Consider $n(\mathbf{r})$, N, $\upsilon_1(\mathbf{r})$, ψ_1 and E_1 be non-degenerate ground state density, number of electrons, ground state potential, wave function and ground state energy of a system respectively (Hohenberg & Kohn, 1964a). Then:

$$E_1 = \langle\psi_1|\hat{H}_1|\psi_1\rangle = \int \upsilon_1(\mathbf{r})n(\mathbf{r})d\mathbf{r} + \langle\psi_1|(\hat{T} + \hat{V}_{ee})|\psi_1\rangle \tag{3.25}$$

where, $\hat{H}_1$, $\hat{T}$ and $\hat{V}_{ee}$ represent hamiltonian of $\upsilon_1(\mathbf{r})$, kinetic energy and interaction energy operators respectively. Again, if we consider a second potential υ_2 $(\mathbf{r})$ which is not equal to $\upsilon_1(\mathbf{r})$ + constant, with ground state wave function ψ_2. Then:

$$E_2 = \int \upsilon_2(\mathbf{r})n(\mathbf{r})d\mathbf{r} + \langle\psi_2|(\hat{T} + \hat{V}_{ee})|\psi_2\rangle \tag{3.26}$$

Here, ψ_1 is supposed to be non-degenerate, the variational principle for ψ_1 gives rise to the inequality (Gross et al., 1988):

$$E_1 < \langle\Psi_2|\ H_1|\Psi_2\rangle = \int \upsilon_1(\mathbf{r})n(\mathbf{r})d\mathbf{r} + \langle\psi_2|(T + U)|\psi_2\rangle \tag{3.27}$$

or,

$$E_1 < \langle\Psi_2|\ H_1|\Psi_2\rangle = E_2 + \int [\upsilon_1(\mathbf{r}) - \upsilon_2(\mathbf{r})]n(\mathbf{r})d\mathbf{r} \tag{3.28}$$

Likewise,

$$E_2 \leq \langle\Psi_1|\ H_1|\Psi_1\rangle = E_1 + \int [\upsilon_2(\mathbf{r}) - \upsilon_1(\mathbf{r})]n(\mathbf{r})d\mathbf{r} \tag{3.29}$$

where, $\leq$ is used since Ψ_2 is not assumed to be non-degenerate. On adding (3.28) and (3.29), we get

$$E_1 + E_2 < E_1 + E_2 \tag{3.30}$$

This contradicts the existence of $\upsilon_2(\mathbf{r})$, and is not equal to $\upsilon_1(\mathbf{r})$ + constant. But it yields yet the same $n(\mathbf{r})$ must be wrong. This reflects, there is unique potential $\upsilon(\mathbf{r})$ which leads to the ground state density $n(\mathbf{r})$ and the converse is also true.

Using this theorem, we can calculate the total energy of the system in terms of density. After minimizing this functional we find the ground state energy. The total energy is given by the sum of total kinetic energy of electrons $T[n]$, potential energy between electron-electron interactions $V_{ee}[n]$, and exterinal potential energy $V_{ext}[n]$ (Hohenberg & Kohn, 1964a), i. e.,

$$E_v[n] = T[n] + V_{ee}[n] + V_{ext}[n] \tag{3.31}$$

where,

$$V_{ext}[n] = \int v(\mathbf{r})\, n(\mathbf{r})\, d\mathbf{r} \tag{3.32}$$

This shows that $V_{ext}[n]$ is system dependent. To account the other universally valid part, we define a new HK function as:

$$F_{HK}[n(\mathbf{r})] = \langle\psi|\hat{T} + \hat{V}_{ee})|\psi\rangle \tag{3.33}$$

reasonalble for any number of the particles and any external potential $v(\mathbf{r})$. Therefore, the energy functional, $E[n(\mathbf{r})]$, in equation (3.31) becomes,

$$E_v[n(\mathbf{r})] = \int v(\mathbf{r})\, n(\mathbf{r})\, d\mathbf{r} + F_{HK}[n(\mathbf{r})] \tag{3.34}$$

$F_{HK}[n(\mathbf{r})]$ functional is referred to as universal functional as it is independent of N, Z, and R_0. It has the functionals for $T[n]$ and V_{ee}, the explicit forms of which are totally unknown. If it were known exactly, the exact solution of Schrodinger equation would have been obtained without any approximations. For convenience, we remove the classical Coulomb energy from $V_{ee}[n]$ and write (Hohenberg & Kohn, 1964a):

$$F_{HK}[n(\mathbf{r})] = \frac{1}{2}\int \frac{n(\mathbf{r})\, n(\mathbf{r}')}{|\mathbf{r} - \mathbf{r}'|}\, d\mathbf{r}d\mathbf{r}' + G[n(\mathbf{r})] \tag{3.35}$$

where, $G[n]$ is a functional containing $T[n]$ and all the non-classical grants.

The total energy $E_v[n]$ is equal to the ground state energy E_0 for the correct $n(\mathbf{r})$. In order to minimize $E_v[n]$, we apply the variational principle. For this, let $n'(\mathbf{r})$ be the trial density satisfying the necessary boundary conditions; $n'(\mathbf{r}) \geq 0$, and for the Hamiltonian $\hat{H}$, $\int n'(\mathbf{r})d\mathbf{r} = N$. In addition, if $\psi'(\mathbf{r})$ is the trial wave function corresponding to $n'(\mathbf{r})$, then

$$\langle\psi'|\hat{H}|\psi'\rangle = \int v(\mathbf{r})n'(\mathbf{r})d\mathbf{r} + F_{HK}[n'] = E_v[n'] \geq E_0[n] = \langle\psi|\hat{H}|\psi\rangle \tag{3.36}$$

In compact form, $E_0[n] \leq E_v[n']$.

Second Hohenberg-Kohn (HK) Theorem

The second Hohenberg-Kohn (HK) theorem, commonly known as HK variational principle. It states that "the exact ground state energy $E_0[n]$ of a system with an external potential ($V_{ext}(\mathbf{r})$) is given by global minimum value of the energy functional $E[n(\mathbf{r})]$ and the density that minimizes the functional is the ground state density $n_0(\mathbf{r})$".

The minimization of energy functional is required for ground state density within the constraint

$$N[n] \equiv \int n(\mathbf{r})\, d\mathbf{r} = N \tag{3.37}$$

We use Lagrangian undetermined multipliers method and take the stationary principle. It has to satisfy the ground state density as:

$$\delta \left\{ E - \mu \left[\int n(\mathbf{r})\, d\mathbf{r} - N \right] \right\} = 0 \tag{3.38}$$

Solving for undetermined multiplier μ, we get the Euler-Lagrange equation:

$$\mu = \frac{\delta E[n(\mathbf{r})]}{\delta n(\mathbf{r})} = v_{ext}(\mathbf{r}) + \frac{\delta F[n(\mathbf{r})]}{\delta n(\mathbf{r})} \tag{3.39}$$

where μ is the chemical potential. Explicit forms of functionals introduced in HK theorems is unknown and this scheme is not practically useful without further development.

3.5.3 Kohn-Sham (KS) Formalism

Kohn and Sham (Kohn & Sham, 1965), led to the establishment for the application of DFT in computational modern physics and chemistry by introducing the concept of atomic orbitals (one electron functions) in 1965. Hence, the exact kinetic energy can be calculated, leaving only a small residual correlation term which is obtained separately. Kohn and Sham considered non-interacting particle approximation instead of interacting many body problems, by taking exchange-correlation functional. From which it gives exact ground state electron density $n(\mathbf{r})$.

$$\hat{H}_s = -\frac{1}{2} \sum_{i=1}^{N} {\nabla_i}^2 + \sum_{i=1}^{N} v_s(\mathbf{r}) \tag{3.40}$$

Kinetic energy of this system is:

$$T_s = \langle \psi_s | - \frac{1}{2} \sum_{1}^{N} \nabla_i^2 | \psi_s \rangle \tag{3.41}$$

where the ground state wave function (ψ_s) can be given by HF theory in the form of Slater determinant (Kohn & Sham, 1965; Slater, 1937) as:

$$\psi_s = \frac{1}{\sqrt{N!}} \begin{vmatrix} \phi_1(\mathbf{r_1}, s_1) & \phi_2(\mathbf{r_1}, s_2) & \dots & \phi_N(\mathbf{r_1}, s_N) \\ \phi_2(\mathbf{r_2}, s_1) & \phi_2(\mathbf{r_2}, s_2) & \dots & \phi_N(\mathbf{r_2}, s_N) \\ \vdots & \vdots & \cdot & \vdots \\ \phi_N(\mathbf{r_N}, s_1) & \phi_2(\mathbf{r_N}, s_2) & \dots & \phi_N(\mathbf{r_N}, s_N) \end{vmatrix} \tag{3.42}$$

where, orbitals ϕ_i are N lowest eigen states of single electron Hamiltonian. We have

$$\hat{H}_s \phi_i = \left[-\frac{1}{2}\nabla^2 + v_s(\mathbf{r}) \right] \phi_i = \epsilon_i \phi_i \tag{3.43}$$

Here, non-interacting potential is given by v_s. The kinetic energy $T_s[n]$ and electron density $n(\mathbf{r})$ are given by using v_s. Thus,

$$T_s[n] = -\frac{1}{2} \sum_i \langle \phi_i | \nabla^2 | \phi_i \rangle \tag{3.44}$$

$$n(\mathbf{r}) = \sum_i^N \sum_s |\phi_i(\mathbf{r}, s)|^2 \tag{3.45}$$

The definition of kinetic energy $T_s[n]$ requires the existence of non-interacting ground state with given $n(\mathbf{r})$. Although, here $T_s[n]$ is uniquely defined for density. This is not the exact kinetic energy. Kohn and Sham (Kohn & Sham, 1965) applied very clever idea to deal with such problems. They rewrite the problem such that T_s become exact kinetic energy by taking the correlation part of kinetic energy T_c to the non-classical contributions. For this, the equation (3.33) can be expressed as (Kohn & Sham, 1965):

$$F_{HK}[n] = T_s[n] + J[n] + E_{xc}[n] \tag{3.46}$$

with $J[n]$ is the classical Coulomb part defined by:

$$J[n] = \frac{1}{2} \int \frac{n(\mathbf{r})\, n(\mathbf{r}')}{|\mathbf{r} - \mathbf{r}'|}\, d\mathbf{r}\, d\mathbf{r}' \tag{3.47}$$

and $E_{xc}[n]$ is the exchange-correlation energy functional contains $T_c[n]$, the small difference between $T[n]$ and T_s, and $E_{ncl}[n]$, the non-classical contribution to V_{ee} apart from $J[n]$.

$$E_{xc}[n] \equiv (T[n] - T_s[n]) + (V_{ee}[n] - J[n]) \tag{3.48}$$

Or,

$$E_{xc}[n] = T_c[n] + E_{ncl}[n] \tag{3.49}$$

By the method of Lagrange's undetermined multiplier μ, we minimize the energy using constraint (3.21) and obtain Euler-Lagrange equation as (Agrawal, 2002):

$$\mu = v_{eff}(\mathbf{r}) + \frac{\delta T_s[n(\mathbf{r})]}{\delta n(\mathbf{r})} \tag{3.50}$$

and finally Kohn-Sham effective potential as:

$$v_{eff}(\mathbf{r}) = v(\mathbf{r}) + \int \frac{n(\mathbf{r}')}{|\mathbf{r} - \mathbf{r}'|} d\mathbf{r}' + v_{xc}(\mathbf{r}) \tag{3.51}$$

where

$$v_{eff}(\mathbf{r}) \equiv v(\mathbf{r}) + \frac{\delta J[n(\mathbf{r})]}{\delta n(\mathbf{r})} + \frac{\delta E_{xc}[n(\mathbf{r})]}{\delta n(\mathbf{r})} \tag{3.52}$$

and

$$v_{xc}(\mathbf{r}) \equiv \frac{\delta E_{xc}[n]}{\delta n} \tag{3.53}$$

One has to solve N one-electron equations:

$$\left(-\frac{1}{2}\nabla^2 + v_{eff}(\mathbf{r})\right) \phi_i(\mathbf{r}) = \epsilon_i \, \phi_i(\mathbf{r}) \tag{3.54}$$

and using that fact

$$n(\mathbf{r}) = \sum_{i=1}^{N} \sum_{s} |\phi_i(\mathbf{r}, s)|^2 \tag{3.55}$$

Three equations (3.51), (3.54) and (3.55) are called self-consistent Kohn-Sham equations (Kohn & Sham, 1965). They have to be solved self-consistently. To solve this, one begins with by assuming $n(\mathbf{r})$, and construct $v_{eff}(\mathbf{r})$ from (3.51) and find a new $n(\mathbf{r})$ from (3.54) and (3.55). This process is repeated until it converges. Eventually, the ground state energy is obtain by the formula:

$$E_0 = \sum_{i}^{N} \epsilon_i + E_{xc}[n(\mathbf{r})] - \int v_{xc}(\mathbf{r}) \, n(\mathbf{r}) \, d\mathbf{r} - \frac{1}{2} \int \frac{n(\mathbf{r}) \, n(\mathbf{r}')}{|\mathbf{r} - \mathbf{r}'|} d\mathbf{r} \, d\mathbf{r}' \tag{3.56}$$

As we discussed above, exchange and correlation (XC) term is the crucial quantity to manage the exactness of the calculations. For this, good approximations are required

to solve Kohn-Sham based density functional theory (KS-DFT). In this way, Kohn-Sham approach relies on some empirical quantities in addition to the universal energy functional which is independent to the material under study.

Solution of KS Equation

The Kohn-Sham approach (Kohn & Sham, 1965) is based on the self-consistent iterative process. It removes one type of problem by an another type by replacing real interacting electrons with a system of non-interacting electrons. The KS equations are solved self-consistently by using the relationship in between ground state energy/electron density and KS potential. The process begins with the initial choice of electron density, based on superposition of electron density of individual atoms, which uniquely determine the KS potential and solves KS equations with this potential. The self-consistent conditions of the system are checked upon finding this new density, where we compare the new and old density/energy or forces by subtracting the new values from the corresponding old ones. Once the difference is smaller than some defined threshold. The system is said to be conversed and the desired properties can be extracted. On the other hand, if the difference is above the threshold value, the density from the previous iteration is mixed with the new ones, and go through the repeated process until satisfying the conditions of convergence. To solve KS equation, we need to obtain KS potential. KS potential consists of external, Hartree potential and exchange-correlation potentials (Kohn & Sham, 1965). Among them, exchange-correlation potential is complex term and requires different approximations, which are described as follows.

3.6 Exchange-Correlation (XC) Functional

Calculation of electron charge density is an important task in Kohn-Sham ansatz. It could be found by solving self-consistent method, which howerver requires KS potential. KS potential is equal to the sum of external, Hartree and exchange-correlation (XC) potentials (Kohn & Sham, 1965). Among these potential, XC term is very complex and requires approximations. We first include the simple and mostly widly used approximations for XC functionals; local density approximation (LDA) and generalized gradient approximation (GGA). The required additions like London dispersion interactions have been considered acccording to their relevancy in the present work.

3.6.1 Local Density Approximation (LDA)

LDA considers a uniform distribution of electron density, where exchange-correlation (XC) term obey the law of homogenous electron gas (HEG). LDA works well for a system of slowly varying density. It covers a wide range of systems where either the electronic system is not too strongly correlated or the electrons in the system feel constant external potential. It is one of the popular traditional methods for geometrical optimization and electronic structure calculations in case of the systems, where the XC energy is local in nature.

The concept of uniform electron density in LDA is consistent with Thomas-Fermi model (Fermi, 1928), and the Hohenberg-Khon themorems (Hohenberg & Kohn, 1964b), where the electrons are treated as homogeneous electron gas. In case of inhomogeneous system, LDA approximates XC functional as an integral over space with a local function of the charge density at each point. Because of elimination of errors in XC terms, LDA is successful to carry very good results than generally expected. For a system of HEG, the total XC functional is givn as:

$$E_{xc}^{LDA}[n] = \int n(\mathbf{r})\epsilon_{xc}[n(\mathbf{r})]d\mathbf{r} \tag{3.57}$$

where, $\epsilon_{xc}[n(\mathbf{r})]$ is a functional, it allows the XC energy per particle in a HEG with electron density $n(\mathbf{r})$. The exchange-correlation energy per particle $\epsilon_{xc}[n(\mathbf{r})]$ is the sum of exchange and correlation parts:

$$\epsilon_{xc}[n(\mathbf{r})] = \epsilon_x[n(\mathbf{r})] + \epsilon_c[n(\mathbf{r})] \tag{3.58}$$

The analytical expression of exchange energy functional (Dirac, 1930) is:

$$E_x^{LDA}[n] = \int n(\mathbf{r})\epsilon_x[n(\mathbf{r})]d\mathbf{r} \tag{3.59}$$

with

$$\epsilon_x[n(\mathbf{r})] = -\frac{3}{4}(\frac{3}{\pi})^{\frac{1}{3}}[n(\mathbf{r})]^{\frac{1}{3}} \tag{3.60}$$

On the other hand, the analytical expression of correlation energy density for HEG is very complicated, and known only for high and low density limits. At low density limit, correlation energy becomes simply the electrostatic energy of point charges, and dominates over the exchange energy. Reversely, at the high density regime, correlation energy becomes less relevant over the exchange energy.

The correlation energy of HEG at the moderate density has been accurately calculated

by Quantum Monte-Carlo (QMC) simulations (Ceperley & Alder, 1980). Interpolated values from these simulations are used in later development of LDAs like Vosko-Wilk-Nusair (VWN) (Vosko et al., 1980), Perdew-Zunger (PZ81) (Perdew & Zunger, 1981), Cole-Perdew (CP) (Cole & Perdew, 1982), and Perdew-Wang (PW92) (Perdew & Wang, 1992).

The real systems are far from the assumptions of homogeneous electron density and hence the fundamental approximation of LDA is not correct. Accurate description for many real systems could be understood by (i) systematic cancellation of error: under-estimated E_c and over-estimated E_x (Levine et al., 2009; Parr & Weitao, 1994), and (ii) spherical description of averaged pair density.

3.6.2 Generalized Gradient Approximation (GGA)

LDA assumption of homogeneous electron gas is far from the reality and can not cover the inhomogeneous electron density of real systems in which distribution of electron is not uniform. It means, electron density $n(\mathbf{r})$ undergoes rapid changes such as in molecules. LDA fails in such cases since the energy given out by true density is approximated with the energy given by a local constant density in LDA. To overcome the limations of LDA, a new approximation was developed which described the non-homogenity of true electron density through the gradient. This is called generalized gradient approximation (GGA). So in GGA, exchange-correlation functional E_{xc} incorporates density gradient corrections in addition to the HEG approximation made by LDA (Perdew & Wang, 1992). Mathematically:

$$E_{xc}^{GGA}[n(\mathbf{r})] = \int \epsilon_{xc}[n(\mathbf{r}),\ |\nabla n(\mathbf{r})|,\ \ldots]d\mathbf{r}\ . \tag{3.61}$$

Similar to LDA, the exchange-correlation energy E_{xc}^{GGA} of GGA contains exchange energy E_x^{GGA} and correlation energy E_c^{GGA} parts, which is expressed as:

$$E_{xc}^{GGA}[n(\mathbf{r})] = E_x^{GGA}[n(\mathbf{r})] + E_c^{GGA}[n(\mathbf{r})] \tag{3.62}$$

There are many different exchange-correlation functionals of the GGA type. Some of popular functionals among them are proposed by Perdew and Wang (PW92) (Perdew & Wang, 1992). In 1996, Perdew, Burke and Ernzerhof purposed a XC funtional in GGA is called PBE functional with GGA (Perdew et al., 1996). Further, exchange part of Becke's formula (Becke, 1988) was combined with Perdew's formula (Perdew, 1986) of correlation. And it also with the correction functional of Lee, Young and Parr (Lee et al., 1988) to give BP88 and BLYP type of GGA functionals. All these functionals generally work well for the materials having chemical bonding like covalent, ionic,

metallic or hydrogen. Among in all functional, XC of PBE with GGA give accurate results for most of the periodic systems. In the present work, we have used PBE form of GGA in our calculations because DFT with PBE have given minimum ground state energy of considered systems than the other fonctionals used in the system of our work. In addition, for van der Waals (vdWs) interactions, however, either we need to adopt some hybrid functionals or add some semi-emprical terms in standard GGA with PBE functionals. Therefore, in the present work, we adopted London dispersion interactions in GGA with PBE functional of DFT is called DFT-D2 approximation.

3.7 London Dispersion Interactions

Density functional theory (DFT) explains the condensed matter physics and quantum chemistry problems with reasonable accuracy based on widly used approximations, LDA and GGA. However, these functionals do not incorporate non-local interactions between the electrons, which are important in chemically non-bonded systems such as bio-molecular systems, atomic packing of crystals, and host guest interactions in gaseous bindings (Israelachvili & Tabor, 1972). These non-local interactions are defined by van der Waals (vdWs) interactions. vdWs interaction includes three different terms known as Keesom, Debye and London interactions (Israelachvili & Tabor, 1972; Ulman et al., 2014). The Keesom term includes the interactions between the permanent dipoles. the The interaction between permanent dipoles and induced dipoles in the system were described by Debye. London dispersion term includes the interactions between instantaneously induced dipoles in the system (Grimme, 2006; Ulman et al., 2014). Among the three different type of interactions, London dispersion interactions is found to be the major contributor of vdWs interactions between the different layers of heterostructure materials (Grimme, 2004; Piacenza & Grimme, 2005), which is one of the prime concerns of the present work.

London dispersion interactions are caused by the effect of charge fluctuations at one region of the system to the electrons residing anywhere on the system. They are weak, attractive and long-ranged. Some of the models to incorporate the dispersion forces (Grimme, 2006; Klimevs & Michaelides, 2012) are still underway to find more effective and cheap algorithms.

Methods to treat vdWs interactions is one of the popular areas in last decade. Grimme's model of DFT-D is well tested (Grimme, 2004) with high accuracy in different applications (Piacenza & Grimme, 2005; Parac et al., 2005). This method has an additional term $-\frac{c}{r^6}$ in normal DFT, where c is a constant term and r is the inter-particle distance between the diploes. It takes care of asympotic behaviour of interactions in between the particles at larger separation. It is also noted that normal DFT accounted the system of

smaller value of r. Hence, total energy E_{total} of a system is given by

$$E_{total} = E_{KS-DFT} + E_{dispersion} \tag{3.63}$$

In equation (3.63), E_{KS-DFT} is the KS-DFT energy with approximated XC functional and $E_{dispersion}$ is the empirical dispersion energy term. The dispersion energy term in DFT-D2 approach (Grimme, 2006) is given by:

$$E_{dispersion} = -s_6 \sum_{i}^{N_{at}-1} \sum_{j>i}^{N_{at}} \frac{c^{ij}}{r_{ij}^6} f_{damp}(r_{ij}) \tag{3.64}$$

In equation (3.64), N_{at} represents the number of atoms in the system, c^{ij} is dispersion coefficient for atom pair ij calculated from a relation coupling ionization potentials and static polarizabilites of isolated atoms. Similarly, s is a global scaling factor for the kind of DFT we use and $f_{damp}(r_{ij})$ is the damping function to avoid singularities at smaller distances r_{ij}. The damping factor is given as:

$$f_{damp}(r_{ij}) = \frac{1}{1 + e^{-d(\frac{r_{ij}}{r_s} - 1)}} \tag{3.65}$$

where r_s as the sum of atomic vdWs radii. DFT-D2 approach considers the pairwise dispersion terms and gives total dispersion due to all pairs of particles. This approach is widly used because of its simplicity and low computational cost. However, the method has some limitations like; it only considers the leading dipole-dipole interaction term, and neglects the many body correlations. Previous studies reveal that the level of accuracy with DFT-D2 calculations is high comparing to traditionl DFT approaches (Joshi & Ghosh, 2013). We use DFT-D2 method to study the interactions between graphene (G) and h-BN in pristine G/h-BN HS, and B, N and C sites vacancy defected G/h-BN HS materials.

3.8 Basis Sets and Pseudopotentials

A basis set is the linear combination of a set of basis functions, to create molecular/atomic orbitals. Atomic orbitals are a type of basis functions. A basis set is the superposition of minimum number of basis functions. It represents all of the electrons on each atom, is called minimal basis set. Depending up on the choice of basis functions, a number of basis sets are available for the expansion of Kohn-Sham orbitals in Kohn-Sham method. We use orthogonalized plane wave basis sets within the pseudopotential scheme, which are popular in the systems where the periodic boundary conditions are applicable (Blochl et al., 1994; Parmenter, 1952). For a periodic system, the solution of

Schrodinger equation satisfies the fundamental property of the Bloch's theorem. It can be written in the form of (Parmenter, 1952):

$$\Psi(\mathbf{r}) = u_k(r)e^{i\mathbf{k}.\mathbf{r}} \tag{3.66}$$

Here, $u_k\,(\mathbf{r})!$ is the periodic potential which is consistent with the period of the unit cell. In this case, the Schrodinger equation can be solved independently for each value of K. The function $e^{i\mathbf{k}.\mathbf{r}}$ are called plane waves and k's are the reciprocal vectors. The plane waves are the choice as basis sets for the expansion of wave functions in periodic systems. Pseudopotentials are especially used in place of external potential of nuclei (Vanderbilt, 1990). Plane waves are orthonormal and independent to the atomic positions and energy. In DFT calculations, KS equation is converted to the simple matrix eigen value problem for the expansion of coefficients. The plane waves are able to perform the correct variational calculations based on a discrete numerical grid (Kohn & Sham, 1965; Slater, 1937). The electronic wave functions in a periodic system require infinite sum of plane waves which however is not practical for the purpose of actual computations. In the real calculations, the wave function should be desribed by plane waves within a certain energy cut-off (E_{cut}).

In all electron DFT calculations, we need to take wave functions for each of the electrons (both core and valence) and solve a large number of basis functions. The valence electrons are responsible for most of the physical and chemical properties of materials, and participate in bonding between the atoms. During the formation of inter-atomic bonds, their wave functions change significantly. On the other hand, core electrons have nothing to do in bonding and their wave functions are only slightly affected during the interatomic interactions. So, core electrons can be neglected if their screening effect is included in some effective potential known as pseudopotential. Pseudopotential replaces the strong electrostatic potential of nuclei and core electrons. This allows the same wave function outside the core as given by the true wave function to introduce the real properties. It means pseudopotential simplyfies the problems by retaining the properties of interest. As we know, a good pseudopotentials should be soft and transferable (Vanderbilt, 1990). The soft and hard pseudopotentials are defined based on their cut-off radius. It means hard pseudopotential has short cut-off radius and soft pseudopotential has long cut-off radius. Short pseudopotential has a less number of valence electrons and requires less number of plane waves. Among the various pseudopotentials, norm-conserving pseudopotentials are transferable, which conserves the electronic charge with respect to the real system (Hamann et al., 1979), but they require a significant computational cost. The requirement of the computational cost can be reduced by using ultrasoft pseudopotential (USPPs) (Vanderbilt, 1990). Hence, in the present work, we used plane wave basis sets for a wave functions and ultrasoft

pseudopotentials as a pseudopotential.

Here, we have summarized the quantum mechanical methods of calculation for the solution of many body problem (from single particle SWE to DFT method with DFT-D2 approach), which are given as follows:

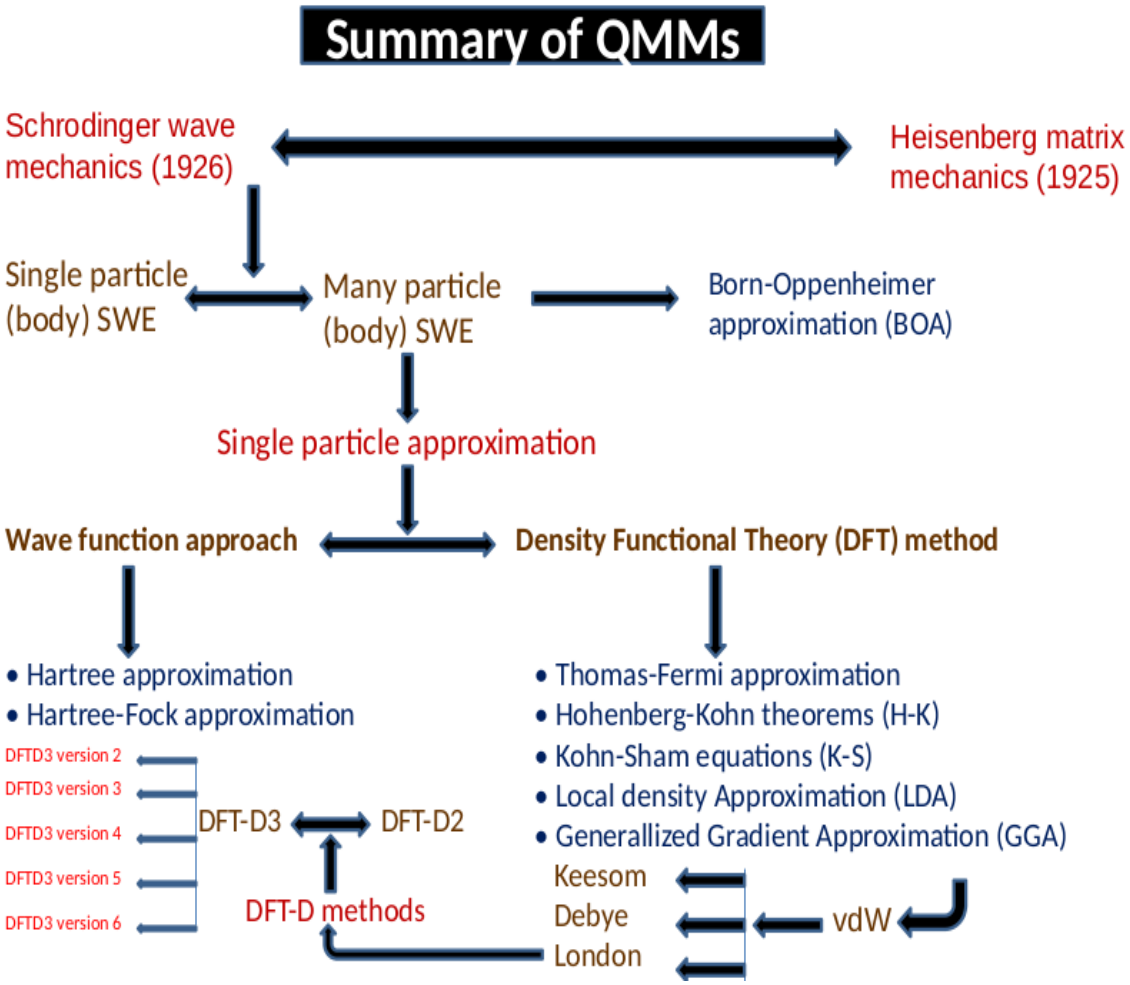

Figure 6: Summary of Quantum mechanical methods.

3.9 Simulation and Software

We basically discuss about our simulations work and the softwares which are used in the calculations. We performed first-principles calculations using Quantum ESPRESSO (QE) software package (Baroni et al., 2005) which is based on the plane wave basis sets. Here, we have explained the optimization of different parameters under the density functional theory (DFT) within the framework of DFT-D2. Moreover, We have used XCrySDen to visualize and interpret the crystal structure, and BoltzTraP software package (Madsen & Singh, 2006) for the calculations of transport properties of considered materials. **XCrySDen** stands for (**X**-window) **Cry**stalline **S**tructures and **Den**sities is a

free software under the terms of GNU general public license (GPL). It is a crystalline and molecular structure visualisation program. It can visualize the crystal structure from pw.x input and output file (Kokalj & Mol, n.d.). We have also used Xmgrace to plot the graphs. Xmgrace is a plotting software in linux operating system used for 2D scientific plots (Guide, n.d.). It is an open source plotting tools used from high school students to experienced scientists. It is highly customizable, it has inbuilt language inside it. Using xmgrace, it is possible to produce good quality plots. Also, we can save the plots in different format such as EPS, PDF, PNG, JPEG, MIF etc. but, to edit the graph we need to save it in .agr format. It is one of the best software for two dimensional plots either using own sets of data or by creating data using formulae button inside it with our desired accuracy. In addition, we discussed about the different codes and their proposes required for our calculations.

3.9.1 Quantum ESPRESSO (QE)

Quantum ESPRESSO (QE) is free, open source package. QE be for Quantum op**E**n-**S**ource **P**ackage for **R**esearch in **E**lectronic **S**tructure, **S**imulation, and **O**ptimization. It is an integrated suite of computer codes for electronic structure calculations and materials modeling (Giannozzi et al., 2009). It is very useful for first-principles calculation in condensed matter physics and material science (periodic and disorder) because, it contains number of codes for different calculations. QE established on density functional theory (DFT), basis sets and pseudopotentials. It's package uses plane wave basis sets for the expansion of wave function, pseudopotentials (norm-conserving and ultra-soft) description of electronic-ion interaction and DFT for the description of electron-ion interactions (Dreizler & Gross, 2012). With the help of QE, we can perform a number of calculations some of which, related to our research work are listed below:

- Ground state calculations of conductors, semiconductors and insulators including self-consistent total energies, forces, stresses, etc.
- Calculations of Kohn-Sham orbitals.
- Exchange-correlation functionals of density functional theory DFT (from LDA to GGA).
- Structural optimization of the system.

Additionally, QE can perform ab-initio molecular dynamics (MD) simulations, which is on electronic ground state (Born-Oppenheimer). It is also used with fictitious electronic kinetic energy (Car-Parrinello). QE is equally important in density functional perturbation theory (DFPT), to analyze energy derivatives and related quantities (Baroni et al., 2001; Giannozzi et al., 2009).

Figure 7: Quantum ESPRESSO logo (Baroni et al., 2005).

We have calculated the ground state energy of graphene unit cell and boron nitride unit cell by using both norm-conserving and ultrasoft pseudopotentials respectively along with plane wave basis sets for the expension of wave function. It was found that ground state energy of both materials have minimum energy values (-22.7979 Ry of graphene and -26.6641 Ry of boron nitride) for ultrasoft pseudopotential rather than norm-conserving. It means, ultrasoft pseudopotential was more appropriate for the calculations of ground state energy.

In this work, we have used Quantum ESPRESSO package (codes) based on DFT within the framework of DFT-D2 approximation. We have taken plane wave basis sets for the expansion of wave function and ultra-soft pseudopotentials with scalar relativistic for first-principles calculations to find binding energy and optimized geometries of pristine graphene (G), pristine h-BN, HS of G/h-BN, and B, N and C sites vacancy defects in G/h-BN HS materials. Also, we use this package (codes) to calculate the band structure, density of states (DOS), projected density of states (PDOS). Then, we can predict the electronic and magnetic properties of considered materials. The main components of this packages related to our work are as follows:

PWscf

Plane Wave self-consistent field (PWscf) was introduced by Baroni *et al*. (Baroni et al., 2001). This code is used to perform different self-consistent calculations of electronic-structure properties using a plane wave (PW) basis sets, and both norm-conserving, and ultrasoft pseudopotentials (USPPs) using different matrix diagonalization methods. PWscf is used for the self consistency calculations, structural relaxation, electronic structure calculations and variable cell molecular dynamics. During structural optimizations, we used Broyden-Fletcher-Goldfarb-Shanno (BFGS) algorithm (Pfrommer et al., 1997) to take into account of the ion dynamics.

The input file of QE consists of the following main parameters (Baroni et al., 2005):

- **calculation:** It represents the type of calculation, what we need, to be performed like relax, scf, nscf, bands etc. For example, if we choose scf as the calculation, then it tells PWscf that this will be self consistent field calculation for the total energy.

- **ibrav:** It gives the information about different types of bravais lattice for the system chosen. There are 14 different types of bravais lattice. To define these bravais lattice, ibrav is assigned from 1 to 14. For example, ibrav = 1 gives cubic structure and ibrav = 4 gives hexagonal structure. Also, we can generate our desired crystal structure by giving ibrav = 0 without mentioning cell dimension but CELL-PARAMETER is necessary. In our system we used ibrav = 4 to represent the hexagonal structure of graphene, boron nitride, and heterostructure of graphene and hexagonal-boron nitride structures.

- **nat:** It represents total number of atoms to be used in the simulating cell. Unit cell of graphene contains 2 atoms. So, we choose nat = 2 for unit cell. Also, we performed further calculations in 4×4 supercell which contains 32 atoms. For this we choose nat = 32. When the 4×4 supercell structure of graphene is combined with the 4×4 supercell structure of hexagonal-boron nitride to form heterostructure of graphene hexagonal-boron nitride. For this we choose 32 carbon atoms, 16 boron atoms, and 16 nitrogen atoms altogether 64 number of atoms in the heterostructure.

- **ntype:** It tells us that the number of types of atoms used in simulating cell. In our case, ntype = 3, it means carbon atoms in graphene structure, boron and nitrogen atoms in hexagonal boron nitride structure.

- **ecutwfc:** It is the kinetic energy cut-off, which truncates the total electronic wave function expanded in terms of infinite plane wave function by PWscf codes, during the calculations, under periodic boundary condition of simulating cell. After the value of cut-off energy, the convergence will not affect. Larger the value of cut-off will increase the accuracy and also it needs more computational cost. It is given in the unit of kinetic energy (Ry). In our case, we have obtained the same value ecutwfc = 35 Ry by optimization of unit cell of graphene and hexagonal boron nitride.

- **celldm(i):** i = 1, 2, 3 specifies the lattice parameters of the crystal. They are given in atomic units. On the other hand, i = 4, 5, 6 denotes the cosines of angle between each pair of lattice vectors. In our case, celldm (1) = a, celldm (2) =$\frac{b}{a}$, and celldm (3) = $\frac{c}{a}$ (for hexagonal lattice a = b), where a, b, c are the lattice vectors along X, Y, Z direction respectively.

- **Atomic_Species:** It referes to the name of atoms with their symbol, their atomic mass (in amu) and name of pseudopotential (PPs) file. For example: In our case, carbon, boron and nitrogen are respectively specified as C 12.01 C.pbe-n-rrkjus_psl.1.0.0.UPF, B 10.8100 B.pbe-n-rrkjus_psl.0.1.UPF, and N 14.0100 N.pbe-n-rrkjus_psl.0.1.UPF respectively.
- **Atomic_Positions:** They represent the position coordinates of the atoms used in simulating cell to define proper structure.
- **k-points:** K-points are the number of sampling points in the reciprocal space. They are used to calculate the actual self consistent minimization of energy. Generally, k-points are taken from convergence test. In our case, we have taken (22×22×1) and (6×6×1) k-points respectively for unit cells of ML graphene and hexagonal-boron nitride, and 4×4 supercell structure of graphene hexagonal-boron nitride HS.

PostProc

The PostProc module holds huge number of codes for post processing. It helps us to analyze the data obtained by PWscf calculations. Basically, we use these codes to calculate band structure, DOS, PDOS. These codes extract the specific data files produced by PWscf calculation, some important codes are as follows:

- **bands.x:** This code extracts the data files produced by PWscf calculation and reports its eigen values at different k-points with comparable energies values.
- **plotband.x:** This code writes the output of bands.x file in a simple format which can be plotted easily by plotting programs like xmgrace or gnuplot and finally it gives band structure.
- **dos.x:** This code is used for the calculations of density of states (DOS) at distinct k-points.
- **projwfc.x:** This code is used to calculate projections of wave function over atomic orbitals that performs population analysis and calculates projected (partical) density of states (PDOS). It helps us to find the contribution of density of states due to different atomic orbitals like s, p, d, f etc.

3.9.2 BoltzTraP

BoltzTraP is the code for calculating band structure dependent quantities which is based on the smoothed Fourier interpolation of bands. This is the program which contains

Boltzmann **Tra**nsport **P**roperties to calculate the semi-classic transport properties (Madsen & Singh, 2006). The input files for BoltzTrap are constructed from Quantum ESPRESSO code. In order to run the program we need a file named *A.intrans*, that contains the parameters for BoltzTraP, where A represents the name of directory. Simiraly, we need the files *A.energy* and *A.struct* for band structure and crystal structure respectively. The *A.intrans* file contains several informations like Fermi energy level, energy grid, energy span around Fermi level, total number of electrons in the systems, numbers of lattice points per k-point, energy range of chemical potential, and maximum temperature with temperature grid as shown in figure (8).

```
GENE                    # Format of DOS
0 0 0 0.0               # iskip (not presently used) idebug setgap shiftgap
-0.0930492878042 0.0005 0.4 256.0    # Fermilevel (Ry), energygrid, energy span around Fermilevel, number of electrons
CALC                    # CALC (calculate expansion coeff), NOCALC read from file
5                       # lpfac, number of latt-points per k-point
BOLTZ                   # run mode (only BOLTZ is supported)
0.15                    # (efcut) energy range of chemical potential
2000.0 20.0              # Tmax, temperature grid
-1.0                    # energyrange of bands given individual DOS output sig_xxx and dos_xxx (xxx is band number)
TETRA
```

Figure 8: Screenshot of *A.intrans* file obtained from QE. This file gives the information of Fermi energy of substance under study and is the input file for BoltzTraP to calculate transport properties of material.

These parameters are required for BoltzTraP input file. After that we have run the BoltzTraP by using *src* and *x_trans* files, (*src* and *x_trans* files are existed in BoltzTraP package) then obtained *A.trace* file. The traces of conductivity tensors are obtained in *A.trace* file. The *A.trace* file includes; energies, temperatures, Seebeck coefficient at different temperatures, ratio of electrical conductivity to the relaxation time, Hall coefficient, ratio of electronic part of thermal conductivity to relaxation time, specific heat capacity, susceptibility and doping concentrations values of materials. The sample of output A.trace file is shown in figure (9).

Ef[Ry]	T [K]	N	DOS(Ef)	S	s/t	R_H	kappa0	c	chi
-0.24251	5.0000	5.39848944	0.12370112E+04	-0.57896102E-11	0.25928814E+21	0.23027E-09	0.26456E+10	0.44444928E-04	0.18467518E-07
-0.24251	10.0000	5.39848700	0.62032607E+03	-0.77830337E-08	0.13002831E+21	0.45929E-09	0.17827E+13	0.29947863E-01	0.92609366E-08
-0.24251	15.0000	5.39845538	0.42914736E+03	-0.70647562E-07	0.89977821E+20	0.66580E-09	0.11131E+14	0.18692909E+00	0.64068024E-08
-0.24251	20.0000	5.39836071	0.35565998E+03	-0.18761682E-06	0.74621099E+20	0.80960E-09	0.24097E+14	0.40413073E+00	0.53096987E-08
-0.24251	25.0000	5.39819901	0.32765351E+03	-0.31274302E-06	0.68812985E+20	0.88874E-09	0.36037E+14	0.60294923E+00	0.48915862E-08
-0.24251	30.0000	5.39798078	0.31724477E+03	-0.42707779E-06	0.66703268E+20	0.93052E-09	0.46206E+14	0.77038041E+00	0.47361926E-08
-0.24251	35.0000	5.39771673	0.31329985E+03	-0.53173074E-06	0.65957159E+20	0.95022E-09	0.55179E+14	0.91585729E+00	0.46772983E-08
-0.24251	40.0000	5.39741458	0.31160027E+03	-0.63043509E-06	0.65690934E+20	0.97693E-09	0.635E9E+14	0.10488233E+01	0.46519251E-08
-0.24251	45.0000	5.39707982	0.31062844E+03	-0.72500458E-06	0.65586873E+20	0.99742E-09	0.71578E+14	0.11747498E+01	0.46374165E-08
-0.24251	50.0000	5.39671661	0.30986113E+03	-0.81577961E-06	0.65535165E+20	0.10184E-08	0.79487E+14	0.12962509E+01	0.46259611E-08
-0.24251	55.0000	5.39632843	0.30912538E+03	-0.90251024E-06	0.65498971E+20	0.104153E-08	0.8731E+14	0.14144839E+01	0.46149770E-08
-0.24251	60.0000	5.39591828	0.30836780E+03	-0.98483861E-06	0.65466237E+20	0.106543E-08	0.9509E+14	0.15299775E+01	0.46036671E-08

Figure 9: Screesshot of *A.trace* file obtained from BoltzTraP. This file contains all the calculations results regarding transport properties of material.

The first column in the figure (9) represents energy in the unit of Rydberg. Second column

gives temperature value in Kelvin. Most important parameter, Seebeck coefficient can be obtained from fifth column at different temperature values in $\frac{V}{K}$. The ratio of electrical conductivity to the relaxation time can be obtained from the sixth column in $\frac{1}{\Omega ms}$. Similarly, Hall coefficient in $\frac{m^3}{C}$, and ratio of electronic part of thermal conductivity to relaxation time in $\frac{W}{mKs}$ can be obtained from columns seven and eight respectively. One can get specific heat capacity in $\frac{J}{molK}$ and molar susceptibility $\frac{m^3}{mol}$ from columns nine and ten respectively. Therefore, we can explore the transport properties of materials by employing the calculated results obtained in $A.trace$ file.

3.10 Computational Details

We have used spin-polarized DFT method incorporating van der Waals (vdWs) interactions DFT-D2 appoach for the study of structural, electronic, magnetic and transport properties of graphene hexagonal-boron nitride (G/h-BN) HS, and boron (B), nitrogen (N) and carbon (C) atoms vacancy defects in G/h-BN HS materials. Computations works are done by using Quantum ESPRESSO (Giannozzi et al., 2009) and BoltzTraP (Madsen & Singh, 2006) codes. PBE form of GGA functional (Perdew et al., 1996) was used for the calcualtions of electronic exchange and correlation effect in our systems. We have used Rappe-Rabe-Kaxiras-Joannopoulos (RRKJ) model (Grimme, 2004) of ultrasoft pseudopotentials (USPPs) from the official website of Quantum ESPRESSO (Baroni et al., 2005; Giannozzi et al., 2009) USPPs accounts the chemically active valence electrons. Thus, USPPs included the effect of chemically active valence electrons in our entire calculations. While doing so, the electronic configurations of C, B and N atoms $1s^2 2s^2 2p^2$, $1s^2 2s^2 2p^1$, $1s^2 2s^2 2p^3$ are treated explicitly as valence electrons in the pseudopotentials description of C, B and N. The interaction effect of inner cores of C, B and N atoms are replaced by ultrasoft pseudopotentials.

During the calculations, the structures are conceded to relax under Broyden-Fletcher-Goldfarb-Shanno (BFGS) (Pfrommer et al., 1997) scheme. For the structure optimization and relaxation, we have used the value of change of total energy between two scf steps is less than 10^{-4} Ry, and each component of force acting is less than 10^{-3} Ry/Bohrs. Self consistent total energy calculations have been done atfter the relax calculations. For this the brillouin zone (BZ) of graphene and hexagonal-boron nitride are sampled in K-space using Monkhorst-Pack scheme (Monkhorst & Pack, 1976) with suitable number of mesh of K-points. They are determined from the convergence test. We have also used Marzarri-Vanderbilt (MV) (Marzari et al., 1999) method of smearing with a small smearing width of 0.001 Ry.The $david$ diagonalization method along with $plain$ mixing mode and mixing factor of default value 0.6 are chosen for self consistency.

3.10.1 Construction of Graphene (G) and Hexagonal-Boron Nitride (h-BN) Monolayers

Graphene (G) and hexagonal-boron nitride (h-BN) have two dimensional (2D) lattice structures with a basis of two atoms in the primitive unit cells. For the construction of input file of unit cells of graphene and h-BN, we have taken the distance between two carbon atoms, a_0 = 1.42 Å, in graphene which was determined experimentally (Neto et al., 2009), and distance between boron and nitrogen atoms, a_0 = 1.45 Å in h-BN, which approaches with the reported value (Y. Liu et al., 2014). The unit cell of ML (specially graphene and BN) can be constructed using QE codes by taking ibrav = 4 (as a bravais lattice index) in the input file since graphene and BN are hexagonal structures. celldm (3) = $\frac{c}{a}$, celldm (2) = $\frac{b}{a}$, and celldm (1) = a are taken in the input file as the parameters. Where, a, b and c represent the lattice constants in Bohr along X, Y and Z-directions respectively. We have taken $b = a$ in the hexagonal structure. To avoid the probability of interaction between two periodic graphene layer, and two periodic h-BN layer respectively in Z-directions, we took the distance between two consecutive layer by 18 Å. In the input file, ATOMIC_SPECIES for each atoms are defined by their atomic symbol keep to by atomic mass (in amu) and ultrasoft pseudopotentials. For example carbon, boron, and nitrogen atoms are mentioned as C 12.01 C.pbe-n-rrkjus_psl.1.0.0.UPF, B 10.8100 B.pbe-n-rrkjus_psl.0.1.UPF, and N 14.0100 N.pbe-n-rrkjus_psl.0.1.UPF respectively, where 12.01 amu is atomic mass of carbon atom and C.pbe-n-rrkjus_psl.1.0.0.UPF is its pseudopotential description; 10.8100 amu is atomic mass of boron atom and B.pbe-n-rrkjus_psl.0.1.UPF is its pseudopotential description, and 14.0100 amu is atomic mass of nitrogen atom and N.pbe-n-rrkjus_psl.0.1.UPF is its pseudopotential description.

After the construction of unit cells, we have to determine important parameters like kinetic energy cut-off (ecutwfc), k-points (n_{kx}, n_{ky}, n_{kz}), and lattice parameter (a). These parameters are calculated from convergence test which are briefly described as follows.

3.10.2 Convergence Tests

We separately determined the three basic parameters namely kinetic energy cut-off (ecutwfc) which is cut-off for wave function expansion, k-points which measures how our discrete grid nearly represents the continuous integral over the brillouin zone (BZ), and lattice parameter (a) which gives cell dimension in first-principles calculations.

Kinetic Energy Cut-off

In Quantum ESPRESSO codes, the plane wave self consistent calculations implements the infinite basis function which are plane wave expansion of ground state wave function and of electronic wave function under the periodic boundary conditions. The plane wave expansion of electronic wave function is given by Bloch's theorem (Parmenter, 1952) as:

$$\Psi(\mathbf{r}) = u_k(r)e^{i\mathbf{k}.\mathbf{r}} \tag{3.67}$$

Here, $\Psi(\mathbf{r})$ and $u_k(\mathbf{r})$ are the electronic wave function and periodic function as in lattice respectively. We truncated the $u_k(\mathbf{r})$ to make it finite known kinetic energy cut-off (ecutwfc). To find the value of ecutwfc, we have performed the scf calculations by using experimental values of lattice parameter a = 4.65 Bohr for graphene and a = 4.70 Bohr for boron nitride respectively. The arbitrary value of k-points as (25×25×1) for different value of ecutwfc (10, 15, 20, 25, 30, 35, 40, 45, 50) are taken in both the materials. Finally we obtained total ground state energy of graphene for each value of ecutwfc using executable pw.x command. The graph between total scf energy (in Ry) and corresponding ecutwfc is shown in figure (10).

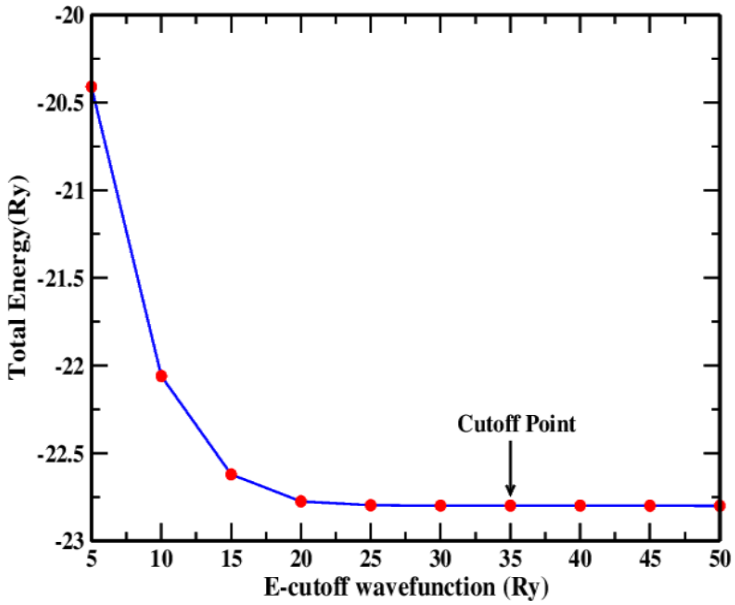

Figure 10: Graph between total energy and kinetic energy cut-off of graphene unit cell.

From the figure (10), the value of total energy is almost constant after the value of energy cut-off is 30 Ry, so we have chosen energy cut-off = 35 Ry for upcoming calculations. Similar results is obtained in h-BN structure. As the value of ecutwfc is known, we then predicted the value of charge density cut-off (ecutrho) which is 10× ecutwfc in the case of ultrasoft pseudopotentials. Thus, ecutrho 350 Ry is used in our calculations.

Convergence of K-points

The points in the momentum space are called K-points. The exact self consistent minimization of energy calculations will be performed by using K-points. We have replaced the continuous integral over the brillouin zone by finite sum over discrete values of k-points in our calculations. To optimize k-points, we used ecutwfc = 35 Ry, ecutrho = 350 Ry and experimental value of lattice parameter (a) = 4.65 Bohr for graphene and 4.70 Bohr for boron nitride structures respectively. Then, we performed scf calculations for different values of k-points (6, 8, 10, 12, 14, 16, 18, 20, 22, 24). Finally, we obtained total energy of graphene for each value of k-points and we have plotted the graph between total energy with number of k-points. Nature of graph is shown in figure (11).

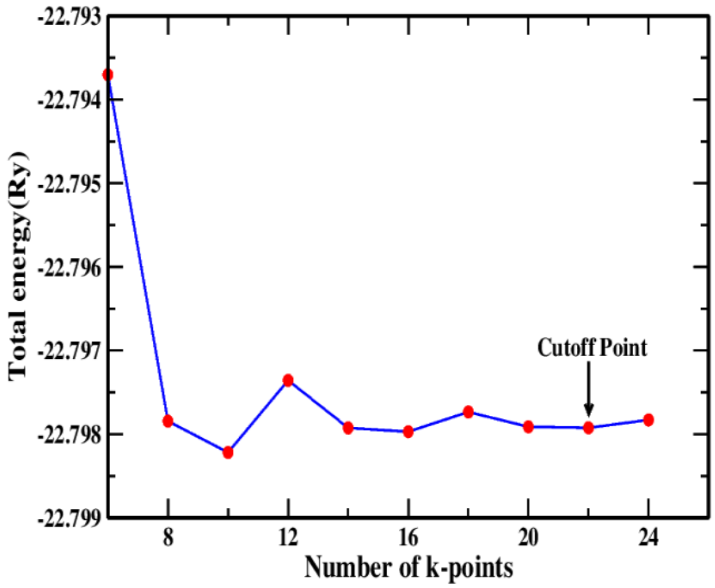

Figure 11: Graph between total energy and number of K-points of graphene unit cell.

Figure (11) shows that, the total energy is almost constant after the value of K-points (20×20×1). So, by calculating successive energy difference between two K-points, we have chosen the K-point grid as 22×22×1. Similar result is obtained for boron nitride structure. Therefore, we used 22×22×1 k-points value in graphene and h-BN structures in further calculations.

Lattice Parameter (a)

After the optimization of kinetic energy cut-off and k-points, we proceeded to find the optimized lattice parameter (a) of graphene and h-BN. For this, we used the optimized value of ecutoff = 35 Ry, ecutrho = 350 Ry, and k-points (n_{kx}, n_{ky} ,n_{kz}) = (22×22×1) in

the input file, and then we performed self consistent calculations for different value of lattice parameter (4.40, 4.45, 4.50, 4.55, 4.60, 4.65, 4.70, 4.75, 4.80, 4.85, 4.90) Bohrs respectively. Finally, we got total energy for each value of lattice parameter and then we plotted a graph of total energy versus lattice parameter (a). The graph between total energy and corresponding lattice parameter of graphene unit cell is shown in figure (12).

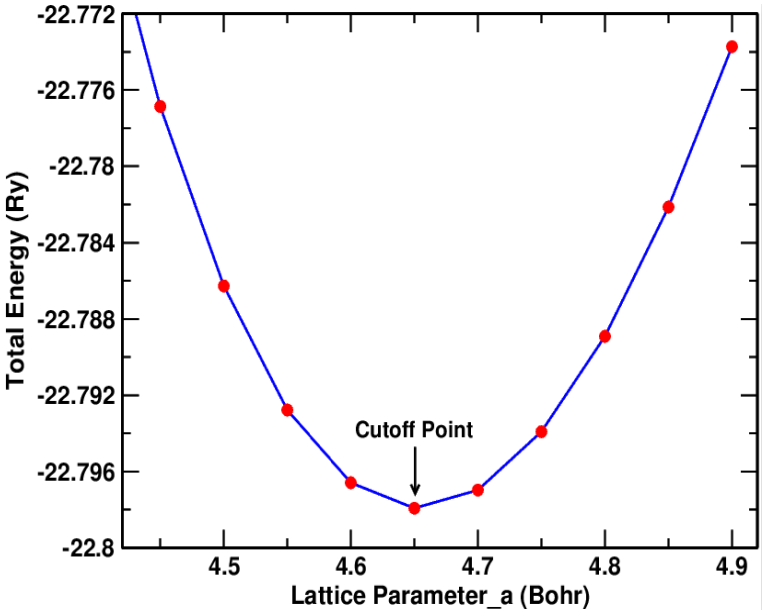

Figure 12: Graph between total energy and lattice parameter *a* of a graphene unit cell.

From figure (12), it is seen that for the value of lattice parameter of graphene unit cell is (a) = 4.65 Bohr, at total minimum energy. This value is similar to the result obtained by Pantha et al. (Pantha et al., 2015) for the unit cell of graphene, and it is also comparable with the experimentally reported value (Chan et al., 2008). Similarly, lattice parameter of boron nitride unit cell is found to be (a) = 4.68 Bohr. This value is also comparable with the reported value (Ooi et al., 2005). The value of lattice parameter depends upon the number of atom per unit cell. Therefore, for 2×2, 3×3 and 4×4 supercell structures of graphene and h-BN, we have chosen the value of lattice parameter as 9.30 Bohrs, 13.95 Bohrs and 18.60 Bohrs respectively.

After the calculations of ecutwfc, k-points and lattice parameter, we used these parameters on input file is called optimized input of graphene and h-BN. The relax calculations are done by using optimized input file of graphene and h-BN respectively. From the optimized and relaxed graphene unit cell structure, the distance between any two nearest carbon atom is found to be 1.4207 Å. This is fairly aggrement to the experimentally reported value 1.42 Å, (Neto et al., 2009). Similarly, the distance between boron and nitrogen atoms from the optimized and relaxed unit cell structure of boron nitride is estimated 1.4542 Å, which is closely agreeable with the experimentally reported value 1.45 Å (Liu et al., 2014). Therefore, we have constructed the 4×4 supercell struc-

tures of graphene and hexagonal-boron nitride. For this, optimized primitive unit cell of graphene and h-BN are extended along X and Y-directions by using XCrySDen respectively as shown in figure (13).

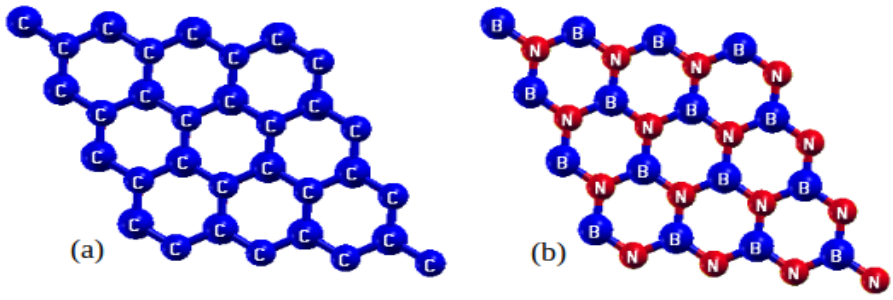

Figure 13: Optimized and relax 4×4 supercell structures of: (a) graphene, (b) hexagonal-boron nitride (h-BN).

The optimized geometries of different supercell are obtained from relax calculations and hence, we have calculated total energy from scf calculations using $pw.x$ executable. Then, the stability of pure graphene sheet and hexagonal boron nitride are studied using the informations obtained from relax and scf calculations.

3.10.3 Construction of Pristine and Vacancy Defected Graphene/Hexagonal-Boron Nitride (G/h-BN) Heterostructures

Two different chemical bonded materials are combined together to form heterostructure (HS) material. The HS materials have diffrent physical and chemical properties than their constituents (Wang et al., 2017). In the present work, we have combined the structural similar materials graphene (G) and h-BN at diffrent orientations to form G/h-BN HS material. The vertical stacking (graphene is combined with h-BN where graphene is at top position and h-BN is as a base) configuration of G/h-BN heterostructure material is more stable than that of other configurations. So, we have chosen 4×4 supercell structure of graphene and 4×4 supercell structure of h-BN materials are vertically stacking to form G/h-BN HS materials, where G/h-BN contains 64 atoms (32 carbon atoms, 16 boron atoms and 16 nitrogen atoms in HS materials) as shown in figure (14). Then, relax calculations are performed to get optimized G/h-BN heterostructure, and then total energy is calculated from scf calculations using pw.x executable.

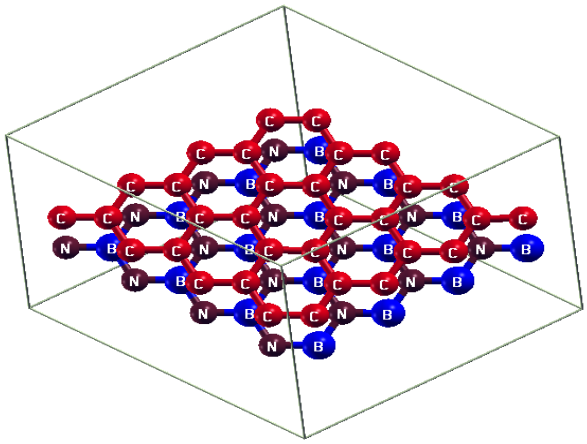

Figure 14: 4×4 supercell structures of graphene and h-BN are combined to form vertical stacking G/h-BN heterostructure material (Neupane, et al., 2021).

Further, we have prepared the boron (B), nitrogen (N), and carbon (C) sites vacancy defected materials from the optimized-relaxed G/h-BN HS. For this, we have constructed 1B vacancy defect in G/h-BN HS (G/h-BN_1B), 1N vacancy defect in G/h-BN HS (G/h-BN_1N), nearest neighbouring 1B and 1N atoms vacancy defects in G/h-BN HS (G/h-BN_nBN), and alternate zone of 1B and 1N atoms vacancy defects in G/h-BN HS (G/h-BN_aBN) from the surface of h-BN of G/h-BN HS material respectively. Also, we have created 1C vacancy defect in G/h-BN HS (G/h-BN_1C), and 2C vacancy defects in G/h-BN HS (G/h-BN_2C) materials by removing one carbon and two carbon atoms respectively from the surface of graphene of G/h-BN HS material. Then, relax calculations are performed to get optimized-relaxed vacancy defected G/h-BN heterostructures. The optimized-relaxed B and N sites vacancy defected G/h-BN materials are shown in figure (15) and C sites vacancy defected G/h-BN materials are shown in figure (16).

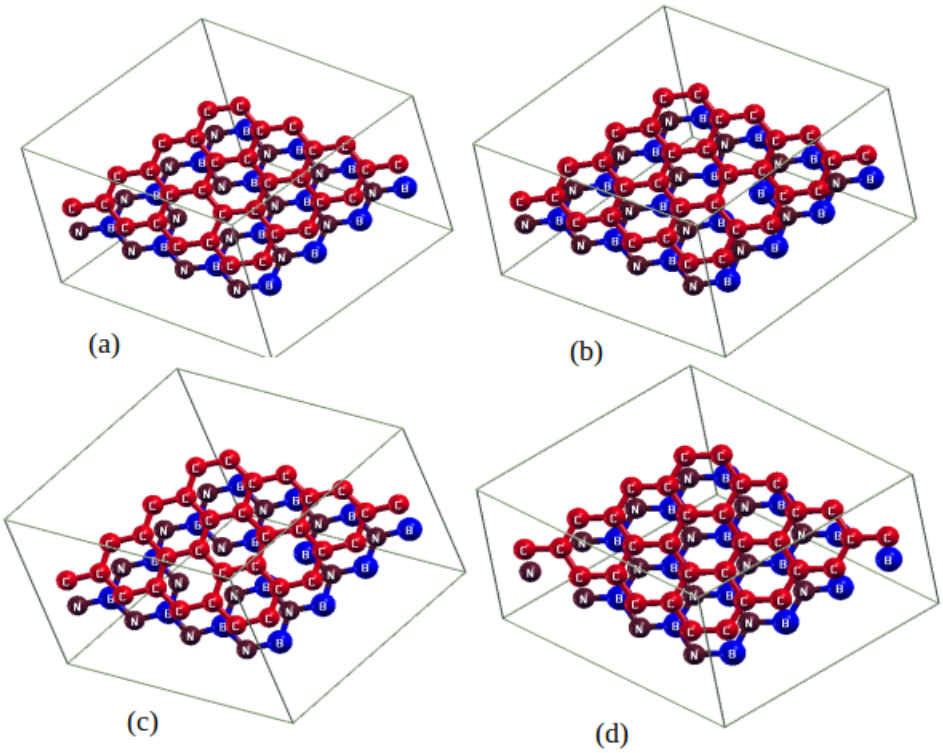

Figure 15: B and N sites vacancy defected G/h-BN HS: (a) G/h-BN_1B, (b) G/h-BN_1N, (c) G/h-BN_nBN, and (d) G/h-BN_aBN HS materials (Neupane, et al., 2021).

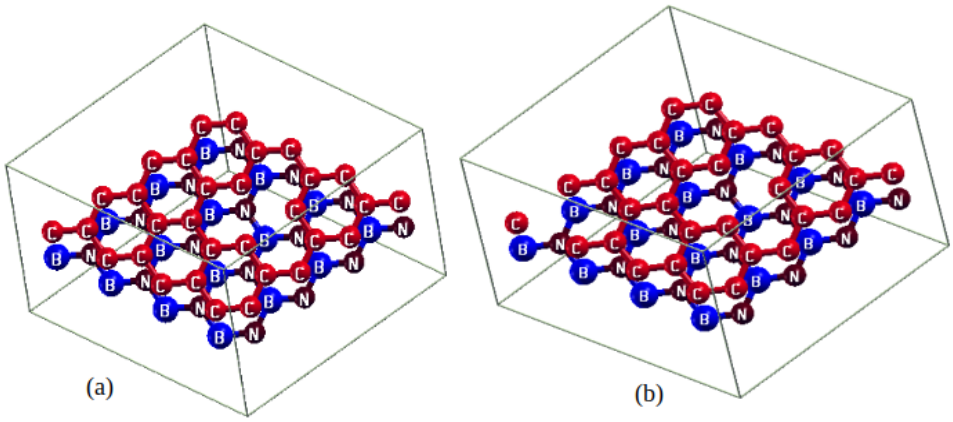

Figure 16: C sites vacancy defected G/h-BN HS: (a) G/h-BN_1C, and (b) G/h-BN_2C HS materials (Neupane, et al., 2022).

To avoid the interactivity between adjacent heterostructures, vaccum length of HS (pristine and defected) is made large enough i.e. 18 Å along Z- axis. We have also developed the band structure of G/h-BN, and B, N and C sites vacancy defected G/h-BN materials. For this, we have chosen Γ**–M–K–**Γ high symmetric points in X-axis. We have also taken 100 K-points in the specific direction of unchangeable brillouin zone (BZ) in order to obtain band structure graph using pw.x and bands.x executable. After that we performed post processing calculations to extract the data for band plotting using executable

plotband.x command. Further, we have estimated the total DOS of considered HS. For the calculations of DOS, first we performed non-self consistent field ($nscf$) calculations using pw.x executable. To run $nscf$ calculations we took just double number of k-point grid than scf calculations in order to obtain fine DOS. Then, we performed DOS and projections of wave functions over atomic orbitals (PDOS) calculations using dos.x and projwfc.x executable. The PDOS calculations help to find the contribution of different orbitals on DOS. In addition, we have studied the transport properties of pristine and vacancy defected G/h-BN HS materials using BoltzTraP computational codes by $dot\ intrans$ and $dot\ trans$ executable. Transport properties of considered materials are estimated through the parameters of Seebeck coefficient, thermoelectric power factor, electrical conductivity and electronic contribution of thermal conductivity. The more details about band, DOS, PDOS, and transport properies calculations of pristine and vacancy defects in G/h-BN HS are discussed in 'Results and Discussion' chapter.

CHAPTER 4

4. RESULTS AND DISCUSSION

4.1 General Consideration

The main findings of the present work have been discussed in this chapter. Also, we have performed the comparision of our obtained results with available experimental reported values. The main aim of our work is to study structural, electronic, magnetic and transport properties of G/h-BN heterostucture (HS) material, and B, N and C sites vacancy defected G/h-BN HS materials. Computational works are carried out through Quantum ESPRESSO (QE) and BoltzTraP (BTP) software packages, on the basis of spin-polarized density functional theory (DFT) within the frame work of van der Waals (vdWs) corrections DFT-D2 approach, and Boltzmann transport equations (BTE). To obtain the optimized kinetic energy cut-off, k-points and lattice parameters, convergence tests have been performed. It gives the most stable structural configurations at minimum ground state energy. We study the band structure, DOS and PDOS of heterostructures we considered in the present work. The electronic and magnetic properties of examined materials are investigated based on band, DOS and PDOS calculations. BoltzTraP package can be used to estimate the transport properties of materials on the basis of their Seebeck coefficient (S), electical conductivity $\frac{\sigma}{\tau}$, thermal conductivity $\frac{\kappa}{\tau}$, theromelectric power factor P = $\frac{S^2\sigma}{\tau}$, figure of merit ZT = $\frac{S^2\sigma T}{\kappa}$, Hall coefficient R_H, and chemical potential μ. Transport properties of graphene, h-BN, G/h-BN HS, and B, N and C sites vacancy defected G/h-BN HS materials are investigated through the calculations of their Seebeck coefficient, electical conductivity, electronic contribution of thermal conductivity, theromelectric power factor.

In section 4.2, we have discussed the structure and stability of pure graphene (G) and hexagonal-boron nitride (h-BN) monolayers (ML), graphene/hexagonal-boron nitride (G/h-BN) heterostructure (HS), and B, N and C atoms vacancy defected G/h-BN HS materials. In section 4.3, we have examined the electronic properties of considered materials on the basis of their band structure calculations. In section 4.4, we have explored the magnetic properties of graphene ML, h-BN ML, G/h-BN HS, and B, N and

C atoms vacancy defected G/h-BN HS on the basis of their DOS and PDOS analysis. Section 4.5 is dedicated to transport properties of materials. The finding of the present work covers the following topics.

- Structural stability of monolayer (ML), different stacking configurations of heterostructure (HS) and vacancy defects in HS materials is determined based on their total ground state energy and binding energy. We have computed the total ground state energy and binding energy of graphene (G) and h-BN supercell structures, heterostructure of G/h-BN HS, 1B defect in G/h-BN HS (G/h-BN_1B), 1N defect in G/h-BN HS (G/h-BN_1N), nearest neighbour 1B and 1N defects in G/h-BN HS (G/h-BN_nBN), alernate zone of 1B and 1N defects in G/h-BN HS (G/h-BN_aBN), 1C defect in G/h-BN HS (G/h-BN_1C), and 2C defects in G/h-BN HS (G/h-BN_2C) materials. The monolayer (ML) of graphene and h-BN supercell structures, vertical stacking configuration of G/h-BN HS, and B, N and C atoms vacancy defected G/h-BN HS materials are found to be stable.

- The nature of material is predicted on the basis of its electronic properties. Here, we have predicted the electronic properties of graphene and h-BN ML, and G/h-BN, G/h-BN_1B, G/h-BN_1N, G/h-BN_nBN, G/h-BN_aBN, G/h-BN_1C and G/h-BN_2C HS materials on the basis of their band structure calculations. We found that graphene is a zero band gap and h-BN is a wide band gap materials as reported in previous works (Novoselov et al., 2004; Watanabe et al., 2004). The pristine (non-defected) G/h-BN, and B and N sites vacancy defects in G/h-BN materials have semimetallic properties. On the other hand, G/h-BN_1C opens small energy band gap of 0.40 eV at K-point of band structure. Hence, it is called an n-type semiconductor. But, band states of G/h-BN_2C HS material are appeared around the Fermi energy level in band structure. Hence, it has metallic properties.

- Magnetic properties (magnetic moment) of spin-polarized system are affected by the distribution of up-and down-spin states of electrons in the orbitals of atoms present in their DOS and PDOS plots. Hence, we have investigated the magnetic properties of considered ML and HS (pristine and vacancy defected) materials through the analysis of their DOS and PDOS. It is found that graphene and h-BN have non-magnetic properties, while G/h-BN, and B, N and C sites vacancy defected HS have magnetic properties.

- Thermoelectric materials are explored based on their transport properties. Here, we have studied the transport properties of considered ML supercell structures, pristine HS, and vacancy defected HS materials based on the calculations of their Seebeck coefficient, electrical conductiviy, electronic contribution of thermal con-

ductivity and thermoelectric power factor, they are found to be good thermoelectric materials.

4.2 Structural Properties

Surface engineering properties of materials are called structural properties. They are used for the purpose of designing the new materials with desired properties as there is an excellent correlation of structure and properties of materials (Novoselov et al., 2004; Ooi et al., 2005). In this section, we discuss the structural properties of graphene, h-BN, HS of G/h-BN, and vacancy defected G/h-BN HS materials.

4.2.1 Graphene (G) and Hexagonal-Boron Nitride (h-BN) Supercell Structures

Structures of graphene and h-BN are similar but they have different physical and chemical properties. Structure and stability of pure graphene and hexagonal boron nitride (h-BN) are described as follows.

Graphene

Graphene's structure can be formed by two carbon atoms bounded covalently per unit cell with a carbon to carbon bond length of (a) = 1.42 Å (Novoselov et al., 2004; Singh & Kroll, 2009). Graphene is made of a set of sp^2 hybridised carbon atoms which form four bonds each, three σ bonds, one with each neighbour, and one π orientated out of plane (Novoselov et al., 2004; Neto et al., 2009; Wang, Ma, & Sun, 2017). Supercell structure of 2D graphene is fabricated by advancing its unit cell along X and Y-directions. Here, we discuss equilibrium configuration of graphene and binding energy of carbon atom in unit cell and supercells containing 2, 8, 18 and 32 number of carbon atoms, because stability of materials are predicted based on their binding energy. The binding energy E_b of graphene is estimated by:

$$E_b = NE_C - E_g \tag{4.1}$$

where, E_C and E_g respectively represent the ground state energy of isolated carbon atom and pure graphene sheet. N is the total number of carbon atoms in a graphene supercell. We have estimated the binding energy per carbon atom using the relation:

$$(E_b)_{percarbonatom} = \frac{NE_C - E_g}{N} \tag{4.2}$$

Before calculating binding energy, we have performed the relax and self consistant field (scf) calculations of isolated carbon atom to get total energy of isolated carbon on same dimension of unit cell and each graphene 2×2, 3×3 and 4×4 supercells. Also, we have relaxed each supercell until the convergence is achieved. Then, we have performed scf calculations to get total energy for different supercells containing 2, 8, 18 and 32 number of carbon atoms. Unit cell and supercell structures of graphene sheet are shown in figure (17).

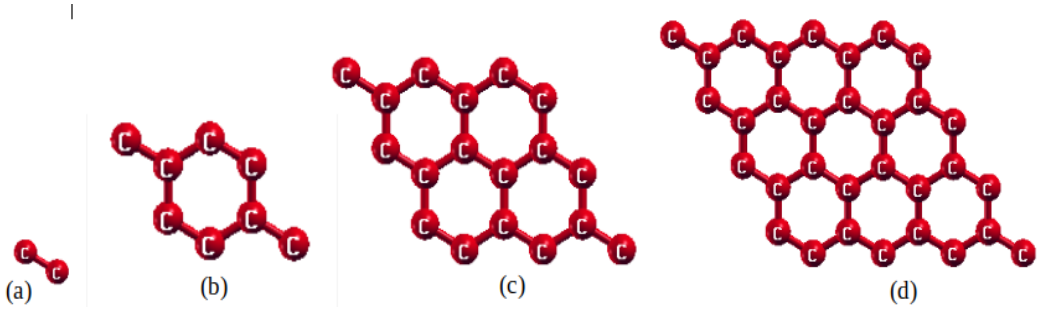

Figure 17: The unit and supercell structures of graphene: (a) A unit cell, (b) 2×2 supercell, (c) 3×3 supercell, and (d) 4×4 supercell.

The total ground state energy, calculated binding energy and binding energy per carbon atom are illustrated in table (1) below.

Table 1: Total ground state energy (Ry), energy of isolated carbon atom (Ry), binding energy of carbon atom (eV) and binding energy per carbon atom (eV/atom) graphene sheet containing 2, 8, 18 and 32 number of carbon atoms.

Number of carbon atoms	Total Energy (Ry)	Energy of isolated carbon atom (Ry)	Binding energy of carbon atom (eV)	B. E. per carbon atom (eV/atom)
C_2	-22.7979	-10.9785	11.4362	5.7181
C_8	-99.4452	-11.8519	62.9680	7.8710
C_{18}	-223.7507	-11.8438	143.6473	7.9804
C_{32}	-397.7808	-11.8437	255.4406	7.9825

From table (1), it is seen that (from numerical calculation), the binding energy increases with increase in the number of carbon atoms. Higher the value of binding energy, more stable the system. Thus, the graphene with large number of carbon atoms is more stable than with less number of carbon atoms. We found that, the binding energy per carbon atom is almost constant at 18 and 32 numbers of carbon atoms. The binding energy per carbon atom of 2×2, 3×3 and 4×4 supercells have 7.8710 eV/atom, 7.9804 eV/atom, and 7.9825 eV/atom values respectively, they are analogous with 7.7890 eV/atom, 7.9010 eV/atom and 7.9040 eV/atom reported values by Pantha et al. (Pantha, Khaniya, & Adhikari, 2015). We concluded that graphene with 3×3 and 4×4 supercells are more stable than smaller sized supercells. With reference to available reported value, the

binding energy per carbon atom for pure graphene sheet (7.9825) eV/atom) containing 32 number of carbon atom agrees within 0.88 % to the previously reported value of 7.9100 eV/atom by Bhattacharya et al. (Bhattacharya et al., 2010) and within 0.62 % to the value 8.0300 eV/atom reported by Oli et al. (Oli et al., 2013). Therefore, 4×4 supercell structure of pure graphene is a stable material. It can be used for further calculations.

Hexagonal Boron Nitride (h-BN)

If we assume hexagonal boron nitride (h-BN) as the structure of graphite (Song et al., 2010). It contains strong in-plane covalent bondings and weak van der Waals (vdWs) interplanner bonding. The unit cell of h-BN is formed by covalently bonded one boron atom and one nitrogen atom together. It is found that bond length between nearest B-N atoms of optimized structure of unit cell has 1.45 Å. This is fairly close with the reported value 1.45 Å, (Liu et al., 2014). Structural (geometrical) optimization gives the strain free lattice constants, atomic coordinates leading to minimum energy configuration. Once all the parameters (lattice parameters, kinetic energy cut-off, k-points and atomic coordinates) required in the input files are fixed. We have carry out relax calculations of the unit cell. It makes small deviates in the atomic coordinates allowing stable and minimum ground state energy of crystal structure. It means, relaxation further gives more minimum energy configuration.

After relaxation, self consistent field (scf) calculations were performed to find the total energy of the system. By extending periodically the unit cell along X- and Y-axes using XCrySDen (Kokalj & Mol, n.d.); we obtained 2×2, 3×3 and 4×4 supercell structures of 2D h-BN which are illustrated in figure (18).

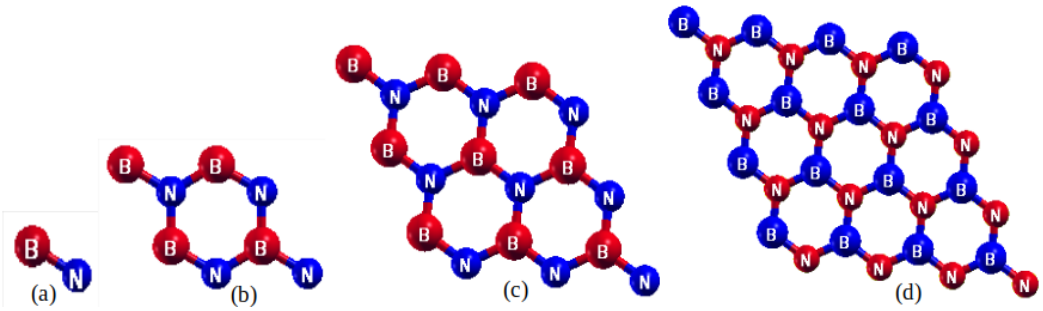

Figure 18: The unit and supercell structures of h-BN: (a) A unit cell, (b) 2×2 supercell, (c) 3×3 supercell, and (d) 4×4 supercell.

Here, 2×2 supercell contains 4 boron (B) and 4 nitrogen (N) atoms, 3×3 supercell contains 9 boron and 9 nitrogen atoms, and 4×4 supercell contains 16 boron and 16 nitrogen atoms. Then, the stability of the supercells are determined from the calculations. Once

the equilibrium configuration of supercells are achieved after the relaxation operations, scf are performed to get total ground state energies of the systems. Thus, the stability of h-BN sheets are then calculated using the relation:

$$E_b = N(E_B + E_N) - E_{h-BN} \tag{4.3}$$

where, E_b and E_{h-BN} respectively represent the binding energy and ground state energy of h-BN supercell under consideration. Let, N is the number of boron atoms and nitrogen atoms in the same supercell. Positive value of binding energy E_b means bounded system can exist in nature. Similarly, the binding energy per boron-nitrogen pair can be estimated as:

$$(E_b)_{BN} = \frac{E_b}{N} = \frac{N(E_B + E_N) - E_{h-BN}}{N} \tag{4.4}$$

Energies of isolated boron and nitrogen atoms are estimated usig the same method as the complex one. Energy of an isolated boron and nitrogen atoms are found to be E_B = -5.9234 Ry and E_N = -19.8117 Ry respectively. The total ground state energy, calculated binding energy and binding energy per B-N atoms are given in table (2).

Table 2: Total ground state energy (Ry), binding energy (eV), and binding energy per B-N atoms (eV/atom) for h-BN sheet containing 2, 8, 18 and 32 number of B-N atoms.

Cell size	Number of B and N atoms	Total ground energy (Ry)	Binding energy B.E. (eV)	Binding energy per B-N atoms (eV/atom)
1×1	2	-26.6641	12.6248	6.3124
2×2	8	-106.6563	50.5345	6.3168
3×3	18	-239.9766	113.7145	6.3175
4×4	32	-426.6251	202.1592	6.3175

Table (2) shows that total binding energy increases with the increase in the number of boron and nitrogen atoms while the ground state energy decreases with the increase in the size of the supercell. It is also found that binding energy per B-N atoms of h-BN supercells have higher values than that of unit cell, and binding energy of h-BN supercells per pair of B-N have almost constant value. The binding energy per B-N atoms of 4×4 h-BN supercell is comparable with the experimentally reported binding energy 6.6000 eV of h-BN (Zunger, 1974). Also, the estimated binding energy value of h-BN is comparable with reported values of graphene (Zunger, 1974; Bhattacharya et al., 2010; Oli et al., 2013). Therefore, 4×4 supercell h-BN structure is a stable, and is used for further calculations.

4.2.2 Graphene/hexagonal-Boron Nitride (G/h-BN) Heterostructure

The graphene based G/h-BN heterostructure (HS) material is modelled using optimized and relaxed 4×4 supercell structure of graphene and 4×4 supercell structure of h-BN with appreciable lattice mismatch (1.4 %) in the present work. This value is approximate with the reported value (Ramasubramaniam et al., 2011; Quhe et al., 2012; Slotman et al., 2015). After that we have performed relax calculations of G/h-BN HS for the appropriate adjustment of atomic coordinates in the structure. The relaxed structure of G/h-BN is illustrated in figure (19).

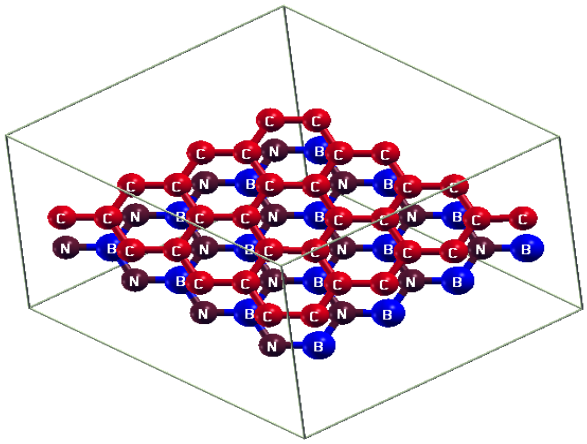

Figure 19: Optimized and relaxed G/h-BN heterostructure (Neupane, et al., 2021).

We have estimated the distance between nearest two B atoms of h-BN in G/h-BN to be 2.48 Å, this is approximate with the values of graphene (2.46 Å) and h-BN (2.50 Å) (Aggoune et al., 2018). Thus, the adjustment of graphene sheet and h-BN are suitable in G/h-BN (Woods et al., 2014). We found the interlayer distance between graphene and h-BN in G/h-BN is 3.28 Å. This lies within 1.50 % with the previously obtained value (Ramasubramaniam et al., 2011; Aggoune et al., 2020). Hence, van der Waals (vdWs) interaction exists in between graphene and h-BN surfaces of G/h-BN heterostructure.

The stability of materials is determined by the value of their binding energy. Higher the value of binding energy (higher negative energy value in the present work), more stable is the system. Thus, we have determined the stability of G/h-BN HS material by finding its binding energy (formation energy) using equation (4.5) (Vu et al., 2020):

$$(E_b)_{G/h-BN} = \frac{E_{G/h-BN} - E_G - E_{h-BN}}{A} \tag{4.5}$$

where, $E_{G/h-BN}$, E_G and E_{h-BN} represent the total ground state energy of G/h-BN, graphene, h-BN respectively. Let A be the area occupied by G/h-BN. The obtained

binding energy of G/h-BN is -41.88 meV/Å^2. This value is comparable with -19.49 meV/Å^2 (Peng et al., 2018) and -31.88 meV/Å^2 (Li et al., 2018) values of other 2D heterostructure materials. The negative binding energy of material reflects that it is strongly stable at ground state. Therefore, we concluded that G/h-BN is a stable 2D vdWs HS material. The estimated parameters regarding to the structural properties of G/h-BN are presented in table (3).

Table 3: Total ground state energy E_t (Ry), binding energy E_b (meV/Å^2), defect formation energy E_d (eV), Interlayer distance r (Å), distance between two carbon (C-C) atoms in graphene d_{CC} (Å), and distance between boron and nitrogen (B-N) atoms d_{BN} (Å) in h-BN of HS materials (Neupane, et al., 2021, 2022).

HS materials	E_t (Ry)	E_b (meV/Å^2)	E_d (eV)	r (Å)	d_{CC} (Å)	d_{BN} (Å)
$G/h-BN$	- 790.6591	- 41.8802	-	3.2824	1.4201	1.4514
$G/h-BN\_1B$	- 771.5331	- 30.3612	0.1912	3.2928	1.4208	1.4612
$G/h-BN\_1N$	- 770.0864	- 38.8331	0.1542	3.2927	1.4206	1.4521
$G/h-BN\_nBN$	- 763.3113	- 23.7924	0.3612	3.3304	1.4203	1.4622
$G/h-BN\_aBN$	- 763.2466	- 28.8342	0.3216	3.3221	1.4203	1.4623
$G/h-BN\_1C$	- 779.0212	- 28.3008	0.1843	3.2923	1.4312	1.4510
$G/h-BN\_2C$	- 767.1102	- 22.8206	0.2444	3.3312	1.4314	1.4511

4.2.3 Vacancy Defected G/h-BN Heterostructures

In this section, we have studied the structural properties of B, N and C sites vacancy defects in G/h-BN HS material. At first, we have constructed 1B defect in G/h-BN (G/h-BN_1B), 1N defect in G/h-BN (G/h-BN_1N), nearest neighbour 1B and 1N defects in G/h-BN (G/h-BN_nBN), alternate-zone of 1B and 1N defects in G/h-BN (G/h-BN_aBN), 1C defect in G/h-BN (G/h-BN_1C), and 2C defects in G/h-BN (G/h-BN_2C) HS materials by detaching 1B atom, 1N atom, nearest neighbour 1B and 1N atoms, alternate-zone of 1B and 1N atoms from h-BN of G/h-BN HS, 1C atom and 2C atoms from graphene of G/h-BN HS material respectively. Then, relax calculations of these materials are performed, since proper atomic coordinates are determined by relax calculations. The optimized and relaxed B and N sites vacancy defects in G/h-BN structures are shown in figure (20), and C sites vacancy defects in G/h-BN structures are emblished in figure (21).

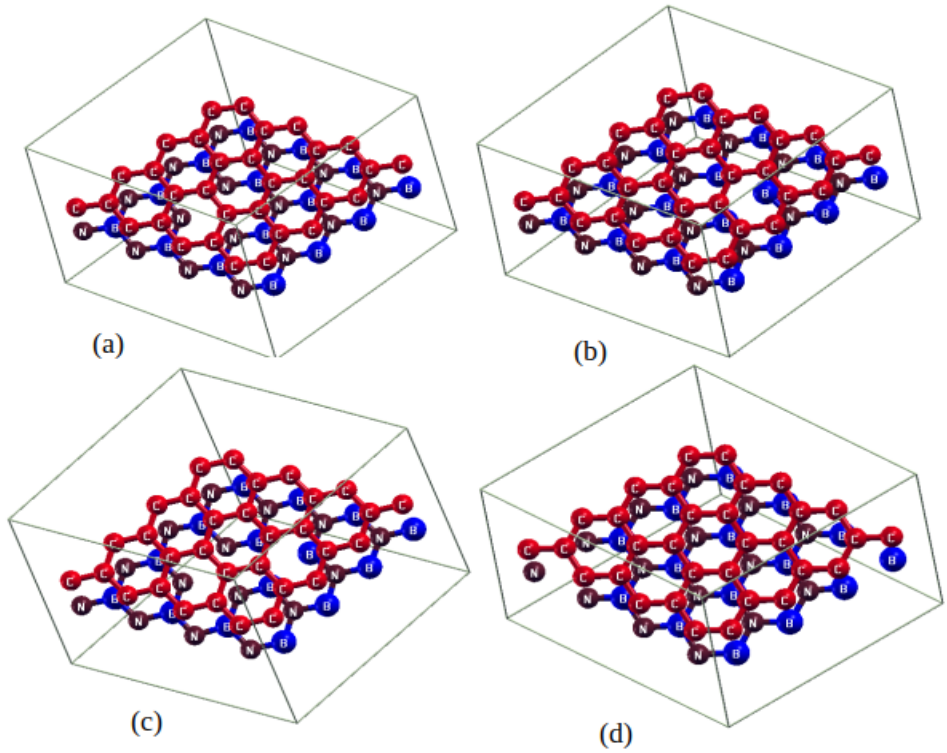

Figure 20: Optimized and relaxed B and N atoms vacancy defected G/h-BN HS materials: (a) G/h-BN_1B HS, (b) G/h-BN_1N HS, (c) G/h-BN_nBN HS, and (d) G/h-BN_aBN HS materials (Neupane, et al., 2021).

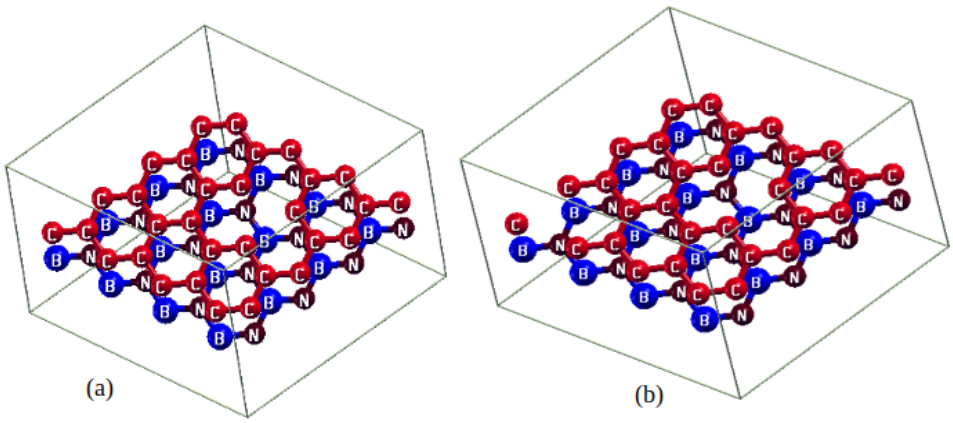

Figure 21: Optimized and relaxed C atom vacancy defected G/h-BN HS materials: (a) G/h-BN_1C HS, and (f) G/h-BN_2C HS materials (Neupane, et al., 2022).

Binding energy of materials are used to predict their stability. Binding energy of G/h-BN_1B, G/h-BN_1N, G/h-BN_nBN, G/h-BN_aBN, materials are calculated by using equation (4.6), and of G/h-BN_1C and G/h-BN_2C materials by using equation (4.7) (Vu et al., 2020; Neupane, et al., 2022):

$$(E_b)_{(G/h-BN)d} = \frac{E_{(G/h-BN)d} - E_G - E_{(h-BN)d}}{A} \tag{4.6}$$

$$(E_b)_{(G/h-BN)d} = \frac{E_{(G/h-BN)d} - E_{(G)d} - E_{h-BN}}{A} \tag{4.7}$$

where, $E_{(G/h-BN)d}$, E_G, $E_{(h-BN)d}$, $E_{(G)d}$, E_{h-BN} and A denote the total ground state energy of B, N and C sites vacancy defected G/h-BN materials, graphene sheet, vacancy defected h-BN, vacancy defected graphene sheet, pristine h-BN sheet, and area occupied by vacancy defected heterostructure materials. The obtained binding energy of G/h-BN_1B, G/h-BN_1N, G/h-BN_nBN, G/h-BN_aBN materials are -30.36 meV/Å^2, -38.83 meV/Å^2, -23.79 meV/Å^2, -28.83 meV/Å^2 respectively (Neupane, et al., 2021), and of G/h-BN_1C and G/h-BN_2C are -28.30 meV/Å^2 and -22.82 meV/Å^2 respectively (Neupane, et al., 2022). These values are comparable with the reported values -31.88 meV/Å^2 and -19.49 meV/Å^2 of other 2D HS materials (like of SiC/graphene HS, Chalcogenides/arsenene HS) (Peng et al., 2018; Li et al., 2018). Therefore, our above mentioned materials are mightily stable at ground state. Among the materials, we considered to study G/h-BN_1N has highest and G/h-BN_2C has lowest stability. Higher the value of binding energy (higher negative values) reveals that they are energetically stable at ground state and exist in nature. We also correlated the binding energy values of vacancy defected materials with the value of pristine G/h-BN material and found that pristine G/h-BN is more stable than defected materials.

In addition, we have estimated the interlayer distance between the constituents of G/h-BN is found to be 3.28 Å, and vacancy defected G/h-BN_1B, G/h-BN_1N, G/h-BN_nBN, G/h-BN_aBN, G/h-BN_1C and G/h-BN_2C are found to be 3.29 Å, 3.29 Å, 3.33 Å, 3.32 Å, 3.29 Å, and 3.33 Å, respectively. They are also comparable with the values 3.80Å, and 3.33Å, of other 2D HS materials (like of SiC/graphene, Chalcobenides/arsenene, graphene/h-BN HS) (Li et al., 2018; Aggoune et al., 2020). It seems that interlayer distances of defected G/h-BN materials are increased than that of pristine G/h-BN. Also, interlayer distance of defected materials are found to be increased with increasing vacancy atom/atoms in G/h-BN HS. Hence, the compactness of material increases with decreasing the defects concentration, and van der Waals interaction (force) exists in between the consistents of HS. Therefore, based on the estimation of binding energy and interlayer distance, we concluded that vacancy defected HS are stable 2D van der Waals HS materials.

In the defected system, it needs to calculate and analyze the defect formation energy because it is also used to predict the stability of materials. Defect formation energy of defected materials are calculated using equation (4.8) (Hou et al., 2012):

$$(E_t)f = (E_t)d - [(E_t)p + n_a\mu_a + n_b\mu_b + n_c\mu_c] \tag{4.8}$$

where, $(E_t)f$, $(E_t)d$, $(E_t)p$, n_a, n_b, n_c, and μ_a, μ_b, μ_c denote the total defect formation energy of a G/h-BN HS material, total ground state energy of defected G/h-BN HS material, total ground state energy of pristine G/h-BN HS material, number of B atom vacancy, N atom vacancy, C atom vacancy in G/h-BN HS material, and chemical potential of B atom, N atom, C atom/s in G/h-BN HS material respectively.

It is found that $(E_t)f$ of G/h-BN_1B, G/h-BN_1N, G/h-BN_nBN and G/h-BN_aBN have values 0.19 eV, 0.15 eV, 0.36 eV and 0.32 eV respectively (Neupane, et al., 2021). And of G/h-BN_1C and G/h-BN_2C materials have values 0.18 eV and 0.24 eV respectively (Neupane, et al., 2022). Lower defect formation energy reflects, materials will be more favorable for the computational work (Hou et al., 2012). The estimated defect formation energy of our study materials are low which reveals that they are suitable materials for the computational research work, and hence these materials are structurally stable and existable in nature. It is seen that single atom vacancy defected HS are more suitable for computational work than double atoms vacancy defected HS materials, since less amount of energy is used to remove the atom from its pristine structure. Therefore, from the analysis of structural properties of pristine G/h-BN and vacancy defected G/h-BN HS materials, they are found to be stable vdWs HS materials. The estimated parameters related to structural properties of vacancy defected G/h-BN HS are illustrated in table (3).

4.3 Electronic Properties

The hardness of solid state matter found on the relative compactness of the constituent atoms (Kwon & Savitskii, 2001). The configuration of electrons of atoms in a material can be predicted by it's energy bands (band structure), thus giving the clear picture of electronic properties of the material (Parmenter, 1952). The energy bands can either be mixed, forbidden or empty, based on which we can say either a solid is a conductor, semiconductor or insulator. Further study of band structure is one of the most broadly used way to study electronic properties of materials (Kittel, 2005). We adopted spin-polarized density functional theory (SDFT) technique (among different techniques like muffin tin approximation, green function approximation, tight binding approximations, nearly free electron approximation) for the calculations of band structures.

4.3.1 Band Structure Calculations

Calculations of band structure of solids come from the solution of Schrdinger equation within the crystal potential. Considering the Kohn Sham equation with effective crystal

potential $v_{eff}(r)$ and energy eigen values ϵ_i:

$$\left(-\frac{\hbar^2}{2m_e}\nabla^2 + v_{eff}(\mathbf{r})\right)\psi_i(\mathbf{r}) = \epsilon_i\,\psi_i(\mathbf{r}) \tag{4.9}$$

To solve this equation within the crystal, we need to know the nature of effective crystal potential. The nature of such effective crystal potential was given by Bloch. According to Bloch theorem, the crystal potential is a periodic potential (Blochl et al., 1994; Parmenter, 1952) i.e. $v_{eff}(\mathbf{r} = v_{eff}(\mathbf{r} + \mathbf{R_l})$ and there always exists a vector k such that the translation of wave function by a lattice vector R_l is equivalent to multiplying by the phase factor, $e^{ik.R_l}$. Mathematically (Parmenter, 1952):

$$\psi_k(\mathbf{r} + \mathbf{R_l}) = e^{ik.R_l}\psi_k(\mathbf{r}) \tag{4.10}$$

The wave vector defined in a Bloch theorem is a good quantum number for a periodic system. As seen in equation (4.10) if k satisfies Bloch theorem, $(\mathbf{k} + \mathbf{R_l})$ also satisfies Bloch theorem, where $\mathbf{R_l}$ is the reciprocal lattice vector. Hence, all possible values of $\mathbf{k}$ can be confined to the unit cell of reciprocal lattice (i.e. confined to the first brillouin zone). In the present work, we have used Quantum ESPRESSO codes (Giannozzi et al., 2009) to calculate band structure of our systems by characterizing the behavior of solids in a first brillouin zone (BZ). The first BZ of our considered heterostructures (hexagonal lattice) with **Γ–M–K–Γ** high symmetric points is shown in figure (22), where **Γ** is the center of the zone, **M** and **K** are two end points of the sides of any face.

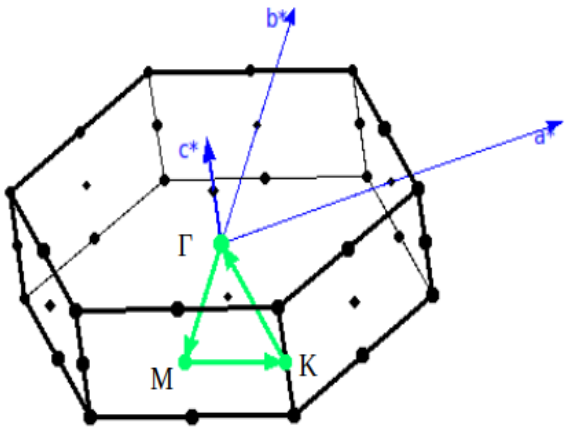

Figure 22: Brillouin zone (BZ) of hexagonal crystal structure showing highly symmetric points **Γ–M–K–Γ**, where **Γ** is the center of the zone, **M** and **K** are two end points of the sides. a^*, b^* and c^* represent the reciprocal lattice vectors along X-, Y- and Z-directions respectively.

For each points on the BZ there are different values of **K** and for each **K**, there are many eigen values of Hamiltonian that are labeled as $\epsilon_n(\mathbf{k})$, where n is the band index. A plot of $\epsilon_n(\mathbf{k})$ versus **K** is called the band structure (Huat et al., 2014). Therefore, Bloch

theorem greatly facillitates the solution of Kohn Sham equations leading the calculations of band structure of solids.

The band structure and density of states calculations involve the integration over BZ. The structure of BZ differs with structure of primitive cell of crystal. There are several methods to perform such integrations over the first BZ, such as Gaussian-broadened sampling integration (Elsasser et al., 1994), Fermi-Dirac-broadened sampling integration (Kratzer & Neugebauer, 2019), and Tetrahedron integration (Blochl et al., 1994). In our calculations, Quantum ESPRESSO uses the modified tetrahedron method which was the modified version of tetrahedron method bt Blochel et al. (Blochl et al., 1994). The possibility of translation symmetry in crystaline solid allows us to define a quantum number called crystal momentum **K**. Therefore, wave functions $\psi_n(\mathbf{k})$ and energy eigen values $\epsilon_n(\mathbf{k})$ are found to be depend on band index n and crystal momentum vector **K**. The modified tetrahedron method involves the BZ integration by the division of irreducible BZ into several tetrahedrons in which energy eigen values and matrix elements are linearized in **K** (Blochl et al., 1994). Energy eigen values and matrix elements are calculated for the k-points which lie at the corners of these tetrahedrons and rest of the eigen values and matrix elements are for whole tetrahedrons are obtained by linear interpolation and integration over that tetrahedron (Blochl et al., 1994). Finally integration is obtained by summing over all tetrahedra.

Band Structure Calculations of Graphene and h-BN

We have performed the band structure calculations of monolayer graphene sheet and h-BN by taking the high symmetry points **Γ–M–K–Γ** on the first brillouin zone (BZ) of hexagonal lattice as shown in figure (22), for which we have taken high symmetric 100 k-points along this specific direction in order to find fine band structure. Each carbon atom in graphene consists of four valence electrons. Valence electrons in $2s$, $2p_x$ and $2p_y$ orbitals of three carbon atoms interact with its three nearest neighbour carbon atoms. An electron in $2p_z$ orbital of carbon atom overlaps with the electron of nearest $2p_z$ orbital of other carbon atoms. The band structure of graphene emanating from $2p_z$-orbital of carbon atoms because electronic properties of graphene are predicted by mobile (loosely bounded) electrons of carbon atoms (Novoselov et al., 2004, 2005). The band structure plots of 4×4 supercell of graphene and 4×4 supercell of h-BN monolayers are shown in figure (23). Where, high symmetric points in the direction of irreducible BZ are taken in X-axis and their corresponding energy are taken in Y-axis.

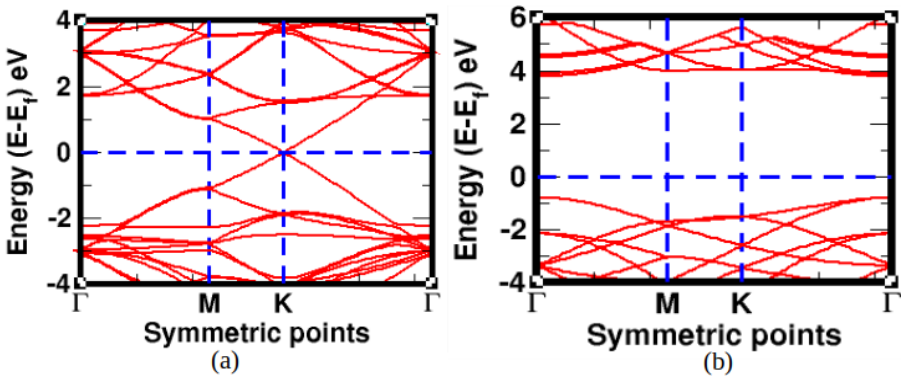

Figure 23: Band structure of graphene and h-BN supercells in spin-polarized calculations, where the Fermi level is set to zero: (a) band structure plot of 4×4 graphene supercell structure, (b) band structure plot of 4×4 h-BN supercell structure (Neupane, et al., 2021).

In figure (23a), the Fermi energy level is denoted by horizontal dotted line. The region above the horizontal dotted line is called conduction band and below the horizontal dotted line is called valence band. Band states in the conduction band indicates to π^* band and band states in the valence band indicates to π band. These π^* and π bands of 4×4 graphene supercell are meet at high symmetric K-point on the Fermi energy level, known as Dirac point (cone) as shown in figure (23a). Hence, valence band and conduction band of graphene supercell do not overlap. Hence, it has zero band gap energy. It indicates that graphene is a zero band gap material. The estimated band gap energy of graphene is E_g = 0 eV. This is fairly in aggreement with experimentally reported value (Novoselov et al., 2004). Graphene is a zero band gap semiconducting material.

In spite of numerous studies that has been done on h-BN till date, nature of h-BN is very controversial with the doubtful band gap. Previously calculated reports suggest that the gap ranges from 3.0 eV to 7.5 eV (Ooi et al., 2005; Abdellaoui et al., 1997; Solozhenko et al., 2001; Watanabe et al., 2009), this might be due to the use of different simulation methods, eventhough such a huge variations seem quite confusing. In the mean time, nature of band structure also seems debatable with some reports suggesting the bands to be direct; while other report to be opposite, indirect, leading to ambiguous conclusions. Therefore, we have performed the band structure calculations of pristine h-BN taking the high symmetry points **Γ–M–K–**Γ on the first (BZ) of hexagonal lattice as shown in figure (23b). Where high symmetric points are plotted in X-axis and represents the high symmetric points and energy values are taken in Y-axis. The horizontal dotted line indicates Fermi enery level which separates the electronic bands. We observed that top of the valance band and bottom of conduction band are located at **Γ** symmetric point of 4×4 h-BN supercell. It indicates the direct nature of band structure with band gap energy of 4.98 eV value. Our estimated band gap lies within the range of experimentally band gap (Watanabe et al., 2004). h-BN is a wide band gap material.

Band Structure Calculations of G/h-BN HS

Band structure calculations of van der Waals (vdWs) G/h-BN heterostructure (HS) material are performed by defining highly symmetric points on the edge of brillouin zone (BZ). A sampling path of **Γ–M–K–**Γ is used for band structure calculations. The K-path is shown in figure (22), and the resulting band structure is shown in (24a), where X-axis represents different symmetric points of BZ and Y-axis represents energy value with reference taken as Fermi energy.

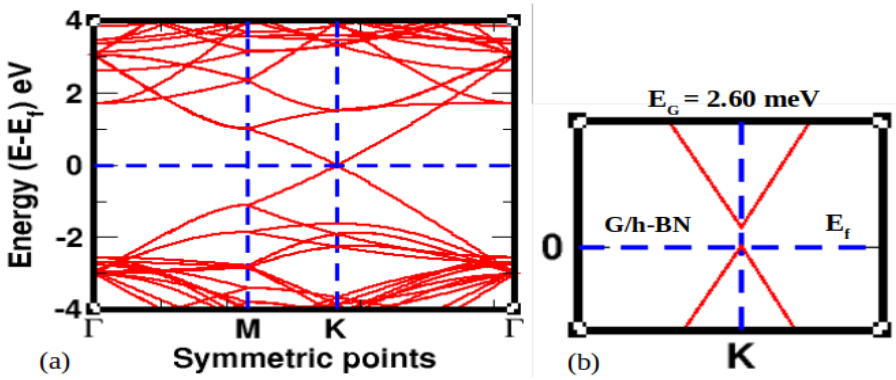

Figure 24: Band structure of vdWs G/h-BN heterostructure in spin-polarized calculations: (a) band structure plot of G/h-BN HS, (b) zoom scale band structure plot of G/h-BN HS, where small band gap is appeared at high symmetric K-point in the first BZ (Neupane, et al., 2021).

In band structure, estimated bands of G/h-BN appeared as a superposition of its constituents. This is because the covalent bonds within the layers are not changed in the establishment of the HS. Fermi energy and total ground states energy of graphene are -2.54 eV and -397.7808 Ry, and of h-BN are -3.20 eV and -426.6251 Ry respectively, while that of G/h-BN are -1.26 eV and -790.6591 Ry. That means, Fermi level shifted towards the conduction band in HS material. Hence, there will be a chance to flow the electrons from valence to conduction band. Hence, it has metallic nature. Moreover, we carefully observed band states around the Fermi energy level. It is found that a small band gap of value 2.60 meV open at K-point in the band state of graphene as shown in figure (24b), because there will be a weak interactions existing in beween graphene and h-BN supercells. Hence, GGA calculations with PBE exchange correlation showed the narrow band gap of 2.60 meV, obtained at top of the valance band and bottom of conduction band, which are located at K-point of first BZ. Therefore, by the analysis of band structure, we predicted that vdWs G/h-BN HS has semimetallic properties.The materials having more than 400 meV band gap energy values, they are called semiconductor.

Band Structure Calculations of B, N and C Sites Vacancy Defected G/h-BN HS

For the study of our queries on the nature of defected G/h-BN HS with B, N and C sites vacancy atoms, we need to calculate their band structures. So, electronic properties of B, N and C atoms vacancy defected G/h-BN HS materials are determined by the inspection of their band structure. Band structure of defected G/h-BN HS materials with B, N and C sites vacancy atoms are illustrated in figures (25), (26) and (27) respectively. We have selected 100 K-points on the specific position of invariant BZ by taking **Γ–M–K–**Γ high symmetric points are taken in X-axis and the energy values are taken in Y-axis. The horizontal dotted line detaches the electronic bands (i.e. region above the horizontal dotted line is called conduction band, and below horizontal dotted line is called valence band). In this work, we have separately studied the band structures of B, N and C atoms vacancy defected HS materials. We found that band states of h-BN in the valence band are very approaching (0.01 eV) to the Fermi energy level. But in conduction band, they appear slightly away (1.70 eV) from the Fermi energy level as shown in figure (25a) (Neupane, et al., 2021). It reflects that p-type Schottky contact has preeminent role than n-type Schottky contact. Therefore, h-BN opens band gap of value 1.71 eV in G/h-BN_1B HS (Neupane, et al., 2021). Nevertheless, band states of graphene are unmoving and seems as like in band plot of G/h-BN HS. We intensely analyzed the band plot of G/h-BN_1B, it is found to be 9.75 meV band gap energy at high symmetric K-point as shown in figure (25b) (Neupane, et al., 2021). Similarly, we have developed and analyzed the band structure of G/h-BN_1N HS material as shown in figure (25c), where 2.45 eV energy gap is obtained by the cause of the contributions of n-type and p-type Schottky contacts in bands structure (Neupane, et al., 2021). The p-type and n-type Schottky contacts have values 2.45 eV and 0 eV respectively (Neupane, et al., 2021), hence n-type Schottky contact has presiding role in G/h-BN_1N. In addition, we conscientiously invistigated the effect of graphene in band structure of G/h-BN_1N. Band gap energy 33.84 meV found at high symmeric K-point in band structure as shown in figure (25d) (Neupane, et al., 2021). Because of two alike C atoms exposed to two distinct electrostatic potentials caused by B and N atoms, small band gaps are obtained in B and N sites vacancy defected materials. Therefore, G/h-BN_1B and G/h-BN_1N materials have semimetallic properties. We also compared the band gap energy of G/h-BN_1B and G/h-BN_1N with non-defected G/h-BN, and found that band gap energy of G/h-BN_1B and G/h-BN_1N have slightly higher values than of G/h-BN, but band gap created by h-BN in defected materials have lower values than of G/h-BN, which are summarized in table (4).

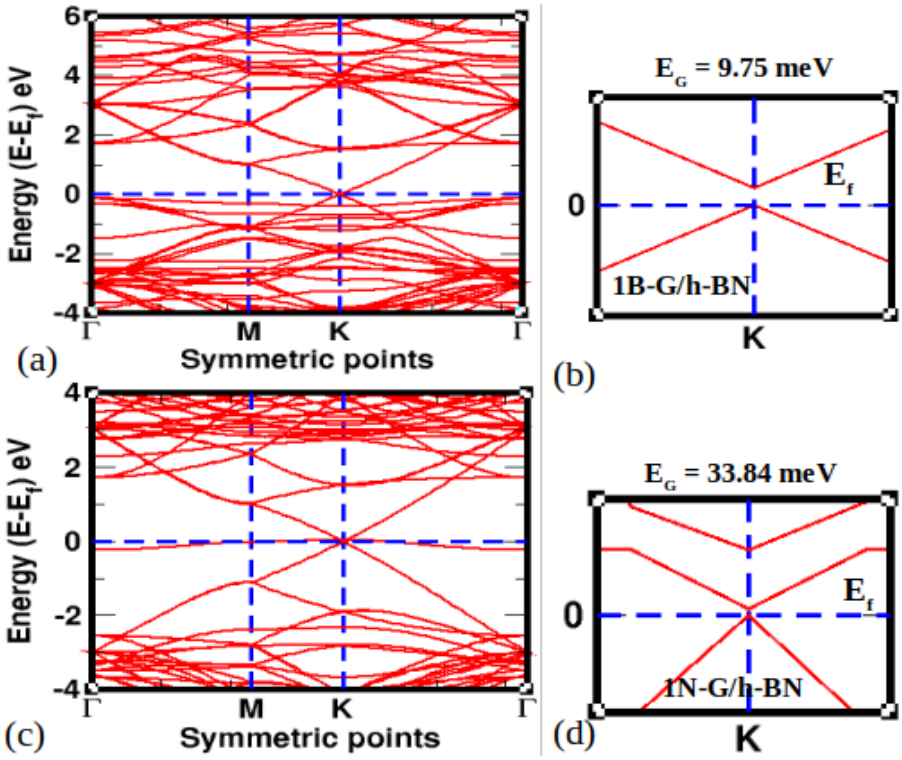

Figure 25: Band structures of B and N sites vacancy defected vdWs G/h-BN heterostructure in spin-polarized calculations: (a) band structure of G/h-BN_1B HS, (b) zoom scale band plot of G/h-BN_1B HS, (c) band structure of G/h-BN_1N HS, (d) zoom scale band plot of G/h-BN_1N HS. In zoom scale of band plots, small band gap is appeared at high symmetric K-point in the first BZ (Neupane, et al., 2021).

In addition, we have analyzed the band structure calculations of G/h-BN_nBN and G/h-BN_aBN materials which are illustrated in figure (26). Highly symmetric points are taken in X-axis and energy values are taken in Y-axis. Also, horizontal dotted line separates the electronic bands in it. We have determined the band states of h-BN in both G/h-BN_nBN and G/h-BN_aBN materials. It is found that they locate closer to the Fermi energy level. Hence, n-type and p-type Schottky contact are formed and found to be 0.35 eV and 1.76 eV of G/h-BN_nBN and of 0.69 eV and 1.22 eV of G/h-BN_aBN respectively. Thus, total band gap energy obtained by h-BN in G/h-BN_nBN and G/h-BN_aBN materials are 2.11 eV and 1.91 eV values respectively. These values are also smaller than that of G/h-BN. It is also observed that n-type Schottky contact are formed in both materials. We precisely calculated the band gap energy of G/h-BN_nBN and G/h-BN_aBN, and found 1.71 meV and 2.73 meV values at high symmetric K-point as shown in figures (26b) and (26d) respectively. Small band gaps are opened in all B and N atoms vacancy defected materials because two unequal C atoms have a equivalent chemical condition. Hence, electronic bands in graphene can go through weakeing at K-point, by forbidding the opening of band gap. Therefore, G/h-BN_1B, G/h-BN_1N, G/h-BN_nBN and G/h-BN_aBN are semimetallic materials.

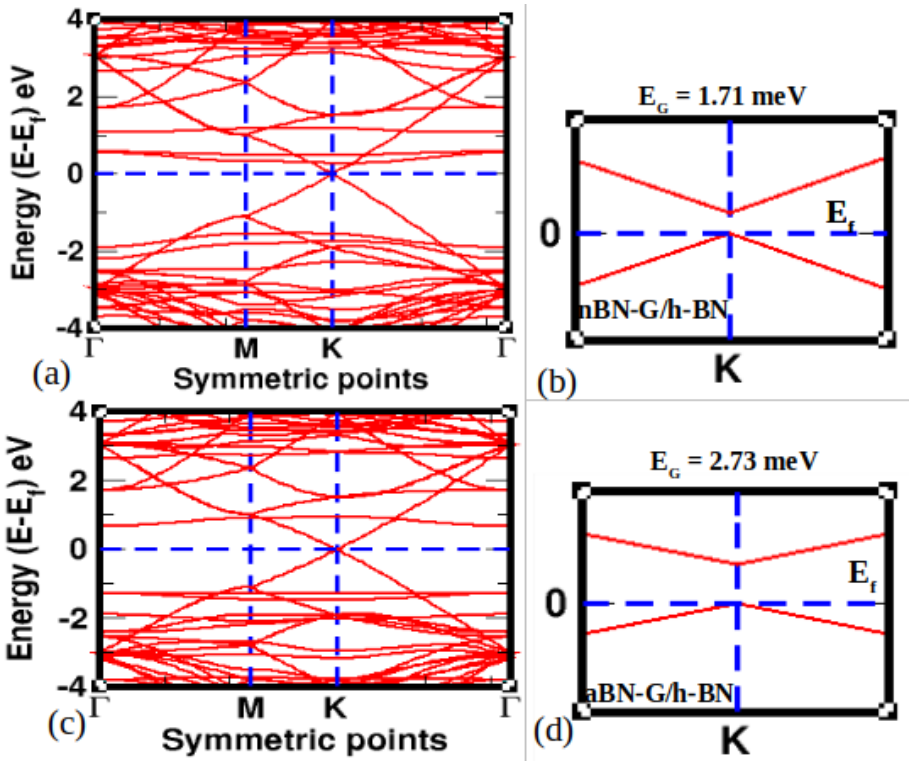

Figure 26: Band structure of B and N sites vacancy defected vdWs G/h-BN heterostructure in spin-polarized calculations: (a) band structure of G/h-BN_nBN HS, (b) zoom scale band plot of G/h-BN_nBN HS, (c) band structure of G/h-BN_aBN HS, (d) zoom scale band plot of G/h-BN_aBN HS. In zoom scale of band plots, small band gap is appeared at high symmetric K-point in the first BZ (Neupane, et al., 2021).

Moreover, we have examined the band structure of G/h-BN_1C and G/h-BN_2C HS materials for the study of their electronic properties, which are shown in figure (27) (Neupane, et al., 2022). The symmetric points that we choose in order to calculate band structure are **Γ–M–K–**Γ taken in X-axis and their energy values taken in Y-axis. Fermi energy level is noted by horizontal dotted line, it distinguishes the electronic bands. The band gap energy of 5.97 eV (Neupane, et al., 2022) is established by h-BN in G/h-BN_1C HS, which is the sum of p-type and n-type Schottky contacts of values 2.28 eV and 3.69 eV respectively. Likewise, we have computated the band gap energy of G/h-BN_2C by the effect of h-BN and found to be 5.99 eV, this is also due to the sum of n-type and p-type Schottky contacts of values 3.63 eV and 2.35 eV respectively. We have compared the calcualted band gap energy of G/h-BN_1C and G/h-BN_2C materials with that of pristine G/h-BN, and found that G/h-BN_1C has slightly higher value than that of pristine HS material because dangling bonds are formed at graphene surface of G/h-BN HS material by 1C vacancy atom. But G/h-BN_2C has lower value than that of G/h-BN. By careful inspection, 1C vacancy atom in graphene of HS disturbs the specific symmetries. Hence, linearly crossing bands present around the Fermi energy level of G/h-BN_1C as shown in figure (27a). We noted that electronic bands associated with dangling bond and revived C-C bond of vacancy develop close to the top of valence band and in the conduction band of G/h-BN_1C HS material as shown in (27a)-(27b).

Hence, G/h-BN_1C has obtained small band gap of value 0.40 eV at K-point in the Fermi energy level of band structure. Thus, G/h-BN_1C is semiconducting in nature. In G/h-BN_2C, no states are attached with dangling bond but reconstructed C-C bond come about on all sides of vacancy atoms. So that band states are elevated in the vicinity of Fermi energy level as illustrated in figures (27c)-(27d). 2C vacancy atoms in graphene of HS interrupts the specified symmetries. The linearly crossing bands are presented at Fermi energy level. They limits the vacancy states correlated to the flat bands observed in band gap. Thus, G/h-BN_2C has continious energy bands at the Fermi enery level. And hence it has zero band gap energy. Therefore, by the analysis of band structure calculations, we found that G/h-BN_2C HS material has metallic properties.

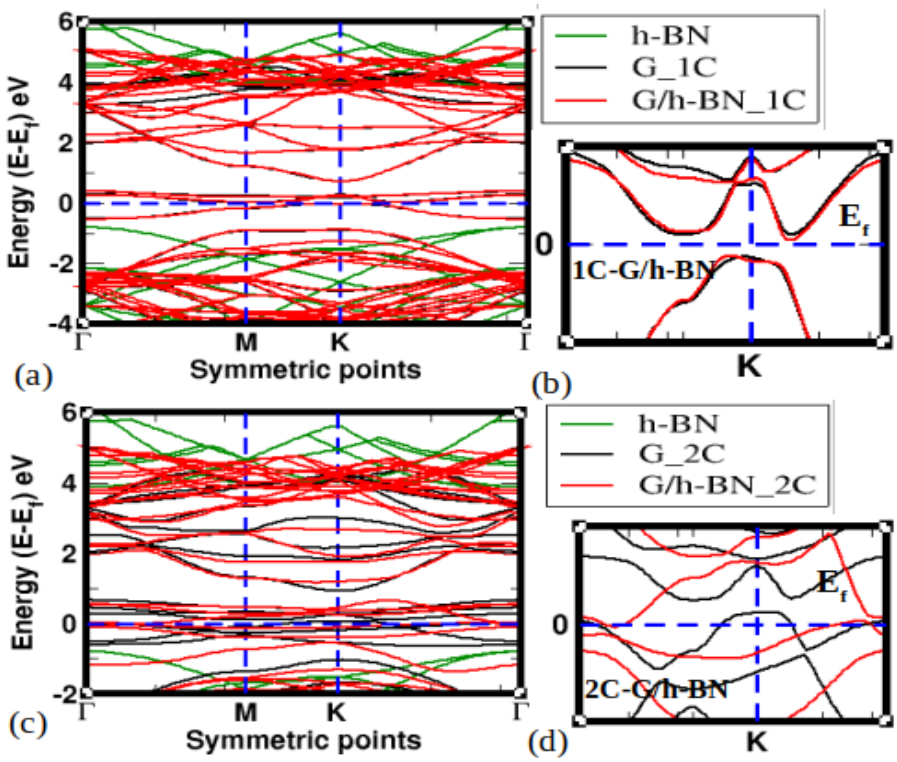

Figure 27: Band plots of C atom/s vacancy defected vdWs G/h-BN HS in spin-polarized calculations: (a) band structure of G/h-BN_1C HS , (b) zoom scale band plot of G/h-BN_1C HS, (c) band structure of G/h-BN_2C HS, (d) zoom scale band plot of G/h-BN_2C HS (Neupane, et al., 2022).

Data regarding to electronic properties of B, N and C sites vacancy defected materials are summarized in table (4).

Table 4: Fermi energy (E_f), band gap energy of graphene in heterostructure (HS) (E_G), band gap energy of h-BN in HS (E_g), change of band gap energy value of h-BN in HS from the calculated band gap energy value (4.98 eV) of monolayer (ML) h-BN (E_{cg}) of G/h-BN, G/h-BN_1B, G/h-BN_1N, G/h-BN_nBN, G/h-BN_aBN, G/h-BN_1C and G/h-BN_2C HS materials (Neupane, et al., 2021, 2022).

ML and HS materials	E_f (eV)	E_G (meV)	E_g (eV)	E_{cg} (eV)	Nature of materials
Graphene	- 2.18	-	-	-	zero band gap
h-BN	- 3.20	-	-	-	wide band gap
G/h-BN	- 1.26	2.60	3.78	1.20	semimetallic
G/h-BN_1B	- 2.18	9.75	1.71	3.27	semimetallic
G/h-BN_1N	- 1.04	33.84	2.45	2.53	semimetallic
G/h-BN_nBN	- 1.31	1.71	2.11	2.87	semimetallic
G/h-BN_aBN	- 1.31	2.73	1.91	3.07	semimetallic
G/h-BN_1C	- 1.65	0.40 eV	5.97	- 0.99	semiconductor
G/h-BN_2C	- 1.64	-	5.99	- 1.01	metallic

4.4 Magnetic Properties

Magnetic properties of materials are great enticing properties because modern technological devices await on the magnetic materials. Magnetic materials have budding employment in the various distinct areas. They are used in biomedicine, catalysis, molecular biology, biochemistry, diagnosis, nanoelectronic materials, sensors: magnetic and pressure sensors, and computers (Makarova et al., 2019; Peng et al., 2016). In this work, we have investigated the magnetic properties of monolayers (ML) graphene (G) and h-BN, and heterostructure (HS) G/h-BN, G/h-BN_1B, G/h-BN_1N, G/h-BN_nBN, G/h-BN_aBN, G/h-BN_1C and G/h-BN_2C materials by the analysis of DOS and PDOS calculations. They are described as follows.

4.4.1 Estimation of DOS and PDOS

DOS is one of very useful quantities that we frequently encounter in electronic structure calculations of solids. It is defined as the number of electronic states per unit energy range per unit cell. It gives an idea about the presence of quantum states in a materials. It provides an insight of different electronic and magnetic properties of solids and is of immense importance in condensed matter physics (Liu, et al., 2005; Neupane, et al., 2020). DOS also helps to find out different thermodynamic properties such as internal energy, the number of particles, thermal conductivity and specific heat c apacity. The nature of materials also depends on the value of DOS. Zero value of DOS means, no states are occupied at the energy level. It is called a forbidden gap. On the other hand,

high value of DOS reflects that many band states are available to occupy in a particular energy level (Kittel, 2005). DOS counts the number of energy states closeby a given energy value in computational physics and chemistry. It means DOS represents the electronic eigen states in energy space of a molecule. Magnetic properties of materials are predicted using certain measuring parameters, which are determined through DOS calcualtions. Therefore, DOS aids in the prediction of magnetic properties of matter with the calculations of certain measuring parameters. The magnetic moment (μ) is given by DOS calculations of the system considered. The total magnetic moment of materials is defined by $\mu = \mathrm{m}\mu_B$, here m denotes the number of unpaired electrons, μ_B is given in SI unit of Bohr magneton. m is calculated on the basis of presented spin states of electrons in the orbitals of atoms present in DOS plot of material.

The DOS projected over any arbitrary state is called PDOS. PDOS calculations are used to investigate the contributions of all individual orbitals of atom in total DOS (TDOS) of material. PDOS grants the relative aiding to TDOS. Hence, it assists to examine impact of each atom or molecule in the whole systems. In present work, we have performed spin-polarized DFT level of approximation for the calculations of DOS and PDOS of graphene and h-BN ML supercell structures, pristine G/h-BN HS, and B, N and C atoms vacancy defects in G/h-BN HS materials. The up-and down-spin states of electrons in the orbitals of atom present in material gives up-DOS (D_u) and down-DOS (D_d) respectively:

$$m = \int_{-\infty}^{\infty} (D_u(\varepsilon) - D_d(\varepsilon)) d\varepsilon \tag{4.11}$$

Equation (4.11) shows if DOS for up-spin electrons and DOS for down-spin elctrons are equal i.e. symmetrical, system will be non-magnetic. If DOS for up-spin electrons is not equal to that for down-spin electrons i.e. asymmetrical, system will be magnetic. Therefore, symmetrically distributed spins-state in the orbitals of atom present in the material reavels that material has non-magnetic properties. It means distrubuted up-and down-spin states of electrons in the orbitals of atom has zero value of total spin (Kittel, 2005). On the other hand, unpaired up and down spins states in the orbitals of atoms present in the material are asymmetrically distributed, causing magnetic moment and hence material has magnetic properties (Kittel, 2005). The detail discussions about DOS and PDOS calculations of considered materials are given as below.

DOS and PDOS Calculations of Graphene and h-BN Monolayers (ML)

To study the magnetic properties of graphene and h-BN ML supercell structures, we have performed spin-polarized DFT method of calculations. At first, we have calculated

the DOS of up and down spins of graphene supercell to explore its magnetic properties. We have plotted the DOS of up and down spin states of graphene as shown in figure (28a). The states above and below the horizontal line respectively represent up-spin and down-spin. It is seen that up and down spin are symmetrically distributed around the Fermi level showing non-magnetic substance i.e. magnetic moment is zero. DOS of up and down spin states meet at a Fermi energy level, and hence DOS of graphene is equal to zero. In order to investigate the magnetic properties of h-BN ML supercell by the analysis of DOS calculations of it. DOS calculations of presented up and down spin states of electrons in the orbital of atoms are separately shown in figure (28b), where Fermi energy is represented by the vertical dotted lines as reference. The forbidden gap corresponding to that in band structure is given by the gap around the Fermi level. In figure (28b), left hand side from the reference level represents valance band whereas right hand side represents the conduction band. The DOS plot of h-BN supercell is found to be perfectly symmetric of up-spin and down-spin as shown in (28b), representing the non-magnetic nature. We have also determined the band gap energy of h-BN and found to be 4.98 eV, it shows that h-BN is a wide band gap semiconductor. Thus, pristine h-BN sheet is a non-magnetic and wide band gap semiconducting material, which agrees with previously reported work (Ooi et al., 2005).

Additionally, for details study of DOS of graphene and h-BN ML, we have computed the projected density of states (PDOS) of different orbitals of carbon atoms in graphene, and orbitals of boron and nitrogen atoms in h-BN. To observe the contributions of valence electrons in PDOS calculations of present work, we have used ultrasoft pseudopotentials (USPPs). The electronic configuration of carbon, boron and nitrogen atoms (valence electrons) are [C] $2s^2 2p^2$, [B] $2s^2 2p^1$ and [N] $2s^2 2p^3$ respectively. Valence electrons present 2p and 2s orbitals of C, N and B atoms. So, we have calculated the contributions of only those two orbitals in PDOS of graphene and h-BN. We found that 2p orbitals of carbon atoms in graphene, and 2p orbitals of boron atoms as well as 2p orbitals of nitrogen atoms in h-BN have significant contributions in total DOS, which appear at periphery of Fermi energy level. 2s orbitals of carbon atoms in graphene, and boron and nitrogen atoms in h-BN have negligible effect to generate the magnetic moment in materials.

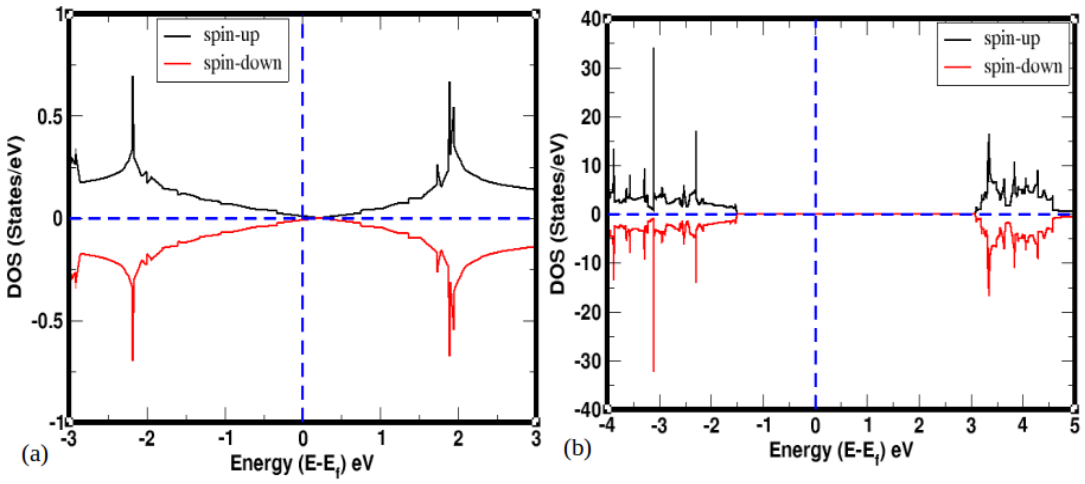

Figure 28: DOS calculations of 2D graphene and h-BN ML: (a) DOS of total up and down spin states of graphene, (b) DOS of total up and down spin states of h-BN. Vertical dot line is a Fermi level and horizontal dot line separates up and down spin states

.

DOS and PDOS Calculations of G/h-BN Heterostructure (HS)

We have performed DFT method within the frame work of DFT-D2 approximation for the calculations of DOS and PDOS of 2D, vdWs G/h-BN HS material. Magnetic properties (magnetic moment) of G/h-BN HS is computed through its DOS and PDOS calculations as shown in figure (29). Total number of states per unit energy range (in eV) and its corresponding energy are plotted in Y-axis and X-axis respectively. Total up and down spin states of electrons in orbitals of atoms present in G/h-BN material are symmetrically distributed in DOS plot, as shown in figure (29a). It indicates that G/h-BN is a non-magnetic material. Also, DOS of up and down spin states are appeared to be zero at Fermi energy level. It reflects that G/h-BN has metallic properties, since there is no possibility of band gap energy. By conscientiously observation in PDOS plot as shown in figure (29b), unpaired up and down spin states of electrons in the orbitals of atoms in G/h-BN are found to be slightly asymmetrical near the Fermi level, depicting the feebly magnetic nature with total magnetic moment 0.04 $\mu_B/cell$. Thus, it behaves as weakly magnetic material. Hence, G/h-BN has a approving state for magnetism (Repellin et al., 2020; Chatterjee et al., 2020; Liu & Dai, 2020). The obtained magnetic moment is contributed by unpaired spin states in the orbitals of valence electrons of carbon, boron and nitrogen atoms, which are shown in figure (29b) and given in table (5). It is found that 2p of carbon atoms have dominant contributions for the magnetism in G/h-BN material. Also, down spin states of electron in 2p of carbon atoms appear at Fermi energy level, while up spin states disappear at Fermi energy level. From the calculations of asymmetrically distributed unpaired up-and down-spin states around the Fermi energy level, we concluded that 2p orbitals of carbon atoms in graphene of G/h-BN has opened

very small (2.60 meV) band gap. G/h-BN has semimetallic and magnetic properties.

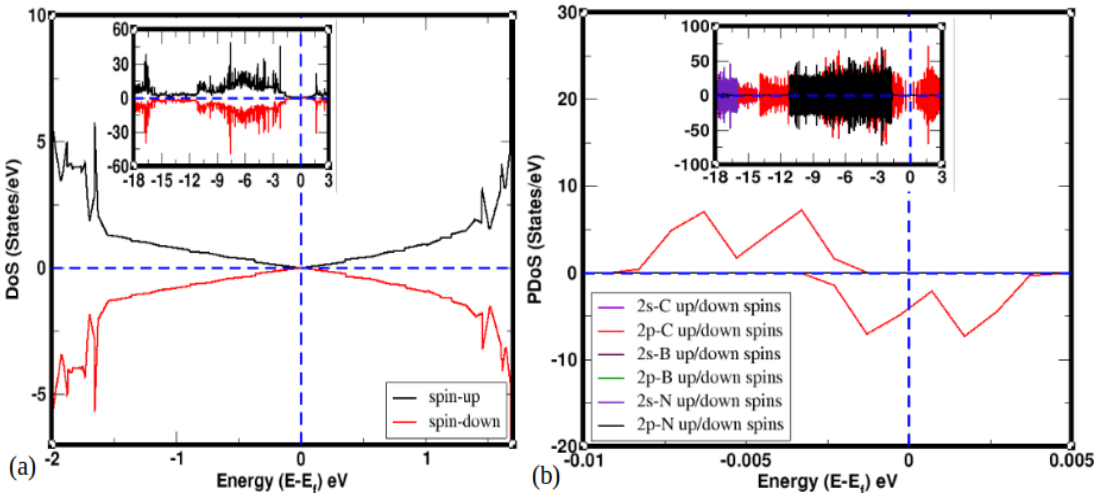

Figure 29: DOS and PDOS calculations of 2D vdWs G/h-BN HS material: (a) DOS of total up and down spin states of G/h-BN HS, (b) PDOS of individual up and down spin states of C, B, and N atoms present in G/h-BN HS. Vertical dot line is a Fermi level and horizontal dot line separates up and down spin states. Insets in the plots signify the spin states having large energy range in X-axis (Neupane, et al., 2021).

.

DOS and PDOS Calculations of Vacancy Defected G/h-BN Heterostructures (HS)

Magnetic properties of vacancy defected G/h-BN HS materials are predicted based on their DOS and PDOS calculations. At first, we have obtained DOS and PDOS plots of G/h-BN_1B HS as shown in figures (30a) and (30b) respectively. In these figures, vertical dot line is a Fermi level and horizontal dot line separates up and down spin states. Regions of left hand side and right hand side from the Fermi energy level denote the valence band and conduction band respectively. Also, X-axis represents the energy of HS material (in eV) taking Fermi energy (reference energy) level set to zero and Y-axis represents the number of energy states per unit energy (in eV^{-1}). It is found that total up and down spin states are asymmetrically distributed in DOS plot of G/h-BN_1B as shown in figure (30a), which noted that G/h-BN_1B has magnetic properties. DOS of total down spin states present at Fermi energy level but DOS of total up spin states are not presented there. It refers to small band gap energy of 9.75 meV at Fermi level, and hence G/h-BN_1B has semimetallic properties. More detail informations regarding to magnetic properties of G/h-BN_1B material are determined through PDOS analysis of it, shown in figure (30b). We found that unpaired up and down spin states of valence electrons in the orbitals of individual atoms are asymmetrically distributed around the Fermi energy level. It reavels that material has magnetic properties. The magnetic moment generated in G/h-BN_1B material due to the preeminent grants from 2p orbitals of carbon, boron and nitrogen atoms. Among them down spin states of valence electron in 2p of N atoms have greater contributions than other orbitals, which are illustrated in

figure (30b) and also in table (5). On the other hand, 2s orbital of valence electrons of carbon, boron and nitrogen atoms has weak impact for the growth of magnetic moment (magnetism) in material. In particular, magnetic moment brought by up and down spin states of valence electrons in 2s, 2p of C atoms is - 0.02 $\mu_B/cell$, - 0.11 $\mu_B/cell$; 2s, 2p of B atoms is - 0.03 $\mu_B/cell$, - 0.91 $\mu_B/cell$; and 2s, 2p of N atoms is - 0.06 $\mu_B/cell$, - 1.83 $\mu_B/cell$ respectively. Total magnetic moment is the sum of magnetic moment given by individual orbitals of valence electrons of atoms in the material. Hence, total magnetic moment (μ_T) of G/h-BN_1B is equal to - 2.96 $\mu_B/cell$. Therefore, G/h-BN_1B has magnetic properties. We have compared the magnetic moment of G/h-BN_1B with that of pristine G/h-BN material, and found that defected HS material has higher value of magnetic moment than that of pristine (non-defected) HS material. The negative sign of magnetic moment indicates that down spin states of electrons in the orbitals of atoms have dominant role for the developement of magnetic moment than the up spin states of electrons in PDOS of G/h-BN_1B.

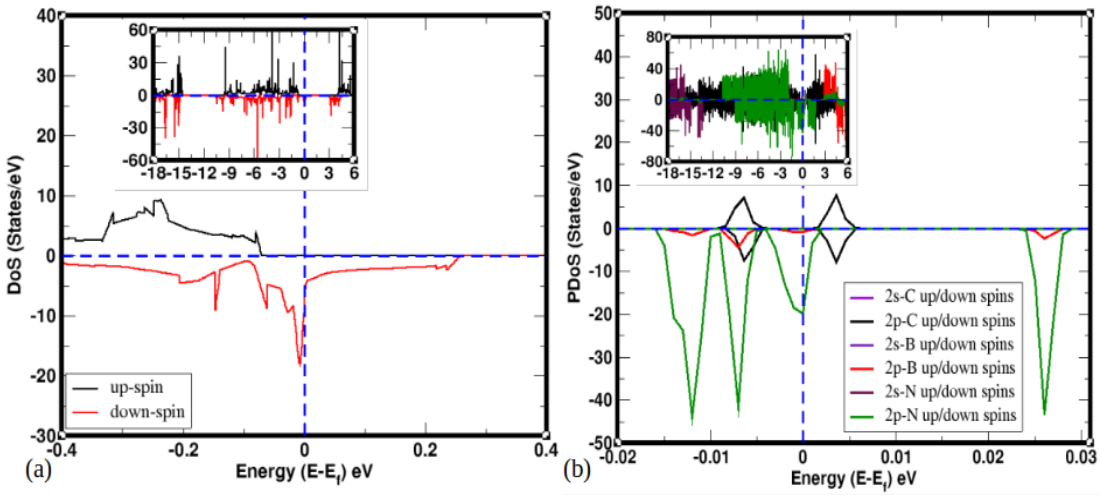

Figure 30: DOS and PDOS calculations of 2D vdWs G/h-BN_1B HS material: (a) DOS of total up and down spin states of G/h-BN_1B HS, (b) PDOS of individual up and down spin states of C, B, and N atoms of G/h-BN_1B HS. Vertical dot line is a Fermi level and horizontal dot line separates up and down spin states. Insets in the plots signify the spin states having large energy range in X-axis (Neupane, et al., 2021).

.

Similarly, we have computed the magnetic moment of G/h-BN_1N HS material through its DOS and PDOS plots. Figure (31a) is a DOS plot of G/h-BN_1N, where X-axis represents the energy of HS material (in eV) taking Fermi energy (reference energy) level set to zero and Y-axis represents the number of energy states per unit energy (in eV^{-1}). Also, vertical dot line is a Fermi level and horizontal dot line separates up and down spin states. Fermi level separates the electronic bands, since regions of left hand side and right hand side from the Fermi level denote valence band and conduction band respectively. We found that total up and down spin states are appeared asymmetrical

around the Fermi energy level in DOS plot of G/h-BN_1N as shown in figure (31a). Hence, G/h-BN_1N has magnetic properties. We have examined the DOS plot and found that DOS of total up spin states present at Fermi energy level, which means orbitals are available for the occupation, whereas DOS of total down spin states are not appeared at the Fermi level, reflects that occupied states are presented there called forbidden gap. It concludes that small band gap (33.84 meV) open at Fermi energy level, hence G/h-BN_1N has semimetallic properties. We have studied the impact of up and down spin states of individual orbital (s and p) of valence electrons of carbon, boron and nitrogen atoms on magnetic moment of G/h-BN_1N HS material through PDOS calculations, which are embellished in figure (31b) and table (5). Detail calculations of magnetic moment are acquired through PDOS analysis. In figure (31b), we can see unpaired up and down spin states of valence electrons in the orbitals of individual atoms are asymmetrically distributed around the Fermi energy level. It implies that G/h-BN_1N has magnetic properties. Magnetic moment in G/h-BN_1N is obtained by the effect of 2p orbitals of valence electrons in boron, nitrogen and carbon atoms. Comparatively, 2p orbital of boron atoms has significant contribution than of nitrogen and carbon atoms. We have calculated the effect on magnetic moment by virtue of 2s orbitals of valence electrons of carbon, boron and nitrogen atoms, and found that magnetic moment is weakly impressed by cause of spin states in 2s orbital, which are obviously given in figure (31b) and table (5). The magnetic moment, as a result of up and down spin states in 2s, 2p of valence electrons in carbon atoms have 0.02 $\mu_B/cell$, 0.09 $\mu_B/cell$; 2s, 2p of valence electrons in boron atoms have 0.03 $\mu_B/cell$, 0.58 $\mu_B/cell$; and 2s, 2p of valence electrons in nitrogen atoms have 0.05 $\mu_B/cell$, 0.20 $\mu_B/cell$ respectively. From these calculations, total magnetic moment of G/h-BN_1N is noted to be 0.97 $\mu_B/cell$. Therefore, G/h-BN_1N has magnetic properties. We found that magnetic moment of G/h-BN_1N is higher than that of pristine G/h-BN material. Because N vacancy atom in HS created unpaired spin states in the orbitals of valence electrons of B and N atoms. Positive sign of magnetic moment reflects that distributed up spin have dominant role for developement of magnetic moment than the down spin states.

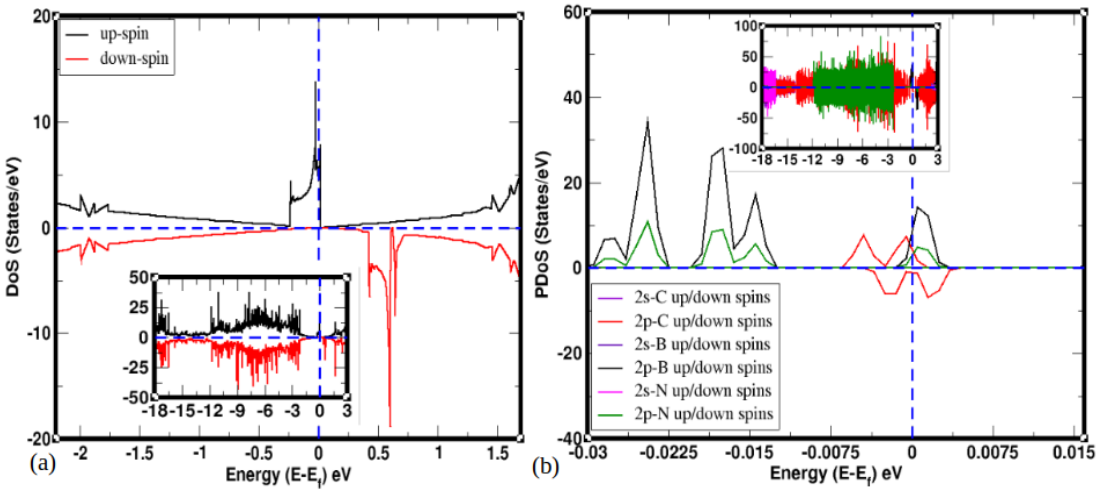

Figure 31: DOS and PDOS calculations of 2D vdWs G/h-BN_1N HS material: (a) DOS of total up and down spin states of G/h-BN_1N HS, (b) PDOS of individual up and down spin states of C, B, and N atoms of G/h-BN_1N HS. Vertical dot line is a Fermi level and horizontal dot line separates up and down spin states. Insets in the plots signify the spin states having large energy range in X-axis (Neupane, et al., 2021).

.

Magnetic moment (properties) of G/h-BN_nBN material is predicted by using its DOS and PDOS. They are illustrated in figure (32a) and (32b) respectively. In figures (32a) and (32b), up and down spin states of DOS/PDOS are taken in Y-axis and their energies are taken in X-axis. Vertical dot line is a Fermi level which is set at zero and horizontal dot line separates up and down spin states. In G/h-BN_nBN, unpaired spin states are created in the orbitals of valence electrons of N and B atoms by reason of 1B and 1N defects in G/h-BN HS. The total unpaired up and down spin states of valence electrons are presented asymmetrically near the Fermi energy level, depicted in DOS plot. As a result, non-zero magnetic moment is obtained which is specified in table (5). Hence, G/h-BN_nBN has magnetic properties. We rigorously computed the magnetic moment of G/h-BN_nBN on the basis of its PDOS calculations. It is found that uneven up and down spin states of individual atoms are asymmetrically assigned around Fermi energy level as illustrated in figure (32b). Particularly, magnetic moment caused by uneven spin of valence electrons in 2s and 2p of boron, carbon and nitrogen atoms have been calculated. It is found that up and down spin states in 2s, 2p of carbon atoms have 0.00 $\mu_B/cell$, - 0.05 $\mu_B/cell$; 2s, 2p of boron atoms have - 0.06 $\mu_B/cell$, - 0.93 $\mu_B/cell$; and 2s, 2p of nitrogen atoms have - 0.08 $\mu_B/cell$, - 0.84 $\mu_B/cell$ values respectively. Total magnetic moment is obtained by adding magnetic moments contributed by individual atoms, and found to be - 1.96 $\mu_B/cell$. This value is greater than the value of pristine G/h-BN HS. Therefore, G/h-BN_nBN has magnetic nature. In G/h-BN_nBN, down spin states have ruling contributions than up spin states. Moreover, we observed that down spin states of 2p of carbons are seen at Fermi energy level but up spin states are not seen at there. Thus, up spin of 2p of carbon atoms open small energy gap (1.71 meV)

at Fermi level. Hence, G/h-BN_nBN is called semimetallic material.

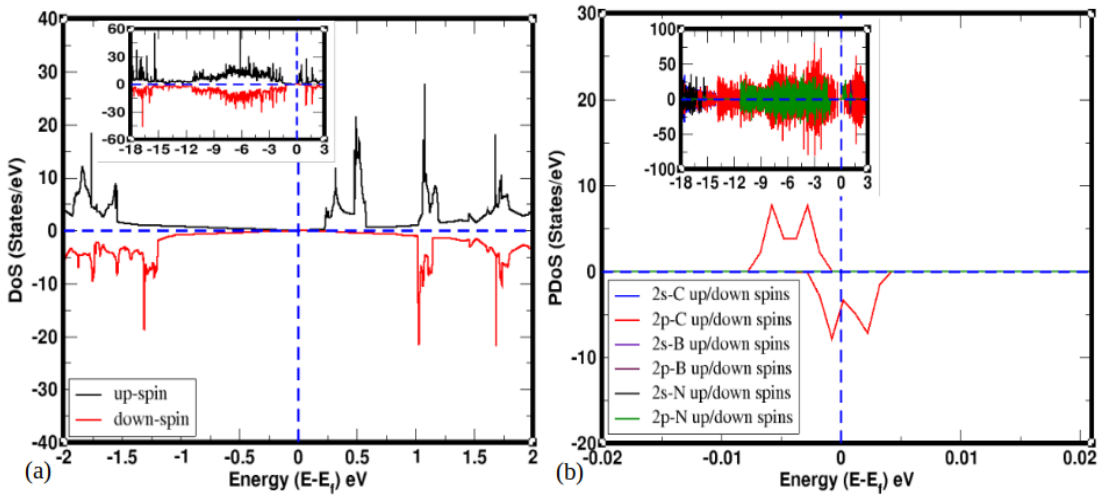

Figure 32: DOS and PDOS calculations of 2D vdWs G/h-BN_nBN HS material: (a) DOS of total up and down spin states of G/h-BN_nBN HS, (b) PDOS of individual up and down spin states of C, B, and N atoms of G/h-BN_nBN HS. Vertical dot line is a Fermi level and horizontal dot line separates up and down spin states. Insets in the plots signify the spin states having large energy range in X-axis (Neupane, et al., 2021).

.

Magnetic properties of G/h-BN_aBN HS material is inspected on basis of its DOS and PDOS calculations, they are exhibited in figures (33a) and (33b) respectively. Total up and down spin are unequally disseminated in DOS plot of G/h-BN_aBN, and hence non-zero magnetic moment is acquired in G/h-BN_aBN material. Thus, G/h-BN_aBN is a magnetic material. For detail informations about the contributions of magnetic moment by cause of different orbitals of valence electrons of carbon, boron and nitrogen atoms on total DOS of G/h-BN_aBN material is computed by its PDOS plot and PDOS calcualtions, which are shown in figure (33b) and table (5) respectively. We found that unpaired up and down spin of valence electrons in 2s and 2p of carbon, boron and nitrogen atoms are disproportionally assigned throughout the Fermi energy level. These asymmetrically allocated unequal up and down spin accord magnetic moment in the material. Therefore, we ensured that G/h-BN_aBN has magnetic nature. Moreover, we have determined the magnetic moment given by 2s and 2p orbitals of valence electrons of carbon, boron and nitrogen atoms present in G/h-BN_aBN. The estimated values caused by up and down spin in 2s, 2p of carbon atoms have 0.01 $\mu_B/cell$, 0.08 $\mu_B/cell$; 2s, 2p of boron atoms have 0.02 $\mu_B/cell$, 0.83 $\mu_B/cell$; and 2s, 2p of nitrogen atoms have 0.08 $\mu_B/cell$, 0.99 $\mu_B/cell$ respectively. Hence, total magnetic moment of G/h-BN_aBN is found to be 2.01 $\mu_B/cell$. According to our above calcualtions, we found that up and down spins in 2p of boron and nitrogen atoms have notable contributions for the development of magnetic moment. On the other hand, spins in 2p of carbon atoms and 2s of carbon, boron and nitrogen atoms jointly allow feeble improvement for

the magnetism. Detail informations regarding to the estimation of magnetic moment of defected materials are given in table (5).

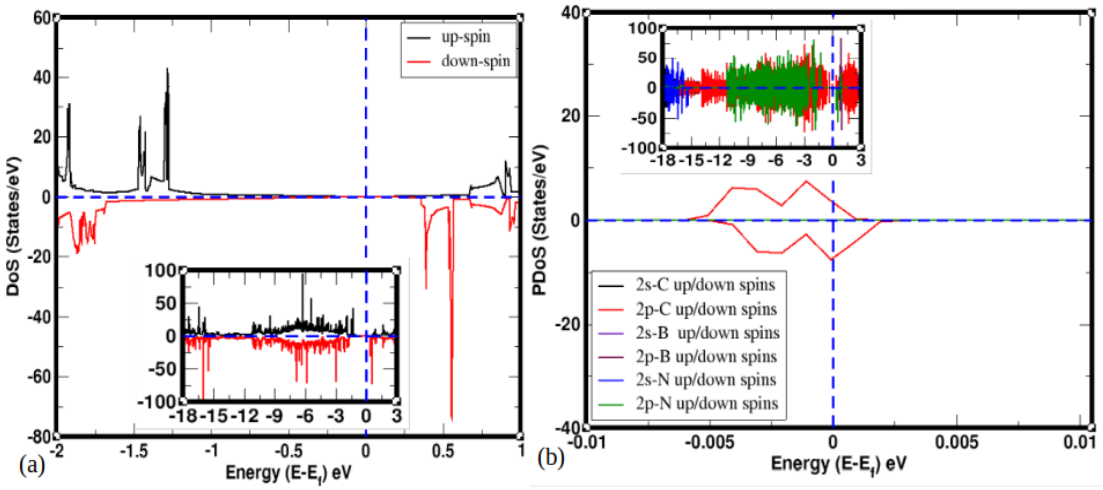

Figure 33: DOS and PDOS calculations of 2D vdWs G/h-BN_aBN HS material: (a) DOS of total up and down spin states of G/h-BN_aBN HS, (b) PDOS of individual up and down spin states of C, B, and N atoms of G/h-BN_aBN HS. Vertical dot line is a Fermi level and horizontal dot line separates up and down spin states. Insets in the plots signify the spin states having large energy range in X-axis (Neupane, et al., 2021).

.

In this work, we have also explored the magnetic properties of C sites vacancy defected G/h-BN HS material. At first, we considered 1C vacancy defect in G/h-BN HS (G/h-BN_1C) material. Magnetic moment of G/h-BN_1C is studied based on its DOS and PDOS calculations, which are given in figures (34a) and (34b) respectively. Vertical dot line is a Fermi level and horizontal dot line separates up and down spin states. Also, total DOS states are taken in Y-axis and energy of DOS states are taken in X-axis. DOS of total up and down spins are appeared asymmetrically throughout the Fermi energy level. It means, non-zero value of magnetic moment is obtained in G/h-BN_1C material. Hence, G/h-BN_1C is a magnetic material. Magnetic moment contributed by unpaired up and down spin in the individual orbitals of carbon, boron and nitrogen atoms are given by PDOS analysis. Therefore, we have studied the PDOS of G/h-BN_1C material, and found its total magnetic moment 0.39 $\mu_B/cell$. This total magnetic moment is obtained as a result of magnetic moment contributed by unpaired both spins of valence electrons in 2s and 2p orbitals of carbon atoms. Magnetic moment generated by 2s and 2p of carbon atoms have 0.12 $\mu_B/cell$ and 0.27 $\mu_B/cell$ values respectively. They are obtained as the arrangement uneven spin of electrons generated by 1C vacancy defect in G/h-BN material. We have computed the magnetic moment given by 2s and 2p of boron and nitrogen atoms, and found to be 0.00 $\mu_B/cell$ value. It means, only 2s and 2p of carbons have dominant grants for the magnetism. The detail calcualtions of magnetic moment of G/h-BN_1C are given in table (5). We also compared the magnetic moment

of G/h-BN_1C with that of pristine G/h-BN, and found that G/h-BN_1C has slightly higher value of magnetic moment than that of pristine one.

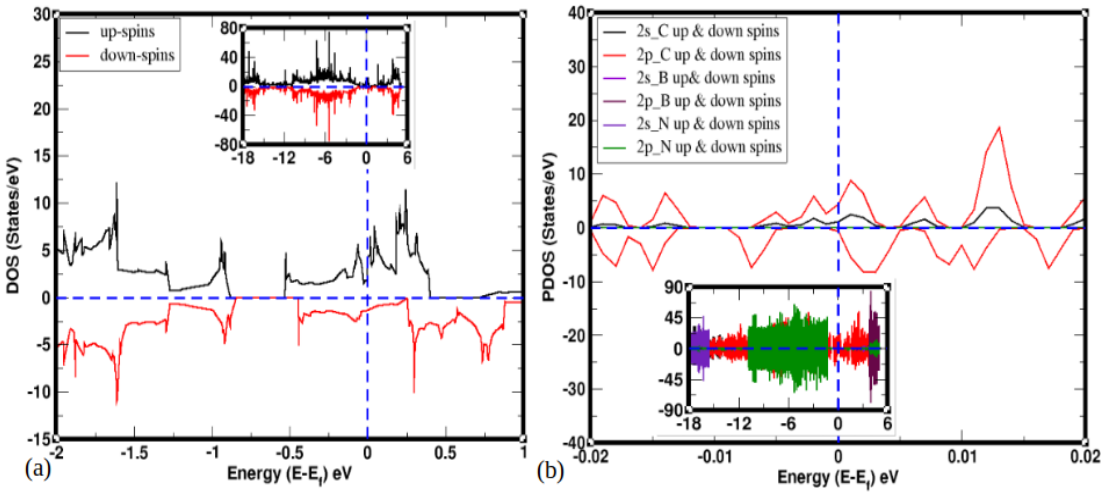

Figure 34: DOS and PDOS calculations of 2D vdWs G/h-BN_1C HS material: (a) DOS of total up and down spin states of G/h-BN_1C HS, (b) PDOS of individual up and down spin states of C, B, and N atoms of G/h-BN_1C HS. Vertical dot line is a Fermi level and horizontal dot line separates up and down spin states. Insets in the plots signify the spin states having large energy range in X-axis (Neupane, et al., 2022).

In addition, we have explored the magnetic properties of G/h-BN_2C HS material by using its DOS and PDOS calculations. DOS and PDOS plots are depicted in figures (35a) and (35b) respectively, where X-axis represents the energy of the DOS/PDOS states (in eV) taking Fermi energy as a reference and Y-axis represents the number of energy states per unit energy range (in eV^{-1}). Also, Vertical dot line is a Fermi level and horizontal dot line separates up and down spin states. It is seen that unoccupied up and down spin states are arrived throughout the Fermi energy level. These unoccupied spin states are appeared asymmetrically near the Fermi energy level. They generate non-zero value of magnetic moment (1.89 $\mu_B/cell$). This is because magnetic properties in the material is developed due to the rearrangement of unpaired distributed spin in the orbitals of atoms. Hence, G/h-BN_2C is a magnetic material. The detail calculations of magnetic moment given by 2s and 2p orbitals of carbon, boron and nitrogen atoms are presented in figure (35b) and table (5). We have estimated the magnetic moment given by 2s, 2p of carbon atoms are 0.48 $\mu_B/cell$, 1.22 $\mu_B/cell$; 2s, 2p of boron atoms are 0.02 $\mu_B/cell$, 0.09 $\mu_B/cell$; and 2s, 2p of nitrogen atoms are 0.01 $\mu_B/cell$, 0.07 $\mu_B/cell$ respectively. From these calculations, we found that 2s and 2p orbitals of carbon atoms have remarkable contributions of magnetic moment in G/h-BN_2C material.

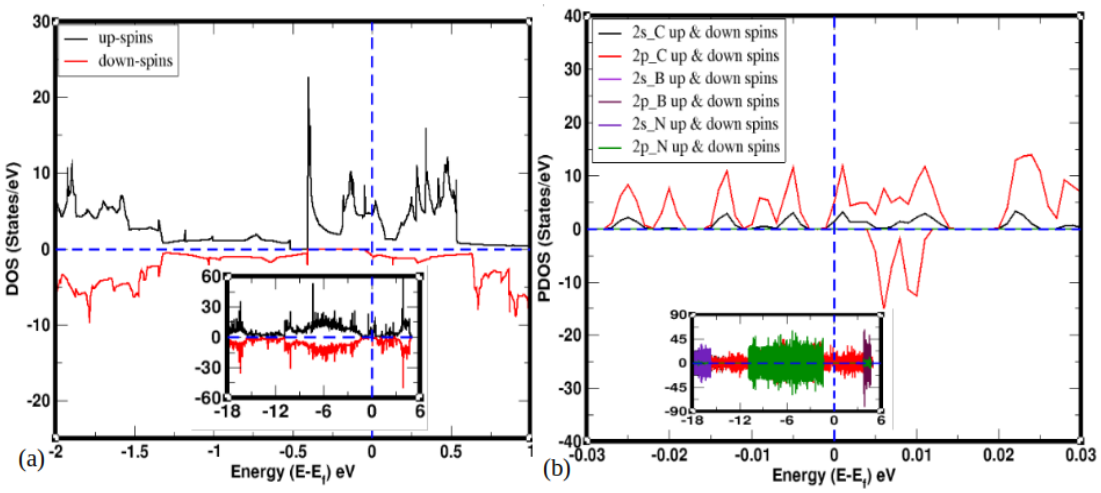

Figure 35: DOS and PDOS calculations of 2D vdWs G/h-BN_2C HS material: (a) DOS of total up and down spin states of G/h-BN_2C HS, (b) PDOS of individual up and down spin states of C, B, and N atoms of G/h-BN_2C HS. Vertical dot line is a Fermi level and horizontal dot line separates up and down spin states. Insets in the plots signify the spin states having large energy range in X-axis (Neupane, et al., 2022).

.

After magnetic moment calculations of pristine and defected materials, we came to an end that all the materials have magnetic properties, and hence they behave as a magnetic material. We have compared the magnetic moment of these materials and found that all the defected materials have higher values of magnetic moment than of pristine HS material. Among the defected HS materials, order of magnetic moment are found to be G/h-BN_1B $\gtrsim$ G/h-BN_aBN $\gtrsim$ G/h-BN_nBN $\gtrsim$ G/h-BN_2C $\gtrsim$ G/h-BN_1N $\gtrsim$ G/h-BN_1C. The detail magnetic moment calculations of pristine and defected HS materials are presented in table (5).

Table 5: The total magnetic moment μ_T (in $\mu_B/cell$) of G/h-BN, G/h-BN_1B, G/h-BN_1N, G/h-BN_nBN, G/h-BN_aBN, G/h-BN_1C and G/h-BN_2C materials are determined by PDOS calculations, where μ_T ($\mu_B/cell$) is the sum of magnetic moment μ ($\mu_B/cell$) given by asymmetrically distributed unpaired spins of individual atoms present in the materials (Neupane, et al., 2021, 2022).

Orbitals of atoms	Pristine G/h-BN ($\mu_B/cell$)	G/h-BN _1B ($\mu_B/cell$)	G/h-BN _1N ($\mu_B/cell$)	G/h-BN _nBN ($\mu_B/cell$)	G/h-BN _aBN ($\mu_B/cell$)	G/h-BN _1C ($\mu_B/cell$)	G/h-BN _2C ($\mu_B/cell$)
C_{2s}	0.01	- 0.02	0.02	0.00	0.01	0.12	0.48
C_{2p}	0.03	- 0.11	0.09	- 0.05	0.08	0.27	1.22
B_{2s}	0.00	- 0.03	0.03	- 0.06	0.02	0.00	0.02
B_{2p}	0.00	- 0.91	0.58	- 0.93	0.83	0.00	0.09
N_{2s}	0.00	- 0.06	0.05	- 0.08	0.08	0.00	0.01
N_{2p}	0.00	- 1.83	0.20	- 0.84	0.99	0.00	0.07
μ_T	0.04	- 2.96	0.97	- 1.96	2.01	0.39	1.89

4.5 Transport Properties

The study of transport properties of materials is typically important for the construction of high-efficiency theromelectric (TE) devices (Dahal et al., 2014, 2015; Bhattarai et al., 2020). TE devices are designed with the intent of harvesting waste heat and converting it into electrical energy, similar to how photocells turn light into electricity (Yang et al., 2012). A good TE material should possess high electrical conductivity (σ), high Seebeck coefficient (S), and lower thermal conductivity (K) (Dahal et al., 2015). The phenomenon of development of steady-state electrostatic potential difference in the specimen when temperature gradient is maintained across the two ends is known as Seebeck effect (Ashcroft et al., 1976). If $\triangle$V is the potential difference induced in specimen due to steady temperature gradient $\triangle$T applied across its ends (Zuev et al., 2009), then

$$\triangle V = S\triangle T \tag{4.12}$$

According to equation (4.12), in order to get more potential difference from the given temperature difference, we need the material with large S. Although, S is the characteristic property of material, it has dependence with parameters like temperature and charge carrier concentration, and effective mass of the charge carrier. For metals or degenerate semiconductors, the Seebeck coefficient is given by (Zuev et al., 2009; Dahal et al., 2014; Reshak, 2016):

$$S = \frac{8\pi^2 K_B^2 m^*}{3eh^2}\left(\frac{\pi}{3n}\right)^{\frac{2}{3}} \tag{4.13}$$

where, K_B, m^* and n are the Boltzmann constant, effective mass of the charge carrier, and charge carrier density respectively. Equation (4.13) suggests that, in order to yield large S, the value of n must be small. However, the small value of n results low electrical conductivity (σ = neμ) where μ is the mobility, which in turn gives small value of thermoelectric power factor P = $S^2\sigma$. The effective mass of charge carrier (m^*) causes another difficulty; for large S, large value of m^* is required but the large value of m^* reduces velocity and hence mobility of charge carriers resulting in the reduction of σ value. Good TE devices require materials with enhanced power factor, for which both S and σ requires being relatively high. Sharma, and co-workers (Sharma et al., 2020) mentioned that thermal conductivity of boron nitride (BN) based materials have structure dependence with its value ranging from $\sim$ 2000 $\mathrm{Wm^{-1}K^{-1}}$ for zigzag boron nitride nanoribbon to $\sim$ 0.3 $\mathrm{nWK^{-1}}$ for boron nitride quantum dots. Compared to graphene, h-BN has much lower thermal conductivity (Lindsay & Broido, 2011). This difference is attributed due to the reduction in frequency of acoustic phonon in h-BN

caused from strong phonon-phonon scattering rates (Sichel et al., 1976; Jo et al., 2013). The thermoelectric (transport) properties of single layer graphene, h-BN and graphene/h-BN/graphene (G/h-BN/G) HS were studied based on their Seebeck coefficient and power factors (Chen et al., 2015; Li et al., 2012; Reshak et al., 2014). But, transport properties of B, N and C atoms vacancy defected G/h-BN HS materials have not been reported in literatures till date. Therefore, we have explored the transport properties of graphene, h-BN, G/h-BN HS, and B, N, and C atoms vacancy defected G/h-BN HS materials in the present work. Transport properties of considered materials are studied by the estimation of their transport parameters. Transport parameters like Seebeck coefficient, thermoelctric power factor, electrical conductivity and electronic contribution to thermal conductivity are estimated by using spin-polarized DFT method within DFT-D2 approach through Quantum ESPRESSO and BoltzTraP computational packages.

4.5.1 Seebeck Coefficient

Study of Seebeck coefficient of material is essential for its transport properties calculations. So, we have determined the transport properties of graphene and h-BN supercell ML, G/h-BN HS, and B, N and C atoms vacancy defected G/h-BN HS materials based on their Seebeck coefficient S (μV/K). In our calcualtions, we used the relaxation time (τ = 1×10^{-14} sec.) since the relaxation time of graphene based HS material has the order of 10^{-14} sec. (D'Souza & Mukherjee, 2016b). The effect of temperature at certain value of energy (E = E_f, since E_f is the Fermi energy) on Seebeck coefficient of graphene, h-BN, and up-down and total-spin states of G/h-BN are illustrated in figure (36a). The total Seebeck coefficient of graphene is gradually increased with increase in temperature and attains the maximum value of about 198 μV/K at low temperature of around 40 K, after which it decreases gradually, however at a slower rate. The S of pristine graphene at 300 K is 42 μV/K, which is fairly in agreement with the value $\sim$ 30.50 μV/K of monolayer graphene and $\sim$ 54 μV/K of multilayer graphene system in the experiment (Li et al., 2012; Reshak et al., 2014; Zuev et al., 2009). Thus, graphene has to be an auspicious thermoelectric material (Yokomizo & Nakamura, 2013). The S of h-BN value is negative for all range of temperatures as shown in figure (36a), which implies that the transport is taking place via electrons. The pristine h-BN has optimum Seebeck coefficient of -209 μV/K at temperature 125 K whereas it possesses room temperature S of -210 μV/K. They are analogous with the layers structure of h-BN (D'Souza & Mukherjee, 2016b). The different value of Seebeck coefficient of h-BN than that of graphene is due to its wide band gap (Yao & Fan, 2021). The change has been observed in the value of S after making the heterostructure G/h-BN as shown in figure (36a). The effect of both spins i.e. up-spin and down-spin system have been studied. It has been found that value of S for

down-spin G/h-BN is positive throughout the whole range of temperature, whereas value of S for up-spin G/h-BN is negative at all temperature ranges. The total S of G/h-BN is however positive whose maximum value has been calculated to be around 112 μV/K at T = $\sim$ 20 K and 8 μV/K at temperature 300 K. The significant positive S value of material reveals that they are promising materials in the thermoelectric devices. To ascertain the relatively large value of S at lower temperatures, the graph of S vs chemical potential (μ) has been plotted at constant different temperatures, shown in figures (38a) and (38b). We have calculated the maximum value of Seebeck coefficient (S) of G/h-BN_1N is 58 μV/K at 80 K temperature. This value is likely with the value of G/h-BN. We have also calculated S of G/h-BN_1N is 35 μV/K at 300 K as shown in figure (36b). This value is greater than that of G/h-BN. The S of material is estimated using the formula given by (Zuev et al., 2009; Dahal et al., 2014; Reshak, 2016):

$$S = \frac{8\pi^2 K_B^2 m^*}{3eh^2}\left(\frac{\pi}{3n}\right)^{\frac{2}{3}} \tag{4.14}$$

where m^* and n are the effective mass of charge carrier and carrier density respectively. This relation shows, S is not only the function of T but also the function of n and m^*. Effective mass m^* of electron depends on the curvature of band (Ilyasov et al., 2014):

$$m^* = \frac{h^2/4\pi^2}{d^2E/d^2K}. \tag{4.15}$$

Smaller is the band curvature greater is the effective mass and vice versa. Band structures of G/h-BN and G/h-BN_1N are shown in figures (24b) and (25d) respectively, show that there is relatively decreased curvature at K-point of G/h-BN_1N which is responsible for the increase in effective mass, and hence the value of S.

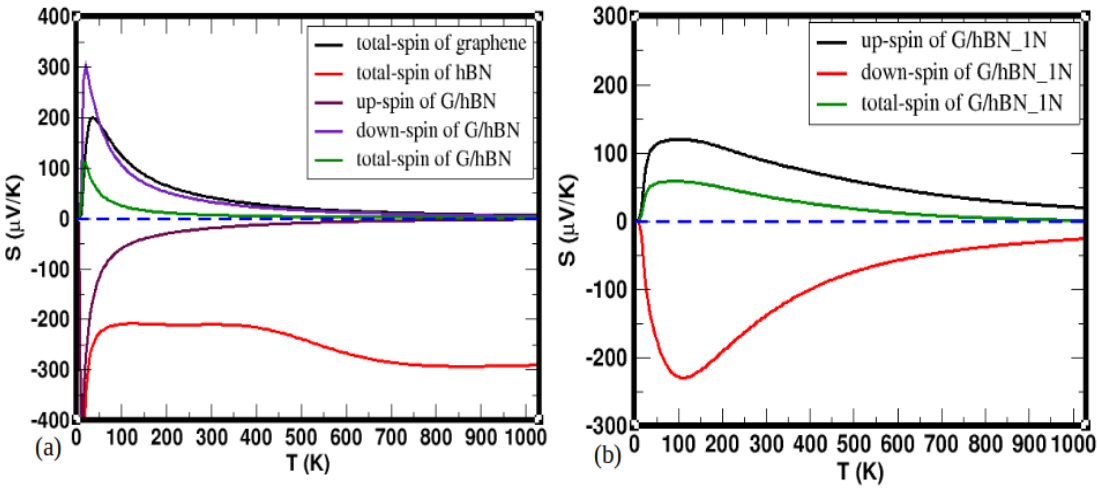

Figure 36: Effect of temperature T (K) on Seebeck coefficient S (μV/K) at constant (Fermi) energy of graphene, h-BN, G/h-BN and G/h-BN_1N materials, (a) Seebeck coefficient with different temperatures of graphene, h-BN and G/h-BN materials, (b) Seebeck coefficient with different temperatures of G/h-BN_1N material.

.

In addition, we have calculated the maximum values of S of G/h-BN_nBN and G/h-BN_aBN, found to be 143 μV/K at 40 K and 231 μV/K at 45 K respectively, and corresponding values are 32 μV/K and 60 μV/K at 300 K respectively as shown in figures (37a) and (37b). The relative increase in the maximum value of S for G/h-BN_nBN and G/h-BN_aBN is attributed due to decrease in carrier concentration (n) and curvature of the band state (as shown in figures 26b and 26d) at K-point, after forming vacancy in their structures. In all cases, value of S increases with increase in temperature attains maxima at particular temperature and then decreases monotonically. This pattern results due to the combined dependence of n, T and m* on the value of S.

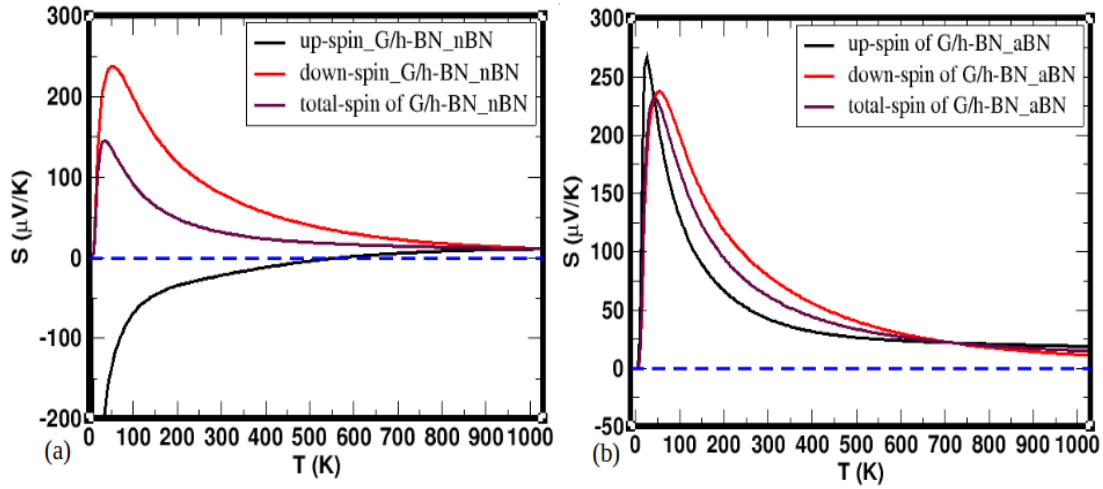

Figure 37: Effect of temperature T (K) on Seebeck coefficient S (μV/K) at constant (Fermi) energy of G/h-BN_nBN and G/h-BN_aBN materials, (a) Seebeck coefficient with different temperatures of G/h-BN_nBN material, (b) Seebeck coefficient with different temperatures of G/h-BN_aBN material.

.

Furthermore, the total value of S results due to the contributions of up-spin and down-spin channels in spin-polarized systems. Figures (38a) and (38b) show that Seebeck coefficient (S) is symmetric about the Fermi level for G/h-BN, G/h-BN_1N, G/h-BN_nBN and G/h-BN_aBN materials. The sign change has been observed at the charge neutrality point (CNP) or the Dirac point. At this point, positive S due to holes (in valance band) encounters with negative S due to the electrons (in the conduction band) (Wang & Lu, 2015). The maximum values of S at different temperatures as obtained from S vs T graphs are shown in figures (36) and (37) are also confirmed by S vs chemical potential (μ) graphs are shown in figure (38) for corresponding materials at corresponding temperatures. The value of S of G/h-BN at room temperature is $\sim$ 230 μV/K, shown in figure (38b), which is comparable with the reported value 300 μV/K (Wang & Lu, 2015; D'Souza & Mukherjee, 2016a). Also, in figure (38b), S of defected ma-terials has equivalent value with HS materials (Wang & Lu, 2015). Therefore, from above discussion, we concluded that considered materials are useful materials for thermoelectric devices.

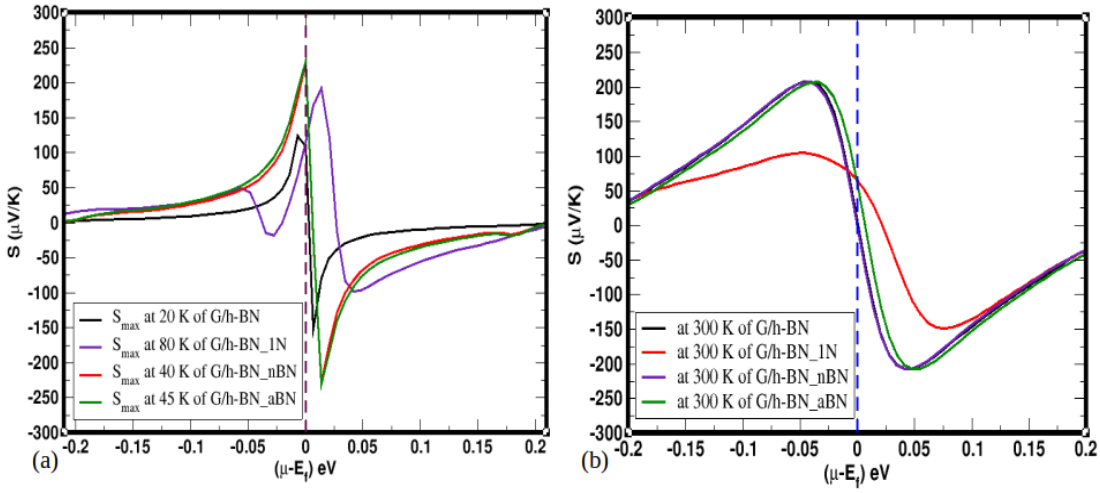

Figure 38: Variation of Seebeck coefficient S (μV/K) (of total-spin channel) with chemical potential μ (eV) at different constant temperature T (K) of G/h-BN, G/h-BN_1N, G/h-BN_nBN, and G/h-BN_aBN materials, (a) Maximum values of S with μ at 20 K of G/h-BN, at 80 K of G/h-BN_1N, at 40 K of G/h-BN_nBN, and at 45 K of G/h-BN_aBN materials, (b) S with μ at 300 K of G/h-BN, G/h-BN_1N, G/h-BN_nBN and G/h-BN_aBN materials.

.

Moreover, S of G/h-BN_1C and G/h-BN_2C are found to be negative throughout the given range of temperatures as shown in figures (39a) and (39b)respectively. The negative S value of these structures at Fermi level is also confirmed by the figure (40b), in which the graph lies below reference line at Fermi level. In graphene, each carbon atom is covalently bonded with three other adjoining carbon atoms. So that one electron is left unbounded for each carbon atom. When one carbon atom is removed from the system, the three carbon atoms are initially bonded with it are each left with two unbounded electrons. The estimated maximum S value of G/h-BN_1C is -16 μV/K at 395 K and -15

μV/K at 300 K respectively, illustrated in figure (39a). The negative value of S is due to negative charge carrier. Similar case happens when two carbon atoms are removed from the surface of Graphene in G/h-BN HS. The maximum S of G/h-BN_2C is -79 μV/K at 1740 K and -22 μV/K at 300 K. Comparatively, S of G/h-BN_1C is smaller than that of G/h-BN_2C owing to the movement of electrons in the materials. So, the increase in number of free electrons explains why these compounds have negative value of S.

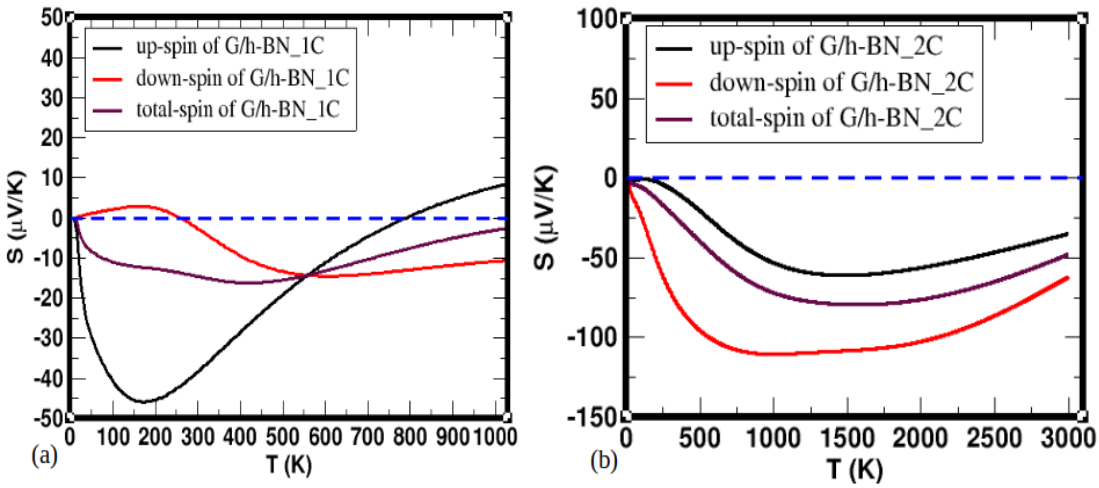

Figure 39: Effect of temperature T (K) on Seebeck coefficient S (μV/K) at constant (Fermi) energy of G/h-BN_1C and G/h-BN_2C materials, (a) Seebeck coefficient with different temperatures of G/h-BN_1C material, (b) Seebeck coefficient with different temperatures of G/h-BN_2C material.

.

Figure (40a) is the plot of Seebeck cofficient S with temperature T of G/h-BN_1B material. S of G/h-BN_1B goes on increasing monotonically with increase in temperature and acquired 15 μV/K value at 300 K. Both up-spin and down-spin channels are contributed to the positive value of S, that results in the monotonically increasing total S of the material. In G/h-BN, each boron atom is covalantly bonded with three adjacent N atoms, so all electrons in the system are involved in bonding. However, when one boron atom is removed, it goes away taking three valance electrons with it. As a results, defficiency of three electrons and the formation of three holes takes place in the structure of a material. The decrease in electron concentration (n) is one of the the main factors in increasing the value of S (Dahal et al., 2014) of G/h-BN_1B.

We have analyzed the plots of S vs chemical potential (μ) at different constant temperatures of G/h-BN, G/h-BN_1B, G/h-BN_1C and G/h-BN_2C materials, shown in figure (40b), and found that charge neutrality point (CNP) is formed at Fermi energy level of G/h-BN due to the equal contribution of electrons and holes at the Fermi level, however it is on conduction band for the G/h-BN_1B. Existence of CNP at Fermi level shows that both, p-type and n-type contributions to S of the system is equal at Fermi level (Wang & Lu, 2015). We have carefully analyzed a figure (40b), it is seen

that S of G/h-BN_1B at 300 K is positive (red colour line) value 20 μV/K at Fermi level, which proves the p-type conduction as a majority contributing factor. Also, the obtained maximum S of G/h-BN_1B at 300 K is equal to 208 μV/K, this value is comparable with the reported value of graphene based HS materials (Wang & Lu, 2015; D'Souza & Mukherjee, 2016a). It reveals that material having high value of S is a useful agent in thermoelectric devices. On the other hand, The CPN of G/h-BN_1C and G/h-BN_2C are formed in valence band because of the effect of negative charge carriers. In figure (40b), we have computed that, maximum S of G/h-BN_1C is 600 μV/K.

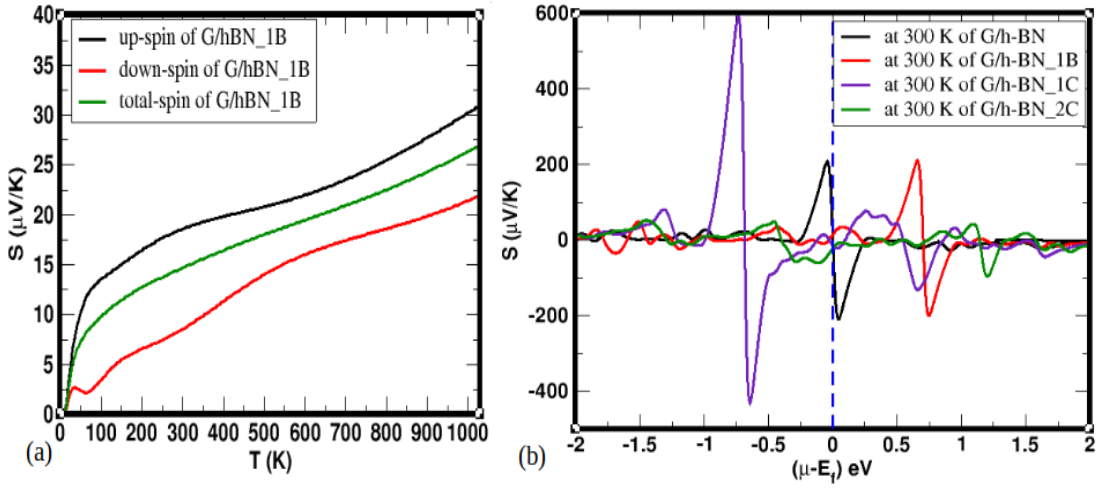

Figure 40: Effect of Seebeck coefficient S (μV/K) with temperature T (K) at constant (Fermi) energy of G/h-BN_1B, and variation of Seebeck coefficient S (μV/K) (of total-spin channel) with chemical potential μ (eV) at constant (300 K) temperature of G/h-BN, G/h-BN_1B, G/h-BN_1C and G/h-BN_2C materials, (a) Seebeck coefficient with different temperatures of G/h-BN_1B material, (b) Seebeck coefficient with chemical potential of G/h-BN, G/h-BN_1B, G/h-BN_1C and G/h-BN_2C materials.

.

This value is greater than that of our calculated value of G/h-BN material. This large increase in S value through the defects is allied to the deformation of density of states in defected materials by establishing resonant states near the Fermi level (Perumal et al., 2019). S of G/h-BN_2C is found to be 49 μV/K at 300 K temperature. It means, efficiency of thermoelectric materials decreases by increasing carbon atom vacancy defects in the material. Therefore, by the analysis of calculated Seebeck coefficient, we concluded that vacancy defected materials are useful materials for the fabrication of thermoelectric devices. Computated data of Seebeck coefficient at different temperatures are summarized in table (6).

Table 6: Computed Seebeck coefficient S (μV/K), thermoelectric power factor P (W/mK^2), electrical conductivity σ (Ω m)$^{-1}$, and electronic contribution of thermal conductivity K (W/mK) values of graphene, h-BN, G/h-BN, G/h-BN_1N, G/h-BN_nBN, G/h-BN_aBN, G/h-BN_1B, G/h-BN_1C and G/h-BN_2C materials.

Materials ↓	S_m(μV/K) at T K	S(μ V/K) 300 K	P_m(W/mK^2 at T K	P(W/mK^2 300 K	σ (Ω m)$^{-1}$ 300 K	K(W/mK) 300 K
Graphene	198 at 40	42	5.03×10^{-6} at 400	4.70×10^{-6}	25.76×10^{2}	1240.08×10^{-4}
h-BN	-209 at 125	-210	-	3.96×10^{-5}	12.20×10^{2}	1505.61×10^{-4}
G/h-BN	112 at 20	08	3.59×10^{-7} at 1840	1.24×10^{-7}	25.70×10^{2}	1240.08×10^{-4}
G/h-BN_1N	58 at 80	35	2.60×10^{-5} at 150	1.71×10^{-5}	24.15×10^{2}	1964.02×10^{-4}
G/h-BN_nBN	143 at 40	32	5.72×10^{-6} at 1070	2.63×10^{-6}	24.95×10^{2}	1226.29×10^{-4}
G/h-BN_aBN	231 at 45	60	1.22×10^{-5} at 530	1.00×10^{-5}	25.08×10^{2}	1205.21×10^{-4}
G/h-BN_1B	-	15	-	6.30×10^{-5}	29.60×10^{4}	2097.75×10^{-3}
G/h-BN_1C	-18 at 420	-15	3.51×10^{-6} at 420	2.76×10^{-5}	13.10×10^{4}	9802.90×10^{-4}
G/h-BN_2C	-80 at 1500	-22	8.60×10^{-5} at 1600	5.91×10^{-5}	13.70×10^{4}	9746.40×10^{-4}

4.5.2 Electrical Conductivity

We have studied electrical conductivity of graphene, h-BN, G/h-BN, G/h-BN_1N, G/h-BN_1B, G/h-BN_nBN,G/h-BN_aBN, G/h-BN_1C and G/h-BN_2C materials. The electrical conductivity (σ) of graphene, h-BN, G/h-BN and G/h-BN_1N, are shown in figures (41a) and (41b). The electrical conductivity is found to be increasing monotonically with temperature for all the systems because with increase in temperature, more charge carriers can transit from valance band to conduction band, and hence movement of free charge density will be increased. Electrical conductivity of pristine graphene at room temperature is found to be 25.76×10^{2} (Ω m)$^{-1}$. There is relatively smaller value of σ (12.20×10^{2} (Ω m)$^{-1}$ for h-BN. The comparatively smaller σ value of h-BN than that of graphene is due to its wide band gap energy. There is no notable change in the value of σ for G/h-BN heterostructure (i.e. 25.70×10^{2} (Ω m)$^{-1}$) compared to pristine graphene, however the removal of 1N has caused significant decrease in the value of

σ with order of magnitude. The electrical conductivity is given by $\sigma = ne\mu$, where charge carrier mobility is $\mu = e\tau/m^*$. This relation shows that, electrical conductivity is inversely proportional to the effective mass of charge carriers. As discussed earlier, value of m^* is relatively large of G/h-BN_1N, which results in decreased μ and hence σ.

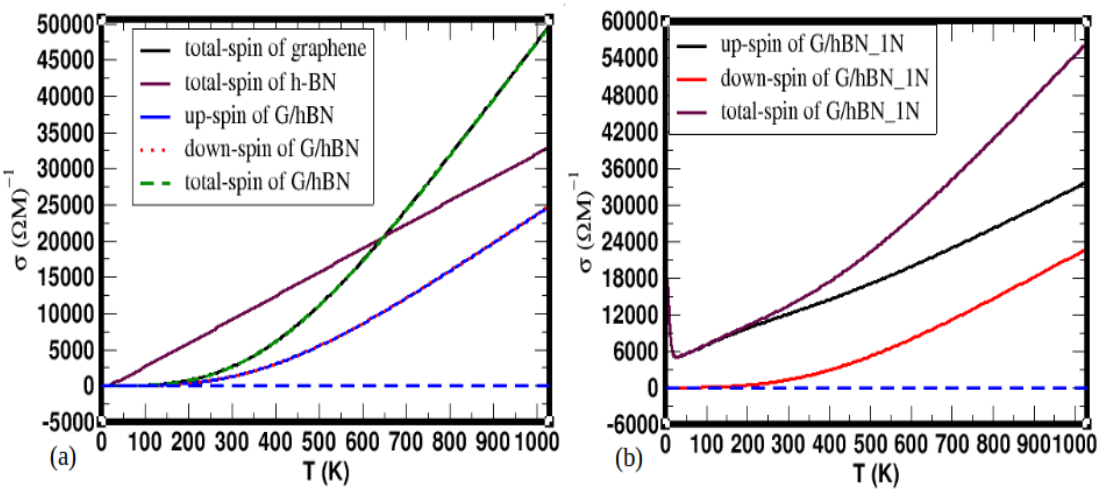

Figure 41: Effect of temperature on electrical conductivity at constant (Fermi) energy of graphene, h-BN, G/h-BN and G/h-BN_1N materials, where X-axis represents the temperature T (K) and Y-axis represents electrical conductivity σ in $(\Omega\ m)^{-1}$, also, horizontal dot line indicates the zero scale along Y-axis: (a) electrical conductivity of graphene, h-BN, G/h-BN materials, (b) electrical conductivity of G/h-BN_1N material.

The electrical conductivity of G/h-BN_nBN and G/h-BN_aBN are shown in figures (42a) and (42b) respectively not crucial different at 300 K than in G/h-BN_1N is illustrated in figure (41a). This is because, the curvature of band state of G/h-BN_nBN and G/h-BN_aBN are to be expected with the curvature of G/h-BN_1N are shown in above figures.

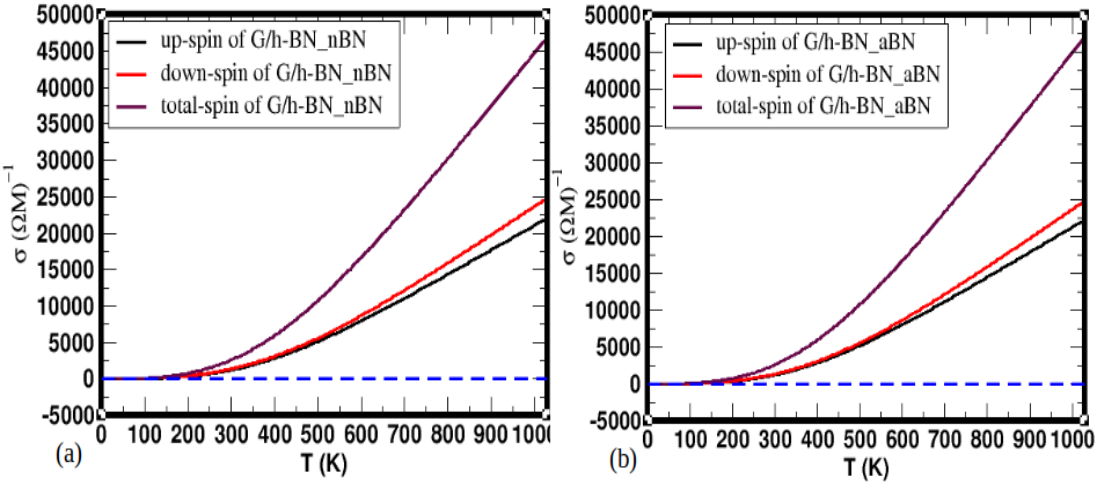

Figure 42: Effect of temperature on electrical conductivity at constant (Fermi) energy of G/h-BN_nBN and G/h-BN_aBN materials, where X-axis represents the temperature T (K) and Y-axis represents electrical conductivity σ in $(\Omega\ \mathrm{m})^{-1}$, also, horizontal dot line indicates the zero scale along Y-axis: (a) electrical conductivity of G/h-BN_nBN material, (b) electrical conductivity of G/h-BN_aBN material.

At room temperature, G/h-BN has electrical conductivity of 25.70 $\times 10^2$ $(\Omega\ \mathrm{m})^{-1}$ which has been increased significantly when boron and carbon sites vacancy defects are made in the material. This is because, band states of valence electrons appeared around the Fermi energy level in band plot of G/h-BN_1B as shown in figure (25a). They crossed the Fermi energy level in band structures of G/h-BN_1C and G/h-BN_2C are shown in figures (27a) and (27c) respectively. As a result, charge carriers are spontaneously moving in the electronic bands. The σ of G/h-BN_1B, G/h-BN_1C and G/h-BN_2C materials have initially maximum values of 12.80 $\times 10^5$ $(\Omega\ \mathrm{m})^{-1}$, 52.00 $\times 10^4$ $(\Omega\ \mathrm{m})^{-1}$ and 54.20 $\times 10^4$ $(\Omega\ \mathrm{m})^{-1}$ at 10 K, and then decreased to the values of 29.60 $\times 10^4$ $(\Omega\ \mathrm{m})^{-1}$, 13.10 $\times 10^4$ $(\Omega\ \mathrm{m})^{-1}$ and 13.70 $\times 10^4$ $(\Omega\ \mathrm{m})^{-1}$ at 300 K respectively are shown in figures (43), (44a) and (44b) respectively, since in boron and carbon sites vacancy defected materials, less number of valence electrons (more number of holes) are presented in the valence band, and hence movement of free charge density will be increased in valence band and decreased in conduction band. From above calculations, it is seen that electrical conductivity of G/h-BN_1B has higher value than the other vacancy defected materials.

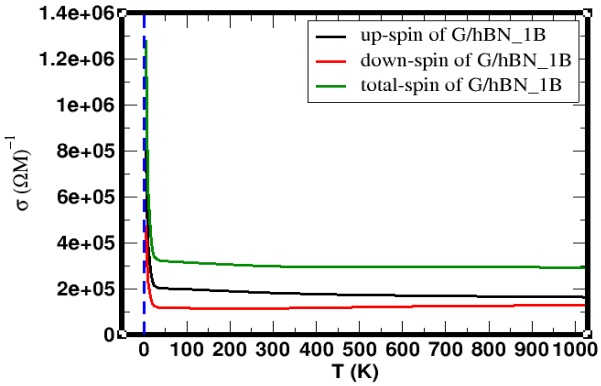

Figure 43: Effect of temperature on electrical conductivity at constant (Fermi) energy of G/h-BN_1B material, where X-axis represents the temperature T (K) and Y-axis represents electrical conductivity σ in $(\Omega\ \mathrm{m})^{-1}$. Also, vertical dot line indicates the zero scale along X-axis.

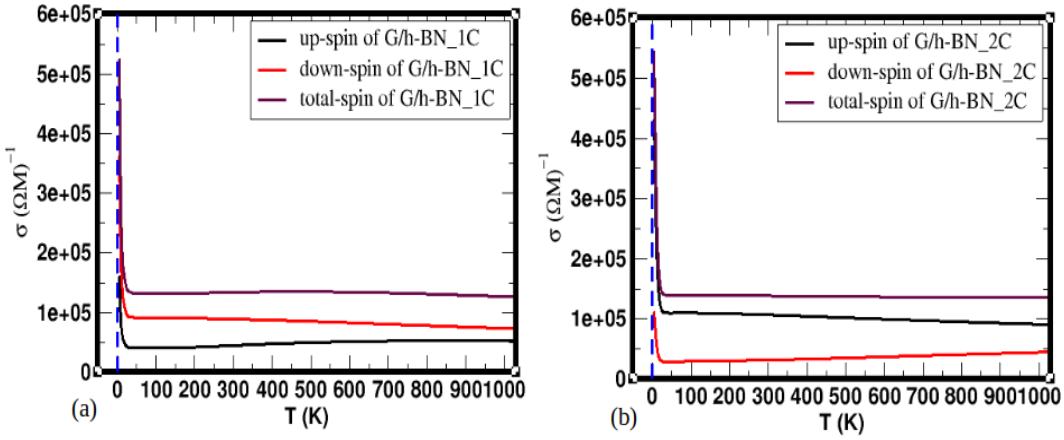

Figure 44: Effect of temperature on electrical conductivity at constant (Fermi) energy of G/h-BN_1C and G/h-BN_2C materials, where X-axis represents the temperature T (K) and Y-axis represents electrical conductivity σ in $(\Omega\ \mathrm{m})^{-1}$,also, vertical dot line indicates the zero scale along X-axis: (a) electrical conductivity of G/h-BN_1C material, (b) electrical conductivity of G/h-BN_2C material.

4.5.3 Electronic Contribution on Thermal Conductivity

The variation of electronic contribution on thermal conductivity (K) with temperature of graphene, h-BN, G/h-BN and G/h-BN_1N materials are presented in figures (45a) and (45b). In these cases, K increases with increase in the temperature. It is due to the increase in concentration of charge carriers at higher temperatures. At room temperature, K of graphene and G/h-BN possess similar value of K which is around 1240×10^{-4} W/mK while K of h-BN and G/h-BN_1N have values 1505×10^{-4} W/mK and 1964.02×10^{-4} W/mK respectively. The value of K however for G/h-BN_1N has been increased slightly because increase in Fermi velocity of electrons near the Fermi level due to reduction in effective mass thereby increasing the mean free path and hence K. On the other hand, K of h-BN is seemed to be decreased than of graphene at higher

temperature (above room temperature), which is due to reduction in the frequency of acoustic phonon in h-BN caused from strong phonon-phonon scattering rates (Lindsay & Broido, 2011; Sichel et al., 1976; Jo et al., 2013).

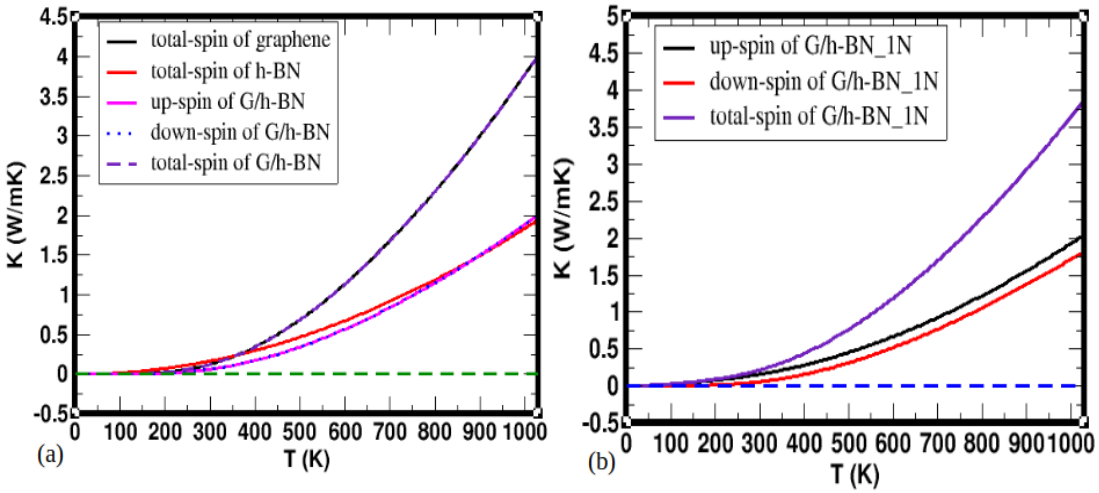

Figure 45: Effect of temperature on electronic thermal conductivity at constant (Fermi) energy of graphene, h-BN, G/h-BN and G/h-BN_1N materials, where X-axis represents temperature T (K) and Y-axis represents electronic thermal conductivity K in (W/mK), also, horizontal dot line indicates the zero scale along Y-axis: (a) electronic thermal conductivity of graphene, h-BN and G/h-BN materials, (b) electronic thermal conductivity of G/h-BN_1N material.

The electronic contribution on thermal conductivity of G/h-BN_nBN and G/h-BN_aBN materials are increased with increase in temperature, shown in figures (46a) and (46b) respectively. At room temperature, K of G/h-BN_nBN and G/h-BN_aBN possess similar value of K of graphene and G/h-BN, which is around 1205×10^{-4} W/mK. The obtained K of graphene, h-BN, G/h-BN, G/h-BN_1N, G/h-BN_nBN and G/h-BN_aBN are summarized in table (6).

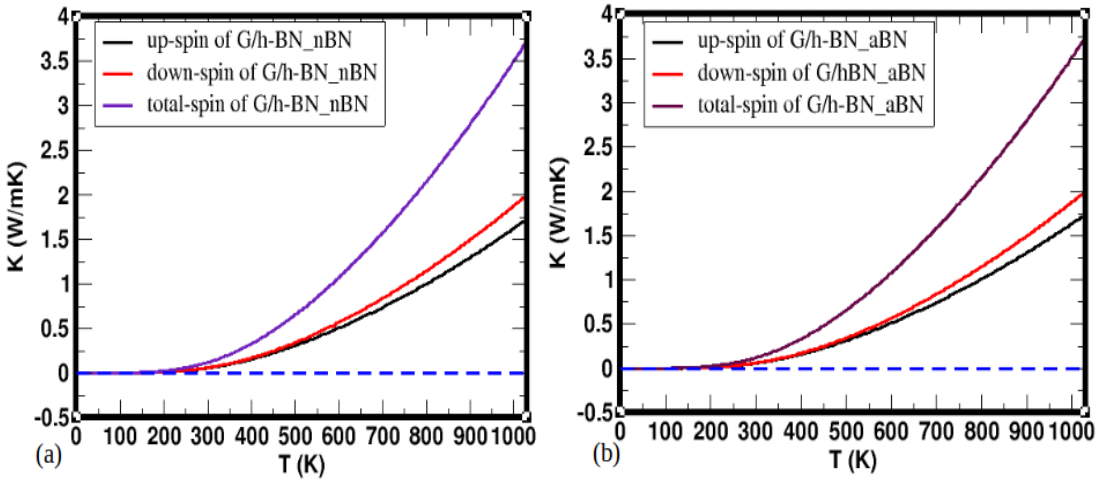

Figure 46: Effect of temperature on electronic thermal conductivity at constant (Fermi) energy of G/h-BN_nBN and G/h-BN_aBN materials, where X-axis represents temperature T (K) and Y-axis represents electronic thermal conductivity K in (W/mK), also, horizontal dot line indicates the zero scale along Y-axis: (a) electronic thermal conductivity of G/h-BN_nBN material, (b) electronic thermal conductivity of G/h-BN_aBN material.

Additionally, we have calculated the electronic contribution on thermal conductivity (K) of G/h-BN_1B, G/h-BN_1C and G/h-BN_2C materials at constant energy. They are found to be increasing with increase in temperature. The graphs of these material have more-less linear nature, which are embellished in figures (47), (48a) and (48b) respectively. Nature of these plots are slightly different than the plot of G/h-BN material because plot of G/h-BN is somehow exponential as shown in figure (45a). The K of G/h-BN_1B, G/h-BN_1C and G/h-BN_2C materials have 2.10 W/mK, 0.98 W/mK and 0.97 W/mK values at 300 K respectively. Comparatively, K of G/h-BN_1B retains high among other materials at 300 K because of increasing in mean free path of electrons. The detail calculations of K with chemical potential (μ) at distinct constant temperature are also supported by the results of K vs T plots. From all above discussions, we confirmed that all the considered materials have intrigued thermo-transport properties; hence, they are promising materials in the fields of thermoelectricity.

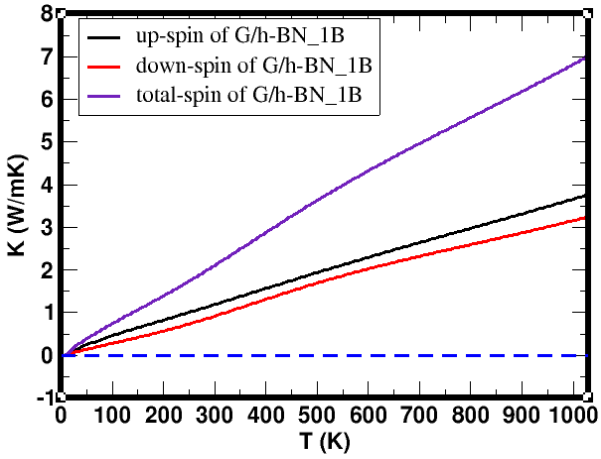

Figure 47: Effect of temperature on electronic thermal conductivity at constant (Fermi) energy of G/h-BN_1B material, where X-axis represents temperature T (K) and Y-axis represents electronic thermal conductivity K in (W/mK). Also, horizontal dot line indicates the zero scale along Y-axis.

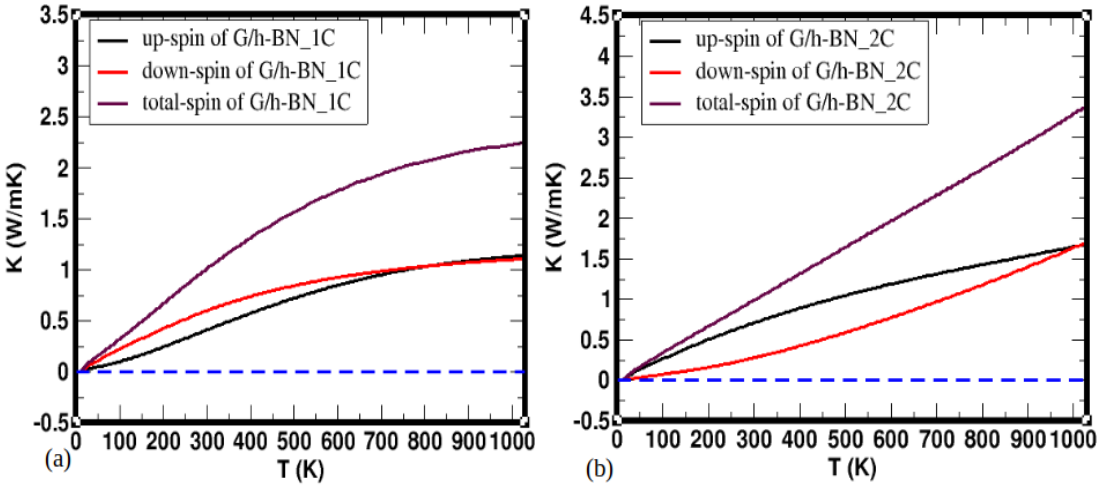

Figure 48: Effect of temperature on electronic thermal conductivity at constant (Fermi) energy of G/h-BN_1C and G/h-BN_2C materials, where X-axis represents temperature T (K) and Y-axis represents electronic thermal conductivity K in (W/mK), also, horizontal dot line indicates the zero scale along Y-axis: (a) electronic thermal conductivity of G/h-BN_1C material, (b) electronic thermal conductivity of G/h-BN_2C material.

4.5.4 Thermoelectric Power Factor

We have calculated the thermoelectric power factor (P) of graphene, G/h-BN and G/h-BN_1N materials. The P of these materials follows similar trend as that of S i.e. the value of P initially increases up to the optimum value and then monotonically decreases. The obtained maximum P of graphene is 5.03×10^{-6} W/mK^2 at 400 K and 4.70×10^{-6} W/mK^2 at room temperature, which are corresponding with outlined values (Reshak et al., 2014). We have calculated P of up-spin, down-spin and total-spin channels of G/h-BN and G/h-BN_1N materials as shown in figures (49a) and (49b) respectively. The

maximum P value of up-spin, down-spin and total-spin of G/h-BN are 4.69×10^{-7} W/mK^2 at 40 K, 1.56×10^{-6} W/mK^2 at 390 K and 3.59×10^{-7} W/mK^2 at 1840 K respectively. Also, we have calculated total P of G/h-BN is 1.24×10^{-7} W/mK^2 at room temperature. P of G/h-BN is lower than that of graphene because P of material also depends on its S. In HS, S of h-BN reduced the S of G/h-BN, and hence obtained P of G/h-BN is slightly less than that of graphene. The obtained maximum P of up-spin, down-spin and total-spin of G/h-BN_1N are 1.15×10^{-4} W/mK^2 at 170 K, 2.90×10^{-5} W/mK^2 at 415 K and 2.60×10^{-5} W/mK^2 at 150 K respectively as shown in figure (49b). The total P value of G/h-BN_1N is obtained 1.71×10^{-5} W/mK^2 at room temperature. This value is slightly greater than that of G/h-BN since vacancy defect is the cause of scattering electron-spins in the materials, which increases its P.

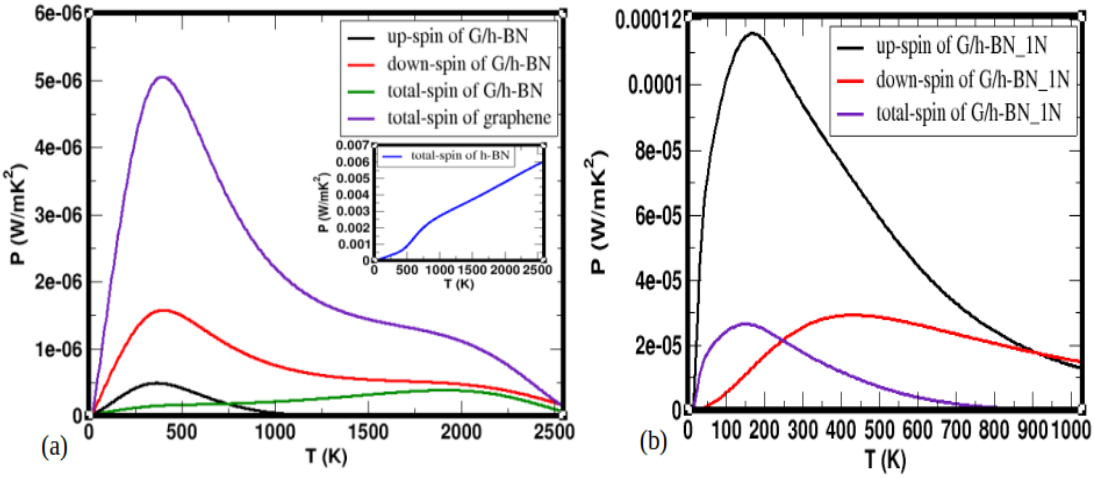

Figure 49: Effect of temperature on thermoelectric power factor (P = S^2 σ) at constant (Fermi) energy of graphene, h-BN, G/h-BN and G/h-BN_1N materials, where X-axis represents temperature T (K) and Y-axis represents thermoelectric power factor P in (W/mK^2), (a) thermoelectric power factor of graphene, h-BN and G/h-BN materials, (b) thermoelectric power factor of G/h-BN_1N material.

Furthermore, we have calcualted the P of G/h-BN_nBN and G/h-BN_aBN materials with differnt temperature at constant Fermi energy level (E=E$_f$) as shown in figures (50a) and (50b) respectively. The nature of plot follows similar trend as that of G/h-BN and G/h-BN_1N. We have calculated the P of up-spin, down-spin, and total-spin of G/h-BN_nBN and G/h-BN_aBN materials. We found that P of G/h-BN_nBN are $3.96\times10^{-}$ W/mK^2 at 1415 K, 9.68×10^{-6} W/mK^2 at 410 K and 5.72×10^{-6} W/mK^2 at 1070 K respectively, and of G/h-BN_aBN are 8.20×10^{-6} W/mK^2 at 1230 K, 9.68×10^{-6} W/mK^2 at 410 K and 1.22×10^{-5} W/mK^2 at 530 K respectively, which are shown in figures (50a) and (50b) respectively.

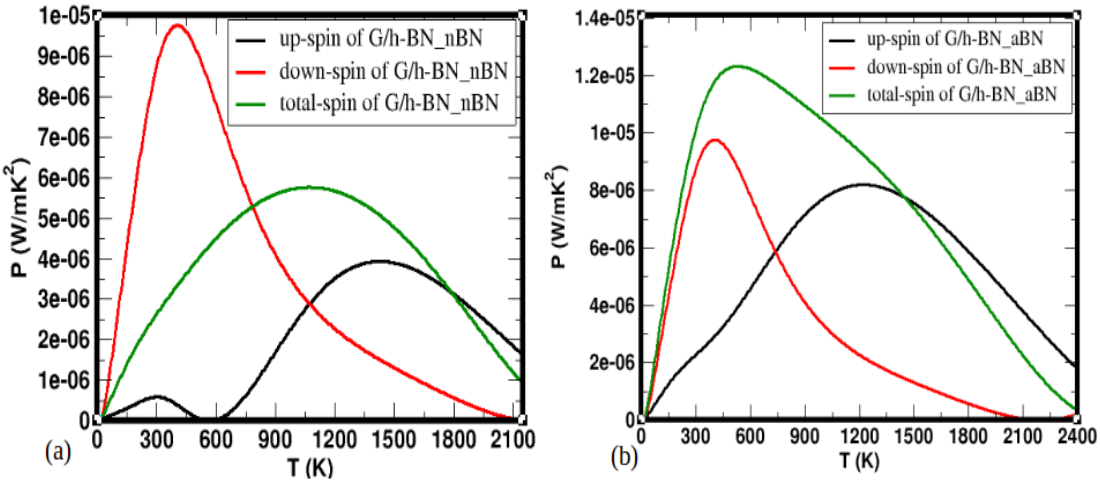

Figure 50: Effect of temperature on thermoelectric power factor ($P = S^2 \sigma$) at constant (Fermi) energy of G/h-BN_nBN and G/h-BN_aBN materials, where X-axis represents temperature T (K) and Y-axis represents thermoelectric power factor P in (W/mK^2), (a) thermoelectric power factor of G/h-BN_nBN material, (b) thermoelectric power factor of G/h-BN_aBN material.

Moreover, we have calculated the value of P of G/h-BN_nBN and G/h-BN_aBN at room temperature and determined 2.63×10^{-6} W/mK^2 and 1.00×10^{-5} W/mK^2 respectively. From these calculations, we found that P values of defected HS materials are higher than that of non-defected HS materials. The materials have more thermoelectric power factor, reflect that they have more efficiency in thermoelectric devices (Baranowski et al., 2014). Hence, boron and nitrogen sites vacancy defected materials are auspicious candidates in the field of thermoelectricity. Some of the calculated data (temperature dependent with constant energy i.e. $E=E_f$) of our considered systems are presented in table (6).

In addition, we have observed the plots P vs chemical potential (μ) of G/h-BN, G/h-BN_1N, G/h-BN_nBN and G/h-BN_aBN materials at different constant temperatures as shown in figure (51). At room temperature, P of G/h-BN is found to be 5×10^{-4} W/mK^2 at 0.12 eV. This is slightly less than P of pristine graphene (Reshak et al., 2014), which is due to less S of h-BN in HS. Similarly, we obtained the P of G/h-BN_1N, G/h-BN_nBN and G/h-BN_aBN and found to be 3.5×10^{-4} W/mK^2 at 0.06 eV, 5×10^{-4} W/mK^2 at 0.12 eV and 5×10^{-4} W/mK^2 at 0.12 eV respectively. They are analogous with the value of G/h-BN. Hence, P vs μ plots also support the results of P vs T plots. Therefore, our considered materials have conceivable thermoelectric properties.

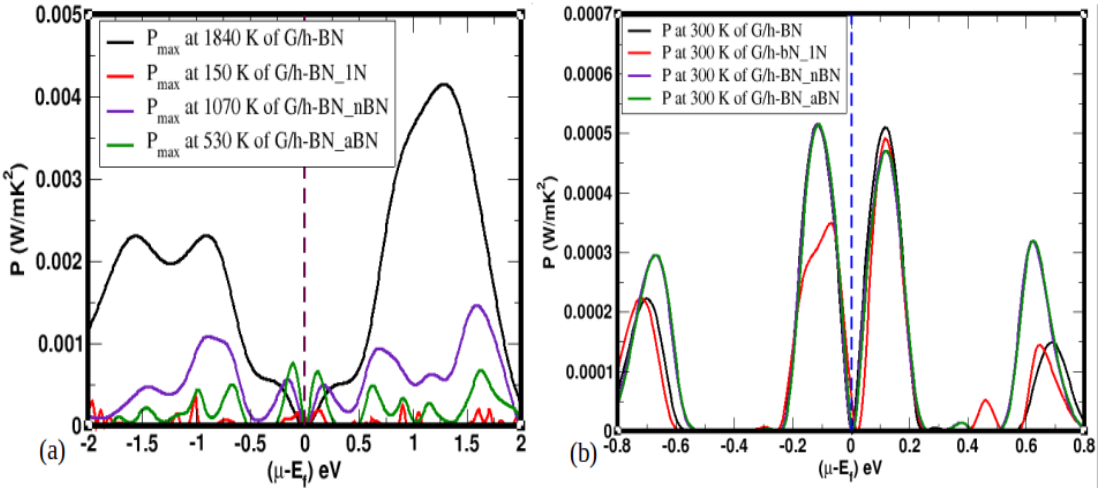

Figure 51: Variation of thermoelectric power factor ($P = S^2\sigma$) with chemical potential μ (energy) of G/h-BN, G/h-BN_1N, G/h-BN_nBN and G/h-BN_aBN materials at different constant temperatures, where X-axis represents chemical potential μ (energy) in eV and Y-axis represents thermoelectric power factor P in (W/mK^2), (a) thermoelectric power factor of G/h-BN, G/h-BN_1N, G/h-BN_aBN, G/h-BN_nBN materials at different constant temperatures , (b) thermoelectric power factor of G/h-BN, G/h-BN_1N, G/h-BN_aBN, G/h-BN_nBN materials at constant 300 K temperature.

The effect of temperature (at constant $E = E_f$) on the thermoelectric power factor P of G/h-BN_1C and G/h-BN_2C materials with the contributions of up-spin, down-spin and total-spin channels are shown in figures (52a) and (52b) respectively. Both the materials possess similar trend in the graphs, that is they initially increased up to the maximum value and then decrease continuously. The maximum P value due to up-spin, down-spin and total-spin channels at constant energy ($E = E_f$) of G/h-BN_1C is 8.68×10^{-5} W/mK^2 at 180 K, 1.70×10^{-5} W/mK^2 at 570 K and 3.53×10^{-5} W/mK^2 at 420 K, and of G/h-BN_2C is 3.08×10^{-4} W/mK^2 at 1330 K, 6.33×10^{-4} W/mK^2 at 1790 K and 8.52×10^{-4} W/mK^2 at 1590 K. Also, P of G/h-BN_1C and G/h-BN_2C materials at 300 K have 2.76×10^{-5} W/mK^2 and 5.91×10^{-5} W/mK^2 respectively, which are according to their Seebeck coefficient.

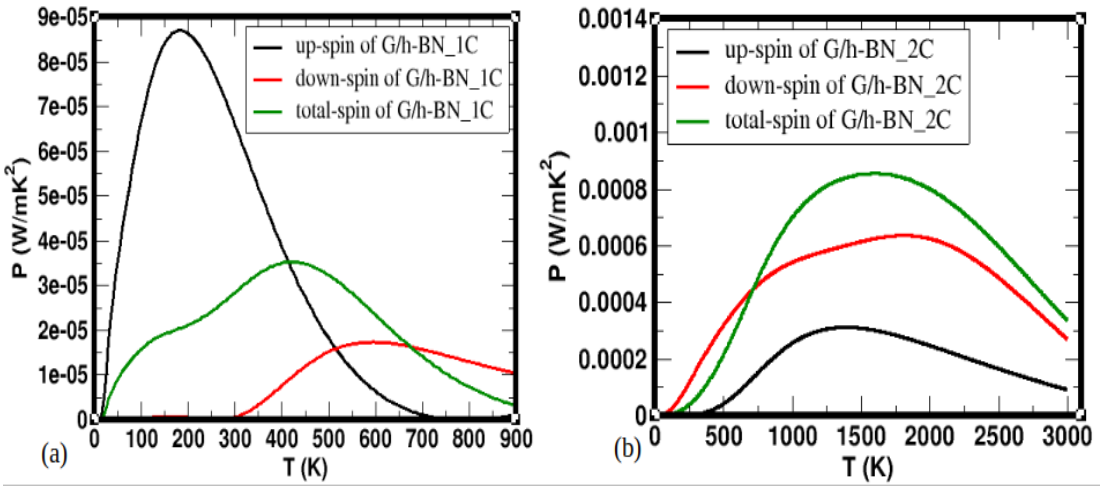

Figure 52: Effect of temperature on thermoelectric power factor (P = $S^2\,\sigma$) at constant (Fermi) energy of G/h-BN_1C and G/h-BN_2C materials, where X-axis represents temperature T (K) and Y-axis represents thermoelectric power factor P in (W/mK^2), (a) thermoelectric power factor of G/h-BN_1C material, (b) thermoelectric power factor of G/h-BN_2C material.

Similarly, we have calcualted the contributions of up-spin, down-spin and total-spin channels on P of G/h-BN_1B with different temperature T at constant E = E_f as shown in figure (53a). The nature of graph is different than of our considered other defected HS materials. The P value of G/h-BN_1B increases continuously with increase in temperature. This difference in the nature of graph comes directly from their variation in the value of S with temperature (i.e. P = $S^2\,\sigma$). P of G/h-BN_1B material at 300 K has 6.30×10^{-5} W/mK^2, which is obtained according to their Seebeck coefficient. In addition, we have developed the graphs between P vs chemical potential (μ) of G/h-BN_1B, G/h-BN_1C and G/h-BN_2C materials at constant temperature as shown in figure (53b). It is found that maximum P of G/h-BN_1B has 1.47×10^{-3} W/mK^2, G/h-BN_1C has 2.40×10^{-3} W/mK^2 and G/h-BN_1C has 5.36×10^{-4} W/mK^2. Based on these calculated P values, we predicted that all the materials are promising candidates in the fields of thermoelectricity.

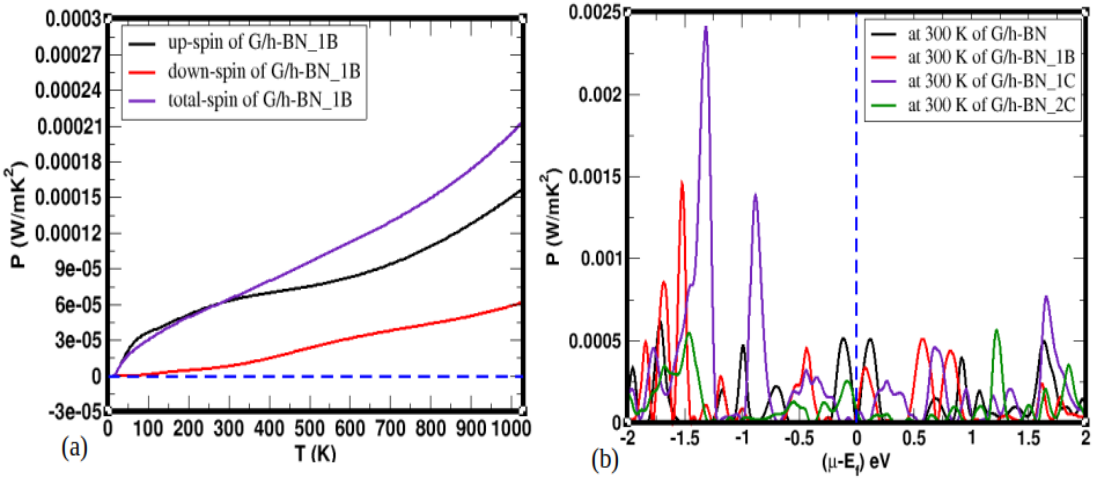

Figure 53: Effect of temperature on thermoelectric power factor ($P = S^2 \sigma$) at constant (Fermi) energy of G/h-BN_1B, and variation of thermoelectric power factor with chemical potential μ (energy) in eV at constant temperature T (K), (a) effect of temperature on thermoelectric power factor of G/h-BN_1B material, where X-axis represents temperature T (K) and Y-axis represents thermoelectric power factor in P in (W/mK^2, (b) variation of thermoelectric power factor P in (W/mK^2) with chemical potential μ (energy) in eV at constant 300 K temperature of G/h-BN, G/h-BN_1B, G/h-BN_1C and G/h-BN_2C materials.

We have summarized the estimated results (data) obtained from the calculations of Seebeck coefficient, electrical conductivity, electronic contribution of thermal conductivity and thermoelectric power factor of graphene, h-BN, G/h-BN, G/h-BN_1N, G/h-BN_nBN, G/h-BN_aBN, G/h-BN_1B, G/h-BN_1C and G/h-BN_2C materials are presented in above table (6).

CHAPTER 5

5. CONCLUSIONS AND RECOMMENDATIONS

Conclusions

We have studied the structural, electronic, magnetic and transport properties of 2D van der Waals G/h-BN HS, and B, N and C atoms vacancy defects in G/h-BN HS materials. Simulations are carried out under spin-polarized DFT method along with vdWs correction DFT-D2 approach. Quantum ESPRESSO (QE) and BoltzTraP (BT) software packages have been employed for the computational work.

Structural stability of materials are measured in terms of their binding energy. The estimated binding energy of G/h-BN HS is found to be -41.88 meV/Å^2, which is good agreement with experimentally reported values in literature within $\approx$ 7 %. Similarly, we have calculated the binding energy of 1B defect in G/h-BN (G/h-BN_1B), 1N defect in G/h-BN (G/h-BN_1N), nearest neighbour 1B and 1N defects in G/h-BN (G/h-BN_nBN), alternate zone of 1B and 1N defects in G/h-BN (G/h-BN_aBN), 1C defect in G/h-BN (G/h-BN_1C) and 2C defects in G/h-BN G/h-BN_2C materials. They have -30.36 meV/Å^2, -38.83 meV/Å^2, -23.79 meV/Å^2, -28.83 meV/Å^2, -28.30 meV/Å^2 and -22.82 meV/Å^2 values respectively. These are comparable values with the values of other 2D HS materials within $\approx$ 9 %. We have also estimated interlayer distance of the constituents of HS materials, which agrees with the experimentally reported values of other 2D HS materials within $\approx$ 6 %. Hence, from the binding energy and interlayer distance calculations, our considered materials are found to be stable 2D vdWs HS materials.

The electronic properties of monolayer (ML), and pristine and defected HS materials are explored based on their band and DOS calculations. It is found that graphene has zero band gap energy (0 eV) and h-BN has wide band gap energy (4.98 eV), they are fairly close with the experimentally reported values. On the other hand, G/h-BN, G/h-BN_1B, G/h-BN_1N, G/h-BN_nBN and G/h-BN_aBN open small energy band gap of values 2.60 meV, 9.75 meV, 33.84 meV, 1.71 meV and 2.73 meV respectively, and are comparable with the reported values. Hence they have semimetallic properties. In addition, we have analyzed the band structure plots of G/h-BN_1C and G/h-BN_2C

materials, and found that G/h-BN_1C has small band gap (0.40 eV) in its band structure. But, band states of G/h-BN_2C are seen near the Fermi energy level. Thus, G/h-BN_1C is a n-type semiconductor (it has the properties of semiconductor) and G/h-BN_2C has metallic properties.

Magnetic properties of our considered materials have been analyzed using their DOS and PDOS plots. It is found that graphene and h-BN have non-magnetic properties. On the other hand, pristine and vacancy defected HS materials have magnetic properties. Magnetic moments of G/h-BN, G/h-BN_1B, G/h-BN_1N, G/h-BN_nBN, G/h-BN_aBN, G/h-BN_1C and G/h-BN_2C materials have values 0.04 $\mu_B/cell$, -2.96 $\mu_B/cell$, 0.97 $\mu_B/cell$, -1.96 $\mu_B/cell$, 2.01 $\mu_B/cell$, 0.39 $\mu_B/cell$ and 1.89 $\mu_B/cell$ respectively. Hence, it is found that non-magnetic ML materials change into weak magnetic G/h-BN HS as the formation of HS, and G/h-BN HS converts into strong magnetic material by virtue of vacancy defects.

Beside the structural, electronic and magnetic properties, we have analyzed transport properties of our considered materials based on their Seebeck coefficient, electrical conductivity, electronic contribution on thermal conductivity and theromelectric power factor due to the effect of different temperatures by taking constant energy (Fermi), and chemical potential (energy) by taking constant temperature. It is found that all the materials are promissing candidates in the fields of thermoelectricity.

Recommendations

Every research work is performed with the vision of ultimately arriving at a fruitful result which can aid in further development. On the same note we hope our work also plays a vital role in further enhancement of vacancy defected G/h-BN system and becomes a reference for those who are interested in this field. The following research works can be further enhancement of our work:

- Study of optical properties of material is crucial, so we can explore the effect of B, N and C sites vacancy defects on optical properties of G/h-BN HS material.
- Physical properties of material are influenced by electric field and stress effect. Hence, we can investigate the physical properties of B, N and C atoms vacancy defected G/h-BN HS materials using electric field and stress effect.
- Physical properties of defected HS materials are tuned by molecular adsorption. Therefore, we can study the structural, electronic, magnetic and transport properties of B and N sites vacancy defected G/h-BN HS material by the adsorption of water molecule.

- The study of transport properties of materials are important for the production of high effiency thermoelectric devices. Thermal properties of materials are determined based on their thermoelectric figure of merit (ZT). ZT depends on Seebeck coefficient, electrical conductivity and total thermal conductivity of materials. Therefore, we can study the transport properties of vacancy defected G/h-BN HS materials on the basis of their thermoelectric figure of merit (ZT).

CHAPTER 6

6. SUMMARY

In this work, structural, electronic, magnetic and transport properties of graphene and h-BN ML, and G/h-BN, G/h-BN_1B, G/h-BN_1N, G/h-BN_nBN, G/h-BN_aBN, G/h-BN_1C and G/h-BN_2C HS materials have been studied using first-principles calculations through DFT with vdWs correction DFT-D2 method. Quantum ESPRESSO and BoltzTraP packages are used as a computational tools. As we know that most of the components in spintonic, electronic, optoelectronic and memory devices are used based on structural, electronic, magnetic and transport properties of materials. Thus, in present work, we have explored the structural, electronic, magnetic and transport properties of our above designed materials. The structural stability of all considered materials are studied, and found to be stable 2D vdWs HS materials. Electronic properties of the materials are determined through band and DOS calculations. On the other hand, magnetic properties of materials are analyzed from DOS and PDOS calculations. It is found that graphene and h-BN ML are non-magnetic zero band gap and wide band gap materials respectively. However, pristine G/h-BN, and B and N atoms vacancy defects in G/h-BN have magnetic and semimetallic properties. Moreover, we have analyzed the band, DOS and PDOS of C sites vacancy defects in G/h-BN. It is found that G/h-BN_1C is a n-type semiconductor having magnetic properties, whereas G/h-BN_2C has metallic and magnetic properties. The nature of material is determined according to the presence of band states around the Fermi energy level in band structure, and distributed spin states around the Fermi energy level in DOS plots. The magnetic properties are predicted on the basis of magnetic moment which are acquired by the results of distributed unpaired spins of valence electrons of atoms in DOS and PDOS plots. Transport properties of materials are determined by the analysis of their transport parameters. Therefore, in the present work we have estimated the Seebeck coefficient, electrical conductivity, electronic contribution on thermal conductivity and thermoelectric power factor of considered materials. It is found that all our considered ML, HS, and B, N and C sites vacancy defects in HS have auspicious thermal properties, and hence they appeal to be in the fields of thermoelectricity.

REFERENCES

Abdellaoui, A., Bath, A., Bouchikhi, B., & Baehr, O. (1997). Structure and optical properties of boron nitride thin films prepared by pecvd. *Materials Science and Engineering: B*, *47*(3), 257–262.

Aggoune, W., Cocchi, C., Nabok, D., Rezouali, K., Belkhir, M. A., & Draxl, C. (2018). Dimensionality of excitons in stacked van der waals materials: The example of hexagonal boron nitride. *Physical Review B*, *97*(24), 241114.

Aggoune, W., Cocchi, C., Nabok, D., Rezouali, K., Belkhir, M. A., & Draxl, C. (2020). Structural, electronic, and optical properties of periodic graphene/h-bn van der waals heterostructures. *Physical Review Materials*, *4*(8), 084001.

Agrawal, O. P. (2002). Formulation of euler–lagrange equations for fractional variational problems. *Journal of Mathematical Analysis and Applications*, *272*(1), 368–379.

Andrew, R. C., Mapasha, R. E., Ukpong, A. M., & Chetty, N. (2012). Mechanical properties of graphene and boronitrene. *Physical Review B*, *85*(12), 125428.

Ashcroft, N. W., Mermin, N. D., et al. (1976). *Solid state physics*. holt, rinehart and winston, new york London.

Avouris, P., Chen, Z., & Perebeinos, V. (2007). Carbon-based electronics. *Nature Nanotechnology*, *2*(10), 605–615.

Balandin, A. A., Ghosh, S., Bao, W., Calizo, I., Teweldebrhan, D., Miao, F., & Lau, C. N. (2008). Superior thermal conductivity of single-layer graphene. *Nano Letters*, *8*(3), 902–907.

Baranowski, L. L., Snyder, G. J., & Toberer, E. S. (2014). The misconception of maximum power and power factor in thermoelectrics. *J. Appl. Phys.*, *115*, 126102.

Barone, V., & Peralta, J. E. (2008). Magnetic boron nitride nanoribbons with tunable electronic properties. *Nano Letters*, *8*(8), 2210–2214.

Baroni, S., Dal Corso, A., De Gironcoli, S., Giannozzi, P., Cavazzoni, C., Ballabio, G., ... others (2005). Quantum espresso: open-source package for research in elec-

tronic structure, simulation, and optimization. *Code available from http://www. quantum-espresso. org*.

Baroni, S., De Gironcoli, S., Dal Corso, A., & Giannozzi, P. (2001). Phonons and related crystal properties from density-functional perturbation theory. *Reviews of Modern Physics*, *73*(2), 515.

Basu, S., & Bhattacharyya, P. (2012). Recent developments on graphene and graphene oxide based solid state gas sensors. *Sensors and Actuators B: Chemical*, *173*, 1–21.

Becke, A. D. (1988). Density-functional exchange-energy approximation with correct asymptotic behavior. *Physical Review A*, *38*(6), 3098.

Beniwal, S., Hooper, J., Miller, D. P., Costa, P. S., Chen, G., Liu, S.-Y., . . . Enders, A. (2017). Graphene-like boron–carbon–nitrogen monolayers. *ACS Nano*, *11*(3), 2486–2493.

Berger, C., Song, Z., Li, X., Wu, X., Brown, N., Naud, C., . . . others (2006). Electronic confinement and coherence in patterned epitaxial graphene. *Science*, *312*(5777), 1191–1196.

Berger, M. (2009). *Nano-society: pushing the boundaries of technology* (Vol. 8). Royal Society of Chemistry.

Berseneva, N., Krasheninnikov, A. V., & Nieminen, R. M. (2011). Mechanisms of postsynthesis doping of boron nitride nanostructures with carbon from first-principles simulations. *Physical Review Letters*, *107*(3), 035501.

Bhattacharya, A., Bhattacharya, S., Majumder, C., & Das, G. (2010). Transition-metal decoration enhanced room-temperature hydrogen storage in a defect-modulated graphene sheet. *The Journal of Physical Chemistry C*, *114*(22), 10297–10301.

Bhattarai, B., Dahal, T., & Adhikari, N. (2020). First principles study of thermoelectric properties of skutterudites: Ir4sb12 and ca0. 04ir4sb12. *Journal of Nepal Physical Society*, *6*(2), 1–9.

Biel, B., Triozon, F., Blase, X., & Roche, S. (2009). Chemically induced mobility gaps in graphene nanoribbons: a route for upscaling device performances. *Nano Letters*, *9*(7), 2725–2729.

Blochl, P. E., Jepsen, O., & Andersen, O. K. (1994). Improved tetrahedron method for brillouin-zone integrations. *Physical Review B*, *49*(23), 16223.

Boldrin, L., Scarpa, F., Chowdhury, R., & Adhikari, S. (2011). Effective mechanical properties of hexagonal boron nitride nanosheets. *Nanotechnology*, *22*(50), 505702.

Born, M., & Oppenheimer, R. (1927). Zur quantentheorie der molekeln. *Annalen der Physik*, *389*(20), 457–484.

Brinkman, W. F. (1986). *Nuclear physics* (Vol. 6). National Academy Press.

Capelle, K. (2006). A bird's-eye view of density-functional theory. *Brazilian Journal of Physics*, *36*, 1318–1343.

Cassabois, G., Valvin, P., & Gil, B. (2016). Intervalley scattering in hexagonal boron nitride. *Physical Review B*, *93*(3), 035207.

Castro, E. V., Novoselov, K., Morozov, S., Peres, N., Dos Santos, J. L., Nilsson, J., ... Neto, A. C. (2007). Biased bilayer graphene: semiconductor with a gap tunable by the electric field effect. *Physical Review Letters*, *99*(21), 216802.

Ceperley, D. M., & Alder, B. J. (1980). Ground state of the electron gas by a stochastic method. *Physical Review Letters*, *45*(7), 566.

Chan, K. T., Neaton, J., & Cohen, M. L. (2008). First-principles study of metal adatom adsorption on graphene. *Physical Review B*, *77*(23), 235430.

Chatterjee, S., Bultinck, N., & Zaletel, M. P. (2020). Symmetry breaking and skyrmionic transport in twisted bilayer graphene. *Physical Review B*, *101*(16), 165141.

Chen, C.-C., Li, Z., Shi, L., & Cronin, S. B. (2015). Thermoelectric transport across graphene/hexagonal boron nitride/graphene heterostructures. *Nano Research*, *8*(2), 666–672.

Chen, J., Badioli, M., Alonso-Gonzalez, P., Thongrattanasiri, S., Huth, F., Osmond, J., ... others (2012). Optical nano-imaging of gate-tunable graphene plasmons. *Nature*, *487*(7405), 77–81.

Chen, J., Jang, C., Xiao, S., Ishigami, M., & Fuhrer, M. S. (2008). Intrinsic and extrinsic performance limits of graphene devices on sio2. *Nature Nanotechnology*, *3*(4), 206–209.

Chopra, N. G., Luyken, R., Cherrey, K., Crespi, V. H., Cohen, M. L., Louie, S. G., & Zettl, A. (1995). Boron nitride nanotubes. *Science*, *269*(5226), 966–967.

Cole, L. A., & Perdew, J. (1982). Calculated electron affinities of the elements. *Physical Review A*, *25*(3), 1265.

Cooper, D., D'Anjou, B., Ghattamaneni, N., Harack, B., Hilke, M., Horth, A., ... others (2012). Isrn condensed matter physics. *Article ID*, *501686*, 56.

Crespi, V. H., Benedict, L. X., Cohen, M. L., & Louie, S. G. (1996). Prediction of a pure-carbon planar covalent metal. *Physical Review B*, *53*(20), R13303.

Dahal, T., Gahlawat, S., Jie, Q., Dahal, K., Lan, Y., White, K., & Ren, Z. (2015). Thermoelectric and mechanical properties on misch metal filled p-type skutterudites mm0. 9fe4- xcoxsb12. *Journal of Applied Physics*, *117*(5), 055101.

Dahal, T., Jie, Q., Joshi, G., Chen, S., Guo, C., Lan, Y., & Ren, Z. (2014). Thermoelectric property enhancement in yb-doped n-type skutterudites ybxco4sb12. *Acta Materialia*, *75*, 316–321.

Dean, C. R., Young, A. F., Meric, I., Lee, C., Wang, L., Sorgenfrei, S., ... others (2010). Boron nitride substrates for high-quality graphene electronics. *Nature Nanotechnology*, *5*(10), 722–726.

Decker, R., Wang, Y., Brar, V. W., Regan, W., Tsai, H.-Z., Wu, Q., ... Crommie, M. F. (2011). Local electronic properties of graphene on a bn substrate via scanning tunneling microscopy. *Nano Letters*, *11*(6), 2291–2295.

Dirac, P. A. (1930). Note on exchange phenomena in the thomas atom. In *Mathematical proceedings of the cambridge philosophical society* (Vol. 26, pp. 376–385).

Dreizler, R. M., & Gross, E. K. (2012). *Density functional theory: an approach to the quantum many-body problem*. Springer Science & Business Media.

D'Souza, R., & Mukherjee, S. (2016a). First principles calculation of thermoelectric parameters of monolayer-and bilayer-graphene and heterostructures of graphene and h-bn. In *Journal of physics: Conference series* (Vol. 759, p. 012040).

D'Souza, R., & Mukherjee, S. (2016b). Thermoelectric transport in graphene/h-bn/graphene heterostructures: A computational study. *Physica E: Low-dimensional Systems and Nanostructures*, *81*, 96–101.

Elias, D. C., Nair, R. R., Mohiuddin, T., Morozov, S., Blake, P., Halsall, M., ... others (2009). Control of graphene's properties by reversible hydrogenation: evidence for graphane. *Science*, *323*(5914), 610–613.

Elsasser, C., Fahnle, M., Chan, C. T., & Ho, K. (1994). Density-functional energies and forces with gaussian-broadened fractional occupations. *Physical Review B*, *49*(19), 13975.

Faccio, R., Fernandezwerner, L., Pardo, H., Goyenola, C., Ventura, O. N., & Mombr'u, A. W. (2010). Electronic and structural distortions in graphene induced by

carbon vacancies and boron doping. *The Journal of Physical Chemistry C*, *114*(44), 18961–18971.

Fedorov, A., Popov, Z., Fedorov, D., Eliseeva, N., Serjantova, M., & Kuzubov, A. (2012). Dft investigation of the influence of ordered vacancies on elastic and magnetic properties of graphene and graphene-like sic and bn structures. *Physica Status Solidi (b)*, *249*(12), 2549–2552.

Fermi, E. (1927). Statistical method to determine some properties of atoms. *Rend. Accad. Naz. Lincei*, *6*(602-607), 5.

Fermi, E. (1928). Eine statistische methode zur bestimmung einiger eigenschaften des atoms und ihre anwendung auf die theorie des periodischen systems der elemente. *Zeitschrift fur Physik*, *48*(1), 73–79.

Fock, V. (1930). Bemerkung zum virialsatz. *Zeitschrift fur Physik*, *63*(11), 855–858.

Gao, R., Yin, L., Wang, C., Qi, Y., Lun, N., Zhang, L., ... Wang, X. (2009). High-yield synthesis of boron nitride nanosheets with strong ultraviolet cathodoluminescence emission. *The Journal of Physical Chemistry C*, *113*(34), 15160–15165.

Gao, T., Song, X., Du, H., Nie, Y., Chen, Y., Ji, Q., ... Liu, Z. (2015). Temperature-triggered chemical switching growth of in-plane and vertically stacked graphene-boron nitride heterostructures. *Nature Communications*, *6*(1), 1–8.

Geim, A., & Novoselov, K. (2007). The rise of graphene. *Nature Materials*, *6*(3), 183–191.

Geim, A. K. (2009). Graphene: status and prospects. *Science*, *324*(5934), 1530–1534.

Geim, A. K. (2011). Random walk to graphene (nobel lecture). *Angewandte Chemie International Edition*, *50*(31), 6966–6985.

Geng, X., Niu, L., Xing, Z., Song, R., Liu, G., Sun, M., ... others (2010). Aqueous-processable noncovalent chemically converted graphene–quantum dot composites for flexible and transparent optoelectronic films. *Advanced Materials*, *22*(5), 638–642.

Giannozzi, P., Baroni, S., Bonini, N., Calandra, M., Car, R., Cavazzoni, C., ... others (2009). Quantum espresso: a modular and open-source software project for quantum simulations of materials. *Journal of Physics: Condensed Matter*, *21*(39), 395502.

Gibertini, M., Tomadin, A., Polini, M., Fasolino, A., & Katsnelson, M. (2010). Electron density distribution and screening in rippled graphene sheets. *Physical Review B*, *81*(12), 125437.

Gomeznavarro, C., Burghard, M., & Kern, K. (2008). Elastic properties of chemically derived single graphene sheets. *Nano Letters*, *8*(7), 2045–2049.

Gomezsantos, G., & Stauber, T. (2011). Measurable lattice effects on the charge and magnetic response in graphene. *Physical Review Letters*, *106*(4), 045504.

Goriachko, A., He, Y., Knapp, M., Over, H., Corso, M., Brugger, T., ... Greber, T. (2007). Self-assembly of a hexagonal boron nitride nanomesh on ru (0001). *Langmuir*, *23*(6), 2928–2931.

Grimme, S. (2004). Accurate description of van der waals complexes by density functional theory including empirical corrections. *Journal of Computational Chemistry*, *25*(12), 1463–1473.

Grimme, S. (2006). Semiempirical gga-type density functional constructed with a long-range dispersion correction. *Journal of Computational Chemistry*, *27*(15), 1787–1799.

Gross, E. K., Oliveira, L. N., & Kohn, W. (1988). Rayleigh-ritz variational principle for ensembles of fractionally occupied states. *Physical Review A*, *37*(8), 2805.

Guide, G. U. (n.d.). Available online: http://plasma-gate. weizmann. ac. il/grace/doc. *UsersGuide. html (accessed on 26 April 2019)*.

Hamann, D., Schluter, M., & Chiang, C. (1979). Norm-conserving pseudopotentials. *Physical Review Letters*, *43*(20), 1494.

Han, S., Garcia, A. V., Oida, S., Jenkins, K. A., & Haensch, W. (2014). Graphene radio frequency receiver integrated circuit. *Nature Communications*, *5*(1), 1–6.

Han, S. W., Yun, W. S., Woo, W. J., Kim, H., Park, J., Hwang, Y. H., ... others (2021). Interface defect engineering of a large-scale cvd-grown mos2 monolayer via residual sodium at the sio2/si substrate. *Advanced Materials Interfaces*, *8*(14), 2100428.

Han, W.-Q., Wu, L., Zhu, Y., Watanabe, K., & Taniguchi, T. (2008). Structure of chemically derived mono-and few-atomic-layer boron nitride sheets. *Applied Physics Letters*, *93*(22), 223103.

Hartree, D. R. (1928). The wave mechanics of an atom with a non-coulomb central field. part ii. some results and discussion. In *Mathematical proceedings of the cambridge philosophical society* (Vol. 24, pp. 111–132).

Hashimoto, A., Suenaga, K., Gloter, A., Urita, K., & Iijima, S. (2004). Direct evidence for atomic defects in graphene layers. *Nature*, *430*(7002), 870–873.

Henck, H., Pierucci, D., Fugallo, G., Avila, J., Cassabois, G., Dappe, Y. J., ... others (2017). Direct observation of the band structure in bulk hexagonal boron nitride. *Physical Review B*, *95*(8), 085410.

Hohenberg, P., & Kohn, W. (1964a). Density functional theory (dft). *Physical Review*, *136*, B864.

Hohenberg, P., & Kohn, W. (1964b). Inhomogeneous electron gas. *Physical Review*, *136*(3B), B864.

Hou, Z., Wang, X., Ikeda, T., Terakura, K., Oshima, M., Kakimoto, M.-a., & Miyata, S. (2012). Interplay between nitrogen dopants and native point defects in graphene. *Physical Review B*, *85*(16), 165439.

Hu, Z., Wu, Z., Han, C., He, J., Ni, Z., & Chen, W. (2018). Two-dimensional transition metal dichalcogenides: interface and defect engineering. *Chemical Society Reviews*, *47*(9), 3100–3128.

Huang, Z., Liu, H., Hu, R., Qiao, H., Wang, H., Liu, Y., ... Zhang, H. (2020). Structures, properties and application of 2d monoelemental materials (xenes) as graphene analogues under defect engineering. *Nano Today*, *35*, 100906.

Huat, B. B., Prasad, A., Asadi, A., & Kazemian, S. (2014). *Geotechnics of organic soils and peat*. CRC Press, Taylor & Francis Group.

Ilyasov, V., Meshi, B., Nguyen, V., Ershov, I., & Nguyen, D. (2014). Tuning the band structure, magnetic and transport properties of the zigzag graphene nanoribbons/hexagonal boron nitride heterostructures by transverse electric field. *The Journal of Chemical Physics*, *141*(1), 014708.

Israelachvili, J. N., & Tabor, D. (1972). The measurement of van der waals dispersion forces in the range 1.5 to 130 nm. *Proceedings of the Royal Society of London. A. Mathematical and Physical Sciences*, *331*(1584), 19–38.

Jiao, L., Zhang, L., Wang, X., Diankov, G., & Dai, H. (2009). Narrow graphene nanoribbons from carbon nanotubes. *Nature*, *458*(7240), 877–880.

Jin, C., Lin, F., Suenaga, K., & Iijima, S. (2009). Fabrication of a freestanding boron nitride single layer and its defect assignments. *Physical Review Letters*, *102*(19), 195505.

Jo, I., Pettes, M. T., Kim, J., Watanabe, K., Taniguchi, T., Yao, Z., & Shi, L. (2013). Thermal conductivity and phonon transport in suspended few-layer hexagonal boron nitride. *Nano Letters*, *13*(2), 550–554.

Joshi, N., & Ghosh, P. (2013). Substrate-induced changes in the magnetic and electronic properties of hexagonal boron nitride. *Physical Review B*, *87*(23), 235440.

Kaloni, T. P., Joshi, R., Adhikari, N., & Schwingenschlogl, U. (2014). Band gap tunning in bn-doped graphene systems with high carrier mobility. *Applied Physics Letters*, *104*(7), 073116.

Kim, K. S., Zhao, Y., Jang, H., Lee, S. Y., Kim, J. M., Kim, K. S., ... Hong, B. H. (2009). Large-scale pattern growth of graphene films for stretchable transparent electrodes. *Nature*, *457*(7230), 706–710.

Kim, Y., Ihm, J., Yoon, E., & Lee, G.-D. (2011). Dynamics and stability of divacancy defects in graphene. *Physical Review B*, *84*(7), 075445.

Kittel, C. (2005). Introduction to solid state physics. john wiley & sons, inc. *New York*.

Klimevs, J., & Michaelides, A. (2012). Perspective: Advances and challenges in treating van der waals dispersion forces in density functional theory. *The Journal of Chemical Physics*, *137*(12), 120901.

Koch, W., & Holthausen, M. C. (2015). *A chemist's guide to density functional theory*. John Wiley & Sons.

Kohn, W., & Sham, L. J. (1965). Self-consistent equations including exchange and correlation effects. *Physical Review*, *140*(4A), A1133.

Kokalj, A., & Mol, J. (n.d.). Graphics modelling, 1999, vol. 17, 176. *Code available from www. xcrysden. org*.

Krasheninnikov, A., & Banhart, F. (2007). Engineering of nanostructured carbon materials with electron or ion beams. *Nature Materials*, *6*(10), 723–733.

Kratzer, P., & Neugebauer, J. (2019). The basics of electronic structure theory for periodic systems. *Frontiers in Chemistry*, *7*, 106.

Kuzmenko, A. B., Van Heumen, E., Carbone, F., & Van Der Marel, D. (2008). Universal optical conductance of graphite. *Physical Review Letters*, *100*(11), 117401.

Kwon, Y., & Savitskii, A. (2001). Solid-state sintering of metal powder mixtures. *Journal of Materials Synthesis and Processing*, *9*(6), 299–317.

Lee, C., Wei, X., Kysar, J. W., & Hone, J. (2008). Measurement of the elastic properties and intrinsic strength of monolayer graphene. *Science*, *321*(5887), 385–388.

Lee, C., Yang, W., & Parr, R. G. (1988). Development of the colle-salvetti correlation-energy formula into a functional of the electron density. *Physical Review B*, *37*(2), 785.

Levine, I. N., Busch, D. H., & Shull, H. (2009). *Quantum chemistry* (Vol. 6). Pearson Prentice Hall Upper Saddle River, NJ.

Lherbier, A., Blase, X., Niquet, Y.-M., Triozon, F., & Roche, S. (2008). Charge transport in chemically doped 2d graphene. *Physical Review Letters*, *101*(3), 036808.

Li, L., Lee, I., Lim, D., Kang, M., Kim, G.-H., Aoki, N., ... Taniguchi, T. (2015). Raman shift and electrical properties of mos2 bilayer on boron nitride substrate. *Nanotechnology*, *26*(29), 295702.

Li, S., Sun, M., Chou, J.-P., Wei, J., Xing, H., & Hu, A. (2018). First-principles calculations of the electronic properties of sic-based bilayer and trilayer heterostructures. *Physical Chemistry Chemical Physics*, *20*(38), 24726–24734.

Li, X., Yin, J., Zhou, J., Wang, Q., & Guo, W. (2012). Exceptional high seebeck coefficient and gas-flow-induced voltage in multilayer graphene. *Applied Physics Letters*, *100*(18), 183108.

Liang, S., Cheng, B., Cui, X., & Miao, F. (2020). Van der waals heterostructures for high-performance device applications: challenges and opportunities. *Advanced Materials*, *32*(27), 1903800.

Lin, Y., Lu, N., Perealopez, N., Li, J., Lin, Z., Peng, X., ... others (2014). Direct synthesis of van der waals solids. *Acs Nano*, *8*(4), 3715–3723.

Lin, Y., Williams, T. V., Xu, T., Cao, W., Elsayedali, H. E., & Connell, J. W. (2011). Aqueous dispersions of few-layered and monolayered hexagonal boron nitride nanosheets from sonication-assisted hydrolysis: critical role of water. *The Journal of Physical Chemistry C*, *115*(6), 2679–2685.

Lindsay, L., & Broido, D. (2011). Enhanced thermal conductivity and isotope effect in single-layer hexagonal boron nitride. *Physical Review B*, *84*(15), 155421.

Liu, J., & Dai, X. (2020). Anomalous hall effect, magneto-optical properties, and nonlinear optical properties of twisted graphene systems. *npj Computational Materials*, *6*(1), 1–10.

Liu, L., & Shen, Z. (2009). Bandgap engineering of graphene: A density functional theory study. *Applied Physics Letters*, *95*(25), 252104.

Liu, Y., Gao, B., Xu, D., Wang, H.-m., & Zhao, J. (2014). Theoretical study on si-doped hexagonal boron nitride (h-bn) sheet: Electronic, magnetic properties, and reactivity. *Physics Letters A*, *378*(40), 2989–2994.

Liu, Z., Song, L., Zhao, S., Huang, J., Ma, L., Zhang, J., ... Ajayan, P. M. (2011). Direct growth of graphene/hexagonal boron nitride stacked layers. *Nano Letters*, *11*(5), 2032–2037.

Lynch, R., & Drickamer, H. (1966). Effect of high pressure on the lattice parameters of diamond, graphite, and hexagonal boron nitride. *The Journal of Chemical Physics*, *44*(1), 181–184.

Madsen, G. K., & Singh, D. J. (2006). Boltztrap. a code for calculating band-structure dependent quantities. *Computer Physics Communications*, *175*(1), 67–71.

Makarova, M., Akaishi, Y., Ikarashi, T., Rao, K., Yoshimura, S., & Saito, H. (2019). Alternating magnetic force microscopy: effect of si doping on the temporal performance degradation of amorphous fecob magnetic tips. *Journal of Magnetism and Magnetic Materials*, *471*, 209–214.

Mansoori, G. A. (2005). *Principles of nanotechnology: molecular-based study of condensed matter in small systems*. World Scientific.

Marzari, N., Vanderbilt, D., De Vita, A., & Payne, M. (1999). Thermal contraction and disordering of the al (110) surface. *Physical Review Letters*, *82*(16), 3296.

Mattausch, A., & Pankratov, O. (2007). Ab initio study of graphene on sic. *Physical Review Letters*, *99*(7), 076802.

Mayorov, A. S., Gorbachev, R. V., Morozov, S. V., Britnell, L., Jalil, R., Ponomarenko, L. A., ... others (2011). Micrometer-scale ballistic transport in encapsulated graphene at room temperature. *Nano Letters*, *11*(6), 2396–2399.

Mikhailov, S. (2011). *Physics and applications of graphene: Experiments*. BoD–Books on Demand.

Monkhorst, H. J., & Pack, J. D. (1976). Special points for brillouin-zone integrations. *Physical Review B*, *13*(12), 5188.

Nag, A., Raidongia, K., Hembram, K. P., Datta, R., Waghmare, U. V., & Rao, C. (2010). Graphene analogues of bn: novel synthesis and properties. *ACS Nano*, *4*(3), 1539–1544.

Nagashima, A., Tejima, N., Gamou, Y., Kawai, T., & Oshima, C. (1995). Electronic structure of monolayer hexagonal boron nitride physisorbed on metal surfaces. *Physical Review Letters*, *75*(21), 3918.

Nair, R. R., Blake, P., Grigorenko, A. N., Novoselov, K. S., Booth, T. J., Stauber, T., ... Geim, A. K. (2008). Fine structure constant defines visual transparency of graphene. *Science*, *320*(5881), 1308–1308.

Neto, A. C., Guinea, F., & Peres, N. M. (2006). Drawing conclusions from graphene. *Physics World*, *19*(11), 33.

Neto, A. C., Guinea, F., Peres, N. M., Novoselov, K. S., & Geim, A. K. (2009). The electronic properties of graphene. *Reviews of Modern Physics*, *81*(1), 109.

Neupane, H., & Adhikari, N. (2020). Structure, electronic and magnetic properties of 2d graphene-molybdenum disulphide (g-mos2) heterostructure (hs) with vacancy defects at mo sites. *Computational Condensed Matter*, *24*, e00489.

Neupane, H. K., & Adhikari, N. P. (2020a). First-principles study of c cites vacancy defects in water adsorbed graphene. *Himalayan Physics*, 19–29.

Neupane, H. K., & Adhikari, N. P. (2020b). Tuning structural, electronic, and magnetic properties of c sites vacancy defects in graphene/mos2 van der waals heterostructure materials: A first-principles study. *Advances in Condensed Matter Physics*, *2020*.

Neupane, H. K., & Adhikari, N. P. (2021a). Effect of vacancy defects in 2d vdw graphene/h-bn heterostructure: First-principles study. *AIP Advances*, *11*(8), 085218.

Neupane, H. K., & Adhikari, N. P. (2021b). First-principles study of structure, electronic, and magnetic properties of c sites vacancy defects in water adsorbed graphene/mos2 van der waals heterostructures. *Journal of Molecular Modeling*, *27*(3), 1–12.

Neupane, H. K., & Adhikari, N. P. (2021c). Structural, electronic and magnetic properties of s sites vacancy defects graphene/mos2 van der waals heterostructures: First-principles study. *International Journal of Computational Materials Science and Engineering*, *10*(02), 2150009.

Neupane, H. K., & Adhikari, N. P. (2022). Adsorption of water on c sites vacancy defected graphene/h-bn: First-principles study. *Journal of Molecular Modeling*, *28*(4), 1–10.

Ni, Z., Wang, H., Kasim, J., Fan, H., Yu, T., Wu, Y., ... Shen, Z. (2007). Graphene thickness determination using reflection and contrast spectroscopy. *Nano Letters*, *7*(9), 2758–2763.

Novoselov, K. S., Geim, A. K., Morozov, S. V., Jiang, D., Katsnelson, M. I., Grigorieva, I., ... Firsov, a. (2005). Two-dimensional gas of massless dirac fermions in graphene. *Nature*, *438*(7065), 197–200.

Novoselov, K. S., Geim, A. K., Morozov, S. V., Jiang, D.-e., Zhang, Y., Dubonos, S. V., ... Firsov, A. A. (2004). Electric field effect in atomically thin carbon films. *Science*, *306*(5696), 666–669.

Oh, D., Shin, B., & Ahn, J. (2010). Band engineering of bilayer graphene by metal atoms: First-principles calculations. *Applied Physics Letters*, *96*(23), 231916.

Okada, M., Sawazaki, T., Watanabe, K., Taniguch, T., Hibino, H., Shinohara, H., & Kitaura, R. (2014). Direct chemical vapor deposition growth of ws2 atomic layers on hexagonal boron nitride. *ACS Nano*, *8*(8), 8273–8277.

Okada, S., & Oshiyama, A. (2001). Magnetic ordering in hexagonally bonded sheets with first-row elements. *Physical Review Letters*, *87*(14), 146803.

Oli, B., Bhattarai, C., Nepal, B., & Adhikari, N. (2013). First-principles study of adsorption of alkali metals (li, na, k) on graphene. In *Advanced nanomaterials and nanotechnology* (pp. 515–529). Springer.

Ooi, N., Rairkar, A., Lindsley, L., & Adams, J. (2005). Electronic structure and bonding in hexagonal boron nitride. *Journal of Physics: Condensed Matter*, *18*(1), 97.

Oshima, C., Itoh, A., Rokuta, E., Tanaka, T., Yamashita, K., & Sakurai, T. (2000). A hetero-epitaxial-double-atomic-layer system of monolayer graphene/monolayer h-bn on ni (111). *Solid State Communications*, *116*(1), 37–40.

Pacile, D., Meyer, J., Girit, c., & Zettl, A. (2008). The two-dimensional phase of boron nitride: Few-atomic-layer sheets and suspended membranes. *Applied Physics Letters*, *92*(13), 133107.

Pankhurst, Q. A., Connolly, J., Jones, S. K., & Dobson, J. (2003). Applications of magnetic nanoparticles in biomedicine. *Journal of Physics D: Applied Physics*, *36*(13), R167.

Pantha, N., Belbase, K., & Adhikari, N. P. (2015). First-principles study of the interaction of hydrogen molecular on na-adsorbed graphene. *Applied Nanoscience*, *5*(4), 393–402.

Pantha, N., Khaniya, A., & Adhikari, N. P. (2015). Hydrogen storage on palladium adsorbed graphene: A density functional theory study. *International Journal of Modern Physics B*, *29*(20), 1550143.

Parac, M., Etinski, M., Peric, M., & Grimme, S. (2005). A theoretical investigation of the geometries and binding energies of molecular tweezer and clip host- guest systems. *Journal of Chemical Theory and Computation*, *1*(6), 1110–1118.

Parmenter, R. (1952). Electronic energy bands in crystals. *Physical Review*, *86*(4), 552.

Parr, R. G., et al. (1989). W. yang density functional theory of atoms and molecules. *Oxford University Press*, *1*, 1989.

Parr, R. G., & Weitao, Y. (1994). Aspects of atoms and molecules. In *Density-functional theory of atoms and molecules.* Oxford University Press.

Partoens, B., & Peeters, F. (2006). From graphene to graphite: Electronic structure around the k point. *Physical Review B*, *74*(7), 075404.

Peng, H.-X., Qin, F., & Phan, M.-H. (2016). *Ferromagnetic microwire composites: from sensors to microwave applications*. Springer.

Peng, Q., Guo, Z., Sa, B., Zhou, J., & Sun, Z. (2018). New gallium chalcogenides/arsenene van der waals heterostructures promising for photocatalytic water splitting. *International Journal of Hydrogen Energy*, *43*(33), 15995–16004.

Perdew, J. P. (1986). Density-functional approximation for the correlation energy of the inhomogeneous electron gas. *Physical Review B*, *33*(12), 8822.

Perdew, J. P., Burke, K., & Ernzerhof, M. (1996). Generalized gradient approximation made simple. *Physical Review Letters*, *77*(18), 3865.

Perdew, J. P., & Wang, Y. (1992). Accurate and simple analytic representation of the electron-gas correlation energy. *Physical Review B*, *45*(23), 13244.

Perdew, J. P., & Zunger, A. (1981). Self-interaction correction to density-functional approximations for many-electron systems. *Physical Review B*, *23*(10), 5048.

Pereira, V. M., Neto, A. C., & Peres, N. (2009). Tight-binding approach to uniaxial strain in graphene. *Physical Review B*, *80*(4), 045401.

Perumal, S., Samanta, M., Ghosh, T., Shenoy, U. S., Bohra, A. K., Bhattacharya, S., ... Biswas, K. (2019). Realization of high thermoelectric figure of merit in gete by complementary co-doping of bi and in. *Joule*, *3*(10), 2565–2580.

Pfrommer, B. G., Cote, M., Louie, S. G., & Cohen, M. L. (1997). Relaxation of crystals with the quasi-newton method. *Journal of Computational Physics*, *131*(1), 233–240.

Phuc, H. V., Hieu, N. N., Hoi, B. D., Phuong, L. T., & Nguyen, C. V. (2018). First principle study on the electronic properties and schottky contact of graphene adsorbed on mos2 monolayer under applied out-plane strain. *Surface Science*, *668*, 23–28.

Piacenza, M., & Grimme, S. (2005). Van der waals interactions in aromatic systems: structure and energetics of dimers and trimers of pyridine. *ChemPhysChem*, *6*(8), 1554–1558.

Quhe, R., Zheng, J., Luo, G., Liu, Q., Qin, R., Zhou, J., ... others (2012). Tunable and sizable band gap of single-layer graphene sandwiched between hexagonal boron nitride. *NPG Asia Materials*, *4*(2), e6–e6.

Radisavljevic, B., Whitwick, M. B., & Kis, A. (2012). Small-signal amplifier based on single-layer mos2. *Applied Physics Letters*, *101*(4), 043103.

Ramasubramaniam, A., Naveh, D., & Towe, E. (2011). Tunable band gaps in bilayer graphene- bn heterostructures. *Nano Letters*, *11*(3), 1070–1075.

Rao, C. e. e., Sood, A. e., Subrahmanyam, K. e., & Govindaraj, A. (2009). Graphene: the new two-dimensional nanomaterial. *Angewandte Chemie International Edition*, *48*(42), 7752–7777.

Repellin, C., Dong, Z., Zhang, Y.-H., & Senthil, T. (2020). Ferromagnetism in narrow bands of moire superlattices. *Physical Review Letters*, *124*(18), 187601.

Reshak, A. (2016). Thermoelectric properties of the spin-polarized half-metallic ferromagnetic cste and rbse compounds. *RSC Advances*, *6*(100), 98197–98207.

Reshak, A., Khan, S. A., & Auluck, S. (2014). Thermoelectric properties of a single graphene sheet and its derivatives. *Journal of Materials Chemistry C*, *2*(13), 2346–2352.

Robertson, A. W., Montanari, B., He, K., Allen, C. S., Wu, Y. A., Harrison, N. M., ... Warner, J. H. (2013). Structural reconstruction of the graphene monovacancy. *ACS Nano*, *7*(5), 4495–4502.

Roy, K., Padmanabhan, M., Goswami, S., Sai, T. P., Ramalingam, G., Raghavan, S., & Ghosh, A. (2013). Graphene–mos2 hybrid structures for multifunctional photoresponsive memory devices. *Nature Nanotechnology*, *8*(11), 826–830.

Rubio, A., Corkill, J. L., & Cohen, M. L. (1994). Theory of graphitic boron nitride nanotubes. *Physical Review B*, *49*(7), 5081.

Saunders, G. (1973). Semimetals and narrow gap semiconductors. *Contemporary Physics*, *14*(2), 149–166.

Schedin, F., Geim, A. K., Morozov, S. V., Hill, E., Blake, P., Katsnelson, M., & Novoselov, K. S. (2007). Detection of individual gas molecules adsorbed on graphene. *Nature Materials*, *6*(9), 652–655.

Schuster, R., Habenicht, C., Ahmad, M., Knupfer, M., & Buchner, B. (2018). Direct observation of the lowest indirect exciton state in the bulk of hexagonal boron nitride. *Physical Review B*, *97*(4), 041201.

Sepioni, M., Nair, R., Rablen, S., Narayanan, J., Tuna, F., Winpenny, R., . . . Grigorieva, I. (2010). Limits on intrinsic magnetism in graphene. *Physical Review Letters*, *105*(20), 207205.

Sharma, V., Kagdada, H. L., Jha, P. K., Spiewak, P., & Kurzydlowski, K. J. (2020). Thermal transport properties of boron nitride based materials: A review. *Renewable and Sustainable Energy Reviews*, *120*, 109622.

Si, M., & Xue, D. (2007). Magnetic properties of vacancies in a graphitic boron nitride sheet by first-principles pseudopotential calculations. *Physical Review B*, *75*(19), 193409.

Sichel, E., Miller, R., Abrahams, M., & Buiocchi, C. (1976). Heat capacity and thermal conductivity of hexagonal pyrolytic boron nitride. *Physical Review B*, *13*(10), 4607.

Singh, J. (2006). *Optical properties of condensed matter and applications* (Vol. 6). John Wiley & Sons.

Singh, R., & Kroll, P. (2009). Magnetism in graphene due to single-atom defects: dependence on the concentration and packing geometry of defects. *Journal of Physics: Condensed Matter*, *21*(19), 196002.

Slater, J. C. (1937). Wave functions in a periodic potential. *Physical Review*, *51*(10), 846.

Slotman, G., Van Wijk, M., Zhao, P.-L., Fasolino, A., Katsnelson, M., & Yuan, S. (2015). Effect of structural relaxation on the electronic structure of graphene on hexagonal boron nitride. *Physical Review Letters*, *115*(18), 186801.

Solozhenko, V., Lazarenko, A., Petitet, J., & Kanaev, A. (2001). Bandgap energy of graphite-like hexagonal boron nitride. *Journal of Physics and Chemistry of Solids*, *62*(7), 1331–1334.

Song, L., Ci, L., Lu, H., Sorokin, P. B., Jin, C., Ni, J., . . . others (2010). Large scale growth and characterization of atomic hexagonal boron nitride layers. *Nano Letters*, *10*(8), 3209–3215.

Sponza, L., Amara, H., Attaccalite, C., Latil, S., Galvani, T., Paleari, F., . . . Ducastelle, F. (2018). Direct and indirect excitons in boron nitride polymorphs: A story

of atomic configuration and electronic correlation. *Physical Review B*, *98*(12), 125206.

Sutter, P. W., Flege, J., & Sutter, E. A. (2008). Epitaxial graphene on ruthenium. *Nature Materials*, *7*(5), 406–411.

Tang, Y., Lee, C. S., Chen, Z., Yuan, G., Kang, Z., Luo, L., ... others (2009). High-quality graphenes via a facile quenching method for field-effect transistors. *Nano Letters*, *9*(4), 1374–1377.

Tetlow, H., De Boer, J. P., Ford, I., Vvedensky, D., Coraux, J., & Kantorovich, L. (2014). Growth of epitaxial graphene: Theory and experiment. *Physics Reports*, *542*(3), 195–295.

Thanh, N. T., Maclean, N., & Mahiddine, S. (2014). Mechanisms of nucleation and growth of nanoparticles in solution. *Chemical Reviews*, *114*(15), 7610–7630.

Thomas, L. H. (1927). The calculation of atomic fields. In *Mathematical proceedings of the cambridge philosophical society* (Vol. 23, pp. 542–548).

Tombros, N., Jozsa, C., Popinciuc, M., Jonkman, H. T., & Van Wees, B. J. (2007). Electronic spin transport and spin precession in single graphene layers at room temperature. *Nature*, *448*(7153), 571–574.

Topsakal, M., Akturk, E., & Ciraci, S. (2009). First-principles study of two-and one-dimensional honeycomb structures of boron nitride. *Physical Review B*, *79*(11), 115442.

Tran, T. T., Bray, K., Ford, M. J., Toth, M., & Aharonovich, I. (2016). Quantum emission from hexagonal boron nitride monolayers. *Nature Nanotechnology*, *11*(1), 37–41.

Tran, V., Pammi, S., Park, B.-J., Han, Y., Jeon, C., & Yoon, S.-G. (2019). Transfer-free graphene electrodes for super-flexible and semi-transparent perovskite solar cells fabricated under ambient air. *Nano Energy*, *65*, 104018.

Ulman, K., Bhaumik, D., Wood, B. C., & Narasimhan, S. (2014). Physical origins of weak h2 binding on carbon nanostructures: insight from ab initio studies of chemically functionalized graphene nanoribbons. *The Journal of Chemical Physics*, *140*(17), 174708.

Valimukhametova, A., Ryan, C., Paz, T., Grote, F., & Naumov, A. V. (2020). Experimental and theoretical inquiry into optical properties of graphene derivatives. *Nanotechnology*, *32*(1), 015709.

Vanderbilt, D. (1990). Soft self-consistent pseudopotentials in a generalized eigenvalue formalism. *Physical Review B*, *41*(11), 7892.

Vosko, S. H., Wilk, L., & Nusair, M. (1980). Accurate spin-dependent electron liquid correlation energies for local spin density calculations: a critical analysis. *Canadian Journal of Physics*, *58*(8), 1200–1211.

Vu, T. V., Hieu, N. V., Phuc, H. V., Hieu, N. N., Bui, H., Idrees, M., ... Nguyen, C. V. (2020). Graphene/wsete van der waals heterostructure: Controllable electronic properties and schottky barrier via interlayer coupling and electric field. *Applied Surface Science*, *507*, 145036.

Wang, E., Lu, X., Ding, S., Yao, W., Yan, M., Wan, G., ... others (2016). Gaps induced by inversion symmetry breaking and second-generation dirac cones in graphene/hexagonal boron nitride. *Nature Physics*, *12*(12), 1111–1115.

Wang, H., Feng, H., & Li, J. (2014). Graphene and graphene-like layered transition metal dichalcogenides in energy conversion and storage. *Small*, *10*(11), 2165–2181.

Wang, H., & Yu, G. (2016). Direct cvd graphene growth on semiconductors and dielectrics for transfer-free device fabrication. *Advanced Materials*, *28*(25), 4956–4975.

Wang, J., Cao, S., Sun, P., Ding, Y., Li, Y., & Ma, F. (2016). Optical advantages of graphene on the boron nitride in visible and sw-nir regions. *RSC Advances*, *6*(112), 111345–111349.

Wang, J., Ma, F., Liang, W., & Sun, M. (2017). Electrical properties and applications of graphene, hexagonal boron nitride (h-bn), and graphene/h-bn heterostructures. *Materials Today Physics*, *2*, 6–34.

Wang, J., Ma, F., & Sun, M. (2017). Graphene, hexagonal boron nitride, and their heterostructures: properties and applications. *RSC Advances*, *7*(27), 16801–16822.

Wang, Q. H., Kalantarzadeh, K., Kis, A., Coleman, J. N., & Strano, M. S. (2012). Electronics and optoelectronics of two-dimensional transition metal dichalcogenides. *Nature Nanotechnology*, *7*(11), 699–712.

Wang, S., Wang, X., & Warner, J. H. (2015). All chemical vapor deposition growth of mos2: h-bn vertical van der waals heterostructures. *ACS Nano*, *9*(5), 5246–5254.

Wang, X.-M., & Lu, S. (2015). First-principles study of the transport properties of graphene-hexagonal boron nitride superlattice. *Journal of Nanoscience and Nanotechnology*, *15*(4), 3025–3028.

Wang, Y., Huang, Y., Song, Y., Zhang, X., Ma, Y., Liang, J., & Chen, Y. (2009). Room-temperature ferromagnetism of graphene. *Nano Letters*, *9*(1), 220–224.

Watanabe, K., Taniguchi, T., & Kanda, H. (2004). Direct-bandgap properties and evidence for ultraviolet lasing of hexagonal boron nitride single crystal. *Nature Materials*, *3*(6), 404–409.

Watanabe, K., Taniguchi, T., Niiyama, T., Miya, K., & Taniguchi, M. (2009). Far-ultraviolet plane-emission handheld device based on hexagonal boron nitride. *Nature Photonics*, *3*(10), 591–594.

Woods, C., Britnell, L., Eckmann, A., Ma, R., Lu, J., Guo, H., ... others (2014). Commensurate–incommensurate transition in graphene on hexagonal boron nitride. *Nature Physics*, *10*(6), 451–456.

Wu, R., Liu, L., Peng, G., & Feng, Y. (2005). Magnetism in bn nanotubes induced by carbon doping. *Applied Physics Letters*, *86*(12), 122510.

Wu, R., Peng, G., Liu, L., & Feng, Y. (2005). Possible graphitic-boron-nitride-based metal-free molecular magnets from first principles study. *Journal of Physics: Condensed Matter*, *18*(2), 569.

Xue, J., Sanchez-Yamagishi, J., Bulmash, D., Jacquod, P., Deshpande, A., Watanabe, K., ... LeRoy, B. J. (2011). Scanning tunnelling microscopy and spectroscopy of ultra-flat graphene on hexagonal boron nitride. *Nature Materials*, *10*(4), 282–285.

Yang, K., Chen, Y., D'Agosta, R., Xie, Y., Zhong, J., & Rubio, A. (2012). Enhanced thermoelectric properties in hybrid graphene/boron nitride nanoribbons. *Physical Review B*, *86*(4), 045425.

Yang, X., Zhai, F., Hu, H., Hu, D., Liu, R., Zhang, S., ... Dai, Q. (2016). Far-field spectroscopy and near-field optical imaging of coupled plasmon–phonon polaritons in 2d van der waals heterostructures. *Advanced Materials*, *28*(15), 2931–2938.

Yankowitz, M., Xue, J., Cormode, D., Sanchez-Yamagishi, J. D., Watanabe, K., Taniguchi, T., ... LeRoy, B. J. (2012). Emergence of superlattice dirac points in graphene on hexagonal boron nitride. *Nature Physics*, *8*(5), 382–386.

Yao, W., & Fan, L. (2021). Defects in graphene/h-bn planar heterostructures: insights into the interfacial thermal transport properties. *Nanomaterials*, *11*(2), 500.

Yazyev, O. V., & Helm, L. (2007). Defect-induced magnetism in graphene. *Physical Review B*, *75*(12), 125408.

Yazyev, O. V., & Louie, S. G. (2010). Topological defects in graphene: Dislocations and grain boundaries. *Physical Review B*, *81*(19), 195420.

Yokomizo, Y., & Nakamura, J. (2013). Giant seebeck coefficient of the graphene/h-bn superlattices. *Applied Physics Letters*, *103*(11), 113901.

Yu, W. J., Li, Z., Zhou, H., Chen, Y., Wang, Y., Huang, Y., & Duan, X. (2013). Vertically stacked multi-heterostructures of layered materials for logic transistors and complementary inverters. *Nature Materials*, *12*(3), 246–252.

Yu, X., Hwang, C., Jozwiak, C. M., Kohl, A., Schmid, A. K., & Lanzara, A. (2011). New synthesis method for the growth of epitaxial graphene. *Journal of Electron Spectroscopy and Related Phenomena*, *184*(3-6), 100–106.

Zhang, C., Zhao, S., Jin, C., Koh, A. L., Zhou, Y., Xu, W., ... Liu, Z. (2015). Direct growth of large-area graphene and boron nitride heterostructures by a co-segregation method. *Nature Communications*, *6*(1), 1–8.

Zhang, S., Xie, M., Li, F., Yan, Z., Li, Y., Kan, E., ... Zeng, H. (2016). Semiconducting group 15 monolayers: a broad range of band gaps and high carrier mobilities. *Angewandte Chemie*, *128*(5), 1698–1701.

Zhang, Y., Tan, Y., Stormer, H. L., & Kim, P. (2005). Experimental observation of the quantum hall effect and berry's phase in graphene. *Nature*, *438*(7065), 201–204.

Zhang, Y., Tang, T., Girit, C., Hao, Z., Martin, M. C., Zettl, A., ... Wang, F. (2009). Direct observation of a widely tunable bandgap in bilayer graphene. *Nature*, *459*(7248), 820–823.

Zhao, J., & Zeng, H. (2016). Two-dimensional germanane and germanane ribbons: density functional calculation of structural, electronic, optical and transport properties and the role of defects. *RSC Advances*, *6*(34), 28298–28307.

Zhi, C., Bando, Y., Tang, C., Kuwahara, H., & Golberg, D. (2009). Large-scale fabrication of boron nitride nanosheets and their utilization in polymeric composites with improved thermal and mechanical properties. *Advanced Materials*, *21*(28), 2889–2893.

Zhou, H., Zhu, J., Liu, Z., Yan, Z., Fan, X., Lin, J., ... others (2014). High thermal conductivity of suspended few-layer hexagonal boron nitride sheets. *Nano Research*, *7*(8), 1232–1240.

Zhou, S. Y., Gweon, G., Fedorov, A., First, d., PN, De Heer, W., Lee, D., ... Lanzara, A. (2007). Substrate-induced bandgap opening in epitaxial graphene. *Nature Materials*, *6*(10), 770–775.

Zhou, W., Qi, S., An, Q., Zhao, H., & Liu, N. (2007). Thermal conductivity of boron nitride reinforced polyethylene composites. *Materials Research Bulletin*, *42*(10), 1863–1873.

Zuev, Y. M., Chang, W., & Kim, P. (2009). Thermoelectric and magnetothermoelectric transport measurements of graphene. *Physical Review Letters*, *102*(9), 096807.

Zunger, A. (1974). A molecular calculation of electronic properties of layered crystals. ii. periodic small cluster calculation for graphite and boron nitride. *Journal of Physics C: Solid State Physics*, *7*(1), 96.

APPENDIX

A. Articles published in International Journals

Neupane, H. K., & Adhikari, N. P. (2022). Adsorption of Water Molecule in Graphene/MoS2 Heterostructure with Vacancy Defects in Mo Sites. *Advances in Condensed Matter Physics*, *2022*.

Neupane, H. K., & Adhikari, N. P. (2022). Adsorption of water on C sites vacancy defected graphene/h-BN: First-principles study. *Journal of Molecular Modeling*, *28*(4), 1–10.

Neupane, H. K., & Adhikari, N. P. (2021). Effect of vacancy defects in 2D vdW graphene/h-BN heterostructure: First-principles study. *AIP Advances*, *11*(8), 085218.

Neupane, H. K., & Adhikari, N. P. (2021). Structural, electronic and magnetic properties of S sites vacancy defects graphene/MoS2 van der Waals heterostructures: First-principles study. *International Journal of Computational Materials Science and Engineering*, *10*(02), 2150009.

Neupane, H. K., & Adhikari, N. P. (2021). First-principles study of structure, electronic, and magnetic properties of C sites vacancy defects in water adsorbed graphene/MoS2 van der Waals heterostructures. *Journal of Molecular Modeling*, *27*(3), 1–12.

Neupane, H. K., & Adhikari, N. P. (2020). Tuning structural, electronic, and magnetic properties of C sites vacancy defects in graphene/MoS2 van der Waals heterostructure materials: A first-principles study. *Advances in Condensed Matter Physics*, *2020*.

Neupane, H. K., & Adhikari, N. P. (2020). Structure, electronic and magnetic properties of 2D Graphene-Molybdenum diSulphide (G-MoS2) Heterostructure (HS) with vacancy defects at Mo sites. *Computational Condensed Matter*, *24*, e00489.

B. Articles published in National Journals

Neupane, H. K., & Adhikari, N. P. (2021). Electronic and magnetic properties of defected MoS2 monolayer. *BIBECHANA*, *18*(2), 68–79.

Neupane, H. K., & Adhikari, N. P. (2021). Structural, Electronic and Magnetic Properties of Defected Water Adsorbed Single-Layer MoS2. *Journal of Institute of Science and Technology*, *26*(1), 43–50.

Neupane, H. K., & Adhikari, N. P. (2021). Structural, Electronic and Magnetic Properties of Impurities Defected Graphene/MoS2 van der Waals Heterostructure: First-principles Study. *Journal of Nepal Physical Society*, *7*(2), 1–8.

Neupane, H. K., & Adhikari, N. P. (2021). First-Principles Study of Vacancy and Impurities Defects in Graphene. *Amrit Research Journal*, *2*(01), 93–102.

Neupane, H. K., & Adhikari, N. P. (2020). First-principles study of C cites vacancy defects in water adsorbed Graphene. *Himalayan Physics*, 19–29.

Neupane, H. K., & Adhikari, N. P. (2020). Path Integral Simulations of Harmonic Oscillator. *Journal of Nepal Physical Society*, *6*(1), 42–49.

C. Participation

- **Study the effect of C sites vacancy defects in Gr/h-BN and water adsorption on defected Gr/h-BN: First-principles calculations.**
  Hari Krishna Neupane, and and Narayan P. Adhikari. International Conference on Frontiers of Physics-2022 (ICFP-2022), organized by Nepal Physical Society, January 22-24, 2022. **Presenter:** Hari Krishna Neupane
- **Effect of S and Mo sites vacancy defects in water adsorbed MoS2: First-principles study.**
  Hari Krishna Neupane, and Narayan P. Adhikari. ANPA conference, July 16-18, 2021. **Presenter:** Hari Krishna Neupane
- **Experimental and Computational Approach of Metal Oxide Thin Film (ECAMOTF).**
  Hari Krishna Neupane. Atomspheric and Material Research Center at the Department of Physics, Amrit Campus with the support of International Science Programme (ISP), Uppsala University, Sweden in collaboration with IEEE/EDS Nepal Chapter, March 18-19, 2021. **Presenter:** Hari Krishna Neupane (as a resource person)
- **First-principles study of C and Mo sites vacancy defects in water adsorbed (HS) Graphene/MoS2 material.**
  Hari Krishna Neupane, and Narayan P. Adhikari. APS March meeting conference, March 15-19, 2021. **Presenter:** Hari Krishna Neupane
- Participated virtually in the conference 10^{th} International Workshop on Compu-

tational Physics and Materials Science: Total Energy and Force Methods at the Adbus Salam International Centre for Theoretical Physics (ICTP), Italy, February 23-25, 2021.

- **Structure, Electronic and Magnetic Properties of C Sites Vacancy Defects in Water adsorbed G/MoS2 heterostructures: First-principles study.**
  Hari Krishna Neupane, and Narayan P. Adhikari. On Scientific Session of 37^{th} Annual Convention, Nepal Physical Society, February 6, 2021. **Presenter:** Hari Krishna Neupane

- **Structure, electronic and magnetic properties of 2D (HS) material G-MoS2 with vacancy defects at C sites.**
  Hari Krishna Neupane, and Narayan P. Adhikari. ANPA conference, July 17-19, 2020. **Presenter:** Hari Krishna Neupane

- Participated in the academic discussion on the Condensed Matter Physics and interacted with the faculty and PhD Scholars at Indian Institute of Technology (IIT), Kharagpur, India, October 14-26, 2019.

Hindawi
Advances in Condensed Matter Physics
Volume 2022, Article ID 2135213, 18 pages
https://doi.org/10.1155/2022/2135213

Research Article

Adsorption of Water Molecule in Graphene/MoS_2 Heterostructure with Vacancy Defects in Mo Sites

Hari Krishna Neupane [1,2] **and Narayan Prasad Adhikari** [2]

[1]*Amrit Campus, Institute of Science and Technology, Tribhuvan University, Kathmandu, Nepal*
[2]*Central Department of Physics, Institute of Science and Technology, Tribhuvan University, Kathmandu, Nepal*

Correspondence should be addressed to Narayan Prasad Adhikari; npadhikari@gmail.com

Received 22 December 2021; Revised 25 February 2022; Accepted 3 March 2022; Published 11 April 2022

Academic Editor: Sefer Bora Lisesivdin

Copyright © 2022 Hari Krishna Neupane and Narayan Prasad Adhikari. This is an open access article distributed under the Creative Commons Attribution License, which permits unrestricted use, distribution, and reproduction in any medium, provided the original work is properly cited.

First-principle calculations based on the spin-polarized density functional theory (DFT) with vdW corrections by DFT-D2 approach have been carried out to study structural, electronic, and magnetic properties of water-adsorbed graphene/MoS_2 heterostructures (system-I), and water-adsorbed graphene/MoS_2 heterostructures with vacancy defects in Mo sites (systems-II). We consider vacancy defects in different Mo sites such as centre-1Mo atom vacancy defect (system-IIa), left-1Mo atom vacancy defect (system-IIb), and 2Mo atom vacancy defects (system-IIc). All the systems considered in this study are structurally stable; however, the stability of defected systems decreases with an increase in defect concentrations. The calculated binding energies of HS used in this study agree with the reported work. Electronic properties of system-I and systems-II reveal that they have metallic characteristics. Our investigation shows that system-I is nonmagnetic and systems-II are magnetic. The magnetic moment in the defected systems (system-IIa, system-IIb, and system-IIc) is developed by unpaired up and down-spins of electrons created in the orbitals of atoms due to vacancy defects in Mo atoms.

1. Introduction

One of the ways to create 2D heterostructures is by two or more monolayers of different materials. The heterostructures improve the functional characteristics and bear novel properties. Therefore, they have intrigued the advanced compliance of researchers to predict other advantageous properties than the constituents [1, 2]. Presently, two-dimensional (2D) van der Waals (vdW) graphene/MoS_2 (G/MoS_2) heterostructure (HS) is a useful tool to design applicable electronic devices [3–6]. Graphene is an atom-thick 2D honeycomb lattice, and has a series of special electronic and physical properties. Its exceptional physical strength, large surface area, high electrical and thermal conductivities, low noise effect, controllable tunable band structure, and many more other interesting properties explore multiple possible applications such as electronic, spintronics, and gas sensors [1, 7–10]. 2D Molybdenum disulphide (MoS_2) is the form of hexagonal plane crystal structure of S atoms on either side of a hexagonal plane of Mo atoms. It has certain bandgap in its electronic band known as the wide bandgap exotic semiconductor [11, 12]. MoS_2 is used in the electronic, spintronic, and optoelectronic devices because of its impressive optical, electronic, and magnetic properties [11–13]. Defects are inherent in any system due to entropic reason. They (vacancy defect/impurity defect) can develop novel properties in 2D materials [14–18], and also electronic and magnetic properties of materials can be modified by defects [15, 19, 20]. People are using the pristine and defected G/MoS_2 HS in electronic devices. Hence, it is highly demanding to study HS of 2D materials with defects. The devices made by pristine G/MoS_2 HS and vacancy-defected G/MoS_2 HS sometimes have to be used in the surrounding (moisture) environment. Due to which, moisture (water molecule) can affect the properties of HS materials [21, 22]. The molecular adsorption in vacancy-defected HS can bring new properties because vacancy defects are very keen locations for molecular adsorption due

to the configuration of atoms around the vacancy. They play a particular role in determining the geometrical arrangement of layered materials [21–23]. Also, electronic and magnetic properties of defected materials can be modified by adsorbed water molecule [23]. Thus, it opens the way to tune novel properties of vacancy-defected HS materials. Therefore, it needs to study the adsorption of water molecule on G/MoS_2 HS (system-I) and Mo sites vacancy defects G/MoS_2 HS (system-II). To our best knowledge, literature studies do not contain a significant study of water-adsorbed 2D G/MoS_2 HS materials with Mo defects. In this study, we have investigated the structural, electronic, and magnetic properties of Mo sites vacancy-defected water-adsorbed 2D G/MoS_2 HS materials by using the spin-polarized density functional theory (DFT)-based first-principle calculations, within the DFT-D2 approach. Our calculations show that system-I and its Mo site vacancy defect (systems-II) materials could be promising candidates for the device applications.

The rest part of the article is arranged as follows. Computational methods, interpretation of findings, and conclusions of this study are given in Sections 2–4, respectively.

2. Methods and Materials

The comprehensive intuition is gained into the physical properties of the system-I and its Mo site vacancy defect systems-II by the spin-polarized density functional theory (DFT) [24]-based first-principle calculations. DFT with the PWscf code of the Quantum ESPRESSO package [25] has been conducted to study the structural, electronic, and magnetic properties of system-I and system-II. The code uses ultra-soft pseudo-potentials (USPPs) to describe the interactions between ion cores and valence electrons. A plane-wave basis set, with cut-off values of 35 Ry and 350 Ry for wave functions and charge densities, respectively, was used. Exchange and correlation interactions were considered by generalized gradient approximation (GGA) [26]. London dispersion contributions for weak vdW force in between the constituents of supercells were described through the DFT-D2 scheme [27]. Self-consistent field (Scf) and structure optimization calculations were executed by Broyden–Fletcher–Goldfarb–Shanno (BFGS) method [28] with Γ-centered Monkhorst-Pack (MP) [29] k-Points mesh commensurate with $(6\times6\times1)$ sampling of the heterostructures of system-I and system-II. The system-I was created by adsorbing water molecule (center position on the surface of MoS_2) at 2.52 Å distance above the top surface of MoS_2 in vertical G/MoS_2 HS as shown in Figure 1, since vertical G/MoS_2 HS was formed by (4×4) supercell structure of graphene and (3×3) supercell structure of MoS_2 with 4.11% lattice mismatch. In HS, the lattice mismatch can be determined via differing the lattice constant, whereas there is no direct chemical bonding between the component layers. Systems-II were constructed by adsorbing water molecule in centre-1Mo atom vacancy defect G/MoS_2 HS (system-IIa), left-1Mo atom vacancy defect G/MoS_2 HS (system-IIb), and 2Mo atom vacancy defect G/MoS_2 HS (system-IIc), which are illustrated in Figure 2. Convergence was sustained by using Marzari–Vanderbilt (MV) [30] smearing with an enlightening of 0.001 Ry. David diagonalization methods with plain mixing mode for self-consistency where a default value of mixing factor 0.6 was used. To reduce the interaction within periodic structures, a vacuum detachment of 18 Å was used along z-direction. All the atoms in structures were allowed to relax by the PBE functional until the forces conversed to less than 10^{-3} Ry/Bohr in each direction and energy to 10^{-4} Ry. To tune electronic and magnetic properties of materials, a mesh of $(6\times6\times1)$ k-points was used for band structure calculations and meshes of $(12\times12\times1)$ k-points were employed for density of states (DOS) and projected density of state (PDOS) calculations.

3. Results and Discussion

In this section, we present, discuss, and analyze the main findings of this study. Findings of system-I and systems-II are obtained from band structure, DOS, and PDOS calculations.

3.1. Structural Study. The water-adsorbed G/MoS_2 HS is constructed by putting water molecule at various locations on graphene and MoS_2 surfaces of the G/MoS_2 HS material as shown in Figures 1(a)–1(d). The adsorbed water molecule (at center position on the surface of MoS_2) at a distance of 2.52 Å above the top surface of MoS_2 in the HS is found to be most stable, as shown in Figure 1(d). To determine the stability, we have calculated the binding energy of system-I by using the following equation [31]:

$$E_b = \frac{E_{w+G/MoS_2\,(HS)} - E_{G/MoS_2\,(HS)} - E_w}{A}, \quad (1)$$

where $E_{w+G/MoS_2\,(HS)}$, $E_{G/MoS_2\,(HS)}$, E_w are the total energy of the system-I, G/MoS_2 HS, and adsorbed water molecule, respectively, and "A" is the surface area of heterostructure. The obtained binding energy of system-I is $-23.82\,meV/Å^2$, which means system-I is energetically stable at the ground state. It means physisorption interaction takes place in between them. The stable optimized system-IIa, system-IIb, and system-IIc are created by adsorbing water molecule in centre-1Mo atom, left-1Mo atom, and 2Mo atom vacancy defect G/MoS_2 HS, respectively, as shown in Figures 2(a)–2(c). To determine the stability of such systems, we have also calculated binding energy using the following formalism [31]:

$$E_b = \frac{E_{w+G/MoS_2\,(HS)Mo-d} - E_{G/MoS_2\,(HS)Mo-d} - E_w}{A}, \quad (2)$$

where $E_{w+G/MoS_2\,(HS)Mo-d}$, $E_{G/MoS_2\,(HS)Mo-d}$, E_w are the ground state energy of Mo site vacancy defect water-adsorbed G/MoS_2 HS (systems-II), Mo site vacancy defect G/MoS_2 HS, and adsorbed water molecule, respectively, and "A" represents the surface area of defected heterostructures. The estimated binding energy of system-IIa, system-IIb, and system-IIc are $-20.09\,meV/Å^2$, $-20.03\,meV/Å^2$, and $-17.40\,meV/Å^2$, respectively. The calculated binding energy

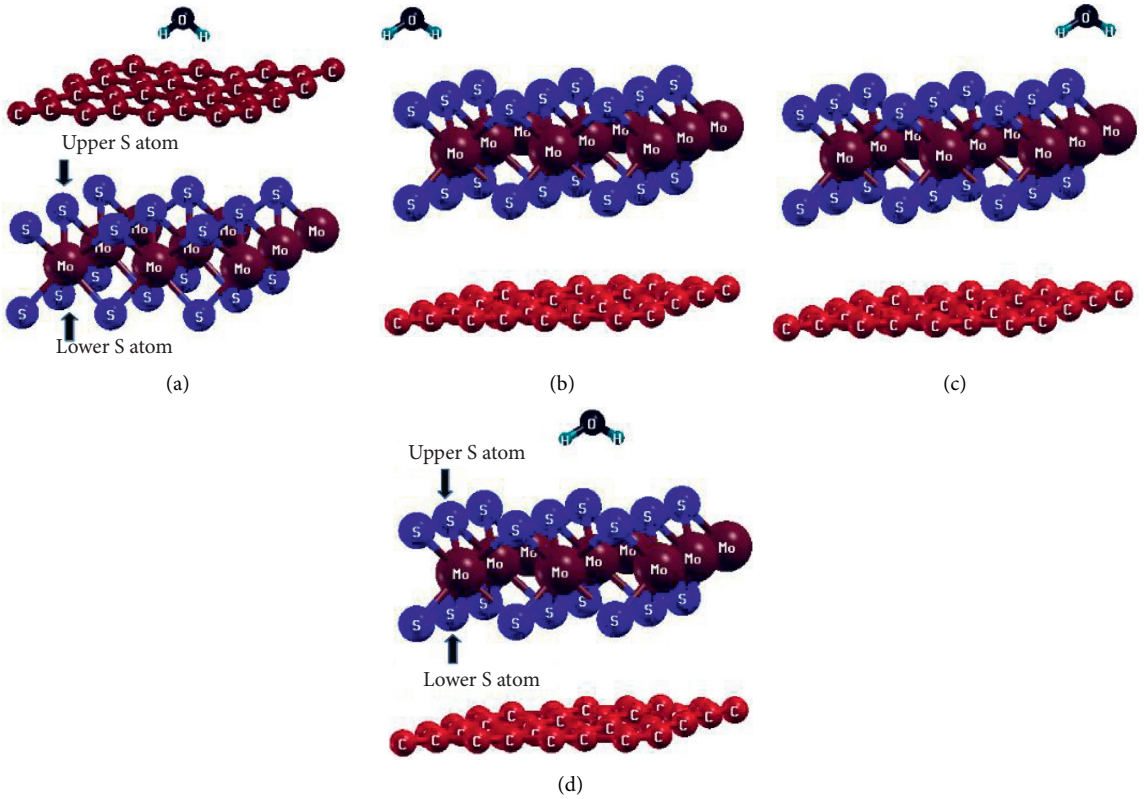

Figure 1: (a) Adsorbed water molecule is at 2.52 Å distance above the top surface of graphene in G/MoS_2 HS. (b) adsorbed water molecule is (left-position) at 2.52 Å distance above the top surface of MoS_2 in G/MoS_2 HS. (c) adsorbed water molecule is (right-position) at 2.52 Å distance above the top surface of MoS_2 in G/MoS_2 HS. (d) adsorbed water molecule is (center position) at 2.52 Å distance above the top surface of MoS_2 in G/MoS_2 HS.

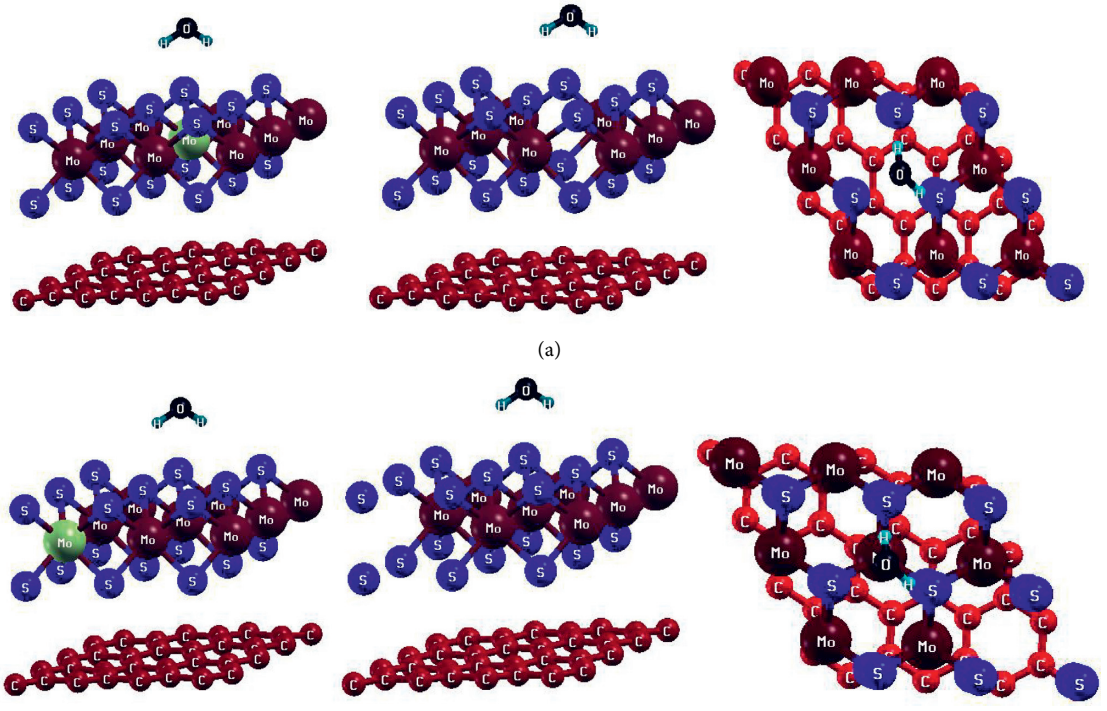

Figure 2: Continued.

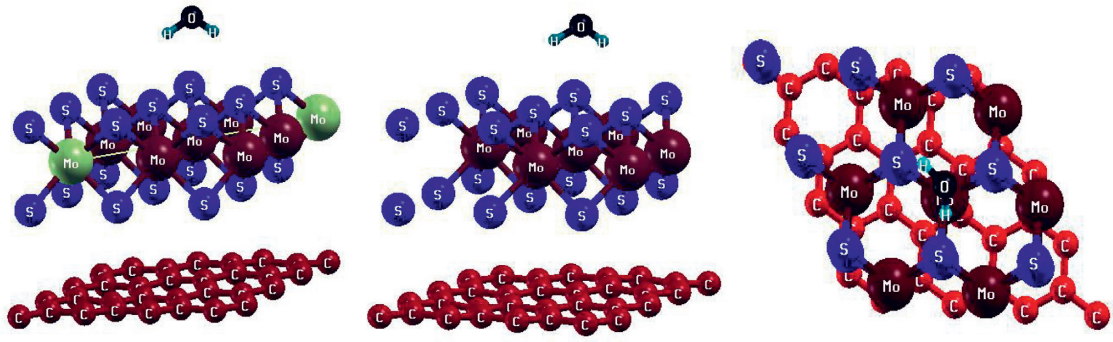

(c)

Figure 2: Side view and top view of Mo site vacancy defect HS materials: (a) center-1Mo atom vacancy defect water-adsorbed G/MoS_2 HS (system-IIa), (b) left-1Mo atom vacancy defect water-adsorbed G/MoS_2 HS (system-IIb), and (c) 2Mo atoms vacancy defects water-adsorbed G/MoS_2 HS (system-IIc).

of system-I, system-IIa, system-IIb, and system-IIc is comparable with the values of other vdW HSs [32, 33]. Thus, considered systems are stable because negative binding energy means that materials are energetically stable at the ground state. Lower value of binding energy indicates that the material is more stable than others. Hence, the stability of the above considered materials is decreased with an increase in the defect concentration. The defect formation energy of system-IIa, system-IIb, and system-IIc is found to be 0.21 eV, 0.21 eV, and 0.40 eV, respectively, which are calculated by using the following equation [34]:

$$E_{\mathrm{df}} = (E_t)_d - \left[(E_t)_p + n_{\mathrm{Mo}}\mu_{\mathrm{Mo}}\right], \tag{3}$$

where $(E_t)_d$, $(E_t)_p$, n_{Mo}, and μ_{Mo} are the total ground state energy of vacancy defect HS (systems-II), total ground state energy of pristine HS (system-I), numbers of vacancy defects (Mo) atoms, and chemical potential of a Mo atom, respectively. Materials have lower defect formation energy, which indicates that they can be favorable for computational work.

In addition, we have also computed the interlayers distance between graphene and monolayer MoS_2 of system-I, system-IIa, system-IIb, and system-IIc materials, and they are 3.72 Å, 3.81 Å, 3.83 Å, and 3.94 Å, respectively. These values are comparable with other graphene-based 2D HS materials [35, 36]. From this analysis, we conclude that system-I is more compact than Mo vacancy-defected systems. In systems-II, compactness of atoms and layers of constituents are increased with a decrease in their defect concentration. The estimation of binding energy and interlayer distance of the above considered systems shows that weak vdW force exists in between graphene and MoS_2.

3.2. Electronic Properties. The electronic properties of the material are predicted based on the electronic band structure. Band structures of system-I, system-IIa, system-IIb, and system-IIc are illustrated in Figures 3(a), 4(a), 5(a), and 6(a), respectively. We know that graphene and monolayer MoS_2 have metallic [1, 9] and semiconducting properties, respectively [12, 13]. Band structure of graphene/MoS_2 HS is a sum of band structures of those constituents in which properties of graphene are preserved, and hence, it also has metallic properties [20, 37]. Impressively, it is noted that Dirac point setup in the conduction band at 0.11 eV distance from the Fermi energy level in the band structure of water adsorbed Graphene/MoS_2 HS (system-I). This small value of the Dirac cone is obtained because of the adsorption of water molecule in G/MoS_2 HS. The formation of the Dirac cone in the conduction band means electrons spontaneously flow from the valence band to the conduction band. Hence, system-I has metallic properties. Also, the property of G/MoS_2 HS is still preserved.

Moreover, we explored band structures of systems-II materials and found that the Dirac cone is formed at 0.72 eV, 0.71 eV, and 0.68 eV distance from the Fermi energy level in system-IIa, system-IIb, and system-IIc materials, respectively, which are shown in Figures 4(a), 5(a) and 6(a). A few numbers of electronic bands of valence electrons cross the Fermi energy level in band structures, which is due to the effect of Mo vacancy atom in structures, which breaks the symmetry of system-I. Hence, defected materials are metallic. In systems-II, unpaired up-spin and down-spin states are appeared by Mo vacancy defects, due to which the movement of interfacial charges is developed in systems. Hence, the different values of the Dirac point, Fermi energy, and shift of the Fermi energy level towards the valence band are obtained in system-IIa, system-IIb, and system-IIc, which are presented in Table 1.

In Table 1, we can see that the values of Fermi energy and Fermi energy shift are increased with an increase in the concentration of Mo vacancy defects, but the distance of the Dirac point from the Fermi energy level decreases with an increase in the defect concentration in the systems. The reason is that vacancies are very precise place for adsorbed molecule. This is because we have calculated the bond length between nearest Mo-Mo atoms, S-S atoms, Mo-S atoms, and distance between adsorbed water molecule to MoS_2 surface in vacancy defects HS and found that the compactness of materials decreases with an increase in defect concentrations. Thus, adsorbed molecule disturbed the atomic configurations in vacancy-defected HS materials, which influences the electronic properties of the systems. Dirac

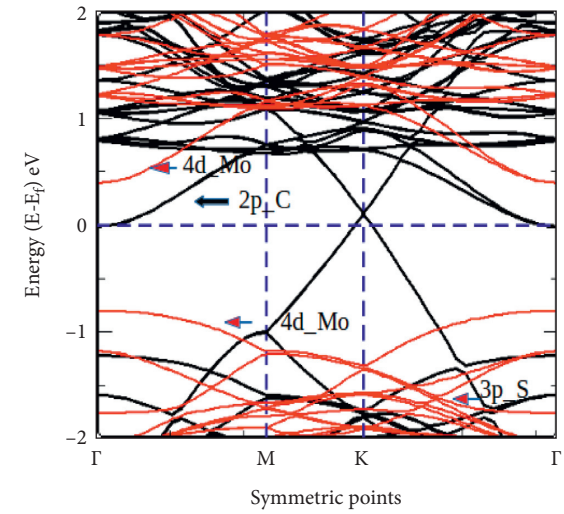

(a)

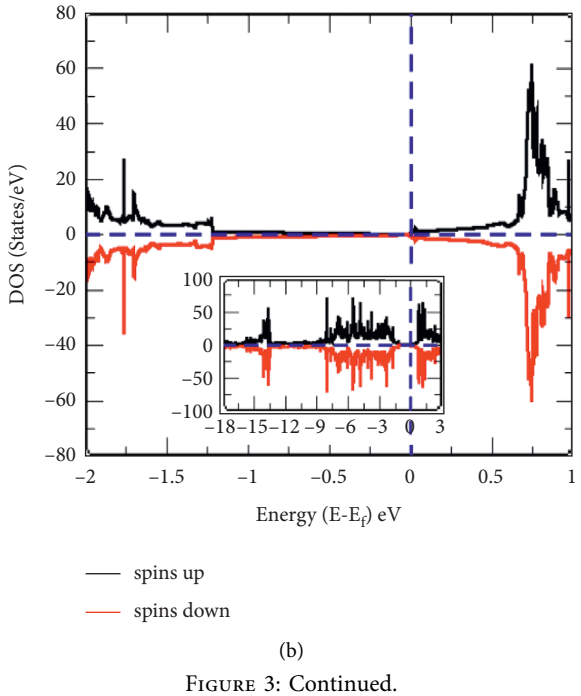

(b)

Figure 3: Continued.

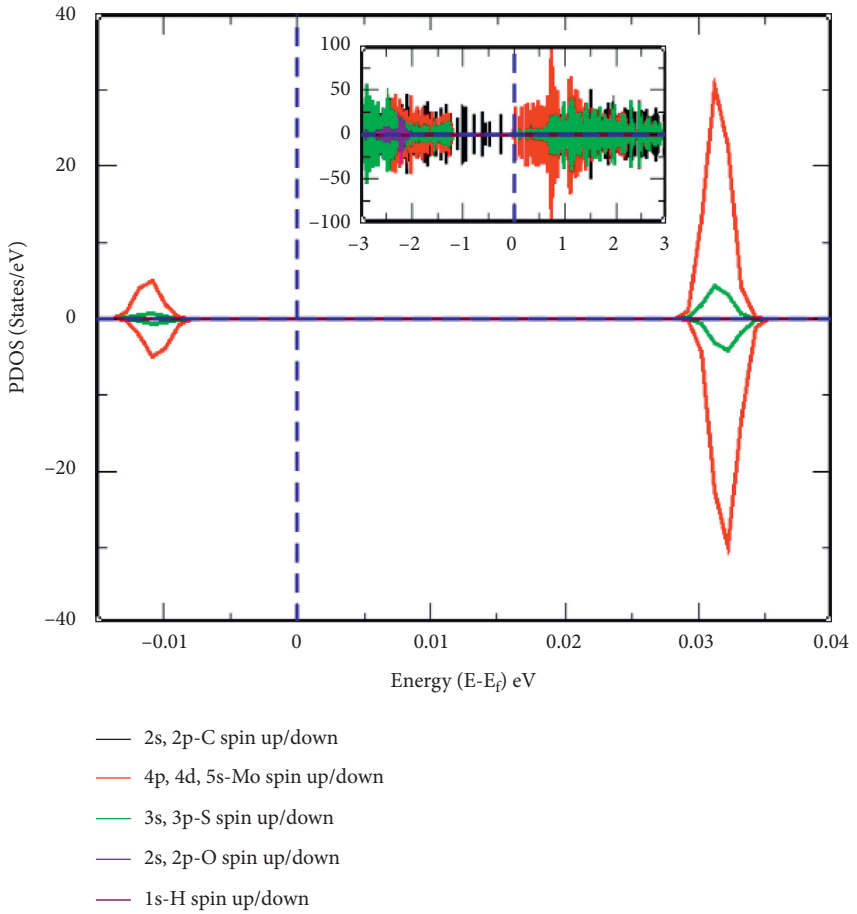

(c)

Figure 3: Continued.

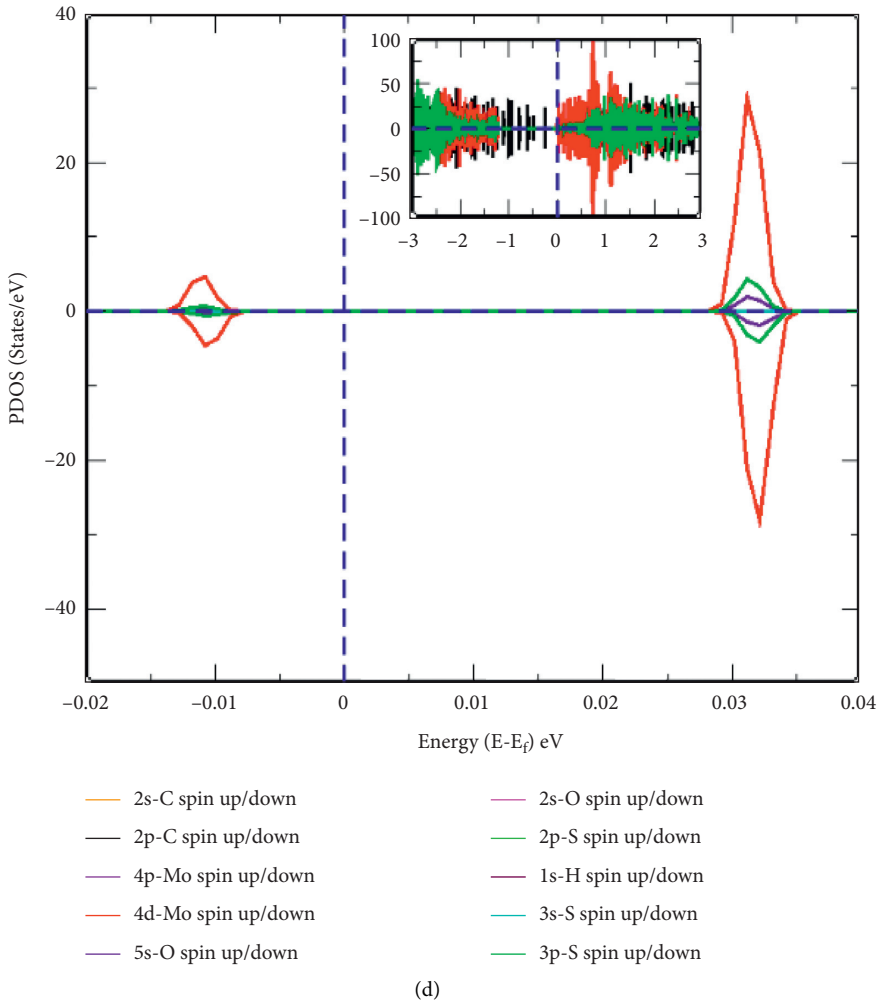

(d)

Figure 3: (a) Band structure of system-I, (b) DOS of up-spin and down-spin states of electrons in the orbitals of C Mo, S O, and H atoms of system-I, (c) PDOS of total up-spin and total down-spin states of electrons in the orbitals of C Mo, S O, and H atoms of system-I, (d) PDOS of individual up-spin and down-spin states of electrons in the orbitals of C Mo, S O, and H atoms of system-I. In all DOS and PDOS, the horizontal dot line separates spin states and the vertical dot line separates the electronic bands, and also in band plot, the horizontal dot line represents the Fermi energy level; insets in DOS and PDOS represent the spin states within a large energy range along *x*-axis.

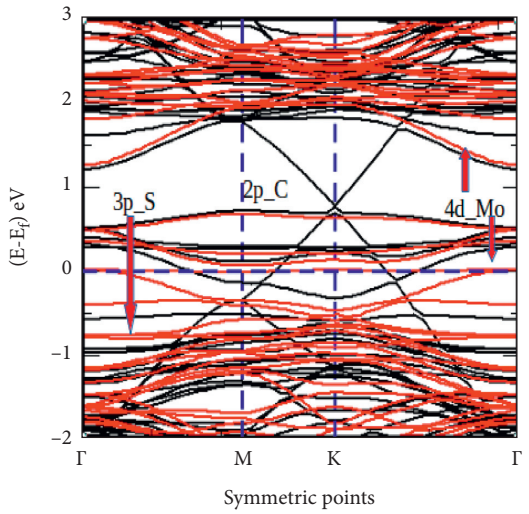

(a)

Figure 4: Continued.

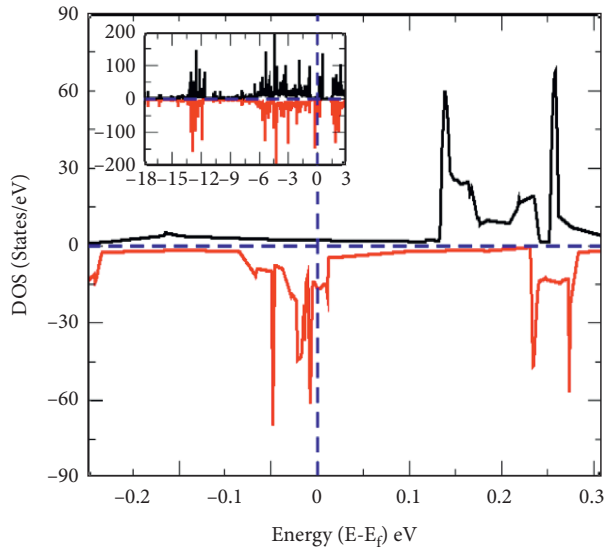

(b)

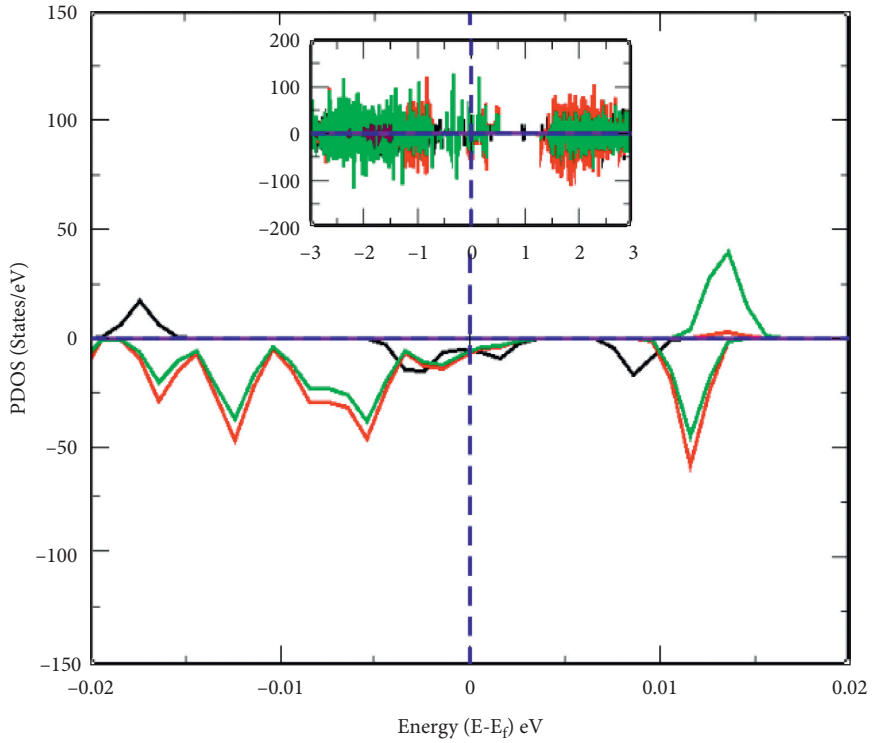

(c)

Figure 4: Continued.

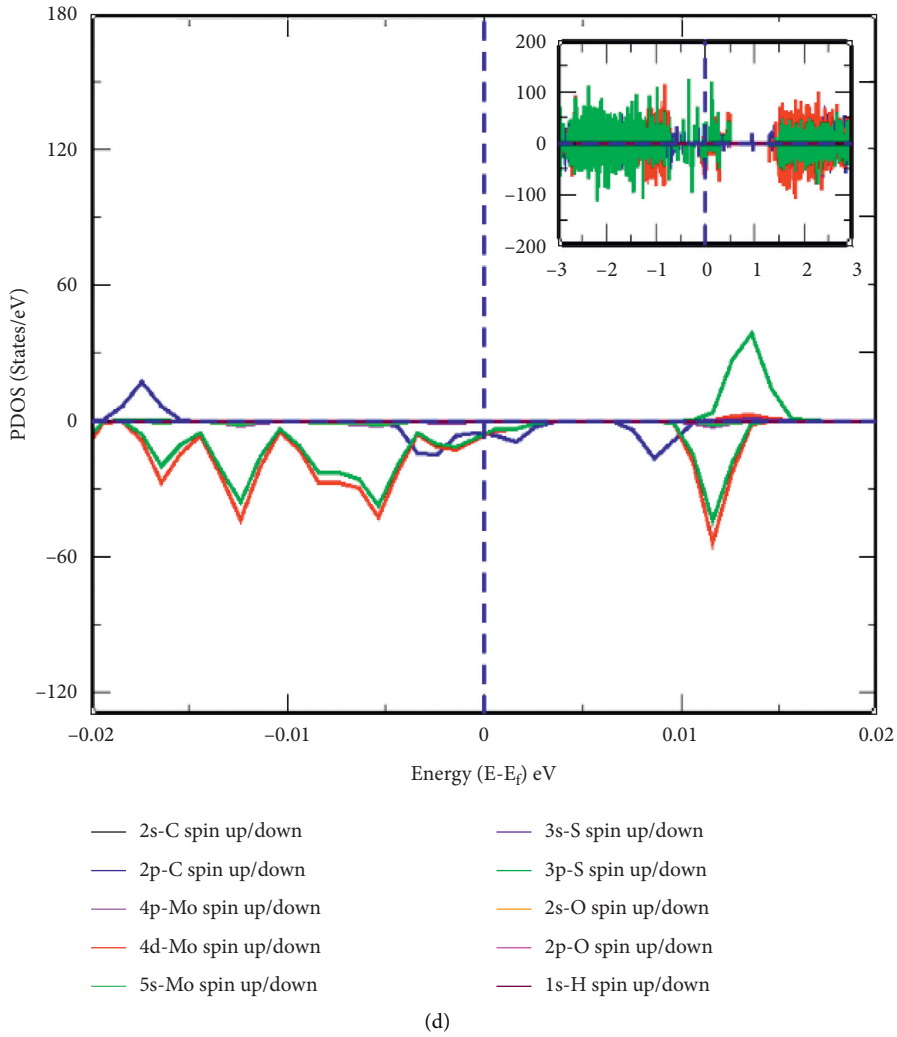

FIGURE 4: (a) Band structure of system-IIa, (b) DOS of up-spin and down-spin states of electrons in the orbitals of C Mo, S O, and H atoms of system-IIa, (c) PDOS of total up-spin and total down-spin states of electrons in the orbitals of C Mo, S O, and H atoms of system-IIa, (d) PDOS of individual up-spin and down-spin states of electrons in the orbitals of C Mo, S O, and H atoms of system-IIa. In all DOS and PDOS, the horizontal dot line separates spin states and the vertical dot line separates the electronic bands, and also in the band plot, the horizontal dot line represents the Fermi energy level. Insets in DOS and PDOS represent spin states within large energy range along x-axis.

point setup in the conduction band reflects that the electron impulsively proceeds from the valence to the conduction band because the flow of current in metals and semiconductors depends on the amplitude of Dirac shift. Hence, system-IIa, system-IIb, and system-IIc have metallic properties.

3.3. Magnetic Properties. The magnetic properties of materials can be studied based on the density of states (DOS) and the projected density of states (PDOS) analysis. DOS are defined as the number of available electronic states per unit energy range. In computational physics/chemistry, it is one of the ways to represent electronic eigen states in the energy space of a molecule, where it counts the number of energy states nearby a given energy value. If Ψ_i and E_i represent the normalized eigen functions and eigen values, respectively, the total density of states (TDOS) can be defined as [17]

$$D(E) = \sum_i \delta(E - E_i), \tag{4}$$

where $D(E)$ represents the density of states, and its integral $\int D(E)\mathrm{dE}$ in between the energies E_1 and E_2 gives the number of states within the specified energy range [38]. The density of states projected over any arbitrary state is defined as the projected density of states (PDOS). The present magnetic moment by reason of spin states of electrons in the individual orbital of atoms in the materials is calculated by using PDOS. It can be expressed as

$$n_0(E) = \sum_i \left|\langle f_0 | \psi_i \rangle\right|^2 \delta(E - E_i), \tag{5}$$

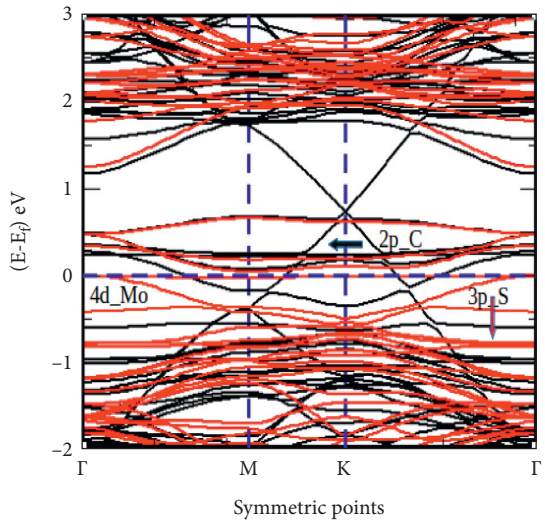

(a)

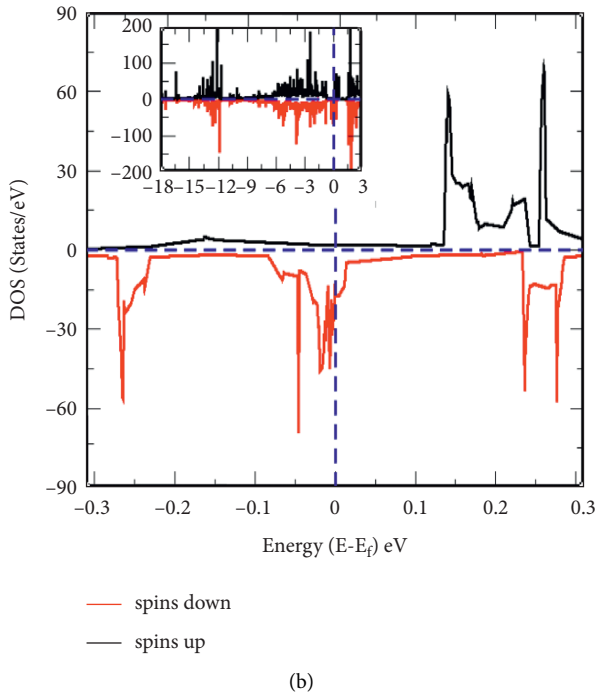

(b)

Figure 5: Continued.

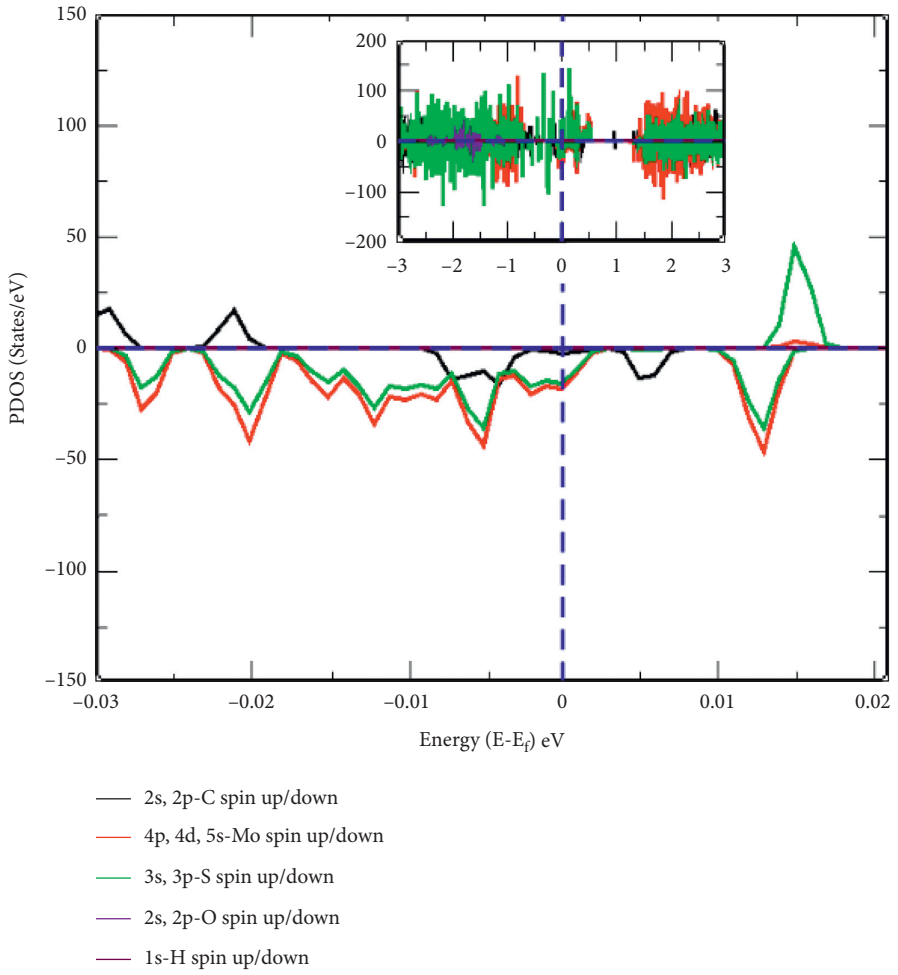

(c)

Figure 5: Continued.

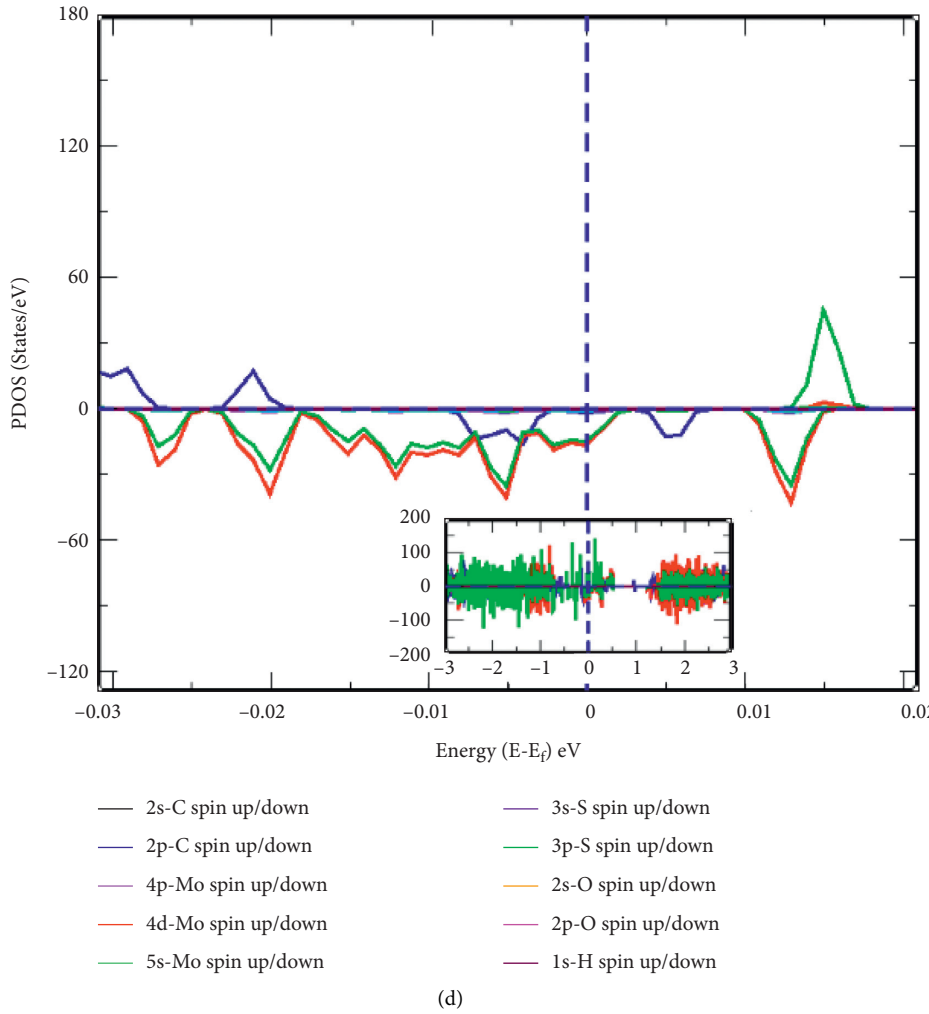

FIGURE 5: (a) Band structure of system-IIb, (b) DOS of up-spin and down-spin states of electrons in the orbitals of C Mo, S O, and H atoms of system-IIb, (c) PDOS of total up-spin and total down-spin states of electrons in the orbitals of C Mo, S O, and H atoms of system-IIb, (d) PDOS of individual up-spin and down-spin states of electrons in the orbitals of C Mo, S O, and H atoms of system-IIb. In all DOS and PDOS, the horizontal dot line separates spin states and the vertical dot line separates the electronic bands, and also in the band plot, the horizontal dot line represents Fermi energy level. Insets in DOS and PDOS represent the spin states within a large energy range along x-axis.

with $\int n_0(E)\mathrm{d}E = 1$, due to the normalization condition of chosen orbital $|f_0>$. When plotted, PDOS gives the relative contributions to TDOS and hence helps to analyze the relative contributions of each atom or molecule in the larger systems. Unpaired up-spin and down-spin states of an isolated atom possess a nonzero value of total spin and cause finite magnetic moment [19]. It means spin states are asymmetrically distributed in DOS and PDOS of materials. Up-spin and down-spin states are totally symmetric in DOS and PDOS, indicating equal contributions of magnetic moment in materials from up- and down-spin electrons. This ensures that those materials have nonmagnetic properties. In the present work, we discuss magnetic properties of water-adsorbed G/MoS_2 HS (system-I) and water-adsorbed Mo sites vacancy defect (systems-II) materials based on DOS and PDOS calculations. Magnetic moments due to spin states of C, Mo, S, O, and H atoms in PDOS of system-I and systems-II are given in Table 2.

DOS and PDOS plots for up-spin and down-spin electrons of system-I, system-IIa, system-IIb, and system-IIc are shown in Figures 3(b)–3(d), Figures 4(b)–4(d), Figures 5(b)–5(d), and Figures 6(b)–6(d), respectively. In Figures 3(b)–3(d), the DOS and PDOS plots for up-spin and down-spin of system-I are found to be symmetric, which means system-I is a nonmagnetic material. The system-IIa and system-IIb behave as strongly magnetic materials with largely asymmetric DOS/PDOS plots for up-spin and down-spin states near the Fermi energy level as shown in Figures 4(b)–4(d) and Figures 5(b)–5(d), while system-IIc is found to be slightly asymmetric as shown in Figures 6(b)–6(d), depicting the weak magnetic nature. We have calculated that the magnetic moment as asymmetrically distributed up-spin and down-spin states of electrons in 2s and 2p orbitals of C atoms are 0.00 μ_B/cell & 0.03 μ_B/cell; 4p, 4d, and 5s orbitals of Mo atoms are −0.03 μ_B/cell, −0.75 μ_B/cell, and −0.02 μ_B/cell;

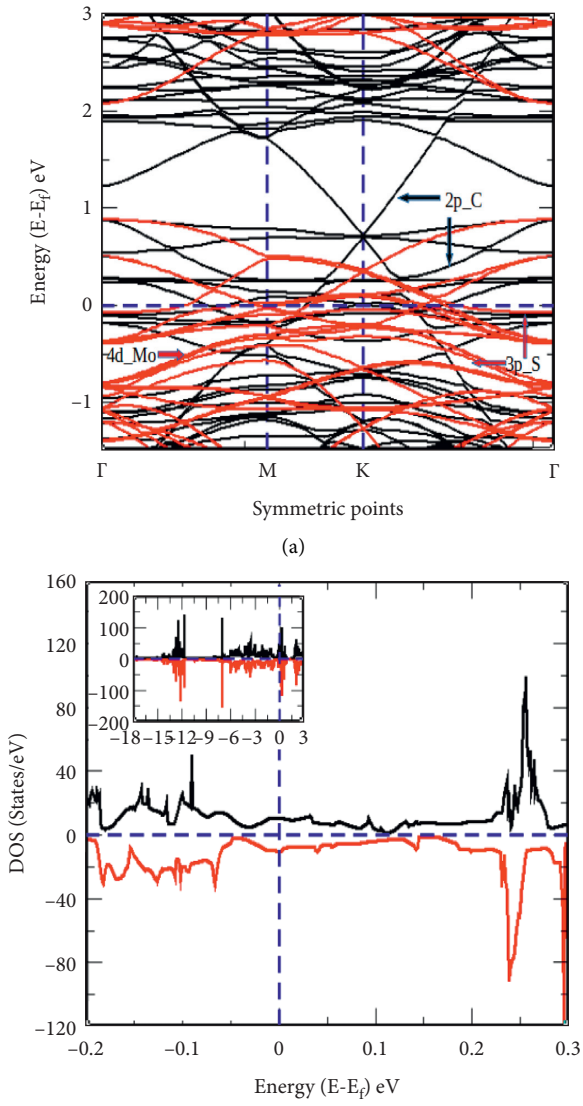

Figure 6: Continued.

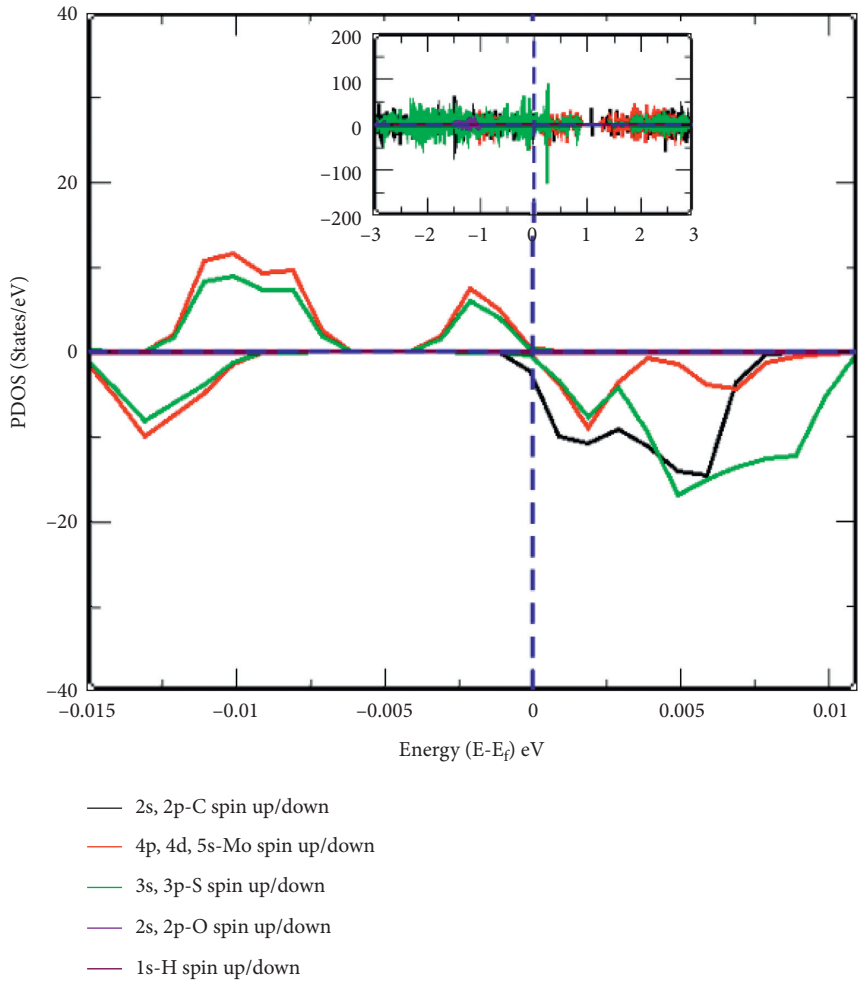

(c)

Figure 6: Continued.

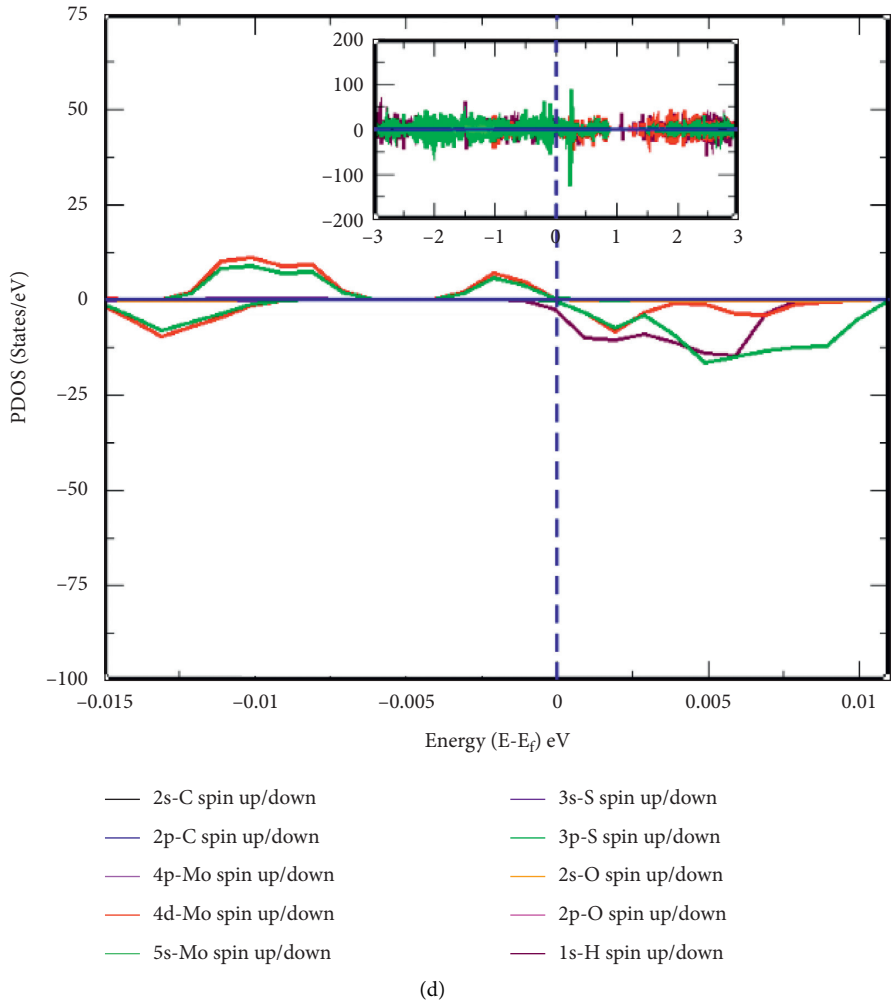

FIGURE 6: (a) Band structure of system-IIc, (b) DOS of up-spin and down-spin states of electrons in the orbitals of C Mo, S O, and H atoms of system-IIc, (c) PDOS of total up-spin and total down-spin states of electrons in the orbitals of C Mo, S O, and H atoms of system-IIc, and (d) PDOS of individual up-spin and down-spin states of electrons in the orbitals of C Mo, S O, and H atoms of system-IIc. In all DOS and PDOS, the horizontal dot line separates the spin states and the vertical dot line separates the electronic bands, and also in the band plot, the horizontal dot line represents the Fermi energy level. Insets in DOS and PDOS represent the spin states within a large energy range along x-axis.

TABLE 1: Fermi energy (E_f), fermi energy shifts (E_s), amplitude of the Dirac point (D_p), Dirac point shifts in defected materials (D_s), defect formation energy (E_{df}), and total binding energy of the systems (E_b).

	System-I:	System-IIa:	System-IIb:	System-IIc:		
Systems ⟶	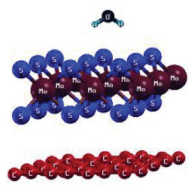	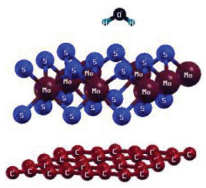	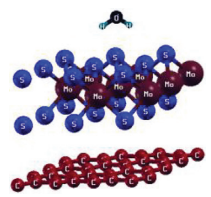	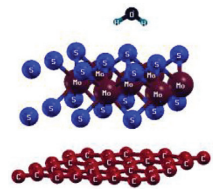		
Systems	E_f (eV)	E_s (eV)	D_p (eV)	D_s (eV)	E_{df} (eV)	E_b (meV/Å^2)
System-I	0.44	—	0.11	—	—	−23.82
System-IIa	−0.61	1.05	0.72	0.61	0.21	−20.09
System-IIb	−0.60	1.04	0.71	0.59	0.21	−20.03
System-IIc	−0.86	1.30	0.68	0.57	0.40	−17.40

Table 2: Total magnetic moment (μ_T) due to up-spin and down-spin state of electrons in the orbitals of C, Mo, S, O, and H atoms in PDOS of system-I, system-IIa, system-IIb, and system-IIc.

μ by up-spin and down-spin in ↓	System-IIc (μ_B/cell)	System-IIb (μ_B/cell)	System-IIa (μ_B/cell)	System-I (μ_B/cell)
2s of C	0.01	0.00	0.00	0.00
2p of C	0.02	0.03	0.03	0.00
4p of Mo	0.00	−0.02	−0.03	0.00
4d of Mo	0.04	−0.75	−0.75	0.00
5s of Mo	0.01	−0.02	−0.02	0.00
3s of S	0.02	−0.03	−0.04	0.00
3p of S	0.07	−1.72	−1.70	0.00
2s of O	0.00	0.00	0.00	0.00
2p of O	0.00	0.00	0.00	0.00
1s of H	0.00	0.00	0.00	0.00
μ_T (μ_B/cell)	+0.17	−2.51	−2.51	0.00

and 3s and 3p orbitals of S atoms are $-0.04\,\mu_B$/cell and $-1.70\,\mu_B$/cell, respectively, of system-IIa. Thus, total magnetic moment of system-IIa has a value of $-2.51\,\mu_B$/cell. Also, we have computed the magnetic moment by asymmetrically distributed unpaired up-spin and down-spin states of electrons in 2s and 2p orbitals of C atoms are $0.01\,\mu_B$/cell and $0.02\,\mu_B$/cell; 4p, 4d, and 5s orbitals of Mo atoms are $-0.02\,\mu_B$/cell, $-0.75\,\mu_B$/cell, and $-0.02\,\mu_B$/cell; 3s and 3p orbitals of S atoms are $-0.03\,\mu_B$/cell and $-1.72\,\mu_B$/cell, respectively, in system-IIb. Hence, the total magnetic moment of system-IIb has a value of $-2.51\,\mu_B$/cell. Similarly, we have determined the magnetic moment of system-IIc material due to asymmetrically distributed up-spin and down-spin states around the Fermi energy level in DoS/PDoS as shown in Figures 6(b)–6(d). The magnetic moments given by total up-spin and total down-spin states of electrons in the orbitals of C, Mo, and S atoms are found to be $0.03\,\mu_B$/cell, $0.05\,\mu_B$/cell, and $0.09\,\mu_B$/cell, respectively. Also, we individually calculated the magnetic moments given by asymmetrically distributed spin states in 2s and 2p orbitals of C atoms, which have values of $0.01\,\mu_B$/cell and $0.02\,\mu_B$/cell, respectively; 4p, 4d, and 5s orbitals of Mo atoms have values of $0.00\,\mu_B$/cell, $0.04\,\mu_B$/cell, and $0.01\,\mu_B$/cell, respectively; and 3s and 3p orbitals of S atoms have values $0.02\,\mu_B$/cell and $0.07\,\mu_B$/cell, respectively, as given in Table 2. Therefore, we found that the total value of magnetic moment of system-IIc is $+0.17\,\mu_B$/cell. In summary, magnetic properties of materials are consistent with the spin-asymmetry theory for the origin of magnetism, where it is understood that the higher the net difference in electronic occupancy in between up-spin and down-spin, the higher the magnetic moment is. The calculated values of magnetic moment in system-IIa and system-IIb (i.e., $-2.51\,\mu_B$/cell and $-2.51\,\mu_B$/cell) are greater than those of system-IIc ($+0.17\,\mu_B$/cell) because unpaired spin states of electrons in the orbitals around the vacancy atoms of system-IIc seem to be more paired by absorbed water molecule than in system-IIa and system-IIb. Therefore, magnetic moment of system-IIc rapidly falls down compared to system-IIa and system-IIb. We also found that there is a bit stronger interaction of water molecule with 1Mo vacancy defects as compared to 2Mo vacancy defects in the systems; this is because of greater polarizability of atoms in system-IIa and system-IIb than in system-IIc.

4. Conclusions

In this work, system-I, system-IIa, system-IIb, and system-IIc materials are constructed and investigated their structural, electronic, and magnetic properties by first-principles calculations based on the spin-polarized DFT-D2 method under computation package Quantum ESPRESSO. By analyzing the structures, we found that system-I is more compact than system-IIa, system-IIb, and system-IIc materials. Compactness of system and defect concentration in structures is related to each other because the more the defect concentrations in structures, the less the compactness of atoms in structures. Therefore, compactness of systems decreases with an increase in its defect concentration. On the analysis of band structures, system-I, system-IIa, system-IIb, and system-IIc have metallic properties. By studying DoS and PDoS calculations, we found that system-I has nonmagnetic properties and system-IIa, system-IIb, and system-IIc have magnetic properties. The total magnetic moment of system-IIa, system-IIb, and system-IIc has values $-2.51\,\mu_B$/cell, $-2.51\,\mu_B$/cell, and $+0.17\,\mu_B$/cell, respectively. Higher values of magnetic moment are claimed by allotted up- and down-spins in 2p orbital of C atoms, 3p orbital of S atoms, and 4d orbital of Mo atoms in defected systems.

Data Availability

All the data to reproduce the figures and tables in the text can be obtained from the corresponding author.

Conflicts of Interest

The authors declare that they have no conflicts of interest.

Acknowledgments

The authors acknowledge the financial support from UGC Nepal grants Ph. D. 075/76-S & T-09, TWAS research grants RG 20-316, and network project NT-14 of ICTP/OEA.

References

[1] K. S. Novoselov, A. K. Geim, S. V. Morozov et al., "Two-dimensional gas of massless dirac fermions in graphene," *Nature*, vol. 438, no. 7065, pp. 197–200, 2005.

[2] E. V. Castro, K. S. Novoselov, S. V. Morozov et al., "Biased bilayer graphene: semiconductor with a gap tunable by the electric field effect," *Physical Review Letters*, vol. 99, no. 21, Article ID 216802, 2007.

[3] L. Britnell, R. V. Gorbachev, R. Jalil et al., "Field-effect tunneling transistor based on vertical graphene heterostructures," *Science*, vol. 335, no. 6071, pp. 947–950, 2012.

[4] C. R. Dean, A. F. Young, I. Meric et al., "Boron nitride substrates for high-quality graphene electronics," *Nature Nanotechnology*, vol. 5, no. 10, pp. 722–726, 2010.

[5] X. Zhong, Y. K. Yap, R. Pandey, and S. P. Karna, "First-principles study of strain-induced modulation of energy gaps of graphene/BN and BN bilayers," *Physical Review B*, vol. 83, no. 19, Article ID 193403, 2011.

[6] L. Debbichi, O. Eriksson, and S. Lebègue, "Electronic structure of two-dimensional transition metal dichalcogenide bilayers fromab initiotheory," *Physical Review B*, vol. 89, no. 20, Article ID 205311, 2014.

[7] F. Schedin, A. K. Geim, S. V. Morozov et al., "Detection of individual gas molecules adsorbed on graphene," *Nature Materials*, vol. 6, no. 9, pp. 652–655, 2007.

[8] S. J. Han, A. V. Garcia, S. Oida, K. A. Jenkins, and W. Haensch, "Graphene radio frequency receiver integrated circuit," *Nature Communications*, vol. 5, no. 1, p. 3086, 2014.

[9] T. Hu, A. Hashmi, and J. Hong, "Transparent half metallic g-C_4N_3 nanotubes: potential multifunctional applications for spintronics and optical devices," *Scientific Reports*, vol. 4, no. 1, pp. 1–7, 2014.

[10] S. Basu and P. Bhattacharyya, "Recent developments on graphene and graphene oxide based solid state gas sensors," *Sensors and Actuators B: Chemical*, vol. 173, pp. 1–21, 2012.

[11] L. Fornarini, F. Stirpe, B. Scrosati, and G. Razzini, "Electrochemical solar cells with layer-type semiconductor anodes: performance of *n*-MoS_2 cells," *Solar Energy Materials*, vol. 5, no. 1, pp. 107–114, 1981.

[12] Y. Zhang, J. Ye, Y. Matsuhashi, and Y. Iwasa, "Ambipolar MoS_2 thin flake transistors," *Nano Letters*, vol. 12, no. 3, pp. 1136–1140, 2012.

[13] B. Radisavljevic, M. B. Whitwick, and A. Kis, "Small-signal amplifier based on single-layer MoS_2," *Applied Physics Letters*, vol. 101, no. 4, Article ID 043103, 2012.

[14] M. M. Ugeda, D. Fernández-Torre, I. Brihuega et al., "Point defects on graphene on metals," *Physical Review Letters*, vol. 107, no. 11, Article ID 116803, 2011.

[15] H. K. Neupane and N. P. Adhikari, "Structural, electronic and magnetic properties of impurities defected graphene/MoS_2 van der waals heterostructure: first-principles study," *Journal of Nepal Paediatric Society*, vol. 7, no. 2, pp. 1–8, 2021.

[16] T. P. Kaloni, R. P. Joshi, N. P. Adhikari, and U. Schwingenschlögl, "Band gap tunning in bn-doped graphene systems with high mobility," 2014, https://arxiv.org/abs/1402.0122.

[17] H. K. Neupane and N. P. Adhikari, "Effect of vacancy defects in 2D vdW graphene/h-BN heterostructure: first-principles study," *AIP Advances*, vol. 11, no. 8, Article ID 085218, 2021.

[18] H. K. Neupane and N. P. Adhikari, "Structural, electronic and magnetic properties of S sites vacancy defects graphene/MoS_2 van der waals heterostructures: first-principles study," *International Journal of Computational Materials Science and Engineering*, vol. 10, Article ID 2150009, 2021.

[19] C. Kittel, *Introduction to Solid State Physics*, John Wiley & Sons, Hoboken, NJ, USA, 2005.

[20] H. K. Neupane and N. P. Adhikari, "Structure, electronic and magnetic properties of 2D graphene-molybdenum disulphide (G-MoS_2) heterostructure (HS) with vacancy defects at Mo sites," *Computational Condensed Matter*, vol. 24, Article ID e00489, 2020.

[21] S. Lamichhane, P. Lage, G. B. Khatri, N. Pantha, N. P. Adhikari, and B. Sanyal, "First-principles study of adsorption of halogen molecules on graphene-MoS_2 bilayer hetero-system," *Journal of Physics: Conference Series*, vol. 765, no. 1, Article ID 012011, 2016.

[22] H. K. Neupane and N. P. Adhikari, "First-principles study of structure, electronic, and magnetic properties of C sites vacancy defects in water adsorbed graphene/MoS_2 van der waals heterostructures," *Journal of Molecular Modeling*, vol. 27, no. 3, pp. 1–12, 2021.

[23] H. K. Neupane and N. P. Adhikari, "Structural, electronic and magnetic properties of defected water adsorbed single-layer MoS_2," *Journal of Institute of Science and Technology*, vol. 26, no. 1, pp. 43–50, 2021.

[24] P. Hohenberg and W. Kohn, "Inhomogeneous electron gas," *Physical Review*, vol. 136, p. 864, 1964.

[25] P. Giannozzi, S. Baroni, N. Bonini et al., "Quantum ESPRESSO: a modular and open-source software project for quantum simulations of materials," *Journal of Physics: Condensed Matter*, vol. 21, no. 39, Article ID 395502, 2009.

[26] J. P. Perdew, K. Burke, and M. Ernzerhof, "Generalized gradient approximation made simple," *Physical Review Letters*, vol. 77, no. 18, pp. 3865–3868, 1996.

[27] S. Grimme, "Accurate description of van der waals complexes by density functional theory including empirical corrections," *Journal of Computational Chemistry*, vol. 25, no. 12, pp. 1463–1473, 2004.

[28] B. G. Pfrommer, M. Côté, S. G. Louie, and M. L. Cohen, "Relaxation of crystals with the quasi-newton method," *Journal of Computational Physics*, vol. 131, no. 1, pp. 233–240, 1997.

[29] J. D. Pack and H. J. Monkhorst, ""Special points for brillouin-zone integrations"-a reply," *Physical Review B*, vol. 16, no. 4, pp. 1748-1749, 1977.

[30] N. Marzari, D. Vanderbilt, A. De Vita, and M. C. Payne, "Thermal contraction and disordering of the Al(110) surface," *Physical Review Letters*, vol. 82, no. 16, pp. 3296–3299, 1999.

[31] T. V. Vu, N. V. Hieu, H. V. Phuc et al., "Graphene/WSeTe van der waals heterostructure: controllable electronic properties and schottky barrier via interlayer coupling and electric field," *Applied Surface Science*, vol. 507, Article ID 145036, 2020.

[32] Q. Peng, Z. Guo, B. Sa, J. Zhou, and Z. Sun, "New gallium chalcogenides/arsenene van der waals heterostructures promising for photocatalytic water splitting," *International Journal of Hydrogen Energy*, vol. 43, no. 33, pp. 15995–16004, 2018.

[33] S. Li, M. Sun, J.-P. Chou, J. Wei, H. Xing, and A. Hu, "First-principles calculations of the electronic properties of SiC-based bilayer and trilayer heterostructures," *Physical Chemistry Chemical Physics*, vol. 20, no. 38, pp. 24726–24734, 2018.

[34] Z. Hou, X. Wang, T. Ikeda et al., "Interplay between nitrogen dopants and native point defects in graphene," *Physical Review B*, vol. 85, no. 16, Article ID 165439, 2012.

[35] S. Deng, L. Li, and P. Rees, "Graphene/MoXY heterostructures adjusted by interlayer distance, external electric

field, and strain for tunable devices," *ACS Applied Nano Materials*, vol. 2, no. 6, pp. 3977–3988, 2019.

[36] K. D. Pham, N. N. Hieu, H. V. Phuc et al., "First principles study of the electronic properties and schottky barrier in vertically stacked graphene on the janus MoSeS under electric field," *Computational Materials Science*, vol. 153, pp. 438–444, 2018.

[37] H. K. Neupane and N. P. Adhikari, "Tuning structural, electronic, and magnetic properties of C sites vacancy defects in graphene/MoS_2 van der waals heterostructure materials: a first-principles study," *Advances In Condensed Matter Physics*, vol. 2020, Article ID 8850701, 11 pages, 2020.

[38] G. Grosso and G. P. Parravicini, *Solid State Physics*, Academic Press, Cambridge, MA, USA, 2005.

Journal of Molecular Modeling (2022) 28:107
https://doi.org/10.1007/s00894-022-05101-2

ORIGINAL PAPER

Adsorption of water on C sites vacancy defected graphene/h-BN: First-principles study

Hari Krishna Neupane[1,2] · **Narayan Prasad Adhikari**[2]

Received: 25 December 2021 / Accepted: 24 March 2022
© The Author(s), under exclusive licence to Springer-Verlag GmbH Germany, part of Springer Nature 2022

Abstract
Heterostructures (HS), vacancy defects in HS, and molecular adsorption on defected HS of 2D materials are fervently inspected for a profusion of applications because of their aptness to form stacked layers that confer approach to an amalgamation of favorable electronic and magnetic properties. In this context, graphene (Gr), hexagonal boron nitride (h-BN), HS of graphene/h-BN (Gr/h-BN), and molecular adsorption on Gr/h-BN offer promising prospects for electronic, spintonic, and optoelectronic devices. In this study, we investigated the structural, electronic, and magnetic properties of C sites vacancy defects in Gr/h-BN HS and adsorption of water molecule on defected Gr/h-BN HS materials by using first-principles calculations based on spin-polarized density functional theory method within van der Waals (vdW) corrections DFT-D2 approach. We found that these considered materials are stable 2D vdW HS. Based on band structure calculations, they are semimetallic, and on density of states and partial density of states analysis, they are magnetic materials. The magnetic moment developed in these defected systems is due to the unpaired up-spin and down-spin states in the orbitals of atoms present in the materials created by the vacancy defects.

Keywords DFT · Heterostructures · Magnetic moment · Molecular adsorption · Vacancy defects

Introduction

Heterostructures (HS) are formed by the incorporation of two distinctive nanomaterials. The properties of HS are different than their constituents [1, 2]. The van der Waals (vdW) HS have strong covalent bonds which provide in-plane stability of the 2D crystals because the atomic layers are attached to each other by a weak force, called vdW force, and the atomically thin layers are not mixed through a chemical reaction [3]. The properties of vdW HS materials can be absolutely restrained by twisting the two stacked atomic layers. The virtue of their novel properties opens the way to use unique degree of freedom for the nano-scale constraint of composite materials and nano-devices in future technologies [4–6]. Thus, vdW HS materials have great interest in device applications by the perspective of basic physics and applied science [7, 8]. The presence of defect will open on to the localization of electron and phonon waves in 2D materials [9]. Tuning defects level in 2D materials beyond notably changing the integrity of the materials remains one of the most difficult challenges, which limits their use in appliances [10, 11]. Defects engineering have focused on the surface of HS because defects engineering are necessary to obtain high-performance functional devices [10, 12, 13]. Thus, defects in HS have compelling role in the performance of devices. In addition, molecular adsorption means a molecule comes to be adsorbed on a surface of another phase. The adsorption of molecules on a surface is basic imperative to in general surface-mediated chemical action [14–16]. Thus, vacancy defects in HS and molecular adsorption on defected HS have novel electronic and magnetic properties based on the type of band structures and density of states (DOS)—partial density of states (PDOS) alignments between the constituent materials [17, 18]. In particular, one such strategy is combining graphene and hexagonal boron nitride with C sites vacancy defects to create vacancy defected Gr/h-BN HS and adsorption of water molecule on such defected HS formed water-adsorbed vacancy defected Gr/h-BN HS. The Gr/h-BN HS is constructed by vertically stacked graphene

✉ Narayan Prasad Adhikari
narayan.adhikari@cdp.tu.edu.np

[1] Amrit Campus, Institute of Science and Technology, Tribhuvan University, Kathmandu, Nepal

[2] Central Department of Physics, Institute of Science and Technology, Tribhuvan University, Kathmandu, Nepal

Published online: 30 March 2022

(Gr) and hexagonal boron nitride (h-BN) with 1.4% lattice mismatch which is comparable with the reported values [19–21]. It has opened stunning prospects because of its very delightful physical properties [22–26]. The monolayers as well as heterostructures of 2D materials have to be used in moisture environment. The adsorbed water molecules modified and deceived the properties of these materials [27–30]. Several recent research works are done about the adsorption of water molecules with the surface of other molecules. The stability and structural, chemical, and physical (electronic, magnetic and tribologic) properties of the materials are affected by the adsorbed water molecule [11, 31–33]. To our best knowledge, the study of structural, electronic, and magnetic properties of 2D vdW Gr/h-BN HS at C sites vacancy defects and adsorption of water molecule on C sites vacancy defected Gr/h-BN HS has not been reported. Therefore, in the present work, we investigated the structural, electronic, and magnetic properties of one carbon atom vacancy defect in Gr/h-BN HS (GBN-1C), two carbon atom vacancy defects in Gr/h-BN HS (GBN-2C), water molecule adsorbed on GBN-1C (w-GBN-1C), and water molecule adsorbed on GBN-2C (w-GBN-2C) materials by using spin-polarized density functional theory (DFT) method within vdW corrections DFT-D2 scheme-based first-principles calculations under Quantum ESPRESSO (QE) codes.

The rest part of this manuscript is outlined as follows: in the "Methods and materials" section, we have explained the methods and materials used in this study. The results and discussion are given in the "Results and discussion" section. The "Conclusions" section is the conclusions of the "Results and discussion" section.

Methods and materials

First-principles calculations for the study of structural, electronic, and magnetic properties of C sites vacancy defects in Gr/h-BN (GBN-1C and GBN-2C) and adsorption of water molecule on vacancy defected Gr/h-BN (w-GBN-1C and w-GBN-2C) have been performed based on spin-polarized density functional theory (DFT) [34] within DFT-D2 approach [35]. The exchange and correlation function are accounted by generalized gradient approximation (GGA) along with Perdew-Burke-Ernzerhof (PBE) plane-wave basis sets and Rabe-Rape-Kaxiras-Joannopoulos (RRKJ) model of ultrasoft pseudopotential (USPP) [36]. They have been taken in order to consider the interactions between ion cores and valence electrons by using Quantum ESPRESSO (QE) computational tool [37]. The heterostructures (HS) are constructed under periodic boundary condition, and then optimized by using Broyden-Fletcher-Goldfarb-Shanno (BFGS) method [38] up to a total energy adjustment that is less than 10^{-4} Ry between the steps of two consecutive self-consistent fields (scf) and each component of force acting that is less than10^{-3} Ry/Bohrs. Brillouin zone is sampled in k-space by suitable number of mesh (i.e., $6\times6\times1$) of k-points. This is obtained from the relation of direct and reciprocal lattice geometries from the convergence test using Γ-centered Monkhorst–Pack (MP) [39]. The Marzari–Vanderbilt (M-V) [40] smearing of 0.001Ry width is used to support the convergence. Moreover, david diagonalization method diagonalizes a subspace of the matrix rather of the whole thing, and gives the first few lowest or highest Eigen values. It is far more cost-efficient, and actually does not require creating the whole matrix in the first place [41]. Hence, we have taken "david" diagonalization method with plain mixing mode of default mixing factor 0.7 for self-consistency, and the kinetic energy cutoff (ecutwfc) for wave function and charge density cutoff (ecutrho) are set to 40Ry and 400Ry respectively.

In addition, computation study using QE begins with the construction of unit cell. At first, boron-nitrogen (BN) and graphene (Gr) unit cells are constructed. After that, we moved forth unit cell along x- and y-axes direction to prepare (4×4) supercell structure of h-BN and (4×4) supercell structure of graphene with suitable lattice parameters. The HS Gr/h-BN is created by using these prepared supercells with 1.4% lattice mismatch. This value is closed with the reported values [19–21]. We used a vacuum region of 18 Å to avert the reactions between the recurrent HS. Single carbon atom vacancy defect (GBN-1C) and double carbon atom vacancy defects (GBN-2C) materials are created by taking out one carbon atom and two carbon atoms respectively from Gr/h-BN HS. Water-adsorbed defected materials are constructed by adsorbing water molecule on GBN-1C (i.e., w-GBN-1C) and GBN-2C (i.e., w-GBN-2C) respectively. These GBN-1C, GBN-2C, w-GBN-1C, and w-GBN-2C materials are allowed to optimize and relax by using BFGS relaxation scheme for additional calculations which are shown in Fig. 1a–d respectively. The total energy and force acting on each component between two consecutive scf steps of optimized water-adsorbed HS (i.e., w-GBN-1C and w-GBN-2C materials) are also found to be less than 10^{-4} Ry and 10^{-3} Ry/Bohrs respectively. A mesh of $(6\times6\times1)$ is used for band structure calculations where 100 k-points are taken along high symmetric points and denser mesh of $(12\times12\times1)$ is used for density of states (DOS) and partial density of states (PDOS) calculations.

Results and discussion

In this section, we put forth the main findings of our work, analyze the results, and interpret them as well as compare with available data from reported works.

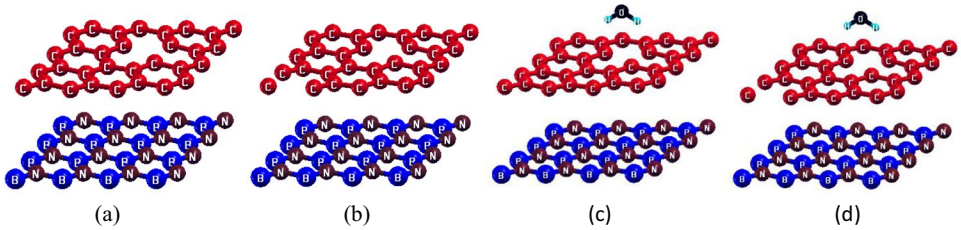

Fig. 1 C sites vacancy defects in graphene/h-BN heterostructure and water adsorption on defected graphene/h-BN heterostructure: **a** GBN-1C material, **b** GBN-2C material, **c** w-GBN-1C material, and **d** w-GBN-2C material

Structural and electronic properties

The 2D Gr/h-BN HS material is the combination of graphene and hexagonal boron nitride. It is one of the most auspicious materials in nanotechnology [1, 4, 6, 42]. Gr/h-BN HS with high perfection of the atomic lattice in the constituents (graphene and hexagonal boron nitride) has outstanding electronic, mechanical, and magnetic properties [43, 44]. Even so, aberration from perfection can be applicable in some appliances, as they make it feasible to tailor the local properties of HS and to accomplish advanced performances [45, 46]. In the present work, we have generated the optimized and relaxed supercell structure of graphene whose lattice parameter and bond length between C–C atoms are found to be 4.65 Å and 1.43 Å respectively, which are comparable to experimentally reported value [47]. Similarly, we have constructed the optimized and relaxed supercell structure of h-BN. The estimated lattice parameter and bond length between B-N atoms of h-BN are 4.74 Å and 1.45 Å respectively. They fairly agree with the reported value [48, 49]. The HS of Gr/h-BN consists of a graphene which is layered on top of an h-BN monolayer with 1.4% lattice mismatch which is in consistent with the reported values [19, 20]. In Gr/h-BN HS, graphene sheet adjusts to the in-plane lattice parameter of h-BN because the estimated in-plane lattice parameter of h-BN is 2.48 Å which is close to the reported values of graphene (2.46 Å) and h-BN (2.50 Å) [50, 51]. The calculated interlayer distance between graphene and h-BN is 3.28 Å, and this is consistent with the reported value [52]. Binding energy of Gr/h-BN determines of its stability which is estimated by using relation (1) [53];

$$E_{\text{binding}} = \frac{E_{\text{Gr}/h-\text{BN}} - E_{\text{Gr}} - E_{h-\text{BN}}}{A} \tag{1}$$

where A stands for surface area of HS and $E_{\text{Gr/h-BN}}$, E_{Gr}, and $E_{\text{h-BN}}$ represent the total ground state energy of Gr/h-BN HS, graphene, and monolayer h-BN respectively. The calculated binding energy of Gr/h-BN is − 41.88 meV/Å^2, and this is equivalent with the value of 2D HS materials [54, 55]. Hence, Gr/h-BN is an energetically stable 2D vdW HS material.

Furthermore, to examine the stability of C sites vacancy defected Gr/h-BN materials, we have modeled the materials GBN-1C and GBN-2C by detaching 1C and 2C atoms respectively from the surface of graphene of Gr/h-BN, and then they are optimized and relaxed before happening more. These optimized and relaxed GBN-1C and GBN-2C geometries are shown in Fig. 1a–b respectively. Later, we calculated binding energy of defected materials because stability of structure is examined based on their binding energy [55, 56]. It is calculated by using Eq. (2) [53];

$$E_{\text{binding}} = \frac{E_{(\text{Gr}/h-\text{BN})d} - E_{(\text{Gr})d} - E_{h-\text{BN}}}{A} \tag{2}$$

where $E_{\text{(Gr/h-BN)d}}$, $E_{\text{(Gr)d}}$, and $E_{\text{h-BN}}$ represent the total ground state energy of vacancy defected Gr/h-BN heterostructure, C sites vacancy defected graphene sheet, and monolayer h-BN respectively, and A denotes surface area of defected HS. The binding energies of GBN-1C and GBN-2C are − 28.30 meV/Å^2 and − 22.82 meV/Å^2 respectively. They are also comparable with other 2D HS materials [54, 55]. Hence, C sites vacancy defected materials are also energetically stable at ground state.

Moreover, we have measured interlayer distance between the consistent of GBN-1C and GBN-2C materials. They are found to be 3.29 Å and 3.33 Å respectively which are also corresponding with the value of other HS [52]. From these measurements, we found that the interlayer distance of defected materials increases with increase in concentration of vacancy defects in Gr/h-BN. Hence, according to binding energy and interlayer distance calculations, we confirmed that C sites vacancy defected geometries are stable vdW HS materials. Also, stability of defected systems can be predicted based on their defects formation energy. Thus, we have calculated defects formation energy of GBN-1C and GBN-2C by using Eq. (3) [57], and found to be 0.18 eV and 0.24 eV respectively.

$$E_f = E_{t-d} - \left(E_{t-\text{nd}} + n_a \mu_a\right) \tag{3}$$

where $E_{\text{t-d}}$, $E_{\text{t-nd}}$, n_{a}, and μ_{a} are the total ground state energy of C sites vacancy defected HS, total ground state energy of pristine HS, number of vacancy defects C atom, and chemical potential of an C atom respectively. The small value of defects formation energy suggests that materials can be agreeable for the computational work. Therefore, GBN-1C and GBN-2C materials can be used for computational study.

Additionally, we have studied the effect of adsorbed water molecule on structural, electronic, and magnetic properties of GBN-1C and GBN-2C materials. For that, water molecule is adsorbed on the top surface of GBN-1C (known as w-GBN-1C) and GBN-2C (known as w-GBN-2C) materials. Regarding our results, adsorption energies of water molecule on GBN-1C and GBN-2C materials are − 0.13 eV and − 0.14 eV respectively. Then, they are optimized and found that distance between adsorbed water molecule and graphene sheet of GBN-1C and GBN-2C is 2.58 Å and 2.59 Å respectively as shown in Fig. 1c and d. The estimated value of binding energy and equilibrium graphene-water distance is close to the reported values 0.17 eV and 3.28 Å respectively [58–60]. We have also calculated the binding energy of w-GBN-1C and w-GBN-2C materials by using Eq. (4) [53];

$$E_{\text{binding}} = \frac{E_{(w-\text{Gr}/h-\text{BN})d} - E_{H_2O} - E_{(\text{Gr}/h-\text{BN})d}}{A} \quad (4)$$

where $E_{(\text{w-Gr/h-BN})\text{d}}$, E_{H2O}, and $E_{(\text{Gr/h-BN})\text{d}}$ denote the total ground state energy of water adsorbed on C sites vacancy defected Gr/h-BN HS, ground state energy of water molecule, and C sites vacancy defected Gr/h-BN HS respectively. "*A*" represents the surface area of water-adsorbed defected HS. The estimated binding energy of w-GBN-1C and w-GBN-2C are − 27.54 meV/Å^2 and − 24.21 meV/Å^2 respectively. We have also calculated the interlayer distance of graphene and h-BN of w-GBN-1C and w-GBN-2C materials and found to be 3.28 Å and 3.31 Å respectively. By the analysis of binding energy and interlayer distance, we found that they are stable 2D vdW HS materials. Therefore, from the analysis of structural properties, it is concluded that all the abovementioned materials are stable 2D vdW HS.

Electronic properties of GBN-1C, GBN-2C, w-GBN-1C, and w-GBN-2C materials are investigated by analyzing their band structures and DOS plots as depicted in Figs. 2a–d and 3a–d respectively. Band structures of these materials contain band states of graphene and h-BN. In graphene, the band above the Fermi level refers to π* and below the Fermi level refers to π band. The π* and π bands meet at a point on the Fermi level called Dirac point which is the vertex of Dirac cones. The conduction band and valence band of graphene do not overlap and have zero band gap [61], which indicates graphene is called zero band gap material. Rather, h-BN is a wide band gap material of value 4.98 eV, which agrees with

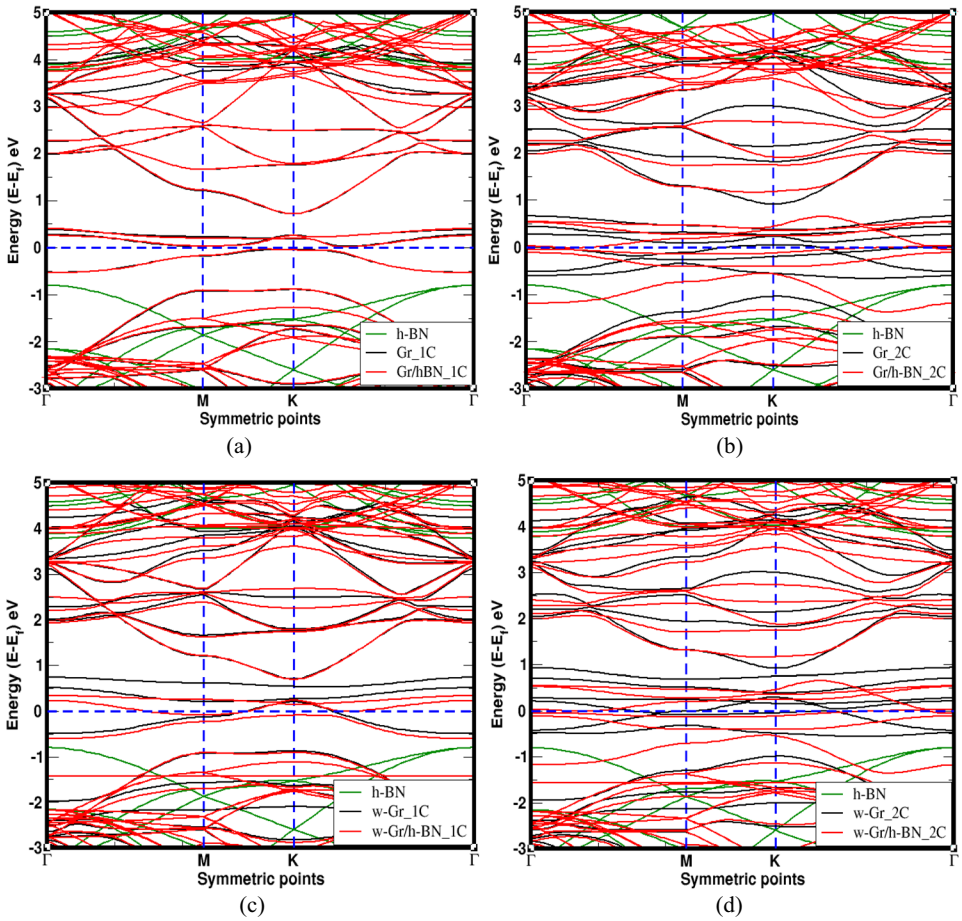

Fig. 2 Band structures of C sites vacancy defects in graphene/h-BN heterostructure and water adsorption on defected graphene/h-BN heterostructure materials: **a** band structure of GBN-1C, **b** band structure of GBN-2C, **c** band structure of w-GBN-1C, **d** band structure of w-GBN-2C. In all band plots, horizontal dotted line represents Fermi energy level, and vertical dotted lines represent symmetric points in brillouin zone. In figures (a and b), green, black, and red lines indicate band states of h-BN, defected graphene, and C sites vacancy defected Gr/h-BN heterostructure respectively. In figures (c and d), green, black, and red lines represent band states of h-BN, water adsorbed in defected graphene, and water adsorbed in C sites vacancy defected Gr/h-BN heterostructure respectively

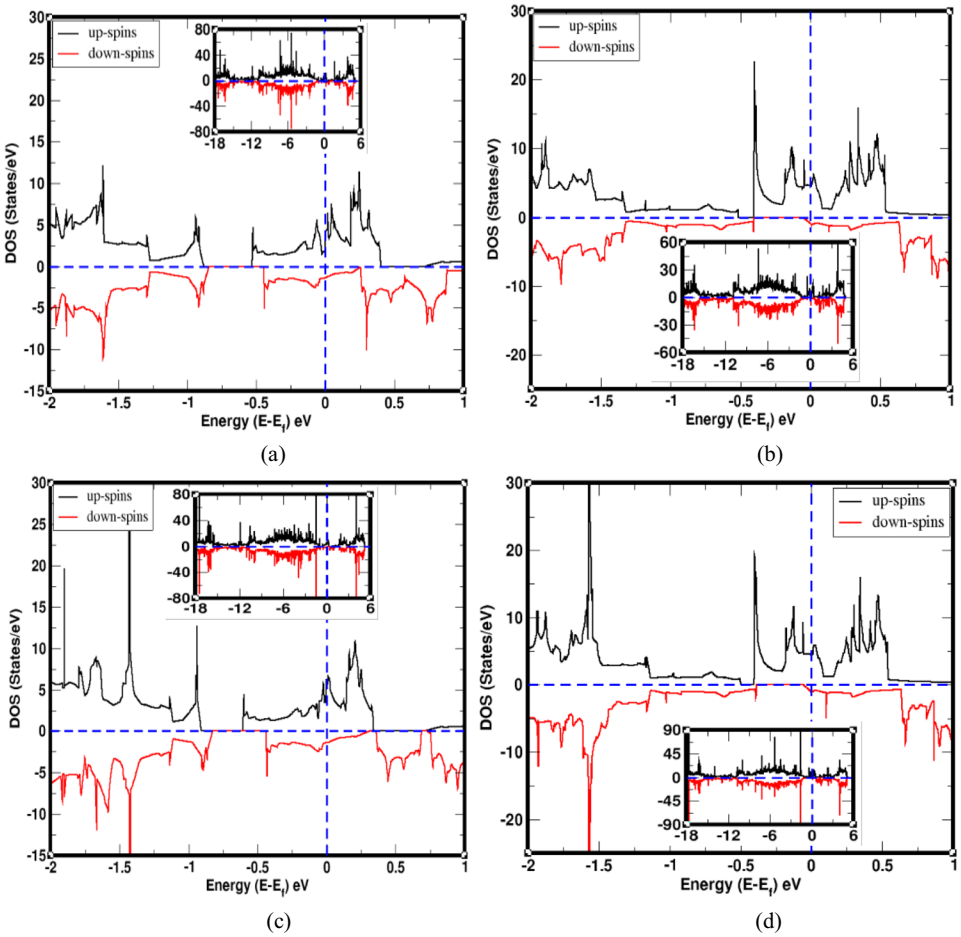

Fig. 3 DOS of total up-spin and total down-spin states of electrons in the orbitals of C, B, N, and H atoms present in C sites vacancy defects in graphene/h-BN heterostructure and water adsorption on defected graphene/h-BN heterostructure materials: **a** DOS of GBN-1C, **b** DOS of GBN-2C, **c** DOS of w-GBN-1C, and **d** DOS of w-GBN-2C. In all DOS, horizontal dotted line distinguishes spin states and vertical dotted line separates the electronic bands. Insets in DOS represent spin states within large energy range along x-axis

the reported value [62]. These different energy band gaps materials are bound together by vdW force to form Gr/h-BN HS. Its band structure is the sum of the band states of its constituents [52], because the covalent bonds within the layers are not altered in the creation of the HS. By the watchful inspection, we found that a small band gap of value 2.60 meV opened at the k point in band states of graphene due to the weak interaction between the two supercells. As well, we have explored the band structures of GBN-1C, GBN-2C, w-GBN-1C, and w-GBN-2C materials which are illustrated in Fig. 2a–d respectively, where 100 k-points are taken along the direction of irreducible brillouin zone by choosing Γ-M–K-Γ symmetric points along x-axis and corresponding energy along y-axis. Horizontal dotted line is called Fermi energy level which separated the electronic bands.

At first, we have discussed the formation of band gap energy of considered defected systems. The calculated band gap energy of GBN-1C is 5.97 eV. This is obtained by the sum of p-type and n-type barrier heights which are 2.28 eV and 3.69 eV respectively as shown in Fig. 2a. Band gap 4.55 eV opens by monolayer h-BN in GBN-1C where n-type and p-type heights are 3.80 eV and 0.75 eV respectively. Hence, band gap of GBN-1C is greater than of monolayer h-BN; this is due to the formation of dangling bonds at graphene surface by the effect of 1C vacancy defects in Gr/h-BN HS. We have calculated band gap energy 5.99 eV of GBN-2C (n-type barrier height 3.63 eV and p-type height 2.35 eV) which is greater than that of GBN-1C. Also, the calculated value of band gap energy in GBN-2C due to monolayer h-BN is 4.70 eV where n- and p-type barrier heights are 3.90 eV and 0.80 eV respectively. Similarly, we have estimated band gap energy of w-GBN-1C and w-GBN-2C as 6.01 eV and 5.98 eV respectively. Band gap energies of monolayer h-BN in such materials are 5.56 eV and 5.69 eV respectively. Moreover, we have compared band gap energy of defected systems and found that band gap energy of w-GBN-2C is smaller than that of GBN-2C because of the rearrangement of band states due to the molecular adsorption on GBN-2C. But, band gap energy of w-GBN-1C is greater than of GBN-1C since more number of unequal energy bands are created by adsorbed water molecule in w-GBN-1C. Additionally, the effects of C sites vacancy defects in Gr/h-BN HS and water adsorption on defected HS are as following: if the mesh of vacancy defects in graphene of HS breaks the specific symmetries, the linearly crossing bands appear at Fermi level. So, C sites vacancy

defected materials GBN-1C, GBN-2C, w-GBN-1C, and w-GBN-2C have linearly crossing bands, and confined vacancy states interrelated to the flat bands are noticed in band gap as shown in Fig. 2a–d respectively. We observed that the states linked with dangling bond and reestablished C–C bond of vacancy occur near the top of valence band and in the conduction band of GBN-1C and w-GBN-1C materials as shown in Fig. 2a and c respectively. In GBN-2C and w-GBN-2C materials, there are no states connected with dangling bond but restructured of C–C bond occurs around the vacancy atoms due to which band states are raised around the Fermi levels as illustrated in Fig. 2b and d. Also, the vacancies are keen regions for molecular adsorption in w-GBN-1C and w-GBN-2C materials due to the engineering of atoms around the vacancy, and hence electronic properties of HS are modified by vacancy defects and molecular adsorption on vacancy defected materials. Therefore, from the band structure analysis, we found that GBN-1C, GBN-2C, w-GBN-1C, and w-GBN-2C materials have semimetallic nature. The calculated data for the analysis of geometrical structures and band structures are given in Table 1.

Magnetic properties

Density of states (DOS) is defined as the number of orbitals (electronic states or quantum states) per unit energy range. DOS calculations are permitted to find out the usual distribution of states as a function of energy and can also rule the energy bands' space in materials. The magnetic properties of materials can be investigated based on their DOS computations because magnetic moment is precisely associated by means of DOS of the materials [63, 64]. The symmetrically distributed DOS of up-spin and down-spin of material reflects non-magnetic properties while asymmetrically distributed DOS of up-spin and down-spin reveals magnetic properties of materials [65, 66]. The reason is that the number of unpaired spin states of electrons gives magnetic moment that can be estimated by counting electrons in the up-spin and down-spin sub-bands. Hence, magnetic moment is calculated owing to unpaired up-spin and down-spin states of electrons in the orbitals of atoms present in materials. In detail, magnetic moment of materials can be explored by partial density of states (PDOS) computations. Thus, both DOS and PDOS computations are used to examine the magnetic properties of materials. In this work, we have investigated the magnetic properties of GBN-1C, GBN-2C, w-GBN-1C, and w-GBN-2C materials by the analysis of DOS and PDOS calculations. The DOS and PDOS plots of the abovementioned materials are illustrated in Figs. 3a–d and 4a–d respectively, where vertical dotted line indicates Fermi energy level and horizontal dotted line distinguishes up-spin and down-spin states of electrons.

Table 1 Fermi energy (E_f), defects formation energy (E_d), binding energy (E_b), interlayer distance (D_I), adsorption energy of water molecule on defected materials (E_a), optimized distance of water molecule from graphene sheet of defected HS materials (D_i), band gap of h-BN (E_g), and band gap of defected heterostructures ($E_{G\text{-}H}$) of GBN-1C, GBN-2C, w-GBN-1C, and w-GBN-2C materials

Materials →	GBN-1C	GBN-2C	w-GBN-1C	w-GBN-2C
E_f (eV)	−1.65	−1.64	−2.11	−2.10
E_d (eV)	0.18	0.24	-	-
E_b (meV/Å^2)	−28.30	−22.82	−27.54	−24.21
D_I (Å)	3.29	3.33	3.28	3.31
E_a (eV)	-	-	−0.13	−0.14
D_i (Å)	-	-	2.58	2.59
E_g (eV)	4.55	4.70	4.56	4.69
$E_{G\text{-}H}$ (eV)	5.97	5.99	6.01	5.98

The DOS of up-spin and down-spin states are asymmetrically distributed and appeared around the Fermi energy level of GBN-1C as shown in Fig. 3a. It means GBN-1C is a magnetic material. We have analyzed the PDOS of GBN-1C which can be used to estimate the magnetic moment contributed by unpaired spin states of electrons in the individual orbital of atom present in material. The magnetic moments given by 2 s and 2p orbitals of C atoms are 0.12 μ_B/cell and 0.27 μ_B/cell respectively which are because of the adjustment of unpaired up-spin and down-spin states of electrons created by 1C vacancy defect in 2 s and 2p orbitals of C atoms in GBN-1C. Alternately, magnetic moment developed through up-spin and down-spin in the orbitals of 2 s and 2p of B, N, and O atoms and 1 s of H atoms is found to be zero (0.00 μ_B/cell). So, only 2 s and 2p orbitals of C atoms have significant role for the buildup of magnetic moment in GBN-1C. Hence, total magnetic moment of GBN-1C is 0.39 μ_B/cell. DOS and PDOS of unoccupied asymmetrically distributed spin states of GBN-2C are seen around the Fermi level as depicted in Figs. 3b and 4b respectively. As a result, magnetic moment is grown up in GBN-2C appearing its magnetic nature. Magnetic moments contributed by 2 s and 2p orbitals of C atoms are 0.48 μ_B/cell and 1.22 μ_B/cell; 2 s and 2p orbitals of B atoms are 0.02 μ_B/cell and 0.09 μ_B/cell; 2 s and 2p orbitals of N atoms are 0.01 μ_B/cell and 0.07 μ_B/cell; 2 s and 2p orbitals of O atom are 0.00 μ_B/cell; and 1 s orbital of H atoms are 0.00 μ_B/cell respectively. From these calculations, we have estimated the total magnetic moment of GBN-2C material is 1.89 μ_B/cell. Hence, GBN-2C is a magnetic material. Likewise, DOS and PDOS of spin states are asymmetrically distributed in w-GBN-1C material as shown in Figs. 3c and 4c respectively, which reveals it has magnetic properties. The magnetic moments given by 2 s and 2p orbitals of C, B, N, and O atoms are 0.21 μ_B/cell and 0.43 μ_B/cell; 0.01 μ_B/cell and 0.04 μ_B/cell; 0.01 μ_B/cell and 0.02 μ_B/cell;

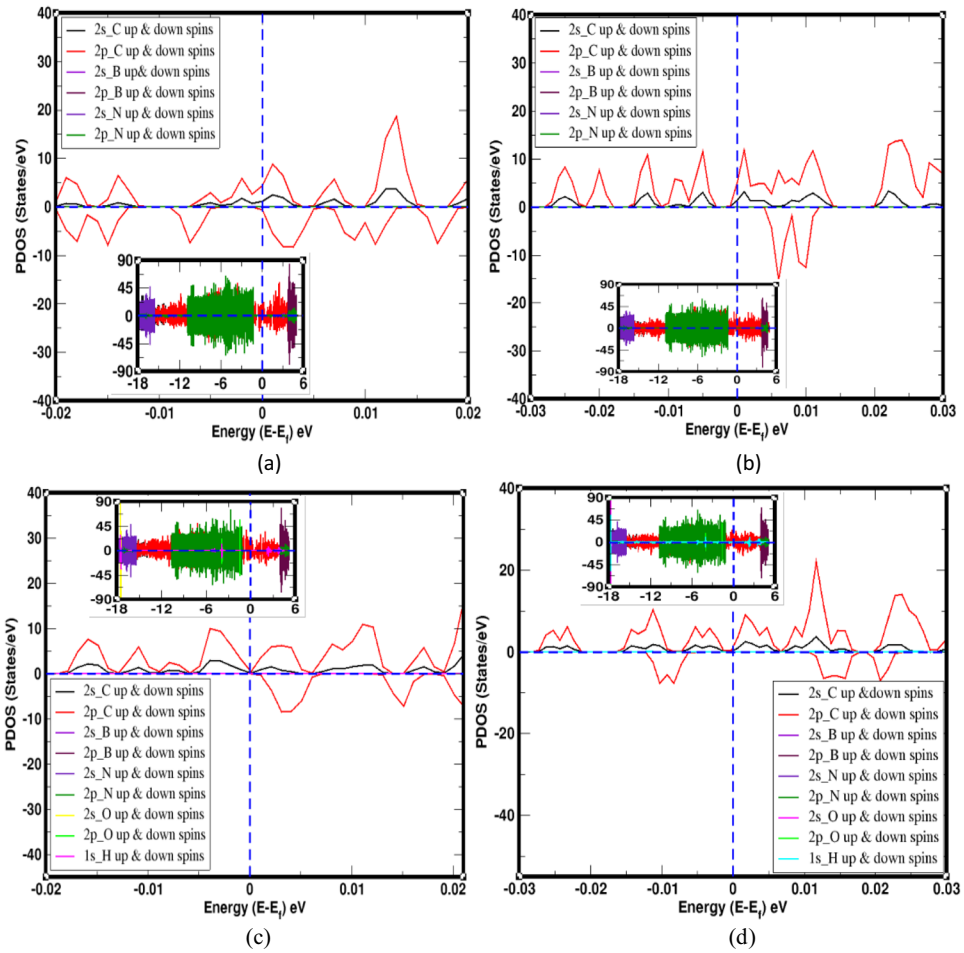

Fig. 4 PDOS of individual up-spin and down-spin states of electrons in the orbitals of C, B, N, O, and H atoms present in C sites vacancy defects in graphene/h-BN heterostructure and water adsorption on defected graphene/h-BN heterostructure materials: **a** PDOS of GBN-1C, **b** PDOS of GBN-2C, **c** PDOS of w-GBN-1C, and **d** PDOS of w-GBN-2C. In all PDOS, horizontal dotted line distinguishes spin states and vertical dotted line separates the electronic bands. Insets in PDOS represent spin states within large energy range along x-axis

and 0.00 μ_B/cell and 0.00 μ_B/cell respectively in w-GBN-1C. Thus, the total magnetic moment of w-GBN-1C is 0.72 μ_B/cell. As well, the magnetic moment of w-GBN-2C is obtained due to the asymmetrically distributed up- and down-spin states in DOS and PDOS as illustrated in Figs. 3d and 4d respectively. Hence, w-GBN-2C is a magnetic material. The total magnetic moment of w-GBN-2C is 1.89 μ_B/cell due to the impact of unpaired spin states present in 2 s and 2p orbitals of C atoms in structures. Total magnetic moments produced in w-GBN-2C by 2 s and 2p orbitals of C atoms are 0.42 μ_B/cell and 1.26 μ_B/cell; 2 s and 2p of B atoms are 0.01 μ_B/cell and 0.06 μ_B/cell; 2 s and 2p of N atoms are 0.00 μ_B/cell and 0.04 μ_B/cell; 2 s and 2p of O atom are 0.00 μ_B/cell and 0.00 μ_B/cell; and 1 s of H atoms are 0.00 μ_B/cell and 0.00 μ_B/cell respectively. Therefore, unpaired spin states in 2 s and 2p orbitals of C atoms in structure have notable role for the production of magnetic properties. The magnetic moment calculations of GBN-1C, GBN-2C, w-GBN-1C, and w-GBN-2C are given in Table 2.

Conclusions

We have conducted the first-principles study to investigate structural, electronic, and magnetic properties of one carbon atom vacancy defect in Gr/h-BN HS (GBN-1C) and two carbon atom vacancy defects in Gr/h-BN HS (GBN-2C) materials, where defects percentage are 3.125% and 6.25% respectively. Also, we have extended our work to study the adsorption of water molecule on GBN-1C (w-GBN-1C) and GBN-2C (w-GBN-2C) materials. All these calculations were carried out under DFT-D2 level of approximation with generalized gradient approximation (GGA) and exchange correlation function including spin-polarized calculation using Quantum ESPRESSO code. The ultrasoft pseudopotentials were used in order to account the interaction between ion cores and valence electrons. We have estimated the binding energy – 28.30 meV/Å^2, – 22.82 meV/Å^2, – 27.54 meV/Å^2, and – 24.21 meV/Å^2 and interlayer distances 3.29 Å, 3.33 Å, 3.28 Å, and 3.31 Å of GBN-1C, GBN-2C, w-GBN-1C, and w-GBN-2C

Table 2 The estimation of total magnetic moment (M_T) by the distributions of up-spin and down-spin states of electrons in the orbitals of C, B, and N atoms in PDOS of GBN-1C, GBN-2C, w-GBN-1C, and w-GBN-2C stacking configurations

Magnetic moment by asymmetrically distributed spin states in the orbitals of C, B, N, O, and H atoms in →	GBN-1C (μ_B/cell)	GBN-2C (μ_B/cell)	w-GBN-1C (μ_B/cell)	w-GBN-2C (μ_B/cell)
Spins in 2 s of C atoms	0.12	0.48	0.21	0.42
Spins in 2p of C atoms	0.27	1.22	0.43	1.26
Spins in 2 s of B atoms	0.00	0.02	0.01	0.01
Spins in 2p of B atoms	0.00	0.09	0.04	0.06
Spins in 2 s of N atoms	0.00	0.01	0.01	0.00
Spins in 2p of N atoms	0.00	0.07	0.02	0.04
Spins in 2 s of O atoms	0.00	0.00	0.00	0.00
Spins in 2p of O atoms	0.00	0.00	0.00	0.00
Spins in 1 s of H atoms	0.00	0.00	0.00	0.00
Total magnetic moment (M_T)	0.39	1.89	0.72	1.89

materials respectively. They indicated that these are stable 2D vdW heterostructure materials. We have calculated the band structure and DOS of GBN-1C and GBN-2C materials and found that band states of graphene cross the Fermi level which gives metallic properties but h-BN opens band gap in band structures. Hence, GBN-1C and GBN-2C materials have semimetallic characteristics. Also, we have analyzed the DOS and PDOS calculations of these materials. In GBN-1C and GBN-2C, DOS/PDOS of up-spin and down-spin states are asymmetrically distributed around the Fermi energy level, which indicates that GBN-1C and GBN-2C are magnetic materials. Moreover, we have studied the adsorption of water molecule on C sites vacancy defected GBN-1C and GBN-2C materials and then analyzed their band structures and DOS and PDOS calculations. We found that, from band and DOS calculations, they are semimetallic, and based on the DOS and PDOS analyses, they have magnetic properties. Hence, GBN-1C, GBN-2C, w-GBN-1C, and w-GBN-2C materials are magnetic materials. Magnetic moments of these materials are found to be 0.39 μ_B/cell, 1.89 μ_B/cell, 0.72 μ_B/cell, and 1.89 μ_B/cell respectively. Magnetic moments are obtained due to the rearrangement of unpaired spin states of electrons in the individual orbitals of atoms present in materials.

Author contribution HKN carried out all the calculations whereas NPA conceived the idea and both the authors analyzed the results and read the manuscript.

Funding The authors acknowledge the financial support from UGC Nepal grants Ph. D. 075/76-S & T-09, TWAS research grants RG 20–316, and network project NT-14 of ICTP/OEA.

Data availability All the data to reproduce the figures and tables of this paper will be provided by the corresponding author on request to do so.

Code availability We used Quantum software to produce all the data in this paper and the code is freely available as an open source code.

Declarations

Conflict of interest The authors declare no competing interests.

References

1. Din HU, Idrees M, Albar A, Shafiq M, Ahmad I, Nguyen CV, Amin B (2019) Rashba spin splitting and photocatalytic properties of GeC− MSSe (M= Mo, W) van der Waals heterostructures. Phys Rev B 100(16):165425
2. Wang J, Ma F, Liang W, Sun M (2017) Electrical properties and applications of graphene, hexagonal boron nitride (h-BN), and graphene/h-BN heterostructures. Mater Today Phys 2:6–34
3. Vu TV, Hieu NV, Phuc HV, Hieu NN, Bui HD, Idrees M, …, Nguyen CV (2020) Graphene/WSeTe van der Waals heterostructure: Controllable electronic properties and Schottky barrier via interlayer coupling and electric field. Appl Surf Sci 507:145036
4. Phuc HV, Hieu NN, Hoi BD, Phuong LT, Nguyen CV (2018) First principle study on the electronic properties and Schottky contact of graphene adsorbed on MoS_2 monolayer under applied out-plane strain. Surf Sci 668:23–28
5. Debbichi L, Eriksson O, Lebègue S (2014) Electronic structure of two-dimensional transition metal dichalcogenide bilayers from ab initio theory. Phys Rev B 89(20):205311
6. Ghorbani-Asl M, Bristowe PD, Koziol K, Heine T, Kuc A (2016) Effect of compression on the electronic, optical and transport properties of MoS2/graphene-based junctions. 2D Mater 3(2):025018
7. Phan AD, Viet NA, Poklonski NA, Woods LM, Le CH (2012) Interaction of a graphene sheet with a ferromagnetic metal plate. Phys Rev B 86(15):155419
8. Yu WJ, Li Z, Zhou H, Chen Y, Wang Y, Huang Y, Duan X (2013) Vertically Stacked multi-heterostructures of layered materials for logic transistors and Complementary inverters. Nat Mater 12(3):246–252
9. Zhu T, Ertekin E (2014) Phonon transport on two-dimensional graphene/boron nitride superlattices. Phys Rev B 90(19):195209
10. Huang Z, Liu H, Hu R, Qiao H, Wang H, Liu Y, Zhang H (2020) Structures, Properties and application of 2D monoelemental materials (Xenes) as graphene analogues Under defect engineering. Nano Today 35:100906
11. Priyadarsini A, Mallik BS (2021) Aqueous Affinity and Interfacial Dynamics of Anisotropic Buckled Black Phosphorous. J Phys Chem B 125(27):7527–7536

12. Hu Z, Wu Z, Han C, He J, Ni Z, Chen W (2018) Two-dimensional transition metal dichalcogenides: interface and defect engineering. Chem Soc Rev 47(9):3100–3128
13. Han SW, Yun WS, Woo WJ, Kim H, Park J, Hwang YH, Nguyen TK, Le CT, Kim YS, Kang M, Ahn CW, Hong SC (2021) Interface defect engineering of a large-scale CVD-grown MoS2 monolayer via residual sodium at the SiO2/Si substrate. Advanced Materials Interfaces 8(14):2100428
14. Kostov MK, Santiso EE, George AM, Gubbins KE, Nardelli MB (2005) Dissociation of water on defective carbon substrates. Phys Rev Lett 95(13):136105
15. Bollinger MV, Lauritsen JV, Jacobsen KW, Nørskov JK, Helveg S, Besenbacher F (2001) One-dimensional metallic edge states in MoS_2. Phys Rev Lett 87(19):196803
16. Neupane HK, Adhikari NP (2021) First-principles study of structure, electronic, and magnetic properties of C sites vacancy defects in water adsorbed graphene/MoS_2 van der Waals heterostructures. J Mol Model 27(3):1–12
17. Xu R, Zou X, Liu B, Cheng HM (2018) Computational design and property predictions for two-dimensional nanostructures. Mater Today 21(4):391–418
18. Bafekry A, Shayesteh SF, Peeters FM (2019) Two-dimensional carbon nitride (2DCN) nanosheets: Tuning of novel electronic and magnetic properties by hydrogenation, atom substitution and defect engineering. J Appl Phys 126(21):215104
19. Ramasubramaniam A, Naveh D, Towe E (2011) Tunable band gaps in bilayer graphene− BN heterostructures. Nano Lett 11(3):1070–1075
20. Slotman GJ, Van Wijk MM, Zhao PL, Fasolino A, Katsnelson MI, Yuan S (2015) Effect of structural relaxation on the electronic structure of graphene on hexagonal boron nitride. Phys Rev Lett 115(18):186801
21. Neupane HK, Adhikari NP (2021) Effect of vacancy defects in 2D vdW graphene/h-BN heterostructure: First-principles study. AIP Adv 11(8):085218
22. Liu Z, Song L, Zhao S, Huang J, Ma L, Zhang J, Ajayan PM (2011) Direct growth of graphene/hexagonal boron nitride stacked layers. Nano Lett 11(5):2032–2037
23 Li L, Lee I, Lim D, Kang M, Kim GH, Aoki N, Taniguchi T (2015) Raman Shift and electrical properties of MoS_2 bilayer on boron nitride substrate. Nanotechnology 26(29):295702
24. Wang S, Wang X, Warner JH (2015) All chemical vapor deposition growth of MoS_2: h-BN vertical van der Waals heterostructures. ACS Nano 9(5):5246–5254
25. Okada M, Sawazaki T, Watanabe K, Taniguch T, Hibino H, Shinohara H, Kitaura R (2014) Direct chemical vapor deposition growth of WS_2 atomic layers on hexagonal boron nitride. ACS Nano 8(8):8273–8277
26. Beniwal S, Hooper J, Miller DP, Costa PS, Chen G, Liu SY, Enders A (2017) Graphene-like boron–carbon–nitrogen monolayers. ACS Nano 11(3):2486–2493
27. Bououden W, Benguerba Y, Darwish AS, Attoui A, Lemaoui T, Balsamo M, Alnashef IM (2021) Surface adsorption of Crizotinib on carbon and boron nitride nanotubes as Anti-Cancer drug Carriers: COSMO-RS and DFT molecular insights. J Mol Liq 338:116666
28. Nakhli A, Bergaoui M, Toumi KH, Khalfaoui M, Benguerba Y, Balsamo M, …, Erto A (2020) Molecular insights through computational modeling of methylene blue adsorption onto low-cost adsorbents derived from natural materials: A multi-model's approach. Comput Chem Eng 140:106965
29. Darwish AS, Warrag SE, Lemaoui T, Alseiari MK, Hatab FA, Rafay R, …, Alamoodi N (2021) Green Extraction of Volatile Fatty Acids from Fermented Wastewater Using Hydrophobic Deep Eutectic Solvents. Fermentation 7(4):226
30. Benabid S, Streit AF, Benguerba Y, Dotto GL, Erto A, Ernst B (2019) Molecular modeling of anionic and cationic dyes adsorption on sludge derived activated carbon. J Mol Liq 289:111119
31. Priyadarsini A, Mallik BS (2021) Effects of Doped N, B, P, and S Atoms on Graphene toward Oxygen Evolution Reactions. ACS Omega 6(8):5368–5378
32. Priyadarsini A, Mallik BS (2021) Amphiphilicity of Intricate Layered Graphene/g- C3N4 Nanosheets. J Phys Chem B 125(42):11697–11708
33. Priyadarsini A, Mallik BS (2022) Site dependent catalytic water dissociation on an anisotropic buckled black phosphorus surface. Phys Chem Chem Phys 24(4):2582–2591. https://doi.org/10.1039/D1CP05249G
34. Hohenberg P, Kohn W (1964) Inhomogeneous electron gas. Phys Rev 136(3B):B864
35. Grimme S (2004) Accurate description of van der Waals complexes by density Functional theory including empirical corrections. J Comput Chem 25(12):1463–1473
36. Perdew JP, Burke K, Ernzerhof M (1996) Generalized gradient approximation made simple. Phys Rev Lett 77(18):3865
37. Giannozzi P, Baroni S, Bonini N, Calandra M, Car R, Cavazzoni C, Dal Corso A (2009) QUANTUM ESPRESSO: modular and open-source software Project for quantum simulations of materials. J Phys Condens Matter 21(39):395502
38. Pfrommer BG, Côté M, Louie SG, Cohen ML (1997) Relaxation of Crystals with the quasi-Newton method. J Comput Phys 131(1):233–240
39. Pack JD, Monkhorst HJ (1977) Special points for Brillouin-zone integrations a reply. Phys Rev B 16(4):1748
40. Marzari N, Vanderbilt D, De Vita A, Payne MC (1999) Thermal Contraction and disordering of the Al (110) surface. Phys Rev Lett 82(16):3296
41. Morgan RB, Scott DS (1986) Generalizations of Davidson's method for computing eigenvalues of sparse symmetric matrices. SIAM J Sci Stat Comput 7(3):817–825
42. Jayaprakash GK, Flores-Moreno R (2018) Regioselectivity in hexagonal boron nitride co-doped graphene. New J Chem 42(23):18913–18918
43. Wang J, Ma F, Sun M (2017) Graphene, hexagonal boron nitride, and their heterostructures: properties and applications. RSC Adv 7(27):16801–16822
44. Pham KD, Nguyen CV (2018) First principles calculations of the geometric structures and electronic properties of van der Waals heterostructure based on graphene, hexagonal boron nitride and molybdenum diselenide. Diam Relat Mater 88:151–157
45. Yao W, Fan L (2021) Defects in Graphene/h-BN Planar Heterostructures: Insights into the Interfacial Thermal Transport Properties. Nanomaterials 11(2):500
46. Kudur Jayaprakash G, Casillas N, Astudillo-Sánchez PD, Flores-Moreno R (2016) Role of defects on regioselectivity of nano pristine graphene. J Phys Chem A 120(45):9101–9108
47. Martin RM (2020) Electronic structure: basic theory and practical methods. Cambridge University Press, Cambridge
48. Liu YJ, Gao B, Xu D, Wang HM, Zhao JX (2014) Theoretical study on Si-doped hexagonal boron nitride (h-BN) sheet: Electronic, magnetic properties, and reactivity. Phys Lett A 378(40):2989–2994
49. Ooi N, Rairkar A, Lindsley L, Adams JB (2005) Electronic structure and bonding in hexagonal boron nitride. J Phys Condens Matter 18(1):97
50. Aggoune W, Cocchi C, Nabok D, Rezouali K, Belkhir MA, Draxl C (2018) Dimensionality of excitons in stacked van der Waals materials: The example of hexagonal boron nitride. Phys Rev B 97(24):241114

51. Woods CR, Britnell L, Eckmann A, Ma RS, Lu JC, Guo HM, Novoselov KS (2014) Commensurate–incommensurate transition in graphene on hexagonal boron nitride. Nat Phys 10(6):451–456
52. Aggoune W, Cocchi C, Nabok D, Rezouali K, Belkhir MA, Draxl C (2020) Structural, electronic, and optical properties of periodic graphene/h-BN van der Waals heterostructures. Phys Rev Mater 4(8):084001
53. Vu TV, Hieu NV, Phuc HV, Hieu NN, Bui HD, Idrees M, Nguyen CV (2020) Graphene/WSeTe van der Waals heterostructure: Controllable electronic properties and Schottky barrier via interlayer coupling and electric field. Appl Surf Sci 507:145036
54. Peng Q, Guo Z, Sa B, Zhou J, Sun Z (2018) New gallium chalcogenides/ Arsenene van der Waals heterostructures promising for photocatalytic water splitting. Int J Hydrogen Energy 43(33):15995–16004
55. Li S, Sun M, Chou JP, Wei J, Xing H, Hu A (2018) First-principles Calculations of the electronic properties of SiC-based bilayer and trilayer heterostructures. Phys Chem Chem Phys 20(38):24726–24734
56. Lamichhane S, Lage P, Khatri GB, Pantha N, Adhikari NP, Sanyal B (2016) First-Principles Study of Adsorption of Halogen Molecules on Graphene-MoS2 Bilayer Hetero-system. In J Phys Conf Ser 765(1):012011
57. Hou Z, Wang X, Ikeda T, Terakura K, Oshima M, Kakimoto MA, Miyata S (2012) Interplay between nitrogen dopants and native point defects in graphene. Phys Rev B 85(16):165439
58. Thierfelder C, Witte M, Blankenburg S, Rauls E, Schmidt WG (2011) Methane adsorption on graphene from first principles including dispersion interaction. Surf Sci 605(7–8):746–749
59. Nasresfahani S, Safaiee R, Sheikhi MH (2017) Influence of Pd/Pd_2 decoration on the structural, electronic and sensing properties of monolayer graphene in the presence of methane molecule: A dispersion-corrected DFT study. Surf Sci 662:93–101
60. Vidali G, Ihm G, Kim HY, Cole MW (1991) Potentials of physical adsorption. Surf Sci Rep 12(4):135–181
61. Neupane HK, Adhikari NP (2020) Structure, electronic and magnetic properties of 2D Graphene-Molybdenum diSulphide (G-MoS2) heterostructure (HS) with vacancy defects at Mo sites. Comput Condens Matter 24:e00489
62. Watanabe K, Taniguchi T, Kanda H (2004) Direct-bandgap properties and Evidence for ultraviolet lasing of hexagonal boron nitride single crystal. Nat Mater 3(6):404–409
63. Neupane HK, Adhikari NP (2020) Tuning structural, electronic, and magnetic properties of c sites vacancy defects in graphene/MoS_2 van der Waals heterostructure materials: a first-principles study. Adv Condens Matter Phys 2020:1–11
64. Neupane HK, Adhikari NP (2021) Structural, electronic and magnetic properties of S sites vacancy defects graphene/MoS2 van der Waals heterostructures: First-principles study. Int J Comput Mater Sci Eng 10(02):2150009
65. Neupane HK, Adhikari NP (2021) Electronic and magnetic properties of defected MoS2 monolayer. BIBECHANA 18(2):68–79
66. Neupane HK, Adhikari NP (2021) Structural, electronic and magnetic properties of defected water adsorbed single-layer MoS2. J Inst Sci Technol 26(1):43–50

Publisher's note Springer Nature remains neutral with regard to jurisdictional claims in published maps and institutional affiliations.

Effect of vacancy defects in 2D vdW graphene/h-BN heterostructure: First-principles study

Cite as: AIP Advances 11, 085218 (2021); doi: 10.1063/5.0059814
Submitted: 12 June 2021 • Accepted: 31 July 2021 •
Published Online: 13 August 2021

View Online Export Citation CrossMark

Hari Krishna Neupane[1,2] and Narayan Prasad Adhikari[2,a)]

AFFILIATIONS

[1] Amrit Campus, Institute of Science and Technology Tribhuvan University, Kathmandu, Nepal
[2] Central Department of Physics, Institute of Science and Technology Tribhuvan University, Kathmandu, Nepal

[a)] Author to whom correspondence should be addressed: narayan.adhikari@cdp.tu.edu.np

ABSTRACT

Graphene (G) and hexagonal Boron Nitride (h-BN) are structurally similar materials but have very different electronic and magnetic properties. Heterostructures formed by the combination of these materials are of great research interest. To assess the role played by the crystalline defects in such heterostructures is also of crucial importance owing to their novel properties. In the present work, we study the structural, electronic, and magnetic properties of the G/h-BN heterostructure and the different possible point defects of B and N atoms in it by using first-principles calculations based on the spin-polarized density functional theory (DFT) method within the van der Waals correction DFT-D2 approach. The structural analysis of these systems shows that they are stable two dimensional van der Waals heterostructure materials. Band structure calculations of these materials reveal their semimetallic nature. On the basis of density of states and partial density of states calculations, the defective systems are magnetic materials. The magnetic moment obtained in these defective systems is due to the unpaired up-spin and down-spin states in the orbitals of C, B, and N atoms created by the vacancy defects. On the other hand, the G/h-BN heterostructure has an approving condition for ferromagnetism due to the presence of flat bands in the neighborhood of the Fermi energy.

© 2021 Author(s). All article content, except where otherwise noted, is licensed under a Creative Commons Attribution (CC BY) license (http://creativecommons.org/licenses/by/4.0/). https://doi.org/10.1063/5.0059814

I. INTRODUCTION

The advent of the field of two dimensional (2D) crystals has grabbed the curiosity of physicists due to their properties worth inquiring.[1,2] Researchers are attracted toward 2D graphene (G) and hexagonal-Boron Nitride (h-BN) materials because of their intriguing properties.[3–6] The honeycomb structure of graphene (zero bandgap energy) is used in the fields of technological applications[7,8] owing to its electronic and mechanical properties. Hexagonal-Boron Nitride (h-BN) is the lowest-energy polymorph[9] of Boron Nitride (BN) just as graphite in the lowest-energy form of carbon. It is sp^2-bonded with alternating boron atom (B) and nitrogen atom (N) compounds. h-BN has a B and N atom stoichiometry ratio of close to 1:1, which are arranged in the honeycomb lattice within each layer. B and N atoms are bound by strong covalent bonds, as in graphene, while the layers are held together by weak van der Waals (vdW) forces, as in graphite.[10] h-BN is isoelectronic with graphite, and its structure is similar except for the difference in the stacking of the layers. In h-BN, because of its partial ionic character, the B and N atoms in the neighboring sheet eclipse each other, which give rise to interaction between the sheets stronger than that in graphite. Wide bandgap energy (≈6 eV) h-BN[11] has attractive properties such as high temperature stability, high mechanical strength, and high thermal conductivity due to which it has a variety of potential applications.[11–13] Heterostructure (HS) materials are created by incorporation of two distinct monolayer constituents. They can possess merged properties superior to those of their individual counterparts. In particular, the vertical stacking configuration of the graphene/h-BN heterostructure (say GBN-I) has opened more impressive perspectives because of its very appealing physical properties.[14–19] The band structure of GBN-I is different from that of pure graphene and monolayer h-BN. Seol and co-workers[20] found that the bandgap of GBN-I can be regulated. It can be transformed from a semiconductor to a semimetal or metal. Thus, GBN-I

© Author(s) 2021

material develops new thermal conductivity and electronic and magnetic properties compared with its constituents.[21,22] In this work, we have constructed the vdW G/h-BN heterostructure (GBN-I) material using graphene and h-BN with a considerable (1.4%) lattice mismatch, which is comparable with reported values.[23–25] Defects are inherent in any crystalline structure. The simplest point defects present on monoatomic sheets with a honeycomb structure are single atom vacancies. The vacancy or impurity defects in monolayer (ML) and HS materials can bring about novel properties, which make defective materials useful in the field of technological applications.[26–31] To the best of our knowledge, the literature does not contain the study of structural, electronic, and magnetic properties of the 2D vdW graphene/h-BN heterostructure (GBN-I) and B and N site vacancy defects in GBN-I materials. Therefore, in the present work, we investigated the structural, electronic, and magnetic properties of the G/h-BN heterostructure without defects (GBN-I), the one B atom vacancy defect in the G/h-BN heterostructure (GBN-IB), the one N atom vacancy defect in the G/h-BN heterostructure (GBN-IN), nearest neighbor one B atom and one N atom vacancy defects in the G/h-BN heterostructure (GBN-NB), and the alternate zone of one B atom and one N atom vacancy defects in G/h-BN heterostructure (GBN-IBIN) materials through band structure analysis and density of states (DoS) and partial density of states (PDoS) calculations. We adopted the spin-polarized density functional theory (DFT) method with semi-empirical DFT-D2 approach based first-principles calculations using the Quantum ESPRESSO (QE) computational package.

This article is organized into four sections. We described the computational methodology used in this study in Sec. II. The results together with a discussion on them are presented in Sec. III followed by conclusions in Sec. IV.

II. COMPUTATIONAL METHODS AND MATERIALS

The spin-polarized DFT method[32] within the vdW correction DFT-D2 approach[33] is performed with the PWscf code of the Quantum ESPRESSO computational package[34] by using the Rappe–Rabe–Kaxiraas–Joannopoulos (RRKJ) model of plane-wave ultra-soft pseudopotential (USPP). The generalized gradient approximation (GGA) used for determination is the Perdew–Burke–Ernzerhof (PBE) exchange-correlation (xc) functional.[35] The kinetic energy cut-off (ecutwfc) for the wave function and the charge density cut-off (ecutrho) are set to 40 and 400 Ry, respectively. The structure optimization and self-consistent field (scf) calculations (of the unit cell, supercell, and HS) are executed by the Broyden–Fletcher–Goldfarb–Shanno (BFGS) method[36]

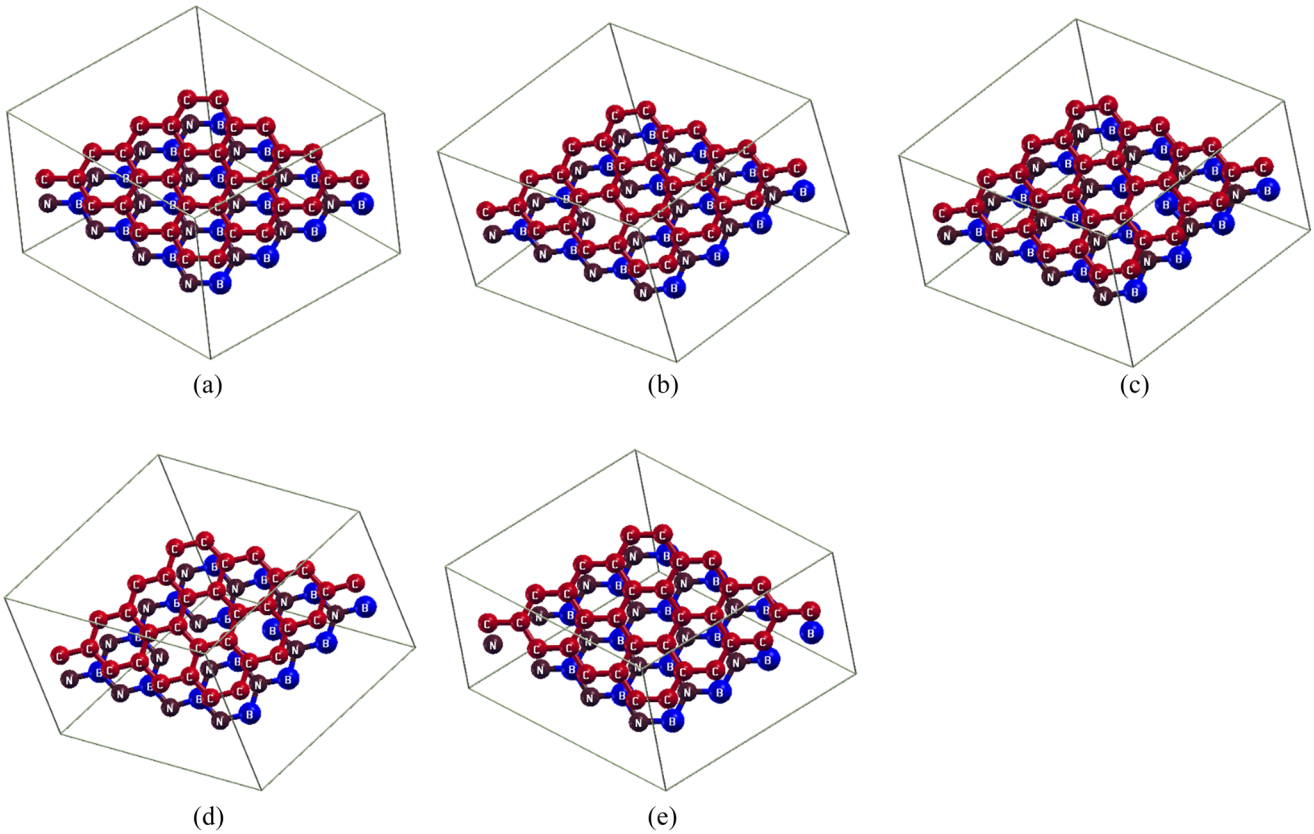

FIG. 1. Pristine and B and N sites vacancy defect heterostructure materials: (a) GBN-I material, (b) GBN-IB material, (c) GBN-IN material, (d) GBN-BN material, and (e) GBN-IBIN material.

© Author(s) 2021

with a Γ-centered Monkhorst–Pack (MP)[37] k-point mesh corresponding to the (6 × 6 × 1) inspect of the heterostructure GBN-I and B and N site vacancy defects in the GBN-I material. During structure optimization, all atoms are fully relaxed until the total energy change is less than 10^{-4} Ry between two consecutive scf steps and each component of the acting force is less than10^{-3} Ry/Bohrs. GBN-I is created by using the (4 × 4) supercell structure of graphene and the (4 × 4) supercell structure of h-BN with 1.4% lattice mismatch. This value agrees with the reported values.[23–25] To avoid the specious interaction between periodic HS, the vacuum thickness is set to 18 Å. The GBN-IB, GBN-IN, GBN-NB, and GBN-IBIN materials are constructed by removing the 1B atom, 1N atom, nearest neighbor 1B atom and 1N atom, and alternate-zone of the 1B atom and 1N atom in the GBN-I material, respectively. Defective materials are also allowed to relax by the BFGS relaxation scheme for further calculations. The optimized and relaxed GBN-I, GBN-IB, GBN-IN, GBN-NB, and GBN-IBIN structures are illustrated in Figs. 1(a)–1(e), respectively. The Marzari–Vanderbilt (M–V)[38] smearing is used to aid convergence with a small smearing width of 0.001 Ry. Furthermore, the mixing factor is taken to be 0.7 for self-consistency while the diagonalization method is chosen as "david." In band structure calculations of HS, 100 k-points are grasped along the high symmetric points associated with the reciprocal space, and a mesh of (6 × 6 × 1) is used. Spin-polarized DFT calculations were employed to investigate the magnetic properties of materials where a mesh of (12 × 12 × 1) k-points is used for DoS and PDoS calculations.

III. RESULTS AND DISCUSSION

In this section, we present the structural analysis of the non-defective and defective G/h-BN materials as well as their electronic and magnetic properties through band structure and DoS and PDoS calculations. Furthermore, the obtained results are compared with the available reported works.

A. Structural analysis

The unit cell of h-BN consists of one B atom and one N atom covalently bonded together. The atomic positions are calculated using the simple geometry of the crystal. Due to the hexagonal crystal structure, we selected ibrav = 4, optimized bond length of B–N as 1.45 Å,[39] bond angle between B–N–B or N–B–N as ~120°, and lattice parameter as 4.74 Å[40] along the x and y directions in the input file, where the interlayer spacing is 18 Å, resulting in nearly free electron theory. Then the structure was optimized. Once all the parameters required in the input files are fixed, we performed relaxation calculation of the unit cell. This causes slight changes in the atomic coordinates, giving a more stable and minimum ground state crystal structure. From the optimized unit cell, we obtained the bond length between N and B atoms to be 1.45 Å, which fairly agrees with the reported value.[39] Similarly, we have created optimized and relax unit cells of graphene by taking a bond length of C–C 1.42 Å[41] and a lattice parameter of 4.65 Å. The bond length between C–C atoms is found to be 1.43 Å, which is comparable to the experimentally reported value.[41] By periodically extending the unit cell along x- and y-axes, we obtained a (4 × 4) supercell of h-BN and a (4 × 4) supercell of graphene. The stability of the supercell is determined based on the scf calculations. Thus, the stability of h-BN is estimated using the following equation:[24]

$$(E_b)_{B-N} = (-N(E_B + E_N) + E_{h-BN})/N, \quad (1)$$

where $(E_b)_{B-N}$ is the binding energy per B–N pair; $E_{h\text{-}BN}$, E_B, and E_N are the ground state energy of the h-BN supercell, single B atom, and single N atom, respectively; and N is the number of B and N atoms in the same supercell. The calculated binding energy of h-BN is −12.63 eV/BN. In addition, the binding energy per C atom in graphene is calculated by using the following equation and was found to be −7.98 eV/atom:

$$(E_b)_C = (E_g - NE_c)/N, \quad (2)$$

where E_g is the ground state energy of the graphene sheet, E_C is the ground state energy of the isolated C atom, and N is the number of C atoms in a graphene supercell. The negative value of binding energy implies the bounded system is stable and can exist in nature. The HS of graphene and h-BN (GBN-I) (containing 32 C atoms, 16 B atoms, and 16 N atoms) considered in this paper is constructed by joining the optimized and relaxed stable supercells of graphene and h-BN. The relaxed GBN-I is illustrated in Fig. 1(a). The estimated lattice mismatch value of GBN-I is 1.4%, consistent with the reported values.[23–25] We have calculated the in-plane lattice parameter of h-BN (distance between nearest two B atoms) in GBN-I to be 2.48 Å, which is comparable with graphene (2.46 Å) and h-BN (2.50Å) values.[42] Therefore, the graphene sheet adjusts to the in-plane lattice parameter of h-BN in GBN-I.[43] We have also calculated the interlayer distance of the graphene and h-BN in GBN-I and found it to be 3.28 Å, which also agrees with the reported value.[23,44] We checked the stability of HS by finding its binding energy (formation energy) from[45]

$$E_b = \frac{E_{G/h-BN} - E_G - E_{h-BN}}{A}, \quad (3)$$

where $E_{G/h\text{-}BN}$, E_G, and $E_{h\text{-}BN}$ represent the total ground state energy of GBN-I, graphene sheet, and h-BN, respectively, and "A" denotes the surface area of HS. The obtained binding energy of GBN-I is −41.88 meV/Å^2. This is comparable with the value of other 2D HS materials.[46,47] The negative binding energy value of GBN-I reveals the fact that it is energetically stable at the ground state. In addition, we predicted that van der Waals (vdW) force exists between the graphene and h-BN of GBN-I through the evidence of the calculated value of the binding energy and interlayer distance. Hence, GBN-I is a 2D vdW heterostructure (HS) material.

In addition, B and N site atom vacancy defects in GBN-I materials are constructed by removing 1B atom (GBN-IB), 1N atom (GBN-IN), the nearest neighbor 1B atom and 1N atom (GBN-NB), and the alternate-zone of the 1B atom and 1N atom (GBN-IBIN) from the GBN-I material; they are then relaxed before proceeding further. The optimized and relaxed stable defective materials are shown in Figs. 1(b)–1(e).

The stability of GBN-IB, GBN-IN, GBN-NB, and GBN-IBIN materials are determined by their binding energy. The values of binding energy of these materials are found to be −30.36, −38.83, −23.79, and −28.83 meV/Å^2, respectively. Hence, they are energetically stable at ground state. The interlayer distances of GBN-IB, GBN-IN, GBN-NB, and GBN-IBIN materials are found to be 3.29, 3.29, 3.33, and 3.32 Å, respectively. From the estimation of binding energy and interlayer distance, we further confirmed that B and N

© Author(s) 2021

site vacancy defective materials are also 2D vdW heterostructures. The defect formation energy of these materials is calculated using[48]

$$E_{df} = E_{td} - (E_{tp} + n_a\mu_a + n_b\mu_b), \quad (4)$$

where E_{td}, E_{tp}, n_a, n_b, μ_a, and μ_b are the total ground state energy of vacancy defected HS, total ground state energy of non-defected HS, number of vacancy defect B atoms, number of vacancy defect N atoms, chemical potential of a B atom, and chemical potential of an N atom, respectively. Defect formation energy of GBN-IB, GBN-IN, GBN-NB, and GBN-IBIN materials are found to be 0.19, 0.15, 0.36, and 0.32 eV, respectively. These defected materials can be more favorable for the computational work owing to their lower value of defect formation energy. Hence, single atom vacancy defective materials are more favorable than double vacancy defective materials. In summary, we concluded that all the considered systems are stable 2D vdW HS materials and GBN-I is more compact than defected materials. Moreover, the compactness of atoms in a defective geometry decreased with an increase in the defect density in it.

B. Electronic properties

To study electronic properties of materials, we begin our discussion with the analysis of band structure calculations of graphene, the h-BN monolayer, and GBN-I, GBN-IB, GBN-IN, GBN-NB, and GBN-IBIN heterostructures. Graphene is a zero bandgap semiconductor because of its two bands—π and π^*— that emerge from the p_z orbitals and meet at six points (at the edges of the Brillouin zone k and k′) in k-space known as the Dirac point, as shown in Fig. 2(a). On the other hand, h-BN is a wide bandgap material of a value of 4.98 eV, as shown in Fig. 2(b), which agrees with the reported value.[49] The band structure of vdW GBN-I seems as a superposition of its constituents, as shown in Fig. 2(c), because the covalent bonds within the layers are not modified in the construction of the heterostructure. However, by careful observation, we found that a small bandgap of a value of 2.60 meV opened at the k point in the band states of graphene, as shown in Fig. 2(h). This is due to the weak interaction between the two supercells. Moreover, we have analyzed the band structures of GBN-IB, GBN-IN, GBN-NB, and GBN-IBIN materials, which are depicted in Figs. 2(d)–2(g),

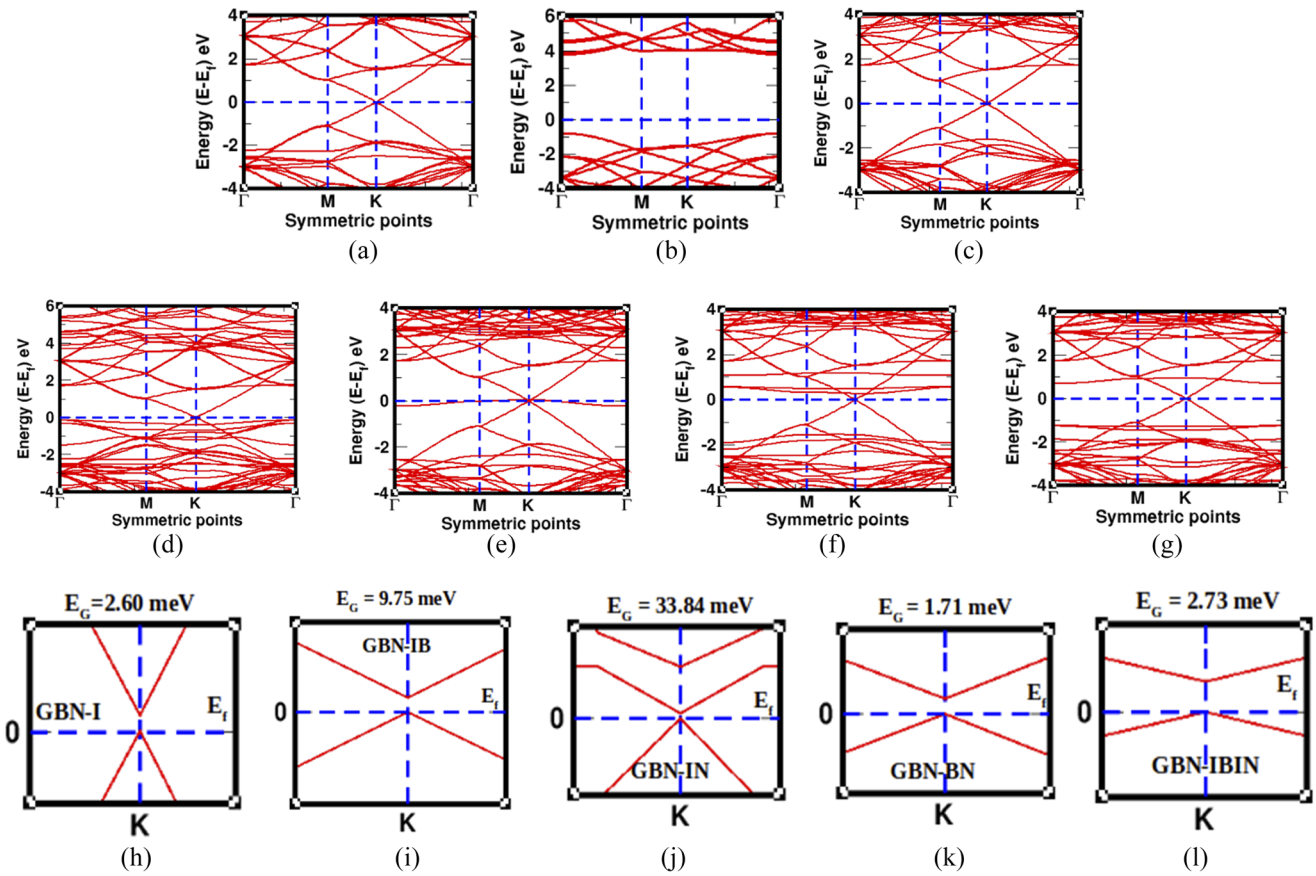

FIG. 2. (a) Band structure of graphene, (b) band structure of h-BN, (c) band structure of GBN-I, (d) band structure of GBN-IB, (e) band structure of GBN-IN, (f) band structure of GBN-BN, (g) band structure of GBN-IBIN, (h) the bandgap opened at the K point by graphene in GBN-I, (i) the bandgap opened at the K point by graphene in GBN-IB, (j) the bandgap opened at the K point by graphene in GBN-IN, (k) the bandgap opened at the K point by graphene in GBN-BN, and (l) the bandgap opened at the K point by graphene in GBN-IBIN. In all band plots, the horizontal dotted line represents the Fermi energy level (E_f), and the vertical dotted lines represent the symmetric points in the Brillouin-zone.

© Author(s) 2021

respectively. In all the considered band structures, 100 k-points are taken along the high symmetric points, and the horizontal dotted line is at the Fermi energy level, which separates the valence and conduction bands. The region below the dotted line is called the valence band, and that above the dotted line is called the conduction band. In GBN-IB, band states of h-BN appear very close to the Fermi level, and p-type Schottky contacts dominate than n-type Schottky contacts since the barrier height of the p-contact is 0.01 eV and that of the n-contact is 1.70 eV. However, graphene states are still preserved similar to pristine GBN-I where the bandgap value of graphene at the k point is 9.75 meV [shown in Fig. 2(i)]. In Fig. 2(e) of GBN-IN, band states of h-BN appear around the Fermi energy level. It has an n-type Schottky contact because the barrier height of the n-contact is almost 0 eV whereas that of the p-contact is 2.45 eV. It means the bandwidth of h-BN in GBN-IN is decreased compared with that of pristine GBN-I while a small bandgap appears at the k-point in the band state of graphene of a value of 33.84 meV [shown in Fig. 2(j)]. This is because two identical C atoms are subjected to two different electrostatic potentials generated by B and N atoms, respectively. The band structures of GBN-BN and GBN-IBIN materials are shown in Figs. 2(f) and 2(g), respectively. In Fig. 2(f), the band states of h-BN come closer to the Fermi level by 0.35 and 1.76 eV from the conduction band and the valence band of GBN-BN, respectively. Similarly, in Fig. 2(g), the band states of h-BN come closer to the Fermi level by 0.69 and 1.22 eV from the conduction band and the valence band of GBN- IBIN, respectively. Hence, the bandgap of h-BN in GBN-BN and GBN-IBIN is 2.11 and 1.91 eV, respectively. It is smaller than that of GBN-I. The bandgap energy in defective HS decreases by B and N vacancy defects. In both (GBN-BN and GBN-IBIN) materials, an n-type Schottky contact is formed. Very small bandgap values of 1.71 and 2.73 meV [shown in Figs. 2(k) and 2(i)] appear at the k symmetric point of graphene in GBN-BN and GBN-IBIN materials, respectively. From the analysis of the above-mentioned band structure calculations, we found that two uneven C atoms have a comparable chemical environment in all GBN-I, GBN-IB, GBN-IN, GBN-NB, and GBN-IBIN configurations. As a result, the valence bands and conduction bands in graphene can endure degeneration at the k-point, thereby prohibiting the opening of the bandgap. Therefore, 2D vdW GBN-I, GBN-IB, GBN-IN, GBN-NB, and GBN-IBIN are semimetallic materials.

The estimated data about structural analysis and electronic properties are reported in Table I.

C. Magnetic properties

The magnetic properties in materials arise due to the unpaired spin states of electrons in the orbital of atoms, which can be observed in the density of states (DoS) and partial density of states (PdoS). DoS is the total number of quantum mechanical states per unit energy range at each energy level available for the electrons to be occupied. In fact, the DoS gives the total number of electronic orbitals per unit energy interval. A high DoS value at a specific energy level means that there are many states available to occupy whereas a DoS value equal to zero represents that no states can be occupied at that energy level as in the case of the forbidden gap.[26] The product of the DoS and probability distribution function gives the number of occupied states per unit volume at a given energy for a system in thermal equilibrium. PDoS calculations are used to study the DoS in detail by incorporating the contributions of different orbitals present in the total DoS of the materials. Thus, the magnetic properties of the materials are predicted by DoS and PDoS calculations. When the DoS of up-spin electrons is equal to that for down-spin electrons, reflection of the spin states of electrons is symmetrically distributed, and the material will be non-magnetic in nature. If the DoS of up-spin and down-spin states of the electrons are asymmetrically distributed, the material will be magnetic in nature. In this paper, we have computed the PDoS of different C, B, and N orbitals present in pristine GBN-I and B and N site vacancy defects in GBN-I. We have used ultrasoft pseudopotential; hence, the contributions of valence orbitals are only shown in the PDoS. The electronic configuration of valence electrons of C, B, and N atoms are $2s^2 2p^2$, $2s^2 2p^1$, and $2s^2 2p^3$, respectively. Here, we can see the valence electrons occupy the 2p and 2s orbitals, suggesting the contributions of only those two orbitals in PDoS of GBN-I, GBN-IB, GBN-IN, GBN-NB, and GBN-IBIN materials. The DoS and PDoS plots of GBN-I are shown in Figs. 3(a) and 4(a), respectively. In DoS and PDoS plots of GBN-I, a few number of up and down spin states appear slightly asymmetric, depicting a weak magnetic nature with a magnetic moment of 0.04 μ_B/cell. This is due to the presence of flat bands in the neighborhood of the Fermi energy as observed in HS. Hence, GBN-I has a favorable condition for ferromagnetism.[50–53]

Furthermore, we investigated the magnetic properties in defective systems by analyzing their DoS and PDoS calculations. The DoS and PDoS of GBN-IB, GBN-IN, GBN-NB, and GBN-IBIN materials are illustrated in Figs. 3(b)–3(e) and 4(b)–4(e), respectively.

TABLE I. Fermi energy (E_f), defect formation energy (E_{df}), binding energy(E_b), interlayer distance (D_d), bandgap energy of graphene in HS ($E_{g\text{-}G}$), bandgap energy of h-BN in HS ($E_{g\text{-}hBN}$), and change in bandgap energy of h-BN in HS from the value (4.98 eV) of monolayer h-BN (E_{gs}) of GBN-I, GBN-IB, GBN-IN, GBN-BN, and GBN-IBIN materials.

Materials	GBN-I	GBN-IB	GBN-IN	GBN-BN	GBN-IBIN
E_f (eV)	−1.26	−2.18	−1.04	−1.31	−1.31
E_{df} (eV)	⋯	0.19	0.15	0.36	0.32
E_b (meV/Å^2)	−41.88	−30.36	−38.83	−23.79	−28.83
D_d (Å)	3.28	3.29	3.29	3.33	3.32
$E_{g\text{-}G}$ (meV)	2.60	9.75	33.84	1.71	2.73
$E_{g\text{-}hBN}$ (eV)	3.78	1.71	2.45	2.11	1.91
E_{gs} (eV)	1.20	3.27	2.53	2.87	3.07

© Author(s) 2021

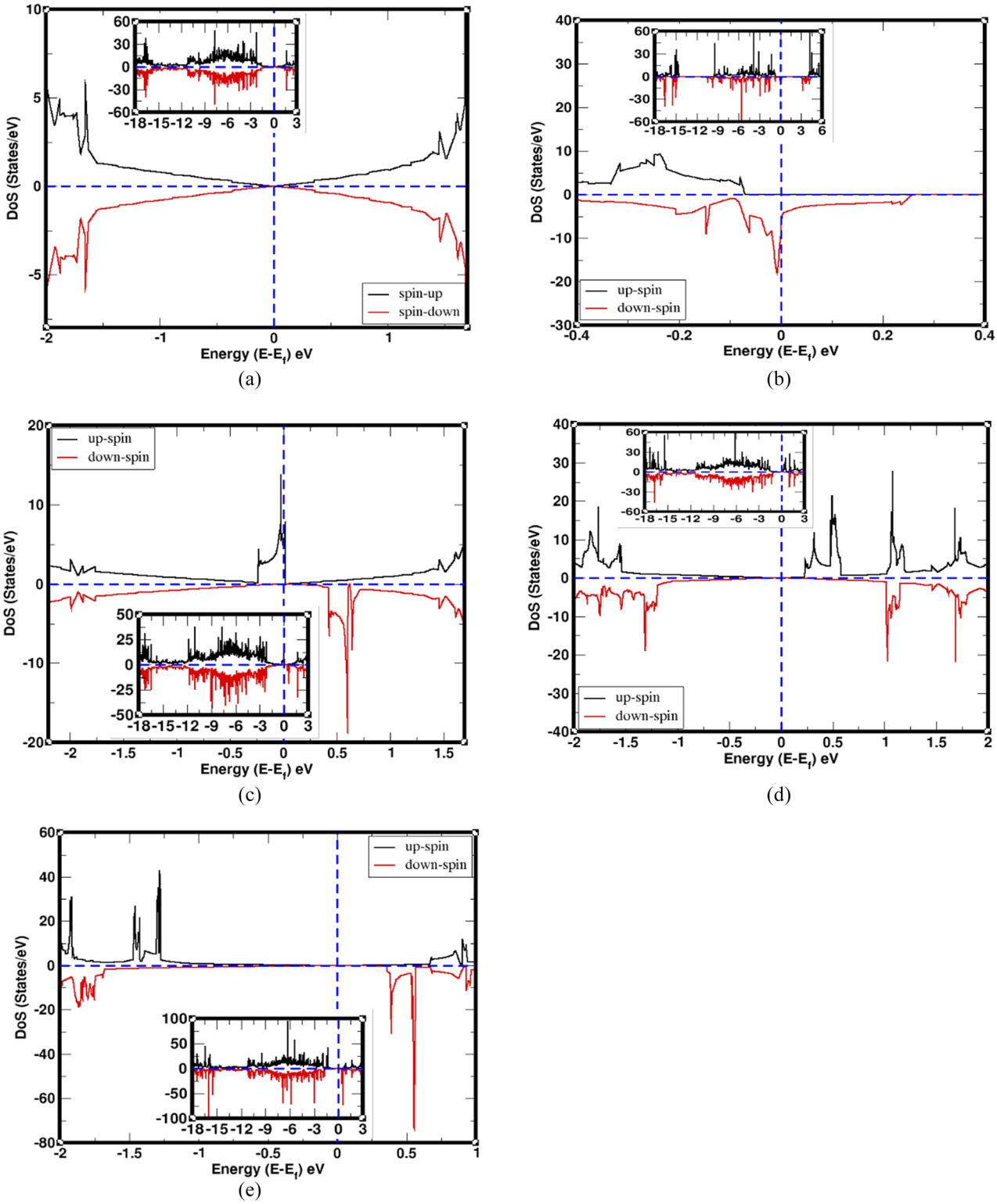

FIG. 3. DoS of total up-spin and total down-spin states of electrons in the orbitals of C, B, and N atoms of (a) GBN-I material, (b) GBN-IB material, (c) GBN-IN material, (d) GBN-BN material, and (e) GBN-IBIN material. In all DoS, the horizontal dotted line separates the spin states, and the vertical dotted line separates the electronic bands. Insets in the DoS represent spin states within a large energy range along the x-axis.

© Author(s) 2021

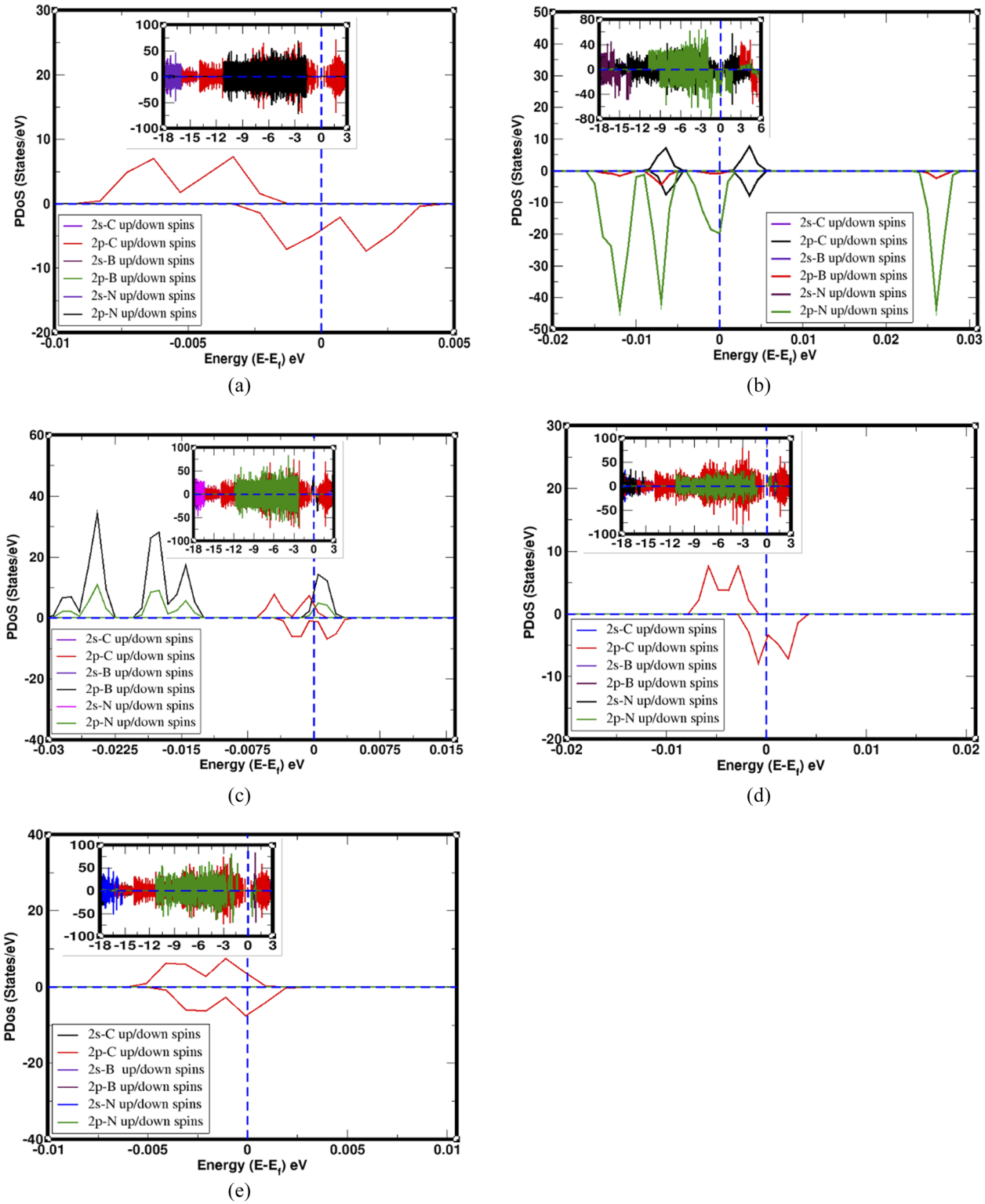

FIG. 4. PDoS of individual up-spin and down-spin states of electrons in the orbitals of C, B, and N atoms of (a) GBN-I material, (b) GBN-IB material, (c) GBN-IN material, (d) GBN-BN material, and (e) GBN-IBIN material. In all PDoS, the horizontal dotted line separates spin states, and the vertical dotted line separates the electronic bands. Insets in the PDoS represent spin states within a large energy range along the x-axis.

© Author(s) 2021

TABLE II. Total magnetic moment (μ_T) obtained due to up-spin and down-spin states of electrons in the orbitals of C, B and N atoms in PDoS of GBN-I, GbN-IB, GBN-IN, GBN-BN and GBN-IBIN stacking configurations.

μby up-spin and down-spin in →	GBN-I (μ_B/cell)	GBN-IB (μ_B/cell)	GBN-IN (μ_B/cell)	GBN-BN (μ_B/cell)	GBN-IBIN (μ_B/cell)
2s of C atoms	0.01	−0.02	0.02	0.00	0.01
2p of C atoms	0.03	−0.11	0.09	−0.05	0.08
2s of B atoms	0.00	−0.03	0.03	−0.06	0.02
2p of B atoms	0.00	−0.91	0.58	−0.93	0.83
2s of N atoms	0.00	−0.06	0.05	−0.08	0.08
2p of N atoms	0.00	−1.83	0.20	−0.84	0.99
Total magnetic moment (μ_T)	0.04	−2.96	0.97	−1.96	2.01

The up-spin and down-spin states are asymmetrically distributed in the DoS and PDoS of GBN-IB, as shown in Figs. 3(b) and 4(b), respectively. It means GBN-IB is a magnetic material. For the detailed information showing the contributions of different orbitals on the total DoS of GBN-IB material, we computed its PDoS. The 1B atom vacancy defective HS (GBN-IB) has a magnetic nature with appreciable contributions from 2p orbitals of N atoms, 2p orbitals of B atoms, and 2p orbitals of C atoms while 2s orbital of N atoms, 2s orbitals of B atoms, and 2s of C atoms have a relatively weak influence. The magnetic moment given by up and down spin states in 2s and 2p orbitals of C atoms is −0.02 and −0.11 μ_B/cell, 2s and 2p orbitals of B atoms is −0.03 and −0.91 μ_B/cell, and 2s and 2p orbitals of N atoms is −0.06 and −1.83 μ_B/cell values, respectively. Thus, the total estimated magnetic moment of GBN-IB is −2.96 μ_B/cell. The high value of magnetic moment is given by 2p orbitals of B and N atoms in the material. Figures 3(c) and 4(c) represent DoS and PDoS plots of GBN-IN where unoccupied asymmetrically distributed up-spin and down-spins states of 2p orbitals of N, B, and C atoms are seen around the Fermi energy level due to which magnetic moment is developed in GBN-IN, showing its magnetic nature. The magnetic moment generated by 2s and 2p orbitals of C atoms is 0.02 and 0.09 μ_B/cell, 2s and 2p orbitals of B atoms is 0.03 and 0.58 μ_B/cell, and 2s and 2p orbitals of N atoms is 0.05 and 0.20 μ_B/cell values, respectively. Here, 2p orbitals of B and N atoms have relatively large contributions than other orbitals of C, B, and N atoms in HS. The total magnetic moment of GBN-IN is 0.97 μ_B/cell. Similarly, in GBN-BN material, the DoS and PDoS of spin states are asymmetrically distributed as shown in Figs. 3(d) and 4(d), respectively, which implies it has magnetic properties. The magnetic moment contributed by 2s and 2p orbitals of C, B, and N atoms is 0.00 and −0.05 μ_B/cell, −0.06 and −0.93 μ_B/cell, and −0.08 and −0.84 μ_B/cell in GBN-BN, respectively. The total magnetic moment of GBN-BN is −1.96 μ_B/cell. In GBN-BN, the appreciable contributions to magnetic moment are given by spins in 2p orbitals of B and N atoms whereas the contributions given by spin states in 2p orbitals of C and 2s orbitals of B and N atoms are weak. Moreover, the influence of 2s orbital of C atoms is negligible. The magnetic moment is obtained in GBN-IBIN due to the asymmetric distribution of up-spins and down-spins in the DoS and PdoS, as shown in Figs. 3(e) and 4(e), respectively. Hence, it is a magnetic material. The total magnetic moment of GBN-IBIN is 2.01 μ_B/cell due to the influence of unpaired spin states present in 2s and 2p orbitals of C, B, and N atoms. Spin states in 2p orbitals of B and N atoms play a significant role in the creation of magnetic moment. On the other hand, 2p orbitals of C atoms and 2s orbitals of C, B, and N atoms collectively give weak contributions for magnetism. The values of magnetic moment due to 2s and 2p orbitals of C, B, and N atoms are 0.01 and 0.08 μ_B/cell, 0.02 and 0.83 μ_B/cell, and 0.08 and 0.99 μ_B/cell, respectively. The detailed calculations of magnetic moment of GBN-I, GBN-IB, GBN-IN, GBN-BN, and GBN-IBIN materials are given in Table II.

IV. CONCLUSIONS

We have presented the first-principles calculations based on the spin-polarized DFT method within the DFT-D2 approach using the Quantum ESPRESSO computational tool. This method has been applied to study the structural, electronic, and magnetic properties of GBN-I, GBN-IB, GBN-IN, GBN-BN, and GBN-IBIN materials. The stability of GBN-I, GBN-IB, GBN-IN, GBN-BN, and GBN-IBIN materials is determined by calculating their binding energy. The values of binding energy of these materials are −41.88, −30.36, −38.83, −23.79, and −28.83 meV/Å^2, respectively. In addition, we have calculated the interlayer distances of GBN-I, GBN-IB, GBN-IN, GBN-BN, and GBN-IBIN materials, which are found to be 3.28, 3.29, 3.29, 3.33, and 3.32 Å, respectively. The estimated values of binding energy and interlayer distance are comparable with the values of other 2D heterostructures. Based on the calculated values of binding energy and interlayer distance, it is concluded that they are 2D vdW HS materials. From the band structure calculations, we found that all the materials are semimetallic. Magnetic properties of considered materials are studied by the analysis of DoS and PDoS calculations, which shows that GBN-I has weak magnetic properties while GBN-IB, GBN-IN, GBN-BN, and GBN-IBIN materials have strong magnetic properties. The values of magnetic moment obtained due to the rearrangement of unpaired spin (up-spin and down-spin) states of electrons in the orbitals of atoms in GBN-I, GBN-IB, GBN-IN, GBN-BN, and GBN-IBIN are 0.04, −2.96, 0.97, −1.96, and 2.01 μ_B/cell, respectively.

ACKNOWLEDGMENTS

This work was supported by network project No. NT-14 of ICTP/OEA and the UGC Nepal under Ph.D. Grants of Award No. Ph.D. 075/76-S and T-09 for HKN. We also acknowledge TWAS Research Grant No. RG 20-316.

© Author(s) 2021

DATA AVAILABILITY

All the data that are used to produce the figures/tables in this paper are available from the corresponding author in case reproduction is needed.

REFERENCES

[1] A. K. Geim and K. S. Novoselov, "The rise of graphene," Nat. Mater. **6**(3), 183–191 (2007).

[2] S. Zhang, M. Xie, F. Li, Z. Yan, Y. Li, E. Kan, W. Liu, Z. Chen, and H. Zeng, "Semiconducting group 15 monolayers: A broad range of band gaps and high carrier mobilities," Angew. Chem. **128**(5), 1698–1701 (2016).

[3] C. H. Ho, C. P. Chang, and M. F. Lin, "Evolution and dimensional crossover from the bulk subbands in ABC-stacked graphene to a three-dimensional Dirac cone structure in rhombohedral graphite," Phys. Rev. B **93**(7), 075437 (2016).

[4] S. Galambosi, L. Wirtz, J. A. Soininen, J. Serrano, A. Marini, K. Watanabe, T. Taniguchi, S. Huotari, A. Rubio, and K. Hämäläinen, "Anisotropic excitonic effects in the energy loss function of hexagonal boron nitride," Phys. Rev. B **83**(8), 081413 (2011).

[5] G. Cassabois, P. Valvin, and B. Gil, "Intervalley scattering in hexagonal boron nitride," Phys. Rev. B **93**(3), 035207 (2016).

[6] T. Q. P. Vuong, G. Cassabois, P. Valvin, V. Jacques, R. Cuscó, L. Artús, and B. Gil, "Overtones of interlayer shear modes in the phonon-assisted emission spectrum of hexagonal boron nitride," Phys. Rev. B **95**(4), 045207 (2017).

[7] K. S. Novoselov, A. K. Geim, S. V. Morozov, D. Jiang, Y. Zhang, S. V. Dubonos, and A. A. Firsov, "Electric field effect in atomically thin carbon films," Science **306**(5696), 666–669 (2004).

[8] E. V. Castro, K. S. Novoselov, S. V. Morozov, N. M. R. Peres, J. M. B. L. Dos Santos, J. Nilsson, F. Guinea, A. K. Geim, and A. H. C. Neto, "Biased bilayer graphene: Semiconductor with A gap tunable by the electric field effect," Phys. Rev. Lett. **99**(21), 216802 (2007).

[9] K. K. Kim, A. Hsu, X. Jia, S. M. Kim, Y. Shi, M. Hofmann, D. Nezich, J. F. Rodriguez-Nieva, M. Dresselhaus, T. Palacios, and J. Kong, "Synthesis of monolayer hexagonal boron nitride on Cu foil using chemical vapor deposition," Nano Lett. **12**(1), 161–166 (2012).

[10] M. Bokdam, G. Brocks, M. I. Katsnelson, and P. J. Kelly, "Schottky barriers at hexagonal boron nitride/metal interfaces: A first-principles study," Phys. Rev. B **90**(8), 085415 (2014).

[11] H. Henck, D. Pierucci, G. Fugallo, J. Avila, G. Cassabois, Y. J. Dappe, M. G. Silly, C. Chen, B. Gil, M. Gatti, F. Sottile, F. Sirotti, M. C. Asensio, and A. Ouerghi, "Direct observation of the band structure in bulk hexagonal boron nitride," Phys. Rev. B **95**(8), 085410 (2017).

[12] A. Rubio, J. L. Corkill, and M. L. Cohen, "Theory of graphitic boron nitride nanotubes," Phys. Rev. B **49**(7), 5081 (1994).

[13] N. G. Chopra, R. J. Luyken, K. Cherrey, V. H. Crespi, M. L. Cohen, S. G. Louie, and A. Zettl, "Boron nitride nanotubes," Science **269**(5226), 966–967 (1995).

[14] Z. Liu, L. Song, S. Zhao, J. Huang, L. Ma, J. Zhang, J. Lou, and P. M. Ajayan, "Direct growth of graphene/hexagonal boron nitride stacked layers," Nano Lett. **11**(5), 2032–2037 (2011).

[15] L. Li, I. Lee, D. Lim, M. Kang, G.-H. Kim, N. Aoki, Y. Ochiai, K. Watanabe, and T. Taniguchi, "Raman Shift and electrical properties of MoS_2 bilayer on boron nitride substrate," Nanotechnology **26**(29), 295702 (2015).

[16] S. Wang, X. Wang, and J. H. Warner, "All chemical vapor deposition growth of MoS_2: h-BN vertical van der Waals heterostructures," ACS Nano **9**(5), 5246–5254 (2015).

[17] Y.-C. Lin, N. Lu, N. Perea-Lopez, J. Li, Z. Lin, X. Peng, C. H. Lee, C. Sun, L. Calderin, P. N. Browning, M. S. Bresnehan, M. J. Kim, T. S. Mayer, M. Terrones, and J. A. Robinson, "Direct synthesis of van der Waals solids," ACS Nano **8**(4), 3715–3723 (2014).

[18] M. Okada, T. Sawazaki, K. Watanabe, T. Taniguch, H. Hibino, H. Shinohara, and R. Kitaura, "Direct chemical vapor deposition growth of WS_2 atomic layers on hexagonal boron nitride," ACS Nano **8**(8), 8273–8277 (2014).

[19] S. Beniwal, J. Hooper, D. P. Miller, P. S. Costa, G. Chen, S.-Y. Liu, P. A. Dowben, E. C. H. Sykes, E. Zurek, and A. Enders, "Graphene-like boron–carbon–nitrogen monolayers," ACS Nano **11**(3), 2486–2493 (2017).

[20] G. Seol and J. Guo, "Bandgap opening in boron nitride confined armchair graphene nanoribbon," Appl. Phys. Lett. **98**(14), 143107 (2011).

[21] T. Gao, X. Song, H. Du, Y. Nie, Y. Chen, Q. Ji, J. Sun, Y. Yang, Y. Zhang, and Z. Liu, "Temperature-triggered chemical switching growth of in-plane and vertically stacked graphene-boron nitride heterostructures," Nat. Commun. **6**(1), 6835–6838 (2015).

[22] C. Zhang, S. Zhao, C. Jin, A. L. Koh, Y. Zhou, W. Xu, Q. Li, Q. Xiong, H. Peng, and Z. Liu, "Direct growth of large-area graphene and boron nitride heterostructures by a co-segregation method," Nat. Commun. **6**(1), 6519 (2015).

[23] A. Ramasubramaniam, D. Naveh, and E. Towe, "Tunable band gaps in bilayer graphene-BN heterostructures," Nano Lett. **11**(3), 1070–1075 (2011).

[24] R. Quhe, J. Zheng, G. Luo, Q. Liu, R. Qin, J. Zhou, D. Yu, S. Nagase, W.-N. Mei, Z. Gao, and J. Lu, "Tunable and sizable band gap of single-layer graphene sandwiched between hexagonal boron nitride," NPG Asia Mater. **4**(2), e6 (2012).

[25] G. J. Slotman, M. M. Van Wijk, P.-L. Zhao, A. Fasolino, M. I. Katsnelson, and S. Yuan, "Effect of structural relaxation on the electronic structure of graphene on hexagonal boron nitride," Phys. Rev. Lett. **115**(18), 186801 (2015).

[26] C. Kittel, P. McEuen, *Introduction to Solid State Physics* (Wiley, New York, 1996), Vol. 8, pp. 140–303.

[27] O. V. Yazyev and L. Helm, "Defect-induced magnetism in graphene," Phys. Rev. B **75**(12), 125408 (2007).

[28] H. K. Neupane and N. P. Adhikari, "Structure, electronic and magnetic properties of 2D Graphene-Molybdenum diSulphide (G-MoS_2) heterostructure (HS) with vacancy defects at Mo sites," Comput. Condens. Matter **24**, e00489 (2020).

[29] H. K. Neupane and N. P. Adhikari, "First-principles study of structure, electronic, and magnetic properties of C sites vacancy defects in water adsorbed graphene/MoS_2 van der Waals heterostructures," J. Mol. Model. **27**(3), 82 (2021).

[30] H. K. Neupane and N. P. Adhikari, "Tuning structural, electronic, and magnetic properties of C sites vacancy defects in graphene/MoS_2 van der Waals heterostructure aterials: A first-principles study," Adv. Condens. Matter Phys. **2020**, 8850701.

[31] H. K. Neupane and N. P. Adhikari, "Structural, electronic and magnetic properties of S sites vacancy defects graphene/MoS_2 van der Waals heterostructures:First-principles study," Int. J. Comput. Mater. Sci. Eng. **10**, 2150009 (2021).

[32] P. Hohenberg and W. Kohn, "Inhomogeneous electron gas," Phys. Rev. **136**(3B), B864 (1964).

[33] S. Grimme, "Accurate description of van der Waals complexes by density Functional theory including empirical corrections," J. Comput. Chem. **25**(12), 1463–1473 (2004).

[34] P. Giannozzi, S. Baroni, N. Bonini, M. Calandra, R. Car, C. Cavazzoni, D. Ceresoli, G. L. Chiarotti, M. Cococcioni, I. Dabo, A. Dal Corso, S. de Gironcoli, S. Fabris, G. Fratesi, R. Gebauer, U. Gerstmann, C. Gougoussis, A. Kokalj, M. Lazzeri, L. Martin-Samos, N. Marzari, F. Mauri, R. Mazzarello, S. Paolini, A. Pasquarello, L. Paulatto, C. Sbraccia, S. Scandolo, G. Sclauzero, A. P. Seitsonen, A. Smogunov, P. Umari, and R. M. Wentzcovitch, "QUANTUM ESPRESSO: Modular and open-source software project for quantum simulations of materials," J. Phys.: Condens. Matter **21**(39), 395502 (2009).

[35] J. P. Perdew, K. Burke, and M. Ernzerhof, "Generalized gradient approximation made simple," Phys. Rev. Lett. **77**(18), 3865 (1996).

[36] B. G. Pfrommer, M. Côté, S. G. Louie, and M. L. Cohen, "Relaxation of Crystals with the quasi-Newton method," J. Comput. Phys. **131**(1), 233–240 (1997).

[37] J. D. Pack and H. J. Monkhorst, "Special points for Brillouin-zone integrations a reply," Phys. Rev. B **16**(4), 1748 (1977).

[38] N. Marzari, D. Vanderbilt, A. De Vita, and M. C. Payne, "Thermal contraction and disordering of the Al (110) surface," Phys. Rev. Lett. **82**(16), 3296 (1999).

[39] Y.-J. Liu, B. Gao, D. Xu, H.-M. Wang, and J.-X. Zhao, "Theoretical study on Si-doped hexagonal boron nitride (*h*-BN) sheet: Electronic, magnetic properties, and reactivity," Phys. Lett. A **378**(40), 2989–2994 (2014).

[40] N. Ooi, A. Rairkar, L. Lindsley, and J. B. Adams, "Electronic structure and bonding in hexagonal boron nitride," J. Phys.: Condens. Matter **18**(1), 97 (2005).

© Author(s) 2021

[41] R. M. Martin, *Electronic Structure: Basic Theory and Practical Methods* (Cambridge University Press, 2020).
[42] W. Aggoune, C. Cocchi, D. Nabok, K. Rezouali, M. A. Belkhir, and C. Draxl, "Dimensionality of excitons in stacked van der Waals materials: The example of hexagonal boron nitride," Phys. Rev. B **97**(24), 241114 (2018).
[43] C. R. Woods, L. Britnell, A. Eckmann, R. S. Ma, J. C. Lu, H. M. Guo, X. Lin, G. L. Yu, Y. Cao, R. V. Gorbachev, A. V. Kretinin, J. Park, L. A. Ponomarenko, M. I. Katsnelson, Y. N. Gornostyrev, K. Watanabe, T. Taniguchi, C. Casiraghi, H.-J. Gao, A. K. Geim, and K. S. Novoselov, "Commensurate–incommensurate transition in graphene on hexagonal boron nitride," Nat. Phys. **10**(6), 451–456 (2014).
[44] W. Aggoune, C. Cocchi, D. Nabok, K. Rezouali, M. A. Belkhir, and C. Draxl, "Structural, electronic, and optical properties of periodic graphene/h-BN van der Waals heterostructures," Phys. Rev. Mater. **4**(8), 084001 (2020).
[45] T. V. Vu, N. V. Hieu, H. V. Phuc, N. N. Hieu, H. D. Bui, M. Idrees, B. Amin, and C. V. Nguyen, "Graphene/WSeTe van der Waals heterostructure: Controllable electronic properties and Schottky barrier via interlayer coupling and electric field," Appl. Surf. Sci. **507**, 145036 (2020).
[46] Q. Peng, Z. Guo, B. Sa, J. Zhou, and Z. Sun, "New gallium chalcogenides/arsenene van der Waals heterostructures promising for photocatalytic water splitting," Int. J. Hydrogen Energy **43**(33), 15995–16004 (2018).
[47] S. Li, M. Sun, J.-P. Chou, J. Wei, H. Xing, and A. Hu, "First-principles calculations of the electronic properties of SiC-based bilayer and trilayer heterostructures," Phys. Chem. Chem. Phys. **20**(38), 24726–24734 (2018).
[48] Z. Hou, X. Wang, T. Ikeda, K. Terakura, M. Oshima, M.-A. Kakimoto, and S. Miyata, "Interplay between nitrogen dopants and native point defects in graphene," Phys. Rev. B **85**(16), 165439 (2012).
[49] K. Watanabe, T. Taniguchi, and H. Kanda, "Direct-bandgap properties and evidence for ultraviolet lasing of hexagonal boron nitride single crystal," Nat. Mater. **3**(6), 404–409 (2004).
[50] C. Repellin, Z. Dong, Y.-H. Zhang, and T. Senthil, "Ferromagnetism in narrow bands of moiré superlattices," Phys. Rev. Lett. **124**(18), 187601 (2020).
[51] S. Chatterjee, N. Bultinck, and M. P. Zaletel, "Symmetry breaking and skyrmionic transport in twisted bilayer graphene," Phys. Rev. B **101**(16), 165141 (2020).
[52] G. Chen, A. L. Sharpe, E. J. Fox, Y.-H. Zhang, S. Wang, L. Jiang, B. Lyu, H. Li, K. Watanabe, T. Taniguchi, Z. Shi, T. Senthil, D. Goldhaber-Gordon, Y. Zhang, and F. Wang, "Tunable correlated Chern insulator and ferromagnetism in a moiré superlattice," Nature **579**(7797), 56–61 (2020).
[53] J. Liu and X. Dai, "Anomalous Hall effect, magneto-optical properties, and nonlinear optical properties of twisted graphene systems," NPJ Comput. Mater. **6**(1), 57 (2020).

© Author(s) 2021

International Journal of Computational Materials
Science and Engineering
Vol. 10, No. 2 (2021) 2150009 (22 pages)
© World Scientific Publishing Europe Ltd.
DOI: 10.1142/S2047684121500093

World Scientific
www.worldscientific.com

Int. J. Comp. Mat. Sci. Eng. 2021.10. Downloaded from www.worldscientific.com
by UNIVERSITA' DEGLI STUDI DI BRESCIA on 06/02/22. Re-use and distribution is strictly not permitted, except for Open Access articles.

Structural, electronic and magnetic properties of S sites vacancy defects graphene/MoS_2 van der Waals heterostructures: First-principles study

Hari Krishna Neupane*,† and Narayan Prasad Adhikari†,‡

*Amrit Campus, Institute of Science
and Technology Tribhuvan University
Kathmandu, Nepal

†Central Department of Physics
Institute of Science and Technology
Tribhuvan University, Kathmandu, Nepal
‡narayan.adhikari@cdp.tu.edu.np

Received 19 October 2020
Revised 15 April 2021
Accepted 16 April 2021
Published 5 June 2021

In this work, we investigated the geometrical structures, electronic and magnetic properties of S sites vacancy defects in heterostructure graphene/molybdenum disulphide ((HS)G/MoS_2) material by performing first-principles calculations based on spin polarized Density Functional Theory (DFT) method within van der Waals (vdW) corrections (DFT-D2) approach. All the structures are optimized and relaxed by BFGS method using computational tool Quantum ESPRESSO (QE) package. We found that both (HS)G/MoS_2 and S sites vacancy defects in (HS)G/MoS_2 (D1S-(HS)G/MoS_2, U1S-(HS)G/MoS_2, 2S-(HS)G/MoS_2 and 3S-(HS)G/MoS_2) are stable materials, and atoms in defects structures are more compact than in pristine (HS)G/MoS_2 structure. From band structure calculations, we found that (HS)G/MoS_2, (D1S-(HS)G/MoS_2, U1S-(HS)G/MoS_2, 2S-(HS)G/MoS_2 and 3S-(HS)G/MoS_2) materials have n-type Schottky contact. The Dirac cone is formed in conduction band of the materials mentioned above. The barrier height of Dirac cones from Fermi energy level of (HS)G/MoS_2, (D1S-(HS)G/MoS_2, U1S-(HS)G/MoS_2, 2S-(HS)G/MoS_2 and 3S-(HS)G/MoS_2) materials have values 0.56 eV, 0.62 eV, 0.62 eV, 0.64 eV and 0.65 eV, respectively, which means they have metallic properties. To study the magnetic properties of materials, we have carried out DoS and PDoS calculations. We found that (HS)G/MoS_2, D1S-(HS)G/MoS_2 and U1S-(HS)G/MoS_2 materials have non-magnetic properties, and 2S-(HS)G/MoS_2 and 3S-(HS)G/MoS_2 materials have magnetic properties. Therefore, the non-magnetic (HS)G/MoS_2 changes to magnetic 2S-(HS)G/MoS_2 and 3S-(HS)G/MoS_2 materials due to 2S and 3S atoms vacancy defects, respectively, in (HS)G/MoS_2 material. Magnetic moment obtained in 2S-(HS)G/MoS_2 and 3S-(HS)G/MoS_2 materials due to the unequal distribution of up and down spin states of electrons in 2s and 2p orbitals of C atoms; 4p, 4d and 5s orbitals of Mo atoms; and 3s and 3p orbitals of S atoms in structures. Magnetic moment of 2S-(HS)G/MoS_2 and 3S-(HS)G/MoS_2 materials is $-0.11\,\mu_B$/cell and $-0.29\,\mu_B$/cell, respectively, and spins of 2p orbital of C atoms, 3p orbital of S atoms

‡Corresponding author.

Scanned with CamScanner

and 4d orbital of Mo atoms have dominant role to create magnetism in 2S–(HS)G/MoS_2 and 3S–(HS)G/MoS_2 materials.

Keywords: DFT; graphene/MoS_2; heterostructures; vacancy defects; vdW.

Int. J. Comp. Mat. Sci. Eng. 2021.10. Downloaded from www.worldscientific.com
by UNIVERSITA' DEGLI STUDI DI BRESCIA on 06/02/22. Re-use and distribution is strictly not permitted, except for Open Access articles.

1. Introduction

The probability of generating and organizing two-dimensional (2D) systems at the nanoscale has expanded the boundary of material science. Among the most auspicious aspirants for new origination of optoelectronic and photonic devices, Graphene and other monolayer materials, such as molybdenum disulphide (MoS_2), hexagonal boron-nitride (h-BN), are performing an exceptional role. It is well known that Graphene is a stable 2D sp^2-hybridized carbon monolayer. It has remarkable electronic, optical, mechanical and magnetic properties so that it is a promising material for mapping future nanoelectronic and related devices [Novoselov *et al.*, 2004; Castro *et al.*, 2007]. On the other hand, MoS_2 is a wide band gap, 2D transition metal dichalcogenide (TMD) material, having stable honeycomb lattice structure. It has attracting properties [Mak *et al.*, 2010; Kadantsev and Hawrylak, 2012]. It is used in producing signal amplifier, integrated logic circuits, flexible optoelectronic devices, transistors, photodetectors, photocatalysts, solar cells, and lubricants [Radisavljevic *et al.*, 2012; Hu *et al.*, 2012; Nguyen, 2018; Phuc *et al.*, 2018]. Hence, it has potential applications in the fields of nanoelectronic and optoelectronic devices. Even more exciting perspectives have been opened by combining these systems in heterostructures, thereby exploiting and enhancing the characteristics of the single components [Din *et al.*, 2019; Vu *et al.*, 2020; Nguyen *et al.*, 2020; Karki and Adhikari, 2014; Oli *et al.*, 2013; Wang *et al.*, 2017]. The vertically stacked van der Waals (vdW) heterostructures formed by graphene (G) and monolayer MoS_2 have received extensive attention. This combination is motivated by the considerable lattice mismatch 4.13% between periodically repeated (4×4) supercell of Graphene and (3×3) supercell of MoS_2. The interfaces of two supercells are equivalent to the term of stoichiometry and geometry. The heterostructure of graphene/molybdenum disulphide (HS(G/MoS_2)) has been reported to be an excellent platform in electronic, photovoltaic and memory devices [Ghorbani-Asi *et al.*, 2016; Ma *et al.*, 2011; Phan *et al.*, 2012; Yu *et al.*, 2013; Choi *et al.*, 2013; Roy *et al.*, 2013], so it has exciting properties such as excellent electronic properties, favorable transport properties, optical transparency, mechanical flexibility and photoconductivity [Phuc *et al.*, 2018; Debbichi *et al.*, 2014]. According to our previous works [Neupane and Adhikari, 2020, 2021], (HS)G/MoS_2 has non-magnetic properties. The magnetic materials have great applications in modern technological devices such as they are used in molecular biology, biochemistry, catalysis, nanoelectronic devices, magnetic sensors, computers, biomedicine, magnetic recording media [Makarova *et al.*, 2019; Peng *et al.*, 2016]. Therefore, to drag the magnetic properties in materials, we have created S sites vacancy defects in vdW (HS)G/MoS_2 material. Defects are inescapable properties in crystalline solids. They are formed

Scanned with CamScanner

Int. J. Comp. Mat. Sci. Eng. 2021.10. Downloaded from www.worldscientific.com
by UNIVERSITA' DEGLI STUDI DI BRESCIA on 06/02/22. Re-use and distribution is strictly not permitted, except for Open Access articles.

due to deviation of atoms or ions from the periodicity. Defects are used to find novel properties as well as to design the new materials, so it impacts the properties of heterostructures material in solids [Kittel *et al.*, 1996]. Therefore, in this work, we studied geometrical structures, electronic and magnetic properties of 2D vdW, (HS)G/MoS_2 and its S atoms vacancy defects (S_{atoms}–(HS)G/MoS_2) materials using spin-polarized Density Functional Theory (DFT) method of calculations within vdW corrections (DFT-D2) approach.

We discussed computational details in Sec. 2. The main findings and their interpretations are given in Sec. 3, conclusions and concluding remarks are given in Sec. 4.

2. Computational Details

The geometrical structures, electronic and magnetic properties of vdW (HS)G/MoS_2 and S_{atoms}–(HS)G/MoS_2 materials are studied by using first-principles calculations, based on spin-polarized Density Functional Theory (DFT) method [Hohenberg and Kohn, 1964], within the framework of vdW corrections (DFT-D2) approach [Grimme, 2004]. The electronic exchange and correlation effects in the systems are treated by Generalized Gradient Approximation (GGA) using Perdew–Burke–Ernzerhof (PBE) [Perdew *et al.*, 1996], also Rappe–Rabe–Kaxiraas–Joannopoulos (RRKJ) model of ultra-soft pseudo-potentials is used in order to replace the complicated effects of the motion of the core electrons of an atom and its nucleus with an effective potential for all atoms in a system, so that only the chemically active valence electrons are included explicitly in calculations [Grimme, 2004]. All the structures are optimized and relaxed by BFGS scheme [Pfrommer *et al.*, 1997] using computational tool Quantum ESPRESSO package [Giannozzi *et al.*, 2009], until total energy change is less than 10^{-4} Ry, and each component of force acting is less than 10^{-3} Ry/Bohrs between two consecutive self-consistent fields. In (3×3) supercell structure of MoS_2, the lattice constant is three times that of the unit cell and a mesh of k-points is reduced to $(6 \times 6 \times 1)$. The reduction of mesh is due to the relation of direct and reciprocal lattice geometries. We have done self-consistent total energy calculations of relaxed structures. For this, a mesh of $(6 \times 6 \times 1)$ k-points is sampled for Brillouin zone integration using Monkhorst–Pack (MP) scheme [Pack and Monkhorst, 1977]. This mesh is determined from the convergence test. The plane-wave expansion with kinetic energy cut-off value 35 Ry is used for wave function and charge density cut-off value 350 Ry is used for charge density. Those values are obtained from the convergence plot of total energy versus energy cut-off wave function. Also, we used Marzarri–Vanderbilt (MV) [Marzari *et al.*, 1999] method of smearing for occupations and 0.001 Ry value of degauss. In addition, we have chosen "David" diagonalization method with "plain" mixing mode and mixing factor of 0.6 for self-consistency. For band structure, and Density of State (DoS), Partial Density of State (PDoS) calculations, a mesh of $(6 \times 6 \times 1)$, and a mesh of $(12 \times 12 \times 1)$ are used, respectively, where 200 k-points are chosen along

Scanned with CamScanner

the high symmetric points connecting the reciprocal space. The (HS)G/MoS_2 is prepared using (4 × 4) and (3 × 3) supercells structures of Graphene and MoS_2 by small (4.13%) lattice mismatch, where we forced vacuum distance greater than 20Å to minimize the interaction between two adjacent layers, as shown in Fig. 1(c). The D1S-(HS)G/MoS_2, U1S–(HS)G/MoS_2, 2S–(HS)G/MoS_2 and 3S–(HS)G/MoS_2 materials are constructed by extracting lower-1S, upper-1S, 2S and 3S atoms from (HS)G/MoS_2 structure, as shown in Fig. 2, then relaxed these structures for further calculations.

3. Results and Discussion

The detail interpretations about structural, electronic and magnetic properties of (HS)G/MoS_2, D1S–(HS)G/MoS_2, U1S–(HS)G/MoS_2, 2S–(HS)G/MoS_2 and 3S–(HS)G/MoS_2 materials are given in this section.

3.1. *Structural properties*

The (4 × 4) supercell structure of Graphene and (3 × 3) supercell structure of monolayer MoS_2 is used in (HS)G/MoS_2 and S_{atoms}–(HS)G/MoS_2 materials, as shown in Fig. 1. These supercell structures are prepared by extending optimized primitive unit cell along x and y directions. At first, we have prepared unit cell of Graphene and MoS_2 by using structure analysis tool XCrySDen and computational tool Quantum ESPRESSO. To construct the unit cell, we used Bravais lattice index, cell dimension parameters and lattice constant in input file. For Graphene unit cell, we have taken experimentally reported value of distance between two carbon atoms that is 1.42 Å [Martin, 2020]. After the construction of Graphene unit cell, we calculated kinetic energy cut-off (ecutwfc), k-points (n_{kx}, n_{ky}, n_{kz}), lattice parameter "a" from convergence test, and found the constant kinetic energy cut-off value 35 Ry. The charge density cut-off value for ultra-soft pseudo potential is calculated by using the relation 10× kinetic energy cut-off, which is 350 Ry. These obtained parameters (kinetic energy cut-off, charge density cut-off, k-points, and lattice parameter) are used in input file to relax our system. We found that the distance between two carbon atoms of relaxed Graphene unit cell is 1.417 Å, which agrees with experimentally reported value [Martin, 2020]. Similarly, we have prepared a unit cell of monolayer MoS_2 by using reported lattice constant value 3.19 Å [Kadantsev and Hawrylak, 2012; Ahmad and Mukherjee, 2014]. Its unit cell contains single layer of two S atoms and one Mo atom. The Mo atom bounds with S atom in a trigonal prismatic arrangement, where each Mo atom is surrounded by six first neighboring S atoms. After the construction of a unit cell, we have calculated its optimized values of kinetic energy cut-off, k-points, lattice parameter, and charge density cut-off as like in Graphene, and then these parameters are used in input file to relax the system. We found that, the value of lattice constant is 3.18 Å, which is close to reported value 3.19 Å [Kadantsev and Hawrylak, 2012;

Int. J. Comp. Mat. Sci. Eng. 2021.10. Downloaded from www.worldscientific.com
by UNIVERSITA' DEGLI STUDI DI BRESCIA on 06/02/22. Re-use and distribution is strictly not permitted, except for Open Access articles.

Scanned with CamScanner

Int. J. Comp. Mat. Sci. Eng. 2021.10. Downloaded from www.worldscientific.com
by UNIVERSITA' DEGLI STUDI DI BRESCIA on 06/02/22. Re-use and distribution is strictly not permitted, except for Open Access articles.

Ahmad and Mukherjee, 2014]. We developed (4 × 4) supercell of Graphene and (3 × 3) supercell of monolayer MoS_2 from these prepared unit cells, by extending along x and y directions, as shown in Figs. 1(a) and 1(b). Furthermore, we have constructed vdW interfaces (HS)G/MoS_2 material by using these supercells with lattice mismatch 4.13% at different stacking configurations. These configurations are relaxed, and found that MoS_2 base (HS)G/MoS_2 structure as shown in Fig. 1(c) is more stable than other configurations, because binding energy of this geometry is greater than other stacking geometries. We know that, stability of structures is determined by binding energy calculations. Higher the value of binding energy, more stable will be the system. Thus, the greater value of binding energy material is more favorable for the calculations.

In addition, we have prepared S sites vacancy defects D1S–(HS)G/MoS_2, U1S–(HS)G/MoS_2, 2S–(HS)G/MoS_2 (U1S and D1S) and 3S–(HS)G/MoS_2 (U2S and D1S) materials by removing lower-1S, upper-1S, 2S and 3S atoms from stable (HS)G/MoS_2 material, where concentration of vacancy defects are found to be 5.56%, 5.56%, 11.11% and 16.67%, respectively. We obtained defects formation energy of D1S–(HS)G/MoS_2, U1S–(HS)G/MoS_2, 2S–(HS)G/MoS_2 and 3S–(HS)G/MoS_2 materials is 1.24 eV, 1.24, 2.05 eV and 2.82 eV, respectively, which are calculated by using standard formalism [Hou *et al.*, 2012]

$$E_d = E_{td} - (E_{tp} + n_s\mu_s), \tag{3.1}$$

where E_{td} and E_{tp} represent total energy of a heterostructure with the defects and total energy of the neutral perfect heterostructure, respectively, n_s is the numbers of S atoms removed from the perfect heterostructure to introduce vacancy, and μ_s is chemical potential of S atom. We then relax these defected structures and found that all are stable materials, as shown in Fig. 2. Figures 1(d)–1(g) represent interlayer and inter-atomic distances measurement geometries of (HS)G/MoS_2 and S sites vacancy defects (S_{atoms}–(HS)G/MoS_2) materials, respectively.

The interlayer and inter-atomic distances measurement parameters of (HS)G/MoS_2 and S_{atoms}–(HS)G/MoS_2 materials are given in Table 1.

From Table 1, we found that S_{atoms}–(HS)G/MoS_2 geometries are more compact than (HS)G/MoS_2 geometry, and also compactness of materials are increased with increase in its defects concentrations.

3.2. *Electronic properties*

To understand the electronic properties of vdW, (HS)G/MoS_2 and S_{atoms}–(HS)G/MoS_2 materials, we first check the electronic properties of the constituents. The optimized structures of Graphene and monolayer MoS_2 are illustrated in Fig. 1. We have calculated the band structures of Graphene and monolayer MoS_2, and found that band gap of Graphene is 0.00 eV and MoS_2 is 1.56 eV. This band gap energy of MoS_2 is close with experimentally reported value 1.80 Å

Scanned with CamScanner

Int. J. Comp. Mat. Sci. Eng. 2021.10. Downloaded from www.worldscientific.com
by UNIVERSITA' DEGLI STUDI DI BRESCIA on 06/02/22. Re-use and distribution is strictly not permitted, except for Open Access articles.

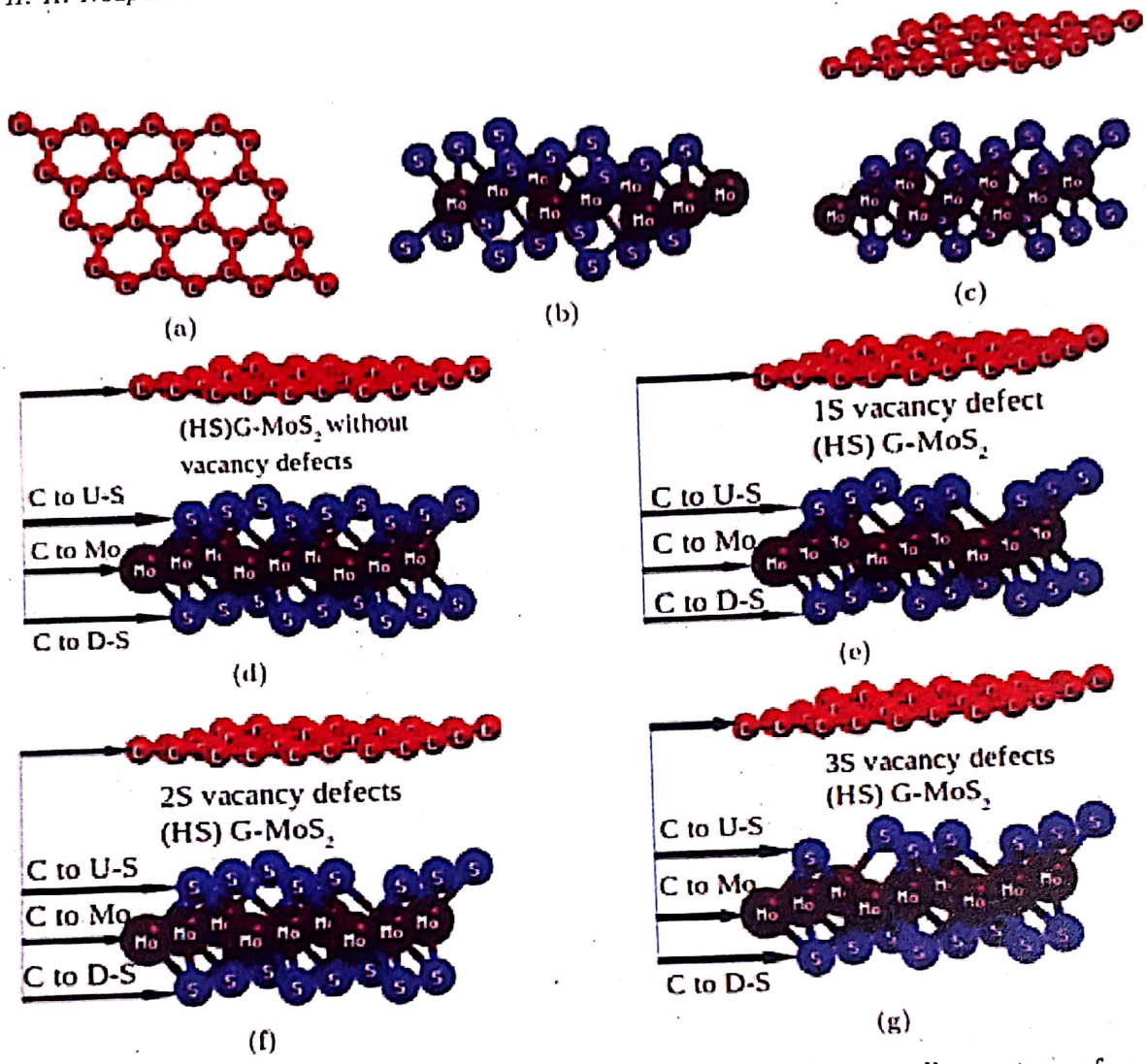

Fig. 1. (a) (4 × 4) supercell structure of Graphene. (b) (3 × 3) supercell structure of monolayer MoS_2. (c) Heterostructure of Graphene/MoS_2. (d) Interlayer and inter-atomic distances measurement structure of (HS)G/MoS_2. (e) Interlayer and inter-atomic distances measurement structure of 1S–(HS)G/MoS_2. (f) Interlayer and inter-atomic distances measurement structure of 2S–(HS)G/MoS_2. (g) Interlayer and inter-atomic distances measurement structure of 3S–(HS)G/MoS_2.

[Ahmad and Mukherjee, 2014]. Thus, MoS_2 is called wide band gap semiconductors. The vertical stacking heterostructure material (HS)G/MoS_2 is formed by using Graphene bonds on MoS_2 with weak vdW interactions. Its different stacking configurations give new properties beyond their single components because vdW (HS)G/MoS_2 has own many physical properties such as carrier mobility, band gap etc. [Pierucci *et al.*, 2016; Zhou *et al.*, 2007; Chen *et al.*, 2019] than individual components. From band structure calculations of (HS)G/MoS_2, we found that its Dirac cone is located in conduction band at 0.56 eV distance from the Fermi energy level as shown in Fig. 3(a). This height is formed due to the positive value of work function difference between (HS)G/MoS_2 and MoS_2. The formation of Dirac cone in the conduction band at 0.56 eV heights from Fermi energy level means electrons are flowing

Scanned with CamScanner

Int. J. Comp. Mat. Sci. Eng. 2021.10. Downloaded from www.worldscientific.com
by UNIVERSITA' DEGLI STUDI DI BRESCIA on 06/02/22. Re-use and distribution is strictly not permitted, except for Open Access articles.

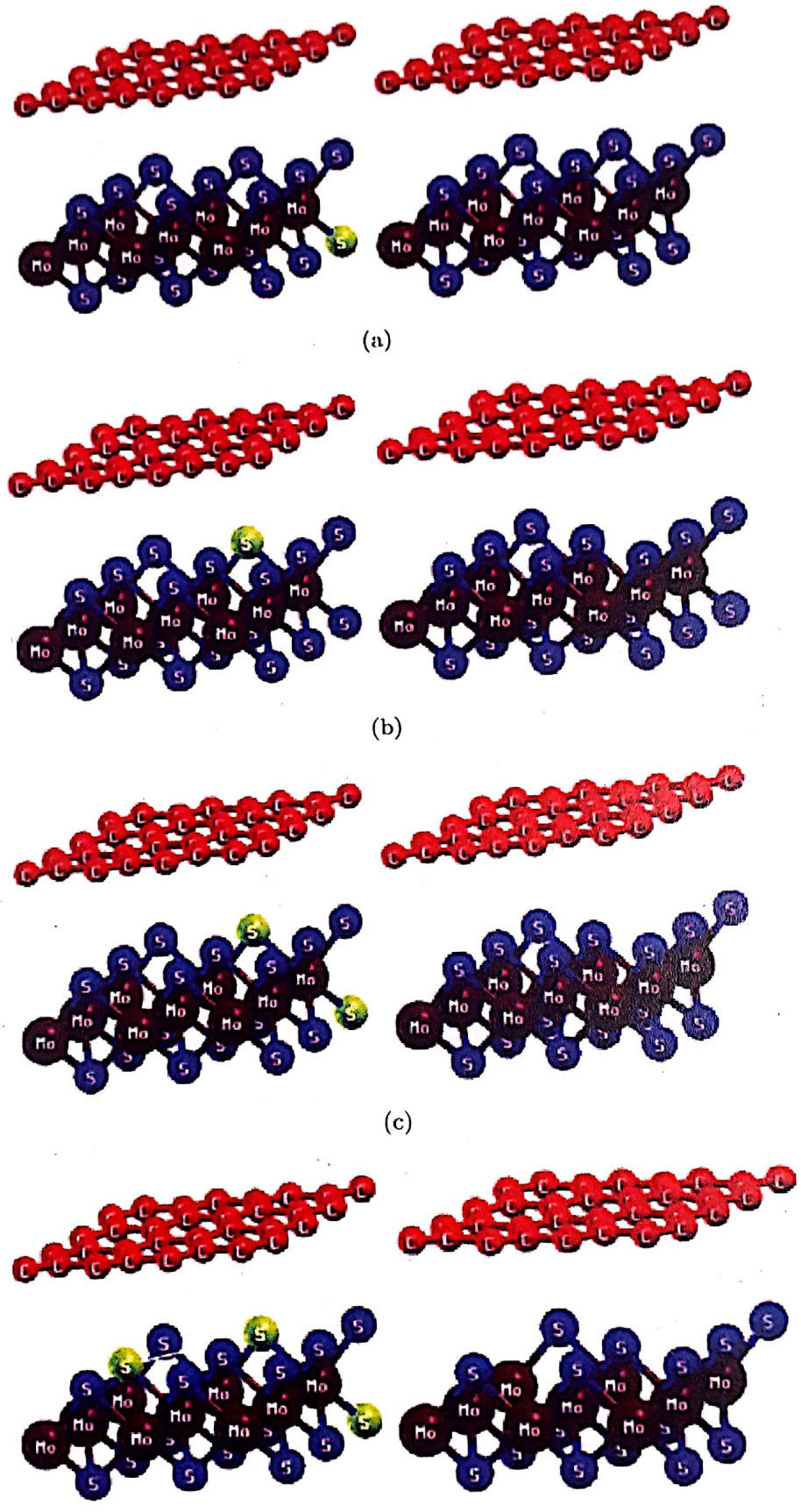

Fig. 2. (a) Stable D1S–(HS)G/MoS_2 structure. (b) Stable U1S–(HS)G/MoS_2 structure. (c) Stable 2S–(HS)G/MoS_2 structure. (d) Stable 3S–(HS)G/MoS_2 structure.

Scanned with CamScanner

Int. J. Comp. Mat. Sci. Eng. 2021.10. Downloaded from www.worldscientific.com
by UNIVERSITA' DEGLI STUDI DI BRESCIA on 06/02/22. Re-use and distribution is strictly not permitted, except for Open Access articles.

Table 1. The interlayer and inter-atomic distances parameters of (HS)G/$MoS_2$and S_{atoms}–(HS)G/MoS_2 structures, where C–Mo, C–US, and C–DU denote distance between carbon atom in Graphene surface to Mo, upper-S and lower-S atoms in MoS_2 structure, respectively.

Interlayer distances of (HS)G/MoS_2 along x, y and z axis	C–Mo	C–US	C–DS
x-axis (Å)	0.29	1.88	0.89
y-axis (Å)	0.25	1.16	1.17
z-axis (Å)	5.92	4.34	7.49
Inter-atomic distances of (HS)G/MoS_2 along x, y and z axis	**x-axis (Å)**	**y-axis (Å)**	**z-axis (Å)**
S–S	0.00	0.00	3.14
Mo–Mo	1.59	2.75	0.00
Mo–S	1.54	0.92	1.57
C–C	0.00	1.39	0.09

Interlayer distances of S_{atoms}–(HS)G/MoS_2 along x, y and z axis	C–Mo			C–US			C–DS		
	3S	2S	1S	3S	2S	1S	3S	2S	1S
x-axis (Å)	0.28	0.28	0.29	1.85	1.87	1.88	0.85	0.87	0.88
y-axis (Å)	0.24	0.24	0.25	1.16	1.16	1.17	1.16	1.17	1.17
z-axis (Å)	5.43	5.79	5.89	4.27	4.31	4.33	7.41	7.44	7.47
Inter-atomic distances of S_{atoms}–(HS)G/MoS_2 along x, y and z axis	**x-axis (Å)**			**y-axis (Å)**			**z-axis (Å)**		
	3S	2S	1S	3S	2S	1S	3S	2S	1S
S–S	0.00	0.00	0.00	0.01	0.00	0.00	3.15	3.14	3.14
Mo–Mo	1.57	1.59	1.59	2.74	2.75	2.75	0.00	0.00	0.00
Mo–S	1.53	1.53	1.54	0.91	0.92	0.92	1.56	1.57	1.57
C–C	0.00	0.00	0.00	1.39	1.38	1.39	0.09	0.09	0.09

from valence band to conduction band due to the interfacial charge transfer. Therefore, we concluded that (HS)G/MoS_2 has metallic properties. Also, we found that (HS)G/MoS_2 has n-type Schottky contact of barrier height value 0.42 eV. This value is close with reported value 0.49 eV [Phuc *et al.*, 2018; Liu *et al.*, 2016]. The n-type Schottky contact is defined as the energy difference between Fermi level and conduction band minimum in metal/semiconductor vdW heterostructures [Chen *et al.*, 2013; Hu *et al.*, 2016].

Moreover, we have done band structure calculations of D1S–(HS)G/MoS_2, U1S–(HS)G/MoS_2, 2S–(HS)G/MoS_2 and 3S–(HS)G/MoS_2 materials, as shown in Figs. 4(a), 5(a), 6(a) and 7(a), respectively, where x-axis represents high symmetric points in the first Brillouin zone and y-axis represents the corresponding energy values. We found that they have Dirac cone in the conduction band at 0.62 eV, 0.62 eV, 0.64 eV and 0.65 eV distances, respectively, from the Fermi energy level. They indicate that S sites vacancy defects in (HS)G/MoS_2 materials have metallic properties. Also, we observed that S sites vacancy defects in (HS)G/MoS_2 materials have n-type Schottky contact. The Fermi energy of (HS)G/MoS_2 has value

Scanned with CamScanner

Int. J. Comp. Mat. Sci. Eng. 2021.10. Downloaded from www.worldscientific.com
by UNIVERSITA' DEGLI STUDI DI BRESCIA on 06/02/22. Re-use and distribution is strictly not permitted, except for Open Access articles.

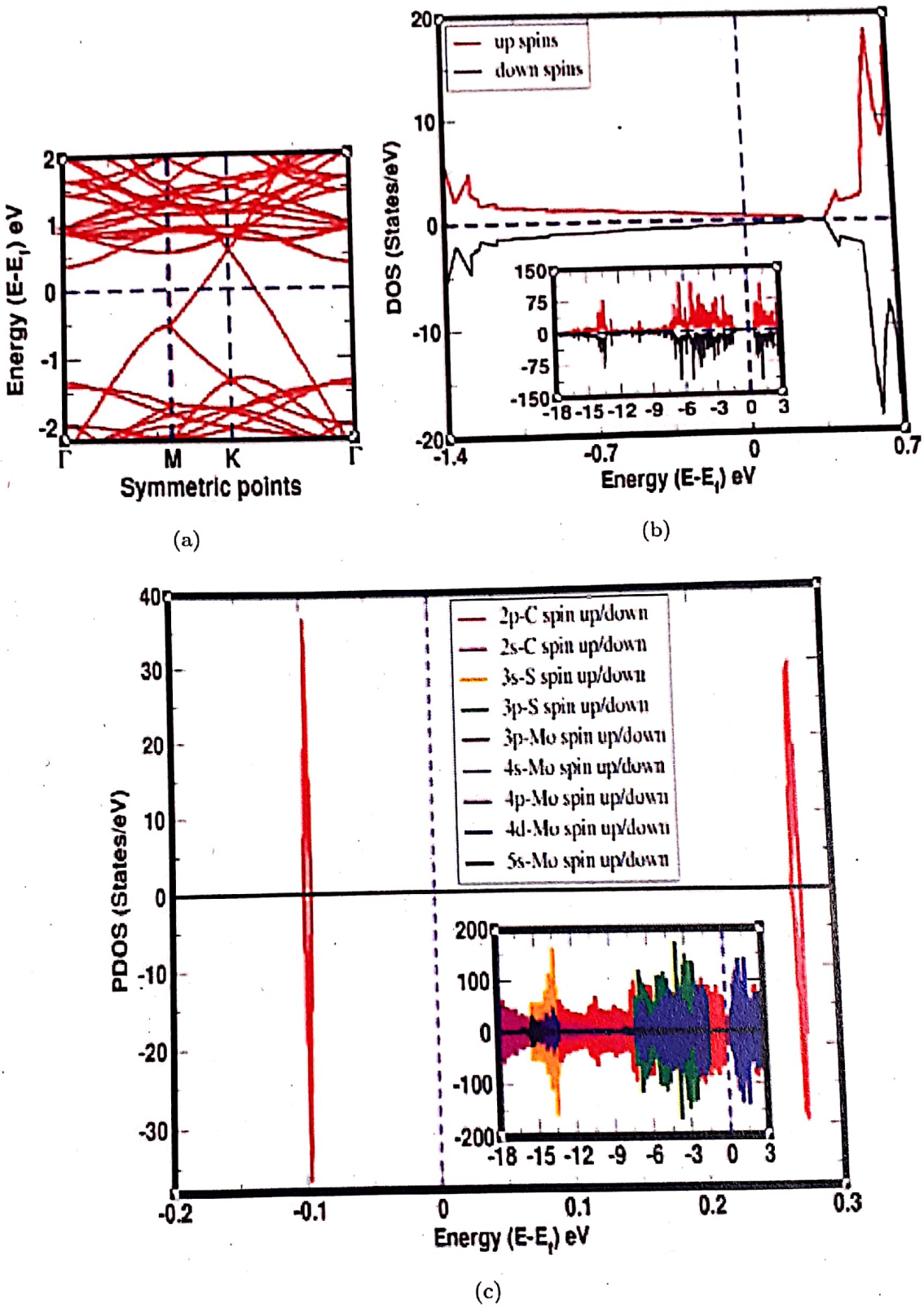

Fig. 3. (a) Band structure of up and down spin states of (HS)G/MoS_2 material. (b) Symmetrically distributed DoS of up and down spin states of electrons in (HS)G/MoS_2 material. (c) Symmetrically distributed PDoS of up and down spin states of electrons in the orbital of atoms present in (HS)G/MoS_2 material. In band structure, horizontal dotted line represents Fermi energy level, and in DoS/PDoS plots, vertical dotted line represents Fermi level. In DoS and PDoS, insets represent the plots of total up and total down spins.

Scanned with CamScanner

Int. J. Comp. Mat. Sci. Eng. 2021.10. Downloaded from www.worldscientific.com
by UNIVERSITA' DEGLI STUDI DI BRESCIA on 06/02/22. Re-use and distribution is strictly not permitted, except for Open Access articles.

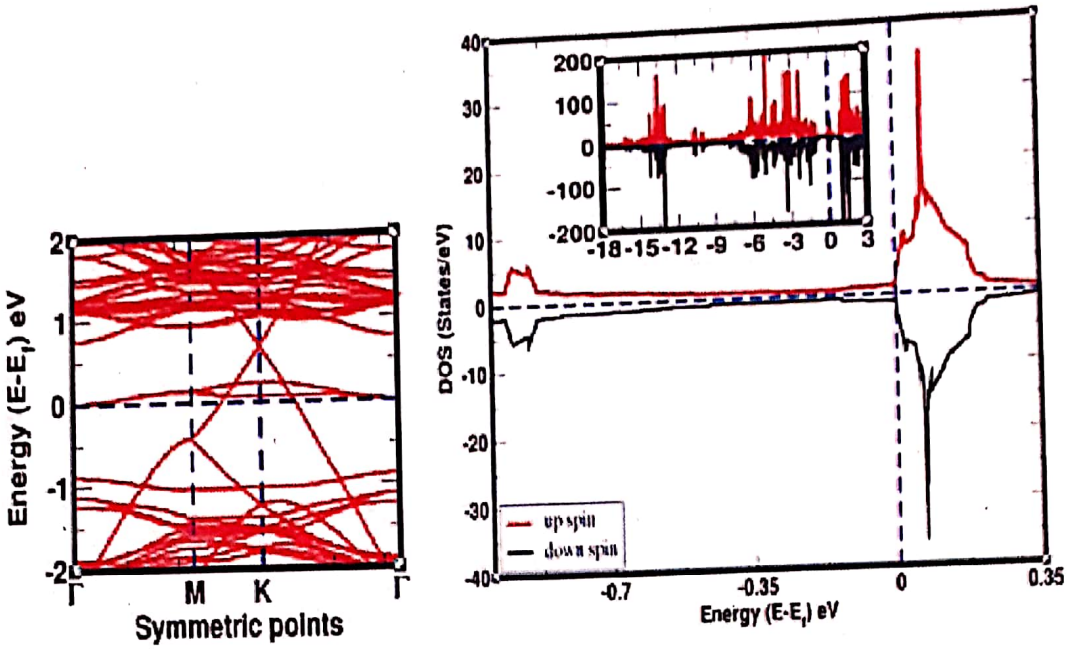

(a) (b)

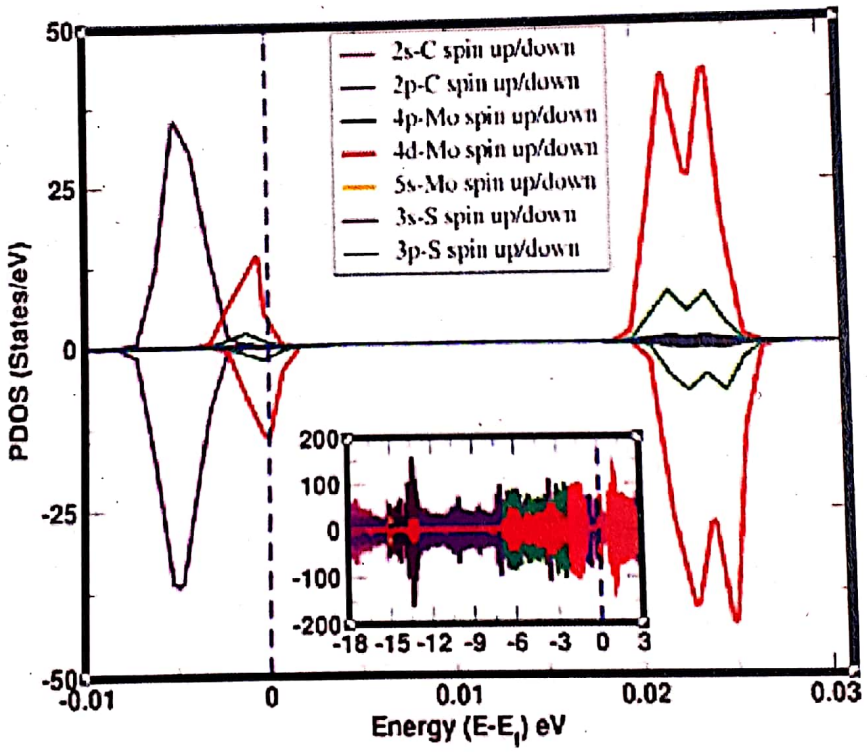

(c)

Fig. 4. (a) Band structure of up and down spin states of D1S–(HS)G/MoS_2 material, (b) DoS of up and down spin states of electrons in D1S–(HS)G/MoS_2 material, (c) PDoS of individual up and down spins states of electrons in the orbital of C, Mo and S atoms in D1S–(HS)G/MoS_2 material, (d) PDoS of total up and down spin states of electrons in the orbital of C, Mo and S atoms in D1S–(HS)G/MoS_2 material. In band structure, horizontal dotted line represents Fermi level, and DoS/PDoS plots, vertical dotted line represents Fermi level. In all DoS and PDoS, insets represent the plots of total up and total down spins.

Scanned with CamScanner

Int. J. Comp. Mat. Sci. Eng. 2021.10. Downloaded from www.worldscientific.com
by UNIVERSITA' DEGLI STUDI DI BRESCIA on 06/02/22. Re-use and distribution is strictly not permitted, except for Open Access articles.

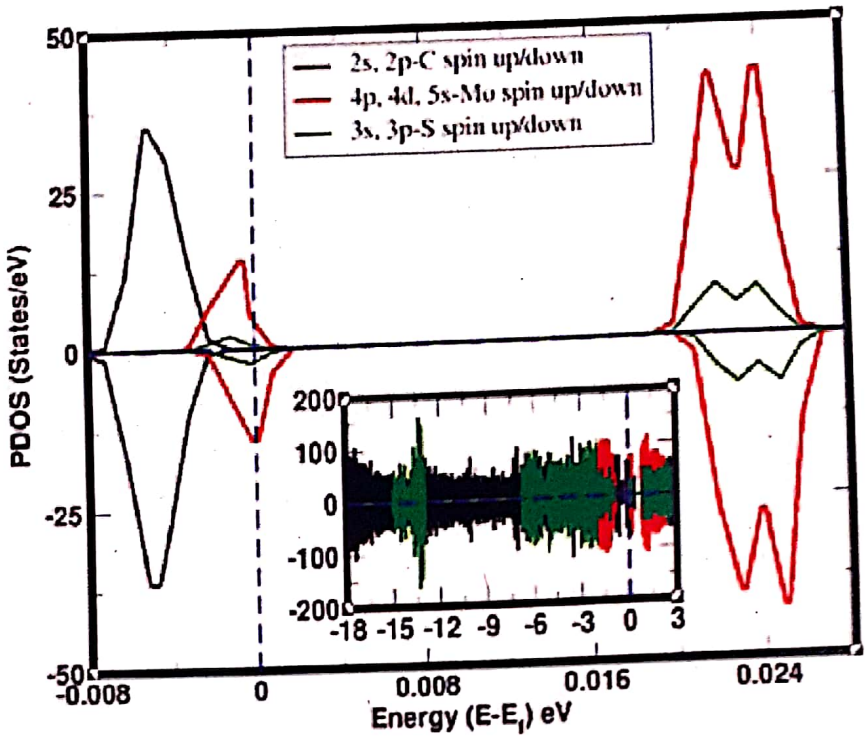

(d)

Fig. 4. (*Continued*)

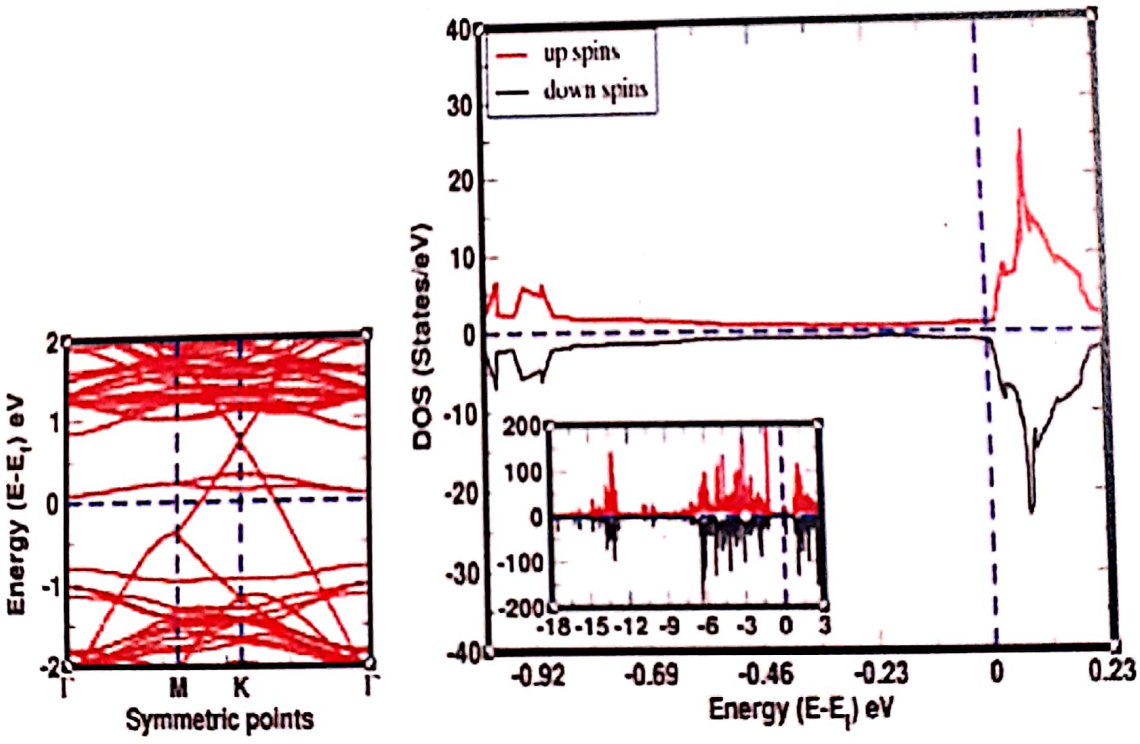

(a) (b)

Fig. 5. (a) Band structure of up and down spin states of U1S–(HS)G/MoS_2 material, (b) DoS of up and down spin states of electrons in U1S–(HS)G/MoS_2 material, (c) PDoS of individual up and down spins states of electrons in the orbital of C, Mo and S atoms in U1S–(HS)G/MoS_2 material, (d) PDoS of total up and down spin states of electrons in the orbital of C, Mo and S atoms in U1S–(HS)G/MoS_2 material. In band structure horizontal dotted line represents Fermi level, and in DoS/PDoS plots, vertical dotted line represents Fermi level. In all DoS and PDoS, insets represent the plots of total up and total down spins.

Scanned with CamScanner

Int. J. Comp. Mat. Sci. Eng. 2021.10. Downloaded from www.worldscientific.com
by UNIVERSITA' DEGLI STUDI DI BRESCIA on 06/02/22. Re-use and distribution is strictly not permitted, except for Open Access articles.

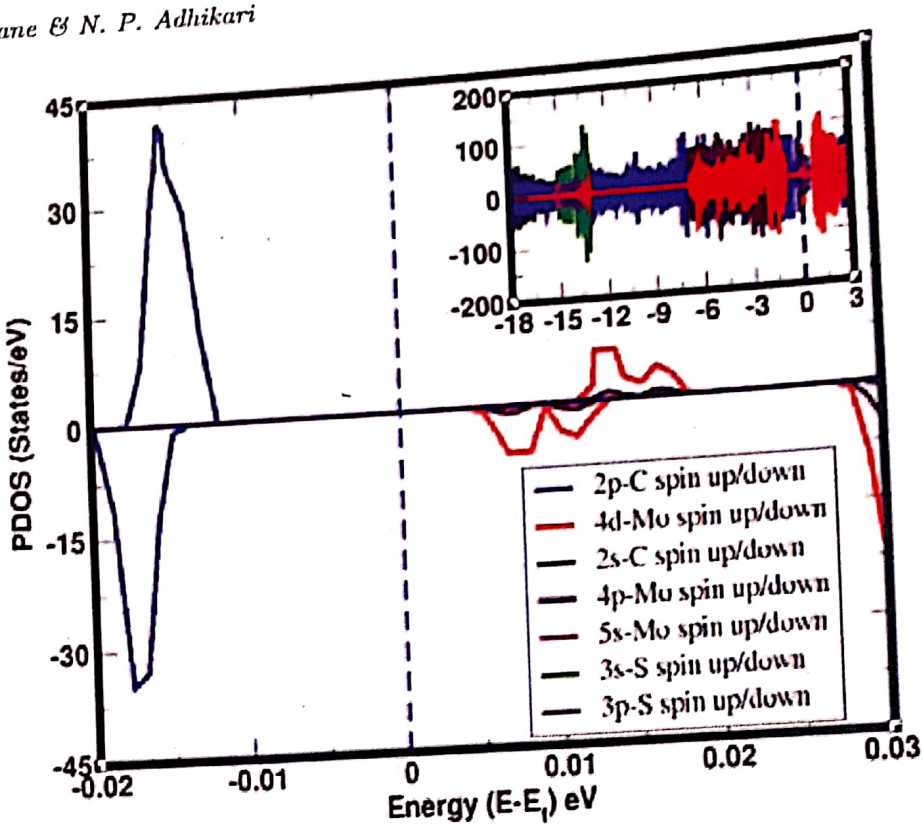

(c)

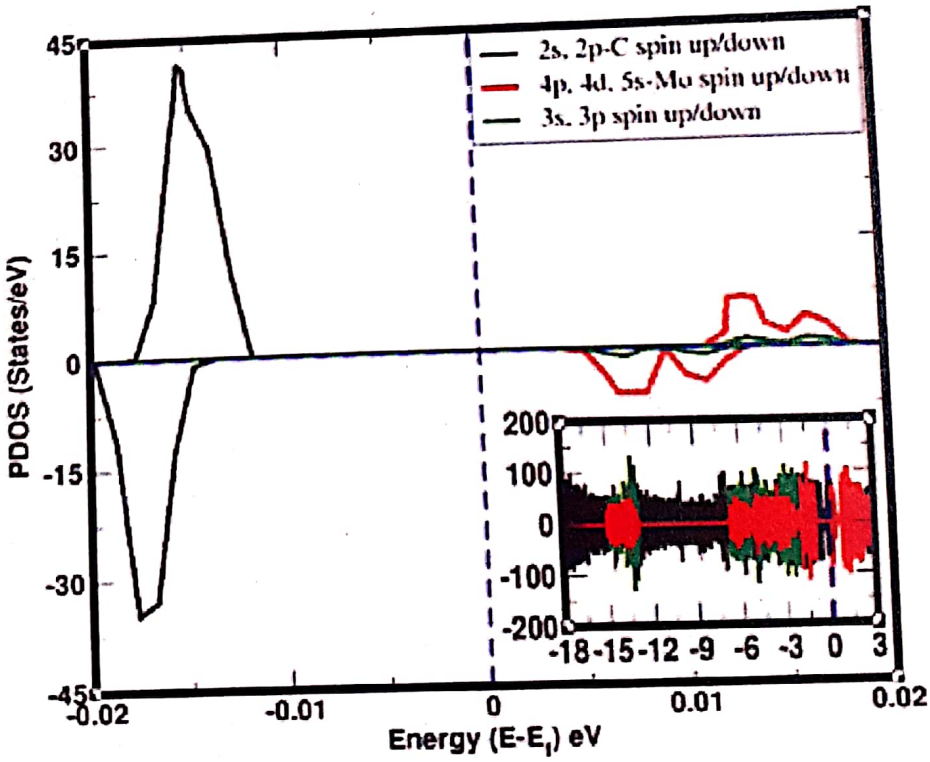

(d)

Fig. 5. (*Continued*)

Scanned with CamScanner

Int. J. Comp. Mat. Sci. Eng. 2021.10. Downloaded from www.worldscientific.com
by UNIVERSITA' DEGLI STUDI DI BRESCIA on 06/02/22. Re-use and distribution is strictly not permitted, except for Open Access articles.

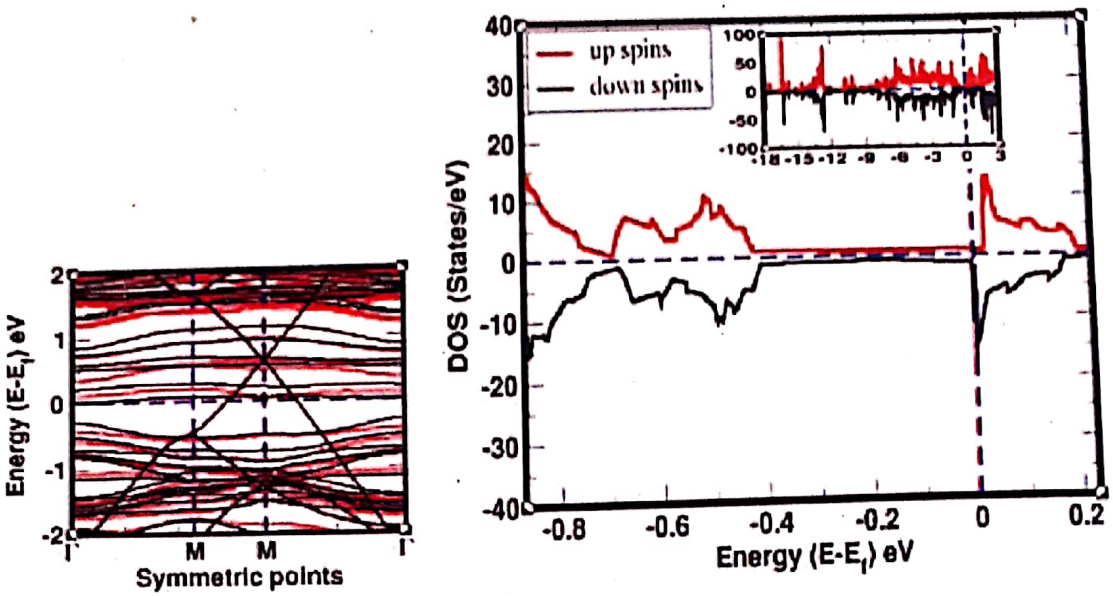

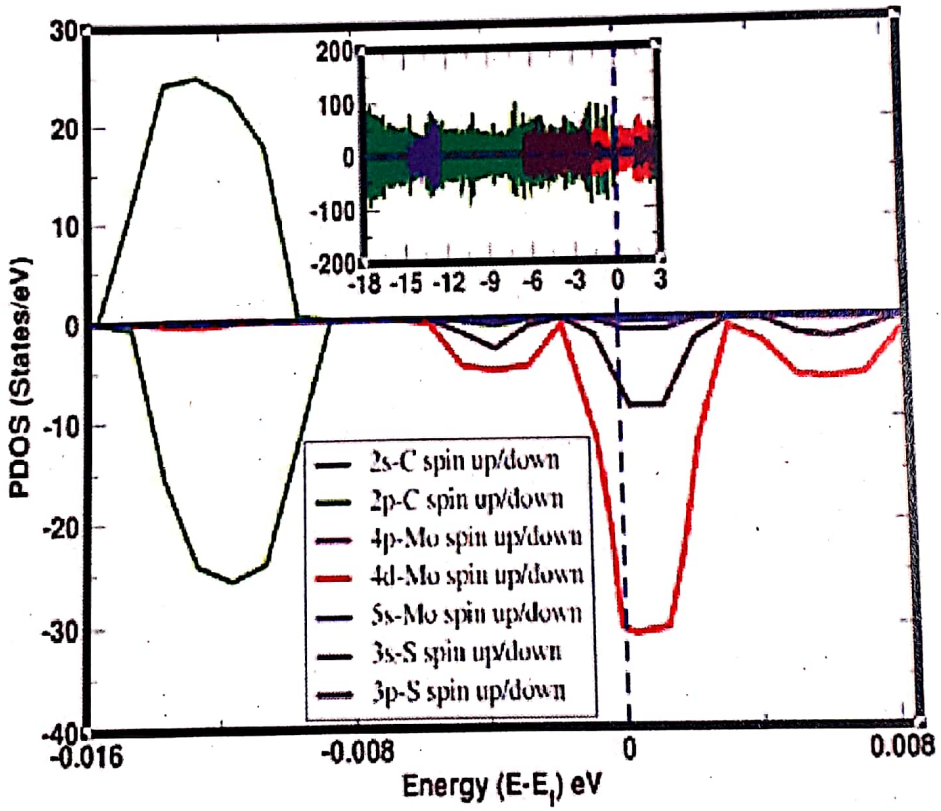

Fig. 6. (a) Band structure of up and down spin states of 2S–(HS)G/MoS_2 material, where red color of bands represent up spin states and black color of bands represent down spin states, (b) DoS of up and down spin states of electrons in 2S–(HS)G/MoS_2 material, (c) PDoS of individual up and down spins states of electrons in the orbital of C, Mo and S atoms in 2S–(HS)G/MoS_2 material, (d) PDoS of total up and down spin states of electrons in the orbital of C, Mo and S atoms in 2S–(HS)G/MoS_2 material. In band structure horizontal dotted line represents Fermi level, and in DoS/PDoS plots, vertical dotted line represents Fermi level. In all DoS and PDoS, insets represent the plots of total up and total down spins.

Scanned with CamScanner

Int. J. Comp. Mat. Sci. Eng. 2021.10. Downloaded from www.worldscientific.com
by UNIVERSITA' DEGLI STUDI DI BRESCIA on 06/02/22. Re-use and distribution is strictly not permitted, except for Open Access articles.

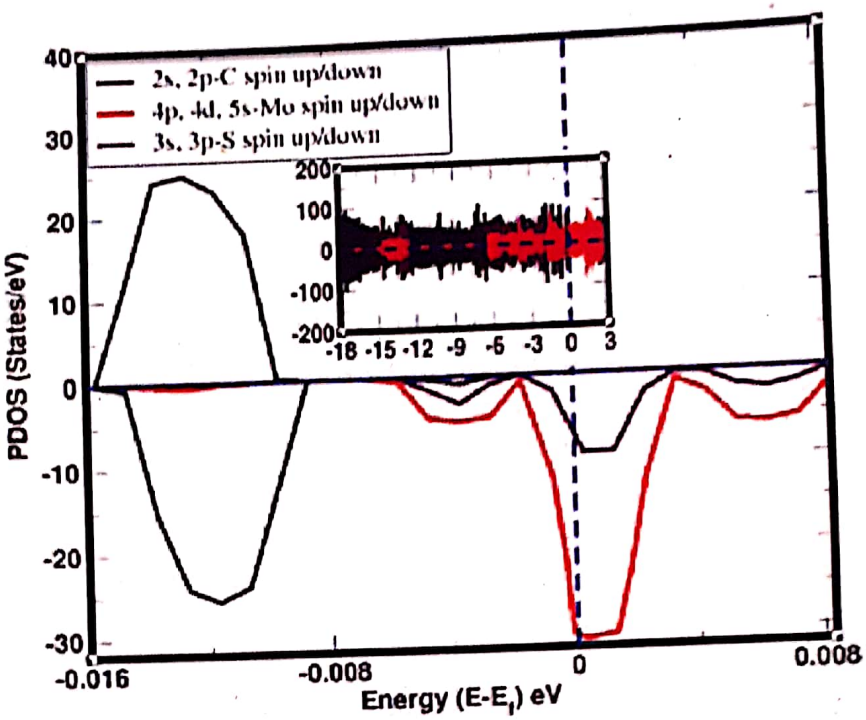

(d)

Fig. 6. (*Continued*)

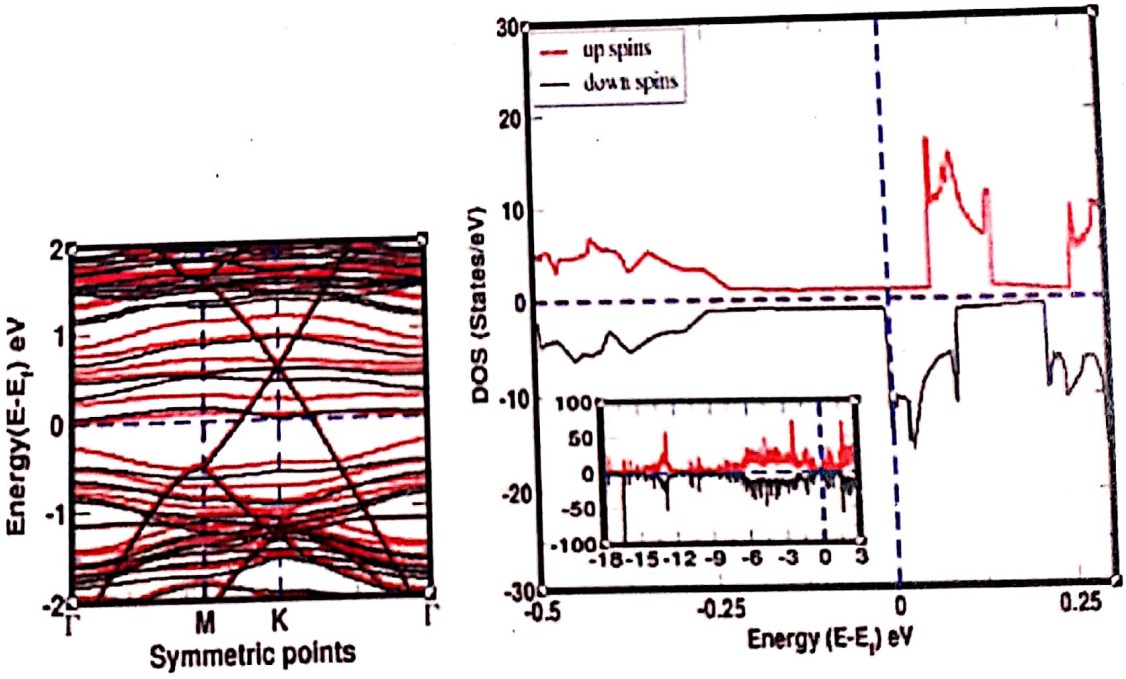

(a) (b)

Fig. 7. (a) Band structure of up and down spin states of 3S–(HS)G/MoS_2 material, where red color of bands represent up spin states and black color of bands represent down spin states, (b) DoS of up and down spin states of electrons in 3S–(HS)G/MoS_2 material, (c) PDoS of individual up and down spins states of electrons in the orbital of C, Mo and S atoms in 3S–(HS)G/MoS_2 material, (d) PDoS of total up and down spin states of electrons in the orbital of C, Mo and S atoms in 3S–(HS)G/MoS_2 material. In band structure horizontal dotted line represents Fermi level, and in DoS/PDoS plots, vertical dotted line represents Fermi level. In all DoS and PDoS, insets represent the plots of total up and total down spins.

Scanned with CamScanner

Int. J. Comp. Mat. Sci. Eng. 2021.10. Downloaded from www.worldscientific.com
by UNIVERSITA' DEGLI STUDI DI BRESCIA on 06/02/22. Re-use and distribution is strictly not permitted, except for Open Access articles.

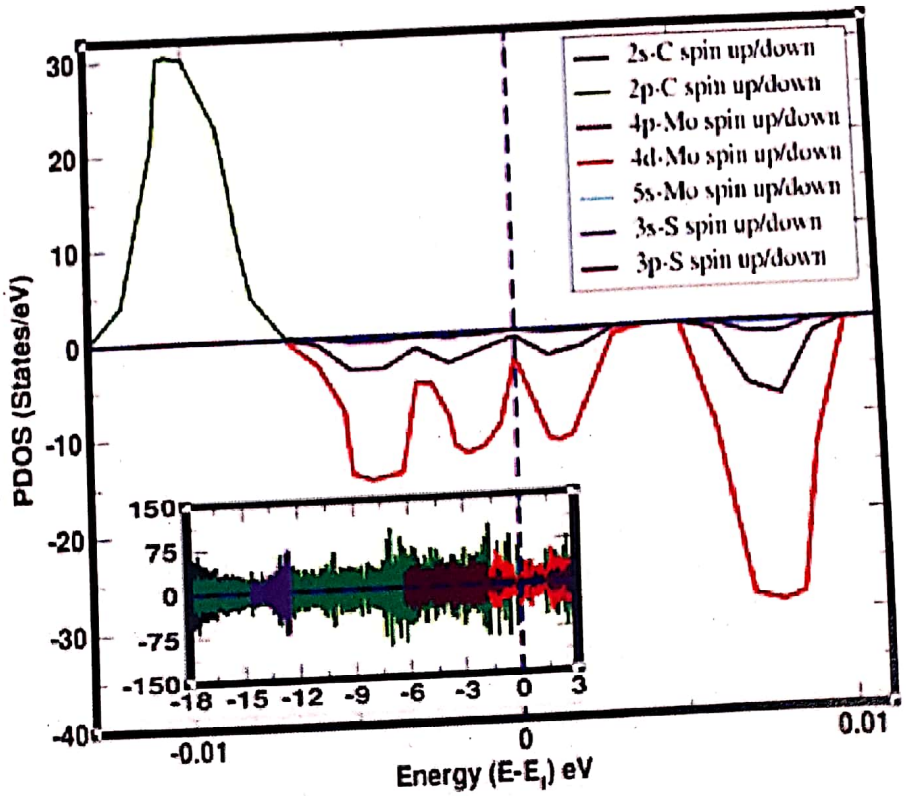

(c)

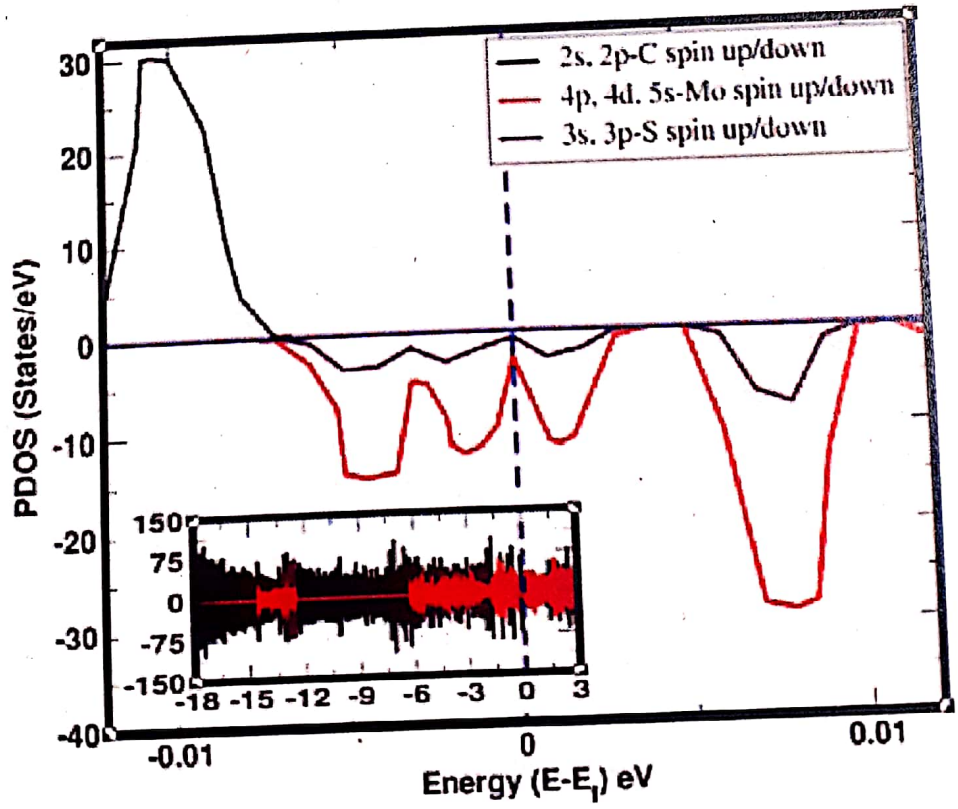

(d)

Fig. 7. (*Continued*)

Scanned with CamScanner

Int. J. Comp. Mat. Sci. Eng. 2021.10. Downloaded from www.worldscientific.com
by UNIVERSITA' DEGLI STUDI DI BRESCIA on 06/02/22. Re-use and distribution is strictly not permitted, except for Open Access articles.

Table 2. Fermi energy (E_f), Fermi energy shift towards valence band (E_s–VB), Dirac point (D_p), Dirac point shift in conduction band (D_s–CB), total value of magnetization value (M_T), defects formation energy (E_d) of (HS)G/MoS_2 and S_{atoms}–(HS)G/MoS_2 materials.

(HS)G/MoS_2 and S_{atoms}–(HS)G/MoS_2 materials	(E_f) eV	(E_s–VB) eV	(D_p) eV	(D_s–CB) eV	(E_d) eV	(M_T) μ_B/cell
(HS)G/MoS_2	0.32	—	0.56	—	—	0.00
D1S–(HS)G–MoS_2	0.04	0.28	0.62	0.06	1.24	0.00
U1S–(HS)G/MoS_2	0.04	0.28	0.62	0.06	1.24	0.00
2S–(HS)G/MoS_2	−0.25	0.57	0.64	0.08	2.05	−0.11
3S–(HS)G/MoS_2	−0.36	0.68	0.65	0.09	2.82	−0.29

0.32 eV, it moves towards valence band of range 0.32 eV to −0.36 eV by S sites vacancy defects in (HS)G/MoS_2, as given in Table 2. The materials having n-type Schottky contact are potential candidates in nanoelectronic devices because they will increase the performance of materials in device applications [Pham *et al.*, 2018]. We can also see in Table 2 the values of Fermi energy shift and Dirac point shift are increased with increase in the concentrations of vacancy defects in the materials. The metal/semiconductor materials are characterized by Fermi shift and Dirac shift values; this is because current/electrons flow in the system based on the amplitude of Dirac shift value.

The magnetic properties of (HS)G/MoS_2 and S_{atoms}–(HS)G/MoS_2 materials are studied by DoS and PDoS analysis. The DoS and PDoS plots of up and down spin states of electrons in the orbital of atoms in (HS)G/MoS_2, D1S–(HS)G/MoS_2, U1S–(HS)G/MoS_2, 2S–(HS)G/MoS_2 and 3S–(HS)G/MoS_2 materials are shown in Figs. 3(b) and 3(c), 4(b)–4(d), 5(b)–5(d), 6(b)–6(d), and 7(b)–7(d), respectively, where the states above the horizontal line represent up spins electrons and states below the horizontal line represents down spins electrons. Also, we have taken large energy range along x-axis (i.e., −18 eV to +3 eV) in insets of DoS/PDoS plots because sometimes we need to know the contributions of spin states in all orbitals of individual atoms in the magnetic properties of the given system.

3.3. *Magnetic properties*

The magnetic and non-magnetic materials are investigated by the analysis of distributed spins of electrons in DoS and PDoS. The asymmetrically and symmetrically distributed up and down spins states of electrons in the orbital of atoms in DoS and PDoS means, materials have magnetic and non-magnetic properties, respectively. Therefore, the magnetic moment (magnetic properties) of materials can be calculated by DoS and PDoS analysis. If the values of DoS have zero or high, there will be no or many states available for occupation. PDoS calculations are used to understand the magnetic moment generated by up and down spins of electrons in the orbital of atoms present in materials. In this work, we have calculated the DoS and PDoS of (HS)G/MoS_2, D1S–(HS)G/MoS_2, U1S–(HS)G/MoS_2, 2S–(HS)G/MoS_2

Scanned with CamScanner

Int. J. Comp. Mat. Sci. Eng. 2021.10. Downloaded from www.worldscientific.com
by UNIVERSITA' DEGLI STUDI DI BRESCIA on 06/02/22. Re-use and distribution is strictly not permitted, except for Open Access articles.

and 3S–(HS)G/MoS_2 materials. It is found that DoS and PDoS of up spins and down spins of electrons in (HS)G/MoS_2 material are symmetrically distributed, as shown in Fig. 3, which means (HS)G/MoS_2 has non-magnetic properties.

In addition, we have calculated DoS and PDoS of D1S–(HS)G/MoS_2, U1S–(HS)G/MoS_2, 2S–(HS)G/MoS_2 and 3S–(HS)G/MoS_2 materials, as shown in Figs. 4–7, respectively. We found that symmetrically distributed DoS and PDoS of up and down spin states of electrons in the orbitals of atoms present in D1S–(HS)G/MoS_2 and U1S–(HS)G/MoS_2 materials. Hence, these materials have non-magnetic properties. The DoS and PDoS of up and down spins states of electrons near the Fermi level are asymmetrically distributed in 2S–(HS)G/MoS_2 and 3S–(HS)G/MoS_2 materials, as shown in Figs. 6(b)–6(d) and 7(b)–7(d), respectively. This is because electron's spins degeneracy of the bands due to S atoms vacancy defects, bands is broken and split. As a result, 2S–(HS)G/MoS_2 and 3S–(HS)G/MoS_2 materials carry magnetic properties. We found that total value of magnetic moment of these materials is $-0.11\,\mu_B$/cell and $-0.29\,\mu_B$/cell, respectively. Therefore, the non-magnetic (HS)G/MoS_2 material changes to magnetic 2S–(HS)G/MoS_2 and 3S–(HS)G/MoS_2 materials due to 2S and 3S atoms vacancy defects, respectively, in (HS)G/MoS_2. The values of magnetic moment of (HS)G/MoS_2, D1S–(HS)G/MoS_2, U1S–(HS)G/MoS_2, 2S–(HS)G/MoS_2 and 3S–(HS)G/MoS_2 materials are given in Table 3.

The PDoS plots of 2s and 2p orbitals of C atoms; 4p, 4d and 5s orbitals of Mo atoms; and 3s and 3p orbital of S atoms in D1S–(HS)G/MoS_2 and U1S–(HS)G/MoS_2 materials are shown in Figs. 4(c) and 4(d) and 5(c) and 5(d), respectively, where symmetrically distributed up and down spin states appear near the Fermi energy level. This means, unoccupied spin states are available there. Magnetic moments given by 2s and 2p orbitals of C atoms; 4p, 4d and 5s orbitals of Mo atoms; and 3s and 3p orbital of S atoms have value $0.00\,\mu_B$/cell in the systems. Total magnetic moment is obtained by calculating net magnetic moment given by up spins and down spin states of electrons in the orbitals of atoms in the materials. We found that magnetic moments given by total up spins and total down spins of electrons in all orbitals of C, Mo, S atoms in D1S–(HS)G/MoS_2 material are $63.15\,\mu_B$/cell and $63.15\,\mu_B$/cell; $64.88\,\mu_B$/cell and $64.88\,\mu_B$/cell; $48.63\,\mu_B$/cell and $48.63\,\mu_B$/cell. And in U1S–(HS)G/MoS_2 material are $63.15\,\mu_B$/cell and $63.15\,\mu_B$/cell; $64.86\,\mu_B$/cell and $64.87\,\mu_B$/cell; $48.64\,\mu_B$/cell and $48.64\,\mu_B$/cell, respectively. Therefore, total magnetic moment of D1S–(HS)G/MoS_2 and U1S–(HS)G/MoS_2 materials has values $0.00\,\mu_B$/cell and $-0.01\,\mu_B$/cell (i.e., $\approx 0.00\,\mu_B$/cell), respectively. Hence, D1S–(HS)G/MoS_2 and U1S–(HS)G/MoS_2 materials have non-magnetic properties.

Similarly, we have calculated the values of magnetic moments given by spins of electrons in 2s and 2p orbitals of C atoms; 4p, 4d and 5s orbitals of Mo atoms, and 3s and 3p orbitals of S atoms are $0.00\,\mu_B$/cell and $0.00\,\mu_B$/cell; $0.00\,\mu_B$/cell, $-0.10\,\mu_B$/cell and $0.00\,\mu_B$/cell, and $0.00\,\mu_B$/cell and $-0.01\,\mu_B$/cell, respectively, in 2S–(HS)G/MoS_2 material. Hence, total value of magnetic moment in 2S–(HS)G/MoS_2 material is $-0.11\,\mu_B$/cell. Also, we have calculated the magnetic moment given by

Scanned with CamScanner

Int. J. Comp. Mat. Sci. Eng. 2021.10. Downloaded from www.worldscientific.com
by UNIVERSITA` DEGLI STUDI DI BRESCIA on 06/02/22. Re-use and distribution is strictly not permitted, except for Open Access articles.

Table 3. The calculated values of magnetic moment (μ) of (HS)G/MoS_2, D1S-(HS)G/MoS_2, U1S-(HS)G/MoS_2, 2S-(HS)G/MoS_2 and 3S-(HS)G/MoS_2 materials due to the distribution of up and down spin states of electrons in the orbital of C, Mo and S atoms in PDoS of the materials.

Magnetic moment given by PDoS of up and down spins states of electrons in the orbitals of C, Mo and S atoms present in (HS)G/MoS_2 and S_{atoms}-(HS)G/MoS_2 materials	3S-(HS)G/MoS_2 (μ_B/cell)	2S-(HS)G/MoS_2 (μ_B/cell)	U1S-(HS)G/MoS_2 (μ_B/cell)	D1S-(HS)G/MoS_2 (μ_B/cell)	(HS)G/MoS_2 (μ_B/cell)
Net μ-due to total spins of electrons in the orbitals of C atoms	−0.04	0.00	0.00	0.00	0.00
Net μ-due to total spins of electrons in the orbitals of Mo atoms	−0.19	−0.10	−0.01	0.00	0.00
Net μ-due to total spins of electrons in the orbitals of S atoms	−0.06	−0.01	0.00	0.00	0.00
μ-due to total up spins in s, p orbitals of C atoms	63.12	63.13	63.15	63.15	63.25
μ-due to total down spins in s, p orbitals of C atoms	63.16	63.13	63.15	63.15	63.25
μ-due to total up spins in s, p, d orbitals of Mo atoms	64.62	64.71	64.86	64.88	64.89
μ-due to total down spins in s, p, d orbitals of Mo atoms	64.81	64.81	64.87	64.88	64.89
μ-due to total up spins in s, p orbitals of S atoms	42.86	45.76	48.64	48.63	51.52
μ-due to total down spins in s, p orbitals of S atoms	42.92	45.77	48.64	48.63	51.52
μ-due to 2s orbital of C atoms	0.00	0.00	0.00	0.00	0.00
μ-due to 2p orbital of C atoms	−0.04	0.00	0.00	0.00	0.00
μ-due to 4p orbital of Mo atoms	0.00	0.00	0.00	0.00	0.00
μ-due to 4d orbital of Mo atoms	−0.18	−0.10	−0.01	0.00	0.00
μ-due to 5s orbital of Mo atoms	−0.01	0.00	0.00	0.00	0.00
μ-due to 3p orbital of S atoms	−0.05	−0.01	0.00	0.00	0.00
μ-due to 3s orbital of S atoms	−0.01	0.00	0.00	0.00	0.00
Total magnetic moment (M_T)	−0.29	−0.11	$-0.01 \approx 0.00$	0.00	0.00

Scanned with CamScanner

Int. J. Comp. Mat. Sci. Eng. 2021.10. Downloaded from www.worldscientific.com
by UNIVERSITA' DEGLI STUDI DI BRESCIA on 06/02/22. Re-use and distribution is strictly not permitted, except for Open Access articles.

spins states of electrons in 2s and 2p orbitals of C atoms have values $0.00\,\mu_B$/cell and $-0.04\,\mu_B$/cell; 4p, 4d and 5s orbitals of Mo atoms have values $0.00\,\mu_B$/cell, $-0.18\,\mu_B$/cell and $-0.01\,\mu_B$/cell; and 3s and 3p orbitals of S atoms have values $-0.01\,\mu_B$/cell and $-0.05\,\mu_B$/cell, respectively, in 3S–(HS)G/MoS_2 material. Thus, total value of magnetic moment in 3S–(HS)G/MoS_2 material is $-0.29\,\mu_B$/cell. From above calculations, we found that 4d orbital of Mo atoms, 3p orbital of S atoms and 2p orbital of C atoms have dominant contributions for the magnetism in 2S–(HS)G/MoS_2 and 3S–(HS)G/MoS_2 materials. Therefore, they seem to be promising in usage in various devices requiring magnetic properties. On the other hand, we have calculated the magnetic moment obtained by total up spins and total down spins of electrons in s and p orbitals of C atoms; s, p and d orbitals of Mo atoms; ands and p orbitals of S atoms in 2S–(HS)G/MoS_2 and 3S–(HS)G/MoS_2 materials are given in Table 3.

Furthermore, we have calculated magnetic moments near to the vacancy defects in S_{atoms}–(HS)G/MoS_2 materials. Unpaired up and down spins states are established near to defects by 3S vacancy atoms in 3S–(HS)G/MoS_2 and 2S vacancy atoms in 2S–(HS)G/MoS_2 materials. They created magnetic moment of values $-0.04\,\mu_B$/cell, $-0.19\,\mu_B$/cell and $-0.06\,\mu_B$/cell, respectively, with C, Mo and S atoms in 3S–(HS)G/MoS_2 material, and $0.00\,\mu_B$/cell, $-0.10\,\mu_B$/cell and $-0.01\,\mu_B$/cell, respectively, with C, Mo and S atoms in 2S–(HS)G/MoS_2 material. Similarly, lower 1S and upper 1S vacancy atoms in D1S–(HS)G/MoS_2 and U1S–(HS)G/MoS_2 materials developed unpaired up and down spins states near to the defects. They created $0.00\,\mu_B$/cell value of net magnetic moment with C, Mo and S atoms in D1S–(HS)G/MoS_2, and $-0.01\,\mu_B$/cell value of net magnetic moment with C, Mo and S atoms in U1S–(HS)G/MoS_2. Hence, 2S–(HS)G/MoS_2 and 3S–(HS)G/MoS_2 have magnetic properties and D1S–(HS)G/MoS_2 and U1S–(HS)G/MoS_2 have non-magnetic properties.

4. Conclusions and Concluding Remarks

In summary, we studied the geometrical structures, electronic and magnetic properties of (HS)G/MoS_2, D1S–(HS)G/MoS_2, U1S–(HS)G/MoS_2, 2S–(HS)G/MoS_2 and 3S–(HS)G/MoS_2 materials by first-principles calculations based on spin-polarized Density Functional Theory (DFT) method within vdW corrections (DFT-D2) approach. Structures are optimized and relaxed by BFGS method using computational tool Quantum ESPRESSO package. First, we studied structural properties and found that all structures mentioned above are stable. For electronic properties, we have calculated band structures, and found that Fermi energy of (HS)G/MoS_2, D1S–(HS)G/MoS_2, U1S–(HS)G/MoS_2, 2S–(HS)G/MoS_2 and 3S–(HS)G/MoS_2 have values 0.32 eV, 0.04 eV, 0.04 eV, −0.25 eV and −0.36 eV, respectively, which means Fermi level shifts towards the valence band in 1S, 2S and 3S vacancy defects (HS)G/MoS_2 materials. Therefore, they have n-type Schottky contact. Dirac cone in (HS)G/MoS_2, D1S–(HS)G/MoS_2, U1S–(HS)G/MoS_2, 2S–(HS)G/MoS_2 and

Scanned with CamScanner

Int. J. Comp. Mat. Sci. Eng. 2021.10. Downloaded from www.worldscientific.com
by UNIVERSITA' DEGLI STUDI DI BRESCIA on 06/02/22. Re-use and distribution is strictly not permitted, except for Open Access articles.

3S–(HS)G/MoS_2 materials is formed at 0.56, 0.62, 0.62, 0.64 and 0.65 eV height, respectively, from the Fermi energy level, which indicates that they have metallic properties. From the analysis of DoS and PDoS calculations, we found that DoS and PDoS of up and down spin states of electrons in the orbitals of atoms are symmetrically distributed in (HS)G–MoS_2, D1S–(HS)G/MoS_2 and U1S–(HS)G/MoS_2 materials, and asymmetrically distributed in 2S–(HS)G/MoS_2 and 3S–(HS)G/MoS_2 materials. Hence, (HS)G MoS_2, D1S (HS)G/MoS_2 and U1S (HS)G/MoS_2 are non-magnetic, and 2S–(HS)G/MoS_2 and 3S–(HS)G/MoS_2 are magnetic materials. Therefore, non-magnetic (HS)G–MoS_2 changes to magnetic 2S–(HS)G/MoS_2 and 3S–(HS)G/MoS_2 materials due to 2S and 3S atoms vacancy defects, respectively. Also, we found that total values of magnetic moment of 2S–(HS)G/MoS_2 and 3S–(HS)G/MoS_2 materials are $-0.11\,\mu_B$/cell and $-0.29\,\mu_B$/cell, respectively, and spins of 2p orbital of C atoms, 3p orbital of S atoms and 4d orbital of Mo atoms have leading contributions for producing magnetic moment in these materials.

Acknowledgments

HKN acknowledges the UGC Nepal Award no. PhD-75/76-S&T-09. NPA acknowledges network project NT-14 of ICTP/OEA and UGC Nepal grants CRG-73/74-S&T-01.

References

Ahmad, S. and Mukherjee, S. [2014] "A comparative study of electronic properties of bulk MoS_2 and its monolayer using DFT technique: Application of mechanical strain on MoS_2 monolayer," *Graphene* **3**, 52–59.

Castro, E. V., Novoselov, K. S., Morozov, S. V., Peres, N. M. R., Dos Santos, J. L., Nilsson, J. and Neto, A. C. [2007] "Biased bilayer graphene: Semiconductor with a gap tunable by the electric field effect," *Phys. Rev. Lett.* **99**(21), 216802.

Chen, H., Zhao, J., Huang, J. and Liang, Y. [2019] "Computational understanding of the structural and electronic properties of the GeS–graphene contact," *Phys. Chem. Chem. Phys.* **21**(14), 7447–7453.

Chen, W., Santos, E. J., Zhu, W., Kaxiras, E. and Zhang, Z. [2013] "Tuning the electronic and chemical properties of monolayer MoS_2 adsorbed on transition metal substrates," *Nano Lett.* **13**(2), 509–514.

Choi, M. S., Lee, G. H., Yu, Y. J., Lee, D. Y., Lee, S. H., Kim, P. and Yoo, W. J. [2013] "Controlled charge trapping by molybdenum disulphide and graphene in ultra-thin hetero structured memory devices," *Nat. Commun.* **4**(1), 1–7.

Debbichi, L., Eriksson, O. and Lebègue, S. [2014] "Electronic structure of two-dimensional transition metal dichalcogenide bilayers from ab initio theory," *Phys. Rev. B* **89**(20), 205311.

Din, H. U., Idrees, M., Albar, A., Shafiq, M., Ahmad, I., Nguyen, C. V. and Amin, B. [2019] "Rashba spin splitting and photocatalytic properties of GeC–MSSe (M = Mo, W) van der Waals heterostructures," *Phys. Rev. B* **100**(16), 165425.

Ghorbani-Asl, M., Bristowe, P. D., Koziol, K., Heine, T. and Kuc, A. [2016] "Effect of compression on the electronic, optical and transport properties of MoS_2/graphene-based junctions," *2D Mater.* **3**(2), 025018.

Scanned with CamScanner

Int. J. Comp. Mat. Sci. Eng. 2021.10. Downloaded from www.worldscientific.com
by UNIVERSITA' DEGLI STUDI DI BRESCIA on 06/02/22. Re-use and distribution is strictly not permitted, except for Open Access articles.

Giannozzi, P., Baroni, S., Bonini, N., Calandra, M., Car, R., Cavazzoni, C. and Dal Corso, A. [2009] "QUANTUM ESPRESSO: Modular and open-source software Project for quantum simulations of materials," *J. Phys. Condens. Matter* **21**(39), 395502.

Grimme, S. [2004] "Accurate description of van der Waals complexes by density functional theory including empirical corrections," *J. Comput. Chem.* **25**(12), 1463–1473.

Hohenberg, P. and Kohn, W. [1964] "Inhomogeneous electron gas," *Phys. Rev.* **136**(3B), B864.

Hou, Z., Wang, X., Ikeda, T., Terakura, K., Oshima, M., Kakimoto, M. A. and Miyata, S. [2012] "Interplay between nitrogen dopants and native point defects in graphene," *Phys. Rev. B* **85**(16), 165439.

Hu, W., Wang, T., Zhang, R. and Yang, J. [2016] "Effects of interlayer coupling and electric fields on the electronic structures of graphene and MoS_2 heterobilayers," *J. Mater. Chem. C* **4**(9), 1776–1781.

Hu, Y., Ruan, M., Guo, Z., Dong, R., Palmer, J., Hankinson, J. and De Heer, W. A. [2012] "Structured epitaxial graphene: Growth and properties," *J. Phys. D: Appl. Phys.* **45**(15), 154010.

Kadantsev, E. S. and Hawrylak, P. [2012] "Electronic structure of a single MoS_2 monolayer," *Solid State Commun.* **152**(10), 909–913.

Karki, D. B. and Adhikari, N. P. [2014] "First-principles study of the stability of graphene and adsorption of halogen atoms (F, Cl and Br) on hydrogen passivated graphene," *Int. J. Mod. Phys. B* **28**(21), 1450141.

Kittel, C., McEuen, P. and McEuen, P. [1996] *Introduction to Solid State Physics*, Vol. 8. (Wiley, New York), pp. 140–303

Liu, B., Wu, L. J., Zhao, Y. Q., Wang, L. Z. and Cai, M. Q. [2016] "First-principles investigation of the Schottky contact for the two-dimensional MoS_2 and graphene heterostructure," *RSC Adv.* **6**(65), 60271–60276.

Ma, Y., Dai, Y., Guo, M., Niu, C. and Huang, B. [2011] "Graphene adhesion on MoS_2 monolayer: An ab initio study," *Nanoscale* **3**(9), 3883–3887.

Mak, K. F., Lee, C., Hone, J., Shan, J. and Heinz, T. F. [2010] "Atomically thin MoS_2: A new direct-gap semiconductor," *Phys. Rev. Lett.* **105**(13), 136805.

Makarova, M. V., Akaishi, Y., Ikarashi, T., Rao, K. S., Yoshimura, S. and Saito, H. [2019] "Alternating magnetic force microscopy: Effect of Si doping on the temporal performance degradation of amorphous FeCoB magnetic tips," *J. Magn. Magn. Mater.* **471**, 209–214.

Martin, R. M. [2020] *Electronic Structure: Basic Theory and Practical Methods* (Cambridge University Press, Cambridge).

Marzari, N., Vanderbilt, D., De Vita, A. and Payne, M. C. [1999] "Thermal contraction and disordering of the Al (110) surface," *Phys. Rev. Lett.* **82**(16), 3296.

Neupane, H. K. and Adhikari, N. P. [2020] "Structure, electronic and magnetic properties of 2D graphene-molybdenum di sulphide (G-MoS2) heterostructure (HS) with vacancy defects at Mo sites," *Comput. Condens. Matter* **24**, e00489.

Neupane, H. K. and Adhikari, N. P. [2020] "Tuning structural, electronic, and magnetic properties of C sites vacancy defects in graphene/MoS_2 van der Waals heterostructure materials: A first-principles study," *Adv. Condens. Matter Phys.* **2020**, 8850701.

Neupane, H. K. and Adhikari, N. P. [2021] "First-principles study of structure, electronic, and magnetic properties of C sites vacancy defects in water adsorbed graphene/MoS_2 van der Waals heterostructures," *J. Mol. Model.* **27**(3), 1–12.

Scanned with CamScanner

Int. J. Comp. Mat. Sci. Eng. 2021.10. Downloaded from www.worldscientific.com
by UNIVERSITA' DEGLI STUDI DI BRESCIA on 06/02/22. Re-use and distribution is strictly not permitted, except for Open Access articles.

Nguyen, C. V. [2018] "Tuning the electronic properties and Schottky barrier height of the vertical graphene/MoS_2 heterostructure by an electric gating," *Superlattices Microstruct.* **116**, 79–87.

Nguyen, C. V., Idrees, M., Phuc, H. V., Hieu, N. N., Binh, N. T., Amin, B. and Vu, T. V. [2020] "Interlayer coupling and electric field controllable Schottky barriers and contact types in graphene/PbI_2 heterostructures," *Phys. Rev. B* **101**(23), 235419.

Novoselov, K. S., Geim, A. K., Morozov, S. V., Jiang, D., Zhang, Y., Dubonos, S. V. and Firsov, A. A. [2004] "Electric field effect in atomically thin carbon films," *Science* **306**(5696), 666–669.

Oli, B. D., Bhattarai, C., Nepal, B. and Adhikari, N. P. [2013] "First-principles study of adsorption of alkali metals (Li, Na, K) on graphene," in *Advanced Nanomaterials and Nanotechnology*, pp. 515–529. Springer, Berlin, Heidelberg.

Pack, J. D. and Monkhorst, H. J. [1977] "Special points for Brillouin-zone integrations a reply," *Phys. Rev. B* **16**(4), 1748.

Peng, H. X., Qin, F. and Phan, M. H. [2016] *Ferromagnetic Microwire Composites: From Sensors to Microwave Applications* (Springer, New York).

Perdew, J. P., Burke, K. and Ernzerhof, M. [1996] "Generalized gradient approximation made simple," *Phys. Rev. Lett.* **77**(18), 3865.

Pfrommer, B. G., Côté, M., Louie, S. G. and Cohen, M. L. [1997] "Relaxation of Crystals with the quasi-Newton method," *J. Comput. Phys.* **131**(1), 233–240.

Pham, K. D., Hieu, N. N., Phuc, H. V., Fedorov, I. A., Duque, C. A., Amin, B. and Nguyen, C. V. [2018] "Layered graphene/GaS van der Waals heterostructure: Controlling the electronic properties and Schottky barrier by vertical strain," *Appl. Phys. Lett.* **113**(17), 171605.

Phan, A. D., Viet, N. A., Poklonski, N. A., Woods, L. M. and Le, C. H. [2012] "Interaction of a graphene sheet with a ferromagnetic metal plate," *Phys. Rev. B* **86**(15), 155419.

Phuc, H. V., Hieu, N. N., Hoi, B. D., Phuong, L. T. and Nguyen, C. V. [2018] "First principle study on the electronic properties and Schottky contact of graphene adsorbed on MoS_2 monolayer under applied out-plane strain," *Surf. Sci.* **668**, 23–28.

Pierucci, D., Henck, H., Avila, J., Balan, A., Naylor, C. H., Patriarche, G. and Asensio, M. C. [2016] "Band alignment and minigaps in monolayer MoS_2-graphene van der Waals heterostructures," *Nano Lett.* **16**(7), 4054–4061.

Radisavljevic, B., Whitwick, M. B. and Kis, A. [2012] "Small-signal amplifier based on single-layer MoS2," *Appl. Phys. Lett.* **101**(4), 043103.

Roy, K., Padmanabhan, M., Goswami, S., Sai, T. P., Ramalingam, G., Raghavan, S. and Ghosh, A. [2013] "Graphene–MoS_2 hybrid structures for multifunctional photo responsive memory devices," *Nat. Nanotechnol.* **8**(11), 826–830.

Vu, T. V., Hieu, N. V., Phuc, H. V., Hieu, N. N., Bui, H. D., Idrees, M. and Nguyen, C. V. [2020] "Graphene/WSeTe van der Waals heterostructure: Controllable electronic properties and Schottky barrier via interlayer coupling and electric field," *Appl. Surf. Sci.* **507**, 145036.

Wang, J., Ma, F., Liang, W. and Sun, M. [2017] "Electrical properties and applications of graphene, hexagonal boron nitride (h-BN), and graphene/h-BN heterostructures," *Mater. Today Phys.* **2**, 6–34.

Yu, W. J., Li, Z., Zhou, H., Chen, Y., Wang, Y., Huang, Y. and Duan, X. [2013] "Vertically stacked multi-heterostructures of layered materials for logic transistors and complementary inverters," *Nat. Mater.* **12**(3), 246–252.

Zhou, S. Y., Gweon, G. H., Fedorov, A. V., First, P. D., De Heer, W. A., Lee, D. H. and Lanzara, A. [2007] "Substrate-induced bandgap opening in epitaxial graphene," *Nat. Mater.* **6**(10), 770–775.

Scanned with CamScanner

Journal of Molecular Modeling (2021) 27: 82
https://doi.org/10.1007/s00894-021-04690-8

ORIGINAL PAPER

First-principles study of structure, electronic, and magnetic properties of C sites vacancy defects in water adsorbed graphene/MoS_2 van der Waals heterostructures

Hari Krishna Neupane[1,2] · Narayan Prasad Adhikari[2]

Received: 14 September 2020 / Accepted: 20 January 2021 / Published online: 12 February 2021
© The Author(s), under exclusive licence to Springer-Verlag GmbH, DE part of Springer Nature 2021

Abstract

We have studied structure, electronic, and magnetic properties of water adsorbed vdW heterostructure graphene/MoS_2 (w-(HS)G/MoS_2) and its C sites vacancy defects materials (w-$C_{atoms\text{-}vacancy}$-(HS)G/MoS_2) by using a spin polarized density functional theory (DFT) method of calculations within DFT-D2 approach to take in to account of vdW interactions. All the structures are optimized and relaxed by BFGS method using computational tool Quantum ESPRESSO package. By structural analysis, we found that both w-(HS)G/MoS_2 and w-$C_{atoms\text{-}vacancy}$-(HS)G/MoS_2 are stable materials. The stability and compactness of these materials decrease with an increase in their defects concentrations. From band structure calculations, our findings show that w-(HS)G/MoS_2 has a metallic nature, and there is formation of n-type Schottky contact of barrier height 0.42 eV. Also, the left 1C atom vacancy defects in w-(HS)G/MoS_2 (L1C-w-(HS)G/MoS_2) and center 1C atom vacancy defects in w-(HS)G/MoS_2 (C1C-w-(HS)G/MoS_2) materials have no band gap for up and down spin electronic states, indicating that they have also a metallic nature. On the other hand, 2C atom vacancy defects in w-(HS)G/MoS_2 (2C-w-(HS)G/MoS_2) has a small band gap for up spins states and no band gap for down spin electronic states which means that the band structure resembles with half metallic nature. Thus, the endowment of metallic nature decreased with increase in the concentrations of defects in structures. To study the magnetic properties in materials, DOS and PDOS calculations are used, and we found that non-magnetic w-(HS)G/MoS_2 material changes to magnetic in all the three different L1C-w-(HS)G/MoS_2, C1C-w-(HS)G/MoS_2, and 2C-w-(HS)G/MoS_2 materials with vacancy. L1C-w-(HS)G/MoS_2, C1C-w-(HS)G/MoS_2, and 2C-w-(HS)G/MoS_2 have magnetic moments of + 0.21 μ_B/cell, + 0.26 μ_B/cell, and − 2.00 μ_B/cell, respectively. The spins of electrons in 2s and 2p orbitals of C atoms give a principal effect of magnetism in w-$C_{atoms\text{-}vacancy}$-(HS)G/MoS_2 materials.

Keywords DFT · Heterostructures · Vacancy defects · Water adsorbed graphene/MoS_2

Introduction

Two dimensional materials, graphene (G), metal monochalcogenides, transition metal dichalcogenides (TMD), and their heterostructures (HS) have great attraction in device (i.e., electronic and optoelectronic devices) applications owing to their excellent physical properties [1–6]. Graphene, a sp^2 hybridized single sheet of carbon atoms organized in a honeycomb lattice, is a zero band gap semiconductor [1]. This emerging material has been the subject of recent intensive research due to the novelty of its structural, electronic, optical, mechanical, and magnetic properties [7–11]. Due to these properties, graphene is a favorable material for the fabrication of electronic devices, transparent electrodes, and spintronics devices [12–14], and a growing array of several other applications that explore the potential of this marvelous material. However, the lack of intrinsic band gap and non-magnetic nature of graphene limits its practical applications in widely expanding field of carbon-based devices. On the other hand, the transition metal dichalcogenides material (TMD)-molybdenum disulphide (MoS_2) has a band gap energy of 1.80 eV [15]. It is a promising material in the field of nanoelectronics and optoelectronics because it has very

✉ Narayan Prasad Adhikari
narayan.adhikari@cdp.tu.edu.np

[1] Amrit Campus, Institute of Science and Technology Tribhuvan University, Kathmandu, Nepal

[2] Central Department of Physics, Institute of Science and Technology Tribhuvan University, Kathmandu, Nepal

sensitive physical properties such as high carrier mobility at room temperature (200 cm^2/Vs), strain, electric field, pressure, and high on/off current ratio of 10^8 [16–19]. The graphene-based heterostructure material G/MoS_2 is formed by using graphene bonds on MoS_2 with weak van der Waals (vdW) interactions. Its different stacking configurations give more new properties beyond their single components because vdW (HS) G/MoS_2 has new and desired physical properties such as carrier mobility and band gap [20–22] than individual components. Thus, (HS) G/MoS_2 is a potential candidate for high speed nanoelectronic and optoelectronic devices. The magnetic properties of materials are great attractive properties, because magnetic materials are used in the fields of biomedicine, molecular biology, biochemistry, diagnosis, catalysis, nanoelectronic devices, and various other industrial applications such as magnetic seals in motors, magnetic sensors, magnetic inks, electrical power generator and transformers, magnetic recording media, and computers [23, 24].

The adsorption of new materials in heterostructure materials tunes more desirable properties than heterostructure materials only. In this work, we investigated the structure, electronic, and magnetic properties of water adsorbed, graphene/MoS_2 heterostructure (w-(HS)G/MoS_2), and its C sites vacancy defects graphene/MoS_2 heterostructure (w-$C_{atoms\text{-}vacancy}$-(HS)G/MoS_2) materials by first-principles calculations using the spin polarized density functional theory within DFT-D2 approximations to consider the vdW corrections.

The rest part of the paper is organized as follows. In Section 2, we discuss details of computational methods. The results and their interpretations are given in Section 3. We closed the paper with main conclusions and outlook of the present work in Section 4.

Computational details

The calculations of structural, electronic, and magnetic properties of w-(HS)G/MoS_2 and w-$C_{atoms\text{-}vacancy}$ (HS)G/MoS_2 have been performed by using the spin polarized density functional theory (DFT) [25], as implemented in a computational package Quantum ESPRESSO (QE) [26]. All electrons in the systems are treated by the generalized gradient approximation (GGA) using Perdew-Burke-Ernzerhof (PBE) [27], with vdW corrections DFT-D2 method [28]. The Rappe-Rabe-Kaxiras-Joannopoulos (RRJK) model of ultra-soft pseudo-potential is used to incorporate the activity of valence electrons in all the calculations. Figures 1a and b and 2a to c show the optimized and relaxed, stable (HS)G/MoS_2, w-(HS)G/MoS_2, and w-$C_{atoms\text{-}vacancy}$-(HS)G/MoS_2 structures respectively. They are prepared under the Broyden-Fletcher-Goldfarb-Shanno (BFGS) scheme [29], until the total energy changes between two consecutive self-consistent field (SCF) steps which is less than 10^{-4} Ry and each component of force acting is less than 10^{-3} Ry/Bohrs. From the convergence test, we determined a k-mesh of (4 × 4 × 1), which is used to calculate the self-consistent total energy. Also, we used kinetic energy cut-off value (35 Ry) and charge density cut-off value (350 Ry) for the expansion of ground state electronic wave function. A vacuum of 20 Å thickness is employed to ensure no unphysical interactions in the stacking direction of (HS)G/MoS2. Moreover, we used the Marzari-Vanderbilt (MV) [30] method of "smearing" with having a width of 0.001 Ry. Also, we have chosen "david" diagonalization method with "plain" mixing mode and mixing factor of 0.6 for self-consistency. We used spin polarized calculations for magnetic properties of the systems. The meshes of (4 × 4 × 1) k-points are used for electronic band structure, and (8 × 8 × 1) k-points are used for DOS and PDOS calculations, where 100 k-points are used along the high symmetric points connecting the reciprocal space for band structure calculations. (HS)G/MoS_2 is constructed by using (4 × 4) super cell of graphene and (3 × 3) super cell of MoS_2 monolayer with 4.13% lattice mismatch as shown in Fig. 1a.

In the present work, we have prepared the stable w-(HS)G/MoS_2, L1C-w-(HS)G/MoS_2, C1C-w-(HS)G/MoS_2, and 2C-w-(HS)G/MoS_2 structures. w-(HS)G/MoS_2 structure is constructed by adding water molecule in stable optimized and relaxed (HS)G/MoS_2 structure. C sites vacancy defect structures L1C-w-(HS)G/MoS_2, C1C-w-(HS)G/MoS_2, and 2C-w-(HS)G/MoS_2 are constructed by removing L-1C atom, C-1C atom, and 2C atoms (L-1C & C-1C atoms) from the graphene surface of w-(HS)G/MoS_2 structure respectively. Here, 1C and 2C atoms create 3.125% and 6.250% vacancy defects respectively in w-(HS)G/MoS_2 structure containing 32 carbon atoms. Then, these stable structures are relaxed by BFGS method, which are used for further calculations as shown in Fig. 2.

Results and discussion

This section mainly focused on the results and interpretations of geometrical structures and stability, band structure, density of states (DOS), and partial density of states (PDOS) of w-(HS)G/MoS_2 and w-$C_{atoms\text{-}vacancy}$-(HS)G/MoS_2 materials using first-principles calculations including spin polarized DFT method incorporating DFT-D2 approach.

Structural properties

The vertical van der Waals heterostructures G/MoS_2 material is made by (4 × 4) and (3 × 3) super cell structures of graphene and MoS_2 with reasonable (4.13%) lattice mismatch. These super cells are obtained by extending optimized primitive unit cell along *x* and *y* directions. The distance between two nearest carbon atoms (in graphene) and distance between Mo and S

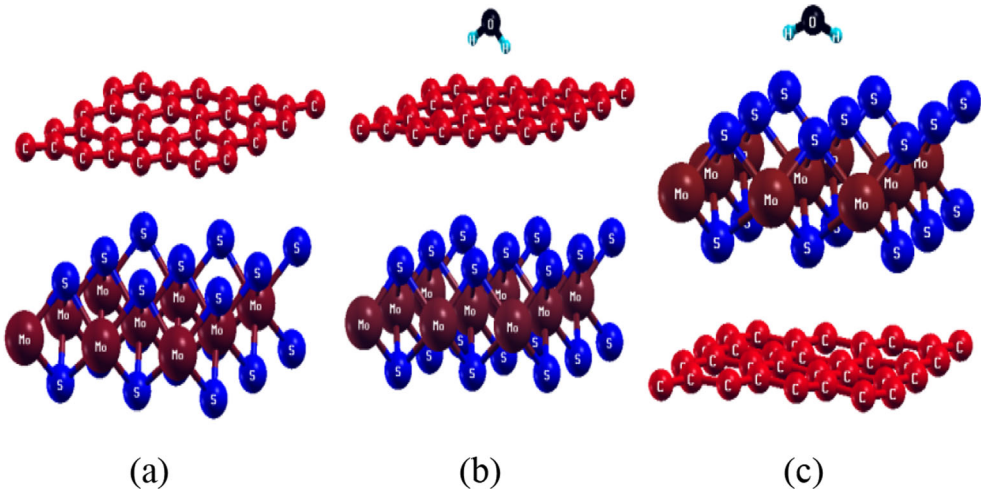

Fig. 1 **a** (HS)G/MoS_2 structure. **b** Water molecule adsorbed on top surface of graphene in MoS_2 base (HS)G/MoS_2 structure. **c** Water molecule adsorbed on top surface of MoS_2 in graphene base (HS)MoS_2/G structure

atoms (in MoS_2) are 1.42 Å and 3.18 Å respectively. These values agree with experimentally reported values 1.42 Å and 3.19 Å [27, 31, 32]. The (HS)G/MoS_2 structure has no dangling bonds present along the external surfaces of the layers of graphene and MoS_2 which therefore show a reduced chemical activity. Physisorption interactions can arise when adsorbing external molecules such as water in this heterostructure. This is evidenced by the adsorption energies we calculated for isolated water physisorption on monolayer graphene (0.12 eV) and MoS_2 (0.13 eV) along with the 2.64 Å distance of the water molecule above the layers. The w-(HS)G/MoS_2 and w-(HS)MoS_2/G structures are prepared by keeping adsorbates' water molecule in a (HS)G/MoS_2 structure at a 2.64 Å distance above the different positions of graphene surface and MoS_2 surface as shown in Fig. **S1** and Fig. **S2** (details of Fig. **S1** and Fig. **S2** are given in the Supplementary information (SI)). The prepared structures are optimized and relaxed using BFGS method [29] and found that water adsorbed on the top surface of graphene (i.e., w-(HS)G/MoS_2) structure (as shown in Fig. 1b) is more stable than water adsorbed on the top surface of MoS_2 (i.e., w-(HS)MoS_2/G) structure. Thus, we used the w-(HS)G/MoS_2 structure for the investigations.

The stability of structures is determined by binding energy calculations. The higher the value of binding energy, the more stable is the system. Thus, the greater value of binding energy material is more favorable for the calculations of its physical properties. The binding energy of w-(HS)G/MoS_2 is calculated by using the following relation:

$$E_b = E_{water} + E_{(HS)G/MoS2} - E_{water} + (HS)G/MoS2 \quad (1)$$

where E_{water}, $E_{(HS)G/MoS2}$, and $E_{water+(HS)G/MoS2}$ represent the ground state energy of a fully relaxed water molecule (H_2O), G/MoS_2 heterostructure, and water adsorbed G/MoS_2 heterostructure material, respectively.

In addition, we have constructed L1C-w-(HS)G/MoS_2, C1C-w-(HS)G/MoS_2, and 2C-w-(HS)G/MoS_2 vacancy defects materials by removing left 1C atom, center 1C atom, and 2C (left 1C and center 1C) atoms respectively from the stable w-(HS)G/MoS_2 structure having defects formation energies 0.20 eV, 0.20 eV, and 0.41 eV. The defects formation energies in our systems are calculated based on the standard formalism [33]:

$$E_f = E_T(\text{defect}) + n_{C_\mu C} - E_T(\text{perfect}) \quad (2)$$

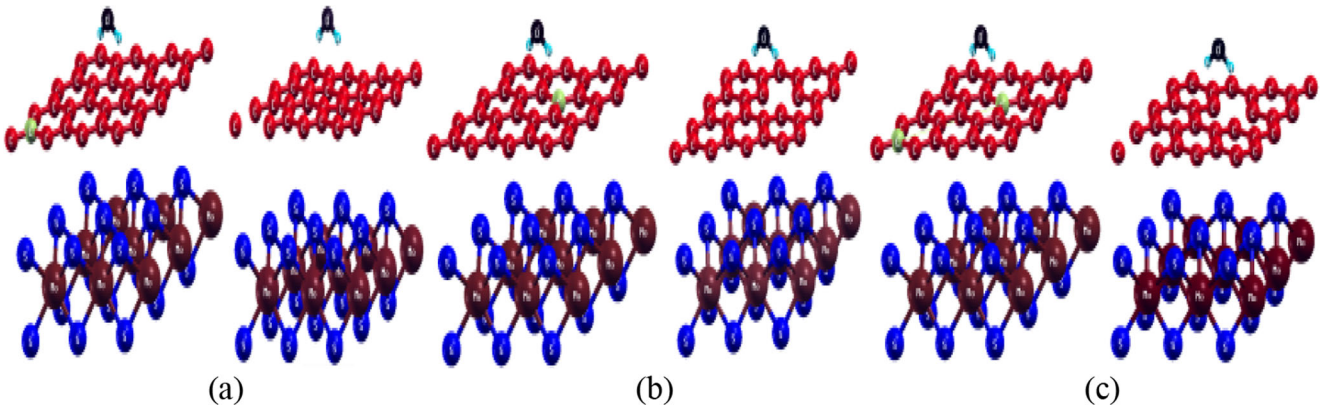

Fig. 2 Optimized and relaxed stable structures of C sites vacancy defects in water adsorbed (HS)G/MoS_2 materials. **a** L1C-w-(HS)G/MoS_2, **b** C1C-w-(HS)G/MoS_2, **c** 2C-w-(HS)G/MoS_2

where E_T (defect) is a total energy of a super cell with the defects, n_C is the numbers of C atoms removed from the perfect super cell to introduce a vacancy, μ_C is the chemical potential of C atom, and E_T(perfect) is the total energy of the neutral perfect super cell. Also, we have analyzed the C sites vacancy defects in water adsorbed at 2.64 Å distance above the different positions of graphene surface of (HS)G/MoS_2 structure (Fig. **S2** in SI) and found that C sites vacancy defects in water adsorbed at 2.64 Å distance above the center position of graphene surface of (HS)G/MoS_2 material are suitable materials for further calculations. These stable L1C-w-(HS)G/MoS_2, C1C-w-(HS)G/MoS_2, and 2C-w-(HS)G/MoS_2 vacancy defects materials are shown in Fig. 2a, b, and c. The order of binding energy of the structures is found to be as w-(HS)G/MoS_2>1C-w-(HS)G/MoS_2>2C-w-(HS)G/MoS_2 which are given in Table 2. The water molecule has stronger intra-atomic bonding in its inert state in w-(HS)G/MoS_2 than in w-$C_{atoms\text{-}vacancy}$-(HS)G/MoS_2. Hence w-(HS)G/MoS_2 material is more stable than C sites vacancy defects w-(HS)G/MoS_2 (w-$C_{atoms\text{-}vacancy}$-(HS)G/MoS_2) materials. The stability of structure is decreased with increase in its defects concentrations.

We have calculated the interlayer distances between the carbon atoms in graphene surface and Mo and upper S and lower S atoms in MoS_2 surface by taking average values along *x*, *y*, and *z* directions. It is possible to take average values, only when the surface of graphene is planar. We have used small size of (4 × 4) super cell structure of graphene in which the value of dihedral angles is found to be 0° (360°). This states that the surface of graphene stays planar even in the defected cases in graphene. The interlayer distance parameters of (HS)G/MoS_2, w-(HS)G/MoS_2, L1C-w-(HS)G/MoS_2, C1C-w-(HS)G/MoS_2, and 2C-w-(HS)G/MoS_2 materials are given in Table 1.

According to the data presented in Table 1, we concluded that w-(HS)G/MoS_2 is more compressed than w-$C_{atoms\text{-}vacancy}$-(HS)G/MoS_2 geometries. The 1C-w-(HS)G/MoS_2 material is more compact than 2C-w-(HS)G/MoS_2 material, and the atoms in w-$C_{atoms\text{-}vacancy}$-(HS)G/MoS_2 structures are slightly extricated than w-(HS)G/MoS_2 structure. Therefore, compactness of materials increases with decrease in its defects concentrations.

Electronic properties

We now explore the electronic properties of w-(HS)G/MoS_2 and w-$C_{atoms\text{-}vacancy}$-(HS)G/MoS_2 materials. As we know, (HS)G/MoS_2 geometry is constructed by combining fully relaxed (4 × 4) super cell structure of graphene and (3 × 3) super cell structure of monolayer MoS_2 with considerable lattice mismatch. It is obvious that (HS)G/MoS_2 is characterized by metal/semiconductor vdW. The Fermi level of vdW, (HS)G/MoS_2 is located in the band gap region of monolayer MoS_2, forming an n-type Schottky barrier contact with the value of 0.56 eV [34], which agrees with the reported value of 0.49 eV [35, 36]. In metal/semiconductor vdW heterostructures, n-type Schottky barrier means the energy difference between Fermi level and conduction band minimum, and p-type Schottky barrier means energy difference between the Fermi level and valence band maximum. Therefore, sum of n-type and p-type Schottky barrier gives energy band gap of semiconductor [37, 38]. The w-(HS)G/MoS_2 structure is prepared by adding water molecule on (HS)G/MoS_2 as shown in Fig. 1b, which is also characterized by metal/semiconductor vdW. The electronic structure of w-(HS)G/MoS_2 depends strongly on the electronic properties of its MoS_2 part. Therefore, it is necessary to investigate Schottky barrier contact by using band structure calculations. For this, 100 k-points are taken along the specific direction of irreducible Brillouin zone to get fine band structure by choosing Γ-M-K-Γ high symmetric points and found n-type Schottky contact of value 0.42 eV as shown in Fig. 3a, where *x*-axis represents high symmetric points in the first Brillouin zone and *y*-axis represents the corresponding energy value. This value is smaller than the experimentally reported (0.49 eV) value [35, 36]. The small Dirac shift amplitude value implies that w-(HS)G/MoS_2 has metallic properties.

Furthermore, w-$C_{atoms\text{-}vacancy}$-(HS)G/MoS_2 materials are constructed by removing L1C, C1C, and 2C atoms respectively from w-(HS)G/MoS_2. The structures after relaxation are shown in Fig. 2. To investigate the electronic properties of L1C-w-(HS)G/MoS_2, C1C-w-(HS)G/MoS_2, and 2C-w-(HS)G/MoS_2 materials, we have analyzed band structures and DOS calculations. In band structures, we have also taken 100 k-points along the specific direction of irreducible Brillouin zone by choosing Γ-M-K-Γ high symmetric points. The few numbers of band states of L1C-w-(HS)G/MoS_2 and C1C-w-(HS)G/MoS_2 are seen around the Fermi level as shown in Figs. 4a and 5a. Also, up and down spins states of electrons are appeared around the Fermi energy level in DOS plots of L1C-w-(HS)G/MoS_2 & C1C-w-(HS)G/MoS_2 materials as shown in Figs. 4(b) and 5(b) respectively. Hence, L1C-w-(HS)G/MoS_2 and C1C-w-(HS)G/MoS_2 materials have metallic properties. The 2C-w-(HS)G/MoS_2 material has an opened small energy band gap for up spin electronic states of value 0.92 eV, and down spins states are appeared around the Fermi level as shown in Fig. 6a and b. Thus, from the band structure and DOS calculations, 2C-w-(HS)G/MoS_2 material shows a half metallic nature. The metallic w-(HS)G/MoS_2 material changes to half metallic 2C-w-(HS)G/MoS_2 material due to 2C vacancy defects. Therefore, the strength of metallic nature of w-(HS)G/MoS_2 material decreases with an increase in its defects concentrations.

We know that electronic configurations of valence electrons in Mo, S, C, O, and H atoms are [Kr] $4d^5$ $5s^1$, [Ne] $3s^2$ $3p^4$, [He] $2s^2$ $2p^2$, [He] $2s^2$ $2p^4$, and $1s^1$ respectively. Each Mo

Table 1 The interlayer distances measurement of vdW, (HS)G/MoS_2, w-(HS)G/MoS_2, and w-$C_{atoms\text{-}vacancy}$(HS)G/MoS_2 materials

Interlayer distances of (HS)G/MoS_2 along *x*, *y*, and *z*-axis	C-Mo		C-US		C-DS	
x-Axis (Å)	0.29		1.88		0.89	
y-Axis (Å)	0.25		1.16		1.17	
z-Axis (Å)	5.88		4.34		7.47	
Interlayer distances of w-(HS)G/MoS_2 along *x*, *y,* and *z*-axis	C-Mo		C-US		C-DS	
x-Axis (Å)	0.26		1.86		0.86	
y-Axis (Å)	0.24		1.14		1.14	
z-Axis (Å)	5.12		3.88		6.91	
Interlayer distances of w-$C_{atoms\text{-}vacancy}$-(HS)G/MoS_2 along *x*, *y,* and *z*-axis	C-Mo		C-US		C-DS	
	2C	1C	2C	1C	2C	1C
x-Axis (Å)	0.28	0.27	1.87	1.87	0.88	0.88
y-Axis (Å)	0.24	0.24	1.16	1.15	1.16	1.15
z-Axis (Å)	5.68	5.38	4.12	3.98	7.24	7.02

These (HS)G/MoS_2, w-(HS)G/MoS_2, and w-$C_{atoms\text{-}vacancy}$(HS)G/MoS_2 represent G/MoS_2 heterostructure, water adsorbed in G/MoS_2 heterostructure, and C sites vacancy defects in water adsorbed G/MoS_2 heterostructure materials respectively. C-Mo, C-US, and C-DS represent the distance between carbon atoms of graphene surface to Mo atoms of MoS_2, carbon atoms of graphene surface to upper S atoms in MoS_2, and carbon atoms of graphene surface to lower S atoms in MoS_2 surface respectively

atom has one unpaired up spin in sub-orbital of 5s orbital, and $4d_{xy}$, $4d_{xz}$, $4d_{yz}$, $4d_{x2\text{-}y2}$, $4d_{z2}$ sub-orbitals of 4d orbital S atom has paired spins (up and down) in $3p_x$ sub-orbital and one unpaired up spin in $3p_y$, $3p_z$ sub-orbital, C atom has single up spin in $2p_x$, $2p_y$ and vacant in $2p_z$ sub-orbital. Similarly, each O atom contains paired spins in $2p_x$ sub-orbital and single unpaired up spin in $2p_y$ and $2p_z$ sub-orbital; H atom has single unpaired up spin in 1s orbital. We prepared L1C-w-(HS)G/MoS_2 and C1C-w-(HS)G/MoS_2 stable structures by pulling out L1C and C1C positions of carbon atoms from w-(HS)G/MoS_2 geometry respectively as shown in Fig. 2a and b. Similarly, 2C-w-(HS)G/MoS_2 stable structure is constructed by eliminating 2C atoms together from w-(HS)G/MoS_2 geometry illustrated in Fig. 2c. L1C position of carbon atom in L1C-w-(HS) G/MoS_2 and C1C position of carbon atom in C1C-w-(HS)G/MoS_2 structures produced unpaired spins in sub-orbital of atoms. Also, 2C vacancy defects atoms developed unpaired spins in sub-orbital of atoms in 2C-w-(HS)G/MoS_2 structure. Due to this, spins arrangement of unpaired up and down spins of electrons in the orbitals of atoms in the defects structures, unequal Fermi energy values are obtained in w-(HS)G/MoS_2 and w-$C_{atoms\text{-}vacancy}$-(HS)G/MoS_2 materials as given in Table 2. The Fermi energy values of w-(HS)G/MoS_2, L1C-w-(HS)G/MoS_2, C1C-w-(HS)G/MoS_2, and 2C-w-(HS)G/MoS_2 materials have values 0.14 eV, 0.23 eV, 0.24 eV, and 0.26 eV respectively. Fermi level shifts upwards by 0.09 eV, 0.10 eV, and 0.12 eV values respectively due to the movement of interfacial charges.

Magnetic properties

The magnetic properties of materials are studied by DOS and PDOS analysis. DOS suggests how densely quantum states are packed in a particular system. High or zero values of DOS means that many or no states are available for occupation. Thus, DOS determines the available states for occupation [39]. The PDOS calculations are used to investigate the magnetic contributions of different orbital of atoms in the system. DOS and PDOS plots of w-(HS)G/MoS_2 and w-$C_{atoms\text{-}vacancy}$-(HS)G/MoS_2, vdW materials are illustrated in Figs. 3(b)-(d), 4(b)-(d), 5(b)-(d), and 6(b)-(d) respectively, where up & down spins states of DOS & PDOS are plotted along y-axis and its corresponding energy values are given in x-axis, also the vertical dotted line represents Fermi energy level and horizontal dotted line separates up & down spins states of electrons in the orbital of all atoms presented in studied materials.

The magnetic and non-magnetic materials are investigated by the analysis of spin distribution in DOS and PDOS plots. The asymmetrically distributed up and down spins of electrons (atoms) in DOS and PDOS plots mean that materials have magnetic properties, and symmetrically distributed up and down spins of electrons in DOS and PDOS plots mean that materials carry non-magnetic properties. We observed that up and down spins states of electrons are symmetrically distributed in DOS and PDOS plots of w-(HS)G/MoS_2 material as shown in Fig. 3b–d. Hence, w-(HS)G/MoS_2 is a non-magnetic material.

In addition, we have carried out the DOS and PDOS analysis of L1C-w-(HS)G/MoS_2, C1C-w-(HS)G/MoS_2, and 2C-w-(HS)G/MoS_2 materials. The PDOS plots of 2s and 2p orbitals of C atoms; 4p, 4d, and 5s orbitals of Mo atoms; 3s and 3p orbitals of S atoms; 2s and 2p orbitals of O atoms; 1s orbital of H atoms; and total spins of electrons in the orbitals of C, Mo, S, O, and H atoms in L1C-w-(HS)G/MoS_2 material are

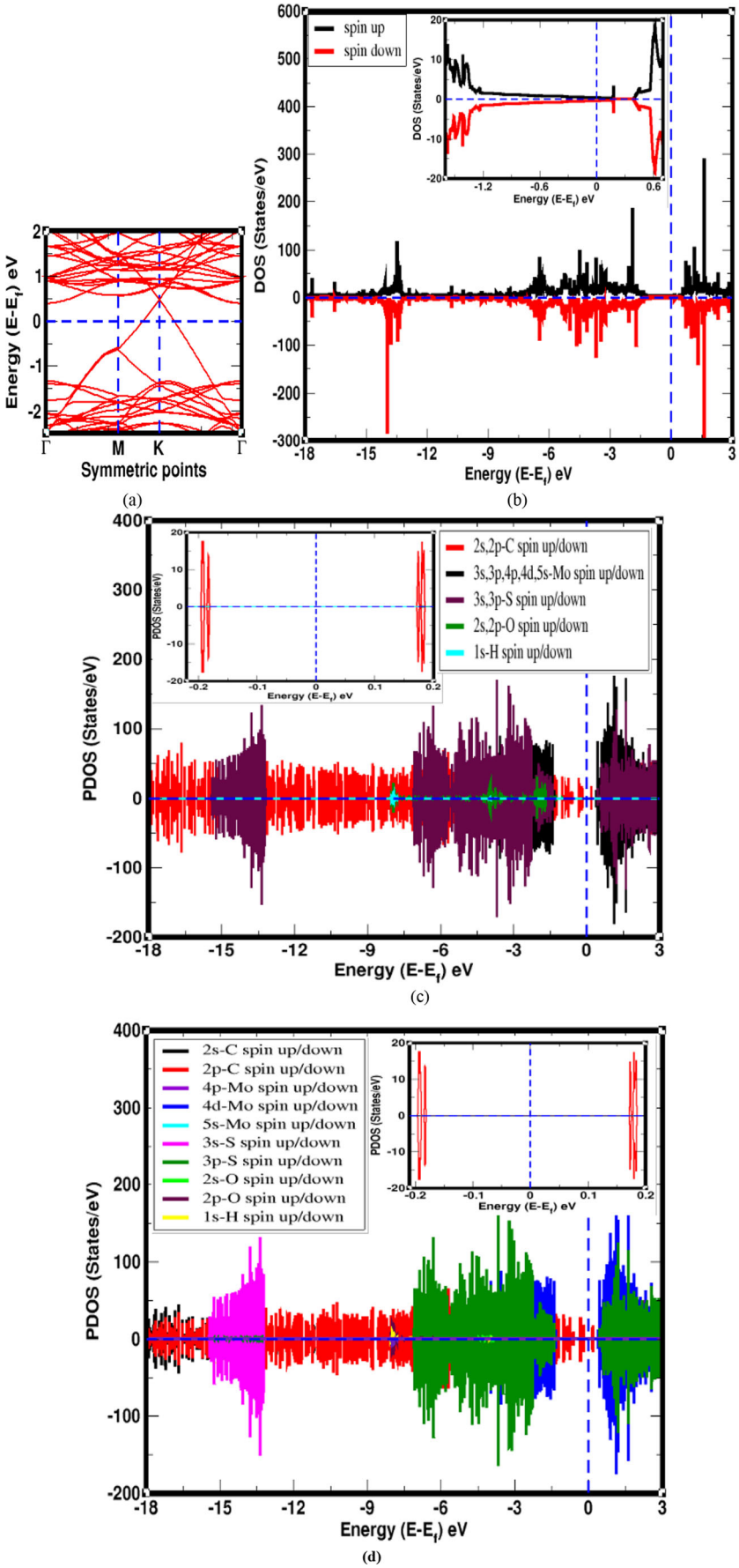

Fig. 3 **a** Band structure of up and down spins states of w-(HS)G/MoS_2 material. **b** DOS of up and down spins states of atoms in the w-(HS)G/MoS_2 material. **c** PDOS of total up and down spins states of all atoms in w-(HS)G/MoS_2 material. **d** PDOS of individual up and down spins states of all atoms in w-(HS)G/MoS_2 material. In band structure, horizontal dotted line represents Fermi energy level, and in DOS and PDOS plots, vertical dotted line represents Fermi energy level. In all DOS and PDOS plots, insets represent the zoom in the scale near the Fermi energy

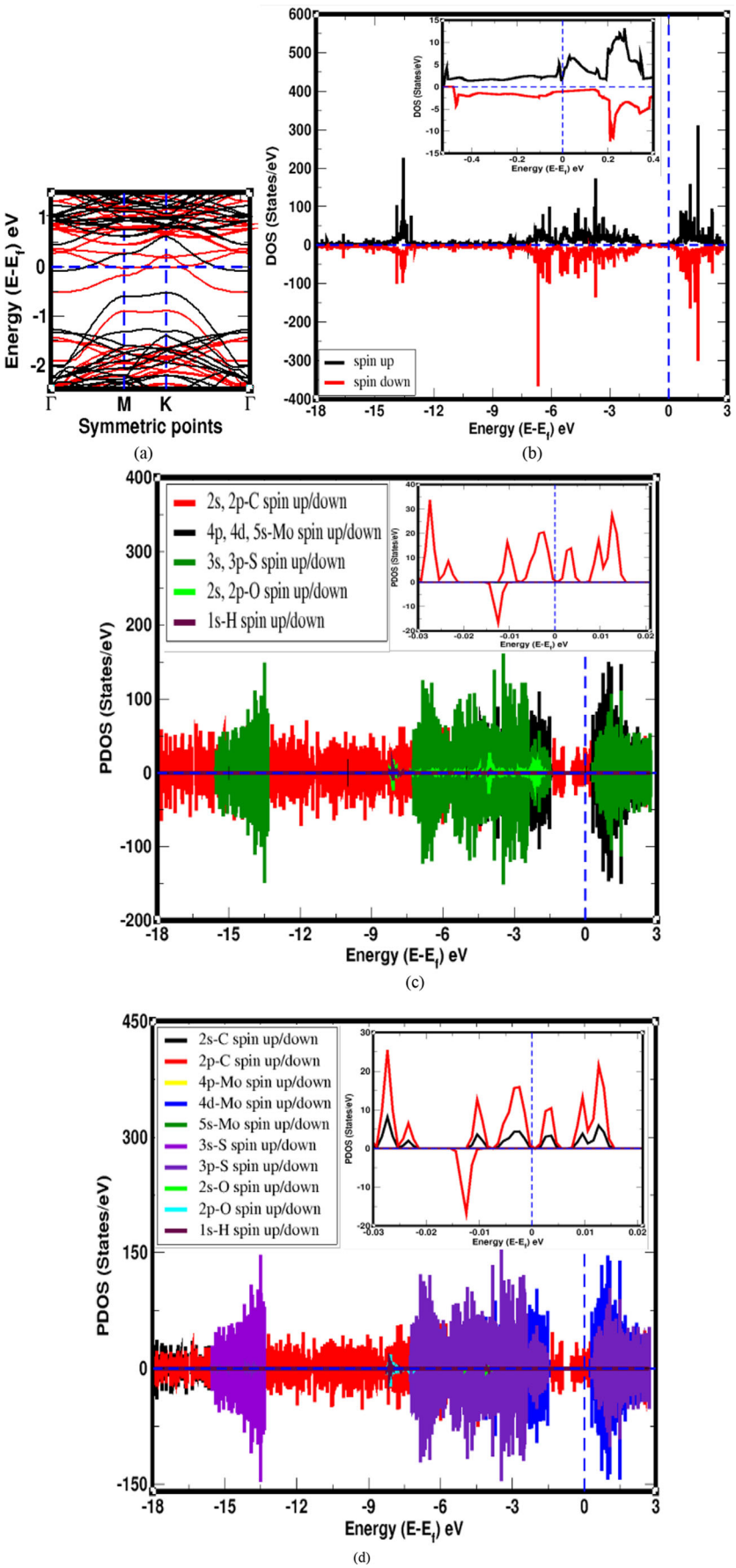

Fig. 4 **a** Band structure of up and down spins states of L1C-w-(HS)G/MoS_2 material, where red color of bands represent up spins states and black color of bands represent down spins states. **b** DOS of up and down spins states of atoms in the L1C-w-(HS)G/MoS_2 material. **c** PDOS of total up and down spins states of all atoms in L1C-w-(HS)G/MoS_2 material. **d** PDOS of individual up and down spins states of all atoms in L1C-w-(HS)G/MoS_2 material. In band structure, horizontal dotted line represents Fermi energy level, and in DOS & PDOS plots, vertical dotted line represents Fermi energy level. In all DOS and PDOS plots, insets represent the zoom in the scale near the Fermi energy

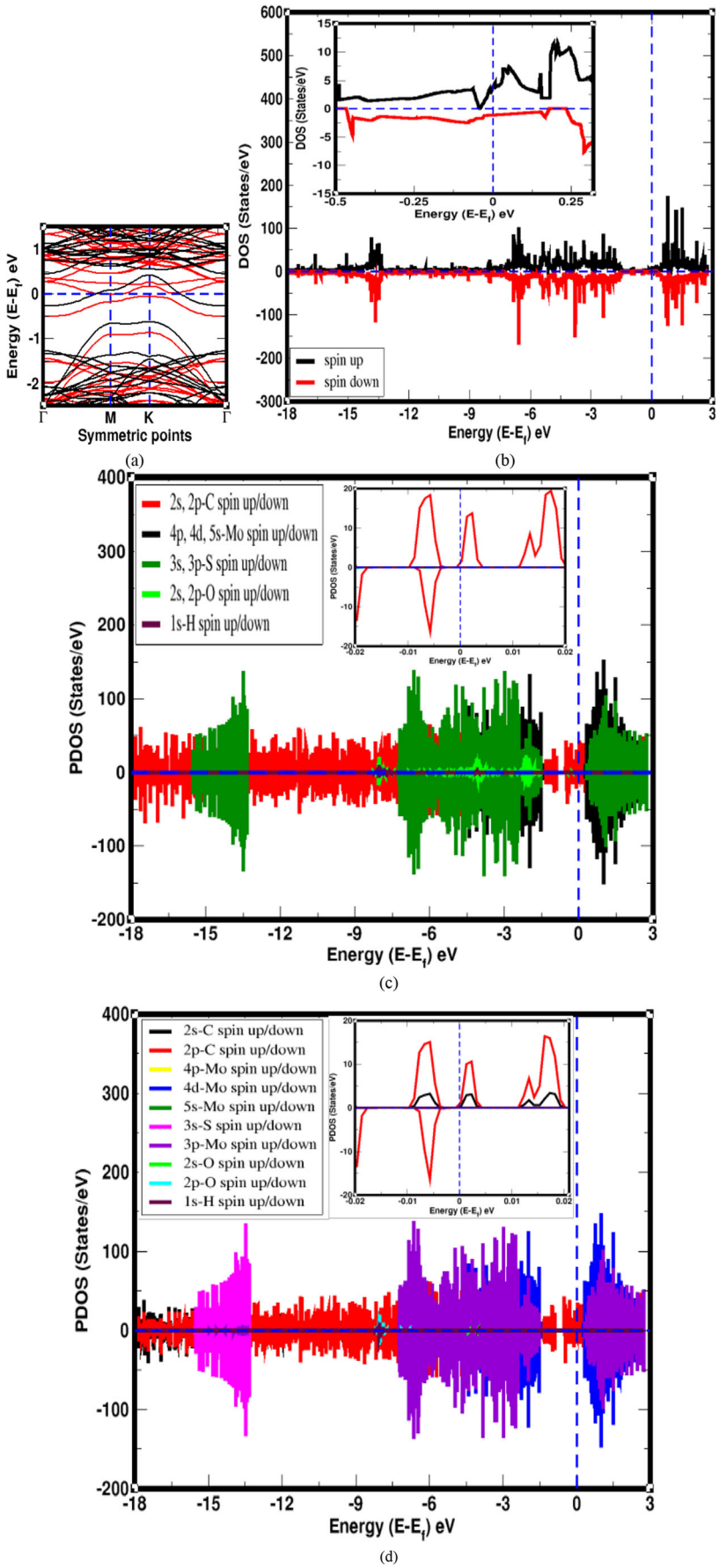

Fig. 5 **a** Band structure of up and down spins states of C1C-w-(HS)G/MoS_2 material, where red color of bands represent up spins states and black color of bands represent down spins states. **b** DOS of up and down spins states of atoms in the C1C-w-(HS)G/MoS_2 material. **c** PDOS of total up and down spins states of all atoms in C1C-w-(HS)G/MoS_2 material. **d** PDOS of individual up and down spins states of all atoms in C1C-w-(HS)G/MoS_2 material. In band structure, horizontal dotted line represents Fermi energy level, and, in DOS & PDOS plots, vertical dotted line represents Fermi energy level. In all DOS and PDOS plots, insets represent the zoom in the scale near the Fermi energy

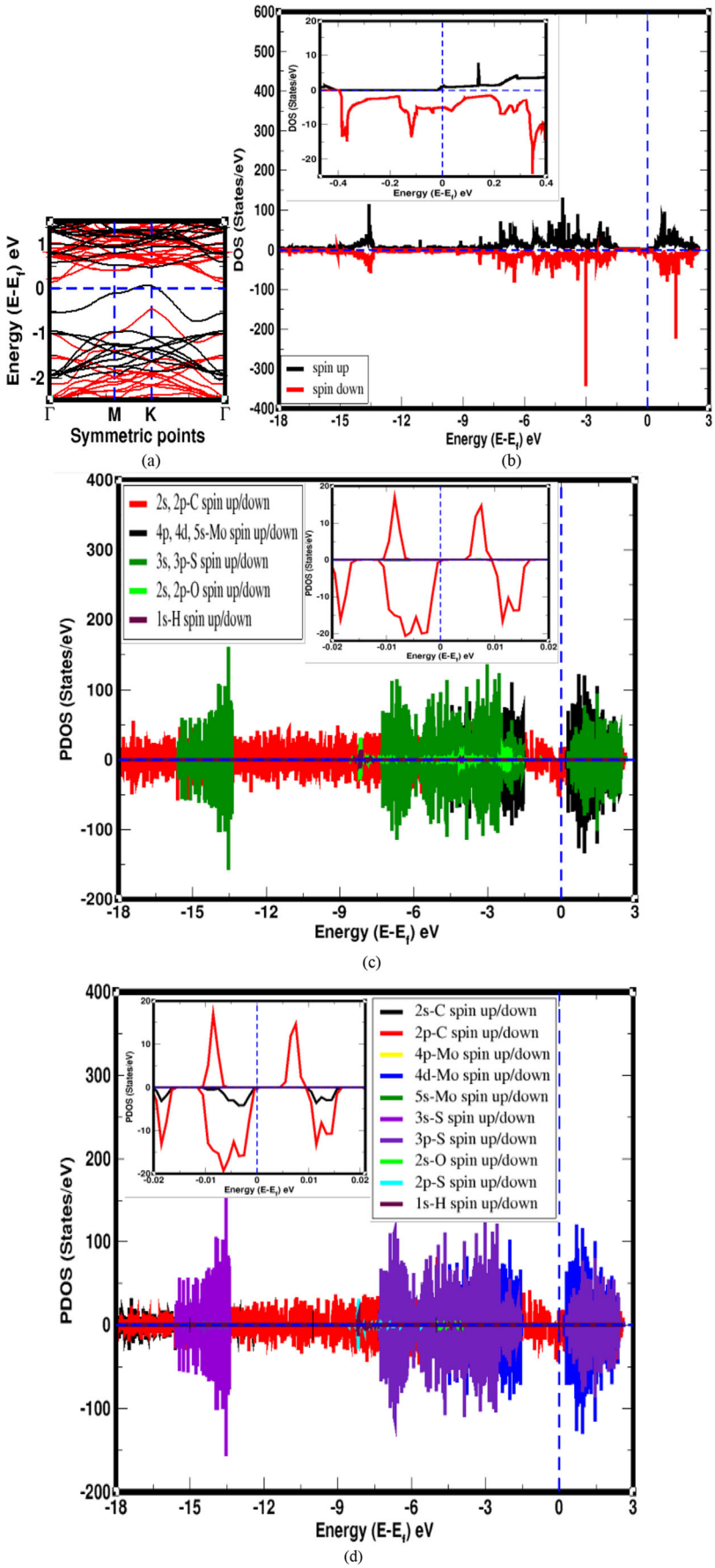

Fig. 6 **a** Band structure of up and down spins states of 2C-w-(HS)G/MoS_2 material, where red color of bands represent up spins states and black color of bands represent down spins states. **b** DOS of up and down spins states of atoms in the 2C-w-(HS)G/MoS_2 material. **c** PDOS of total up and down spins states of all atoms in 2C-w-(HS)G/MoS_2 material. **d** PDOS of individual up and down spins states of all atoms in 2C-w-(HS)G/MoS_2 material. In band structure, horizontal dotted line represents Fermi energy level, and in DOS and PDOS plots, vertical dotted line represents Fermi energy level. In all DOS and PDOS plots, insets represent the zoom in the scale near the Fermi energy

shown in Fig. 4c and d, where unequal distributions of up and down spins states of electrons are presented around the Fermi energy level. These asymmetrically (unequal) distributed spins states of electrons create a magnetic moment. Magnetic moment given by 2s and 2p orbitals of C atoms in the system is 0.06 μ_B/cell and 0.15 μ_B/cell respectively, where magnetic moments are given by p_x, p_y, and p_z sub-orbitals of C atoms have values 0.05 μ_B/cell, 0.08 μ_B/cell, and 0.02 μ_B/cell respectively. The values of magnetic moment are obtained by calculating the net magnetic moment given by up and down spins of electrons in 2s and 2p orbitals of C atoms in structure. Therefore, we found that the total magnetic moment of L1C-w-(HS)G/MoS_2 has a value 0.21 μ_B/cell. The asymmetrically distributed spins states of electrons in DOS and PDOS near the Fermi level gives a magnetic moment as shown in Fig. 5b and c–d. The value of magnetic moment given by 2s and 2p orbitals of C atoms are 0.08 μ_B/cell and 0.18 μ_B/cell (i.e., the values of magnetic moments due to p_x, p_y, and p_z sub-orbitals of C atoms in material are 0.07 μ_B/cell, 0.08 μ_B/cell, and 0.03 μ_B/cell, respectively); 4p, 4d, and 5s orbitals of Mo atoms is 0.00 μ_B/cell; 3s and 3p orbitals of S atoms is 0.00 μ_B/cell; 2s and 2p orbitals of O atom is 0.00 μ_B/cell; and 1s orbital of H atoms is 0.00 μ_B/cell, respectively. These values are obtained by calculating net magnetism given by up and down spins of electrons in the system. These asymmetrically distributed up and down spins states of electrons are given by only 2s and 2p orbitals of C atoms in the structure. Therefore, total value of magnetic moment of C1C-w-(HS)G/MoS_2 material is 0.26 μ_B/cell, due to the dominant contributions of spins of electrons in 2s and 2p orbital of C atoms. Generally, each sigma dangling bond carries a magnetic moment of 1 μ_B. However, in both cases of L1C-w-(HS)G/MoS_2 and C1C-w-(HS)G/MoS_2 materials, we calculated deviated values of magnetic moment; this is due to the rearrangements of unpaired up and down spins of electrons in the sub-orbitals of atoms. Thus, proper arrangements of spins in 2s and 2p orbitals of carbon atoms reduced the values of magnetic moment of L1C-w-(HS)G/MoS_2 and C1C-w-(HS)G/MoS_2 materials. The PDOS plots of 2s and 2p orbital of C atoms; 4p, 4d, and 5s orbital of Mo atoms; 3s and 3p orbitals of S atoms; 2s and 2p orbitals of O atom; and 1s orbital of H atoms in 2C-w-(HS)G/MoS_2 are shown in Fig. 6d. PDOS value near the Fermi level of 2s and 2p orbitals of C atoms reflect that up and down spins states are asymmetrical. We found that the total magnetic moment of 2C-w-(HS)G/MoS_2 has a value of − 2.00 μ_B/cell; this is due to the arrangement of spins of electrons in 2s and 2p orbital of C atoms and 2p orbital of O atom. Also, the magnetic moment given by spins of electrons in 2s and 2p orbitals of C atoms are − 0.46 μ_B/cell and − 1.53 μ_B/cell, and 2p orbital of O atom is − 0.01 μ_B/cell. These magnetic moments are given by p_x, p_y, and p_z sub-orbitals of C atoms which have the values of − 0.59 μ_B/cell, − 0.73 μ_B/cell, and − 0.21 μ_B/cell, respectively, and p_y sub-orbital of O atom has a value of − 0.01 μ_B/cell. The values of magnetic moments are obtained by calculating net magnetic moment given by up and down spin electrons of carbon and oxygen atoms in the structure. This means that spins of other atoms have no role in magnetism of 2C-w-(HS)G/MoS_2. Thus, we found that C atoms and O atom have governing handout of magnetism in 2C-w-(HS)G/MoS_2 material. We compared the magnetic moment of L1C-w-(HS)G/MoS_2, C1C-w-(HS)G/MoS_2, and 2C-w-(HS)G/MoS_2 materials and found that the magnetic moment value of 2C-w-(HS)G/MoS_2 material is greater than the magnetic moment values of L1C-w-(HS)G/MoS_2 and C1C-w-(HS)G/MoS_2 materials. Therefore, the strength of magnetic properties in 2C-w-(HS)G/MoS_2 material is higher than in 1C-w-(HS)G/MoS_2 materials. In all these cases, 2s and 2p orbital of C atoms have major contributions of magnetic moments in w-$C_{atoms\text{-}vacancy}$-(HS)G/MoS_2 materials. Therefore, to tune the magnetic properties in w-$C_{atoms\text{-}vacancy}$-(HS)G/MoS_2 materials, s and p orbital of C atoms provide main contributions.

Conclusions and concluding remarks

The structural, electronic, and magnetic properties of periodic vdW, w-(HS)G/MoS_2, and w-$C_{atoms\text{-}vacancy}$-(HS)G/MoS_2 materials have been studied by using spin polarized density functional theory (DFT) calculations with vdW corrections (DFT-D2) method. At first, we have examined the structures and found that both w-(HS)G/MoS_2 and w-$C_{atoms\text{-}vacancy}$-(HS)G/MoS_2 are stable materials. The stability and compactness of these materials are decreased with increase in the

Table 2 Fermi energy (E_f), Fermi energy shift ($E_{f\text{-}shift}$), band gap energy (E_g), binding energy (E_b), and total value of magnetization (M) of w-(HS)G/MoS_2 and w-$C_{atoms\text{-}vacancy}$-(HS)G/MoS_2 materials

w-(HS)G/MoS_2 & w-$C_{atoms\text{-}vacancy}$-(HS)G/MoS_2 materials	(E_f) eV	($E_{f\text{-}shift}$) eV	(E_g) eV	(E_b) eV	(M) μ_B/cell
w-(HS)G/MoS_2	0.14	–	(Dirac point) 0.42 eV	0.26	0.00
L1C atom vacancy defects w-(HS)G/MoS_2	0.23	0.09	–	0.25	+0.21
C1C atom vacancy defects w-(HS)G/MoS_2	0.24	0.10	–	0.25	+0.26
2C atom vacancy defects w-(HS)G/MoS_2	0.26	0.12	0.92	0.23	−2.00

concentrations of defects in structures. We have done band structure calculations and found that w-(HS)G/MoS_2 has n-type Schottky contact of barrier height 0.42 eV, indicating that the material is metallic in nature. The few numbers of spins states of electrons are appeared around the Fermi level of L1C-w-(HS)G/MoS_2 and C1C-w-(HS)G/MoS_2 materials in bands and DOS plots, which means that they also have a metallic nature. The 2C-w-(HS)G/MoS_2 material has opened a small energy band gap of value 0.92 eV for up spin electronic states and no band gap for down spin electronic states, which implies that 2C-w-(HS)G/MoS_2 resembles with half metallic nature. Thus, the metallic strength of materials decreases with an increase in its defects concentrations. For magnetism, we have analyzed DOS and PDOS calculations and found that spins of electrons are symmetrically distributed in w-(HS)G/MoS_2 material and asymmetrically distributed in L1C-w-(HS)G/MoS_2, C1C-w-(HS)G/MoS_2 and 2C-w-(HS)G/MoS_2 materials. Therefore, non-magnetic w-(HS)G/MoS_2 material changes to magnetic L1C-w-(HS)G/MoS_2, C1C-w-(HS)G/MoS_2, and 2C-w-(HS)G/MoS_2 materials due to C sites vacancy defects. Magnetic moment values of L1C-w-(HS)G/MoS_2, C1C-w-(HS)G/MoS_2, and 2C-w-(HS)G/MoS_2 materials are 0.21 μ_B/cell, 0.26 μ_B/cell, and − 2.00 μ_B/cell, respectively. The prevalent contributions to magnetism in defects materials are given by spins of electrons in the 2s and 2p orbitals of C atoms. Recently, Koda et al. have carried out HSE06 type of functional in DFT to include the effects of quasiparticles [40]. Their investigations show that strong orbital overlaps are observed in the hetero-bilayers (of Ph/MoSe2 and Ph/WSe2) influencing band offsets and, hence, emphasizing the importance of quasiparticle calculations over standard density functional theory ones. The present work has limitations of inclusion of quasiparticles effects by HSE06 exchange correlations functionals.

Supplementary Information The online version contains supplementary material available at https://doi.org/10.1007/s00894-021-04690-8.

Acknowledgments HKN acknowledges the UGC Nepal Award no. PhD-75/76-S&T-09. NPA acknowledges network project NT-14 of ICTP/OEA and UGC Nepal Grants CRG 073/74 -S&T -01.

Code availability We used Quantum Espresso which is open-source software for ab initio simulation of solids.

Authors' contributions HKN carried the calculations, NPA suggested problem, and both the authors analyzed the results.

Funding This study was supported by UGC Nepal and ICTP.

Data availability The corresponding author will provide any data required for reproduction.

Declarations

Conflict of interest The authors declare no conflict of interest.

References

1. Geim AK, Novoselov KS (2007) The rise of graphene. Nat Mater 6(3):183–191
2. Zhang S, Xie M, Li F, Yan Z, Li Y, Kan E et al (2016) Semiconducting group 15 monolayers: a broad range of band gaps and high carrier mobilities. Angew Chem 128(5):1698–1701
3. Wang H, Feng H, Li J (2014) Graphene and graphene-like layered transition metal dichalcogenides in energy conversion and storage. Small 10(11):2165–2181
4. Wang QH, Kalantar-Zadeh K, Kis A, Coleman JN, Strano MS (2012) Electronics and optoelectronics of two-dimensional transition metal dichalcogenides. Nat Nanotechnol 7(11):699–712
5. Song L, Ci L, Lu H, Sorokin PB, Jin C, Ni J et al (2010) Large scale growth and characterization of atomic hexagonal boron nitride layers. Nano Lett 10(8):3209–3215
6. Tran TT, Bray K, Ford MJ, Toth M, Aharonovich I (2016) Quantum emission from hexagonal boron nitride monolayers. Nat Nanotechnol 11(1):37–41
7. Xu M, Liang T, Shi M, Chen H (2013) Graphene-like two-dimensional materials. Chem Rev 113(5):3766–3798
8. Mayorov AS, Gorbachev RV, Morozov SV, Britnell L, Jalil R, Ponomarenko LA et al (2011) Micrometer-scale ballistic transport in encapsulated graphene at room temperature. Nano Lett 11(6): 2396–2399
9. Morozov SV, Novoselov KS, Katsnelson MI, Schedin F, Elias DC, Jaszczak JA, Geim AK (2008) Giant intrinsic carrier mobilities in graphene and its bilayer. Phys Rev Lett 100(1):016602
10. Novoselov KS, Geim AK, Morozov SV, Jiang D, Katsnelson MI, Grigorieva I et al (2005) Two-dimensional gas of massless Dirac fermions in graphene. Nature 438(7065):197–200
11. Castro EV, Novoselov KS, Morozov SV, Peres NMR, Dos Santos JL, Nilsson J, Neto AC (2007) Biased bilayer graphene: semiconductor with a gap tunable by the electric field effect. Phys Rev Lett 99(21):216802
12. Lei JC, Zhang X, Zhou Z (2015) Recent advances in MXene: preparation, properties, and applications. Front Phys 10(3):276–286
13. Dávila ME, Xian L, Cahangirov S, Rubio A, Le Lay G (2014) Germanene: a novel two-dimensional germanium allotrope akin to graphene and silicene. New J Phys 16(9):095002
14. Balendhran S, Walia S, Nili H, Sriram S, Bhaskaran M (2015) Elemental analogues of graphene: silicene, germanene, stanene, and phosphorene. Small 11(6):640–652
15. Mak KF, Lee C, Hone J, Shan J, Heinz TF (2010) Atomically thin MoS_2: a new direct-gap semiconductor. Phys Rev Lett 105(13): 136805
16. Zhang Y, Ye J, Matsuhashi Y, Iwasa Y (2012) Ambipolar MoS2 thin flake transistors. Nano Lett 12(3):1136–1140
17. Radisavljevic B, Whitwick MB, Kis A (2012) Small-signal amplifier based on single-layer MoS_2. Appl Phys Lett 101(4):043103
18. Fornarini L, Stirpe F, Scrosati B, Razzini G (1981) Electrochemical solar cells with layer-type semiconductor anodes. Performance of n-MoS2 cells. Solar Energy Mater 5(1):107–114
19. Hu KH, Hu XG, Wang J, Xu YF, Han CL (2012) Tribological properties of MoS_2 with different morphologies in high-density polyethylene. Tribol Lett 47(1):79–90
20. Pierucci D, Henck H, Avila J, Balan A, Naylor CH, Patriarche G et al (2016) Band alignment and minigaps in monolayer MoS2-graphene van der Waals heterostructures. Nano Lett 16(7):4054–4061
21. Zhou, S. Y., Gweon, G. H., Fedorov, A. V., First, P. D., De Heer, W. A., Lee, D. H.,..& Lanzara, A. (2007). Substrate-induced bandgap opening in epitaxial graphene. Nat Mater, 6(10), 770–775

22. Chen H, Zhao J, Huang J, Liang Y (2019) Computational understanding of the structural and electronic properties of the GeS–graphene contact. Phys Chem Chem Phys 21(14):7447–7453
23. Makarova MV, Akaishi Y, Ikarashi T, Rao KS, Yoshimura S, Saito H (2019) Alternating magnetic force microscopy: effect of Si doping on the temporal performance degradation of amorphous FeCoB magnetic tips. J Magn Magn Mater 471:209–214
24. Peng HX, Qin F, Phan MH (2016) Ferromagnetic microwire composites: from sensors to microwave applications. Springer
25. Hohenberg P, Kohn W (1964) Inhomogeneous electron gas. Phys Rev 136(3B):B864
26. Giannozzi P, Baroni S, Bonini N, Calandra M, Car R, Cavazzoni C, Dal Corso A (2009) QUANTUM ESPRESSO: modular and open-source software project for quantum simulations of materials. J Phys Condens Matter 21(39):395502
27. Perdew JP, Burke K, Ernzerhof M (1996) Generalized gradient approximation made simple. Phys Rev Lett 77(18):3865
28. Grimme S (2004) Accurate description of van der Waals complexes by density functional theory including empirical corrections. J Comput Chem 25(12):1463–1473
29. Pfrommer BG, Côté M, Louie SG, Cohen ML (1997) Relaxation of crystals with the quasi-Newton method. J Comput Phys 131(1): 233–240
30. Marzari N, Vanderbilt D, De Vita A, Payne MC (1999) Thermal contraction and disordering of the Al (110) surface. Phys Rev Lett 82(16):3296
31. Martin RM, Martin RM (2004) Electronic structure: basic theory and practical methods. Cambridge university press
32. Kadantsev ES, Hawrylak P (2012) Electronic structure of a single MoS_2 monolayer. Solid State Commun 152(10):909–913
33. Hou Z, Wang X, Ikeda T, Terakura K, Oshima M, Kakimoto MA, Miyata S (2012) Interplay between nitrogen dopants and native point defects in graphene. Phys Rev B 85(16):165439
34. Neupane HK, Adhikari NP (2020) Structure, electronic and magnetic properties of 2D graphene-molybdenum diSulphide (G-MoS2) Heterostructure (HS) with vacancy defects at Mo sites. Comput Condens Matter:e00489
35. Phuc HV, Hieu NN, Hoi BD, Phuong LT, Nguyen CV (2018) First principle study on the electronic properties and Schottky contact of graphene adsorbed on MoS_2 monolayer under applied out-plane strain. Surf Sci 668:23–28
36. Liu B, Wu LJ, Zhao YQ, Wang LZ, Cai MQ (2016) First-principles investigation of the Schottky contact for the two-dimensional MoS_2 and graphene heterostructure. RSC Adv 6(65):60271–60276
37. Chen W, Santos EJ, Zhu W, Kaxiras E, Zhang Z (2013) Tuning the electronic and chemical properties of monolayer MoS2 adsorbed on transition metal substrates. Nano Lett 13(2):509–514
38. Hu W, Wang T, Zhang R, Yang J (2016) Effects of interlayer coupling and electric fields on the electronic structures of graphene and MoS_2 heterobilayers. J Mater Chem C 4(9):1776–1781
39. Kittel C, McEuen P, McEuen P (1996) Introduction to solid state physics, vol 8. Wiley, New York, pp 140–303
40. Koda DS, Bechstedt F, Marques M, Teles LK (2017) Tuning electronic properties and band alignments of phosphorene combined with MoSe2 and WSe2. J Phys Chem C 121(7):3862–3869

Publisher's note Springer Nature remains neutral with regard to jurisdictional claims in published maps and institutional affiliations.

Hindawi
Advances in Condensed Matter Physics
Volume 2020, Article ID 8850701, 11 pages
https://doi.org/10.1155/2020/8850701

Research Article

Tuning Structural, Electronic, and Magnetic Properties of C Sites Vacancy Defects in Graphene/MoS_2 van der Waals Heterostructure Materials: A First-Principles Study

Hari Krishna Neupane [1,2] **and Narayan Prasad Adhikari** [2]

[1]*Amrit Campus, Institute of Science and Technology Tribhuvan University, Kathmandu, Nepal*
[2]*Central Department of Physics, Institute of Science and Technology Tribhuvan University, Kathmandu, Nepal*

Correspondence should be addressed to Narayan Prasad Adhikari; npadhikari@gmail.com

Received 28 August 2020; Revised 31 October 2020; Accepted 17 November 2020; Published 29 November 2020

Academic Editor: Da-Ren Hang

Copyright © 2020 Hari Krishna Neupane and Narayan Prasad Adhikari. This is an open access article distributed under the Creative Commons Attribution License, which permits unrestricted use, distribution, and reproduction in any medium, provided the original work is properly cited.

In this work, we systematically studied the structure, and electronic and magnetic properties of van der Waals (vdWs) interface Graphene/MoS_2 heterostructure (HS-G/MoS_2) and C sites vacancy defects in HS-G/MoS_2 materials using first-principles calculations. By the structural analysis, we found that nondefects geometry is more compact than defects geometries. To investigate the electronic and magnetic properties of HS-G/MoS_2 and C sites vacancy defects in HS-G/MoS_2 materials, we have studied band structure, density of states (DOS), and partial density of states (PDOS). By analyzing the results, we found that HS-G/MoS_2 is metallic in nature but C sites vacancy defects in HS-G/MoS_2 materials have a certain energy bandgap. Also, from the band structure calculations, we found that Fermi energy level shifted towards the conduction band in vacancy defects geometries which reveals that the defected heterostructure is n-type Schottky contacts. From DOS and PDOS analysis, we obtained that the nonmagnetic HS-G/MoS_2 material changes to magnetic materials due to the presence of C sites vacancy defects. Right 1C atom vacancy defects (R-1C), left 1C atom vacancy defects (L-1C), centre 1C atom vacancy defects (C-1C), and 2C (1C right and 1C centre) atom vacancy defects in HS-G/MoS_2 materials have magnetic moments of −0.75 μ_B/cell, −0.75 μ_B/cell, −0.12 μ_B/cell, and +0.39 μ_B/cell, respectively. Electrons from 2s and 2p orbitals of C atoms have main contributions for the magnetism in all these materials.

1. Introduction

Graphene has a honeycomb lattice of carbon atoms; each atom in a lattice contains four valence electrons and interacts with its three nearest neighbor carbon through σ-bond due to sp^2 hybridization of 2s, $2p_x$, and $2p_y$ orbitals of three valence electrons. The fourth electron occupies the $2p_z$ orbital which overlaps with the nearest $2p_z$ electrons and forms a π-bond perpendicular to the Graphene plane. These electrons are loosely bound, and most of the electronic properties of the pure Graphene are dictated by these delocalized electrons [1, 2]. The band structure of the pure Graphene (two bands π and π^*) originating from p_z-orbital meets at six points in k-space known as Dirac points. Dirac points of Graphene are formed at the Fermi energy level, so it is called zero bandgap semiconductors. The structure of Graphene containing Dirac points bears astonishing electronic, optical, mechanical, and magnetic properties, so electronic devices, transparent electrodes, and spintronics devices can be manufactured by using Graphene [1–3]. In nanoscience research, a keen interest is given by the researchers for the study of two-dimensional hexagonal structural materials. Like Graphene, MoS_2 monolayer is a 2D transition metal dichalcogenide (TMDC) honeycomb structure material with a direct bandgap of the value of 1.80 eV [4]. It also has winsome properties, because of which it can be applied in industry for producing signal amplifier, integrated logic circuits, flexible optoelectronic devices, transistors, photodetectors, photocatalysts, optoelectronic devices, solar cells, and lubricants. Fundamentally, also it is

interesting as it is just a single-layered material [5–10]. The Graphene-based research in 2D materials has made enormous success [11–13]. The metal/semiconductor interface such as G/MoS_2 is a new contact type of the Graphene-based van der Waals (vdWs) interface, known as heterostructures (HS) material. The heterostructures can be used to wipe out the unwanted properties of the constituents and hence give rise to desired properties than the constituents [14]. The first-principles study of HS-G/MoS_2 can be done in periodically repeated supercells. The supercells contain two interfaces which are equivalent to the term of stoichiometry and geometry [15]. This G/MoS_2 vdWs interface was studied by various research groups [15, 16]. The report presented that the structure contains some innovative properties which can create different components in the electronic devices [17]. Also, vdWs HS-G/MoS_2 has intriguing electronic properties, transport properties, optical transparency, mechanical flexibility, and photoconductivity. Thus, it can be highly recommended in the application of electronic, photovoltaic, and memory devices [18–21].

In our previous work, we studied structural, electronic, and magnetic properties of Mo sites vacancy defects in HS-G/MoS_2 materials by first-principles calculations using vdWs correction in the DFT-D2 approach [22]. To the best of our knowledge, C sites vacancy defects in HS-G/MoS_2 materials have not been studied. Therefore, in the present work, we investigated the structural, electronic, and magnetic properties of vdWs interfaces, HS-G/MoS_2, and C sites vacancy defects in HS-G/MoS_2 materials using first-principles calculations with the DFT-D2 approach. The vacancy defects in solids cause deviation of atoms or ions from the periodicity, and they are used to find innovative properties. They can be used to design new materials [23]. Also, the magnetic materials can be applied in various fields such as biomedicine, molecular biology, biochemistry, diagnosis, catalysis, nanoelectronic devices, and various other industrial applications like magnetic seals in motors, magnetic sensors, magnetic inks, electrical power generator, transformers, magnetic recording media, and computers [24, 25].

The rest part of the paper is organized as follows. The computational details will be discussed in Section 2 whereas Section 3 contains results and discussion. We close the paper with the main conclusions and outlook of the present work in Section 4.

2. Computational Model and Methods

We have performed the first-principles calculations to investigate the structural, electronic, and magnetic properties of HS-G/MoS_2 and C atom vacancy defects in HS-G/MoS_2 materials within the framework of density functional theory (DFT) [26], with van der Waals (vdWs) corrections taken into account by DFT-D2 [27] approach using Quantum ESPRESSO (QE) computational package [28]. To incorporate the electronic exchange and correlation effects in the density functional theory, Generalized Gradient Approximation (GGA) was used via Perdew-Burke-Ernzerhof (PBE) exchange correlations [29]. Grimme's Rappe-Rabe-Kaxiras-Joannopoulos (RRJK) model of ultrasoft pseudopotentials is used to replace the complicated effects of the motion of the core (i.e., nonvalence) electrons of an atom and its nucleus with an effective potential for all atoms in a system. It helps to deal with only the chemically active valence electrons which are included explicitly in our calculations. The electronic configurations of valence electrons in C, Mo, and S atoms of our system are C:[He] $2s^2 2p^2$, Mo:[Kr] $4d^5 5s^1$, and S:[Ne] $3s^2 3p^4$, respectively. All the structures are optimized and relaxed by the BFGS scheme [30], using Quantum ESPRESSO code [28], until the total energy changes are less than 10^{-4} Ry and force acting between two consecutive self-consistent fields is less than 10^{-3} Ry/Bohr. After the relax calculations, we have done self-consistent total energy calculations, for this Brillouin zone of heterostructure is sampled in k-space using Monkhorst-Pack (MP) scheme [31], with an appropriate number of mesh $(4 \times 4 \times 1)$ of k-points, which is determined from the convergence test. The Marzari-Vanderbilt (MV) [32] smearing of the small width of 0.001 Ry is used. In addition, we have chosen the "David" diagonalization method with a "plain" mixing mode and mixing factor of 0.6 for self-consistency. For band structure calculations, a mesh of $(4 \times 4 \times 1)$ k-points is used, and for the density of states (DOS) and partial density of states (PDOS) calculations, an automatic denser mesh of $(8 \times 8 \times 1)$ k-points is used, where, in both the cases, 100 k-points are chosen along the high symmetric points connecting the reciprocal space.

In this work, we have prepared the HS-G/MoS_2 by using (4×4) supercell structure of Graphene and (3×3) supercell structure of monolayer MoS_2 with lattice mismatch about 4.13%, where we maintained vacuum distance greater than 20 Å to avoid the interactions between two adjacent layers as shown in Figure 1(c). For the construction of these supercell structures, at first, we have created a unit cell of Graphene and MoS_2 by using structural analysis tool XCrySDen and computational tool Quantum ESPRESSO. To construct the unit cell, we used the Bravais lattice index, cell dimension parameters, and lattice constant in the input file. For the Graphene unit cell, we have taken the experimentally reported value of the distance between two carbon atoms that is 1.42 Å [31]. After the construction of the Graphene unit cell, we calculated the kinetic energy cut-off value, k-points, and lattice parameters from the convergence test and found the constant kinetic energy cut-off value 35 Ry. The charge density cut-off value for ultrasoft pseudopotential is calculated by using the relation $10 \times$ kinetic energy cut-off, which is 350 Ry. These obtained parameters (kinetic energy cut-off, charge density cut-off, k-points, and lattice parameters) are used in the input file to relax our system. We found the distance between two carbon atoms of the relaxed Graphene unit cell to be 1.42 Å, which is very close to the starting value for relaxation [31]. The unit cell of MoS_2 is prepared by using the experimental value of 3.19 Å [6, 33]. Its unit cell contains a single layer of two S and one Mo atoms. The Mo atom bounds with the S atom in a trigonal prismatic arrangement, where each Mo atom is surrounded by six first neighboring S atoms. After the construction of a unit cell, we have calculated its optimized values of kinetic energy cut-off, k-points, lattice parameters, and charge

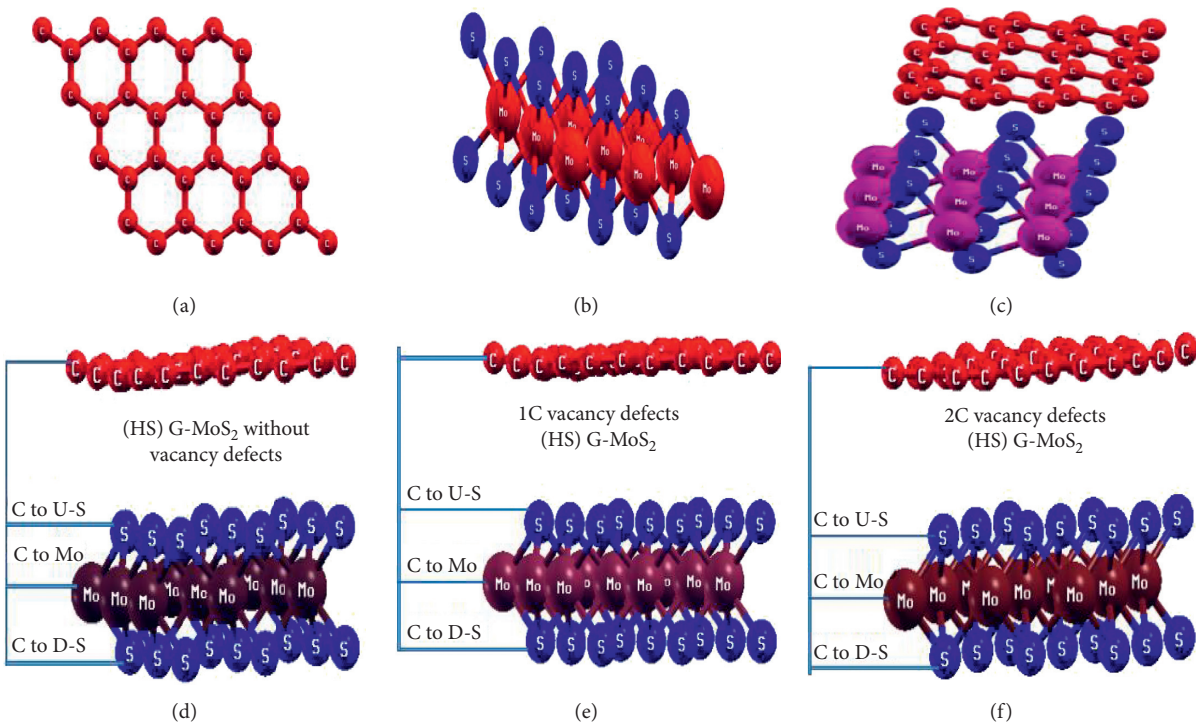

FIGURE 1: (a) (4 × 4) supercell structure of Graphene. (b) (3 × 3) supercell structure of MoS_2. (c) Heterostructure of G/MoS_2. (d) Interlayer and interatomic distances measurement geometry of HS-G/MoS_2. (e) Interlayer and interatomic distances measurement geometry of 1C atom vacancy defects in HS-G/MoS_2. (f) Interlayer and interatomic distances measurement geometry of 2C atom vacancy defects in HS-G/MoS_2.

density cut-off values as in Graphene, and then these parameters are used in the input file to relax the system. We found that the value of the lattice constant to be 3.18 Å, which is also close to the experimentally reported value of 3.19 Å [6, 33]. We then developed (4 × 4) supercell structure of Graphene and (3 × 3) supercell of monolayer MoS_2 from these prepared unit cells, by extending along x and y direction as shown in Figures 1(a) and 1(b), respectively. After that, we have constructed the stable and relaxed structures of right 1C atom vacancy defects (R-1C), left 1C atom vacancy defects (L-1C), centre 1C atom vacancy defects (C-1C), and 2C (1C right and 1C centre) atom vacancy defects in HS-G/MoS_2 as shown in Figure 2. These prepared structures are used for further investigations.

3. Results and Discussion

In the present work, we have carried out a first-principles study of C sites vacancy defects in HS-G/MoS2 heterostructures. In this section, we present the main findings and their interpretations from the investigation of the heterostructures.

3.1. Structural Analysis. The Graphene-based stable heterostructure materials in G/MoS_2 is prepared by using (4 × 4) supercell structure of Graphene and (3 × 3) supercell structure of monolayer MoS_2 with considerable (4.13%) lattice mismatch as shown in Figures 1(a)–1(c). The stability of the structure is determined by binding energy calculations. The higher the value of binding energy is, the more stable the system is. Thus, the greater value of binding energy material is more favorable for the calculations of its physical properties. The binding energy (E_b) of HS-G/MoS_2 is calculated by using the following relation: $E_b = E_{Graphene} + E_{MoS2} - E_{HS\text{-}G/MoS2}$, where $E_{Graphene}$, E_{MoS2}, and $E_{HS\text{-}G/MoS2}$ represent the ground state energy of a fully relaxed (4 × 4) supercell of Graphene, (3 × 3) supercell of MoS_2, and heterostructure of G/MoS_2, respectively. The heterostructures of carbon atom vacancy defects are prepared by using optimized and relaxed HS-G/MoS_2 material as shown in Figure 2, where out of 32C atoms, the concentrations of the vacancy defects of R-1C, L-1C, C-1C, and 2C in HS-G/MoS_2 materials are found to be 3.13%, 3.13%, 3.13%, and 6.25%, respectively. These are also stable structures. The order of binding energy of the structures is found to be as HS-G/MoS_2 > 1C atoms HS-G/MoS_2 > 2C atoms HS-G/MoS_2 as given in Table 1. So, the stability of the structure is decreased with an increase in its defects concentrations. Among the various carbon atom vacancy defects in HS-G/MoS_2 configurations, we have used the most stable R-1C, L-1C, C-1C, and 2C atom vacancy defects in HS-G/MoS_2 materials. R-1C, L-1C, C-1C, and 2C atom vacancy defects in HS-G/MoS_2 have defects formation energies of 0.20 eV, 0.20 eV, 0.20 eV, and 0.41 eV, respectively. These energy values are less than the defects formation of energy values of other vacancy defects configurations. The defects formation energies in our systems are calculated based on the standard formalism [34]; $E_f = E_T(defect) + n_C\mu_C - E_T(perfect)$, where E_T $(defect)$ is the

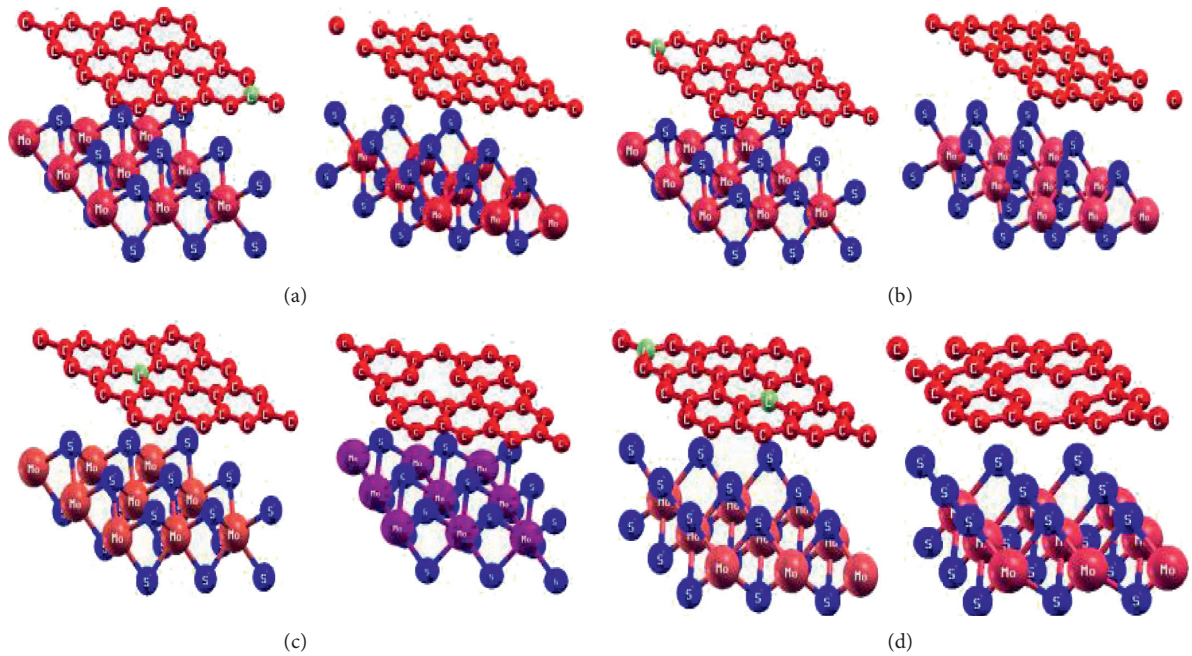

Figure 2: Optimized and relaxed structures of C sites vacancy defects in HS-G/MoS_2 materials. (a) R-1C atom vacancy defects in HS-G/MoS_2. (b) L-1C atom vacancy defects in HS-G/MoS_2. (c) C-1C atom vacancy defects in HS-G/MoS_2. (d) 2C atom vacancy defects in HS-G/MoS_2.

Table 1: Fermi energy level (E_f), Fermi energy level shift towards conduction band (E_s), the energy gap between the bottom of the conduction band and top of the valence band (E_g), the total value of magnetism (M), and binding energy (E_b) of HS-G/MoS_2 and C sites vacancy defects in HS-G/MoS_2 materials.

HS-G/MoS_2 and C sites vacancy defects in HS-G/MoS_2 materials	E_f (eV)	E_s (eV)	E_g (eV)	M (μ_B/cell)	E_b (eV)
HS-G/MoS_2	0.32	—	—	0.00	0.25
R-1C vacancy defects in HS-G/MoS_2	0.52	0.20	0.15	−0.75	0.24
L-1C vacancy defects in HS-G/MoS_2	0.53	0.21	0.13	−0.75	0.24
C-1C vacancy defects in HS-G/MoS_2	0.54	0.22	0.14	−0.12	0.24
2C vacancy defects in HS-G/MoS_2	0.56	0.24	0.37	+0.39	0.23

total energy of a supercell with the defects, n_C *is* the numbers of C atoms removed from the perfect supercell to introduce a vacancy, μ_C is chemical potentials of C atoms, and E_T *(perfect)* is the total energy of the neutral perfect supercell, respectively. Figures 1(d)–1(f) are interlayer and interatomic distances measurement geometries of HS-G/MoS_2, 1C, and 2C atom vacancy defects in HS-G/MoS_2 geometries, respectively.

We have analyzed the structural properties of HS-G/MoS_2 and C sites vacancy defects in HS-G/MoS_2 materials and then obtained the data of interlayer distances which are given in Table 2. Also, interatomic distances of HS-G/MoS_2 and its C sites vacancy defects in HS-G/MoS_2 materials are given in SI (Table S1).

From Table 2, we found that HS-G/MoS_2 geometry is more compressed than C sites vacancy defects in HS-G/MoS_2 geometries, and compactness of material increases with a decrease in its defects concentrations. Also, we found that the C-1C vacancy defects structure is slightly compact than other R-1C and L-1C vacancy defects structures.

3.2. Electronic and Magnetic Properties. To know the electronic and magnetic properties of HS-G/MoS_2 and C sites vacancy defects in HS-G/MoS_2 materials, we first consider the key characteristics of freestanding Graphene supercell, monolayer MoS_2 supercell, and G/MoS_2 heterostructure. From band structure calculations, Graphene has zero bandgap energy because the states below the Fermi level characterized by π bonds and states above the Fermi level characterized by π^* antibonding states and corresponding bands meet at Fermi level that is Dirac cone. The monolayer MoS_2 is an intrinsic semiconductor with a direct band of value 1.65 eV; this value is close to the experimentally reported value of 1.80 eV [10, 33]. The zero-bandgap energy material (Graphene) and wide-bandgap energy material (MoS_2) are joined together to form vdWs HS-G/MoS_2 material with 4.13% of the lattice mismatch as shown in Figure 1(c). In HS-G/MoS_2, n-type Schottky contact is formed with a Schottky barrier height of 0.56 eV as shown in Figure 3(a). Figure 3(a) represents the band structure plot of HS-G/MoS_2, where the x-axis represents high symmetric points in the first Brillouin zone and the y-axis represents the corresponding energy values. We have taken 100 k-points along the specific direction of the irreducible Brillouin zone to get a fine band structure by choosing Γ-M-K-Γ high

Table 2: The interlayer distances of (i) HS-G/MoS_2 and (ii) C sites vacancy defects in HS-G/MoS_2 materials.

	Interlayer distances of HS-G/MoS_2 along x-, y-, and z-axis			Interlayer distances of C sites vacancy defects in HS-G/MoS_2 materials along x-, y-, and z-axis											
				C-Mo				C-US				C-DS			
	C-Mo	C-US	C-DS	2C	C-1C	R-1C	L-1C	2C	C-1C	R-1C	L-1C	2C	C-1C	R-1C	L-1C
x-axis (Å)	0.29	1.88	0.89	0.30	0.29	0.29	0.29	1.89	1.87	1.88	1.88	0.90	0.89	0.89	0.89
y-axis (Å)	0.25	1.16	1.17	0.28	0.26	0.26	0.27	1.18	1.17	1.17	1.18	1.18	1.16	1.16	1.17
z-axis (Å)	5.88	4.34	7.47	5.92	5.90	5.91	5.91	4.38	4.36	4.36	4.37	7.50	7.48	7.49	7.49

Here, (C-Mo), (C-US), and (C-DS) represent distance from C atom in Graphene to Mo atom in MoS_2, distance from C atom in Graphene to upper S atom in MoS_2, and distance from C atom in Graphene to down S atom in MoS_2, respectively.

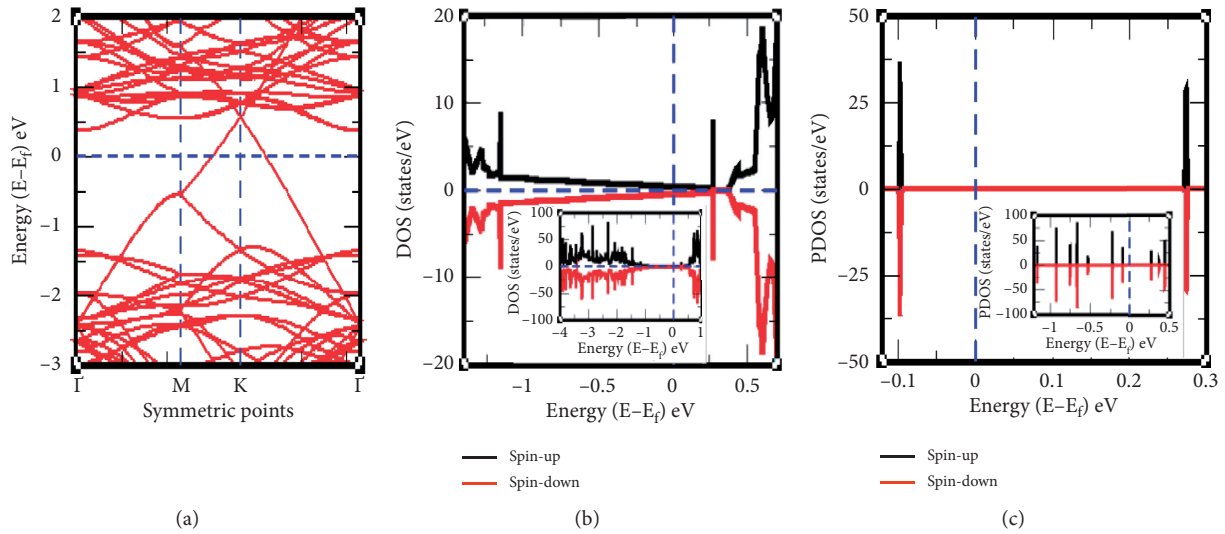

Figure 3: (a) Band structure of HS-G/MoS_2, where horizontal dotted line represents the Fermi level. (b) Spin-up and spin-down electrons are symmetrically distributed in the DOS plot of HS-G/MoS_2. (c) Spin-up and spin-down electrons are symmetrically distributed in the PDOS plot of HS-G/MoS_2. In all DOS and PDOS plots, the vertical dotted line represents the Fermi level. States above the horizontal dotted line represent spin-up electrons and states below the horizontal dotted line represents spin-down electrons.

symmetric points. We found that the Dirac point shifted 0.56 eV above the Fermi level in HS-G/MoS_2, which shows that HS-G/MoS_2 is metallic in nature. The shift in the Dirac point is in good agreement with the previously reported value of 0.49 eV [10, 35]. The Dirac point is formed at 0.56 eV height from the Fermi level in HS-G/MoS_2, because higher values of potential barrier existed between the positions of C and S atoms in Graphene and monolayer MoS_2 surfaces separately. The work function value of HS-G/MoS_2 is greater than MoS_2; as a result, electrons are moved from Graphene to MoS_2 surface making n-type Schottky contact [5, 36]. Figures 3(b) and 3(c) represent the density of states (DOS) and partial density of states (PDOS) plots of HS-G/MoS_2, where the y-axis represents spin-up and spin-down electrons states of DOS/PDOS and the x-axis represents the corresponding energy values.

In addition, to tune the electronic properties at C sites vacancy defects in HS-G/MoS_2 materials, we used band structure calculations of R-1C, L-1C, C-1C, and 2C atom vacancy defects in HS-G/MoS_2 materials as shown in Figure 4, where the x-axis represents high symmetric points in the first Brillouin zone and the y-axis represents the corresponding energy values. We have also taken 100 k-points along the specific direction of the irreducible Brillouin zone by choosing Γ-M-K-Γ high symmetric points.

We found that the Dirac point is not formed in electronic band structures and a small energy gap formed between the lower energy level of the conduction band and upper energy level of the valence band in R-1C, L-1C, C-1C, and 2C atom vacancy defects in HS-G/MoS_2 materials. These R-1C, L-1C, C-1C, and 2C vacancy defects materials have opened narrow bandgap of values 0.15 eV, 0.13 eV, 0.14 eV, and 0.37 eV, respectively. Thus, the strength of metallic nature decreased with an increase in the concentration of defects. It is obvious that electronic configurations of valence electrons in C, Mo, and S atoms are [He] $2s^2\ 2p^2$, [Kr] $4\,d^5\ 5s^1$, and [Ne] $3s^2\ 3p^4$, respectively. Each C atom has a single spin-up in $2p_x$ and $2p_y$ and vacancy in $2p_z$ suborbital; Mo atom has one unpaired spin-up in suborbital 5s and $4d_{xy}$, $4d_{xz}$, $4d_{yz}$, $4d_x^2$-$_y^2$, and $4d_z^2$; S atom has paired spins (up and down) in $3p_x$ suborbital and one unpaired spin-up in $3p_y$ and $3p_z$ suborbital. We have prepared a stable structure of 2C atom vacancy defects in HS-G/MoS_2 materials by removing two C atoms

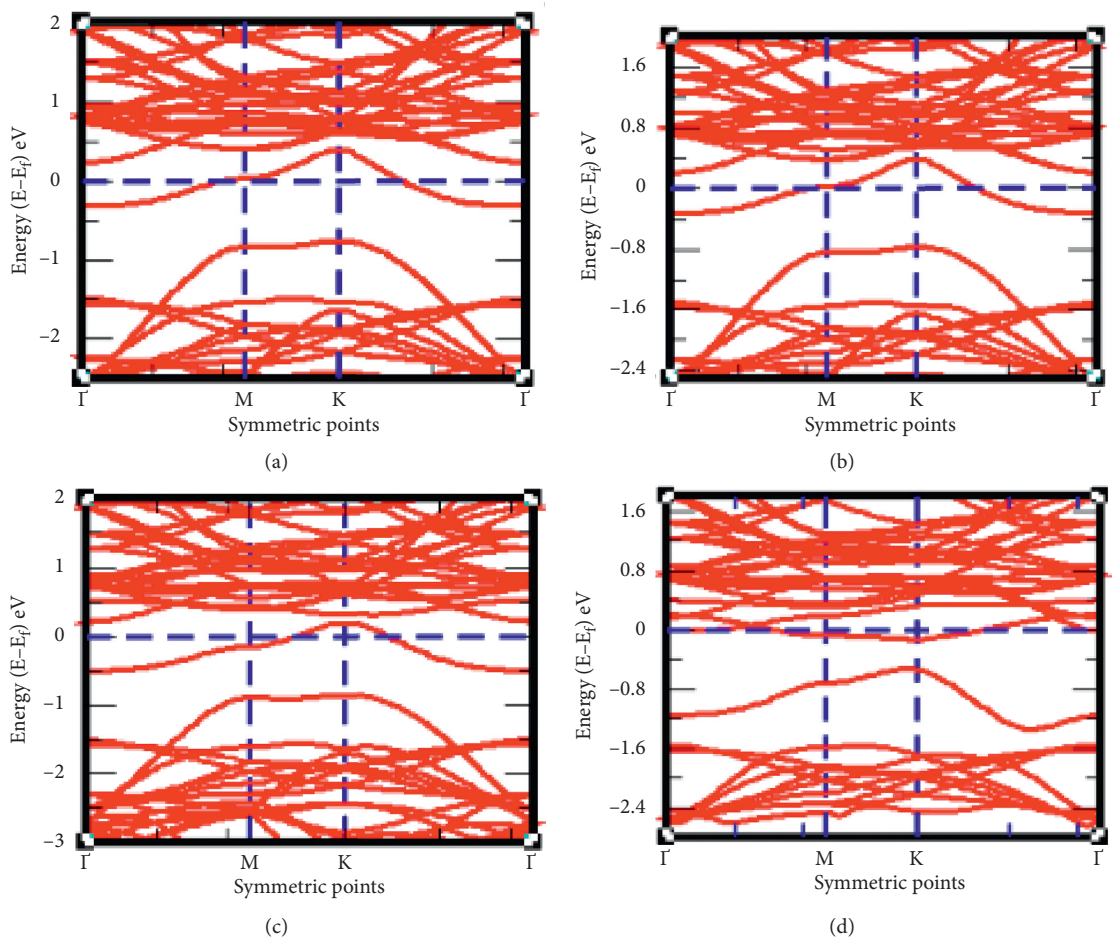

Figure 4: (a) Band structure of R-1C atom vacancy defects in HS-G/MoS_2, (b) band structure of L-1C atom vacancy defects in HS-G/MoS_2, (c) band structure of C-1C atom vacancy defects in HS-G/MoS_2, and (d) band structure of 2C atom vacancy defects in HS-G/MoS_2, where the horizontal dotted line represents Fermi level.

together from HS-G/MoS_2 material containing 59 atoms, as shown in Figure 2(d). Similarly, R-1C, L-1C, and C-1C atom vacancy defects in HS-G/MoS_2 stable materials are prepared by pulling out right 1C, left 1C, and centre 1C positions of carbon atoms from HS-G/MoS_2 structure having 59 atoms, respectively, as shown in Figures 2(a)–2(c). These vacancy positions of carbon atoms developed unpaired spin electrons in suborbital of atoms of 2C defects in HS-G/MoS_2 structure. Similarly, carbon atom vacancy in R-1C, L-1C, and C-1C defects in HS-G/MoS_2 materials produced unpaired spin electrons in the suborbital of atoms. Due to the unpaired total spin-up and total spin-down electrons in the orbitals of atoms in the system, unequal Fermi energy values are obtained in HS-G/MoS_2 and its C sites vacancy defect materials. Therefore, we found that the Fermi energy of HS-G/MoS_2 material has value 0.32 eV and R-1C, L-1C, C-1C, and 2C atom vacancy defects in HS-G/MoS_2 materials have values 0.52 eV, 0.53 eV, 0.54 eV, and 0.56 eV, respectively. It means that the Fermi level shifted upwards (towards conduction band) by 0.20 eV, 0.21 eV, 0.22 eV, and 0.24 eV values, respectively, which means Schottky barrier transition from p-type to n-type Schottky contact by the movement of interfacial charges [35]. The formation of n-type Schottky contact can provide important information for enhancing the power given by high efficiency Schottky nanoelectronic devices [37]. The parameters of Fermi level shift and energy gap look to be associated with each other. Also, they are increased with an increase in its vacancy defects concentrations in materials as shown in Table 1.

To get well competency of electronic and magnetic properties of materials, we have carried out DOS and PDOS calculations [23]. Figures 5(a)–5(d) represent DOS plots of R-1C, L-1C, C-1C, and 2C atom vacancy defects in HS-G/MoS_2 materials, respectively, and Figures 6(a)–6(d) represent PDOS plots of R-1C, L-1C, C-1C, and 2C atom vacancy defects in HS-G/MoS_2 materials, respectively, where the vertical dotted line represents Fermi energy level and the horizontal line separates states of spin-up and spin-down electrons in the orbitals of C, Mo, and S atoms; i.e., the states above the horizontal line represent spin-up electrons and a state below the horizontal line represents spin-down electrons.

The magnetic properties of materials can be investigated by the analysis of spins of electrons distributed in DOS and PDOS plots. The asymmetrically distributed spin-up and spin-down of atoms in DOS and PDOS plots mean that

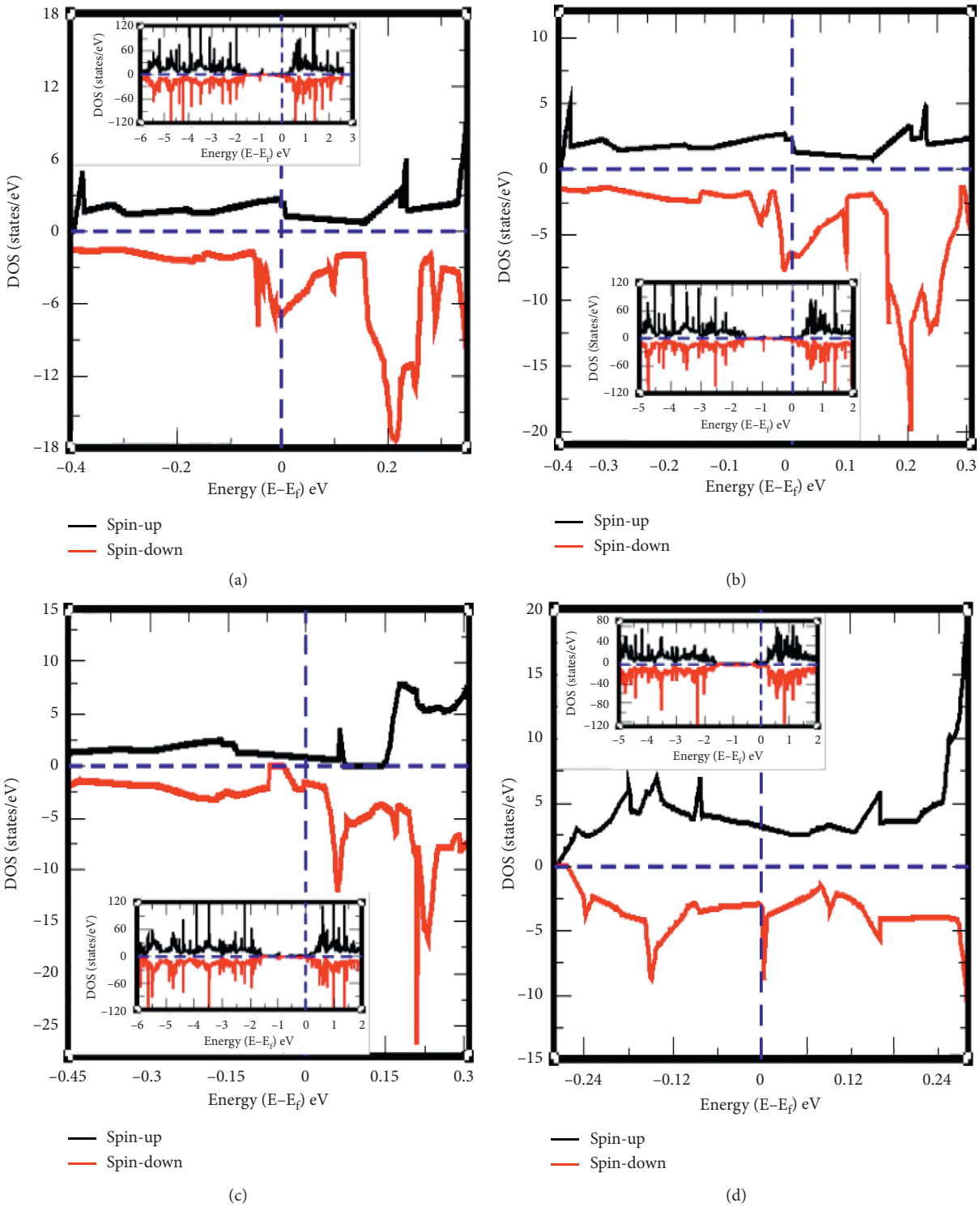

Figure 5: DOS plot of up and down states of spin electrons in the orbitals of C, Mo, and S atoms in (a) R-1C vacancy defects in HS-G/MoS_2 material, (b) L-1C vacancy defects in HS-G/MoS_2 material, (c) C-1C vacancy defects in HS-G/MoS_2 material, and (d) 2C vacancy defects in HS-G/MoS_2 material, where the states above the horizontal dotted line represent spin-up electrons and a state below the horizontal dotted line represents spin-down electrons.

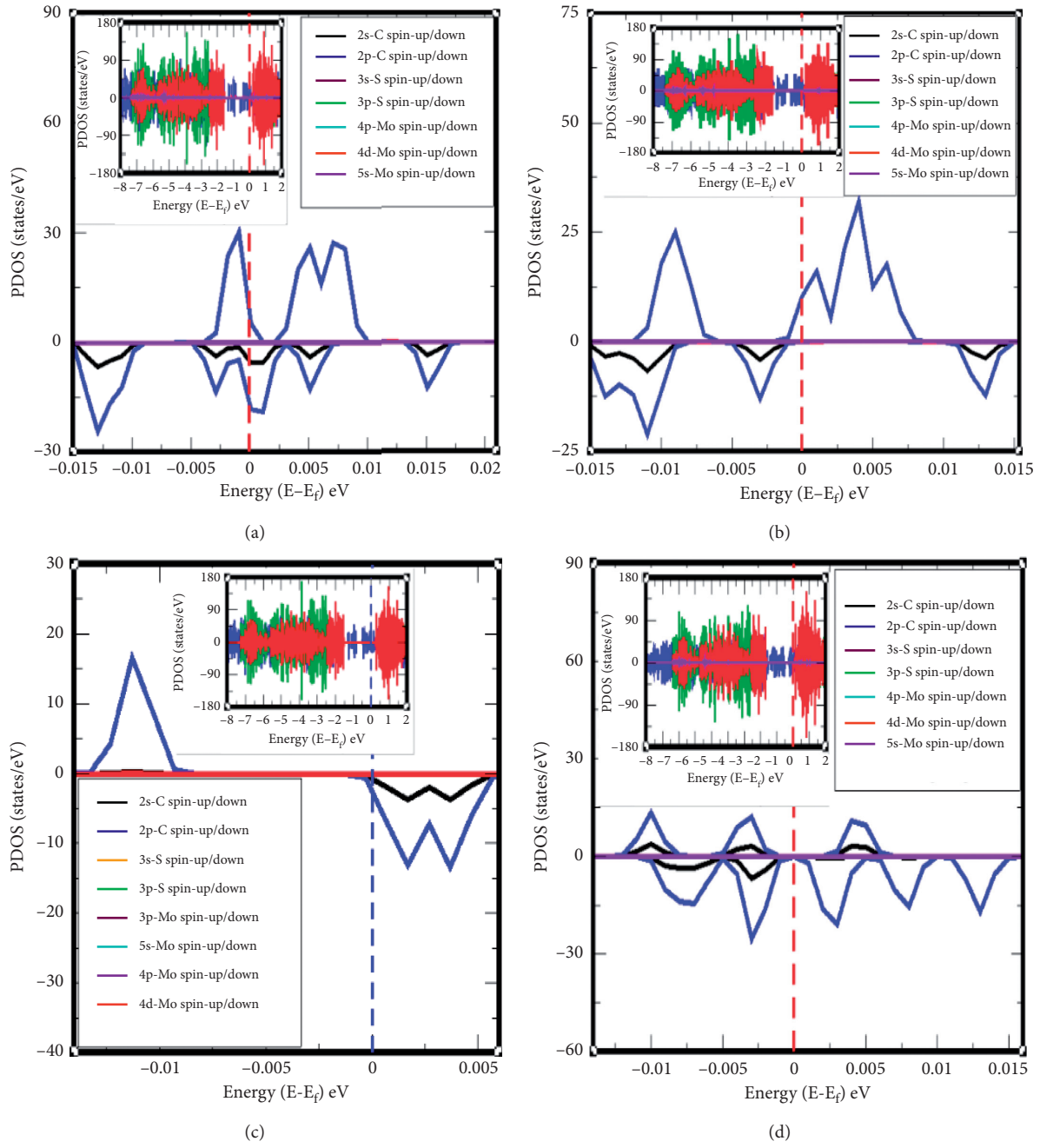

Figure 6: (a) PDOS plot of individual spin-up and spin-down electrons orbital of all atoms in R-1C atom vacancy defects in HS-G/MoS_2. (b) PDOS plot of individual spin-up and spin-down electrons orbital of all atoms in L-1C atom vacancy defects in HS-G/MoS_2. (c) PDOS plot of individual spin-up and spin-down electrons orbital of all atoms in C-1C atom vacancy defects in HS-G/MoS_2. (d) PDOS plot of individual spin-up and spin-down electrons orbital of all atoms in 2C atom vacancy defects in HS-G/MoS_2, where the states above the horizontal line represent spin-up electrons and a state below the horizontal line represents spin-down electrons.

materials have magnetic properties. Similarly, symmetrically distributed spin-up and spin-down of atoms in DOS and PDOS plots mean that materials carry nonmagnetic properties. We observed the spin-up and spin-down states of electrons, which are symmetrically distributed in the DOS and PDOS plot of HS-G/MoS_2 material as shown in Figures 3(b) and 3(c). Hence, HS-G/MoS_2 is a nonmagnetic material.

In addition, we have done the DOS and PDOS analysis of R-1C, L-1C, C-1C, and 2C atom vacancy defects in HS-G/MoS_2 materials. The data of magnetic moment calculations of these materials are given in SI (Table S2). The PDOS plots of 2s and 2p orbital of C atoms, 4p, 4d, and 5s orbital of Mo atoms, and 3s and 3p orbitals of S atoms in R-1C atom vacancy defects in HS-G/MoS_2 material are shown in Figure 6(a). PDOS value near the Fermi level of 2s and 2p orbitals of C atoms reflects that spin-up and spin-down states are asymmetrical. We found that the total magnetic moment of R-1C in HS-G/MoS_2 has a value −0.75 μ_B/cell;

this is due to 2s and 2p spins electrons in the orbitals of C atoms. Also, the magnetic moment given by spins of electrons in 2s and 2p orbitals of C atoms is separately calculated, which have −0.24 $\mu_{B/}$cell and −0.51 $\mu_{B/}$cell values, respectively. These values are obtained by calculating the net magnetic moment given by spin-up and spin-down electrons of carbon atoms in the structure. The negative values of magnetic moment reveal that spin-down electrons of atoms have a principal role compared to spin-up electrons of atoms for magnetism in the system. This means that other atoms do not play a role in the magnetism of R-1C atom vacancy defects in HS-G/MoS_2. In Figure 6(b), the unoccupied spin-up electron states in the 2p orbital of C atoms and spin-down electron states in the 2s and 2p orbital of C atoms are asymmetrically distributed near the Fermi level. Magnetic moment values given by 2s and 2p orbital of C atoms are $-0.23\mu_B$/cell and $-0.52\mu_B$/cell, respectively. Therefore, the total value of the magnetic moment of L-1C vacancy defects in HS-G/MoS_2 material is $-0.75\mu_B$/cell, due to dominant contributions of spin electrons in 2s and 2p orbital of C atoms in the system. Similarly, in Figure 6(c), the only unoccupied spin-down electron states are seen near the Fermi level, which reflects that spin states are asymmetrical. We have evaluated PDOS of C-1C defects in HS-G/MoS_2 material and found that the values of the magnetic moment due to spin electrons in 2s and 2p orbital of C atoms are $-0.07\mu_B$/cell & $-0.05\mu_B$/cell, respectively. Therefore, the total value of the magnetic moment given by spin electrons in the orbital of C atoms in the system is $-0.12\mu_B$/cell. In Figure 6(d), we saw that the asymmetrically distributed spin-up and spin-down electron states are presented beyond −0.0025 eV energy in the valence band and above 0.0024 eV energy in the conduction band. The magnetic moment given by 2s and 2p orbital of C atoms in the system has values $0.7\mu_B$/cell and $0.31\mu_B$/cell, respectively. These values are obtained by calculating net magnetism given by spin-up and spin-own electrons of atoms existing in the system. Therefore, the total value of the magnetic moment of 2C atom vacancy defects in HS-G/MoS_2 material is $+0.39\mu_B$/cell. The positive value of magnetic moment means that spin-up electrons of atoms have a preeminent role compared to spin-down electrons of atoms in the magnetism. In all these cases, 2s and 2p orbitals of C atoms have major contributions of magnetic moments in C sites vacancy defects in HS-G/MoS_2 materials, which are also shown in SI (Figure S1).

4. Conclusions

We have constructed HS-G/MoS_2 and C sites vacancy defects in HS-G/MoS_2 structures and investigated their structural, electronic, and magnetic properties by first-principle calculations with van der Waals corrections in the DFT-D2 levels of approximation. We studied structures of HS-G/MoS_2 and C sites vacancy defects in HS-G/MoS_2 materials and found that the nondefects structure is more compressed than defects structures. The binding energy of these materials is decreased with an increase in its defects concentrations. Then, we investigated the electronic and magnetic properties of these materials from the band structure calculations and DOS/PDOS analysis. From band structure calculations of HS-G/MoS_2, we found that it is metallic in nature. R-1C, L-1C, C-1C, and 2C atom vacancy defects in HS-G/MoS_2 materials have small energy gap of values 0.15 eV, 0.13 eV, 0.14 eV, and 0.37 eV, respectively. Thus, the strength of metallic nature decreased with an increase in the concentration of vacancy in structures. Also, we have calculated the Fermi energy level of pure and vacancy defects geometries, which shows that n-type Schottky barrier contact is formed due to the interfacial charge transfer. For better comprehension of the electronic and magnetic properties of materials, we have performed the DOS and PDOS calculations. We found that DOS and PDOS states of spin-up and spin-down electrons are symmetrically distributed in HS-G/MoS_2 and asymmetrically distributed in C sites vacancy defects in HS-G/MoS_2 materials. Therefore, HS-G/MoS_2 is a nonmagnetic material but C sites vacancy defects in HS-G/MoS_2 materials carry magnetic properties. The total magnetic moment in R-1C, L-1C, C-1C, and 2C atom vacancy defects in HS-G/MoS_2 materials is found to be $-0.75\mu_B$/cell, $-0.75\mu_B$/cell, $-0.12\mu_B$/cell, and $+0.39\mu_B$/cell, respectively. The spins of electrons in 2s and 2p orbitals of C atoms have the main role to bring a magnetic moment in all these materials. The strength of magnetic properties is developed in C sites vacancy defects in HS-G/MoS_2 materials due to the convenient arrangement of spin electrons in the structures.

Data Availability

The data used to support the findings of this study are available from the corresponding author upon request.

Conflicts of Interest

The authors declare that they have no conflicts of interest.

Acknowledgments

HKN acknowledges the UGC Nepal Award no. PhD-75/76-S&T-09 and network project NT-14 of ICTP/OEA. NPA acknowledges UGC Nepal (Grant CRG 073/74 -S&T -01).

Supplementary Materials

Table S_1: the interatomic distances measurement of HS-G/MoS_2 and C sites vacancy defects in HS-G/MoS_2 geometries, where (S-S), (Mo-Mo), and (C-C), respectively, represent the interatomic distance between two sulpher atoms in MoS_2, two molybdenum atoms, and two carbon atoms in Graphene. Table S_2: magnetic values generated by total and individual spin-up and spin-down electron orbital of C, Mo, and S atoms in pure and C sites vacancy defects (HS) in G/MoS_2 geometries from PDOS analysis. Figure S_1: (a) PDOS plot of total spin-up and spin-down electron orbital of all atoms in R-1C atom vacancy defects in HS-G/MoS_2. (b) PDOS plot of total spin-up and spin-down electron orbital of all atoms in L-1C atom vacancy defects in HS-G/MoS_2. (c) PDOS plot of total spin-up and spin-down

electron orbital of all atoms in C-1C atom vacancy defects in HS-G/MoS_2. (d) PDOS plot of total spin-up and spin-down electron orbital of all atoms in 2C atom vacancy defects in HS-G/MoS_2, where the states above the horizontal line represent spin-up electrons and a state below the horizontal line represents spin-down electrons. (*Supplementary Materials*)

References

[1] K. S. Novoselov, A. K. Geim, S. V. Morozov et al., "Electric field effect in atomically thin carbon films," *Science*, vol. 306, no. 5696, pp. 666–669, 2004.

[2] K. S. Novoselov, A. K. Geim, S. V. Morozov et al., "Two-dimensional gas of massless dirac fermions in graphene," *Nature*, vol. 438, no. 7065, pp. 197–200, 2005.

[3] E. V. Castro, K. S. Novoselov, S. V. Morozov et al., "Biased bilayer graphene: semiconductor with a gap tunable by the electric field effect," *Physical Review Letters*, vol. 99, no. 21, p. 216802, 2007.

[4] C. V. Nguyen and N. N. Hieu, "Effect of biaxial strain and external electric field on electronic properties of MoS_2 monolayer: a first-principle study," *Chemical Physics*, vol. 468, pp. 9–14, 2016.

[5] K. F. Mak, C. Lee, J. Hone, J. Shan, and T. F. Heinz, "Atomically thin MoS_2: a new direct-gap semiconductor," *Physical Review Letters*, vol. 105, no. 13, p. 136805, 2010.

[6] E. S. Kadantsev and P. Hawrylak, "Electronic structure of a single MoS_2 monolayer," *Solid State Communications*, vol. 152, no. 10, pp. 909–913, 2012.

[7] B. Radisavljevic, M. B. Whitwick, and A. Kis, "Small-signal amplifier based on single-layer MoS_2," *Applied Physics Letters*, vol. 101, no. 4, p. 043103, 2012.

[8] Y. Hu, M. Ruan, Z. Guo et al., "Structured epitaxial graphene: growth and properties," *Journal of Physics D: Applied Physics*, vol. 45, no. 15, p. 154010, 2012.

[9] C. V. Nguyen, "Tuning the electronic properties and Schottky barrier height of the vertical graphene/MoS_2 heterostructure by an electric gating," *Superlattices and Microstructures*, vol. 116, pp. 79–87, 2018.

[10] H. V. Phuc, N. N. Hieu, B. D. Hoi, L. T. T. Phuong, and C. V. Nguyen, "First principle study on the electronic properties and Schottky contact of graphene adsorbed on MoS_2 monolayer under applied out-plane strain," *Surface Science*, vol. 668, pp. 23–28, 2018.

[11] H. U. Din, M. Idrees, A. Albar et al., "Rashba spin splitting and photocatalytic properties of GeC–MSSe (M=Mo, W) van der Waals heterostructures," *Physical Review B*, vol. 100, no. 16, p. 165425, 2019.

[12] T. V. Vu, N. V. Hieu, H. V. Phuc et al., "Graphene/WSeTe van der Waals heterostructure: controllable electronic properties and Schottky barrier via interlayer coupling and electric field," *Applied Surface Science*, vol. 507, p. 145036, 2020.

[13] C. V. Nguyen, M. Idrees, H. V. Phuc et al., "Interlayer coupling and electric field controllable Schottky barriers and contact types in graphene/PbI_2 heterostructures," *Physical Review B*, vol. 101, no. 23, p. 235419, 2020.

[14] J. Wang, F. Ma, W. Liang, and M. Sun, "Electrical properties and applications of graphene, hexagonal boron nitride (h-BN), and graphene/h-BN heterostructures," *Materials Today Physics*, vol. 2, pp. 6–34, 2017.

[15] M. Ghorbani-Asl, P. D. Bristowe, K. Koziol, T. Heine, and A. Kuc, "Effect of compression on the electronic, optical and transport properties of MoS_2/graphene-based junctions," *2D Materials*, vol. 3, no. 2, p. 025018, 2016.

[16] Y. Ma, Y. Dai, M. Guo, C. Niu, and B. Huang, "Graphene adhesion on MoS_2 monolayer: an ab initio study," *Nanoscale*, vol. 3, no. 9, pp. 3883–3887, 2011.

[17] A. D. Phan, N. A. Viet, N. A. Poklonski, L. M. Woods, and C. H. Le, "Interaction of a graphene sheet with a ferromagnetic metal plate," *Physical Review B*, vol. 86, no. 15, p. 155419, 2012.

[18] W. J. Yu, Z. Li, H. Zhou et al., "Vertically stacked multi-heterostructures of layered materials for logic transistors and complementary inverters," *Nature Materials*, vol. 12, no. 3, pp. 246–252, 2013.

[19] M. S. Choi, G. H. Lee, Y. J. Yu et al., "Controlled charge trapping by molybdenum disulphide and graphene in ultrathin heterostructured memory devices," *Nature Communications*, vol. 4, no. 1, pp. 1–7, 2013.

[20] K. Roy, M. Padmanabhan, S. Goswami et al., "Graphene-MoS_2 hybrid structures for multifunctional photoresponsive memory devices," *Nature Nanotechnology*, vol. 8, no. 11, pp. 826–830, 2013.

[21] L. Debbichi, O. Eriksson, and S. Lebègue, "Electronic structure of two-dimensional transition metal dichalcogenide bilayers from ab initio theory," *Physical Review B*, vol. 89, no. 20, p. 205311, 2014.

[22] H. K. Neupane and N. P. Adhikari, "Structure, electronic and magnetic properties of 2D Graphene-Molybdenum diSulphide (G-MoS_2) heterostructure (HS) with vacancy defects at Mo sites," *Computational Condensed Matter*, vol. 24, p. e00489, 2020.

[23] C. Kittel, P. McEuen, and P. McEuen, *Introduction to solid state Physics*, vol. 8, pp. 140–303, Wiley, New York, NY, USA, 1996.

[24] M. V. Makarova, Y. Akaishi, T. Ikarashi, K. S. Rao, S. Yoshimura, and H. Saito, "Alternating magnetic force microscopy: effect of Si doping on the temporal performance degradation of amorphous FeCoB magnetic tips," *Journal of Magnetism and Magnetic Materials*, vol. 471, pp. 209–214, 2019.

[25] H. X. Peng, F. Qin, and M. H. Phan, *Ferromagnetic Microwire Composites: From Sensors to Microwave Applications*, Springer, New York, NY, USA, 2016.

[26] P. Hohenberg and W. Kohn, "Inhomogeneous electron gas," *Physical Review*, vol. 136, no. 3B, p. B864, 1964.

[27] S. Grimme, "Accurate description of van der Waals complexes by density functional theory including empirical corrections," *Journal of Computational Chemistry*, vol. 25, no. 12, pp. 1463–1473, 2004.

[28] P. Giannozzi, S. Baroni, N. Bonini et al., "Quantum ESPRESSO: a modular and open-source software project for quantum simulations of materials," *Journal of Physics: Condensed Matter*, vol. 21, no. 39, p. 395502, 2009.

[29] J. P. Perdew, K. Burke, and M. Ernzerhof, "Generalized gradient approximation made simple," *Physical Review Letters*, vol. 77, no. 18, p. 3865, 1996.

[30] B. G. Pfrommer, M. Côté, S. G. Louie, and M. L. Cohen, "Relaxation of crystals with the quasi-Newton method," *Journal of Computational Physics*, vol. 131, no. 1, pp. 233–240, 1997.

[31] R. M. Martin and R. M. Martin, *Electronic Structure: Basic Theory and Practical Methods*, Cambridge University Press, Cambridge, UK, 2004.

[32] N. Marzari, D. Vanderbilt, A. De Vita, and M. C. Payne, "Thermal contraction and disordering of the Al(110) surface," *Physical Review Letters*, vol. 82, no. 16, p. 3296, 1999.

[33] S. Ahmad and S. Mukherjee, "A comparative study of electronic properties of bulk MoS_2 and its monolayer using DFT technique: application of mechanical strain on MoS_2 monolayer," *Graphene*, vol. 3, no. 4, pp. 52–59, 2014.

[34] Z. Hou, X. Wang, T. Ikeda et al., "Interplay between nitrogen dopants and native point defects in graphene," *Physical Review B*, vol. 85, no. 16, p. 165439, 2012.

[35] B. Liu, L.-J. Wu, Y.-Q. Zhao, L.-Z. Wang, and M.-Q. Cai, "First-principles investigation of the Schottky contact for the two-dimensional MoS_2 and graphene heterostructure," *RSC Advances*, vol. 6, no. 65, pp. 60271–60276, 2016.

[36] N. N. Hieu, H. V. Phuc, V. V. Ilyasov et al., "First-principles study of the structural and electronic properties of graphene/MoS2 interfaces," *Journal of Applied Physics*, vol. 122, no. 10, p. 104301, 2017.

[37] K. D. Pham, N. N. Hieu, H. V. Phuc et al., "Layered graphene/GaS van der Waals heterostructure: controlling the electronic properties and Schottky barrier by vertical strain," *Applied Physics Letters*, vol. 113, no. 17, p. 171605, 2018.

Computational Condensed Matter 24 (2020) e00489

Contents lists available at ScienceDirect

Computational Condensed Matter

journal homepage: http://ees.elsevier.com/cocom/default.asp

Structure, electronic and magnetic properties of 2D Graphene-Molybdenum diSulphide (G-MoS_2) Heterostructure (HS) with vacancy defects at Mo sites

H.K. Neupane [a, b], N.P. Adhikari [b, *]

[a] Amrit Campus, Institute of Science and Technology Tribhuvan University, Kathmandu, Nepal
[b] Central Department of Physics, Institute of Science and Technology Tribhuvan University, Kathmandu, Nepal

ARTICLE INFO

Article history:
Received 9 May 2020
Received in revised form
14 June 2020
Accepted 15 June 2020

Keywords:
DFT
Heterostructres
Graphene
MoS_2
defects

ABSTRACT

First-principles calculations have been performed to study Structure, Electronic and Magnetic properties of 2D Graphene-Molybdenum diSulphide G-MoS_2 heterostructure (HS) materials with vacancy defects at Mo sites. All the calculations have been performed within the framework of the first-principles Density Functional Theory (DFT) under the Perdew-Burke-Ernzerhof (PBE) form of the Generalized Gradient Approximation (GGA). The ven der Waals (vdW) interactions have been taken into account (considered via Grimme's model) by DFT-D_2 approach. The G-MoS_2 heterostructure without Mo sites defects and with Mo sites defects have been optimized using BFGS methods implemented in Quantum ESPRESSO. Our investigations show that the defects materials are more compact than the pure material. Further, we have studied the Electronic and Magnetic properties of pure and defects G-MoS_2 heterostructures from the band structure calculations and DOS-PDOS analysis. The results show that the pure and defects heterostructures are metallic in nature and they can be useful for low power consumption electronic devices. From the band structures calculation, it is seen that Fermi energy level shifted toward the valence band in single Mo atom and two Mo atoms vacancy defects both the cases means p-type Schottky defects. The analysis of the magnetic properties show that the nonmagnetic pure G-MoS_2 heterostructure changes to magnetic materials by Mo sites defects. It is also found that total magnetism values of C-1Mo, L-1Mo and 2Mo atoms vacancy defects have 2.61 (Bohr-Mag/cell), 2.65 (Bohr-Mag/cell) and 5.25 (Bohr-Mag/cell) respectively and 2p orbital of C atoms, 3p orbital of S atoms and 4d orbital of Mo atoms have main contributions to the magnetism in all three configurations.

© 2020 Elsevier B.V. All rights reserved.

1. Introduction

Graphene is basic unit of graphite. Its hexagonal structure is stable in which each carbon atom bonds with the surrounding carbon atoms by sp^2 hybridization where non-bonding electrons move freely between the layers. A sp^2 hybridized single sheet of carbon atoms can be organized in a honeycomb lattice. Its two bands π and π^* emerge from the p_z orbitals and meet at six points in k-space known as Dirac points which are at the edges of the Brillouin zone k and k', shows Graphene is a zero band gap semiconductor. Because of the existing Dirac point in Graphene structure, it has remarkable properties such as electronic, optical, mechanical and magnetic etc. [1]. Due to these properties, Graphene is a favorable material for the fabrication of electronic devices, transparent electrodes and spintronics devices [1,2]. The study of two dimensional hexagonal structural materials have become of great interest to many researchers for nanoscience. Complementary to Graphene, Molybdenum diSulphide (MoS_2) is one of the two dimensional transition metal dichalcogenide [3] honeycomb structure with certain gap in its electronic band known as wide band gap exotic semiconductor. Mo and S atoms are stacked together to give S-Mo-S arrangement [4] which has intriguing properties. MoS_2 is a wide band semiconductor. It has potential applications in academic as well as industrial sectors. It is

* Corresponding author.
E-mail address: narayan.adhikari@cdp.tu.edu.np (N.P. Adhikari).

https://doi.org/10.1016/j.cocom.2020.e00489
2352-2143/© 2020 Elsevier B.V. All rights reserved.

used to produce transistors, integrated logic circuits, signal amplifier, photodetectors, flexible optoelectronic devices, solar cells, photocatalysts and lubricants [5–8]. The basic applied research in new 2D materials based on Graphene has made great progress [9–11]. When combined with other new 2D materials with different chemical bonds and the formation of different physical and chemical properties of new lattice structures known as heterostructures [12–14].

Heterostructures can be used to eliminate the undesired properties and drag desirable properties of constituents; they are beyond the capacities of constituents. They have more applications by tuning the desired properties [7,13,14]. Therefore, Graphene (G) and Molybdenum diSulphide (MoS_2) are joined together to form Graphene-Molybdenum diSulphide (G-MoS_2) heterostructure (HS). It can be studied periodically repeated super cells, which allow for a conventional reciprocal space formulation of the problem. Typically, super cells are chosen in such a way that they contain two interfaces that are equivalent to the term of stoichimetry and geometry, for avoiding electric fields due to unbalanced charges [15]. Both theoretical and experimental research groups studied Graphene based van der Waals (vdW) heterostructures G-MoS_2 interfaces [15,16]; they reported it has some novel properties for creating individual components in electronic devices [17]. It becomes potential candidate for applications in electronic, photovoltaic and memory devices [18–20]. Therefore, HS of G-MoS_2 has intriguing properties like excellent mechanical flexibility, electronic properties, optical transparency, photoconductivity and favorable transport properties [8,21]. Although, (HS) G-MoS_2 provides helpful information to design, fabricate and understand the physics mechanism in the Graphene based 2D van der Waals heterostructure materials [7,8], we found that it has non-magnetic nature. But, we intend to investigate magnetic properties in 2D Graphene based van der Waals heterostructures; we need the vacancy defects geometries of (HS) G-MoS_2 material. The defects in solid are any deviation of atoms or ions from the periodicity. The defects are one unavoidable properties of crystalline structure, they are used to find not only novel properties but also design the new materials, so it influences the properties of heterostructures material in solids [22]. However, Structure, Electronic and Magnetic properties of 2D (HS) material G-MoS_2 at Mo sites vacancy defects has not been reported to the best of our knowledge. Therefore, we focus to study Structural, Electronic and Magnetic properties of 2D, (HS) G-MoS_2 with Mo sites vacancy defects. In present work, we considered Mo cites vacancy defects of G-MoS_2 hetero system using DFT method of calculations. We focus our attention for studying electronic band structure, Density of States (DOS) and Partial Density of States (PDOS) and hence the magnetic properties. We found the values of magnetic moment in Mo atoms vacancy defects (HS) G-MoS_2 materials. Due to the appearance of magnetism, Mo sites vacancy defects (HS) G-MoS_2 seems to be promising in usage in various devices requiring magnetic properties. Many of our modern technological devices rely on magnetism and magnetic materials. Novel nanomagnetic materials have potential applications in the fields of biomedicine, molecular biology, biochemistry, diagnosis, catalysis, nanoelectronic devices and various other industrial applications such as magnetic seals in motors, magnetic sensors, magnetic inks for bank checks, electrical power generator and transformers, magnetic recording media and computers etc. [23,24]. Therefore, the understanding of novel electronic and magnetic properties on random Mo atoms, vacancy defects may provide significant outlines for the material to device applications.

The remaining part of this paper is organized in the following way. In section 2, we discuss the computational details related to the present work. Main finding are presented and discussed in section 3. We have closed by making conclusions and outlook of the work.

2. Computational details

To investigate the Structural, Electronic and Magnetic properties of heterostructure (HS) material G-MoS_2 with vacancy defects at Mo sites, the calculations are performed using Density Functional Theory (DFT) [25] implemented in the quantum ESPRESSO (QE) code [26]. The Perdew-Burke-Ernzerhof (PBE) variant of the Generalized Gradient Approximation (GGA) [27] incorporating van der Waals (vdW) interactions has been considered. It is well known that the weak interactions are not well described by the standard PBE functional. So a semi-empirical dispersion-correlated Density Functional Theory (DFT-D_2) approach proposed by Grimme's was adopted [28]. Grimme's model was widely used and explained to give better description of weak van der Waals interactions. Grimme's used Rappe-Rabe-Kaxiraas-Joannopoulos (RRJK) model of ultra-soft pseudopotentials to take into account the weak van der Waals interactions. The plane wave expansion with kinetic energy cut-off values of 35 Ry (476 eV) and 350 Ry (4760 eV) respectively, are used for wave function and charge density after the convergence plot of total energy versus cut-off energy. A mesh of $4 \times 4 \times 1$ k-points are taken for the (HS) and further calculations on the basis of the plot of total energy versus number of k-points. The vacuum distance greater than 20 A^0 is maintained to minimize the interactions between two adjacent layers. All the structures are optimized using the Broyden-Fletcher-Goldfarb-Shanno (BFGS) [29] scheme until the total energy change is less than 10^{-4} Ry and force acting is less than 10^{-3} Ry/Bohr's between two consecutive SCF steps. The Marzarri-Vanderbilt [30] smearing or cold smearing with a small broadening width of 0.001 Ry is used. Furthermore, diagonalization method is chosen as 'devid' with mixing factor 0.6 for self consistency. Spin polarized calculations are accommodated to study the magnetic properties of the systems. For band structure calculations, 100 k-points are chosen along the high symmetric points connecting the reciprocal space. For the DOS and PDOS calculations, we have used an automatic denser mesh of $8 \times 8 \times 1$ k-points. Fig. 1 presents the super cell structure of G-MoS_2 heterostructure. The super cell contains one (4×4) Graphene layer and one (3×3) MoS_2 monolayer. The (3×3) MoS_2 monolayer was used to match (4×4) Graphene sheet so that (HS) G-MoS_2 is modeling with due to consideration of the lattice mismatch about 4.13% which is reasonably small and thus it does not affect main results. In this work we have created the vacancy defects of Molybdenum (Mo) atoms by random removal from G-MoS_2 hetero system then optimized these geometries for calculations as shown in Fig. 2.

3. Results and discussion

In this section, we present our main findings and their interpretation. During our work, we have carried out spin polarized DFT calculation to study Structural, Electronic and Magnetic properties of (HS) G-MoS_2 at Mo sites vacancy defects. All these calculations were performed within the first-principles study with van der Waals (vdW) interaction in DFT-D_2 level of approximation using GGA, implemented with Quantum ESPRESSO code.

3.1. Structural properties

For the construction of unit cell Graphene, the atomic positions are chosen in such a way that, the distance between two carbon atoms is 1.42 A^0 which was obtained experimentally [31]. The unit cell of Graphene is hexagonal and it can be easily created using QE codes by writing bravais lattice index, 'ibrav = 4' in the input file. The input file contains the parameters, celldm(1) = a, celldm(2) = b/a celldm(3) = c/a, where (a), (b) and (c) are lattice constants in Bohr along x, y, z directions respectively. In order to

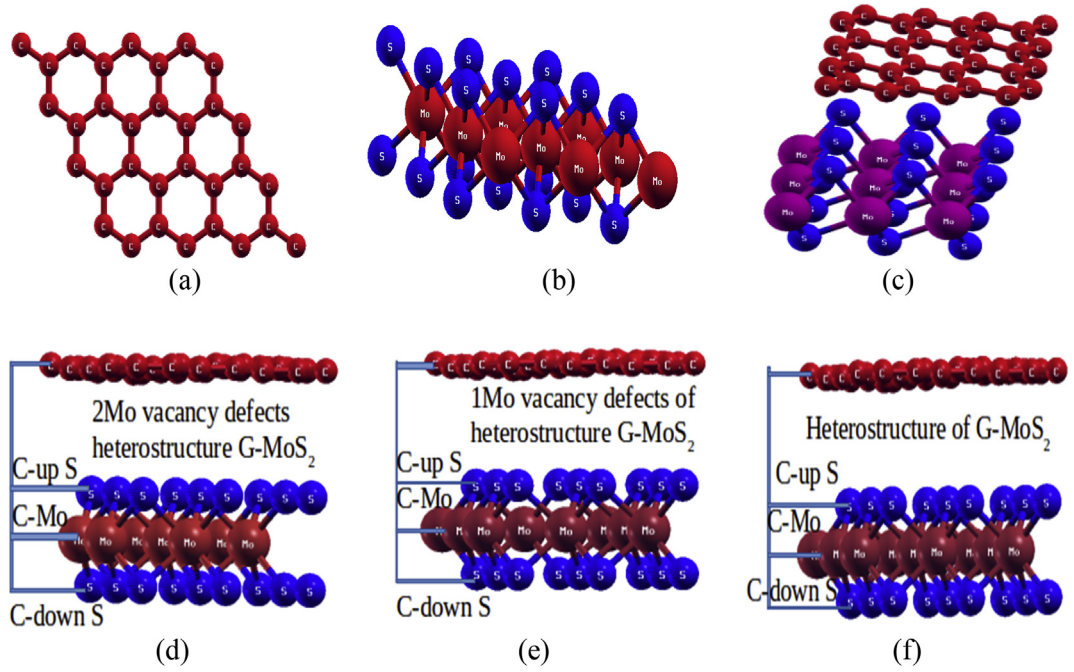

Fig. 1. Super cell structures, where multiple number of unit cells are used to form super cell structures of Graphene and MoS_2. Unit cell consists of a single Mo atom intercalated between two S atoms at a bond length of 2.42 A^0 and S-Mo-S of lattice constant 3.18 A^0 since, 1S atom and 1Mo atom are covalently bounded with 3Mo atoms and 6S atoms respectively to form hexagonal structure, these super cell of Graphene and MoS_2 are joined together to form (HS) of G-MoS_2 (a) (4 × 4) super cell of Graphene (b) (3 × 3) super cell of MoS_2 (c) G-MoS_2 hetero structure (d) interlayer & inter-atomic distances measurement of 2Mo vacancy defects (HS) G-MoS_2 (e) interlayer & inter-atomic distances measurement of 1Mo vacancy defects (HS) G-MoS_2 (f) interlayer & inter-atomic distances measurement of (HS) G-MoS_2.

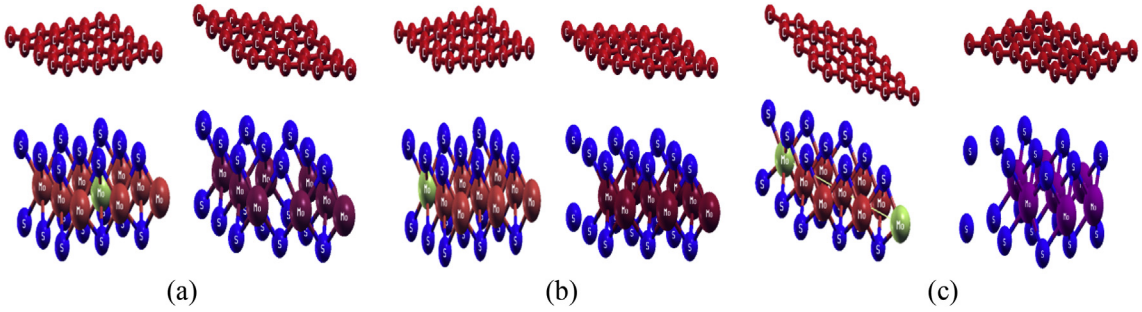

Fig. 2. Mo sites vacancy defects where Mo vacancy defects are created by random removal of 1Mo atom from centre, 1Mo atom from left hand side and 2Mo atoms from both left and right sides respectively in (HS) G-MoS_2 (a) C-1Mo atom vacancy defects (b) L-1Mo atom vacancy defects (c) 2Mo (both left hand side 1Mo and right hand side 1Mo) atoms vacancy defects.

prevent any possibility of interaction between two Graphene layer in z-direction, we kept the distance between two consecutive layers by 20 A^0, that is why we define celldm(3) according to this value. The atomic species for each atom are defined by their atomic symbol followed by atomic mass unit and ultra-soft pseudopotential. After construction of unit cell, we have calculated kinetic energy cut-off ($E_{cut\text{-}off}$), k-points (n_{kx}, n_{ky}, n_{kz}) and lattice parameter (a) from convergence test then used these parameters on input file and relaxed our system. From this relaxed-optimized structure of Graphene unit cell, the distance between two neighboring carbon atoms is found to be 1.42 A^0, which is much closer to the experimental value [31]. Therefore, we constructed the (4 × 4) super cell by extending optimized primitive unit cell along x and y directions using XCrySDen as shown in Fig. 1(a). A hexagonal unit cell of monolayer MoS_2 with the basis of three (1-Mo and 2-S) atoms in honeycomb lattice structure is initially constructed by using experimental value [4,32]. It is built up by single layers of S-Mo-S atoms. It consists of two planes of Sulpher (S) atoms and an intercalated plane of Molybdenum (Mo) atom which bounds with the Sulpher atoms in a trigonal prismatic arrangement. Each Mo atom is surrounded by six first nearest neighboring S atoms. After the construction of unit cell, the structure is optimized with respect to lattice parameter (a), kinetic energy cut-off ($E_{cut\text{-}off}$) for plane wave and the number of k-points along x-axis and y-axis respectively by BFGS method. Based on the convergence tests, we obtained the lattice constant (a) for the MoS_2 equal to 3.18 A^0 which agree with the experimentally reported value 3.19 A^0 [4,27]. The (3 × 3) super cell of monolayer MoS_2 is constructed by using the lattice constant which is three times that of the unit cell as shown in Fig. 1 (b). Further, the plot of the total energy versus the number of k-points shows that the energy of unit cell of monolayer MoS_2 is almost constant when the number of k-points ($n_{kx} = n_{ky}$) crosses 10. A mesh of 10 × 10 × 1 k-points is therefore, used for Brilouin-zone integration of unit cells and a mesh of 4 × 4 × 1 k-points are taken for (3 × 3) super cell. A plane wave basis set with energy cut-off value of 35Ry for the wave function and 350Ry for the

charge density is used for the expansion of the ground state electronic wave function. The (HS) G-MoS_2 is modeling using optimized (3×3) super cell of MoS_2 (9-Mo atoms and 18-S atoms) and (4×4) super cell of Graphene (32-C atoms) with due to consideration (i.e. 4.13%) of the lattice mismatch as shown in Fig. 1(c). The (HS) material G-MoS_2 at Mo sites defects are also constructed after random removal of centre 1Mo atom (C-1Mo), left hand side 1Mo atom (L-1Mo) and 2Mo atoms (both left and right sides) in (HS) G-MoS_2. Thus, out of 9 Mo atoms, vacancy defects of C-1Mo, L-1Mo and 2Mo atoms are found to be 11.11% (1/9 = 0.1111), 11.11% (1/9 = 0.1111) and 22.22% (2/9 = 0.2222) in the system, then we optimized them by using BFGS method [29] shown in Fig. 2(a), 2(b) and 2(c) respectively. Fig. 1(d), 1(e) and 1(f) represent interlayer and inter-atomic distances measurement geometries of Mo sites vacancy defects (HS) G-MoS_2 and pure (HS) G-MoS_2.

The interlayer and inter-atomic distances of pure and defects geometries of (HS) G-MoS_2 are given in Table 1.

From Table 1, we can see that, distance parameters like C atom in Graphene to Mo atom in monolayer MoS_2, C atom in Graphene to up S atom in monolayer MoS_2 and C atom in Graphene to down S atom in monolayer MoS_2 of materials are decreased after formation of Mo sites vacancy defects. This means, configuration of vacancy defects materials are more compact than original configuration material. Also, compactness of material increased with increased its defects concentrations.

3.2. Electronic and magnetic properties

The electronic and magnetic properties of (HS) G-MoS_2 materials are studied from the optimized-relaxed structures. All the structures are optimized using the BFGS [29] method within first-principles calculations and PBE variant of the GGA [27], incorporating van der Waals interaction has been considered via Grimme's model. Grimme's model used RRKJ model of ultra-soft pseudopotential to take in to account the interaction between ion cores and valence electrons [28]. Figs. 1(c), Fig. 2(a) and 2(b), 2(c) show the fully optimized and relaxed atomic structures of pure and C-1Mo, L-1Mo, 2Mo atoms, vacancy defects (HS) G-MoS_2 materials. The electronic configurations of valence electrons in C, Mo and S atoms are C:[He] $2s^2 2p^2$, Mo:[Kr] $4d^5 5s^1$ and S:[Ne] $3s^2 3p^4$ respectively, they are used in pure and vacancy defects geometries of (HS) G-MoS_2. To understand the impact of Mo atoms vacancy defects in (HS) G-MoS_2, we first need to understand the Electronic properties of Graphene, MoS_2 and (HS) G-MoS_2. In the case of Graphene, the states below the Fermi level (E_f) characterized by π bonds and states above the Fermi level (E_f) characterized by π^* anti-bonding states and corresponding bands meet at Fermi level (Dirac point) employing zero band gap energy. So, it is called a zero band gap semiconductor. On the analysis of bands structure of MoS_2, it is an intrinsic semiconductor with direct band of value 1.65eV in which the Fermi energy (E_f) is at exactly between the valence band maxima (VBM) and conduction band minima (CBM) i.e. the direct band transition along k-symmetric points between VBM and CBM. This band gap is still smaller than that of the experimentally reported results 1.80eV [32]. In (HS) G-MoS_2 material, the higher the potential barrier has been observed between positions of C atoms in isolated Graphene surface and S atoms in monolayer MoS_2 surface. The difference in the work function value in case of (HS) G-MoS_2 and isolated monolayer MoS_2 (i.e. work function of (HS) G-MoS_2 - work function of monolayer MoS_2) is greater than zero electron volts [35], it means electrons will be transferred from Graphene to MoS_2 surface, making the n-type contact. That is why; Dirac cone of Graphene is up-shifted towards the higher binding energy in G-MoS_2 heterostructure material. As a result, n-type Schottky contact is formed in the (HS) G-MoS_2 with the Schottky barrier height (Dirac shift amplitude) of 0.56eV as shown in Fig. 3(a). That Dirac shift amplitude value of (HS) G-MoS_2 geometry is in good agreement with the reported values [7,8,33]. The energy bands structure, DOS and PDOS analysis plots of heterostructure G-MoS_2 are shown in Fig. 3(a), 3(b) and 3(c) respectively where, x-axis

Table 1
The interlayer and inter-atomic distances of pure and defects geometries of (HS) G-MoS_2.

Interlayer distances of (HS) G-MoS_2 along x, y and z axis	Distance between C atom in graphene & Mo atom in MoS_2	Distance between C atom in graphene & up S atom in MoS_2	Distance between C atom in graphene & down S atom in MoS_2
x-axis (A^0)	0.29	1.88	0.89
y-axis (A^0)	0.25	1.16	1.17
z-axis (A^0)	5.89	4.32	7.47

Inter-atomic distances of (HS) G-MoS_2 along x, y and z axis	x-axis (A^0)	y-axis (A^0)	z-axis (A^0)
S-S	0.00	0.00	3.14
Mo-Mo	1.59	2.75	0.00
R1Mo - C1Mo	4.76	2.75	0.00
C1Mo - L1Mo	4.76	2.75	0.00
L1Mo - R1Mo	9.53	5.50	0.00
Mo-S	1.53	0.92	1.57
C-C	0.00	1.38	0.09

Interlayer distances of Mo sites vacancy defects of (HS) G-MoS_2 along x, y and z axis	Distance between C atom in graphene & Mo atom in MoS_2		Distance between C atom in graphene & up S atom in MoS_2		Distance between C atom in graphene & down S atom in MoS_2	
	2 Mo	1 Mo	2 Mo	1 Mo	2 Mo	1 Mo
x-axis (A^0)	0.28	0.29	1.87	1.88	0.87	0.88
y-axis (A^0)	0.25	0.25	1.16	1.17	1.16	1.17
z-axis (A^0)	5.00	5.42	3.44	3.86	6.59	7.01

Inter-atomic distances of Mo sites vacancy defects of (HS) G-MoS_2 along x, y and z axis	x-axis (A^0)		y-axis (A^0)		z-axis (A^0)	
	2Mo	1Mo	2Mo	1Mo	2Mo	1Mo
S − S	0.00	0.00	0.01	0.00	3.15	3.14
Mo-Mo	1.50	1.59	2.76	2.75	0.00	0.00
Mo-S	1.54	1.53	0.92	0.92	1.57	1.57
C-C	0.00	0.00	1.38	1.38	0.09	0.09

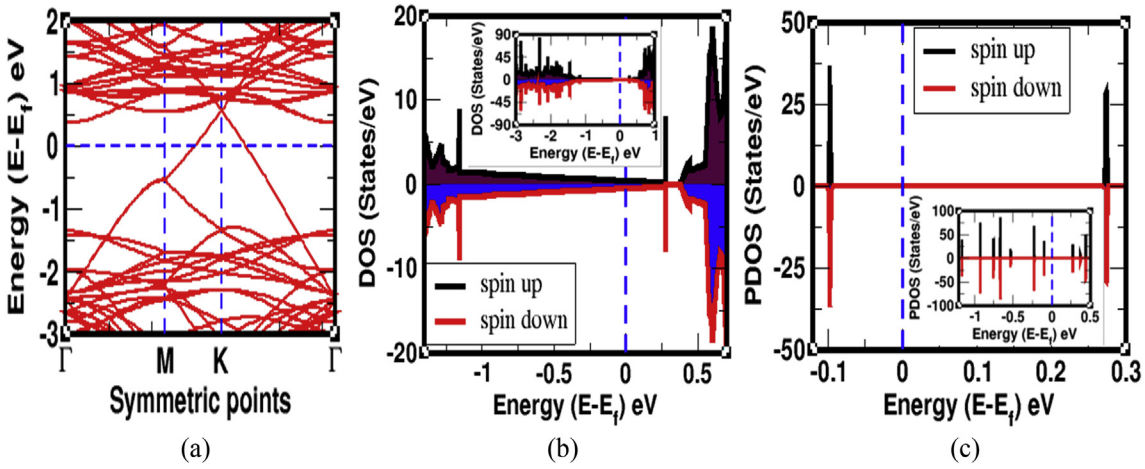

Fig. 3. Band structure, DOS and PDOS plots of (HS) G-MoS_2 where horizontal dotted line represents Fermi level in band structure plot and vertical dotted line represents Fermi level in DOS and PDOS plots (a) band structure (b) spin up electrons and spin down electrons DOS are symmetrical (c) spin up electrons and spin down electrons PDOS are symmetrical.

represents high symmetric points in the first Brillouin zone and y-axis represents the corresponding energy values in bands plot and in DOS-PDOS plots, y-axis represents spin up electrons and spin down electrons of DOS-PDOS and x-axis represents the corresponding energy values.

Furthermore, we studied the electronic and magnetic properties at Mo sites vacancy defects in (HS) G-MoS_2 material. The electronic bands structures at C-1Mo, L-1Mo and 2Mo atoms vacancy defects (HS) G-MoS_2 materials are shown in Fig. 4(a), Fig. 5(a) and Fig. 6(a) respectively where we have taken 100 k-points along the specific direction of irreducible Brillouin zone to get fine bands structure by choosing Γ-*M*-K-Γ high symmetric points. In Fig. 4(a), 5(a) and Fig. 6(a), we found that Dirac point lies in the conduction band and hence values of Dirac point amplitude at C-1Mo, L-1Mo and 2Mo atoms, vacancy defects in (HS) G-MoS_2 have 0.65eV, 0.65eV and 0.67eV. The Fermi energy level of pure (HS) G-MoS_2 is at 0.32eV whereas after creation of vacancy defects at 1Mo and 2Mo atoms sites, Fermi energy levels are at −0.43 eV and −0.70eV respectively. It means, Fermi level shifted downwards (towards valence band) by 0.75 eV and 1.02 eV respectively. They show that, there is more numbers of holes (electrons deficiency) present in the valence band, i.e. the Fermi level shift determine the Schottky barrier transition from n-type Schottky contact to p-type Schottky contact due to the interfacial charge transfer [33]. To improve the performance of high efficiency Schottky nano-electronic devices, useful information are provided by the transformation of n-type to p-type Schottky contact [10,11,36]. The Fermi level shift towards the valence band is related to Dirac point shift towards the conduction band. We show that, greater amount of Fermi energy levels shift to the valence band with respect to greater amount of Dirac amplitude values shift to the conduction band shown by data in Table 2. It implies that, there is probability to flow electrons in conduction band. Dirac point at the Fermi level is preserved but shifted in the formation of heterostructure which shows the impurity states leading from modeled part is different from initial position of host material [7,8,36]. Interestingly, in all these defects geometries of (HS) G-MoS_2, the Fermi level shift towards the valence band indicates, the formation of holes in valence band, this is called p-type Schottky defects.

As we know in Table 2, Fermi levels shift and amplitudes of Dirac point shift are related parameters, they increased with increased the concentration of vacancy defects in the materials. The amplitude of Dirac shift is one of most important properties of metal/semiconductor system because the current flow crossing the system depends strongly on the amplitude of Dirac shift. The formed Dirac point in Fermi level and in or towards the conduction band indicates that electrons are spontaneously flow from the valence band to conduction band. Therefore, (HS) G-MoS_2 materials at Mo sites vacancy defects have metallic characters. To get better understanding of Electronic and Magnetic properties of these materials, we have performed the DOS and PDOS analysis. DOS of a system is the number of states per unit energy range available for the particles to be occupied. It indicates how densely quantum states are packed in a particular system. High DOS at a specific energy level reflects that many states are available for occupation. If there are no available states for occupation in an energetic level, the value for the DOS will be zero [22]. Magnetic properties (magnetic moment) are directly related to DOS and PDOS of the considered system. The total magnetic moment is given by $\mu = m\mu_B$, where m is the number of unpaired electrons and μ_B is the Bohr magnetron. Number of unpaired electrons can be obtained by counting electrons in the spin up and spin down sub-bands. If DOS for the spin up electrons and spin down electrons are exactly same i.e. symmetrically distributed, then system will be non-magnetic. In order to investigate the contributions of spin up and spin down electrons in different orbital of atoms, we have required PDOS analysis. From the DOS-PDOS analysis of (HS) G-MoS_2, spin up electrons and spin down electrons of DOS and PDOS are symmetrically distributed as shown in above Fig. 3(b) and Fig. 3(c) and both total and absolute values of magnetization are zero. Hence, (HS) G-MoS_2 has non-magnetic nature. Furthermore, we have discussed DOS and PDOS analysis of (HS) G-MoS_2 at Mo sites vacancy defects. We obtained DOS and PDOS plots for spin up electrons and spin down electrons states of C-1Mo, L-1Mo and 2Mo atoms, vacancy defects taking a reference of Fermi energy as shown Fig. 4(c), 4(b), 4(d), Fig. 5(c), 5(b), 5(d) and Fig. 6(c), 6(b), 6(d) respectively. The states above the horizontal line represent spin up electrons and states below the horizontal line represents spin down electrons. We see that spin up and spin down electrons are not symmetrically distributed showing magnetic properties. From PDOS analysis of pure and Mo sites vacancy defects heterostructure materials G-MoS_2, we found that, magnetism is developed only due to the vacancy defects. Also, from scf.out and pdos.out calculations, we got greater magnetic values of 2Mo atoms than L-1Mo, C-1Mo atoms vacancy defects which are given 5.25 Bohr-Mag/cell, 2.65 Bohr-Mag/cell and 2.61 Bohr-Mag/cell respectively.

The magnetism of considered defects materials explained based on the contributions of electrons spins in orbitals of C, Mo and S

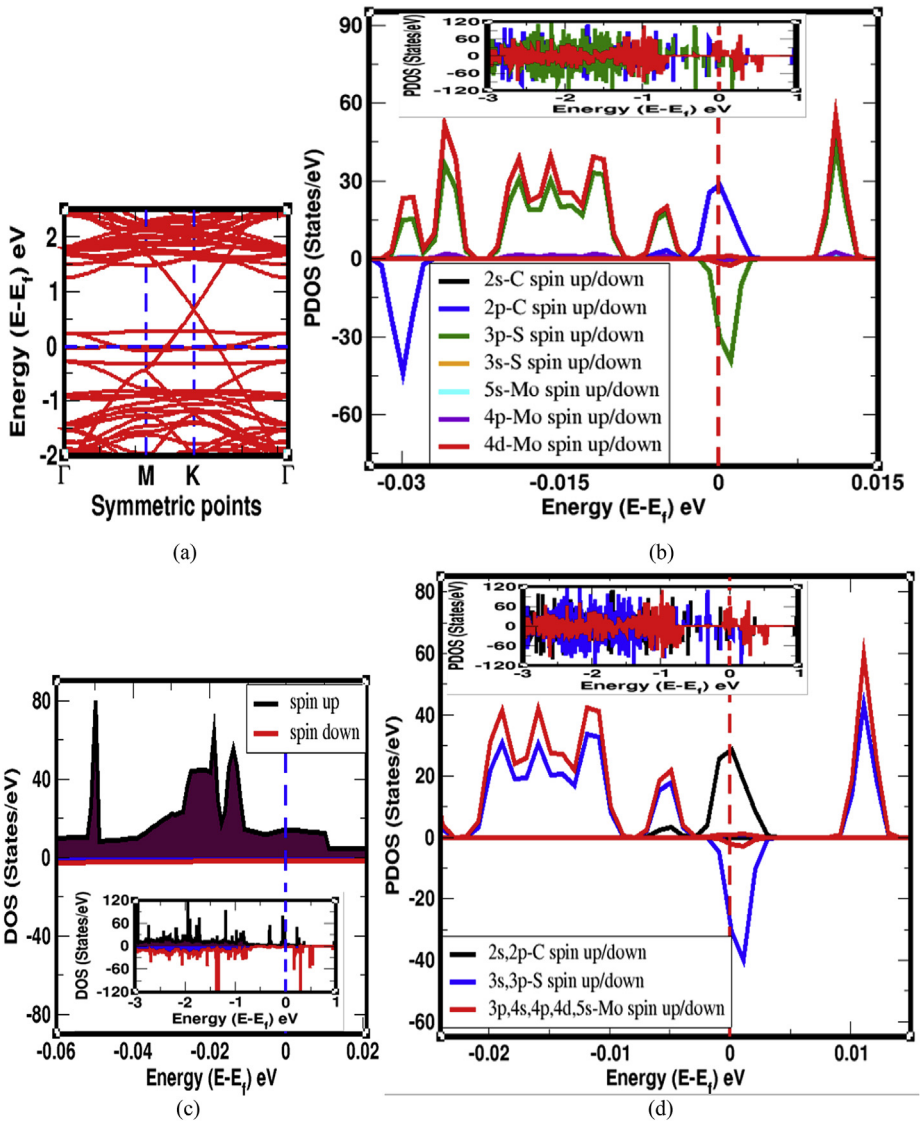

Fig. 4. Band structure, DOS and PDOS plots of C-1Mo atom vacancy defects (HS) G-MoS_2 where horizontal dotted line represents Fermi level in band structure plot and vertical dotted line represents Fermi level in DOS and PDOS plots (a) band structure (b) individual spin up electrons and spin down electrons PDOS orbitals of C, Mo, S atoms (c) DOS of spin up electrons and spin down electrons (d) total spin up electrons and spin down electrons PDOS orbitals of C, Mo, S atoms.

atoms at Mo sites vacancy defects are given in Table 3.

As shown in Fig. 4 (b) and 4(d), high PDOS value near the Fermi level of 2p orbital of C atoms, 4d orbital of Mo atoms and 3p orbital of S atoms reflects that many states are available for occupation. The values of magnetism carried by all spin up and spin down electrons in orbitals of C atoms have 63.09$\mu_{B/}$cell, 63.12$\mu_{B/}$cell, Mo atoms have 58.10$\mu_{B/}$cell, 57.29$\mu_{B/}$cell, and S atoms have 52.78$\mu_{B/}$cell, 50.95$\mu_{B/}$cell at C-1Mo sites vacancy defects material (HS) G-MoS_2. Therefore, total magnetism produced by C, Mo and S atoms have values −0.03$\mu_{B/}$cell, 0.81$\mu_{B/}$cell and 1.83$\mu_{B/}$cell, it means, unpaired spin up and spin down electrons in sub-orbital of S atoms produce more magnetic value (magnetism) than Mo atoms and C atoms in C-1Mo (HS) G-MoS_2 material. Also, we have calculated magnetic contributions of 2p orbital of C atoms, 4d orbital of Mo atoms and 3p orbital of S atoms only have −0.02$\mu_{B/}$cell, 0.78$\mu_{B/}$cell, and 1.81$\mu_{B/}$cell values respectively. These calculations show that almost all magnetic contributions in the system carried by 2p orbital of C atoms, 4d orbital of Mo atoms and 3p orbital of S atoms. In L-1Mo (HS) G-MoS_2 geometry, high PDOS value of 2p orbital of C atoms, 4d orbital of Mo atoms and 3p orbital of S atoms around Fermi level reveals that many states are available for occupation as shown in Fig. 5(b) and 5(d). From PDOS calculations, we got the magnetic values of all spin up and spin down electrons in orbitals of C atoms have 63.07$\mu_{B/}$cell, 63.12$\mu_{B/}$cell, Mo atoms have 58.09$\mu_{B/}$cell, 57.26$\mu_{B/}$cell, and S atoms have 52.83$\mu_{B/}$cell, 50.96$\mu_{B/}$cell respectively. Hence, total magnetism produced by C, Mo and S atoms are −0.05$\mu_{B/}$cell, 0.83$\mu_{B/}$cell and 1.87$\mu_{B/}$cell respectively, which are obtained by subtracting the magnetic values of spin down electrons in orbitals of all atoms from spin up electrons in orbitals of all atoms in the system. It means orbitals of all S atoms have more magnetic contributions than Mo and C atoms; also Mo atoms have more magnetic contributions than C atoms. These calculations show that if higher the PDOS value, lesser will be the contributions in magnetic effect in L-1Mo (HS) G-MoS_2 material. Also, we found that total magnetism of only 2p orbital of C atoms, 4d orbital of Mo atoms and 3p orbital of S atoms have values −0.04$\mu_{B/}$cell, 0.68$\mu_{B/}$cell and 1.84$\mu_{B/}$cell respectively given in Table 3, means magnetic contributions in the considered system dominated by 2p,

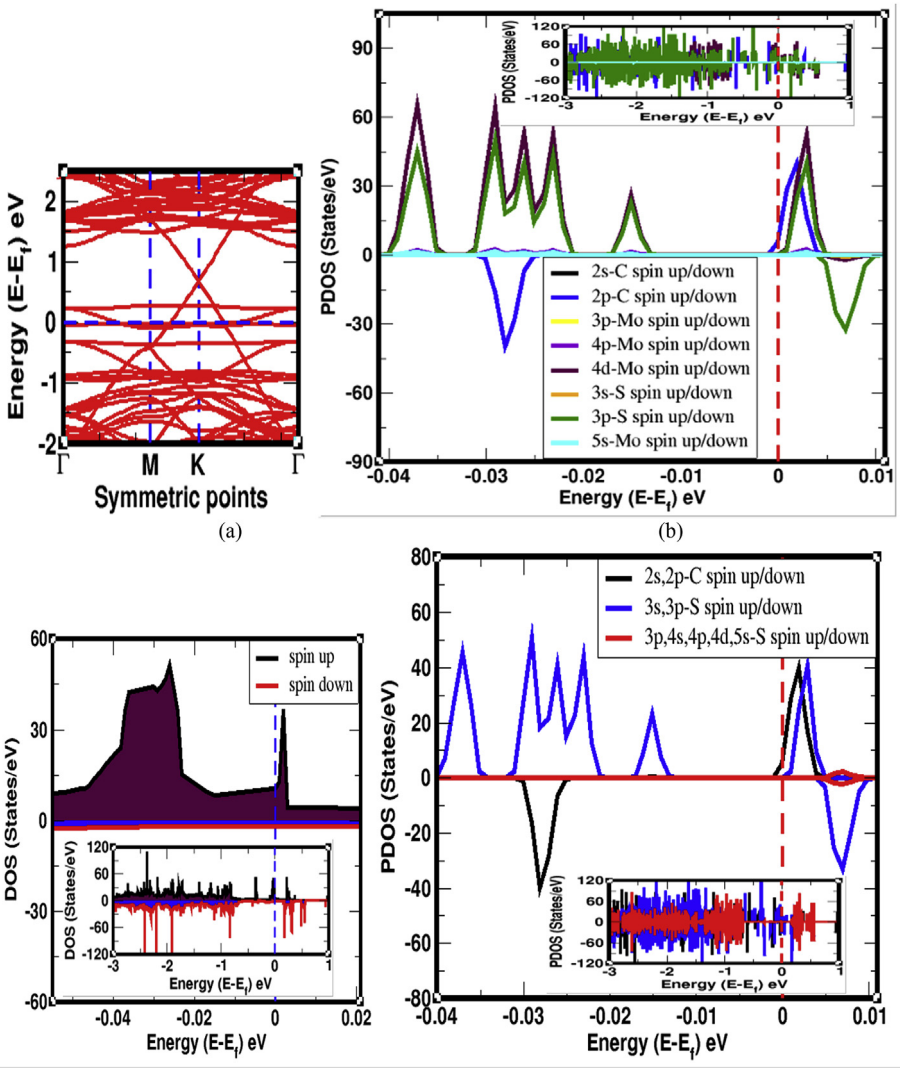

Fig. 5. Band structure, DOS and PDOS plots of L-1Mo atom vacancy defects (HS) G-MoS_2 where horizontal dotted line represents Fermi level in band structure plot and vertical dotted line represents Fermi level in DOS and PDOS plots (a) band structure (b) individual spin up electrons and spin down electrons PDOS orbitals of C, Mo, S atoms (c) DOS of spin up electrons and spin down electrons (d) total. spin up electrons and spin down electrons PDOS orbitals of C, Mo, S atoms.

4d and 3p electronic orbitals of C, Mo and S atoms. In Fig. 6(b) and 6(d), it is seen that high PDOS value near the Fermi level of 2p orbital of C atoms, 4d orbital of Mo atoms and 3p orbital of S atoms implies that many states are available for occupation. From PDOS analysis, we have the magnetic values of all spin up and spin down electrons in orbitals of C atoms have 63.12$\mu_{B/}$cell, 63.13$\mu_{B/}$cell, Mo atoms have 51.19$\mu_{B/}$cell, 49.75$\mu_{B/}$cell, and S atoms have 54.01$\mu_{B/}$cell, 50.19$\mu_{B/}$cell at 2Mo vacancy defects of (HS) G-MoS_2 material. Therefore, magnetism produced by total C, Mo and S atoms have values −0.01$\mu_{B/}$cell, 1.44$\mu_{B/}$cell and 3.82$\mu_{B/}$cell, which are obtained by subtracting the magnetic values of spin down electrons in orbitals of all atoms from spin up electrons in orbitals of all atoms in the system. It also shows that orbitals of S atoms have more contributions to magnetism than Mo and C atoms. Additionally, we found that magnetic values of 2p orbital of C atoms, 4d orbital of Mo atoms and 3p orbital of S atoms have −0.01$\mu_{B/}$cell, 1.39$\mu_{B/}$cell and 3.75$\mu_{B/}$cell respectively, it means 2p, 4d and 3p electrons orbitals of C, Mo, S atoms in the 2Mo (HS) GMoS_2 material have dominant contributions in magnetism. Based on the above calculations, we have concluded that high value of PDOS means less value of magnetism.

As we know in 2Mo vacancy defects configuration, 33 and 41 positions of Mo atoms are removed from 59 atoms geometry of (HS) G-MoS_2. The vacancy created by these atoms in structure established asymmetrically distributed DOS-PDOS plots. Due to that reason, unpaired spin up and spin down orbitals electrons have magnetic values 15.14$\mu_{B/}$cell and 13.70$\mu_{B/}$cell. That means, 1.44$\mu_{B/}$cell magnetism value is obtained by 33 and 41 positions of Mo vacancy atoms in structure. On the other hand, total spin up and spin down orbitals of S atoms in 2Mo defects structure produce 3.82$\mu_{B/}$cell magnetism. Similarly, unpaired spin up and spin down orbitals electrons of L-1Mo vacancy defects atom have magnetic values of 7.63$\mu_{B/}$cell and 6.80$\mu_{B/}$cell at 41 positions, and it produces 0.83$\mu_{B/}$cell magnetism. Also, unpaired spin up and spin down orbitals electrons of C-1Mo vacancy defects atom have magnetic values of 7.60$\mu_{B/}$cell and 6.79$\mu_{B/}$cell at 37 positions and creates 0.81$\mu_{B/}$cell magnetism. In addition, the total contributions of S atoms orbital electrons in structures produce 1.87$\mu_{B/}$cell and 1.83$\mu_{B/}$cell magnetism by L-1Mo and C-1Mo atoms vacancy defects. The magnetic contributions of all orbitals electrons of Mo and S atoms in vacancy defects G-MoS_2 hetero system, 4d of Mo and 3p of S have dominant contributions. Thus, due to the appearance of

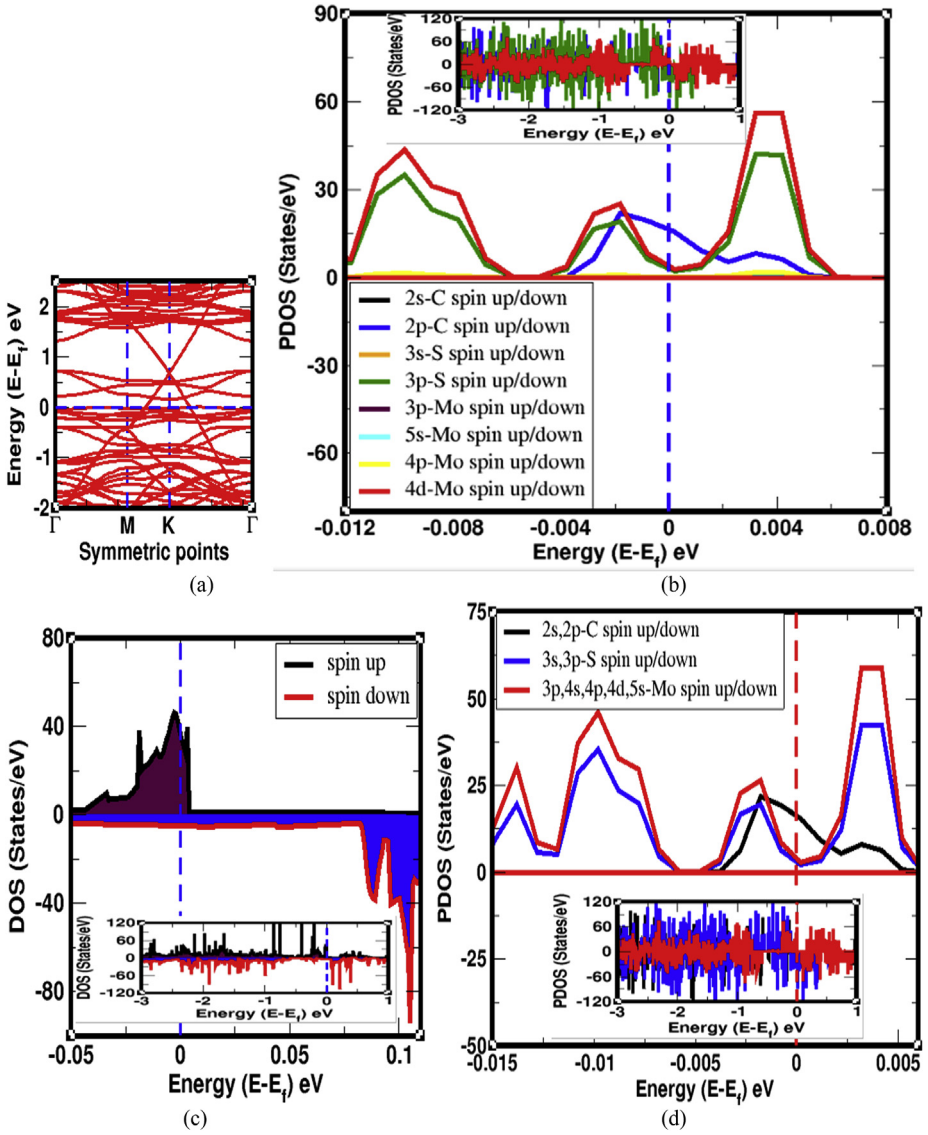

Fig. 6. Band structure, DOS and PDOS plots of 2Mo atoms vacancy defects (HS) G-MoS_2 where horizontal dotted line represents Fermi level in band structure plot and vertical dotted line represents Fermi level in DOS and PDOS plots (a) band structure (b) individual spin up electrons and spin down electrons PDOS orbitals of C, Mo, S atoms (c) DOS of spin up electrons and spin down electrons (d) total spin up electrons and spin down electrons PDOS orbitals of C, Mo, S atoms.

Table 2
Fermi energy level (E_f), Fermi energy level shift to valence band (E_{shift}-VB), Dirac point in conduction band (D_{point}-CB), Dirac point of defects configurations shift from pure material geometry in conduction band (D_{shift}-CB), total (T_m) and absolute (A_m) magnetization values of pure and at Mo sites vacancy defects material (HS) G-MoS_2.

Pure and defects geometry of (HS) G-MoS_2	(E_f) (eV)	(E_{shift}-VB) (eV)	(D_{point}-CB) (eV)	(D_{shift}-CB) (eV)	T_m (Bohr-Mag/cell)	A_m (Bohr-Mag/cell)
(HS) G-MoS_2	0.32	–	0.56	–	0.00	0.00
C-1Mo vacancy defects (HS) G-MoS_2	−0.43	0.75	0.65	0.09	2.61	3.12
L-1Mo vacancy defects (HS) G-MoS_2	−0.43	0.75	0.65	0.09	2.65	3.38
2Mo vacancy defects (HS) G-MoS_2	−0.70	1.02	0.67	0.11	5.25	5.58

magnetism, Mo sites vacancy defects (HS) G-MoS_2 material seems to be promising in usage in various devices requiring magnetic properties. Based on PDOS analysis, we know that top of the valence band is contributed by d orbital of Mo atom and p orbital of S atom and bottom of conduction band is mainly contributed by d orbital of Mo atom. Thus, d orbital of Mo and p orbital of S atom are hybridized with each other at the top of the valence band and $2p_z$ state of C atom in freestanding Graphene at Mo sites vacancy defects configurations.

4. Conclusions

We have investigated the Structural, Electronic and Magnetic properties of pure and defects geometries (HS) G-MoS_2 by using the first-principles calculations. All the calculations were performed under DFT-D_2 level of approximation with GGA, exchange correlation functional including spin polarized calculation using Quantum ESPRESSO code. At first, we studied structural properties of pure and Mo sites vacancy defects (HS) G-MoS_2 materials. We

Table 3
Total and individual atomic orbital contributions of C, Mo and S atoms in PDOS analysis of pure and defect geometries of (HS) G-MoS_2.

Magnetic Contributions of C, Mo, S atomic orbitals in pure and Mo sites vacancy defects (HS) G-MoS_2	2Mo atoms (Bohr-Mag/cell)	L-1Mo atom (Bohr-Mag/cell)	C-1Mo atom (Bohr-Mag/cell)	G-MoS_2 (Bohr-Mag/cell)
total orbital of C atoms (spin up-spin down)	−0.01	−0.05	−0.03	0.00
total orbital of Mo atoms (spin up-spin down)	1.44	0.83	0.81	0.00
total orbital of S atoms (spin up-spin down)	3.82	1.87	1.83	0.00
spin up s, p orbitals of C atoms	63.12	63.07	63.09	63.25
spin down s, p orbitals of C atoms	63.13	63.12	63.12	63.25
spin up s, p, d orbitals of Mo atoms	51.19	58.09	58.10	64.89
spin down s,p,d orbitals of Mo atoms	49.75	57.26	57.29	64.89
spin up s, p orbitals of S atoms	54.01	52.83	52.78	51.52
spin down s, p orbitals of S atoms	50.19	50.96	50.95	51.52
2s orbital of C atoms	−0.01	−0.01	−0.01	0.00
2p orbital of C atoms	0.00	−0.04	−0.02	0.00
4p orbital of Mo atoms	0.03	0.02	0.02	0.00
4d orbital of Mo atoms	1.39	0.68	0.78	0.00
5s orbital of Mo atoms	0.02	0.02	0.02	0.00
3p orbital of S atoms	3.75	1.84	1.81	0.00
Total magnetism	5.25	2.65	2.61	0.00

found that, Mo sites vacancy defects geometries of (HS) G-MoS_2 are more compact than pure (HS) G-MoS_2 geometry. Further, we have studied the Electronic and Magnetic properties of pure and vacancy defects materials (HS) G-MoS_2. From the bands structure calculations of these materials, we found that pure and Mo atoms vacancy defects of (HS) G-MoS_2 structures are metallic in nature. Additionally, we saw that Fermi energy level shifted towards the valence band in single Mo atom and two Mo atoms vacancy defects, both the cases lead to p-type Schottky defects. To understand the Magnetic properties of materials, we used DOS and PDOS analysis. We found that DOS and PDOS for spin up and spin down electrons are symmetrically distributed in (HS) G-MoS_2 and asymmetrically distributed in C-1Mo, L-1Mo and 2Mo atoms, vacancy defects (HS) G-MoS_2. It means non-magnetic (HS) G-MoS_2 changes to magnetic materials by Mo sites vacancy defects. It was also found that total magnetism values of C-1Mo, L-1Mo and 2Mo atoms vacancy defects have 2.61 (Bohr-Mag/cell), 2.65 (Bohr-Mag/cell) and 5.25 (Bohr-Mag/cell) respectively and 2p orbital of C atoms, 3p orbital of S atoms and 4d orbital of Mo atoms have main contributions to the magnetism in all three configurations.

Declaration of competing interest

The authors declare that they have no known competing financial interests or personal relationships that could have appeared to influence the work reported in this paper.

Acknowledgements

We acknowledge the UGC Nepal Award no. CRG-73/74-S&T-01 and network project NT-14 of ICTP/OEA. Discussions with Saran Lamichhane and Nurapti Pantha were quite helpful.

References

[1] K.S. Novoselov, A.K. Geim, S.V. Morozov, D. Jiang, Y. Zhang, S.V. Dubonos, A.A. Firsov, Electric field effect in atomically thin carbon films, Science 306 (5696) (2004) 666–669.
[2] E.V. Castro, K.S. Novoselov, S.V. Morozov, N.M.R. Peres, J.L. Dos Santos, J. Nilsson, A.C. Neto, Biased bilayer graphene: semiconductor with a gap tunable by the electric field effect, Phys. Rev. Lett. 99 (21) (2007) 216802.
[3] K.F. Mak, C. Lee, J. Hone, J. Shan, T.F. Heinz, Atomically thin MoS_2: a new direct-gap semiconductor, Phys. Rev. Lett. 105 (13) (2010) 136805.
[4] E.S. Kadantsev, P. Hawrylak, Electronic structure of a single MoS_2 monolayer, Solid State Commun. 152 (10) (2012) 909–913.
[5] B. Radisavljevic, M.B. Whitwick, A. Kis, Small-signal amplifier based on single-layer MoS2, Appl. Phys. Lett. 101 (4) (2012), 043103.
[6] Y. Hu, M. Ruan, Z. Guo, R. Dong, J. Palmer, J. Hankinson, W.A. De Heer, Structured epitaxial graphene: growth and properties, J. Phys. Appl. Phys. 45 (15) (2012) 154010.
[7] C.V. Nguyen, Tuning the electronic properties and Schottky barrier height of the vertical graphene/MoS_2 heterostructure by an electric gating, Superlattice. Microst. 116 (2018) 79–87.
[8] H.V. Phuc, N.N. Hieu, B.D. Hoi, L.T. Phuong, C.V. Nguyen, First principle study on the electronic properties and Schottky contact of graphene adsorbed on MoS_2 monolayer under applied out-plane strain, Surf. Sci. 668 (2018) 23–28.
[9] H.U. Din, M. Idrees, A. Albar, M. Shafiq, I. Ahmad, C.V. Nguyen, B. Amin, Rashba spin splitting and photocatalytic properties of GeC– MSSe (M= Mo, W) van der Waals heterostructures, Phys. Rev. B 100 (16) (2019) 165425.
[10] T.V. Vu, N.V. Hieu, H.V. Phuc, N.N. Hieu, H.D. Bui, M. Idrees, C.V. Nguyen, Graphene/WSeTe van der Waals heterostructure: controllable electronic properties and Schottky barrier via interlayer coupling and electric field, Appl. Surf. Sci. 507 (2020) 145036.
[11] C.V. Nguyen, M. Idrees, H.V. Phuc, N.N. Hieu, N.T. Binh, B. Amin, T.V. Vu, Interlayer coupling and electric field controllable Schottky barriers and contact types in graphene/PbI_2 heterostructures, Phys. Rev. B 101 (23) (2020) 235419.
[12] D.B. Karki, N.P. Adhikari, First-principles study of the stability of graphene and adsorption of halogen atoms (F, Cl and Br) on hydrogen passivated graphene, Int. J. Mod. Phys. B 28 (21) (2014) 1450141.
[13] B.D. Oli, C. Bhattarai, B. Nepal, N.P. Adhikari, First-Principles study of adsorption of alkali metals (Li, Na, K) on graphene, in: Advanced Nanomaterials And Nanotechnology, Springer, Berlin, Heidelberg, 2013, pp. 515–529.
[14] J. Wang, F. Ma, W. Liang, M. Sun, Electrical properties and applications of graphene, hexagonal boron nitride (h-BN), and graphene/h-BN heterostructures, Materials Today Physics 2 (2017) 6–34.
[15] M. Ghorbani-Asl, P.D. Bristowe, K. Koziol, T. Heine, A. Kuc, Effect of compression on the electronic, optical and transport properties of MoS2/graphene-based junctions, 2*D Mater.* 3 (2) (2016), 025018.
[16] Y. Ma, Y. Dai, M. Guo, C. Niu, B. Huang, Graphene adhesion on MoS_2 monolayer: an ab initio study, Nanoscale 3 (9) (2011) 3883–3887.
[17] A.D. Phan, N.A. Viet, N.A. Poklonski, L.M. Woods, C.H. Le, Interaction of a graphene sheet with a ferromagnetic metal plate, Phys. Rev. B 86 (15) (2012) 155419.
[18] W.J. Yu, Z. Li, H. Zhou, Y. Chen, Y. Wang, Y. Huang, X. Duan, Vertically Stacked multi-heterostructures of layered materials for logic transistors and complementary inverters, Nat. Mater. 12 (3) (2013) 246–252.
[19] M.S. Choi, G.H. Lee, Y.J. Yu, D.Y. Lee, S.H. Lee, P. Kim, W.J. Yoo, Controlled charge trapping by molybdenum disulphide and graphene in ultrathin heterostructured memory devices, Nat. Commun. 4 (1) (2013) 1–7.
[20] K. Roy, M. Padmanabhan, S. Goswami, T.P. Sai, G. Ramalingam, S. Raghavan, A. Ghosh, Graphene–MoS 2 hybrid structures for multifunctional photoresponsive memory devices, Nat. Nanotechnol. 8 (11) (2013) 826–830.
[21] L. Debbichi, O. Eriksson, S. Lebègue, Electronic structure of two-dimensional transition metal dichalcogenide bilayers from ab initio theory, Phys. Rev. B 89 (20) (2014) 205311.
[22] C. Kittel, P. McEuen, P. McEuen, Introduction to Solid State Physics, vol. 8, Wiley, New York, 1996, pp. 140–303.
[23] M.V. Makarova, Y. Akaishi, T. Ikarashi, K.S. Rao, S. Yoshimura, H. Saito, Alternating Magnetic Force Microscopy: effect of Si doping on the temporal performance degradation of amorphous FeCoB magnetic tips, J. Magn. Magn Mater. 471 (2019) 209–214.
[24] H.X. Peng, F. Qin, M.H. Phan, Ferromagnetic Microwire Composites: from Sensors To Microwave Applications, Springer, 2016.
[25] P. Hohenberg, W. Kohn, Inhomogeneous electron gas, Phys. Rev. 136 (3B) (1964) B864.

[26] P. Giannozzi, S. Baroni, N. Bonini, M. Calandra, R. Car, C. Cavazzoni, A. Dal Corso, Quantum ESPRESSO: modular and open-source software Project for quantum simulations of materials, J. Phys. Condens. Matter 21 (39) (2009) 395502.
[27] J.P. Perdew, K. Burke, M. Ernzerhof, Generalized gradient approximation made simple, Phys. Rev. Lett. 77 (18) (1996) 3865.
[28] S. Grimme, Accurate description of van der Waals complexes by density Functional theory including empirical corrections, J. Comput. Chem. 25 (12) (2004) 1463−1473.
[29] B.G. Pfrommer, M. Côté, S.G. Louie, M.L. Cohen, Relaxation of Crystals with the quasi-Newton method, J. Comput. Phys. 131 (1) (1997) 233−240.
[30] N. Marzari, D. Vanderbilt, A. De Vita, M.C. Payne, Thermal Contraction and disordering of the Al (110) surface, Phys. Rev. Lett. 82 (16) (1999) 3296.
[31] R.M. Martin, R.M. Martin, Electronic Structure: Basic Theory and Practical Methods, Cambridge university press, 2004.
[32] S. Ahmad, S. Mukherjee, A Comparative Study of Electronic Properties of Bulk MoS2 and its Monolayer Using DFT Technique: Application of Mechanical Strain on MoS2 Monolayer, 2014.
[33] B. Liu, L.J. Wu, Y.Q. Zhao, L.Z. Wang, M.Q. Cai, First-principles Investigation of the Schottky contact for the two-dimensional MoS_2 and graphene heterostructure, RSC Adv. 6 (65) (2016) 60271−60276.
[35] N.N. Hieu, H.V. Phuc, V.V. Ilyasov, N.D. Chien, N.A. Poklonski, N. Van Hieu, C.V. Nguyen, First-principles study of the structural and electronic properties of graphene/MoS2 interfaces, J. *Appl. Phys.* 122 (10) (2017) 104301.
[36] K.D. Pham, N.N. Hieu, H.V. Phuc, I.A. Fedorov, C.A. Duque, B. Amin, C.V. Nguyen, Layered graphene/GaS van der Waals heterostructure: controlling the electronic properties and Schottky barrier by vertical strain, Appl. Phys. Lett. 113 (17) (2018) 171605.

BIBECHANA
ISSN 2091-0762 (Print), 2382-5340 (Online)
Journal homepage: http://nepjol.info/index.php/BIBECHANA
Publisher: Department of Physics, Mahendra Morang A.M. Campus, TU, Biratnagar, Nepal

Electronic and magnetic properties of defected MoS_2 monolayer

Hari Krishna Neupane[1, 2], Narayan Prasad Adhikari[2*]
[1]Amrit Campus, Institute of Science and Technology Tribhuvan University, Kathmandu, Nepal
[2]Central Department of Physics, Institute of Science and Technology Tribhuvan University, Kathmandu, Nepal
[*]Email: narayan.adhikari@cdp.tu.edu.np

Article Information:
Received: December 28, 2020
Accepted: April 17, 2021

Keywords:
DFT
Magnetic moment
Monolayer
Spins
Vacancy defects

ABSTRACT

It is interesting to understand the effect of defects in 2D materials, because vacancy defects in 2D materials have novel electronic and magnetic properties. In this work, we studied electronic and magnetic properties of 1S vacancy defect ($1S_v$-MoS_2), 2S vacancy defects ($2S_v$-MoS_2), 1Mo vacancy defect (Mo_v-MoS_2), and (1Mo & 1S) vacancy defects ($(Mo\text{-}S)_v$-MoS_2) in 2D MoS_2 material by first-principles calculations within spin-polarized density functional theory (DFT) method. To understand the electronic properties of materials, we have analyzed band structures and DOS calculations, and found that $1S_v$-MoS_2 & $2S_v$-MoS_2 materials have semiconducting nature. This is because, $1S_v$-MoS_2 & $2S_v$-MoS_2 materials open small energy band gap of values 0.68 eV & 0.54 eV respectively in band structures. But, in Mo_v-MoS_2 & $(Mo\text{-}S)_v$-MoS_2 materials, energy bands around the Fermi level mix with the orbital's of Mo and S atoms. As a result, bands are split and raised around and above the Fermi energy level. Therefore, Mo_v-MoS_2 & $(Mo\text{-}S)_v$-MoS_2 materials have metallic nature. We found that MoS_2, $1S_v$-MoS_2 & $2S_v$-MoS_2 materials have non-magnetic properties, and Mo_v-MoS_2 & $(Mo\text{-}S)_v$-MoS_2 materials have magnetic properties because magnetic moment of MoS_2, $1S_v$-MoS_2 & $2S_v$-MoS_2 materials have 0.00 μ_B/cell value and Mo_v-MoS_2 & $(Mo\text{-}S)_v$-MoS_2 materials have 2.72 μ_B/cell & 0.99 μ_B/cell respectively. Therefore, non-magnetic MoS_2 changes to magnetic Mo_v-MoS_2 & $(Mo\text{-}S)_v$-MoS_2 materials due to Mo and (1Mo & 1S) vacancy defects. Magnetic moment obtained in Mo_v-MoS_2 & $(Mo\text{-}S)_v$-MoS_2 materials due to the distribution of up and down spins in 4p, 4d & 5s orbitals of Mo atoms and 3s & 3p orbitals of S atoms in structures. The significant values of magnetic moment are given by distributed spins in 4d orbital of Mo atoms and 3p orbital of S atoms.

DOI: https://doi.org/10.3126/bibechana.v18i2.33905
This work is licensed under the Creative Commons CC BY-NC License. https://creativecommons.org/licenses/by-nc/4.0/

1. Introduction

Two dimensional (2D) materials with atomic thickness have become candidates for wearable electronic devices in the future. Graphene and transition metal sulfides have received extensive attention in logic computing and sensing applications due to their lower power dissipation [1-3]. However, the lack of intrinsic band gap and non-magnetic nature of graphene limits its practical applications in widely expanding field of carbon-based devices. Therefore, the transition metal dichalcogenides material (TMD) Molybdenum diSulphide (MoS_2) is a suitable candidate for logic computing (logic computing is the sequence of operations (hardware or software) performed by computers) and sensing (devices) applications. MoS_2 is made by Mo and S atoms stacked together to give S-Mo-S in a triangular prismatic arrangement [4]. The band structure of MoS_2 depends on the number of layers, and the single layer MoS_2 has a direct band gap of energy 1.80 eV [5]. The band is opened in between the lower energy band of conduction band and higher energy band of valence band. Due to the wide band gap (1.80 eV), MoS_2 provides huge opportunities for electrical and optoelectronics [6-9]. In recent years, a lot of research has been carried out surrounding MoS_2, and various new electronic devices based on MoS_2 have emerged, including gas sensors, resistive memory, photo detectors, integrated logic circuits, signal amplifiers, flexible optoelectronic devices, solar cells and lubricants etc. [10-13].

Electronic and magnetic properties of 2D pristine and defected materials are attracting properties in solid-state physics because they have potential applications in industrial as well as academic sectors. Hence, it is interesting to understand the effect of defects in 2D materials [14-16]. The vacancy defects in solids causes deviation of atoms or ions from the periodicity and they are used to find innovative properties. They can be used to design new materials [17]. To our best knowledge, Mo and S atoms vacancy defects (i.e. 1Mo atom only, 1Mo and 1S atoms together) in monolayer MoS_2 material have not been reported [5, 18-21]. These Mo and S atoms vacancy defects in MoS_2 may provide significance outline for the material in device applications. Therefore, in this work, we focus on the electronic and magnetic properties of Mo and S atoms vacancy defects in monolayer MoS_2 through first-principles calculations within the frame work of density functional theory (DFT), using computational tool quantum ESPRESSO.

The remaining part of this paper is arranged as follows. In section 2, we introduce the computational details. Main finding and their interpretation are presented in section 3. Finally we draw conclusions in section 4.

2. Computational Methods

In this work, we used spin-polarized density functional theory (DFT) [22], with the quantum ESPRESSO simulation package [23] and structure visualization program XCrySDen [24], to perform all the calculations. The Generalized Gradient Approximation (GGA) of Perdew-Burke-Ernzerhof (PBE) [25] is used to describe the exchange correlation interactions. The Rappe-Rabe-Kaxiraas-Joannopoulos (RRKJ) model of ultra-soft pseudo-potentials is used to describe chemically active valence electrons in calculations. The kinetic energy cut-off and charge density cut-off values are set to 35 Ry and 350 Ry respectively for the plane-wave expansion. The first Brillouin zone is sampling of a (10×10×1) Monkhorst-Pack (MP) [26] k-points grid, which is used to perform geometric optimizations. All the structures are fully relaxed by Broyden-Fletcher-Goldfarb-Shanno (BFGS) scheme [27], until the energy and force are converged less than 10^{-4} Ry and 10^{-3} Ry/Bohr values respectively. The mesh of (6×6×1) k-points grid is used to perform all bands structure calculations and automatic denser mesh (12×12×1) k-points is used for density of states (DoS) and partial density of states (PDoS) calculations, where in both the cases, 100 k-points are chosen along the high symmetric points connecting the reciprocal space. The Marzarri-Vanderbilt (MV) [28]

smearing of small width 0.001 Ry is used. In addition, we have chosen 'david' diagonalization method with 'plain' mixing mode and mixing factor of 0.6 for self consistency.

In present work, we have constructed (3×3) supercell structure of monolayer MoS_2 from the unit cell by extending along x and y direction as shown in figure 1(a). Then, we have generated stable and relaxed structures of 1S vacancy defect in MoS_2 ($1S_v$-MoS_2), 2S vacancy defects in MoS_2 ($2S_v$-MoS_2), 1Mo vacancy defect in MoS_2 (Mo_v-MoS_2) and (1Mo & 1S) vacancy defects in MoS_2 $(Mo\text{-}S)_v$-MoS_2 materials as shown in figures 1(b-i). These prepared structures are used for further investigations.

3. Results and Discussion

In this section, we reported first-principles calculations within the frame work of spin-polarized DFT method to study electronic and magnetic properties of Mo and S atoms vacancy defects in MoS_2 material.

3.1 Electronic Properties

The electronic properties of $1S_v$-MoS_2, $2S_v$-MoS_2, Mo_v-MoS_2 and $(Mo\text{-}S)_v$-MoS_2 materials are studied by the analysis of band structures and DoS calculations using DFT method. The optimized and relaxed structures of MoS_2, $1S_v$-MoS_2, $2S_v$-MoS_2, Mo_v-MoS_2 and $(Mo\text{-}S)_v$-MoS_2 materials are shown in figures 1(a-i) respectively. Before study the band structures and DoS calculations of $1S_v$-MoS_2, $2S_v$-MoS_2, Mo_v-MoS_2 and $(Mo\text{-}S)_v$-MoS_2 materials, we need to understand the electronic properties of pure MoS_2 material. We know that the electronic configurations of valence electrons in Mo and S atoms are [Kr] $4d^5\ 5s^1$ and [Ne] $3s^2\ 3p^4$ respectively. A hexagonal unit cell of monolayer MoS_2 on the basis of three (1Mo & 2S) atoms in honeycomb lattice structure is initially constructed by using reported value [29, 30]. It is built up by single layers of S-Mo-S atoms. It consists of two planes of Sulphur (S) atoms and an intercalated plane of Molybdenum (Mo) atom which bounds with the Sulphur atoms in a trigonal prismatic arrangement. Each Mo atom is surrounded by six first nearest neighboring S atoms. Based on convergence test, we obtained the lattice constant 'a' for MoS_2 equals to 3.137Å, which agrees with the reported value 3.19Å [31]. The (3×3) supercell structure of monolayer MoS_2 is constructed by using the lattice constant which is three times that of the unit cell as shown in figure 1(a).

We have done band structure calculations of MoS_2 supercell structure, and obtained band gap energy value 1.23 eV, this value is close to reported value 1.80 eV [26]. Therefore, we also concluded that monolayer MoS_2 is a wide band gap semiconductor. The band structure of monolayer MoS_2 is shown in figure 2(a), where x-axis represents high symmetric points in the first Brillouin zone and y-axis represents the corresponding energy values.

In addition, we have prepared stable and relaxed structures of $1S_v$-MoS_2, $2S_v$-MoS_2, Mo_v-MoS_2 and $(Mo\text{-}S)_v$-MoS_2 by removing 1S, 2S, 1Mo and (1Mo & 1S) atoms in supercell structure of MoS_2, with defects formation energy 0.52 eV, 0.76 eV, 0.64 eV and 0.87 eV respectively. These defects formation energy are calculated by using the standard formalism [32];

$$E_d = E_{T\text{-}d} - (E_{T\text{-}p} + n_d\mu_d) \quad \ldots (1)$$

where, $E_{T\text{-}d}$ is a total energy of a supercell with the defects, n_d, is the numbers of atom removed from the perfect super cell to introduce a vacancy, μ_d is chemical potentials of defected atom in structures, $E_{T\text{-}p}$ is the total energy of the neutral perfect supercell respectively. Defects formation energy values of these materials are given in table 1. The stability of these structures is observed by binding energy calculations. Higher the value of binding energy means, systems are more stable. The binding energy of materials depends upon calculated total energy of the systems, which are also given in table 1.

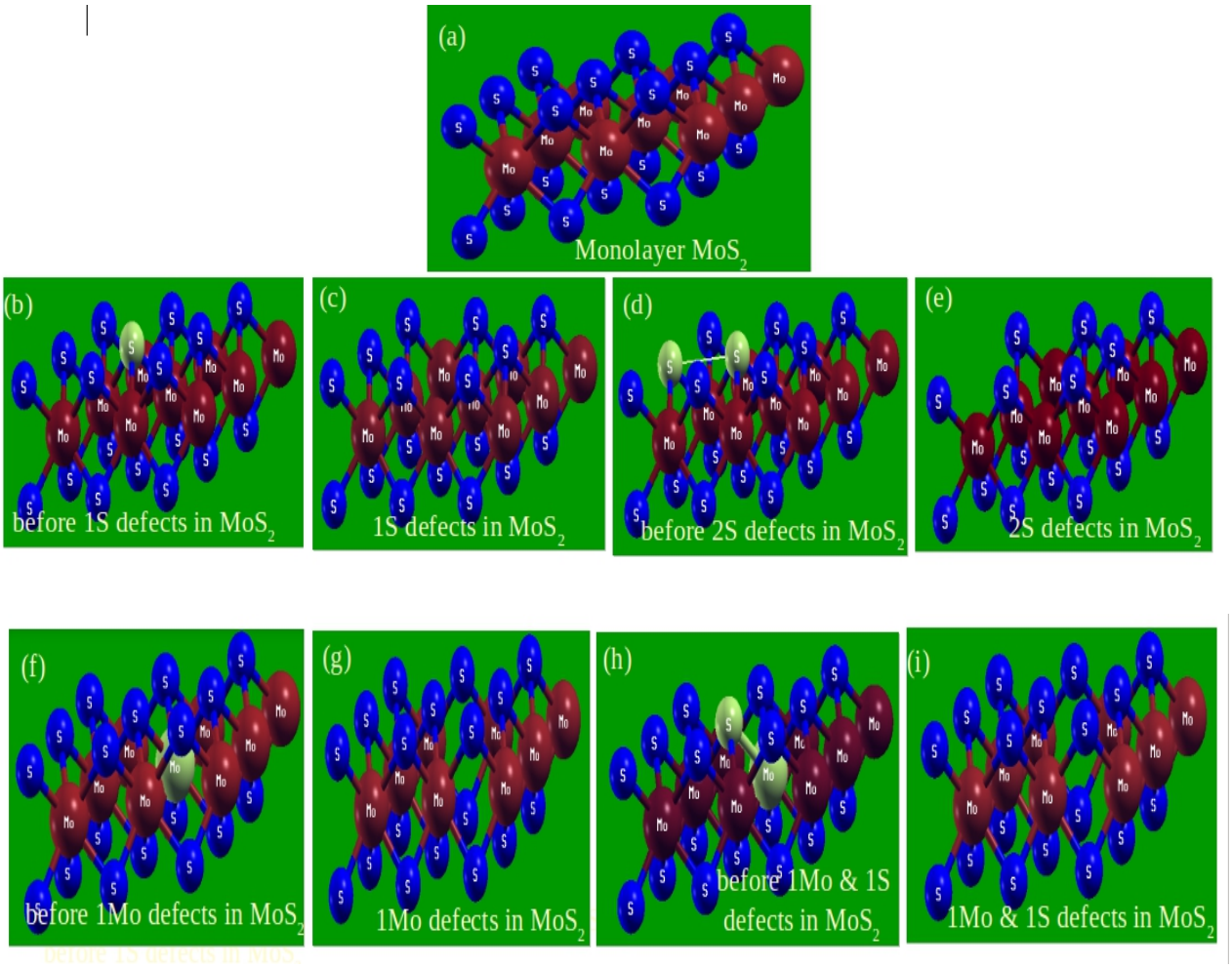

Fig. 1: (a) (3×3) supercell structure of monolayer MoS_2 (b) Before 1S vacancy defect in (3×3) supercell structure of monolayer MoS_2 (c) 1S vacancy defect in (3×3) supercell structure of monolayer MoS_2 (d) before 2S vacancy defects in (3×3) supercell structure of monolayer MoS_2 (e) 2S vacancy defects in (3×3) supercell structure of monolayer MoS_2 (f) Before 1Mo vacancy defect in (3×3) supercell structure of monolayer MoS_2 (g) 1Mo vacancy defect in (3×3) supercell structure of monolayer MoS_2 (h) Before 1Mo & 1S vacancy defects in (3×3) supercell structure of monolayer MoS_2 (i) 1Mo & 1S vacancy defects in (3×3) supercell structure of monolayer MoS_2.

We calculated the inter-atomic distances of atoms in pristine and defected MoS_2 monolayer. It is found that compactness of the materials is decreased due to vacancy defects in structure. This is because, inter-atomic bondings are broken due to vacancy defect atom (atoms) in structures, and remaining atoms are loosely bounded to each other. The inter–atomic distances in pristine and vacancy defected MoS_2 materials are given in table 2.

Table 1: Fermi energy (E_f), Fermi energy shift (E_s), bandgap energy (E_g), total energy of system (E_t), defects formation energy (E_d), total value of magnetic moment (M), and magnetic moment due to total up & down spins states of electrons (μ) in 4p, 4d & 5s orbitals of Mo atoms; 3s & 3p orbitals of S atoms in $1S_v$-MoS_2, $2S_v$-MoS_2, Mo_v-MoS_2, and $(Mo\text{-}S)_v$-MoS_2 materials.

Data of band structures, DoS and PDoS calculations of MoS_2, S_v-MoS_2, Mo_v-MoS_2 & $(Mo\text{-}S)_v$-MoS_2 materials	MoS_2	$1S_v$-MoS_2	$2S_v$-MoS_2	Mo_v-MoS_2	$(Mo\text{-}S)_v$-MoS_2
E_f (eV)	-1.89	-1.97	-2.02	-2.30	-2.33
E_s (eV)	-	0.08	0.13	0.41	0.44
E_g (eV)	1.23	0.68	0.54	-	-
E_t (Ry)	-1741.61	-1718.60	-1696.58	-1593.42	-1570.53
E_d (eV)	---	0.52	0.76	0.64	0.87
μ due to 4p of Mo atoms (μ_B/cell)	0.00	0.00	0.00	0.03	0.01
μ due to 4d of Mo atoms (μ_B/cell)	0.00	0.00	0.00	0.73	0.23
μ due to 5s of Mo atoms (μ_B/cell)	0.00	0.00	0.00	0.03	0.01
μ due to 3s of S atoms (μ_B/cell)	0.00	0.00	0.00	0.04	0.02
μ due to 3p of S atoms (μ_B/cell)	0.00	0.00	0.00	1.89	0.72
T Total value of magnetic moment M (μ_B/cell)	0.00	0.00	0.00	2.72	0.99

Table 2: Inter-atomic distances in pristine MoS_2 and vacancy defects MoS_2 materials, where S-S, Mo-Mo and Mo-S represent inter-atomic bonding in between any two neighbouring Sulphur atoms, any two Molybdenum atoms and nearest neighbour 1Mo and 1S atoms in structures.

Inter-atomic distances of pristine MoS_2 and defected MoS_2 monolayer along x, y and z axis	x-axis (Å)			y-axis (Å)			z-axis (Å)		
	S–S	Mo-Mo	Mo-S	S-S	Mo-Mo	Mo-S	S-S	Mo-Mo	Mo-S
Pristine MoS_2	0.00	1.57	1.52	0.00	2.74	0.90	3.13	0.00	1.56
1S defect MoS_2	0.00	1.57	1.54	0.00	2.74	0.91	3.14	0.00	1.57
2S defects MoS_2	0.00	1.58	1.56	0.00	2.75	0.92	3.15	0.00	1.58
1Mo defect MoS_2	0.00	1.61	1.58	0.00	2.78	0.95	3.15	0.03	1.60
1Mo & 1S defects MoS_2	0.02	1.62	1.59	0.02	2.78	0.97	0.01	0.03	0.62

We have done band structures calculations of $1S_v$-MoS_2, $2S_v$-MoS_2, Mo_v-MoS_2 and $(Mo\text{-}S)_v$-MoS_2 materials as shown in figures 2(b-e) respectively, where 100 k-points are taken along the specific direction of irreducible Brillouin zone by choosing Γ-M-K-Γ high symmetric points. Also, high symmetric points in the first Brillouin zone are taken along x-axis and corresponding energies are taken along y-axis.

The $1S_v$-MoS_2 and $2S_v$-MoS_2 materials have opened narrow band gap of values 0.68 eV and 0.54 eV respectively as shown in figures 2(b-c). Hence, the materials resemble with the nature of semiconductors. The band gap energy value of defected materials decreases with increase in defects concentrations in MoS_2 structure, which determines the conductivity strength of materials. Thus, the strength of conductivity in $2S_v$-MoS_2 is greater than $1S_v$-MoS_2. Also, conductivity of defected materials is higher than non-defected monolayer MoS_2 supercell structure. On the other hand, bands states of Mo_v-MoS_2 and $(Mo\text{-}S)_v$-MoS_2 materials split and cross the Fermi energy level as shown in figures 2(d-e) respectively. Bands around Fermi level mix with the orbital's of Mo vacancy in Mo_v-MoS_2, and (1Mo & 1S) vacancies in $(Mo\text{-}S)_v$-MoS_2. The states associated with the dangling bond and reconstructed Mo-S bond of vacancy occurs near the top of valence band and in conduction band, and appear as flat bands as shown in figures 2(d) and 2(e). Therefore, from the band calculations, Mo_v-MoS_2 and $(Mo\text{-}S)_v$-MoS_2 materials have metallic nature. The vacancies position of S and Mo atoms in structures creates unpaired spins of electrons in sub-orbitals of Mo-S atoms in structures. We have calculated the Fermi energy of $1S_v$-MoS_2, $2S_v$-MoS_2, Mo_v-MoS_2 and $(Mo\text{-}S)_v$-MoS_2 materials and found -1.97 eV, -2.02 eV, -2.30 eV and -2.33 eV values respectively. These obtained different values of Fermi energy are, due to unpaired total up & down spins states of electrons and movement of charges carriers in structures.

We have analyzed DoS and PDoS calculations for the investigation of magnetic properties in materials. Figures 3(a) and 3(b) represent DoS and PDoS plots of pure monolayer MoS_2; figures 4(a) and 4(b) represent total DoS plots of S_v-MoS_2 and $2S_v$-MoS_2 materials, figures 4(c) and 4(d) represent total PDoS plots of $1S_v$-MoS_2 and $2S_v$-MoS_2 materials, figures 5(a) and 5(b) represent total DoS plots of Mo_v-MoS_2 and $(Mo\text{-}S)_v$-MoS_2 materials, and figures 5(c) and 5(d) represent total PDoS plots of Mo_v-MoS_2 and $(Mo\text{-}S)_v$-MoS_2 materials respectively, where the states above the horizontal line represents up spin states of electrons and a state below the horizontal line represents down spin states of electrons.

3.2 Magnetic Properties

The induced magnetization in the materials is obtained by analysis of DoS and PDoS calculations of materials. The asymmetrically distributed up and down spins states of electrons in DoS and PDoS plots reflect, materials have magnetic properties, and symmetrically distributed up and down spins states of electrons in DoS and PDoS plots means, materials carry non-magnetic properties. Up and down spins states of electrons in the orbitals of Mo & S atoms are symmetrically distributed in DoS and PDoS plots of MoS_2, $1S_v$-MoS_2 and $2S_v$-MoS_2 materials are shown in figures 3(a) & 3(b), figures 4(a) & 4(c), and 4(b) & 4(d) respectively. Magnetic moment due to up and down spins states of electrons in 4p, 4d & 5s orbitals of Mo atoms and 3s & 3p orbitals of S atoms in MoS_2, $1S_v$-MoS_2 and $2S_v$-MoS_2 have value 0.00 μ_B/cell, which are given in table 1. Therefore, MoS_2, $1S_v$-MoS_2 and $2S_v$-MoS_2 materials have non-magnetic properties.

We have investigated magnetic properties of Mo_v-MoS_2 and $(Mo\text{-}S)_v$-MoS_2 materials from the DoS and PDoS calculations using spin-polarized DFT method. The DoS and PDoS of up and down spins states of electrons near the Fermi level are asymmetrically distributed in Mo_v-MoS_2 material as shown in figures 5(a) & 5(c) respectively.

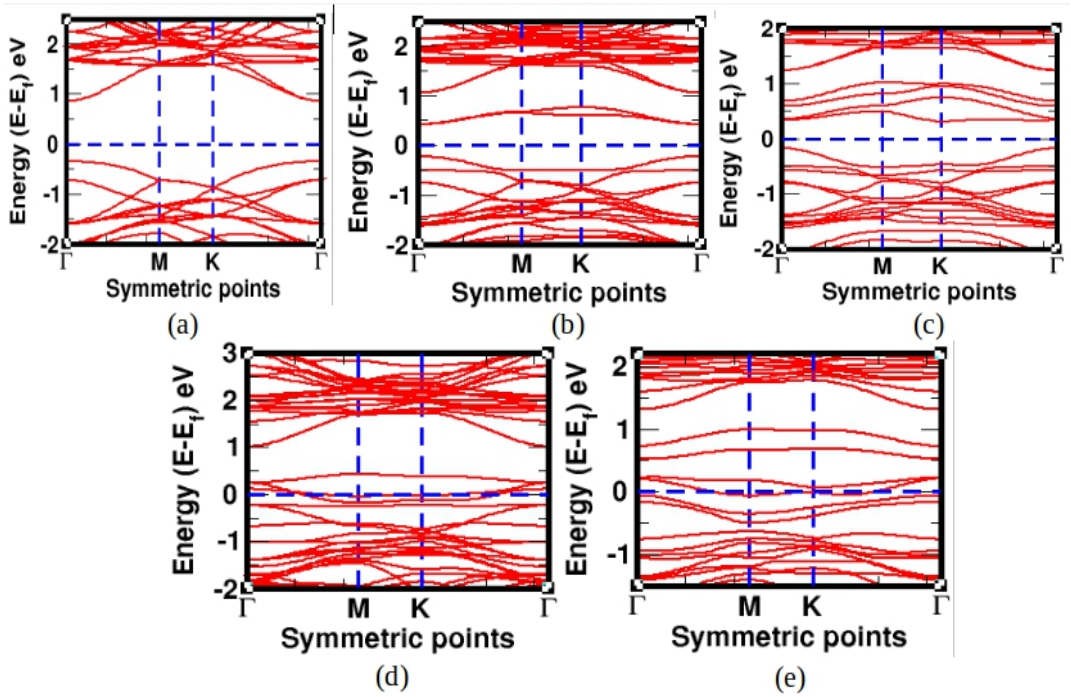

Fig. 2: (a) Band structure of monolayer MoS_2 (b) Band structure of 1S vacancy defect in monolayer MoS_2 (c) Band structure of 2S vacancy defects in monolayer MoS_2 (d) Band structure of 1Mo vacancy defect in monolayer MoS_2 (e) Band structure of (1Mo & 1S) vacancy defects in monolayer MoS_2. In all band structure plots, horizontal dotted line represents Fermi energy level.

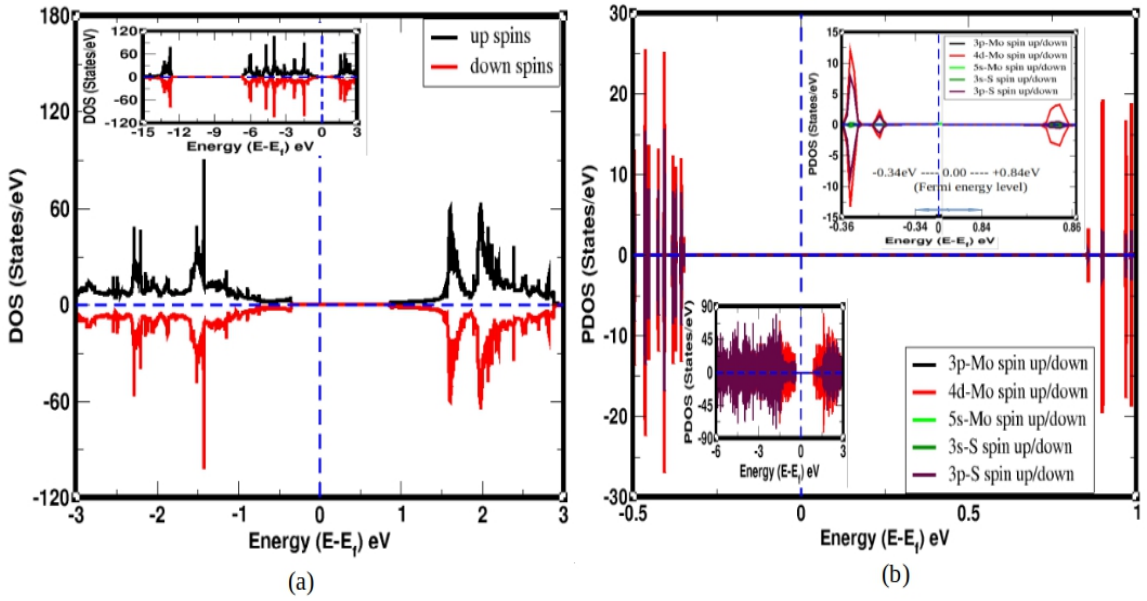

Fig. 3: (a) Total DoS of (3×3) supercell structure of monolayer MoS_2 (b) PDoS of up and down spins states of electrons in the individual orbitals of Mo & S atoms in (3×3) supercell structure of MoS_2 material. In DoS and PDoS plots, vertical dotted line represents Fermi energy level.

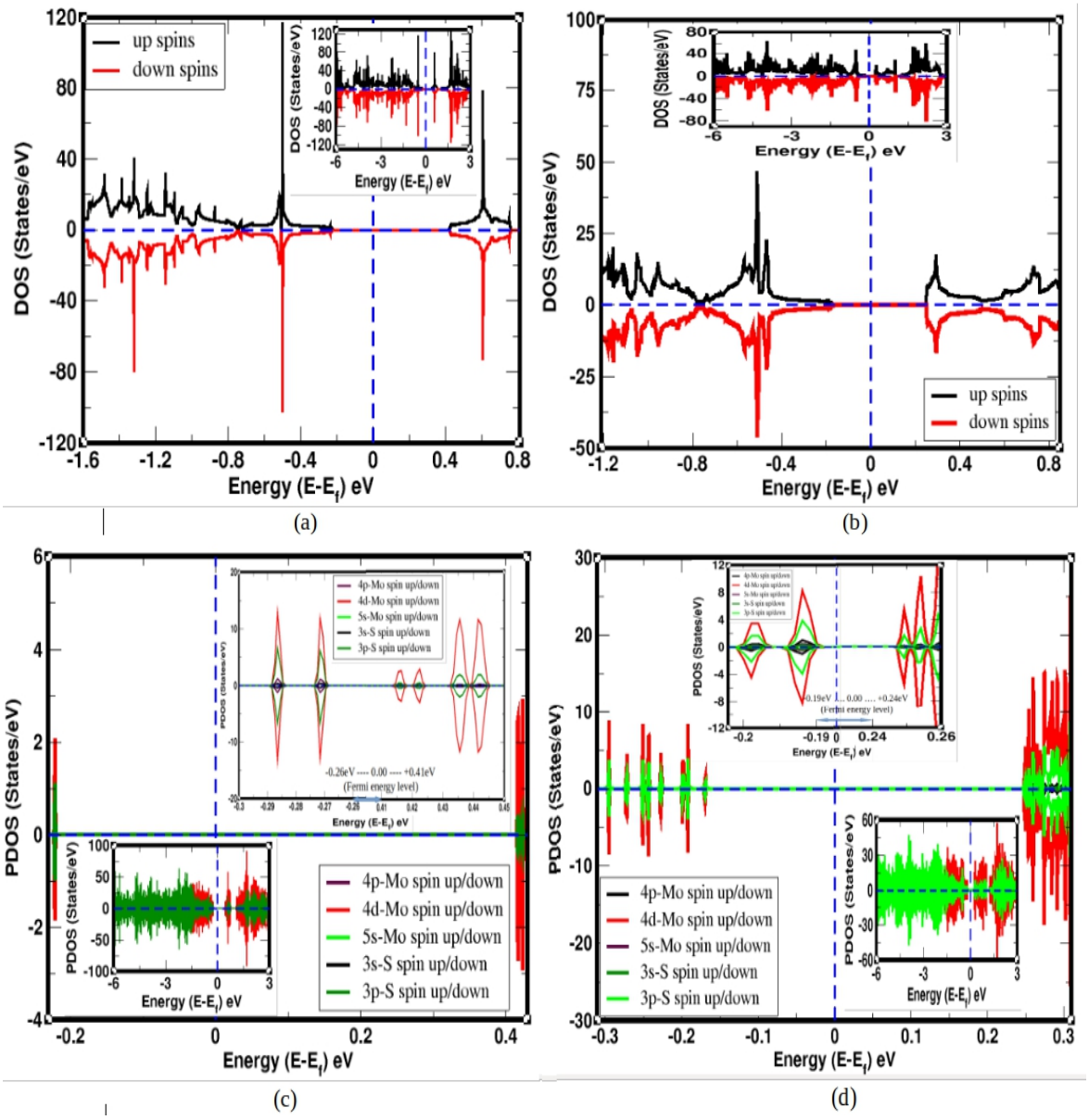

Fig. 4: (a) Total DoS of up & down spins states of electrons in the orbitals of Mo & S atoms in 1S vacancy defect in MoS_2 material (b) Total DoS of up & down spins states of electrons in the orbitals of Mo & S atoms in 2S vacancy defects in MoS_2 material (c) PDoS of up & down spins states of electrons in the individual orbital of Mo & S atoms in 1S vacancy defect MoS_2 material (d) PDoS of up & down spins states of electrons in the individual orbital of Mo & S atoms in 2S vacancy defects MoS_2 material. In DoS and PDoS plots, vertical dotted line represents Fermi energy level.

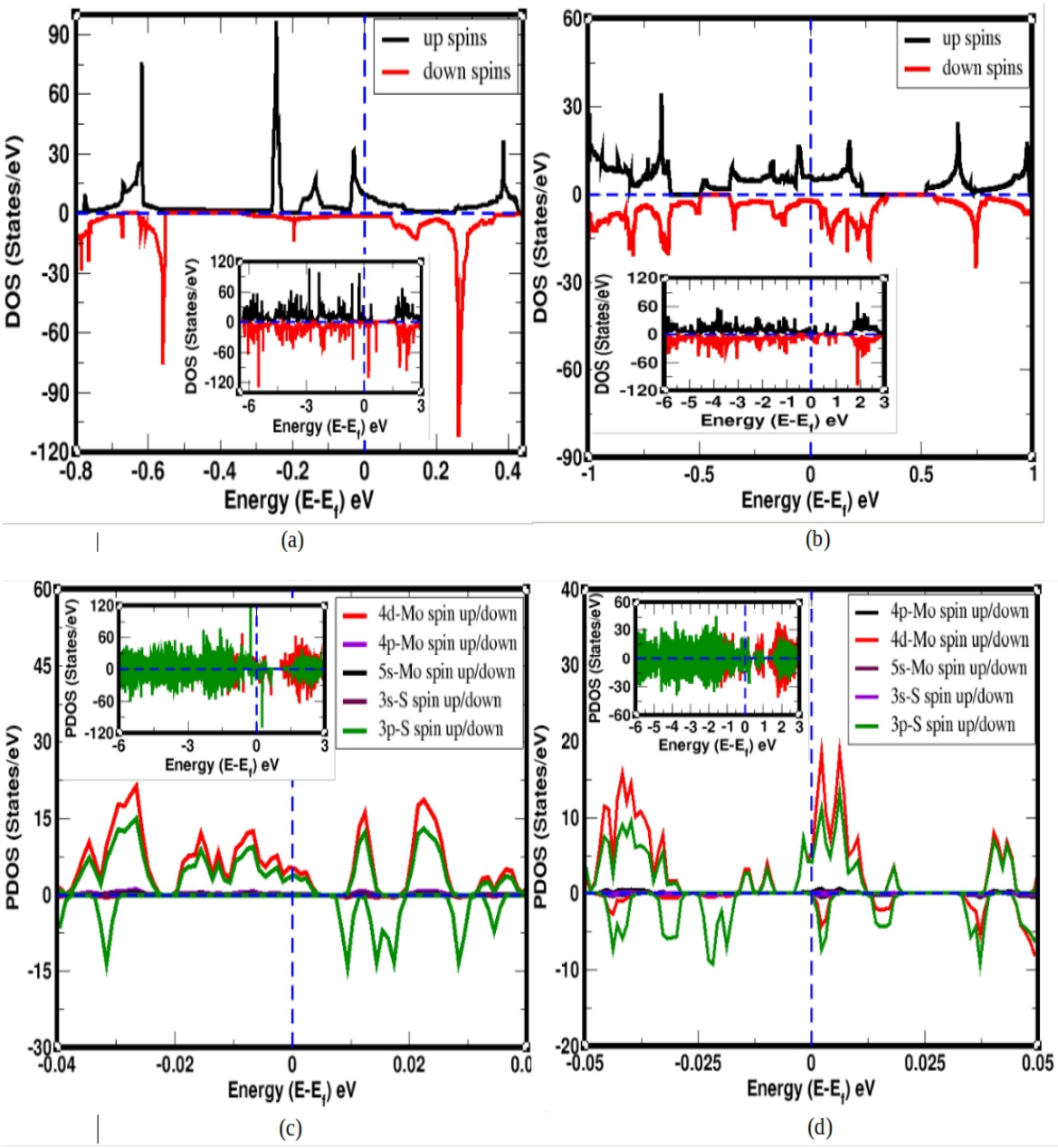

Fig. 5: (a) Total DoS of up & down spins states of electrons in the orbitals of Mo & S atoms in 1Mo vacancy defect in MoS_2 material (b) Total DoS of up & down spins states of electrons in the orbitals of Mo & S atoms in (1Mo & 1S) atoms vacancy defects MoS_2 material (c) PDoS of up & down spins states of electrons in the individual orbital of Mo & S atoms in 1Mo vacancy defect in MoS_2 material (d) PDoS of up & down spins states of electrons in the individual orbital of Mo & S atoms in (1Mo & 1S) atoms vacancy defects MoS_2 material. In DoS and PDoS plots, vertical dotted line represents Fermi energy level.

This is because, electron's spins degeneracy of the bands due to Mo vacancy defects, bands are broken and splited. As a result, Mo_v-MoS_2 material bears magnetic properties. We have also calculated the magnetic moments given by spins of electrons in 4p, 4d & 5s orbitals of Mo atoms and 3s & 3p orbitals of S atoms having values 0.03 μ_B/cell, 0.73 μ_B/cell & 0.03 μ_B/cell; and 0.04 μ_B/cell & 1.89

μ_B/cell in Mo_v-MoS_2 material respectively. Hence, total value of magnetic moment in Mo_v-MoS_2 material is 2.72μ_B/cell. From above calculations, we know that spins states of electrons in 4d orbital of Mo atoms, and 3p orbital of S atoms have dominant contributions for magnetism. Similarly, the spins states of electrons in the orbital of Mo & S atoms of $(Mo\text{-}S)_v$-MoS_2 material near the Fermi energy level are asymmetrically distributed in DoS and PDoS plots as shown in figures 5(b) & 5(d) respectively. Magnetic moment is given by spins states of electrons in 4p, 4d & 5s orbitals of Mo atoms; and 2s & 2p orbitals of S atoms; in structure have values 0.01 μ_B/cell, 0.23 μ_B/cell & 0.01 μ_B/cell; and 0.02 μ_B/cell & 0.72 μ_B/cell respectively. The total magnetic moment in $(Mo\text{-}S)_v$-MoS_2 material has value 0.99 μ_B/cell. Therefore, $(Mo\text{-}S)_v$-MoS_2 material has magnetic properties. 4d orbital of Mo and 3p orbital of S atoms give greater values of magnetic moment than magnetic moment given by other orbitals of atoms in the material. Magnetic moment of Mo_v-MoS_2 is higher than that of $(Mo\text{-}S)_v$-MoS_2 material because unequal unpaired (dangling) bonds are present in structures. These dangling bonds are formed due to the effects of 1Mo atom vacancy defects and (1Mo & 1S) atoms vacancy defects in the materials. It is also seen that spins polarization of atoms in (1Mo &1S) atoms vacancy defects structure is less than 1Mo atom vacancy defects structure.

4. Conclusions and Concluding Remarks

The novel properties in MoS_2 material are developed due to Mo and S atoms vacancy defects. The electronic and magnetic properties of $1S_v$-MoS_2, $2S_v$-MoS_2, Mo_v-MoS_2 and $(Mo\text{-}S)_v$-MoS_2 materials are studied through first-principles calculations within the frame work of spin-polarized DFT method using computational tool quantum ESPRESSO. We have prepared stable structures of these materials, and then analyzed their band structures, DoS and PDoS calculations. From the band structure calculations, we found that $1S_v$-MoS_2 and $2S_v$-MoS_2 materials have open small energy band gap of value 0.68 eV and 0.58 eV in both up and down spins electronic states, which implies that $1S_v$-MoS_2 and $2S_v$-MoS_2 resemble with the nature of semiconductors. Thus, conductivity of material increases with increase in its defects concentrations. On the other hand, Mo_v-MoS_2 and $(Mo\text{-}S)_v$-MoS_2 materials have metallic properties because bands around the Fermi level mix with the orbital's of Mo vacancy in Mo_v-MoS_2, and (Mo & S) vacancies in $(Mo\text{-}S)_v$-MoS_2. The states associated with the dangling bond and reconstructed Mo-S bond of vacancy occurs near the top of valence band and in conduction band, and appear as flat bands. The charge densities associated in these bands are localized. From the analysis of DoS and PDoS calculations, we found that MoS_2, $1S_v$-MoS_2 and $2S_v$-MoS_2 materials have non-magnetic properties. The non-magnetic MoS_2 material changes to magnetic Mo_v-MoS_2 and $(Mo\text{-}S)_v$-MoS_2 materials, due to 1Mo atom vacancy defects in monolayer MoS_2 and (1Mo & 1S) atoms vacancy defects in monolayer MoS_2 structure respectively. Total magnetic moment of Mo_v-MoS_2 and $(Mo\text{-}S)_v$-MoS_2 materials have values 2.72 μ_B/cell and 0.99 μ_B/cell respectively. Significant values of magnetic moment are obtained due to the distribution of electrons spins in 4p, 4d, & 5s orbitals of Mo atoms and 3s & 3p orbitals of S atoms in both materials.

Acknowledgments

Hari Krishna Neupane and Narayan Prasad Adhikari acknowledge the UGC Nepal award no. PhD-75/76-S&T-09 and grants CRG 073/74 -S&T -01 respectively. Also, Narayan Prasad Adhikari acknowledges network project NT-14 of ICTP/OEA.

References

[1] J. C. Lei, X. Zhang, and Z. Zhou, Recent advances in MXene: Preparation, properties, and applications, Frontiers of Physics 10(3) (2015) 276-286.

[2] M. E. Dávila, et al., Germanene: a novel two-dimensional germanium allotrope akin to graphene andsilicene, New Journal of Physics 16(9) (2014) 095002.

[3] S.N.Balendhran, et al., Bhaskaran, Elementalanalogues of graphene: silicene, germanene, stanene, and phosphorene small 11(6) (2015) 640-652.

[4] E. S. Kadantsev, and P. Hawrylak, Electronic structure of a single MoS_2 monolayer Solid State Communications 152(10) (2012) 909-913.

[5] K. F. Mak, et al., Atomically thin MoS_2: a new direct-gap semiconductor Physical review letters 105 (13) (2010) 136805.

[6] Y. Zhang, et al., Ambipolar MoS_2 thin flake transistors, Nano Letters *12*(3) (2012) 1136-1140.

[7] B. Radisavljevic, M. B. Whitwick, and A. Kis, Small-signal amplifier based on single-layer MoS_2, Applied Physics Letters, 101(4) (2012) 043103.

[8] L. Fornarini, et al., Electrochemical solarcells with layer-type semiconductor anodes. Performance of n-MoS_2 cells, Solar Energy Materials 5(1) (1981) 107-114.

[9] K. H. Hu, et al., Tribologicalproperties of MoS_2 with different morphologies in high-density polyethylene, Tribology Letters 47(1) (2012) 79-90.

[10] Y. Zhang, et al., Ambipolar MoS_2 thin flake transistors, Nano letters 12(3) (2012) 1136-1140.

[11] B. Radisavljevic, M. B. Whitwick, and A. Kis, Small-signal amplifier based on single-layer MoS_2, Applied Physics Letters 101(4) (2012) 043103.

[12] L. Fornarini, et al., Electrochemical solarcells with layer-type semiconductor anodes. Performance of n-MoS_2 cells, Solar Energy Materials 5(1) (1981) 107-114.

[13] K. H. Hu, et al., Tribological properties of MoS_2 with different morphologies in high-density polyethylene, Tribology Letters 47(1) (2012) 79-90.

[14] H. K. Neupane, and N. P. Adhikari, Structure, electronic and magnetic properties of 2D Graphene-Molybdenum diSulphide (G-MoS_2) Heterostructure (HS) with vacancy defects at Mo sites, Computational Condensed Matter e00489 (2020).

[15] H. K. Neupane, and N. P. Adhikari, Tuning Structural, Electronic, and Magnetic Properties of C Sites Vacancy Defects in Graphene/MoS_2 van der Waals Heterostructure Materials: A First-Principles Study, Advances in Condensed Matter Physics (2020).

[16] H. K. Neupane, and N. P. Adhikari, First-principles study of structure, electronic, and magnetic properties of C sites vacancy defects in water adsorbed graphene/MoS_2 van der Waals Heterostructures, Journal of Molecular Modeling, 27(3) (2021) 1-12.

[17] C. Kittel, P. McEuen, and P. McEuen, Introduction to solid state Physics (Vol. 8, pp. 140-303). New York: Wiley (1996).

[18] A. Splendiani, et al., Emerging photoluminescence in monolayer MoS_2, Nano Letters, 10(4) (2010) 1271-1275.

[19] H. Schmidt, et al., Transport properties of monolayer MoS_2 grown by chemical vapor deposition, Nano Letters, 14(4) (2014)1909-1913.

[20] B. Radisavljevic, and A. Kis, Mobility engineering and a metal–insulator transition in monolayer MoS_2, Nature materials 12(9) (2013) 815-820.

[21] D. P. Rai, et al., Electronic and optical properties of 2D monolayer (ML) MoS_2 with vacancy defect at S sites, Nano-Structures & Nano-Objects 21 (2020) 100404.

[22] P. Hohenberg, and W. Kohn, Inhomogeneous electron gas, Physical Review 136 (3B) (1964): B864.

[23] P.Giannozzi, et al., QUANTUM ESPRESSO: modular and open-source software project for quantum simulations of materials *J*ournal of physics Condensed Matter 21(39) (2009) 395502.

[24] A. Kokalj, XcrySDen-a new program for displaying crystalline structures and electron densities, Journal of molecular Graphics and modeling 17.3-4 (1999) 176-179.

[25] J. P. Perdew, K. Burke, and M. Ernzerhof, Generalized gradient approximation made simple, Physical review letters *77*(18) (1996) 3865.

[26] R. M. Martin, Electronic structure: basic theory andpractical methods, Cambridge University Press (2004).

[27] B. G. Pfrommer, et al., Relaxation of Crystals with the quasi-Newton method, Journal of Computational Physics 131(1) (1997) 233-240.

[28] N. Marzari, et al., Thermal contraction and disordering of the Al (110) surface, Physical Review Letters 82(16) (1999) 3296.

[29] E. S. Kadantsev, and P. Hawrylak, Electronic structure of a single MoS_2monolayer, Solid State Communications 152(10) (2012) 909-913.

[30] S. Ahmad, and S. Mukherjee, A comparative study of electronic properties of bulk MoS2 and its monolayer using DFT technique: application of mechanical strain on MoS2 monolayer (2014).

[31] J. P. Perdew, K. Burke, and M. Ernzerhof, Generalized gradient approximation made simple. Physical Review Letters 77(18) (1996) 3865.

[32] Z. Hou, et al., Interplay between nitrogen dopants and native point defects in graphene, Physical Review B 85 (16) (2012) 165439.

Journal of Institute of Science and Technology, 26(1), 43-50 (2021)
ISSN: 2469-9062 (print), 2467-9240 (e)
https://doi.org/10.3126/jist.v26i1.37817
© IOST, Tribhuvan University
Research Article

STRUCTURAL, ELECTRONIC AND MAGNETIC PROPERTIES OF DEFECTED WATER ADSORBED SINGLE LAYER MoS_2

Hari Krishna Neupane[1,2], **Narayan Prasad Adhikari**[2*]

[1]*Department of Physics, Amrit Campus, Tribhuvan University, Kathmandu, Nepal*
[2]*Central Department of Physics, Tribhuvan University, Kathmandu, Nepal*
[*]*Corresponding author: narayan.adhikari@cdp.tu.edu.np*

*(**Received**: January 19, 2021; **Revised**: May 05, 2021; **Accepted**: June 04, 2021)*

ABSTRACT

Water adsorbed in MoS_2 (w_{ad}-MoS_2), 1S atom vacancy defect in w_{ad}-MoS_2 (1S-w_{ad}-MoS_2), 2S atoms vacancy defects in w_{ad}-MoS_2 (2S-w_{ad}-MoS_2), and 1Mo atom vacancy defect in w_{ad}-MoS_2 (Mo-w_{ad}-MoS_2) materials were constructed, and their structural, electronic, and magnetic properties were studied by spin-polarized density functional theory (DFT) based first-principles calculations. The w_{ad}-MoS_2, 1S-w_{ad}-MoS_2, 2S-w_{ad}-MoS_2, and Mo-w_{ad}-MoS_2 materials were found stable. From band structure calculations, w_{ad}-MoS_2, 1S-w_{ad}-MoS_2 and 2S-w_{ad}-MoS_2 materials open energy bandgap of values 1.19 eV, 0.65 eV and 0.38 eV respectively. Also, it was found that the conductivity strength of the material increases with an increase in the concentration of S atom vacancy defects in the structure. On the other hand, the Mo-w_{ad}-MoS_2 material has metallic properties because energy bands of electrons crossed the Fermi energy level in the band structure. For the investigation of magnetic properties, the density of states (DoS) and partial density of states (PDoS) calculations were used and found that w_{ad}-MoS_2, 1S-w_{ad}-MoS_2, and 2S-w_{ad}-MoS_2 are non-magnetic materials, while Mo-w_{ad}-MoS_2 is a magnetic material. The total magnetic moment of Mo-w_{ad}-MoS_2 has a value of 2.66 μ_B/cell, due to the arrangement of unpaired up-spin and down-spin of electrons in 3s & 3p orbitals of S atoms; and 4p, 4d & 5s orbitals of Mo atoms in the material.

Keywords: DFT, Magnetic moment, Spins, Vacancy defects, Water adsorbed MoS_2.

INTRODUCTION

Molybdenum disulphide (MoS_2) is a two dimensional (2D) transition metal dichalcogenides (TMDS) material. It has a direct band gap semiconductor of band gap energy 1.80 eV (Mak *et al.,* 2010), although it was reported 1.16 eV in the bulk state using density functional theory implemented in tight binding linear Muffin-tin orbital approach (Sedhain & Kaphle, 2017). The band gap is opened between the lowest energy of the conduction band and the highest energy of the valence band at the k-point. MoS_2 has a high carrier mobility of 200 cm^2/Vs, and a high on/off current ratio of 10^8 at room temperature, so it is used in the field of FETs and photo-detectors (Radisavljevic *et al.,* 2011; Jean & Konor, 2007). Both the theoretical and experimental research groups have studied the physical properties of monolayer MoS_2.

The physical properties are very sensitive to pressure, electric field and strain, because transitions from semiconductors to metal are observed in monolayer MoS_2 due to strain and electric field (Yun *et al.,* 2012; Ataca & Ciraci, 2011; Ataca *et al.,* 2011; Johari & Shenoy, 2012; Kumar & Ahluwalia, 2012; Scalise *et al.,* 2012; Li & Chen, 2014). So, MoS_2 is used in the field of optoelectronics and nanoelectronics devices, as solid lubricants and as catalytic surfaces for hydrogen storage (Novoselov *et al.,* 2012; Neto *et al.,* 2009; Li & Zhu, 2015; Radisavljevic *et al.,* 2011). Hence, it is known as some of the most studied nano-materials due to their different array of technological and industrial applications. MoS_2 has also been studied for the adsorption of water molecules because the devices made by MoS_2 sometimes have to be used in a moisture environment. The physical properties (electronic, magnetic, and tribologic) are affected by adsorbed molecules (like water molecule, hydrogen atom) in monolayer MoS_2 (Panitz *et al.,* 1988; Zhao *et al.,* 2010; Pantha & Adhikari, 2015; Pantha *et al.,* 2020). Hence, the adsorption of a water molecule in monolayer MoS_2 is one of the promising approaches to modify and deceive unwanted properties of any constituent. The water adsorbed MoS_2 losses its lubricity because water-driven oxidation in MoS_2 material leads to the formation of molybdenum trioxide (MoO_3) (Liang *et al.,* 2008; Liang *et al.,* 2011).

Defects in the structure are one of the promising approaches to adapt and exploit the unwanted properties of materials. Hence, they influence the properties of materials in solids (Kettel *et al.,* 1996). The electronic and magnetic properties are attractive properties of the materials. Mo vacancy defect in material develops magnetic properties (Neupane & Adhikari, 2020). Magnetic materials have conceivable applications in the fields of biomedicine, molecular biology, biochemistry, diagnosis, catalysis, nanoelectronic devices, magnetic sensors, computers, magnetic recording media, electric power generators, and transformers (Makarova *et al.,* 2019; Peng *et al.,* 2016).

To our best knowledge, electronic and magnetic properties Mo vacancy defect and S vacancy defect respectively in water adsorbed MoS_2 material have not been reported. Therefore, in present work, we studied the structural, electronic, and magnetic properties of Mo vacancy defect in water adsorbed MoS_2 material, and S vacancy defects in water adsorbed MoS_2 material by spin-polarized DFT theory based first-principles calculations.

MATERIALS AND METHODS

First-principles calculation was performed to investigate the structural, electronic, and magnetic properties of water adsorbed in MoS_2, and Mo & S atoms vacancy defects in water adsorbed MoS_2 materials within the framework of DFT theory (Hohenberg & Kohn, 1964), using Quantum ESPRESSO (QE) computational package (Giannozzi *et al.,* 2009), and structure visualization program XCrySDen (Kokalj, 1999). The electronic exchange and correlation effects in the systems were treated by generalized gradient approximation (GGA) using Perdew-Burke-Ernzerhof (PBE) (Perdew *et al.,* 1996). Rappe-Rabe-Kaxiraas-Joannopoulos (RRKJ) model of ultra-soft pseudo-potentials was used to explain the chemically active valence electrons in our calculations. The Broyden-Fletcher-Goldfarb-Shanno (BFGS) algorithm (Pfrommer *et al.,* 1997) was used to relax the structures until the total energy change was less than 10^{-4} Ry between two consecutive self-consistent field (SCF) steps and each component of force acting was less than 10^{-3} Ry/Bohrs to get geometrically optimized structures. The unit cell was optimized to lattice parameter (a), kinetic energy cut-off (E_{cut}) for plane-wave and the number of k-points along 'x' and 'y' axes, respectively.

The values of lattice constant (a = 3.18 Å), kinetic energy cut-off (E_{cut} = 35 Ry), charge density cut-off (ρ = 350 Ry), and a mesh of (16×16×1) k-points of MoS_2 unit cell were obtained from the convergence test. A mesh of (16×16×1) k-points of MoS_2 unit cell was found from the plot of the total energy versus the number of k-points, where the energy of the unit cell of monolayer MoS_2 was almost constant after n_{kx} =16. Hence, in the unit cell of MoS_2, a mesh of (16×16×1) k-points was used for the Brillouin-zone integration. For the (3×3) supercell structure of MoS_2, the lattice constant was three times that of the unit cell and a mesh of k-points was reduced to (6×6×1). The reduction of the mash was due to the relation of direct and reciprocal lattice geometries. The Marzarri-Vanderbilt (MV) (Marzari *et al.,* 1999), method of smearing with a small width of 0.001Ry was used. In addition, 'david' diagonalization method was chosen with 'plain' mixing mode and a mixing factor of 0.6 for self-consistency. Spin-polarized calculations were allowed to study the magnetic properties of the systems. For band structure calculations, 100 k-points were chosen along the high symmetric points connecting the reciprocal space. For the density of states (DoS) and partial density of states (PDoS) calculations, denser meshes of (12×12×1) k-points were taken.

In the present work, water adsorbed MoS_2 structure, and Mo & S atoms vacancy defects in water adsorbed MoS_2 structures were prepared. At first, w_{ad}-MoS_2 material was constructed by adsorbing water molecules at 2.52 Å distance above the surface of MoS_2. Then, a Mo atom vacancy defect in the w_{ad}-MoS_2 structure (Mo-w_{ad}-MoS_2) was created by removing 1Mo atom in w_{ad}-MoS_2. Similarly, 1S and 2S atoms vacancy defects in w_{ad}-MoS_2 structure (i.e. 1S-w_{ad}-MoS_2 & 2S-w_{ad}-MoS_2) were constructed by removing upper-1S atom in w_{ad}-MoS_2 and 2S (upper-1S & lower-1S) atoms in w_{ad}-MoS_2 structure respectively. All these structures were then optimized and relaxed by using the BFGS scheme for further calculations. Fig. 1 represents stable and relaxed water adsorbed in MoS_2 (w_{ad}-MoS_2), Mo atom vacancy defect in water adsorbed MoS_2 (Mo-w_{ad}-MoS_2), 1S (upper-S atom) vacancy defect in water adsorbed MoS_2 (1S-w_{ad}-MoS_2), and 2S (1S-upper & 1S-lower) atoms vacancy defects in water adsorbed MoS_2 (2S-w_{ad}-MoS_2) materials.

RESULTS AND DISCUSSION

The main findings and their interpretations are presented in this section. Spin-polarized DFT calculations were carried out for the first-principles study of w_{ad}-MoS_2, Mo-w_{ad}-MoS_2, 1S-w_{ad}-MoS_2, and 2S-w_{ad}-MoS_2 materials using computational tools Quantum ESPRESSO.

Structural analysis

The (3×3) supercell structure of monolayer MoS_2 was prepared by extending optimized primitive unit cell along 'x' and 'y' directions using structural visualization tool XCrySDen. The distance between Mo and S atoms in MoS_2 was equal to 3.18 Å. This value agrees with the experimentally reported value of 3.19 Å (Kadantsev & Hawrylak, 2012). Different stacking configurations of w_{ad}-MoS_2 material were prepared by keeping water molecules at different positions on the surface of MoS_2 material. It found that the optimized and relax structure of w_{ad}-MoS_2 material formed by adsorbing water molecules at 2.52 Å distance above the top surface of MoS_2 was more stable than other configurations. This stable structure is shown in Fig. 1(a).

The stability of structures was determined by binding energy calculations. The greater value of binding energy was more favorable for the stability of the system. The binding energy of w_{ad}-MoS_2 was calculated by using the relation (Vu *et al.,* 2020), as depicted in equation (1);

$$E_b = E_{water} + E_{MoS2} - E_{water/MoS2} \quad (1)$$

Where, E_{water}, $E_{MoS2,}$ and $E_{water/MoS2}$ represent ground state energy of relaxing water molecule, monolayer MoS_2, and water adsorbed in monolayer MoS_2 materials, respectively.

After that, Mo-w_{ad}-MoS_2, 1S-w_{ad}-MoS_2, and 2S-w_{ad}-MoS_2 structures were prepared by removing 1Mo atom, upper-1S atom, and 2S (upper-1S & lower-1S) atoms, respectively, in the w_{ad}-MoS_2 structure. Where, out of 9 Mo atoms in w_{ad}-MoS_2, the concentration of Mo atom in Mo vacancy defect w_{ad}-MoS_2 structure was found to be 11.11 %. Also, the concentration of S atoms in 1S vacancy defect w_{ad}-MoS_2 and 2S vacancy defects w_{ad}-MoS_2 structures were found to be 3.04 % and 7.41 %, respectively. The defects formation energy of these materials was calculated by the relation (Hou *et al.*, 2012), as given by equation (2);

$$E_f = E_{Td} + n_d\mu_d - E_{TP} \quad (2)$$

Where E_{Td} is the total energy of a supercell with the defects, n_d is the numbers of defects atoms removed from the perfect supercell to introduce a vacancy, μ_d is chemical potential of defects atoms, E_{TP} is the total energy of the neutral perfect supercell. The calculated defect formation energy of Mo-w_{ad}-MoS_2, 1S-w_{ad}-MoS_2 and 2S-w_{ad}-MoS_2 materials have values 0.68 eV, 0.58 eV and 0.82 eV, respectively. The lower value of defect formation energy means, materials are more stable. Thus, 1S-w_{ad}-MoS_2 is more stable than 2S-w_{ad}-MoS_2 & Mo-w_{ad}-MoS_2 materials. The obtained defect formation energy values are comparable with the defect formation energy of other 2D materials (Neupane & Adhikari, 2021). The defective structures were then relaxed by using the BFGS method. The relaxed-stable Mo-w_{ad}-MoS_2, 1S-w_{ad}-MoS_2 & 2S-w_{ad}-MoS_2 materials are shown in Figs. 1(c), 1(e) & 1(g), respectively. The binding energy of these materials is given in Table 1.

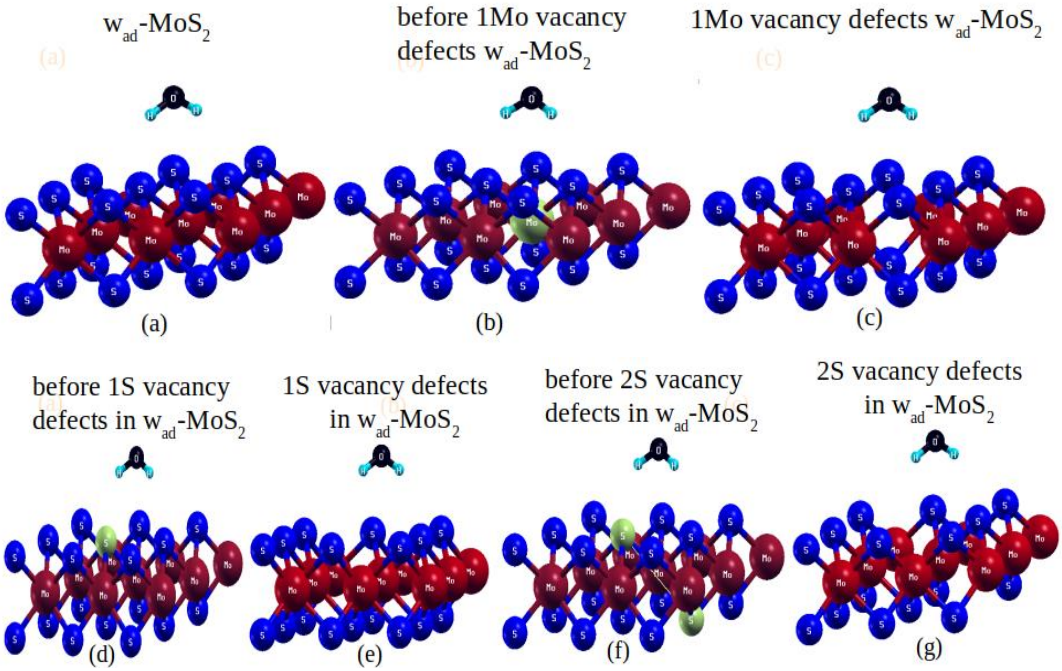

Fig. 1. (a) Water adsorbed MoS_2 structure, (b) Before 1Mo atom vacancy defect in water adsorbed MoS_2 structure, (c) 1Mo atom vacancy defect in water adsorbed MoS_2 structure, (d) Before upper-1S atom vacancy defect in water adsorbed MoS_2 structure, (e) Upper-1S atom vacancy defect in water adsorbed MoS_2 structure, (f) Before 2S atoms vacancy defects in water adsorbed MoS_2 structure (g) 2S atoms vacancy defects in water adsorbed MoS_2 structure

Electronic properties

The electronic properties of w_{ad}-MoS_2, Mo-w_{ad}-MoS_2, 1S-w_{ad}-MoS_2, and 2S-w_{ad}-MoS_2 materials were studied by the analysis of band structure calculations. To know the effect of the adsorbed water molecule in (3×3) supercell of monolayer MoS_2, first need to understand the electronic properties of (3×3) supercell structure of MoS_2. It is a wide band gap semiconductor of band gap value 1.65 eV (Neupane & Adhikari, 2020), this value is close to the experimentally reported value of 1.80 eV (Phuc *et al.*, 2018). The bandgap energy of w_{ad}-MoS_2 was found to be 1.19 eV which is less than the reported band gap energy value of supercell MoS_2.

Therefore, the band gap energy of w_{ad}-MoS_2 was reduced due to the adsorption of the water molecule in pure MoS_2 super cell structure as shown in Fig. 2(a). Similarly, we have calculated the band gap energy values of 1S-w_{ad}-MoS_2 and 2S-w_{ad}-MoS_2 materials from their band structure plots as shown in Figs. 2(b) & 2(c), respectively, wherein all band structure plots, the x-axis represents high symmetric points in the first Brillouin-zone and the y-axis represents the corresponding energy values.

The band gap energy value of these materials was found to be 0.65 eV and 0.38 eV, respectively. These values are less than the band gap energy value of w_{ad}-MoS_2. Hence, from all these calculations, we concluded that w_{ad}-MoS_2, 1S-w_{ad}-MoS_2, and 2S-w_{ad}-MoS_2 materials resemble the nature of semiconductors. But, the conductivity strength of the material increases with an increase in its defect concentration. Also, the band structure of Mo-w_{ad}-MoS_2 was analyzed, and found that the energy band of electrons crossed the Fermi energy level as shown in Fig. 2(d). Hence, Mo-w_{ad}-MoS_2 is metallic in nature.

Table 1. Fermi energy (E_f), Fermi energy shift (E_s), band gap energy (E_g), binding energy (E_b), defects formation energy (E_d), total magnetic moment (M), and magnetic moment (μ) due to up-spin and down-spin of electrons in 4p, 4d & 5s orbitals of Mo atoms; 3s & 3p orbitals of S atoms; 2s & 2p orbitals of O atom; 1s orbital of H atoms; of w_{ad}-MoS_2, 1S-w_{ad}-MoS_2, 2S-w_{ad}-MoS_2 and Mo-w_{ad}-MoS_2 materials

	w_{ad}-MoS_2	1S-w_{ad}-MoS_2	2S-w_{ad}-MoS_2	Mo-w_{ad}-MoS_2
E_f (eV)	-2.04	-2.02	-2.10	-2.48
E_s (eV)	-	0.02	0.06	0.44
E_g (eV)	1.19	0.65	0.38	-
E_b (eV)	0.15	0.13	0.10	0.08
E_d (eV)	-	0.58	0.82	0.68
μ-due to 4p of Mo atoms (μ_B/cell)	0.00	0.00	0.00	0.20
μ-due to 4d of Mo atoms (μ_B/cell)	0.00	0.00	0.00	0.66
μ-due to 5s of Mo atoms (μ_B/cell)	0.00	0.00	0.00	0.02
μ-due to 3s of S atoms (μ_B/cell)	0.00	0.00	0.00	0.04
μ-due to 3p of S atoms (μ_B/cell)	0.00	0.00	0.00	1.74
μ-due to 2s of O atom (μ_B/cell)	0.00	0.00	0.00	0.00
μ-due to 2p of O atom (μ_B/cell)	0.00	0.00	0.00	0.00
μ-due to 1s of H atoms (μ_B/cell)	0.00	0.00	0.00	0.00
Total magnetic moment M (μ_B/cell)	0.00	0.00	0.00	2.66

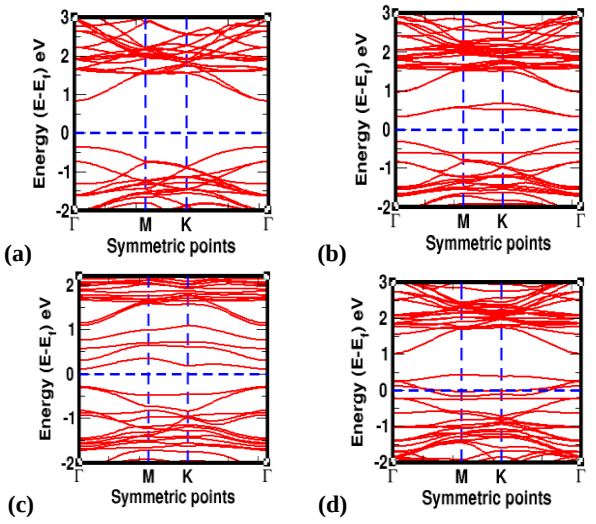

Fig. 2. (a) Band structure of (a) water adsorbed MoS_2 material, (b) upper-1S atom vacancy defect in water adsorbed MoS_2 material, (c) 2S atoms vacancy defects in water adsorbed MoS_2 material, (d) 1Mo atom vacancy defect in water adsorbed MoS_2 material

The metallic and semiconductor nature in defected materials were obtained because the edges and vacancies are very sensitive locations for molecular adsorption due to the under-coordination of atoms in the edge or around the vacancy. They also play a special role either in determining the geometrical conformation of layered materials and inducing modifications of the electronic properties of the layers themselves. It is know that electronic configurations of valence electrons in Mo, S, O and H atoms are [Kr] $4d^5$ $5s^1$, [Ne] $3s^2$ $3p^4$, [He] $2s^2$ $2p^4$ and $1s^1$, respectively. Each Mo atom has one unpaired up-spin in sub-orbital 5s and $4d_{xy}$, $4d_{xz}$, $4d_{yz}$, $4d_{x^2-y^2}$, $4d_{z^2}$; S atom has paired spins (up-spin and down-spin) in $3p_x$ sub-orbital and one unpaired up-spin in $3p_y$, $3p_z$ sub-orbital, and each O atom contains paired spins in $2p_x$ sub-orbital and single unpaired up-spin in $2p_y$ and $2p_z$ sub-orbital, H atom has single unpaired up-spin in 1s orbital. Due to the arrangement of unpaired up and down spin states of electrons in the orbitals of atoms in all w_{ad}-MoS_2, 1S-w_{ad}-MoS_2, 2S-w_{ad}-MoS_2 and Mo-w_{ad}-MoS_2 materials developed different values of Fermi energy. The Fermi energy values of w_{ad}-MoS_2, 1S-w_{ad}-MoS_2, 2S-w_{ad}-MoS_2 and Mo-w_{ad}-MoS_2 materials were found -2.04 eV, -2.02

eV, -2.10 eV and -2.48 eV, respectively. Besides, shifting of Fermi energy values of 1S-w_{ad}-MoS_2, 2S-w_{ad}-MoS_2 and Mo-w_{ad}-MoS_2 materials are 0.02 eV, 0.06 eV and 0.44 eV, respectively, which are given in Table 1. This is due to the movement of charges in the structures. Moreover, we have carried out DoS and PDoS calculations to understand the electronic and magnetic properties of materials. The DoS and PDoS plots of w_{ad}-MoS_2, 1S-w_{ad}-MoS_2, 2S-w_{ad}-MoS_2, and Mo-w_{ad}-MoS_2 materials are shown in Figs. 3(a-d) and Figs. 4(a-d), respectively, where the vertical dotted line represents Fermi energy levels of respective structures.

Magnetic properties

The magnetic moment of materials can be calculated from DoS and PDoS analysis. DoS and PDoS of up and down spin states of electrons in the orbitals of atoms in the materials were symmetrically distributed means, materials have non-magnetic properties, and asymmetrically distributed means, and materials have magnetic properties. The DoS and PDoS plots of w_{ad}-MoS_2, 1S-w_{ad}-MoS_2, 2S-w_{ad}-MoS_2, and Mo-w_{ad}-MoS_2 materials are shown in Figs. 3(a-d) and Figs. 4(a-d), respectively. We have anatomized PDoS calculations to know the contributions of the magnetic moment given by the up-spin and down-spin of electrons in the individual orbital of atoms in materials. The detailed calculations of the magnetic moment due to spin states of electrons in the orbitals of Mo, S, O, and H atoms in PDoS of w_{ad}-MoS_2, 1S-w_{ad}-MoS_2, and 2S-w_{ad}-MoS_2 materials are given in Table 1. DoS and PDoS plots of these materials are seen symmetrically distributed near the Fermi energy level as shown in Figs. 3(a-c) and Figs. 4(a-c), respectively.

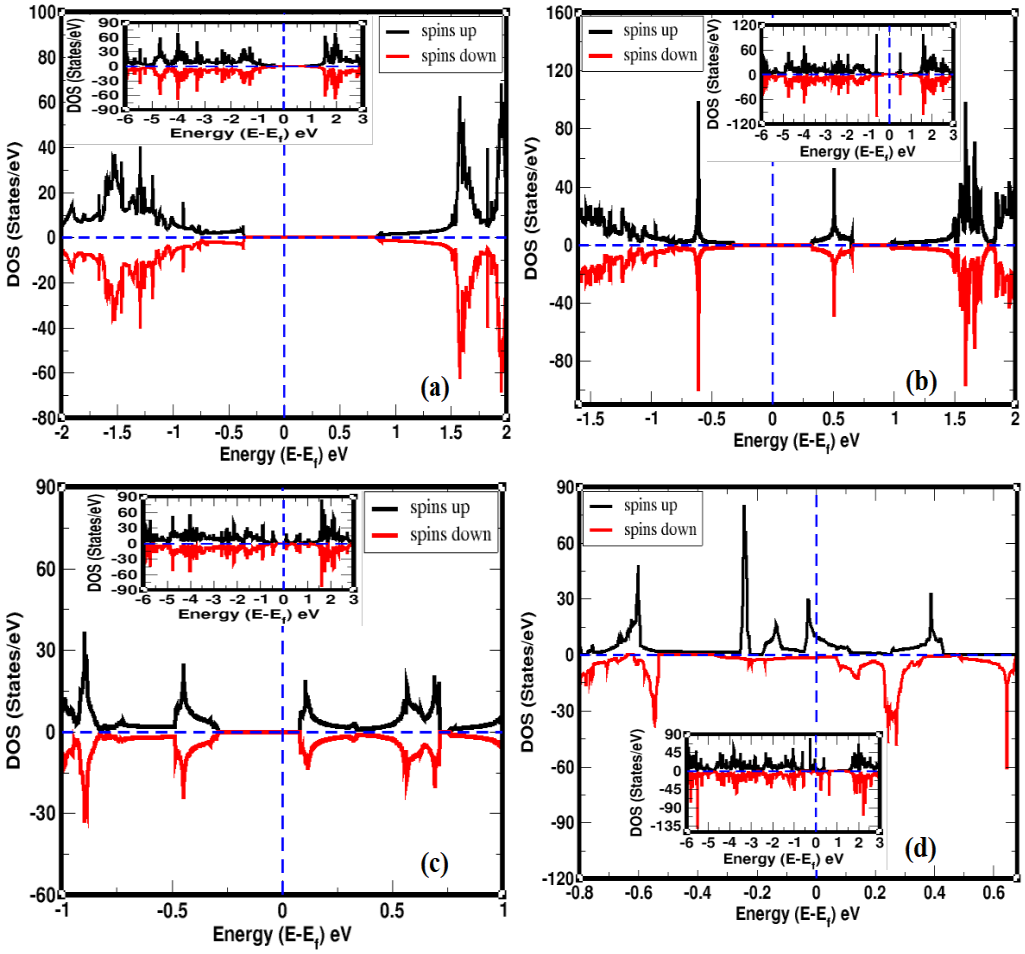

Fig. 3. (a) Total DoS of water adsorbed MoS_2 material, (b) total DoS of upper-1S atom vacancy defect in water adsorbed MoS_2 material, (c) total DoS of 2S atoms vacancy defects in water adsorbed MoS_2 material, (d) total DoS of 1Mo atom vacancy defect in water adsorbed MoS_2 material

Also, it was found that net magnetic moment given by up and down spin of electrons in 4p, 4d & 5s orbitals of Mo atoms; 3s & 3p orbitals of S atoms; 2s & 2p orbitals of O atom; and 1s orbital of H atoms have zero value. This is because; adsorbed water molecule reduces chemical activity in the lattice structures of w_{ad}-MoS_2, 1S-w_{ad}-MoS_2

and 2S-w_{ad}-MoS_2 materials. Physisorption interactions can arise when a water molecule is adsorbed in this type of structure. Therefore, w_{ad}-MoS_2, 1S-w_{ad}-MoS_2, and 2S-w_{ad}-MoS_2 materials have non-magnetic properties.

Furthermore, the DoS/PDoS calculation of Mo-w_{ad}-MoS_2 material was analyzed. The DoS and PDoS of up-spin and down-spin states of electrons near the Fermi level were asymmetrically distributed, as shown in Figs. 3(d) and 4(d). Hence, the Mo-w_{ad}-MoS_2 material has magnetic properties. Also, the contributions of the magnetic moment due to the distribution of spins of electrons in the individual orbital of atoms presented in Mo-w_{ad}-MoS_2 material are given in Table 1. The magnetic moment developed in the material due to up-spin and down-spin of electrons in 4p, 4d & 5s orbitals of Mo atoms are 0.20 μ_B/cell, 0.66 μ_B/cell & 0.02μ_B/cell; 3s & 3p orbitals of S atoms were 0.04μ_B/cell & 1.74μ_B/cell; and 2s & 2p orbitals of O atom, 1s orbital of H atoms were 0.00 μ_B/cell values, respectively. It means dominant contributions of magnetic moments are given by spins of 4p & 4d orbitals of Mo atoms and 3s & 3p orbitals of S atoms in the material. These values of the magnetic moment were calculated by subtraction between the values of the magnetic moment given by total up-spins and total down-spins of electrons in the orbitals of atoms present in Mo-w_{ad}-MoS_2 material. Hence, from these calculations, we found that the total magnetic moment of Mo-w_{ad}-MoS_2 has a value of 2.66 μ_B/cell. The positive value of magnetic moment means the up-spin electrons of atoms have a dominant role over the down-spin electrons of atoms. In Mo-w_{ad}-MoS_2 material, 3p orbital of S atoms and 4d orbital of Mo atoms have the principal role for the development of magnetic moment.

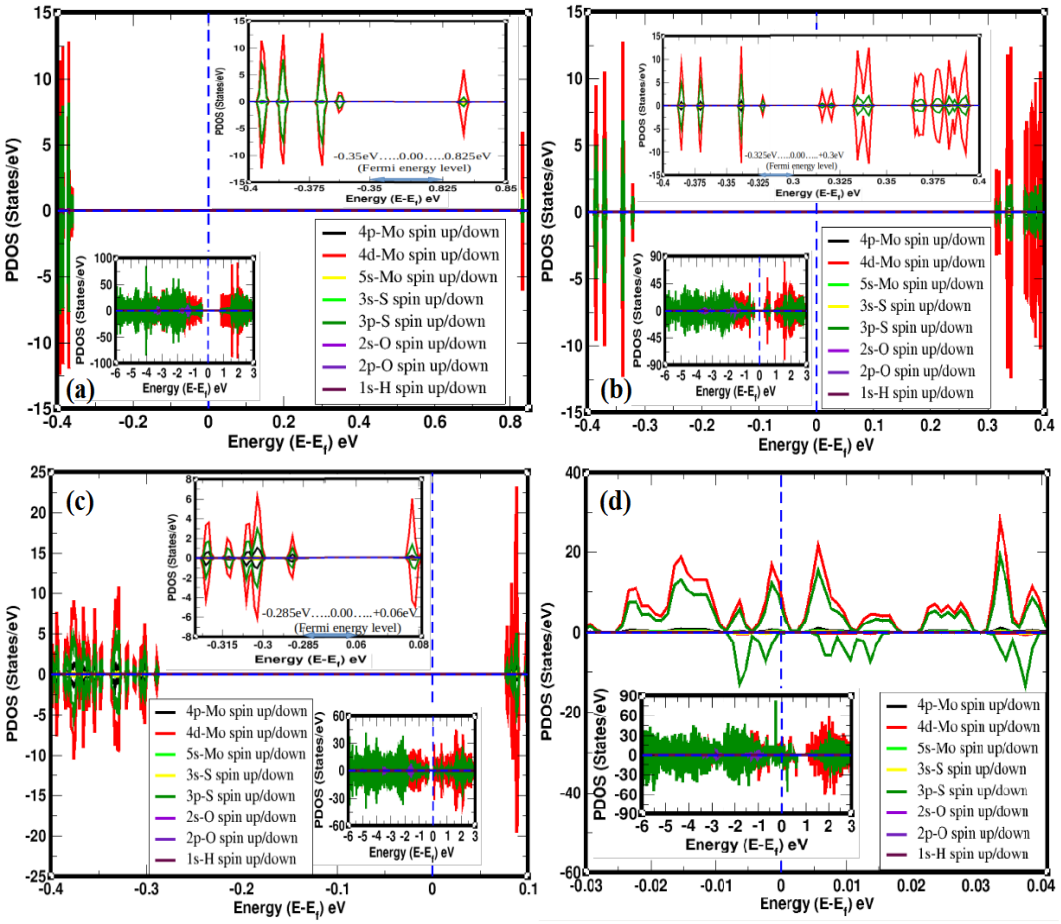

Fig. 4. PDoS of individual orbital of Mo, S, O, H atoms in (a) water adsorbed MoS_2 material, (b) upper-1S atom vacancy defect water adsorbed MoS_2 material, (c) 2S atoms vacancy defects water adsorbed MoS_2 material, and (d) 1Mo atom vacancy defect water adsorbed MoS_2 material

CONCLUSIONS

In the present work, the structural, electronic, and magnetic properties of w_{ad}-MoS_2, 1S-w_{ad}-MoS_2, 2S-w_{ad}-MoS_2, and Mo-w_{ad}-MoS_2 materials were studied by first-principles calculations based on the spin-polarized density functional theory (DFT) method. The Quantum ESPRESSO package was used for the computational work

and the XCrySDen program was used for structure visualization. By analyzing the structures, the w_{ad}-MoS_2, 1S-w_{ad}-MoS_2, 2S-w_{ad}-MoS_2, and Mo-w_{ad}-MoS_2 were found to be stable materials. From the band structure calculations, the band gap energy of w_{ad}-MoS_2, 1S-w_{ad}-MoS_2, and 2S-w_{ad}-MoS_2 materials calculated as 1.19 eV, 0.65 eV, and 0.38 eV, respectively. Therefore, these materials behave as a semiconductor. But, energy bands of electrons were crossed the Fermi energy level in the band structure of Mo-w_{ad}-MoS_2 material. Hence, Mo-w_{ad}-MoS_2 material has metallic properties. From DoS and PDoS calculations, w_{ad}-MoS_2, 1S-w_{ad}-MoS_2, and 2S-w_{ad}-MoS_2 materials are non-magnetic materials, while Mo-w_{ad}-MoS_2 is a magnetic material. Therefore, non-magnetic w_{ad}-MoS_2 changes to magnetic Mo-w_{ad}-MoS_2 material due to the presence of Mo vacancy defect. The total magnetic moment of Mo-w_{ad}-MoS_2 material has a value of 2.66 μ_B/cell. The high value of magnetic moment in Mo-w_{ad}-MoS_2 is given by distributed up-spin and down-spin in 3p orbital of S atoms and 4d orbital of Mo atoms.

ACKNOWLEDGEMENTS

HKN acknowledges the UGC Nepal for awarding the Ph. D. scholarship (PhD-75/76-S&T-09), and NPA acknowledges network project NT-14 of ICTP/OEA and UGC Nepal Grants CRG 073/74 -S&T -01.

REFERENCES

Ataca, C., & Ciraci, S. (2011). Functionalization of single-layer MoS_2 honeycomb structures. *The Journal of Physical Chemistry C*, *115*(27), 13303-13311.

Ataca, C., Sahin, H., Akturk, E., & Ciraci, S. (2011). Mechanical and electronic properties of MoS_2 nanoribbons and their defects. *The Journal of Physical Chemistry C*, *115*(10), 3934-3941.

Giannozzi, P., Baroni, S., Bonini, N., Calandra, M., Car, R., Cavazzoni, C. & Dal Corso, A. (2009). Quantum ESPRESSO: modular and open-source software project for quantum simulations of materials. *Journal of Physics: Condensed Matter*, *21*(39), 395502. https://doi.org/10.1088/0953-8984/21/39/395502

Hohenberg, P., & Kohn, W. (1964). Inhomogeneous electron gas. *Physical Review B*, *136*(3), 864. https://doi.org/10.1103/PhysRev.136.B864

Hou, Z., Wang, X., Ikeda, T., Terakura, K., Oshima, M., Kakimoto, M. A., & Miyata, S. (2012). Interplay between nitrogen dopants and native point defects in graphene. *Physical Review B*, *85*(16), 165439. https://doi.org/10.1103/PhysRevB.85.165439

Jena, D., & Konar, A. (2007). Enhancement of carrier mobility in semiconductor nanostructures by dielectric engineering. *Physical Review Letters*, *98*(13), 136805. https://doi.org/10.1103/PhysRevLett.98.136805

Johari, P., & Shenoy, V. B. (2012). Tuning the electronic properties of semiconducting transition metal dichalcogenides by applying mechanical strains. *ACS Nano*, *6*(6), 5449-5456.

Kadantsev, E. S., & Hawrylak, P. (2012). Electronic structure of a single MoS_2 monolayer. *Solid State Communications*, *152*(10), 909-913.

Kittel, C., McEuen, P., & McEuen, P. (1996). *Introduction to solid state physics* (Vol. 8, pp. 105-130). New York, USA: Wiley. ISBN: 978-81-265-3518-7

Kokalj, A., (1999). XCrySDen-a new program for displaying crystalline structures and electron densities. *Journal of Molecular Graphics and Modeling*, *17*(3-4), 176-179.

Kumar, A., & Ahluwalia, P. K. (2012). A first principle comparative study of electronic and optical properties of 1H-MoS_2 and 2H-MoS_2. *Materials Chemistry and Physics*, *135*(2-3), 755-761.

Li, X., & Zhu, H. (2015). Two-dimensional MoS_2: Properties, preparation, and applications. *Journal of Materiomics*, *1*(1), 33-44.

Li, Y., & Chen, Z. (2014). Tuning electronic properties of germanane layers by external electric field and biaxial tensile strain: a computational study. *The Journal of Physical Chemistry C*, *118*(2), 1148-1154.

Liang, T., Sawyer, W. G., Perry, S. S., Sinnott, S. B., & Phillpot, S. R. (2008). First-principles determination of static potential energy surfaces for atomic friction in MoS_2 and MoO_3. *Physical Review B*, *77*(10), 104105. https://doi.org/10.1103/PhysRevB.77.104105

Liang, T., Sawyer, W. G., Perry, S. S., Sinnott, S. B., & Phillpot, S. R. (2011). Energetics of oxidation in MoS_2 nanoparticles by density functional theory. *The Journal of Physical Chemistry C*, *115*(21), 10606-10616. https://doi.org/10.1021/jp110562n

Mak, K. F., Lee, C., Hone, J., Shan, J., & Heinz, T. F. (2010). Atomically thin MoS_2: a new direct-gap semiconductor. *Physical Review Letters*, *105*(13), 136805. https://doi.org/10.1103/PhysRevLett.105.136805

Makarova, M. V., Akaishi, Y., Ikarashi, T., Rao, K. S., Yoshimura, S., & Saito, H. (2019). Alternating magnetic force microscopy: Effect of Si doping on

the temporal performance degradation of amorphous FeCoB magnetic tips. *Journal of Magnetism and Magnetic Materials, 471*, 209-214.

Marzari, N., Vanderbilt, D., De Vita, A., & Payne, M. C. (1999). Thermal contraction and disordering of the Al (110) surface. *Physical Review Letters, 82*(16), 3296. https://doi.org/10.1103/PhysRevLett.82.3296

Neto, A. C., Guinea, F., Peres, N. M., Novoselov, K. S., & Geim, A. K. (2009). The electronic properties of graphene. *Reviews of Modern Physics, 81*(1), 109. https://doi.org/10.1103/RevModPhys.81.109

Neupane, H. K., & Adhikari, N. P. (2020). Structure, electronic and magnetic properties of 2D Graphene-Molybdenum diSulphide (G-MoS_2) Heterostructure (HS) with vacancy defects at Mo sites. *Computational Condensed Matter*, 24, e00489. https://doi.org/10.1016/j.cocom.2020.e00489

Neupane, H. K., & Adhikari, N. P. (2020). Tuning structural, electronic, and magnetic properties of C sites vacancy defects in graphene/MoS2 van der Waals heterostructure materials: A first-principles study. *Advances in Condensed Matter Physics, 2020*, 8850701. https://doi.org/10.1155/2020/8850701

Neupane, H. K., & Adhikari, N. P. (2021). First-principles study of structure, electronic, and magnetic properties of C sites vacancy defects in water adsorbed graphene/MoS_2 van der Waals heterostructures. *Journal of Molecular Modeling, 27*(3), 1-12.

Novoselov, K. S., Fal, V. I., Colombo, L., Gellert, P. R., Schwab, M. G., & Kim, K. (2012). A roadmap for graphene. *Nature, 490*(7419), 192-200.

Panitz, J. K. G., Pope, L. E., Lyons, J. E., & Staley, D. J. (1988). The tribological properties of MoS_2 coatings in a vacuum, low relative humidity, and high relative humidity environments. *Journal of Vacuum Science & Technology A: Vacuum, Surfaces, and Films, 6*(3), 1166-1170.

Pantha, N., & Adhikari, N. (2015). Structure and symmetrization of hydrogen bonding in ices VIII and X at high pressure: A density functional theory approach. *Journal of Institute of Science and Technology, 19*(2), 14-18.

Pantha, N., Thapa, S., & Adhikari, N. (2020). First-principles study of molecular adsorption of hydrogen/s on Co-adatom graphene. *Journal of Institute of Science and Technology, 25*(1), 15-23.

Peng, H. X., Qin, F., & Phan, M. H. (2016). *Ferromagnetic microwire composites: from Sensors to microwave applications*. Switzerland: Springer International Publishing. https://doi.org/10.1007/978-3-319-29276-2

Perdew, J. P., Burke, K., & Ernzerhof, M. (1996). Generalized gradient approximation made simple. *Physical Review Letters, 77*(18), 3865. https://doi.org/10.1103/PhysRevLett.77.3865

Pfrommer, B. G., Cote, M., Louie, S. G., & Cohen, M. L. (1997). Relaxation of crystals with the quasi-Newton method. *Journal of Computational Physics, 131*(1), 233-240.

Phuc, H. V., Hieu, N. N., Hoi, B. D., Phuong, L. T., & Nguyen, C. V. (2018). First principle study on the electronic properties and Schottky contact of graphene adsorbed on MoS_2 monolayer under applied out-plane strain. *Surface Science, 668*, 23-28.

Radisavljevic, B., Radenovic, A., Brivio, J., Giacometti, V., & Kis, A. (2011). Single-layer MoS_2 transistors. *Nature Nanotechnology, 6*(3), 147-150.

Scalise, E., Houssa, M., Pourtois, G., Afanas'ev, V., & Stesmans, A. (2012). Strain-induced semiconductor to metal transition in the two-dimensional honeycomb structure of MoS_2. *Nano Research, 5*(1), 43-48.

Sedhain, R., & Kaphle, G. (2017). Structural and electronic properties of transition metal dichalcogenides (MX_2) M=(Mo, W) and X=(S, Se) in bulk state: A first-principles study. *Journal of Institute of Science and Technology, 22*(1), 41-50.

Vu, T. V., Hieu, N. V., Phuc, H. V., Hieu, N. N., Bui, H. D., Idrees, M.,.. & Nguyen, C. V. (2020). Graphene/WSeTe van der Waals heterostructure: Controllable electronic properties and Schottky barrier via interlayer coupling and electric field. *Applied Surface Science, 507*, 145036. https://doi.org/10.1016/j.apsusc.2019.145036

Yun, W. S., Han, S. W., Hong, S. C., Kim, I. G., & Lee, J. D. (2012). Thickness and strain effects on electronic structures of transition metal dichalcogenides: 2H-MX_2 semiconductors (M = Mo, W; X = S, Se, Te). *Physical Review B, 85*(3), 033305. https://doi.org/10.1103/PhysRevB.85.033305

Zhao, X., & Perry, S. S. (2010). The role of water in modifying friction within MoS_2 sliding interfaces. *ACS Applied Materials & Interfaces, 2*(5), 1444-1448.

JNPS 7 (2): 1-8 (2021)
ISSN: 2392-473X (Print), 2738-9537 (Online)
Research Article *© Nepal Physical Society*
DOI: https://doi.org/10.3126/jnphyssoc.v7i2.38578

Structural, Electronic and Magnetic Properties of Impurities Defected Graphene/MoS_2 Van Der Waals Heterostructure: First-principles Study

H. K. Neupane[1, 2] and N. P. Adhikari[2, *]
[1]Amrit Campus, Institute of Science and Technology, Tribhuvan University, Kathmandu, Nepal
[2]Central Department of Physics, Institute of Science and Technology,
Tribhuvan University, Kathmandu, Nepal
[*]Corresponding Email: narayan.adhikari@cdp.tu.edu.np

Received: *14 May, 2021;* ***Revised:*** *13 June, 2021;* ***Accepted:*** *25 June, 2021*

ABSTRACT

Two-dimensional (2D) pristine and defected van der Waals (vdW) heterostructure (HS) materials open up fortune in nanoelectronic and optoelectronic devices. So, they are compatible for designing in the fields of device applications. In the present work, we studied structural, electronic and magnetic properties of vdW (HS) graphene/MoS_2 ((HS)G/MoS_2), Nb impurity defect in vdW (HS) graphene/MoS_2 (Nb-(HS)G/MoS_2), and Tc impurity defect in vdW (HS) graphene/MoS_2 (Tc-(HS)G/MoS_2) materials by using spin-polarized DFT-D2 method. We examined the structure of these materials, and found that they are stable. Based on band structure analysis, we found that (HS)G/MoS_2, Nb-(HS)G/MoS_2 and Tc-(HS)G/MoS_2 have metallic characteristics. Also, (HS)G/MoS_2 and Tc-(HS)G/MoS_2 materials have n-type Schottky contact, while Nb-(HS)G/MoS_2 material has p-type Schottky contact. To understand the magnetic properties of materials, we have used DoS, IDoS and PDoS calculations. We found that (HS)G/MoS_2 is a non-magnetic material, but Nb-(HS)G/MoS_2 and Tc-(HS)G/MoS_2 are magnetic materials. Magnetic moment of Nb-(HS)G/MoS_2 and Tc-(HS)G/MoS_2 materials are -0.24 μ_B/cell and +0.07μ_B/cell values respectively from DoS/PDoS calculations, and 0.26 μ_B/cell and 0.08μ_B/cell values respectively from IDoS calculations. Up-spin and down-spin states of electrons in 2p orbital of C atoms, 3p orbital of S atoms, 4d orbital of Mo atoms, 4d orbital of Tc atom in Tc-(HS)G/MoS_2, and 2p orbital of C atoms, 3p orbital of S atoms, 4p & 4d orbitals of Mo atoms, 4p & 4d orbitals of Nb atom in Nb-(HS)G/MoS_2 have major contribution for the development of magnetic moment.

Keywords: DFT-D2; Heterostructure; Impurity defects; Magnetic moment; Spin states.

1. INTRODUCTION

Graphene is two dimensional (2D) stretchable, sp^2-hybridized, zero band gap and honeycomb lattice structure of carbon atoms. It has good electronic properties such as, high carrier mobility and high thermal conductivity, observable Quantum Hall effect at room temperature and existence of two dimensional gases of massless Dirac fermions [1-4]. Due to these properties, it has potential applications in the areas of nanoelectronic, optoelectronic, sensing and hydrogen storage devices [5-7]. Thus, graphene is a favorable material for the researchers to predict additional desirable properties [4, 8]. Molybdenum disulphide (MoS_2) is 2D transition metal dichalcogenide (TMD) wide band gap semiconductor of band gap 1.80 eV [9]. It can be constructed by assembling Mo and S atoms (i.e. S-Mo-S) in a triangular prismatic configuration [10]. MoS_2 has great applications in the fields of nanoelectronic and optoelectronic devices [11-14]. However, 2D materials, graphene due to zero bandgap energy, and monolayer MoS_2 due to wide gap energy have limited properties. Therefore, to tune the desirable properties in 2D materials, graphene is combined with other 2D materials and formed heterostructure

(HS). The graphene based 2D (HS) materials (G/MoS_2, G/h-BN) are used to produce novel ways for engineering electronic and optoelectronic devices [15-17]. The (HS)G/MoS_2 (heterostructure of graphene with MoS_2) offers mechanical, electronic, optical, and transport properties. Thus, it can be used in the fields of device applications [18]. Moreover, the substitution of any atom by foreign atom (impurity defect) in (HS)G/MoS_2 or removal of any atom (vacancy defect) from (HS)G/MoS_2 structure is one of the promising approaches to modify and exploit unwanted properties of any constituent. The impurity of Technetium (Tc) atom or Niobium (Nb) atom in (HS)G/MoS_2 changes its electronic and magnetic properties. Defects in (HS) give peculiar properties and carry out the new materials [19-22]. Hence, defects impact the properties of (HS) materials [23]. To our knowledge, effect of impurity defects on structural, electronic and magnetic properties of vdW (HS)G/MoS_2 material have not been reported yet. Therefore, in this paper, we learned the structural, electronic and magnetic properties of vdW (HS)G/MoS_2, and effect of Nb impurity defect in vdW (HS)G/MoS_2 (Nb-(HS)G/MoS_2) material & Tc impurity defects in vdW (HS)G/MoS_2 (Tc-(HS)G/MoS_2) material by spin-polarized DFT-D2 method based on first-principles calculations. Figs. 1(a-c) illustrated pristine (HS)G/MoS_2, Nb-(HS)G/MoS_2 and Tc-(HS)G/MoS_2 materials respectively.

2. METHODS AND MATERIALS

We used spin-polarized DFT-D2 method to learn the structural, electronic and magnetic properties of (HS)G/MoS_2 and impurity defects (Nb and Tc impurity defects) in vdW (HS)G/MoS_2 using Quantum ESPRESSO (QE) computational tool [24-26]. The electronic exchange and correlation effects in the systems are treated by Generalized Gradient Approximation (GGA) using Perdew-Burke-Ernzerhof (PBE) [27]. Rappe-Rabe-Kaxiraas-Joannopoulos (RRKJ) model of ultra-soft pseudo-potentials is used to deal the chemically active valence electrons in the systems. All structures are optimized and relaxed by Broyden-Fletcher-Goldfarb-Shanno (BFGS) [28] method. At first we have prepared G/MoS_2 heterostructure material by (4×4) supercell structure of graphene and (3×3) supercell structure of monolayer MoS_2 with 4.11% lattice mismatch. To avoid the physical interactions in the stacking direction of (HS)G/MoS_2 material, we kept a vacuum distance greater than 18 Å. The Nb impurity defect in (HS)G/MoS_2 (i.e. Nb-(HS)G/MoS_2) and Tc Impurity defect in (HS)G/MoS_2 (i.e. Tc-(HS)G/MoS_2) are obtained by replacing centre Mo atom of (HS)G/MoS_2 by Nb atom and Tc atom respectively. Then, we obtained relax Nb-(HS)G/MoS_2 and Tc-(HS)G/MoS_2 structures by using BFGS method as shown in figs. 1(b-c). We performed self consistent total energy calculation after relax calculations. For this, the Brillouin-zone of (HS) is figured out in k-space using Monkhorst-Pack scheme [29] with suitable number of mesh (6×6×1) of k-points, which is determined from the convergence test. The plane-wave expansion with kinetic energy cut-off 35 Ry and charge density cut-off 350 Ry are used for wave function and charge density respectively. Kinetic energy cut-off and charge density cut-off values are calculated from convergence plot of total energy versus energy cut-off wave function. We used Marzarri-Vanderbilt [30] method of smearing for occupations and 0.001 Ry value of degauss. We have taken "david" diagonalization method with "plain" mixing mode for self consistency with 0.6 mixing factor. Also, we have taken a mesh of (6×6×1) k-points for band structure calculations (100 k-points are chosen along the high symmetric points), and meshes of (12×12×1) k-points are used for density of states (DoS) and projected density of states (PDoS) calculations.

3. RESULTS AND DISCUSSION

In this section, we discussed in details about structural, electronic and magnetic properties of pristine (HS)G/MoS_2, and Nb & Tc impurity defected (HS)G/MoS_2 materials based on spin-polarized DFT-D2 method.

3.1 Structural Analysis

We have prepared vertical stacking configuration of vdW (HS)G/MoS_2 material by keeping supercell of graphene and supercell of MoS_2. The lattice mismatch is found to be 4.11% in vdW (HS)G/MoS_2. Lattice mismatch is fixed by differing the lattice constant because there is no direct chemical bonding between the constituent layers. Stability of (HS)G/MoS_2 material is checked by its calculated binding energy. Binding energy (-0.40 eV) of it is obtained by using equation (1), [31];

$$E_b = E_{(HS)G/MoS2} - E_G - E_{MoS2} \ldots (1)$$

Where, $E_{(HS)G/MoS2}$, E_G and E_{MoS2} represent total ground state energy of (HS)G/MoS_2, supercell of

graphene and supercell of MoS_2 respectively. The obtained binding energy (-0.40 eV) of (HS)G/MoS_2 indicates that material is energetically stable at ground state because negative value of binding energy of materials implies that they are energetically stable at ground state. We have also calculated the inter-layer distance the constituents of (HS) and found 3.37 Å value. Our calculated values of binding energy and inter-layer distance are comparable with other 2D VdW heterostructure materials [32]. In addition, we have created the stable Nb-(HS)G/MoS_2 and Tc-(HS)G/MoS_2 impurity defects materials as shown in figs. 1(b-c). The binding energy of Nb-(HS)G/MoS_2 is -0.35 eV and Tc-(HS)G/MoS_2 is -0.38 eV are calculated by using equation (2), [31]; because binding energy determines the stability of materials.

$$E_b = E_{(HS\text{-}G/MoS2)i\text{-}d} - E_G - E_{(MoS2)i\text{-}d} \ldots (2)$$

Where, $E_{(HS\text{-}G/MoS2)i\text{-}d}$, $E_{(MoS2)i\text{-}d}$ & E_G represent total ground state energy of impurity (Nb atom or Tc atom) defected (HS)G/MoS_2, impurity defected monolayer MoS_2 & graphene respectively. We measured the inter-layer distances between graphene and MoS_2 in Nb-(HS)G/MoS_2 and Tc-(HS)G/MoS_2 materials, and found that they are 3.54 Å and 3.42 Å respectively, which are comparable to other 2D heteostructure materials of values 3.31 Å and 3.19 Å [32]. Thus, the estimated binding energies and inter-layer distances of impurity defected materials are also comparable with other vdW heterostructure materials [32]. We can also test the stability of impurity defected materials relative to pristine material; we can calculate the defects formation energy (E_f). Defects formation energy is obtained by using the values of total energy of impurity defects in (HS)G/MoS_2 (E_{t1}), total energy of pristine (HS)G/MoS_2 (E_{t2}), energy of impurity (Nb or Tc) atom (E_1), and energy of isolated (replaced) Mo atom (E_2) by equation (3), [33];

$$E_f = (E_{t1}\text{-}E_{t2}) - (E_1\text{-}E_2) \ldots (3)$$

Defects formation energy of Nb-(HS)G/MoS_2 and Tc-(HS)G/MoS_2 materials are found to be 2.54 eV and 2.56 eV respectively. The negative value of formation energy indicates that the system is more stable than the pristine one, while positive value of formation energy implies that the system requires external energy for the formation of impurity defects in material. Also, lower value of defects formation energy means, materials can be favorable in computation work.

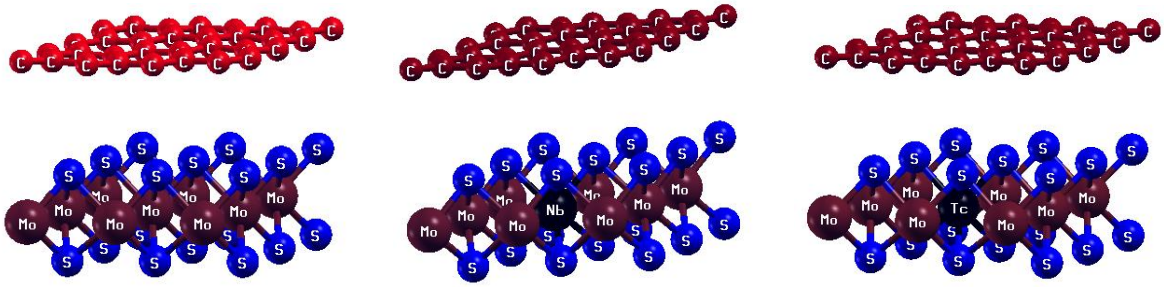

Fig. 1: (a) Structure of pristine (HS)G/MoS_2 material, (b) Structure of Nb-(HS)G/MoS_2 material, (c) Structure of Tc-(HS)G/MoS_2 material.

From the structural analysis of pristine (HS)G/MoS_2 and impurity defects Nb-(HS)G/MoS_2 & Tc-(HS)G/MoS_2 materials, we found that all are stable and compactness of pristine has greater than that of impurity defects materials.

3.2 Electronic and Magnetic Properties

Solid state matter is rigid and its degree of rigidity depends upon the relative compactness of the constituent atoms. In an isolated atom, the electrons occupy atomic orbitals each of which has a discrete energy level while atomic orbitals overlap when two identical atoms join together to form a molecule. In solid with N identical atoms, each atomic orbital splits into N discrete molecular orbitals, each with a different energy. In a macroscopic piece of solid, the number of atoms is large ($N \approx 10^{23}$), so is the number of orbitals and is very closely spaced in energy (10^{-22} eV). Thus, they

form continuum of energy as 'energy band'. Electronic properties of material can be predicted by the analysis of its band structure. In this section, we discuss electronic and magnetic properties of (HS)G/MoS_2, Nb-(HS)G/MoS_2 and Tc-(HS)G/MoS_2 materials on the basis of their band structures and density of states (DoS), integrated density of states (IDoS) and projected density of states (PDoS) analysis. The band structures of (HS)G/MoS_2, Nb-(HS)G/MoS_2 and Tc-(HS)G/MoS_2 materials are shown in fig. 2(a), fig. 3(a) and fig. 4(a) respectively. In band structures, x-axis represents Γ-centre symmetric points (Γ-M-K-Γ) in the first Brillouin-zone, where 100 k-points are kept along the particular direction of irreducible Brillouin-zone, and y-axis represents the corresponding energy values, also horizontal dotted line represents the Fermi energy level. In band structure of pristine (HS)G/MoS_2, Dirac cone is formed in the conduction band at 0.56 eV distance from Fermi energy level. It means electrons flow from valence band to conduction band. Hence, (HS)G/MoS_2 has metallic properties. Also, n-type Schottky contact is formed with Schottky barrier height of 0.42 eV in (HS)G/MoS_2. This value agrees with the reported value 0.49 eV [34, 35]. In band structures of impurity defects Nb-(HS)G/MoS_2 and Tc-(HS)G/MoS_2 materials, Dirac cone is formed in conduction band at 0.70 eV and 0.01 eV distances from the Fermi energy level as shown in fig. 3(a) and fig. 4(a) respectively. In both materials, electrons flow from valence band to conduction band, hence they have metallic properties. The n-type Schottky contact is still preserved in Tc-(HS)G/MoS_2, while in Nb-(HS)G/MoS_2 material p-type Schottky contact is formed. Therefore, n-type Schottky contact of (HS)G/MoS_2 shifts to p-type Schottky contact due to Nb impurity atom in it. We know that electronic configurations of valence electrons in Mo, Tc, Nb, S & C atoms present in the materials are [Kr] $4d^5$ $5s^1$, [Kr] $4d^5$ $5s^2$, [Kr] $4d^4$ $5s^1$, [Ne] $3s^2$ $3p^4$ & [He] $2s^2$ $2p^2$ respectively. Each Mo atom has one unpaired up-spin in 5s orbital and $4d_{xy}$, $4d_{xz}$, $4d_{yz}$, $4d_{x^2-y^2}$, $4d_{z^2}$ sub-orbitals; Tc atom has paired spins in 5s orbital and one unpaired up-spin in $4d_{xy}$, $4d_{xz}$, $4d_{yz}$, $4d_{x^2-y^2}$, $4d_{z^2}$ sub-orbitals; Nb atom has one unpaired up-spin in 5s orbital, $4d_{xy}$, $4d_{xz}$, $4d_{yz}$, $4d_{x^2-y^2}$ sub-orbitals and vacant in $4d_{z^2}$ sub-orbital; S atom has paired spins (up-spin & down-spin) in $3p_x$ sub-orbital and one unpaired up-spin in $3p_y$, $3p_z$ sub-orbitals; C atom has single up-spin in $2p_x$, $2p_y$ and vacant in $2p_z$ sub-orbitals. By the configurations of unpaired (up-spin and down-spin) spins of electrons in the orbital of atoms in (HS)G/MoS_2, Nb-(HS)G/MoS_2 and Tc-(HS)G/MoS_2 materials created different values of Fermi energy and Dirac (cone) point. The different values of Fermi energy, Dirac point, Dirac shift, Fermi shift, total energy, binding energy and inter-layer distances of above mentioned materials are given in table 1.

Table 1: Fermi energy (E_f), Fermi energy shift (E_s), Dirac (point) cone (D_p), Dirac (point) cone shift (D_s), total energy (E_t), binding energy (E_b) and inter-layer distances (D_{I-d}) of (HS)G/MoS_2, Nb-(HS)G/MoS_2 and Tc-(HS)G/MoS_2 materials.

(HS)G/MoS_2, Nb-(HS)G/MoS_2 and Tc-(HS)G/MoS_2 materials	E_f (eV)	E_s (eV)	D_p (eV)	D_s (eV)	E_t (Ry)	E_b (eV)	D_{I-d} (Å)
(HS)G/MoS_2	0.32	-	0.56	-	-2106.17	-0.40	3.37
Nb-(HS)G/MoS_2	-0.50	-0.82	0.70	+0.14	-2076.54	-0.35	3.54
Tc-(HS)G/MoS_2	0.78	+0.46	0.01	-0.55	-2138.61	-0.38	3.42

Based on DoS and PDoS calculations, we can investigate the magnetic properties of materials. Symmetrically distributed total up-spin and total down-spin in DoS/PDoS of materials means, materials has non-magnetic properties, and asymmetrically distributed unpaired up-spin and down-spin of electrons in the orbital of atom give magnetic properties of materials. The DoS and PDoS plots of (HS)G/MoS_2, Nb-(HS)G/MoS_2 and Tc-(HS)G/MoS_2 materials are given in figs 2(b-c), figs. 3(b-c) and figs. 4(b-c) respectively, where vertical dotted line distinguished energy bands (the region below zero scale is called valence band and the region above zero scale is called conduction band), and horizontal dotted line separates distributed up-spin and down-spin states of electrons in the orbitals of atoms in materials.

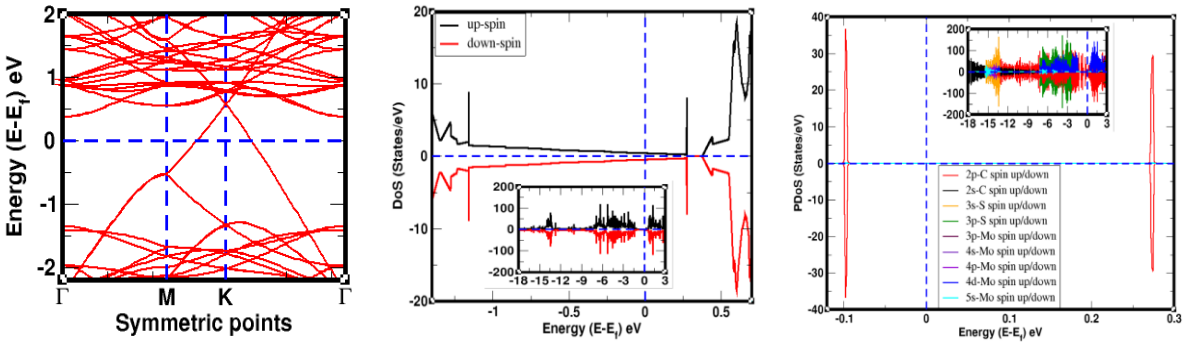

(a) (b) (c)

Fig. 2: (a) Band structure of (HS)G/MoS_2 material, (b) DoS of up-spin and down-spin states of electrons in the orbitals of C, Mo & S atoms of (HS)G/MoS_2 material (c) PDoS of individual up-spin and down-spin states of electrons in the orbitals of C, Mo & S atoms of (HS)G/MoS_2 material, where in band structure, horizontal dotted line represents Fermi level and in DoS/PDoS plots, vertical dotted line represents Fermi level. In all DoS and PDoS plots, insets represent the symmetrically distributed total up-spin and total down-spin of electrons in the orbital of atoms present in (HS)G/MoS_2 material.

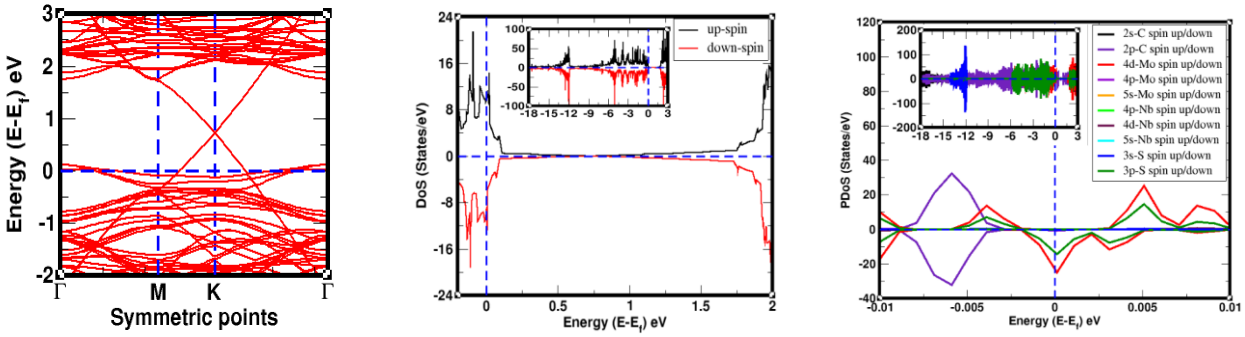

(a) (b) (c)

Fig. 3: (a) Band structure of Nb-(HS)G/MoS_2 material, (b) DoS of up-spin and down-spin states of electrons in the orbitals of C, Mo, S & Nb atoms of Nb-(HS)G/MoS_2 material (c) PDoS of individual up-spin and down-spin states of electrons in the orbitals of C, Mo, S & Nb atoms of Nb-(HS)G/MoS_2 material, where in band structure, horizontal dotted line represents Fermi level and in DoS/PDoS plots, vertical dotted line represents Fermi level. In all DoS and PDoS plots, insets represent the asymmetrically distributed total up-spin and total down-spin of electrons in the orbital of atoms present in Nb-(HS)G/MoS_2 material.

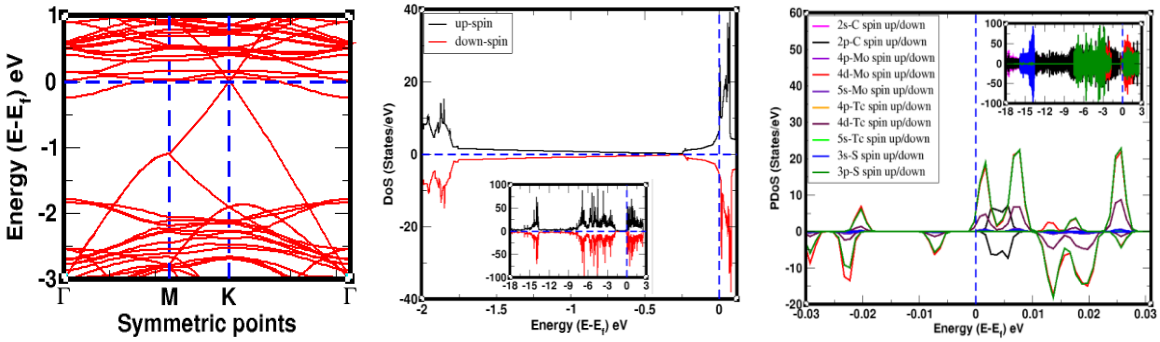

(a) (b) (c)

Fig. 4: (a) Band structure of Tc-(HS)G/MoS_2 material, (b) DoS of up-spin and down-spin states of electrons in the orbitals of C, Mo, S & Tc atoms of Tc-(HS)G/MoS_2 material (c) PDoS of individual up-spin and down-spin states of electrons in the orbitals of C, Mo, S & Tc atoms of Tc-(HS)G/MoS_2 material, where in band structure, horizontal dotted line represents Fermi level and in DoS/PDoS plots, vertical dotted line represents Fermi level. In all DoS and PDoS plots, insets represent the asymmetrically distributed total up-spin and total down-spin of electrons in the orbital of atoms present in Tc-(HS)G/MoS_2 material.

The detail calculations of magnetic moment due to spin states of electrons in the orbitals of C, Mo, S, Nb & Tc atoms in PDoS of (HS)G/MoS_2, Nb-(HS)G/MoS_2 and Tc-(HS)G/MoS_2 materials are given in table 2.

Table 2: Total magnetic moment (μ_T) of Nb-(HS)G/MoS2 and Tc-(HS)G/MoS_2 materials are obtained by asymmetrically distributed up-spin and down-spin of electrons in 2s & 2p orbitals of C atoms; 4p, 4d & 5s orbitals of Mo atoms; 3s & 3p orbitals of S atoms; 4p, 4d & 5s orbitals of Nb atoms, and 4p, 4d & 5s orbitals of Tc atoms in the materials.

Magnetic moments (μ) of (HS)G/MoS_2, Nb-(HS)G/MoS_2 and Tc-(HS)G/MoS_2 materials	Nb-(HS)G/MoS_2 (μ_B/cell)	Tc-(HS)G/MoS_2 (μ_B/cell)
μ of C atoms by distributed spins in 2s orbital	0.00	0.00
μ of C atoms by distributed spins in 2p orbital	-0.01	0.01
μ of Mo atoms by distributed spins in 4p orbital	-0.03	0.00
μ of Mo atoms by distributed spins in 4d orbital	-0.10	0.02
μ of Mo atoms by distributed spins in 5s orbital	0.00	0.00
μ of S atoms by distributed spins in 3s orbital	0.00	0.00
μ of S atoms by distributed spins in 3p orbital	-0.08	0.04
μ of Nb atom by distributed spins in 4p orbital	-0.01	-
μ of Nb atom by distributed spins in 4d orbital	-0.01	-
μ of Nb atom by distributed spins in 5s orbital	0.00	-
μ of Tc atom by distributed spins in 4p orbital	-	0.00
μ of Tc atom by distributed spins in 4d orbital	-	0.01
μ of Tc atom by distributed spins in 5s orbital	-	0.00
Total magnetic moment (μ_T) μ_B/cell	-0.24	0.07

We observed that in DoS and PDoS plots of (HS)G/MoS_2 material, up-spin and down-spin states are symmetrically distributed near the Fermi energy level as shown in figs. 2(b-c). And we obtained the value of net magnetic moment given by up-spin down-spin of electrons in all individual orbital of C, Mo, & S atoms are of zero (0.00μ_B/cell) value. We also calculated the magnetic moment due to integrated DoS and found that it is 0.00μ_B/cell. Therefore, (HS)G/MoS_2 has non-magnetic properties.

Additionally, PDoS of up-spin and down-spin states of electrons near the Fermi level of Nb-(HS)G/MoS_2 are asymmetrically distributed as shown in figs. 3(b-c). The magnetic moment developed due to the distributed up-spin and down-spin in 2s & 2p orbitals of C atoms are 0.00 μ_B/cell & -0.01μ_B/cell; 4p, 4d & 5s orbitals of Mo atoms are -0.03μ_B/cell, -0.10 μ_B/cell & -0.0oμ_B/cell; 3s & 3p orbitals of S atoms are 0.00μ_B/cell & -0.08 μ_B/cell; 4p, 4d & 5s orbitals of Nb atoms are -0.01μ_B/cell, -0.01 μ_B/cell & 0.00 μ_B/cell values respectively. We obtained the total magnetic moment of Nb-(HS)G/MoS_2 material is -0.24 μ_B/cell. Also, we have estimated the magnetic moment of Nb-(HS)G/MoS_2 material based on integrated density of states (IDoS) is 0.26 μ_B/cell. Therefore, Nb-(HS)G/MoS_2 material is called magnetic material. PDoS of up-spin and down-spin states of electrons are asymmetrically distributed around the Fermi energy level of Tc-(HS)G/MoS_2 material as shown in figs. 4(b-c). Magnetic moment developed in material due to unpaired up-spin and down-spin of electrons in 2s & 2p orbitals of C atoms are 0.00 μ_B/cell & 0.01 μ_B/cell; 4p, 4d & 5s orbitals of Mo atoms are 0.00 μ_B/cell, 0.02 μ_B/cell & 0.00 μ_B/cell; 3s & 3p orbitals of S atoms are 0.00 μ_B/cell & 0.04 μ_B/cell; 4p, 4d & 5s orbitals of Tc atoms are 0.00 μ_B/cell, 0.01 μ_B/cell & 0.00 μ_B/cell values respectively. The calculated value of total magnetic moment of Tc-(HS)G/MoS_2 material is 0.07 μ_B/cell. We calculated the magnetic moment of Tc-(HS)G/MoS_2 based on IDoS, which is 0.08 μ_B/cell value. Hence, Tc-(HS)G/MoS_2 material is also called magnetic material. Therefore, non-magnetic (HS)G/MoS_2 changes to magnetic Nb-

(HS)G/MoS_2 and Tc-(HS)G/MoS_2 materials due to Nb and Tc impurity defects respectively. In impurity defected Nb-(HS)G/MoS_2 material, major contribution of magnetic moment is given by distributed spin states in 4p, 4d orbitals of Mo atoms and 3p orbital of S atoms, while distributed spin states in 4d orbital of Mo atoms and 3p orbital of S atoms have dominant role for the development of magnetic moment in Tc-(HS)G/MoS_2 material.

4. CONCLUSIONS

Structural, electronic and magnetic properties of (HS)G/MoS_2, Nb-(HS)G/MoS_2 and Tc-(HS)G/MoS_2 materials have been studied using spin-polarized DFT with vdW corrections DFT-D2 approach. By analyzing the structures, we found that (HS)G/MoS_2 is more compact than impurity defected Nb-(HS)G/MoS_2 and Tc-(HS)G/MoS_2 materials. From the band structure calculations, we found that all the materials have metallic properties. It is found that n-type Schottky contact is formed in pristine (HS)G/MoS_2 and Tc impurity defect Tc-(HS)G/MoS_2 materials, and p-type Shottky contact is formed in Nb impurity defect Nb-(HS)G/MoS_2 material. Therefore, n-type Schottky contact of (HS)G/MoS_2 changes to p-type Schottky contact due to Nb impurity defect in (HS)G/MoS_2 material. To investigate the magnetic properties, we have carried out DoS and PDoS calculations, and found that (HS)G/MoS_2 is non-magnetic material, while Nb-(HS)G/MoS_2 and Tc-(HS)G/MoS_2 are magnetic materials. The total magnetic moment of Nb-(HS)G/MoS_2 and Tc-(HS)G/MoS_2 have values -0.24μ_B/cell and 0.07 μ_B/cell respectively. High value of magnetic moment is given by distributed unpaired up-spin and down-spin of electrons in 4p & 4d orbitals of Mo atoms; 3p orbital of S atoms in Nb-(HS)G/MoS_2 material, and 4d orbital of Mo atoms; 3p orbital of S atoms in Tc-(HS)G/MoS_2 material.

ACKNOWLEDGEMENTS

HK Neupane and NP Adhikari acknowledge to UGC Nepal, PhD grants of award no. PhD - 75/76 - S & T - 09, and UGC grants CRG 073/74 - S & T - 01 respectively. Also, NP Adhikari acknowledges to network project NT - 14 of ICTP/OEA.

REFERENCES

[1] Xu, M.; Liang, T.; Shi, M.; and Chen, H. Graphene-like two-dimensional materials. *Chemical Reviews*, **113**(5): 3766-3798 (2013).

[2] Mayorov, A. S.; Gorbachev, R. V.; Morozov, S. V.; Britnell, L.; Jalil, R.; Ponomarenko, L. A.; and Geim, A. K. Micrometer-scale ballistic transport in encapsulated graphene at room temperature. *Nano Letters*, **11**(6): 2396-2399 (2011).

[3] Morozov, S. V.; Novoselov, K. S.; Katsnelson, M. I.; Schedin, F.; Elias, D. C.; Jaszczak, J. A.; and Geim, A. K. Giant intrinsic carrier mobilities in graphene and its bilayer. *Physical Review Letters*, **100**(1): 016602 (2008).

[4] Novoselov, K. S.; Geim, A. K.; Morozov, S. V.; Jiang, D.; Katsnelson, M. I.; Grigorieva, I.; and Firsov, A. A. Two-dimensional gas of massless Dirac fermions in graphene. *Nature*, **438**(7065): 197-200 (2005).

[5] Lei, J. C.; Zhang, X.; and Zhou, Z. Recent advances in MXene: Preparation, properties, and applications. *Frontiers of Physics*, **10**(3): 276-286 (2015).

[6] Dávila, M. E.; Xian, L.; Cahangirov, S.; Rubio, A.; and Le Lay, G. Germanene: a novel two-dimensional germanium allotrope akin to graphene and silicene. *New Journal of Physics*, **16**(9): 095002 (2014).

[7] Balendhran, S.; Walia, S.; Nili, H.; Sriram, S.; and Bhaskaran, M. Elemental analogues of graphene: silicene, germanene, stanene, and phosphorene. *Small*, **11**(6): 640-652 (2015).

[8] Castro, E. V.; Novoselov, K. S.; Morozov, S. V.; Peres, N. M. R.; Dos Santos, J. L.; Nilsson, J.; and Neto, A. C. Biased bilayer graphene: semiconductor with a gap tunable by the electric field effect. *Physical Review Letters*, **99**(21): 216802 (2007).

[9] Mak, K. F.; Lee, C.; Hone, J.; Shan, J.; and Heinz, T. F. Atomically thin MoS_2: a new direct-gap semiconductor. *Physical Review Letters*, **105**(13): 136805 (2010).

[10] Kadantsev, E. S.; and Hawrylak, P. Electronic structure of a single MoS_2 monolayer. *Solid State Communications*, **152**(10): 909-913 (2012).

[11] Zhang, Y.; Ye, J.; Matsuhashi, Y.; and Iwasa, Y. Ambipolar MoS_2 thin flake transistors. *Nano Letters*, **12**(3): 1136-1140 (2012).

[12] Radisavljevic, B.; Whitwick, M. B.; and Kis, A. Small-signal amplifier based on single-layer MoS_2. *Applied Physics Letters*, **101**(4): 043103 (2012).

[13] Fornarini, L.; Stirpe, F.; Scrosati, B.; and Razzini, G. Electrochemical solar cells with layer-type semiconductor anodes. Performance of n-MoS2 cells. *Solar Energy Materials*, **5**(1): 107-114 (1981).

[14] Hu, K. H.; Hu, X. G.; Wang, J.; Xu, Y. F.; and Han, C. L. Tribological properties of MoS_2 with different morphologies in high-density

polyethylene. *Tribology Letters*, **47**(1): 79-90 (2012).

[15] Britnell, L.; Gorbachev, R. V.; Jalil, R.; Belle, B. D.; Schedin, F.; Mishchenko, A.; and Peres, N. M. R. Field-effect tunneling transistor based on vertical graphene heterostructures. *Science*, **335**(6071): 947-950 (2012).

[16] Dean, C. R.; Young, A. F.; Meric, I.; Lee, C.; Wang, L.; Sorgenfrei, S.; and Hone, J. Boron nitride substrates for high-quality graphene electronics. *Nature Nanotechnology*, **5**(10): 722-726 (2010).

[17] Zhong, X.; Yap, Y. K.; Pandey, R.; and Karna, S. P. First-principles study of strain-induced modulation of energy gaps of graphene/BN and BN bilayers. *Physical Review B*, **83**(19): 193403 (2011).

[18] Debbichi, L.; Eriksson, O.; and Lebègue, S. Electronic structure of two-dimensional transition metal dichalcogenide bilayers from ab initio theory. *Physical Review B*, **89**(20): 205311 (2014).

[19] Neupane, H. K.; and Adhikari, N. P. Structure, electronic and magnetic properties of 2D Graphene-Molybdenum diSulphide (G-MoS2) Heterostructure (HS) with vacancy defects at Mo sites. *Computational Condensed Matter*, e00489 (2020).

[20] Neupane, H. K.; and Adhikari, N. P. Tuning Structural, Electronic, and Magnetic Properties of C Sites Vacancy Defects in Graphene/MoS2 van der Waals Heterostructure Materials: A First-Principles Study. *Advances in Condensed MatterPhysics*, *2020* (2020).

[21] Neupane, H. K.; and Adhikari, N. P. First-principles study of structure, electronic, and magnetic properties of C sites vacancy defects in water adsorbed graphene/MoS 2 van der Waals heterostructures. *Journal of Molecular Modeling*, **27**(3): 1-12 (2021).

[22] Neupane, H. K.; and Adhikari, N. P. Structural, electronic and magnetic properties of S sites vacancy defects graphene/MoS2 van der Waals heterostructures: First-principles study. *International Journal of Computational Materials Science and Engineering*, 2150009 (2021).

[23] Kittel, C.; McEuen, P.; and McEuen, P. Introduction to solid state Physics. *New York: Wiley*, **8**: 140-303 (1996).

[24] Hohenberg, P.; and Kohn, W. Inhomogeneous electron gas. *Physical Review*, **136**(3B): B864 (1964).

[25] Grimme, S. Accurate description of van der Waals complexes by density Functional theory including empirical corrections. *Journal of Computational Chemistry*, **25**(12): 1463-1473 (2004).

[26] Giannozzi, P.; Baroni, S.; Bonini, N.; Calandra, M.; Car, R.; Cavazzoni, C.; and Dal Corso, A. QUANTUM ESPRESSO: modular and open-source software Project for quantum simulations of materials. *Journal of Physics: Condensed Matter*, **21**(39): 395502 (2009).

[27] Perdew, J. P.; Burke, K.; and Ernzerhof, M. Generalized gradient approximation made simple. *Physical review letters*, **77**(18): 3865 (1996).

[28] Pfrommer, B. G.; Côté, M.; Louie, S. G.; and Cohen, M. L. Relaxation of Crystals with the quasi-Newton method. *Journal of Computational Physics*, **131**(1): 233-240 (1997).

[29] Pack, J. D.; and Monkhorst, H. J. Special points for Brillouin-zone integrations a reply. *Physical Review B*, **16**(4): 1748 (1977).

[30] Marzari, N.; Vanderbilt, D.; De Vita, A.; and Payne, M. C. Thermal Contraction and disordering of the Al (110) surface. *Physical review Letters*, **82**(16): 3296 (1999).

[31] Vu, T. V.; Hieu, N. V.; Phuc, H. V.; Hieu, N. N.; Bui, H. D.; Idrees, M.; and Nguyen, C. V. Graphene/WSeTe van der Waals heterostructure: Controllable electronic properties and Schottky barrier via interlayer coupling and electric field. *Applied Surface Science*, **507**: 145036 (2020).

[32] Alam, Q.; Muhammad, S.; Idrees, M.; Hieu, N. V.; Binh, N. T.; Nguyen, C.; and Amin, B. First-principles study of the electronic structures and optical and photocatalytic performances of van der Waals heterostructures of SiS, P and SiC monolayers. *RSC Advances*, **11**(24): 14263-14268 (2021).

[33] Hou, Z.; Wang, X.; Ikeda, T.; Terakura, K.; Oshima, M.; Kakimoto, M. A.; and Miyata, S. Interplay between nitrogen dopants and native point defects in graphene. *Physical Review B*, **85**(16): 165439 (2012).

[34] Phuc, H. V.; Hieu, N. N.; Hoi, B. D.; Phuong, L. T.; and Nguyen, C. V. First principle study on the electronic properties and Schottky contact of graphene adsorbed on MoS_2 monolayer under applied out-plane strain. *Surface Science*, **668**: 23-28 (2018).

[35] Liu, B.; Wu, L. J.; Zhao, Y. Q.; Wang, L. Z.; and Cai, M. Q. First-principles Investigation of the Schottky contact for the two-dimensional MoS_2 and graphene heterostructure. *RSC advances*, **6**(65): 60271-60276 (2016).

A | R | J
Amrit Research Journal June 2021, Vol. 2, Issue 1, 93-102
ISSN: 2738-9553 (print)
RESEARCH ARTICLE

First-Principles Study of Vacancy and Impurities Defects in Graphene

Hari Krishna Neupane*[1, 2]*, Narayan Prasad Adhikari*[2]
[1]*Amrit Campus, Institute of Science and Technology Tribhuvan University, Kathmandu, Nepal*
[2]*Central Department of Physics, Institute of Science and Technology Tribhuvan University, Kathmandu, Nepal*
E-mail: narayan.adhikari@cdp.tu.edu.np

(Received:29 January 2021, Received in revised form: 18 April, Accepted: 25 June 2021, Available Online)

Highlights

- Electronic and magnetic properties of vacancy and impurity defects in graphene are studied by using first-principles calculations through computational tool Quantum ESPRESSO.
- From band and DOS calculations, all the defected materials are found to be metallic.
- By the analysis of DOS and PDOS calculations, 1C vacancy and 1N impurity defects in graphene have magnetic properties, but 1O mpurity defect in graphene has non-magnetic properties.

Abstract

In this work, we have studied the electronic and magnetic properties of 1C atom vacancy defects in graphene ($1C_{v\text{-}d}$-G), 1N atom impurity defects in graphene ($1N_{I\text{-}d}$-G) and 1O atom impurity defects in graphene ($1O_{I\text{-}d}$-G) materials through first-principles calculations based on spin-polarized density functional theory (DFT) method, using computational tool Quantum ESPRESSO (QE) code. From band structure and density of states (DOS) calculations, we found that supercell structure of monolayer graphene is a zero bandgap material. But, electronic bands of $1C_{v\text{-}d}$-G, $1N_{I\text{-}d}$-G and $1O_{I\text{-}d}$-G materials split around the Fermi energy level and DOS of up & down spins states appear in the Fermi energy level. Thus, $1C_{v\text{-}d}$-G, $1N_{I\text{-}d}$-G and $1O_{I\text{-}d}$-G materials have metallic properties. We have studied the magnetic properties of pure and defected materials by analyzing density of states (DOS) and partial density of states (PDOS) calculations. We found that graphene and $1O_{I\text{-}d}$-G materials have non-magnetic properties. On the other hand, 1C vacancy atom and 1N impurity atom induced magnetization in $1C_{v\text{-}d}$-G & $1N_{I\text{-}d}$-G materials by the rebonding of dangling bonds and acquiring significant magnetic moments of values -0.75μ_B/cell & 0.05μ_B/cell respectively through remaining unsaturated dangling bond. Therefore, non-magnetic graphene changes to magnetic $1C_{v\text{-}d}$-G and $1N_{I\text{-}d}$-G materials due to 1C atom vacancy defects and 1N atom impurity defects. The 2p orbital of carbon atoms has main contribution of magnetic moment in these defected structures.

Keywords: *DFT; vacancy defects; impurity defects; graphene; magnetic moment*

Introduction

Graphene is a two dimensional (2D) stretchable, sp^2 hybridized single sheet of carbon atoms organized in a honeycomb lattice structure. Its hexagonal structure is stable in which each carbon atom bonds with the surrounding carbon atoms and non-bonding electrons move freely between the layers. Dirac cones provided by the linearly crossing π and π* bands meet at six points in k-space, and is called zero band gap semiconductor [1]. Graphene has series of special physical properties such as high mechanical strength, chemical stability, massless Dirac fermions behavior, ambipolar effect, unique electronic

*Corresponding author

and magnetic properties [2-5]. It is used for the fabrication of electronic devices, transparent electrodes and spintronics devices [6-8]. Therefore, it opened up appealing opportunities for developing nanoelectronic devices. Because of growing allotropes and tunable thermal, electronic and mechanical properties through appropriate modifications, graphene has recently become a leading section of solid state physics and material science. However, the lack of intrinsic band gap and non-magnetic nature of graphene limits its practical applications in widely expanding field of carbon-based devices.

The defects in solids cause deviation of atoms or ions from the periodicity and they are used to find innovative properties. They can be used to design new materials. Among the different type of defects in solids, point defects play important role in solid-state physics. Point defect is classified in to vacancy defects and impurity defects [9-11]. The magnetic ordering in graphene is often explained by the presence of vacancies and impurities defects. Defects are expected to play key roles in the chemical functionally and electronic transport properties of graphene based materials [12-15]. So, defects in graphene provide an opportunity for the researchers. The theoretical and experimental research groups have studied the defects in monolayer structures of graphene and found that a single carbon atom vacancy defects in graphene is able to induce local magnetic moments due to the three carbon dangling bond atoms surrounding a single vacancy [16-24]. The adsorption of new atom in graphene tunes more desirable properties than pristine graphene and vacancy defects graphene. To our best knowledge, electronic and magnetic properties of graphene structure due to the impurities defects by Nitrogen (N) atom and Oxygen (O) atom has not been reported. Therefore, in present work, we have investigated the electronic and magnetic properties of 1C atom vacancy defects, 1N atom and 1O atom; impurities defects in (4×4) supercell structure of monolayer graphene using first-principles approaches based on spin-polarized density functional theory (DFT) method.

In sections 2 and 3, we will discuss details of computational methods and interpretations of finding respectively. We closed the paper with main conclusions of the present work in section 4.

Computational details

We used first-principles calculations based on spin-polarized density functional theory (DFT) [25], within the generalized gradient approximation (GGA) using computational tool Quantum ESPRESSO package [26, 27], and structure analysis tool XCrySDen. The exchange-correlation potential is approximated with Perdew-Burke-Ernzerhof (PBE) functional [27]. Ultra-soft pseudo-potential contained in Rappe-Rabe-Kaxiraas-Joannopoulos (RRJK) model is used to describe the chemical activity of valence electrons in calculations. At first, we have prepared optimized primitive unit cell of graphene, then we have created (4×4) supercell structure of monolayer graphene by extending optimized primitive unit cell along x and y directions. Vacancy defects structure is prepared by removing 1C atom from the (4×4) supercell structure of monolayer graphene sheet. Also, Impurities defects structures are constructed by replacing 1C atom by 1N atom and 1O atom respectively in (4×4) supercell structure of monolayer graphene sheet. The Brillouin zone of all structures was sampled by (6×6×1) k-points in the Monkhorst-Pack (MP) scheme [28]. A plane-wave basis set with energy cut-off value of (35 Ry) and charge density cut-off value (350 Ry) was used for the expansion of ground state electronic wave function. Atomic positions were optimized by using the Broyden-Fletcher-Goldfarb-Shanno (BFGS) scheme [29], until the total energy changes between two consecutive self consistent field (SCF) steps is less than 10^{-4} Ry and each component of force acting is less than 10^{-3} Ry/Bohrs. And, we used Marzarri-Vanderbilt (MV) [30] method of 'smearing' having width of 0.001 Ry. Spin-polarized DFT was used for the magnetic properties calculations of the systems. The meshes of (6×6×1) k-points is used for electronic band structure and (12×12×1) k-points is used for density of states (DOS) and partial density of states (PDOS) calculations, where 100 k-points are used along the high symmetric points connecting the reciprocal space for bands structure calculations. In present work, we have prepared 1C atom vacancy defects, 1N atom impurity defects and 1O atom impurity defects in (4×4) supercell structure of monolayer graphene material as shown in figures 1(a-d). These impurities defected materials are formed by replacing centre position 1C atom of graphene sheet by 1N atom and 1O atom respectively. The defected structures are then optimized and relaxed by BFGS method, which are used for further calculations.

Results and Discussion

In this section, we present our results for the two types of defects mentioned above and their interpretations.

Electronic properties

The (4×4) supercell structure of Graphene is made by extending optimized primitive unit cell along x and y directions. The distance between two nearest carbon atoms in graphene is 1.417 Å [21]. This value agrees with experimentally reported value 1.42 Å [30]. Here, we have also done the relax calculation of (4×4) supercell structure of graphene until the convergence is achieved, then we performed self-consistent field (SCF) calculations of supercell structure to get total energy, binding energy and binding energy per atom. The binding energy and binding energy per atom of supercell structure are calculated by using the relation;

$$E_b = NE_c - E_g \quad \ldots (1)$$

Where, E_g is the ground state energy of pure graphene sheet, E_c is ground state energy of isolated carbon atom and N is the number of carbon atom in a graphene supercell. Similarly, the binding energy per carbon atom is calculated by the relation;

$$E_{b/C\text{-}atom} = (NE_c - E_g)/N \quad \ldots (2)$$

The calculated values of total ground state energy, energy of isolated carbon atom, binding energy, and binding energy per carbon atom for graphene sheet containing 32C atoms (i.e. 32 carbon atoms are presented in (4×4) supercell structure of graphene) are -397.78 Ry, -11.84 Ry, 255.44 eV and 7.98 eV/atom respectively. In this work, we have investigated the electronic and magnetic properties of vacancy and impurities defects in supercell structure of graphene. The defects are localized states. They give rise to localized states in the band gap. In our work, we studied two types of defects in graphene. The 1C atom vacancy defects ($1C_{v\text{-}d}$-G) material is created by removing 1C (centre 1C) atom from (4×4) supercell structure of graphene as shown in figure 1(b), where defects concentration of 1C atom in structure is 3.125%. The 1N atom impurity defects ($1N_{s\text{-}d}$-G) and 1O atom impurity defects ($1O_{s\text{-}d}$-G) materials are prepared by replacing 1C atom with 1N atom and 1O atom respectively in supercell structure of graphene as shown in figures 1(c-d).

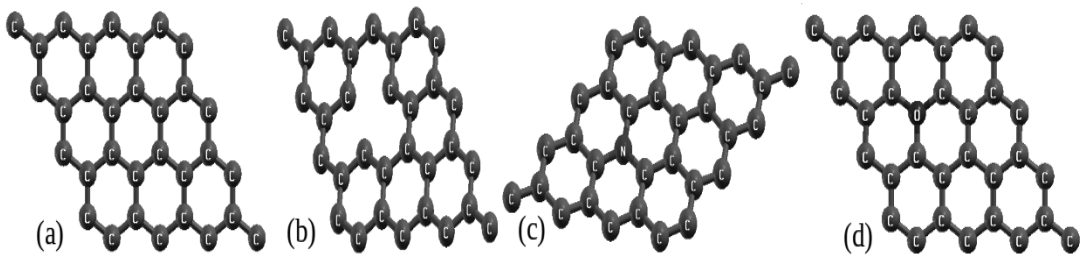

Fig. 1: *Optimized and relaxed; (a) (4×4) supercell structure of graphene, (b) 1C atom vacancy defects in (4×4) supercell structure of graphene, (c) 1N atom impurity defects in (4×4) supercell structure of graphene, (d) 1O atom impurity defects in (4×4) supercell structure of graphene.*

Electronic properties of materials are investigated by analyzing band and DOS structures calculations. Band and DOS plots of pristine graphene are shown in figures 2(a-b), where we have taken 100 k-points along the specific direction of irreducible Brillouin zone to get fine band structure by choosing Γ-M-K-Γ high symmetric points, x-axis represents high symmetric points in the first Brillouin zone and y-axis represents the corresponding energy value. Up & down spins states of DOS are plotted along y-axis and its corresponding energy values are plotted in x-axis, and the vertical dotted line represents Fermi energy level and horizontal dotted line separates up & down spins states of electrons in the orbital of all atoms present in material. We can see that Dirac point of graphene lies at the Fermi energy level in band structure and no DOS states appear at the Fermi energy level in DOS plot as shown in figures 2(a-b). So that pure graphene is a zero bandgap material.

In addition, 1C atom vacancy defects with above mentioned concentration in graphene is seen still have linearly crossing bands, and localized vacancy states corresponding to the flat impurities bands in bandgaps. Due to symmetry of the supercell having 1C vacancy defects, the linearly crossing bands split and they are raised slightly above the Fermi energy level, it means n-type Schottky barrier (contact) is formed. The states associated with the dangling bond and reconstructed C-C bond of vacancy occurs near the top of valence band and in the conduction band appear as flat bands and charge densities are associated these bands are localized as shown in figure 3(a). The band plots of 1N & 1O impurities defects in graphene are shown in figures 4(a) & 5(a) respectively where, electronic bands split. As a result, they cross the Fermi energy level and appear in valence band, it means

p-type Schottky barriers of impurities defects are formed in both structures. Thus, π and π* bands around Fermi level mix with the orbitals of vacancy and impurities defects. In metal and semiconductor, n-type Schottky barrier means, the energy difference between Fermi energy level and conduction band minimum, and p-type Schottky barrier means energy difference between the Fermi energy level and valence band maximum. Therefore, sum of n-type and p-type Schottky barrier give energy bandgap of semiconductor [31, 32]. Also, in DOS plots of $1C_{v\text{-}d}$-G, $1N_{I\text{-}d}$-G & $1O_{I\text{-}d}$-G materials, we observed that spins of up-DOS & down-DOS states are appeared around the Fermi level. Therefore, from the analysis of band and DOS calculations, we found that vacancy defects material $1C_{v\text{-}d}$-G and impurities defects materials $1N_{I\text{-}d}$-G & $1O_{I\text{-}d}$-G have metallic nature. We know that the electronic configurations of valence electrons in C, N and O atoms are [He] $2s^2$ $2p^2$, [He] $2s^2$ $2p^3$ and [He] $2s^2$ $2p^4$ respectively. Each C atom has single up spin in $2p_x$, $2p_y$ and vacant in $2p_z$ sub-orbital, each N atom has single up spin in $2p_x$, $2p_y$ and $2p_z$ sub-orbitals and each O atom contains paired spins in $2p_x$ sub-orbital and single unpaired up spin in $2p_y$ and $2p_z$ sub-orbital. Due to the arrangement of unpaired up and down spins states of electrons in the orbitals of atoms in all $1C_{v\text{-}d}$-G, $1N_{I\text{-}d}$-G & $1O_{I\text{-}d}$-G materials obtained different values of Fermi energy. We found that Fermi energy values of these materials are -2.93 eV, -1.64 eV and -1.75 eV respectively. Also, we calculated Fermi energy shift values of $1C_{v\text{-}d}$-G, $1N_{I\text{-}d}$-G & $1O_{I\text{-}d}$-G material from Fermi energy value of pure graphene are 0.38 eV, -0.91 eV & -0.80 eV respectively as given in table 1.

Table 1: Fermi energy (E_f); Fermi energy shift from pure graphene (E_s); total energy (E_T); binding energy per carbon atom of graphene (G), vacancy defects ($1C_{v\text{-}d}$-G), impurities defects ($1N_{I\text{-}d}$-G & $1O_{I\text{-}d}$-G) structures (E_b); total value of magnetic moment (M); and magnetic moment due to total up & down spins of electrons in 2s, 2p orbitals of C, N & O atoms (μ); in pristine graphene (G), 1C atom vacancy in graphene ($1C_{v\text{-}d}$-G), 1N atom impurity defects in graphene ($1N_{I\text{-}d}$-G) and 1O atom impurity defects in graphene ($1O_{I\text{-}d}$-G).

Data obtained from band, DOS & PDOS analysis of $1C_{v\text{-}d}$-G, $1N_{I\text{-}d}$-G & $1O_{I\text{-}}$-G materials	G	$1C_{v\text{-}d}$-G	$1N_{I\text{-}d}$-G	$1O_{I\text{-}d}$-G
E_f (eV)	-2.55	-2.93	-1.64	-1.75
E_s (eV)	-	0.38	-0.91	-0.80
E_T (Ry)	- 397.78	-352.50	-373.46	-403.67
E_b (eV)	7.98	7.46	7.92	7.97
μ due to 2s of C atoms (μ_B/cell)	0.00	-0.22	0.01	0.00
μ due to 2p of C atoms (μ_B/cell)	0.00	-0.53	0.03	0.00
μ due to 2s of O atom (μ_B/cell)	-	-	-	0.00
μ due to 2p of O atom (μ_B/cell)	-	-	-	0.00
μ due to 2s of N atom (μ_B/cell)	-	-	- 0.00	-
μ due to 2p of N atom (μ_B/cell)	-	-	0.01	-
Total value of magnetic moment M (μ_B/cell)	0.00	-0.75	0.05	0.00

To understand the electronic and magnetic properties of materials more clearly, here we have carried out density of states (DOS) and partial density of states (PDOS) calculations. The DOS and PDOS plots of $1C_{v\text{-}d}$-G, $1N_{I\text{-}d}$-G & $1O_{I\text{-}d}$-G materials are shown in figures 3(b-c), 4(b-c) & 5(b-c) respectively, where vertical dotted line represents Fermi energy levels and horizontal dotted line separates up & down spins states of electrons in the orbital of atom in present in respective structures.

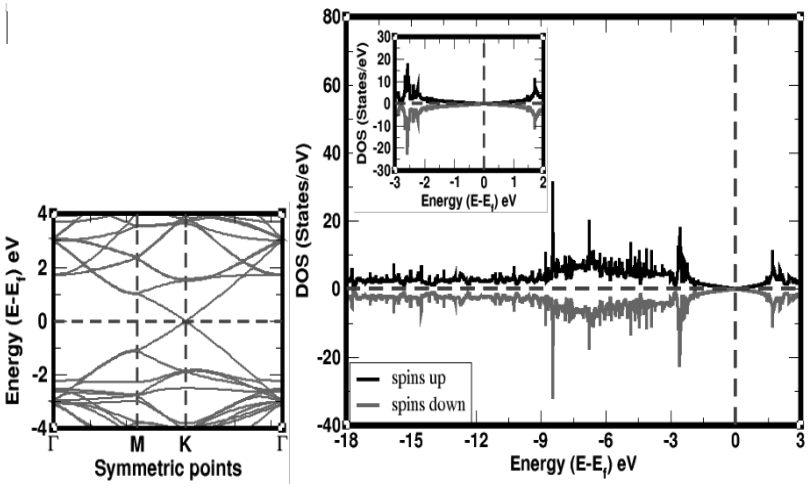

Fig. 2: (a) Band plot of (4×4) supercell structure of graphene, (b) DOS of up & down spins states of atoms in (4×4) supercell structure of graphene. In band structure, horizontal dotted line represents Fermi energy level, and in DOS plot, vertical dotted line represents Fermi energy level.

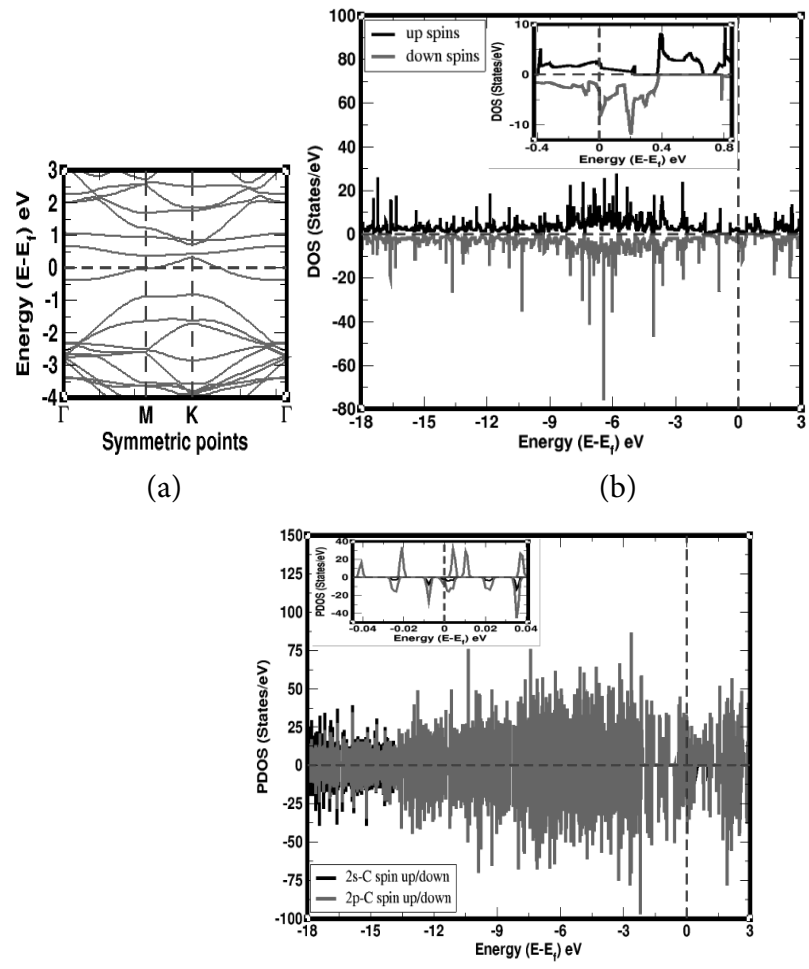

Fig. 3: *(a) Band plot of 1C atom vacancy defects in (4×4) supercell structure of graphene, (b) DOS of up & down spins states of 1C atom vacancy defects in (4×4) supercell structure of graphene (c) PDOS of individual up & down spins states of orbitals of 1C atom vacancy defects in (4×4) supercell structure of graphene. In band structure, horizontal dotted line represents Fermi energy level, and in DOS/PDOS plots, vertical dotted line represents Fermi energy level.*

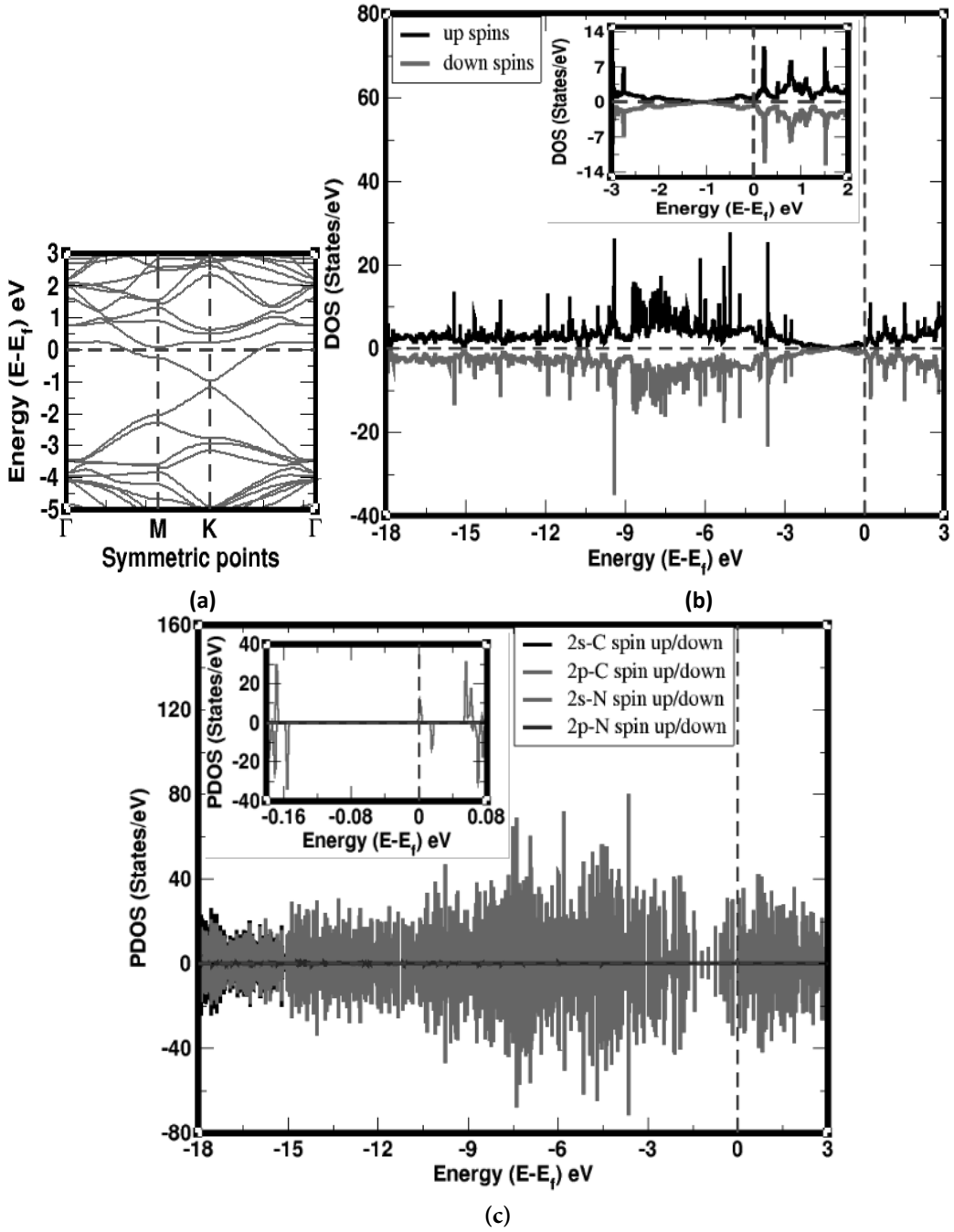

Fig. 4: *(a) Band plot of 1N atom impurity defects in (4×4) supercell structure of graphene, (b) DOS of up & down spins states of 1N atom impurity defects in (4×4) supercell structure of graphene (c) PDOS of individual up & down spins states of electrons in the orbitals of C & N atoms in 1N atom impurity defects in (4×4) supercell structure of graphene. In band structure, horizontal dotted line represents Fermi energy level, and in DOS/PDOS plots, vertical dotted line represents Fermi energy level.*

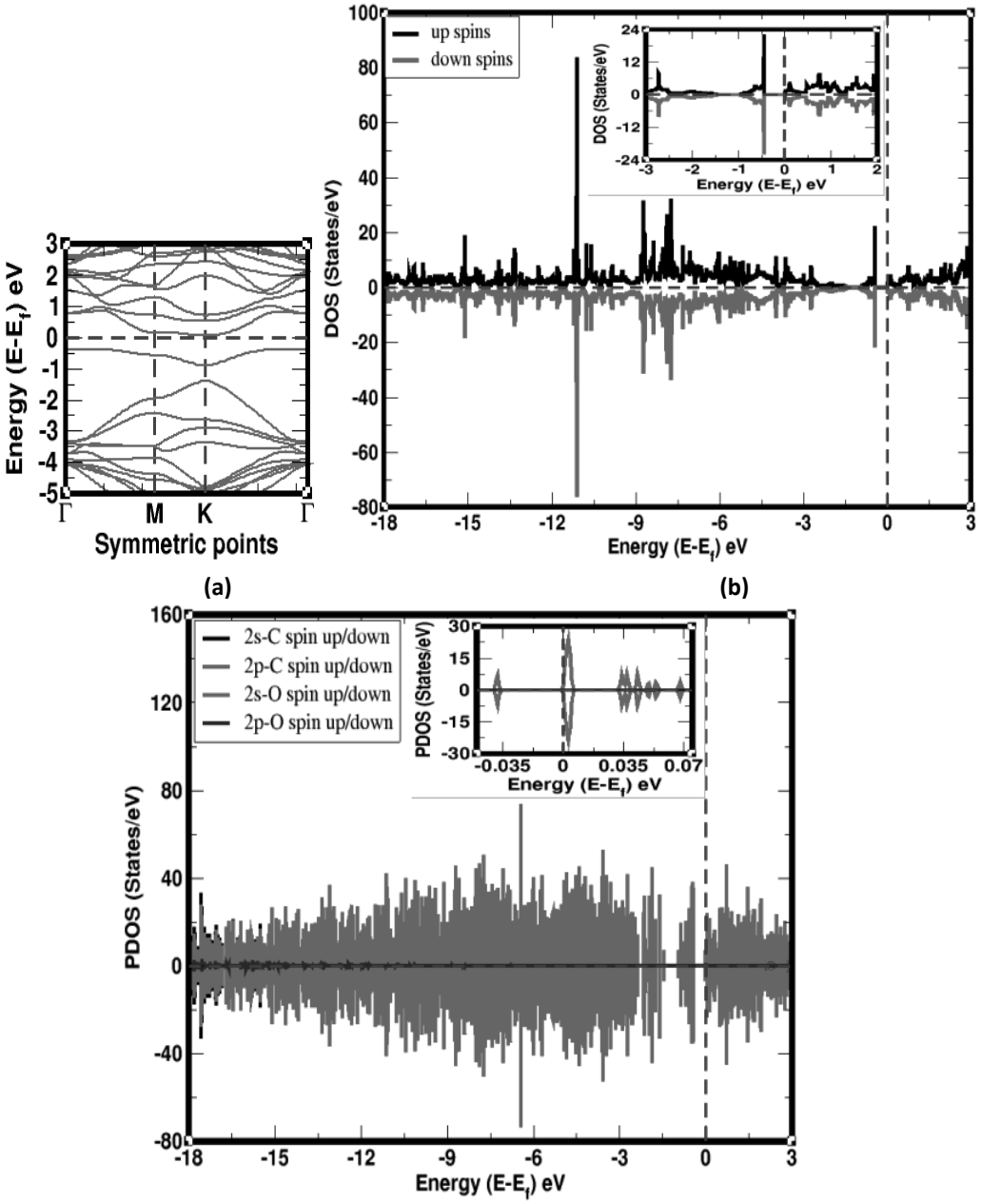

Fig. 5: *(a) Band plot of 1O atom impurity defects in (4×4) supercell structure of graphene, (b) DOS of up & down spins states of 1O atom impurity defects in (4×4) supercell structure of graphene (c) PDOS of individual up & down spins states of electrons in the orbitals of C & O atoms in 1O atom impurity defects in (4×4) supercell structure of graphene. In band structure, horizontal dotted line represents Fermi energy level, and in DOS/PDOS plots, vertical dotted line represents Fermi energy level.*

Magnetic properties

The magnetic properties of materials are studied by DOS and PDOS analysis. DOS suggests how densely quantum states are packed in a particular system. High or zero values of DOS reflects, many or no states are available for occupation. The PDOS calculations are used to investigate the magnetic moment given by distributed up & down spins states of electrons in the orbital of atoms in a system. The asymmetrically distributed up & down spins states of electrons in DOS and PDOS means, materials have magnetic properties, and symmetrically distributed up & down spins states of electrons in DOS and PDOS means, materials carry non-magnetic properties. We observed that up & down spin states of electrons are asymmetrically distributed near the Fermi energy level in DOS and PDOS plots of 1C atom vacancy defects supercell structure of graphene ($1C_{v\text{-}d}$-G) as shown in

figures 3(b-c). This is because electron spins degeneracy of the bands is broken and bands split. Hence, $1C_{v\text{-}d}$-G material has magnetic properties. Also, we have calculated the contributions of magnetic moment due to the distribution of spins of electrons in the individual orbital of atoms presented in $1C_{v\text{-}d}$-G material as given in table 1. The magnetic moment developed in material due to up & down spins of electrons in 2s & 2p orbitals of C atoms have values $-0.22\mu_B$/cell & $-0.53\mu_B$/cell respectively. It means, dominant contributions of magnetic moment are given by spins of 2p orbital of C atoms in material. Hence, from these calculations, we found that total magnetic moment of $1C_{v\text{-}d}$-G material has value $-0.75\mu_B$/cell. Therefore, $1C_{v\text{-}d}$-G material has magnetic properties.

Similarly, we have calculated the magnetic moment in 1N atom impurity defects in graphene ($1N_{I\text{-}d}$-G) material and 1O atom impurity defects in graphene ($1O_{I\text{-}d}$-G) material respectively. The DOS and PDOS of up and down spins states of electrons are asymmetrically distributed near the Fermi energy level of $1N_{I\text{-}d}$-G material as shown in figures 4(b-c). Magnetic moment is given by spins states of electrons in the 2s and 2p orbitals of carbon atoms are $0.01\mu_B$/cell and $0.03\mu_B$/cell respectively, and 2s and 2p orbitals of N atom are $0.00\mu_B$/cell and $0.01\mu_B$/cell respectively. Hence, total value of magnetic moment of $1N_{I\text{-}d}$-G material is $0.05\mu_B$/cell. Thus, $1N_{I\text{-}d}$-G material has magnetic properties. On the other hand, we have calculated the magnetic moment in 1O atom impurity defects in graphene ($1O_{I\text{-}d}$-G) material. The DOS and PDOS of up and down spins states of electrons are symmetrically distributed near the Fermi energy level of $1O_{I\text{-}d}$-G material as shown in figures 5(b-c). Magnetic moment is given by spins states of electrons in the 2s and 2p orbitals of carbon and oxygen atoms are $0.00\mu_B$/cell. Thus, total value of magnetic moment of this material has zero value. Therefore, a 1O atom impurity defects in graphene ($1O_{I\text{-}d}$-G) material is a non-magnetic material.

Conclusions

The electronic and magnetic properties of $1C_{v\text{-}d}$-G, $1N_{I\text{-}d}$-G and $1O_{I\text{-}d}$-G materials are investigated by first-principles calculations based on spin-polarized density functional theory. Computational of this work has been done by using Quantum ESPRESSO package. At first, we have prepared (4×4) supercell structure of monolayer graphene sheet, then constructed 1C atom vacancy defects, and 1N atom, 1O atom respectively impurities defects in monolayer graphene supercell structure. We found that binding energy of defected structures is less than non-defects structure. From the band structure calculations, we found the Dirac cone is formed at the Fermi energy level in graphene material; hence it is called zero bandgap semiconductors. But, electronic band states cross and split around the Fermi energy level in vacancy and impurities defects materials. Hence, defected materials have metallic properties. From the DOS and PDOS calculations, we found that defected $1C_{v\text{-}d}$-G and $1N_{I\text{-}d}$-G materials have magnetic properties, but impurity defects $1O_{I\text{-}d}$-G material has non-magnetic properties. The non-magnetic nature of graphene supercell structure changes to magnetic materials due to the 1C atom vacancy defects and 1N atom impurity defects in supercell structure of monolayer graphene sheet. The total magnetic moment of $1C_{v\text{-}d}$-G and $1N_{I\text{-}d}$-G materials have values $-0.75\mu_B$/cell and $0.05\mu_B$/cell respectively. The high value of magnetic moment is given by up and down spins states of electrons in 3p orbital of C atoms in both defected materials.

We can further study about above-mentioned materials by investigating their physical properties using electric field and stress effect.

Acknowledgements

HKN acknowledges the UGC Nepal Award no. PhD-75/76-S &T-09. NPA acknowledges network project NT-14 of ICTP/OEA and UGC Nepal Grants CRG 073/74 -S & T -01.

References

1. L. A. Ponomarenko, R. V. Gorbachev, G. L. Yu, D. C. Elias, R. Jalil, A. A. Patel, A.K. Geim. Cloning of Dirac fermions in grapheme superlattices, *Nature*, 2013, **497**(7451), 594-597**. (**DOI**:**https://doi.org/10.1038/nature12187).

2. M. Xu, T. Liang, M. Shi, H. Chen. Graphene-like two-dimensional materials, *Chemical reviews*, 2013, **113**(5), 3766-3798. **(**DOI**:** https://doi.org/10.1021/cr300263a).

3. S. Mayorov, R. V. Gorbachev, S. V. Morozov, L. Britnell, R. Jalil, L. A. Ponomarenko, A. K. Geim. Micrometer-scale ballistic transport in encapsulated graphene at room temperature, *Nano letters*, 2011, **11**(6), 2396-2399. (DOI: https://doi.org/10.1021/nl200758b).
4. S. V. Morozov, K. S. Novoselov, M. I. Katsnelson, F. Schedin, D. C. Elias, J. A. Jaszczak, A. K. Geim. Giant intrinsic carrier mobilities in graphene and its bilayer, *Physical review letters*, 2008, **100**(1), 016602. **(**DOI**:** https://doi.org/10.1103/PhysRevLett.100.016602).
5. K. S. Novoselov, A. K. Geim, S. V. Morozov, D. Jiang, M. I. Katsnelson, I. Grigorieva, A. A. Firsov. Two-dimensional gas of massless Dirac fermions in grapheme, *Nature*, 2005,**438**(7065), 197-200.**(**DOI**:**https://doi.org/10.1038/nature04233).
6. J. C. Lei, X. Zhang, Z. Zhou. Recent advances in MXene. Preparation, properties, and applications. *Frontiers of Physics*, 2015, **10**(3), 276-286**. (**DOI**:** https://doi.org/10.1007/s11467-015-0493-x).
7. M. E. Dávila, L. Xian, S. Cahangirov, A. Rubio, G. Le Lay Germanene. A novel two-dimensional germanium allotrope akin to graphene and silicene. *New Journal of Physics*, 2014, **16**(9)**,** 095002. **(**DOI**:**10.1088/1367-2630/16/9/095002).
8. S. Balendhran, S. Walia, H. Nili, S. Sriram, M. Bhaskaran, Elemental analogues of graphene: silicene, germanene, stanene, and phosphorene, *Small*, 2015, **11**(6)**,** 640-652. **(**DOI**:** https://doi.org/10.1002/smll.201402041).
9. C. Kittel, P. McEuen, P. McEuen. *Introduction to solid state Physics,* New York: Wiley, 1996**,** pp.140-303. (ISBN: 978-81-265-3518-7).
10. H. Lee, Y. W. Son, N. Park, S. Han, J. Yu. Magnetic ordering at the edges of graphitic fragments: Magnetic tail interactions between the edge-localized states, *Physical Review B*, 2005, *72*(17)**,** 174431.**(**DOI**:** https://doi.org/10.1103/PhysRevB.72.174431).
11. S. Okada, A. Oshiyama. Magnetic ordering in hexagonally bonded sheets with first-row elements, *Physical review letters*, 2001, **87**(14), 146803. **(**DOI**:**https://doi.org/10.1103/PhysRevLett.87.146803).
12. Y. H. Kim, J. Choi, K. J. Chang, D. Tománek. Defective fullerenes and nanotubes as molecular magnets: an ab initio study, *Physical Review B*, 2003, **68**(12), 125420. **(**DOI**:** https://doi.org/10.1103/PhysRevB.68.125420).
13. P. O. Lehtinen, A. S. Foster, Y. Ma, A. V. Krasheninnikov, R. M. Nieminen. Irradiation-induced magnetism in graphite: a density functional study, *Physical review letters*, 2004, **93**(18), 187202. **(**DOI**:** https://doi.org/10.1103/PhysRevLett.93.187202).
14. E. J. Duplock, M. Scheffler, P. J. Lindan, Hallmark of perfect grapheme, *Physical review letters*, 2004, **92**(22), 225502. **(**DOI**:** https://doi.org/10.1103/PhysRevLett.92.225502).
15. J. M. Carlsson, M. Scheffler. Structural, electronic, and chemical properties of nanoporous carbon, *Physical review letters*, 2006, **96**(4), 046806. **(**DOI**:** https://doi.org/10.1103/PhysRevLett.96.046806).
16. O. V. Yazyev, S. G. Louie. Topological defects in graphene: Dislocations and grain boundaries, *Physical Review B*, 2010, **81**(19), 195420. **(**DOI**:** https://doi.org/10.1103/PhysRevB.81.195420).
17. Hashimoto, K. Suenaga, A. Gloter, K. Urita, S. Iijima. Direct evidence for atomic defects in graphene layers, *Nature*, 2004, **430**(7002), 870-873. **(**DOI**:**https://doi.org/10.1038/nature02817).
18. V. Krasheninnikov, F. J. N. M. Banhart. Engineering of nanostructured carbon materials with electron or ion beams, *Nature materials*, 2007, **6**(10), 723-733. **(**DOI**:**https://doi.org/10.1038/nmat1996).
19. H. K. Neupane, N. P. Adhikari. Structure, electronic and magnetic properties of 2D Graphene-Molybdenum disulphide (G-MoS_2) Heterostructure (HS) with vacancy defects at Mo sites, *Computational Condensed Matter***,** 2020, **e00489. (**DOI**:**https://doi.org/10.1016/j.cocom.2020.e00489).
20. W. Robertson, B. Montanari, K. He, C. S. Allen, Y. A. Wu, N. M. Harrison, J. H. Warner. Structural reconstruction of the graphene monovacancy, *ACS nano*, 2013, **7**(5), 4495-4502. **(**DOI**:**https://doi.org/10.1021/nn401113r).

21. H. K. Neupane, N. P. Adhikari. Tuning Structural, Electronic, and Magnetic Properties of C Sites Vacancy Defects in Graphene/MoS_2 van der Waals Heterostructure Materials: A First-Principles Study. *Advances in Condensed Matter Physics*, 2020**, 2020. (**DOI**:**https://doi.org/10.1155/2020/8850701).

22. S. Fedorov, Z. I. Popov, D. A. Fedorov, N. S. Eliseeva, M. V. Serjantova, A. A. Kuzubov. DFT investigation of the influence of ordered vacancies on elastic and magnetic properties of graphene and graphene-like SiC and BN structures, *Physica status solidi (b)*, 2012, **249**(12), 2549-2552. (DOI:https://doi.org/10.1002/pssb.201200105).

23. R. Faccio, L. Fernández-Werner, H. Pardo, C. Goyenola, O. N. Ventura, Á. W. Mombrú. Electronic and structural distortions in graphene induced By carbon vacancies and boron doping, *The Journal of Physical Chemistry C*, 2010, **114**(44), 18961-18971. **(**DOI**:**https://doi.org/10.1021/jp106764h).

24. H. K. Neupane, N. P. Adhikari. First-principles study of structure, electronic, and magnetic properties of C sites vacancy defects in water adsorbed graphene/MoS_2 van der Waals heterostructures, *Journal of Molecular Modeling*, 2021, **27**(3), 1-12**. (**DOI**:**https://doi.org/10.1007/s00894-021-04690-8).

25. P. Hohenberg, W. Kohn. Inhomogeneous electron gas. *Physical Review*, 1964**, 136**(3B), B864**. (**DOI**:** https://doi.org/10.1103/PhysRev.136.B864).

26. P. Giannozzi, S. Baroni, N. Bonini, M. Calandra, R. Car, C. Cavazzoni, A. Dal Corso. QUANTUM ESPRESSO: modular and open-source software Project for quantum simulations of materials, *Journal of Physics: Condensed Matter*, 2009, **21**(39), 395502. **(**DOI**:**10.1088/0953-8984/21/39/395502).

27. J. P. Perdew, K. Burke, M. Ernzerhof. Generalized gradient approximation made simple, *Physical review letters*, 1996, **77**(18), 3865. **(**DOI**:** https://doi.org/10.1103/PhysRevLett.77.3865).

28. R. M. Martin, *Electronic structure: basic theory and Practical methods*. Cambridge university press, **(2020). (**DOI**:** 10.1017/9781108555586).

29. B. G. Pfrommer, M. Côté, S. G. Louie, M. L. Cohen. Relaxation of Crystals with the quasi-Newton method. *Journal of Computational Physics*, 1997, **131**(1), 233-240**. (**DOI**:**https://doi.org/10.1006/jcph.1996.5612).

30. N. Marzari, D. Vanderbilt, A. De Vita, M. C. Payne. Thermal Contraction and disordering of the Al (110) surface. *Physical review Letters*, 1999, **82(16),** 3296. **(**DOI**:** https://doi.org/10.1103/PhysRevLett.82.3296).

31. W. Chen, E. J. Santos, W. Zhu, E. Kaxiras, Z. Zhang, Tuning the electronic and chemical properties of monolayer MoS2 adsorbed on transition metal substrates, *Nano letters*, 2013, **13(2),** 509-514. **(**DOI**:**https://doi.org/10.1021/nl303909f).

32. W. Xiong, C. Xia, X. Zhao, T. Wang, Y. Jia, Effects of strain and electric field on electronic structures and Schottky barrier in graphene and SnS hybrid heterostructures, *Carbon*, 2016, **109**, 737-746. **(**DOI**:**https://doi.org/10.1016/j.carbon.2016.08.082).

Him. Phys. **9** 19-29, (2020)

Himalayan Physics

First-principles study of C cites vacancy defects in water adsorbed Graphene

Research Article

Hari Krishna Neupane[1,2], Narayan Prasad Adhikari[2]*

1 Amrit Campus, Institute of Science and Technology Tribhuvan University, Kathmandu, Nepal

2 Central Department of Physics, Institute of Science and Technology Tribhuvan University, Kathmandu, Nepal

Abstract: The electronic and magnetic properties of water adsorbed graphene ($w_{ad}-G$), single carbon (1C) atom vacancy defects in water adsorbed graphene ($1C_{atom\text{-}vacancy}-w_{ad}-G$) and double carbon (2C) atoms vacancy defects in water adsorbed graphene ($2C_{atoms\text{-}vacancy}-w_{ad}-G$) materials are studied by first-principles calculations within the frame work of density functional theory (DFT) using computational tool Quantum ESPRESSO (QE) code. We have calculated the binding energy of $w_{ad}-G$, $1C_{atom\text{-}vacancy}-w_{ad}-G$ and $2C_{atoms\text{-}vacancy}-w_{ad}-G$ materials, and then found that non-defects geometry is more compact than vacancy defects geometries. From band structure calculations, we found that $w_{ad}-G$ is zero band gap semiconductor, but $1C_{atom\text{-}vacancy}-w_{ad}-G$ and $2C_{atoms\text{-}vacancy}-w_{ad}-G$ materials have metallic properties. Hence, zero band gap semiconductor changes to metallic nature due to C sites vacancy defects in its structures. We have investigated the magnetic properties of $w_{ad}-G$ and its C sites vacancy defects materials by using Density of States (DOS) and Partial Density of States (PDOS) calculations. We found that $w_{ad}-G$ is non- magnetic material. 1C atom vacancy defects in graphene surface of $w_{ad}-G$ is induced magnetization by the rebonding of two dangling bonds and acquiring significant magnetic moment ($-0.11\ \mu_B/\text{cell}$) through remaining unsaturated dangling bond. But, 2C atoms vacancy defects in graphene surface of $w_{ad}-G$ induced low value of magnetic moment ($+0.03\ \mu_B/\text{cell}$) than 1C atom vacancy defects in structure, which is due to no dangling bonds present in the structure. Therefore, non-magnetic $w_{ad}-G$ changes to magnetic $1C_{atom\text{-}vacancy}-w_{ad}-G$ and $2C_{atoms\text{-}vacancy}-w_{ad}-G$ materials due to C sites vacancy defects in $w_{ad}-G$ structure. The 2p orbital of carbon atoms has main contribution of magnetic moment in defects structures.

Keywords: • DFT • Vacancy defects • Water adsorbed Graphene • Magnetic moment

1. Introduction

Graphene is a carbon allotrope with a two dimensional (2D) honeycomb lattice. The honeycomb network made by planar and three-folded sp^2 hybrid orbitals acquires planar stability through $\pi-\pi$ orbital interaction and achieves high in-plane stiffness [1]. Dirac cones provided by the linearly crossing π and π^* bands meet as six points in k -space, and is called zero band gap semiconductor. Graphene has various exceptional properties, such as high mechanical strength, chemical stability, massless Dirac fermions behavior, ambipolar effect, unique electronic and magnetic properties [2–5] . It is used for the fabrication of electronic devices, transparent electrodes

* *Corresponding Author: narayan.adhikari@cdp.tu.edu.np*

and spintronics devices [6–8]. So, graphene has opened up exciting opportunities for developing nanoelectronic devices. However, the lack of intrinsic band gap and non-magnetic nature of graphene limits its practical applications in widely expanding field of carbon- based devices. The chemical and physical properties of materials are affected by the structural defects in low dimensional systems. Defects are expected to play key roles in the chemical functionally and electronic transport properties of graphene based materials. The understanding of the mechanical, electrical and magnetic properties of defects in graphene is an important applied physics goal [1, 9]. So, defects in graphene provide an opportunity for the researchers. The vacancies in monolayer structures of graphene have attracted various experimental and theoretical studies [10–16]. Vacancy defects graphene material enhanced the catalytic activities of materials. So, scientists developed vacancy defects in 2D honeycomb structure of graphene, although it has high defects formation energy in comparison with other 2D materials [17, 18]. Both theoretical and experimental research groups have studied the mechanical, electronic and magnetic properties of single carbon atom vacancy defects in graphene. They found that a single carbon atom vacancy defects in graphene is able to induce local magnetic moments due to the three carbon dangling bond atoms surrounding a single vacancy [19–22]. The adsorption of new material in graphene and its vacancy defects materials tunes more desirable properties than pristine graphene only. To our best knowledge, electronic and magnetic properties of carbon atom vacancy defects in water adsorbed graphene structure have not been reported. Therefore, in present work, we have investigated the electronic and magnetic properties of single and double carbon atom vacancy defects in water adsorbed graphene structure through first-principles calculations within spin polarized density functional theory (DFT) method, using computational tool Quantum ESPRESSO package.

The rest part of the paper is organized as follows. In section 2, we discuss details of computational methods. The results and their interpretations are given in section 3. We closed the paper with main conclusions and outlook of the present work in section 4.

2. Computational Details

We have performed spin polarized Density Functional Theory (DFT) calculations [23] , within the generalized gradient approximation (GGA) using computational tool Quantum ESPRESSO package [24, 25] and structure analysis tool XCrySDen. The exchange-correlation potential is approximated with Perdew-Burke-Ernzerhof (PBE) functional [25]. The Rappe-Rabe-Kaxiraas-Joannopoulos (RRJK) model of ultra-soft pseudo-potential is used to incorporate the activity of valence electrons in all the calculations. A vacancy defects honeycomb structure is represented by (4×4) the super cell structure of monolayer graphene sheet. The brillouin zone was sampled by $(6 \times 6 \times 1)$ k-points in the Monkhorst-Pack (MP) scheme [26], where the convergence in energy as a function of the number of k-points was tested. A plane wave basis set with energy cut- off value of (35Ry) and charge density cut-off value (350Ry) was used for the expansion of ground state electronic wave function. Atomic positions were optimized by using the Broyden-Fletcher-Goldfarb-Shanno (BFGS) scheme [27], until the total energy changes

between two consecutive self consistent field (SCF) steps is less than 10^{-4}Ry and each component of force acting is less than 10^{-3}Ry/Bohrs. Moreover, we used Marzarri-Vanderbilt (MV) [28] method of 'smearing' having width of 0.001 Ry. Also, we have chosen 'david' diagonalization method with 'plain' mixing mode and mixing factor of 0.6 for self consistency. We used spin polarized calculations for magnetic properties of the systems. The meshes of $(6 \times 6 \times 1)$ k-points is used for electronic band structure and $(12 \times 12 \times 1)$ k-points is used for DOS & PDOS calculations, where 100 k-points are used along the high symmetric points connecting the reciprocal space for bands structure calculations. In the present work, we have prepared water adsorbed in (4×4) super cell structure of graphene and 1C & 2C atoms vacancy defects in water adsorbed graphene structure as shown in fig. $1(a-e)$. These 1C and 2C atoms vacancy defects in water adsorbed graphene structures are constructed by removing centre 1C atom and 2C (left 1C & centre 1C) atoms in (4×4) super cell structure of graphene. After that, these structures are optimized and relaxed by BFGS method, which are used for further calculations as shown in fig. 1 .

3. Results and Discussion

This section mainly focused on the results and interpretations of geometrical structures band structure calculations, Density of States (DOS), and Partial Density of States (PDOS) calculations, of 1C & 2C atoms vacancy defects in graphene surface of water adsorbed graphene by first-principles calculations including spin polarized DFT method using computational tool Quantum ESPRESSO code.

Electronic Properties

The (4×4) super cell structure of Graphene is made by extending optimized primitive unit cell along x and y directions. The distance between two nearest carbon atoms in graphene is 1.42 [29] . This value agrees with experimentally reported value 1.42 [28]. Here, we have also done the relax calculation of (4×4) super cell structure of graphene until the convergence is achieved, then we performed self consistent field (SCF) calculations of super cell structure to get total energy, binding energy and binding energy per atom. The binding energy and binding energy per atom of super cell structure are calculated by using following formalism;

$$E_b = NE_c - E_g \tag{1}$$

Where, E_g is the ground state energy of pure graphene sheet, E_c is ground state energy of isolated carbon atom and N is the number of carbon atom in a graphene super cell. Similarly, the binding energy per carbon atom is calculated by the relation;

$$\mathrm{E_{b/C-atom}} = \left(\mathrm{NE_c} - \mathrm{E_g}\right)/\mathrm{N} \tag{2}$$

The calculated values of total ground state energy, energy of isolated carbon atom, binding energy, and binding energy per carbon atom for graphene sheet containing $2C$ and 32C atoms (i.e. 32 carbon atoms are presented in

(4×4) super cell structure of graphene) are; −22.80 Ry, −10.98 Ry, 11.44 eV, 5.72 eV/atom, and −397.78 Ry, −11.84 Ry, 255.44 eV, 7.98 eV/atom respectively. The adsorption of water molecule at 2.64 distance above the surface of (4 × 4) super cell structure of graphene as shown in fig. 1(a) does not bring significant changed in the values of pure graphene structure. Also, band structure plot of water adsorbed in graphene ($w_{ad} - G$) as shown in fig. 2(a) is similar with band plot of pure super cell structure of graphene. This is because; the $w_{ad} - G$ structure has no dangling bonds present along the external surface of Graphene which therefore show a reduced chemical activity. Only physisorption interactions can arise when adsorbing water molecule in this structure. This is evidenced by the adsorption energy we calculated for isolated water physisorption on monolayer Graphene (0.12eV) at 2.64 distance of water molecule above the graphene. In the present work, we intended to investigate physical properties of C sites vacancy defects in graphene surface of water adsorbed graphene super cell structure.

Vacancy defects are localized states. They give rise to localized states in the band gap. In our study, we treated the vacancy defects by removing 1C (centre 1C) atom in $w_{ad} - G$ structure ($1C_{\text{atom-vacancy}} - w_{ad} - G$) and 2C (1 left & 1C centre) atoms in $w_{ad} - G$ structure ($2C_{\text{atoms-vacancy}} - w_{ad} - G$) as shown in fig. 1(b − c) and fig. 1(d − e) respectively.

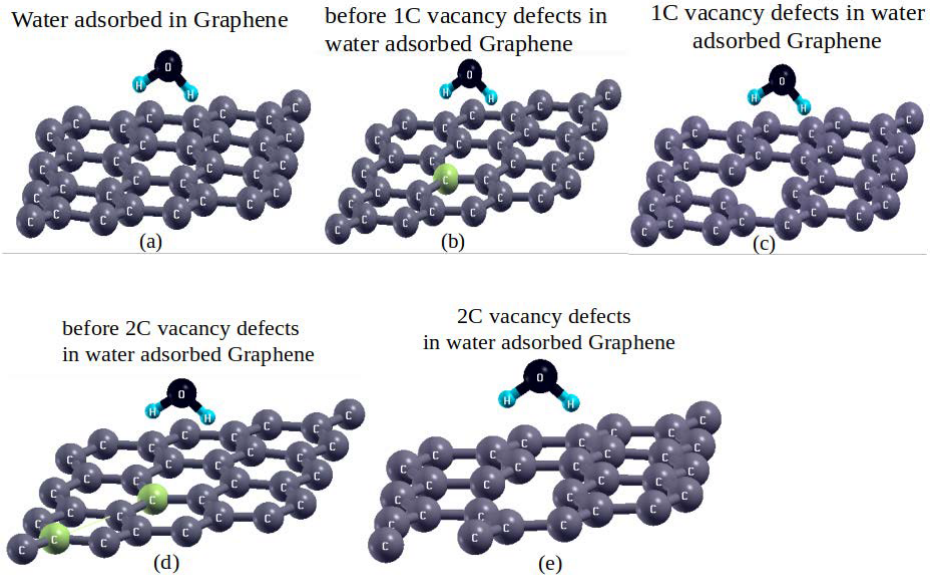

Figure 1. Optimized and relaxed structures of Graphene and C sites vacancy defects in water adsorbed Graphene, where adsorbed water molecule is at 2.64 distance above the surface of Graphene. These structures are constructed by removing 1C & 2C atoms in water adsorbed Graphene material (a) Water adsorbed Graphene structure (b) Before 1C atom vacancy defects in water adsorbed Graphene structure (c) 1C atom vacancy defects in water adsorbed Graphene structure (d) Before 2C atoms vacancy defects in water adsorbed Graphene structure (e) 2C atoms vacancy defects in water adsorbed Graphene structure.

The defects formation energy of single and double carbon atoms vacancy defects in $w_{ad} - G$ structure are 7.6 eV and 7.0 eV respectively, because binding energy of 1C defects is greater than 2C defects in $w_{ad} - G$ structure

as given in table 1. Defects formation energy values of these materials are calculated by using the relation [30].

$$E_f = E_T(defect) + n_C\mu_C - E_T(perfect) \tag{3}$$

Where, E_T (defect) is a total energy of a super cell with the defects, n_C is the numbers of C atoms removed from the perfect super cell to introduce a vacancy, μ_C is chemical potential of C atom, E_T (perfect) is the total energy of the neutral perfect super cell. Defects concentrations of 1C and 2C atoms in structures are 3.125% and 6.25% respectively. For $w_{ad} - G$, if the mesh of vacancy defects in $2D$ hexagonal lattice breaks the specific symmetries of parent pristine $w_{ad} - G$ structure the linearly crossing bands at Fermi level. So, C sites vacancy defects with above mentioned concentrations in $w_{ad} - G$ are seen still have linearly crossing bands, and localized vacancy states corresponding to the flat impurities bands in band gaps as shown in fig. 3 (a) & 4 (a) respectively. Due to symmetry of the super cell having 1C vacancy defects, the linearly crossing bands split and they are raised slightly above the Fermi level. The π and π^* bands around Fermi level mix with the orbitals of vacancy. The states associated with the dangling bond and reconstructed $C - C$ bond of vacancy occurs near the top of valence band and in the conduction band appear as flat bands and charge densities are associated these bands are localized as shown in fig. 3 (a). But, in 2C vacancy defects in $w_{ad} - G$ structure, there is no states associated with dangling bond and reconstructed $C - C$ bond of vacancy occurs around the Fermi energy level as shown in fig. 4 (a). In C sites vacancy defects $w_{ad} - G$ structures, the edges and vacancies are very sensitive locations for molecular adsorption due to the under-coordination of atoms in the edge or around the vacancy. They also play a special role either in determining the geometrical conformation of layered materials and inducing modifications of the electronic properties of the layers itself. Therefore, from the band structures analysis, we found that $1C_{atom\text{-}vacancy} - w_{ad} - G$ and $2C_{atoms\text{-}vacancy} - w_{ad} - G$ materials have metallic nature. We know that the electronic configurations of valence electrons in C, O and H atoms are [He] $2s^2\ 2p^2$, [He] $2s^2\ 2p^4$ and $1s^1$ respectively. Each C atom has single up spin in $2p_x, 2p_y$ and vacant in $2p_z$ sub - orbital, each O atom contains paired spins in $2p_x$ sub - orbital and single unpaired up spin in $2p_y$ and $2p_z$ sub - orbital, and H atom has single unpaired up spin in 1s orbital. Due to the arrangement of unpaired up and down spins states of electrons in the orbitals of atoms in all $w_{ad} - G$, $1C_{atom\text{-}vacancy} - w_{ad} - G$ and $2C_{atoms\text{-}vacancy} - w_{ad} - G$ materials develop different values of Fermi energy. We found that Fermi energy values of these materials are -2.91 eV, -3.29 eV and -3.42 eV respectively. Also, we calculated Fermi energy shift values of $1C_{atom\text{-}vacancy} - w_{ad} - G$ and $2C_{atoms\text{-}vacancy} - w_{ad} - G$ materials are 0.38 eV and 0.51 eV respectively as given in table 1.

Table 1. Fermi energy (E_f), Fermi energy shift (E_s), adsorption energy of water molecule in graphene (E_a), defects formation energy (E_d), binding energy per carbon atom of pure graphene and vacancy defects graphene in $w_{ad}-G$ structures (E_b), total value of magnetic moment (M), and magnetic moment due to total up & down spins of electrons in 2s, 2p orbitals of C & O atoms and 1s orbital of H atoms (μ) in water adsorbed Graphene ($w_{ad}-G$) and C sites vacancy defects in water adsorbed Graphene ($C_{atom\text{-}vacancy}-w_{ad}-G$) materials.

Data of band structures and DOS/PDOS plots of $w_{ad}-G$ & $C_{atom\text{-}vacancy}-w_{ad}-G$	$w_{ad}-G$	$1C_{atom\text{-}vacancy}$ $w_{ad}-G$	$2C_{atom\text{-}vacancy}$ $w_{ad}-G$
E_f(eV)	-2.91	-3.29	-3.42
E_s(eV)	-	0.38	0.51
E_a(eV)	0.12	-	-
E_d(eV)	-	7.60	7.00
E_b(eV)	7.98	7.46	6.82
μ due to 2s of C atoms (μ_B/cell)	0.00	-0.01	0.01
μ due to 2p of C atoms (μ_B/cell)	0.00	-0.10	0.02
μ due to 2s of O atoms (μ_B/cell)	0.00	0.00	0.00
μ due to 2p of O atoms (μ_B/cell)	0.00	0.00	0.00
μ due to 1s of H atoms (μ_B/cell)	0.00	0.00	0.00
Total value of magnetic moment M (μ_B/cell)	0.00	-0.11	+0.03

In addition, we have carried out Density of States (DOS) and Partial Density of States (PDOS) calculations to understand the electronic and magnetic properties of materials more clearly. The DOS and PDOS plots of $w_{ad}-G$, $1C_{atom\text{-}vacancy}-w_{ad}-G$ and $2C_{atom\text{-}vacancy}-w_{ad}-G$ materials are shown in fig. 2(b−c), fig. 3(b−c) and fig. 4(b − c) respectively, where vertical dotted line represents Fermi energy levels of respective structures.

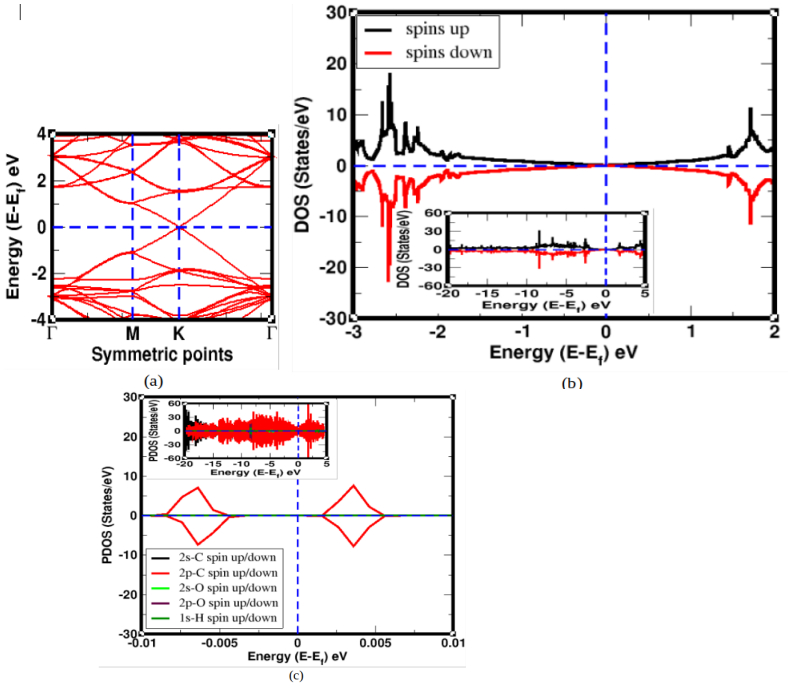

Figure 2. (a) Band structure plot of water adsorbed Graphene (b) Total DOS of up and down spins states of atoms in water adsorbed Graphene (c) PDOS of individual up and down spins states of all atoms in water adsorbed Graphene. In band structure, horizontal dotted line represents Fermi energy level, and in DOS/PDOS plots, vertical dotted line represents Fermi energy level.

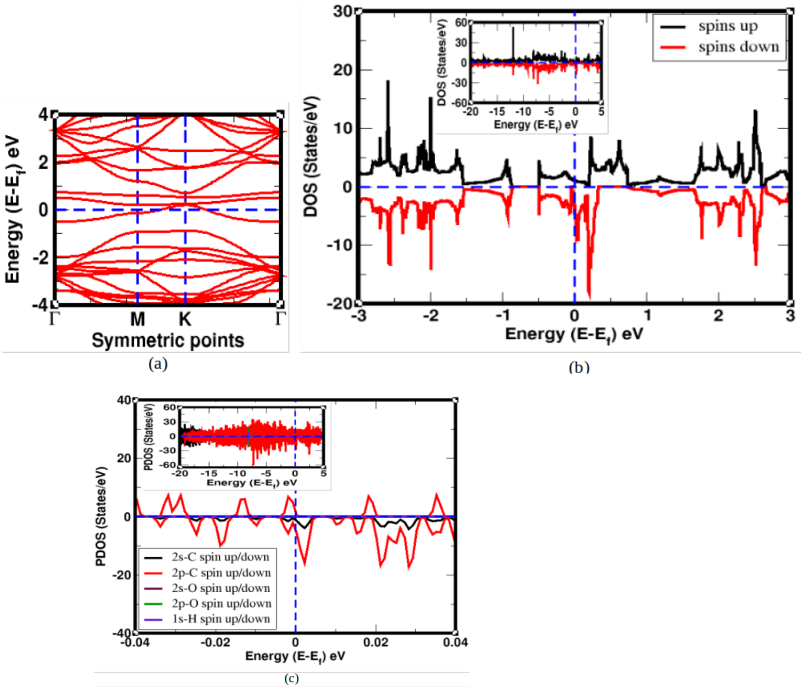

Figure 3. (a) Band structure plot of 1C atom vacancy defects in water adsorbed Graphene (b) Total DOS of up and down spins states of 1C atom vacancy defects in water adsorbed Graphene (c) PDOS of individual up and down spins states of orbitals of 1C atom vacancy defects in water adsorbed Graphene. In band structure, horizontal dotted line represents Fermi energy level, and in DOS/PDOS plots, vertical dotted line represents Fermi energy level.

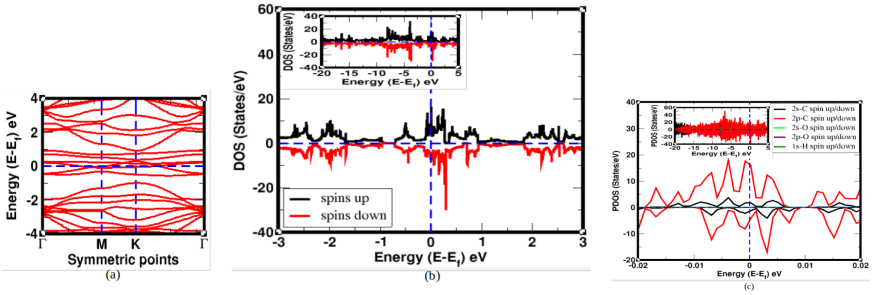

Figure 4. (a) Band structure plot of 2C atoms vacancy defects in water adsorbed Graphene (b) Total DOS of up and down spins states of 2C atoms vacancy defects in water adsorbed Graphene (c) PDOS of individual up and down spins states of orbitals of 2C atoms vacancy defects in water adsorbed Graphene. In band structure, horizontal dotted line represents Fermi energy level, and in DOS/PDOS plots, vertical dotted line represents Fermi energy level.

Magnetic properties

The magnetic and non-magnetic materials are investigated by the analysis of spins distribution in DOS and PDOS plots. The asymmetrically distributed up and down spins states of electrons in DOS and PDOS plots means, materials have magnetic properties, and symmetrically distributed up and down spins states of electrons

in DOS and PDOS plots means, materials carry non-magnetic properties. We observed that up and down spin states of electrons are symmetrically distributed in DOS and PDOS plots of $w_{ad} - G$ material as shown in fig. $2(b - c)$. Net values of magnetic moment are given by up and down spins states of electrons in 2s & 2p orbitals of C & O atoms, and 1s orbital of H atoms in structure is $0.00\mu_B$/cell. Hence, $w_{ad} - G$ is non-magnetic material.

Furthermore, we have analyzed the DOS/PDOS calculations of $1C_{atom\text{-}vacancy} - w_{ad} - G$ and $2C_{atoms\text{-}vacancy} - w_{ad} - G$ materials. The DOS and PDOS of up and down spins states of electrons near the Fermi level are asymmetrically distributed in $1C_{atom\text{-}vacancy} - w_{ad} - G$ as shown in Fig. 3(b−c), because electrons spins degeneracy of the bands are broken and bands split. Hence, $1C_{atom\text{-}vacancy} - w_{ad} - G$ material has magnetic properties. Also, we have calculated the contributions of magnetic moment due to the distribution of spins of electrons in the individual orbital of atoms presented in $1C_{atom\text{-}vacancy} - w_{ad} - G$ material as given in table 1. The magnetic moment developed in material due to up and down spins of electrons in 2s & 2p orbitals of C atoms only which are -0.01 μ_B/cell & -0.10 μ_B/cell respectively. It means, dominant contributions of magnetic moment are given by spins of 2p orbital of C atoms only in the material. The values of magnetic moment are calculated by subtraction between the values of magnetic moment given by total up & down spins states of electrons in the orbitals of atoms present in $1C_{atom\text{-}vacancy} - w_{ad} - G$ material. Hence, from these calculations, we found that total magnetic moment of $1C_{atom\text{-}vacancy} - w_{ad} - G$ has value -0.11 μ_B/cell. Similarly, we have calculated the magnetic moment in $2C_{atoms\text{-}vacancy} - w_{ad} - G$. We know that double vacancy defects in graphene have zero value of magnetic moment because no dangling bonds are formed there. However, in our case, we have obtained small value of magnetic moment which is due to the adsorption of water molecule in double vacancy defects graphene sheet. The DOS/PDOS of up and down spins states of electrons are asymmetrically distributed near the Fermi energy level as shown in fig. 4(b − c). Magnetic moment is given by spins states of electrons in the 2s & 2p orbitals of carbon atoms in structure are 0.01 μ_B/cell & 0.02 μ_B/cell respectively. Hence, total value of magnetic moment of $2C_{atoms\text{-}vacancy} - w_{ad} - G$ material is 0.03 μ_B/cell. The negative value of magnetic moment means, down spins of electrons have dominant role than up spins of electrons, and positive value of magnetic moment means, up spins electrons of atoms have commanding role than down spins electrons in the systems. The magnetic properties developed in $1C_{atom\text{-}vacancy} - w_{ad} - G$ and $2C_{atoms\text{-}vacancy} - w_{ad} - G$ materials are due to the distribution of unpaired electrons spins in 2s & 2p orbitals of carbon atoms in structures.

4. Conclusions

The physical properties of $w_{ad} - G$, $1C_{atom\text{-}vacancy} - w_{ad} - G$ and $2C_{atoms\text{-}vacancy} - w_{ad} - G$ materials are investigated through first-principles plane wave calculations within the Density Functional Theory. Computational of this work has been done by using Quantum ESPRESSO package. At first, we have prepared stable water adsorbed graphene super cell structure, and then constructed C sites vacancy defects in it. We found that binding energy of defects structures are less than non-defects structure. The value of binding energy decreases

with increase in defects concentrations in graphene material. From the band structure calculations, we found the Dirac cone is formed at the Fermi energy level in $w_{ad} - G$ material; hence it is called zero band gap semiconductor. But, electrons band states are crossing and split, and they are raised slightly above the Fermi energy level in $1C_{atom\text{-}vacancy} - w_{ad} - G$ and $2C_{atoms\text{-}vacancy} - w_{ad} - G$ materials. Hence, C sites vacancy defects in $w_{ad} - G$ material have metallic properties. We have analyzed the DOS and PDOS calculations, and found that $w_{ad} - G$ is non-magnetic material. The non- magnetic $w_{ad} - G$ material changes to magnetic $1C_{atom\text{-}vacancy} - w_{ad} - G$ and $2C_{atoms\text{-}vacancy} - w_{ad} - G$ materials due to the presence of C sites vacancy defects in $w_{ad} - G$ structure. The total magnetic moment of $1C_{atom\text{-}vacancy} - w_{ad} - G$ and $2C_{atoms\text{-}vacancy} - w_{ad} - G$ materials have values $-0.11\ \mu_B$/cell and $0.03\ \mu_B$/cell respectively. The high value of magnetic moment is given by up and down spins states of electrons in 3p orbital of C atoms in vacancy defects structures.

5. Acknowledgements

HKN acknowledges the UGC Nepal Award no. PhD-75/76-S&T-09. NPA acknowledges network project NT-14 of ICTP/OEA and UGC Nepal Grants CRG 073/74 -S & T-01.

References

[1] Geim A, Novoselov K. The rise of graphene. naturematerials, 6: 183–191. March. 2007;.

[2] Xu M, Liang T, Shi M, Chen H. Graphene-like two-dimensional materials. Chemical reviews. 2013;113(5):3766–3798.

[3] Mayorov AS, Gorbachev RV, Morozov SV, Britnell L, Jalil R, Ponomarenko LA, et al. Micrometer-scale ballistic transport in encapsulated graphene at room temperature. Nano letters. 2011;11(6):2396–2399.

[4] Morozov S, Novoselov K, Katsnelson M, Schedin F, Elias D, Jaszczak JA, et al. Giant intrinsic carrier mobilities in graphene and its bilayer. Physical review letters. 2008;100(1):016602.

[5] Novoselov KS, Geim AK, Morozov SV, Jiang D, Katsnelson MI, Grigorieva I, et al. Two-dimensional gas of massless Dirac fermions in graphene. nature. 2005;438(7065):197–200.

[6] Lei JC, Zhang X, Zhou Z. Recent advances in MXene: Preparation, properties, and applications. Frontiers of Physics. 2015;10(3):276–286.

[7] Dávila M, Xian L, Cahangirov S, Rubio A, Le Lay G. Germanene: a novel two-dimensional germanium allotrope akin to graphene and silicene. New Journal of Physics. 2014;16(9):095002.

[8] Balendhran S, Walia S, Nili H, Sriram S, Bhaskaran M. Elemental analogues of graphene: silicene, germanene, stanene, and phosphorene. small. 2015;11(6):640–652.

[9] Lehtinen PO, Foster AS, Ma Y, Krasheninnikov A, Nieminen RM. Irradiation-induced magnetism in graphite: a density functional study. Physical review letters. 2004;93(18):187202.

[10] Yazyev OV, Louie SG. Topological defects in graphene: Dislocations and grain boundaries. Physical Review B. 2010;81(19):195420.

[11] Hashimoto A, Suenaga K, Gloter A, Urita K, Iijima S. Direct evidence for atomic defects in graphene layers. nature. 2004;430(7002):870–873.

[12] Krasheninnikov A, Banhart F. Engineering of nanostructured carbon materials with electron or ion beams. Nature materials. 2007;6(10):723–733.

[13] Crespi VH, Benedict LX, Cohen ML, Louie SG. Prediction of a pure-carbon planar covalent metal. Physical Review B. 1996;53(20):R13303.

[14] Kim Y, Ihm J, Yoon E, Lee GD. Dynamics and stability of divacancy defects in graphene. Physical Review B. 2011;84(7):075445.

[15] Singh R, Kroll P. Magnetism in graphene due to single-atom defects: dependence on the concentration and packing geometry of defects. Journal of Physics: Condensed Matter. 2009;21(19):196002.

[16] Faccio R, Fernández-Werner L, Pardo H, Goyenola C, Ventura ON, Mombrú ÁW. Electronic and structural distortions in graphene induced by carbon vacancies and boron doping. The Journal of Physical Chemistry C. 2010;114(44):18961–18971.

[17] Topsakal M, Aktürk E, Sevinçli H, Ciraci S. First-principles approach to monitoring the band gap and magnetic state of a graphene nanoribbon via its vacancies. Physical Review B. 2008;78(23):235435.

[18] Balog R, Jørgensen B, Nilsson L, Andersen M, Rienks E, Bianchi M, et al. Bandgap opening in graphene induced by patterned hydrogen adsorption. Nature materials. 2010;9(4):315–319.

[19] Robertson AW, Montanari B, He K, Allen CS, Wu YA, Harrison NM, et al. Structural reconstruction of the graphene monovacancy. ACS nano. 2013;7(5):4495–4502.

[20] Yazyev OV, Helm L. Defect-induced magnetism in graphene. Physical Review B. 2007;75(12):125408.

[21] Neupane HK, Adhikari NP. Tuning Structural, Electronic, and Magnetic Properties of C Sites Vacancy Defects in Graphene/MoS2 van der Waals Heterostructure Materials: A First-Principles Study. Advances in Condensed Matter Physics. 2020;2020.

[22] Fedorov A, Popov Z, Fedorov D, Eliseeva N, Serjantova M, Kuzubov A. DFT investigation of the influence of ordered vacancies on elastic and magnetic properties of graphene and graphene-like SiC and BN structures. physica status solidi (b). 2012;249(12):2549–2552.

[23] Hohenberg P, Kohn W. Inhomogeneous electron gas. Physical review. 1964;136(3B):B864.

[24] Giannozzi P, Baroni S, Bonini N, Calandra M, Car R, Cavazzoni C, et al. QUANTUM ESPRESSO: a modular and open-source software project for quantum simulations of materials. Journal of physics: Condensed matter. 2009;21(39):395502.

[25] Perdew JP, Burke K, Ernzerhof M. Generalized gradient approximation made simple. Physical review letters. 1996;77(18):3865.

[26] Martin RM. Electronic structure: basic theory and practical methods. Cambridge university press; 2004.

[27] Pfrommer BG, Côté M, Louie SG, Cohen ML. Relaxation of crystals with the quasi-Newton method. Journal of Computational Physics. 1997;131(1):233–240.

[28] Marzari N, Vanderbilt D, De Vita A, Payne M. Thermal contraction and disordering of the Al (110) surface. Physical review letters. 1999;82(16):3296.

[29] Neupane H, Adhikari N. Structure, electronic and magnetic properties of 2D Graphene-Molybdenum diSulphide (G-MoS2) heterostructure (HS) with vacancy defects at Mo sites. Computational Condensed Matter. 2020;24:e00489.

[30] Hou Z, Wang X, Ikeda T, Terakura K, Oshima M, Kakimoto Ma, et al. Interplay between nitrogen dopants and native point defects in graphene. Physical Review B. 2012;85(16):165439.

JNPS ***6*** *(1), 42-49 (2020)* ***Research Article*** *© Nepal Physical Society*
ISSN: 2392-473X (Print), 2738-9537 (Online) *DOI: http://doi.org/10.3126/jnphyssoc.v6i1.30516*

Path Integral Simulations of Harmonic Oscillator

H. K. Neupane[1, 2] and N. P. Adhikari[2, *]
[1] Amrit Campus, Institute of Science and Technology Tribhuvan University, Kathmandu, Nepal
[2] Central Department of Physics, Institute of Science and Technology Tribhuvan University, Kathmandu, Nepal
[*]Corresponding Email: narayan.adhikari@cdp.tu.edu.np

Received: *15 May, 2020;* ***Revised:*** *15 Jun., 2020;* ***Accepted:*** *28 Jun., 2020*

Abstract

To study the interaction of atoms present in the two rings polymer molecule system, we have performed path integral, Monte Carlo simulations method using FORTRAN code. In literature, we found that the interaction of atoms present in two rings polymer molecule was done by path integral, Monte Carlo simulations method. Also, we found that less the number of atoms present in the rings polymer molecule i.e. P = 2, 4, 8, 16, more will be the probability of getting classical result. But, if the numbers of atoms are increased in the rings, we can reach near exact quantum mechanical result. When the value of P is ∞ the average interaction energy value of atoms present in two rings was found to be 0.5, which was exact zero point energy value of harmonic oscillator. As given in literature, we have studied the interaction of atoms present in two rings polymer system using path integral, Monte Carlo simulations method, the result we produced was as same as in literature, where the value of P were 2, 4, 8, 16 and ∞. We have done additional work by taking the values of P = 32, 64, 128, 256 and calculated the variation of average interaction energy with temperature, and found that the value of average interaction energy <E> = 0.5 at low temperature T ≈ 0K. This value is called zero point energy value of quantum harmonic oscillator. Here, the value of P = 256 and P = ∞ can resemble with each other. For this, we took P = 256 and observed the interaction, and found that the average interaction energy value of atoms present in rings was 0.5 at T ≈ 0K. Therefore, by this additional work we can say more clearly that increasing the number of atoms in two rings polymer molecule will result to the high possibility of getting exact value of average interaction energy in the system.

Keywords: FORTRAN, Path integral, Monte Carlo, Harmonic Oscillator, Interaction.

1. INTRODUCTION

Schrodinger's equation and Heisenberg's matrix mechanics are based on Hamiltonian classical mechanics, which provides a direct connection between classical and quantum mechanics [1-3]. In 1933, Dirac [4, 5] proposed an approach to quantum mechanics based on the Lagrangian, he considered it as more basic than the Hamiltonian. Dirac suggested that in quantum mechanics, transition amplitude is also known as the propagator which correlates to the quantity $e^{iS/\eta}$ where S is the classical action calculated along the path taken by particles. In 1948, Feynman [6] extended Dirac's idea and formulated quantum mechanics based on sum over all paths between fixed initial and final states. The amplitudes of paths combined by superposition principle, in which each path contributes a pure phase $e^{iS/\eta}$ to the propagator, as suggested by Dirac. This sum over paths is typically an integral over continuum of paths is known as path-integral method. Feynman derived the path integral methods and applied into many areas of Physics [1], most notably in non-relativistic quantum mechanics, many body Physics, quantum field theory and statistical mechanics etc. [7, 8]. In quantum mechanics, path integral leads to phenomena like tunneling, double-slit experiment etc. To interpret these experiments, path integral provides a fascinating basis [9]. Path integral is an explicit expression for the probability amplitude. The actual calculation of these amplitudes depends on the problem of interest such as harmonic oscillator, the path integral can be evaluated exactly, but typically either an approximate solution is found or a perturbative expansion is done. The various others established methods like mean field theory,

renormalization group etc. are obtaining exact or approximate solution from path integrals [10], however there are some situations approximate solution are ineffective for example in Quantum Chromo Dynamics (QCD), where calculations based on perturbation theory have been successful. In the strong interaction regime provides non-perturbative numerical evaluation of amplitudes and matrix elements, which are based on Monte Carlo methods [11-13].

The Monte Carlo simulations method is a large class of algorithms that simulates quantum systems with the idea of solving the quantum many body problems like Schrodinger wave equation [14]. It makes use of random numbers to make a series of random moves, an algorithm is then used to accept or reject the move. Depending on the Monte Carlo method used, a specific function is applied to old and new configurations. The move is either accepted or rejected by comparing the results of this function before and after the move. Also, Monte Carlo simulations [15], is a method for analyzing the behavior of any activity or process that involves uncertainty so that this method is used random numbers and probability statistics to solve the problems. As we know, it may be easy to solve the equations which described the interaction between the two atoms but solving the same equations for hundreds or thousands of atoms is often impossible. Monte Carlo methods can be sampled a large system with a number of small random configurations and that data can be used to analyze the overall system.

Thus, Monte Carlo simulations method is widely used in different fields that range from economics to nuclear physics [16]. In Monte Carlo algorithms, the entire system, which may be an equation involving hundreds or thousands of variables is simulated or evaluated a large number of times. Each time the equation is simulated, the unknown variables are sampled. The system is then simulated numerous times and the performance of the system can be commutated. At the end of the simulations, the result is a large number of samples which describe the possible state of the system. These results are combined into probability distributions of possible outcomes. As a result, the outputs are not single values but probability distributions.

In this project, we focused path integral method on quantum mechanical treatment of two rings polymer system using FORTRAN code based on Monte Carlo simulations method.

2. SIMULATIONS METHOD

We have done path integral simulations of two rings polymer molecule by using Monte Carlo simulations method based on FORTRAN code. FORTRAN is a programming language which was conceived in early 1950s [17, 18]. In present work, we have considered two rings polymer molecule as a system, where P represents the number of atoms present in a system. This system is an example of Harmonic oscillator. Here, we have taken FORTRAN code for a considered polymer molecule at different values of P with different values of temperature. In this FORTRAN program, program name is given as *qmc-pi-sho.f90* which is a simple path integral, Monte Carlo simulations program. We have used this path integral, Monte Carlo simulations method to study the variation of average interaction energy between the atoms in the rings polymer molecule at different temperatures.

The *Math-module* and *average-module* in FORTRAN program are incorporated in intrinsic and others different conditions are used as a code in designed FORTRAN program. We have taken different values of P and temperature at constant values of *nstep, nblock, nequil* and *dx-max,* and also we have taken 20 numbers of blocks for production, 10 numbers of blocks for equilibration, 50000 numbers of steps per block in simulations and value 1.00 for maximum displacement in FORTRAN code. Here, we considered P is an integer and temperature, *dx-max*, and classical and quantum potentials are taken as real. This program is run in Linux by using *gfortran……f90,* we got different data and plots, and they are discussed in results and discussion section.

3. RESULTS AND DISCUSSION

In this section, we discussed the interaction of atoms in two rings polymer molecule by using path integral, Monte Carlo simulations method based on FORTRAN code and we compared our main findings, their interpretation with reported results.

3.1 Path-Integral Simulations

To arrive at the path integral formulation of quantum mechanics, we consider the problem of calculating the probability of a particle leaving a position like q_i and arriving at a position q_f under the action of a potential V(q) in a time T [16]. We used Dirac path integral formalism; the probability is given by $< q_f / e^{-iHT} / q_i >$. The interpretation is

that we divide time axis in N times slices and then compute the probability amplitude for the particle leaving a position q_i at time t_i and reaching the position q_{i+1} at time t_{i+1}. The next step is to multiply these amplitudes to obtain the probability amplitude for the particle leaving q_i arrive at q_f in time T through a specific path. We repeat this for all possible paths and sum the amplitudes for each path to obtain the total probability amplitude $< q_f / e^{-iHT} / q_i >$. The path integral evaluate analytical solutions numerically, for this we relate the path integral with the partition function on statistical mechanics and use the metropolis algorithm to make Monte Carlo simulations. In our considered system, nuclei of the atoms are modeled by quantum mechanically which incorporated quantum effects in simulations [19]. So our attempts have been made to incorporate quantum effects in simulations within the limitation of classical simulations. To estimate quantum corrections of thermodynamics function by expanding the partition function of N atoms in powers of Planck constant in expression of partition function [19, 20],

$$Q_{NVT} = \frac{1}{a\Lambda^{3N} N!}\int dr[1-\frac{\beta\eta^2}{24m}\sum_{i=1}^{N}(\nabla_{r_i}\beta V(r))^2]e^{-\beta V(r)} ....(1)$$

Where, $\Lambda = \left(\frac{h^2}{2\pi m K_B T}\right)^{\frac{1}{2}}$

The corrections to the thermodynamic properties, extra term is added in the classical Hamiltonian, [21] which is given by;

$$H^{qu} = H^{cl} + \frac{\eta^2\beta}{24m}[-\frac{\beta}{m}(\sum_i P_i.\nabla_{ri})^2 V^{cl} + 3\sum_i \nabla^2{}_{ri} V^{cl} - \beta\sum_i (\nabla_{ri} V^{cl}) ....(2)$$

But, correction term obtained was done by molecular dynamics (MD) simulation model which was numerically instabilities. Therefore, to treat the nuclei quantum mechanically, we have needed quantum partition function which is obtained by the path integral formulation of quantum mechanics, by taking non-normalize quantum mechanical density operator $\rho = e^{-\beta H}$ [1, 21, 22],

$$Q_{NVT}(\beta) \approx \frac{1}{NP!}\left(\frac{M}{2\pi\beta\eta^2}\right)^{\frac{3NP}{2}}\int dr e^{-\beta V(r)} ....(3)$$

Where, r represents the position of all the molecules. Using equation (3), some properties like thermodynamics properties, static and dynamic structure properties are estimated. We first take for one particle then generate to N particles then get [23] the partition function is;

$$Q_{NVT}(\beta) \approx \frac{1}{NP!}\left(\frac{M}{2\pi\beta\eta^2}\right)^{\frac{3NP}{2}}\int dr e^{-\beta V(r)} ....(3)$$

Where, *mp=M*,

Or,

$$V(r) = V^{cl}(r) + V^{qu}(r) ....(4).$$

Since, $V^{cl}(r)$ and $V^{qu}(r)$ represent the Classical and Quantum potential respectively. Thus, a Monte Carlo simulation of the classical ring polymer system with potential energy V(r) is given by equation (4). As the number of particles P in our ring polymer increases, we get a better approximation of quantum partition function and become formally exact as P = ∞. We can see the theoretical graph, the finite P valued energy curves deviate from the true result as temperature decreases, leaving the zero point level $E = \frac{1}{2}\eta\omega$ and dropping to classical value < E > = 0 at T = 0 as shown in Fig. 1(b) [22].

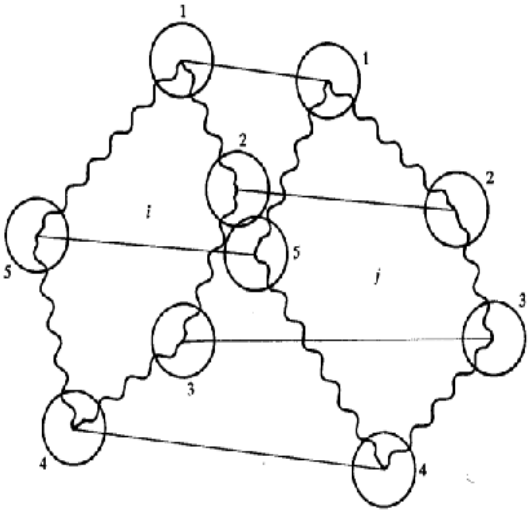

(a)

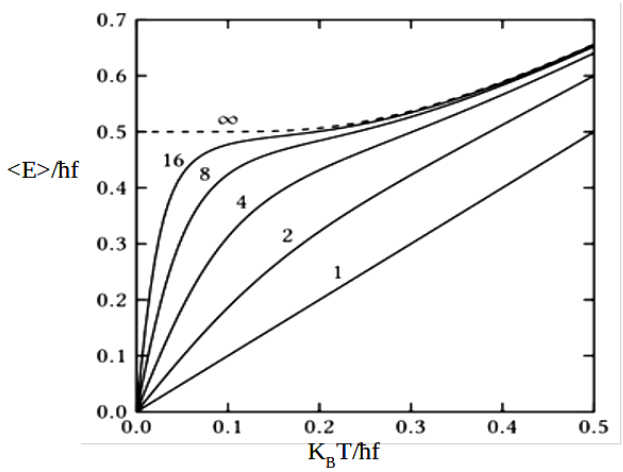

(b)

Fig. 1: *(a) Two rings polymer molecule (P = 5) representing the interaction between two atoms in a path integral simulation (b) The average energy of the path integral approximation to the Quantum Harmonic Oscillator of frequency as a function of temperature [22].*

In literature [22], we found a system of two rings polymer molecule shown in Fig. 1(a), in which atoms are presented in each ring. In Fig. 1(a), i and j represent two rings polymer structure where each ring contains P number of atoms. The atoms in one ring are interacted with atoms in another ring like a quantum harmonic oscillator since atoms having two rings are seemed to be bounded like an ideal spring. So that, the interaction between atoms present in the two rings looks like harmonic oscillator problem. The interaction of two rings polymer system was studied by path integral, Monte Carlo simulations method using FORTRAN program. The reported graph shown in Fig. 1(b) was obtained by doing path integral, Monte Carlo simulation in a considered polymer system where average interaction energy (<E>/hf) between the atoms in rings were taken along y-axis and different values of temperature (thermal energy K_BT/hf) were taken along x-axis. We saw that, number of atoms present in each ring (P = 1) in our considered system gives classical result, i.e. the value of average interaction energy was zero at zero temperature. But, we know that, quantum harmonic oscillator has zero point energy value ($\hbar\omega/2$) at zero temperature. Similarly, the value of P gradually increased up to 16, (i.e. P = 2, 4, 8, 16) also provided classical result (i.e. <E> = 0) at zero temperature, but quantum mechanically, average values of interaction energy between the atoms in two rings polymer molecule have greater value (i.e. 0.5) at low temperature region (i.e. T = 0K). It means, the value of average interaction energy between more numbers of atoms present in rings polymer using path integral, Monte Carlo simulations method provides approximate quantum mechanical result at absolute zero temperature. So that, at P = ∞ has given zero point energy value (<E> = 0.5) at T = 0K, shown in Fig. 1(b), otherwise (P = 2, 4, 8, 16) have slightly deviated result from quantum mechanical treatment of harmonic oscillator problem. Therefore, according to the result reported in literature, we can reach to the conclusion that, if number of atoms in two rings polymer system has greater amount, (i.e. P > >16 to ∞), the average value of interaction energy between the atoms in the rings polymer system would be 0.5 at zero temperature, which is called exact average interaction energy (zero point energy of harmonic oscillator) in the two rings polymer system.

In this work, as reported in literature we have taken two rings polymer system. The atoms present in the rings interact with each other which resembles with the harmonic oscillator interaction. So that the two rings polymer system is also called an example of harmonic oscillator. Here, we have taken the number of atoms P = 2, 4, 8, 16, 32, 64, 128, 256, ∞ in our assumed system. We used path integral, Monte Carlo simulations method based on FORTRAN code to study the variation of average interaction energy of atoms in our considered system at different values of temperature. We found that, if the value of P is less (i.e. P = 2, 4, 8, 16)

classical result will be obtained at T ≈ 0K as shown in Figs. 2 (a), 2(b), 2(c), 2(d) respectively. These plots are resembled exactly to the plots reported in Fig. 1(b). And, if the values of P is gradually increased from P = 32, 64, 128, 256, ……., the average interaction energy will be seen near the exact value (0.5) at T ≈ 0K temperature as shown in Figs. 3(a), 3(b), 3(c), 3(d) respectively.

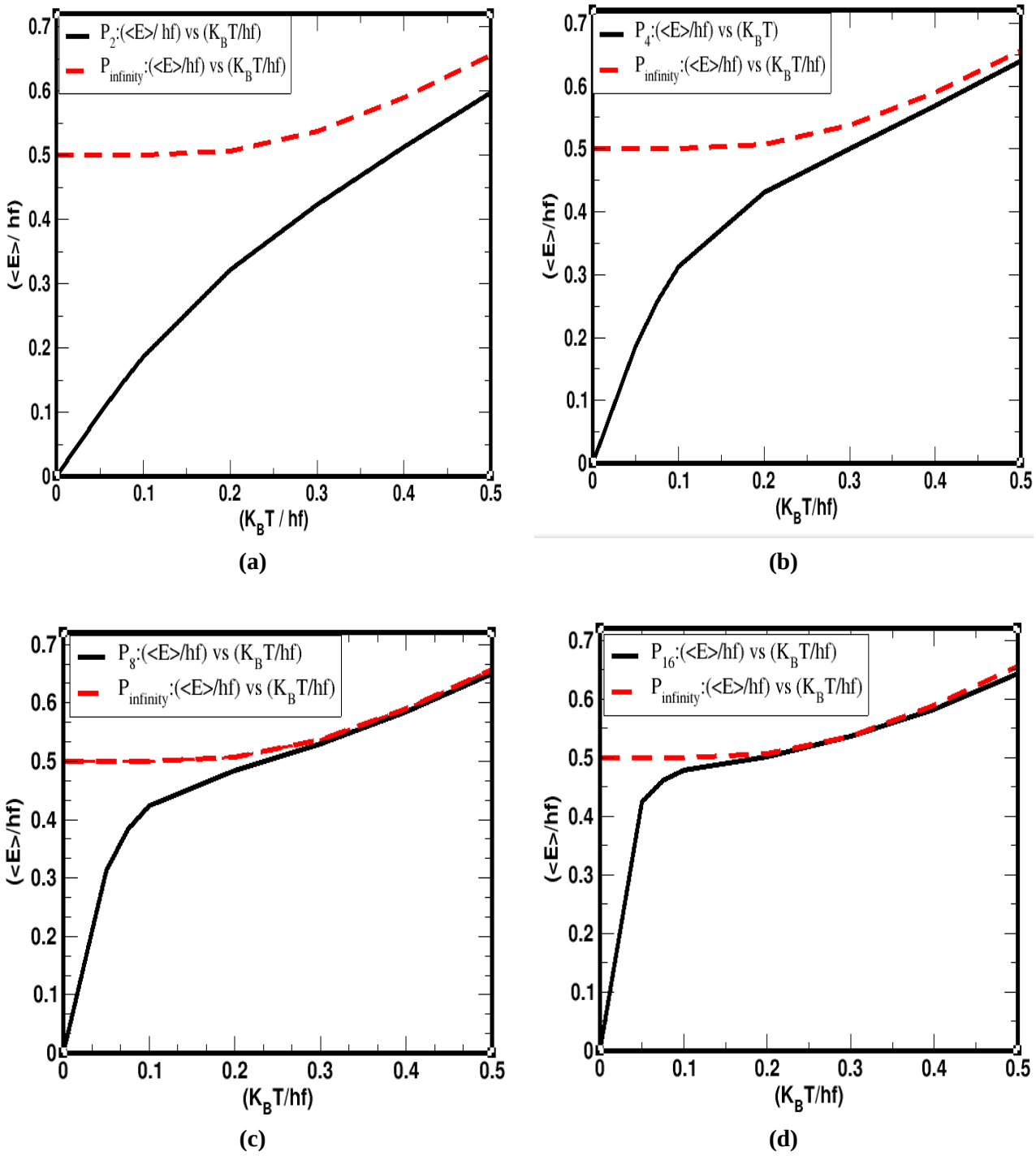

***Fig. 2**: Two rings polymer molecule represents the interaction between the atoms as an example of harmonic oscillator (a) The plot of average interaction energy at P = 2 and ∞ as a function of temperature (b) The plot of average interaction energy at P = 4 and ∞ as a function of temperature (c) The plot of average interaction energy at P = 8 and ∞ as a function of temperature (d) The plot of average interaction energy at P = 16 and ∞ as a function of temperature.*

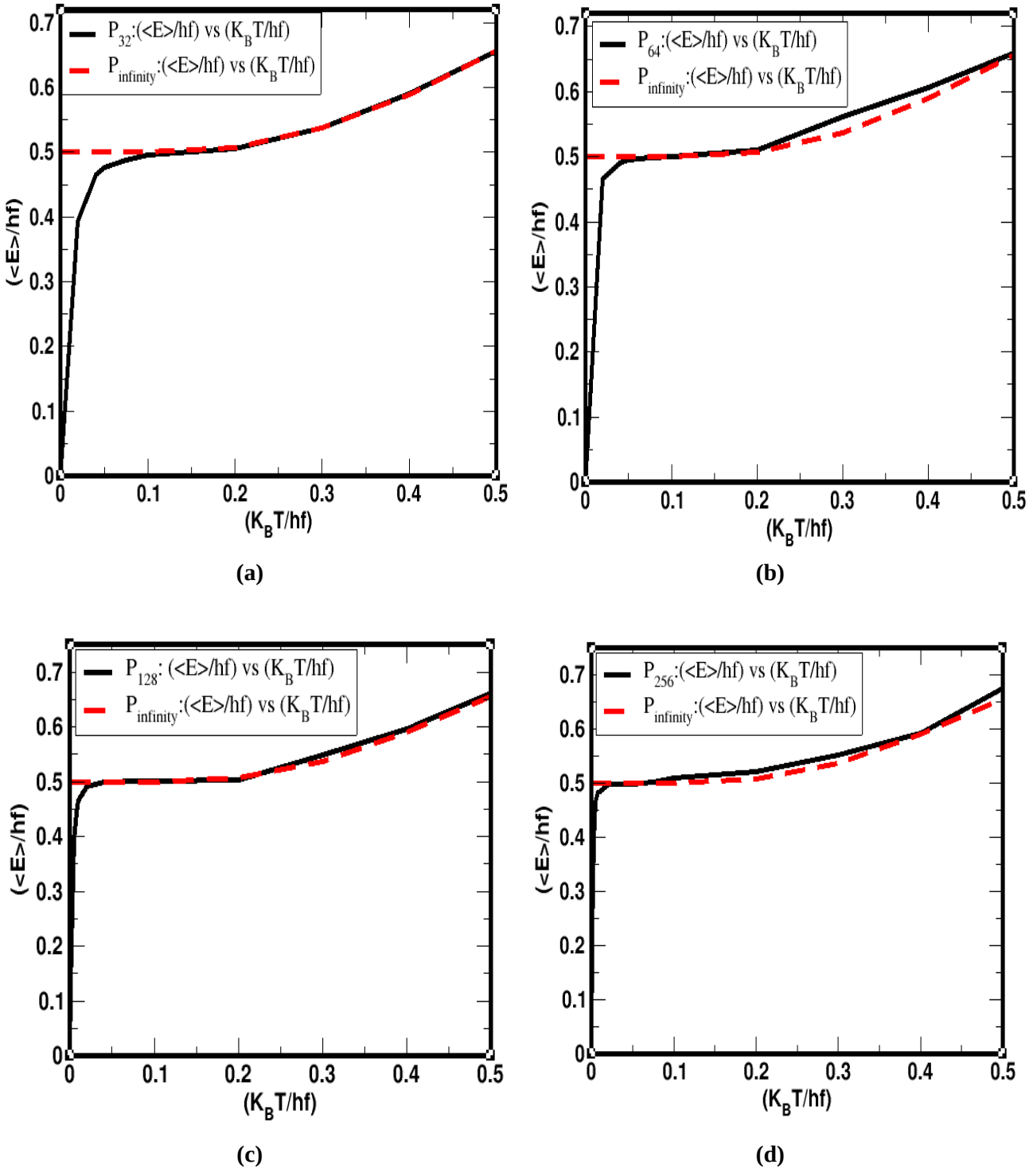

Fig. 3*: Two rings polymer molecule represents the interaction between the atoms as an example of harmonic oscillator (a) plot of average interaction energy at P = 32 and ∞ as a function of temperature (b) plot of average interaction energy at P = 64 and ∞ as a function of temperature (c) plot of average interaction energy at P = 128 and ∞ as a function of temperature (d) plot of average interaction energy at P = 256 and ∞ as a function of temperature.*

Here, we have presented the simulated data of average interaction energy values of atoms in two rings polymer system at P = 2, 4, 8, 16, 32, 64, 128, 256 and ∞ with different values of temperature in table 1, where P = ∞ is obtained from the large numbers of iteration in Monte Carlo simulations method.

Table 1: Data of thermal energy in term of temperature (K_BT/hf) and average interaction energy between the atoms in i and j rings polymer molecules in term of (<E>/hf) are obtained from the path integral, Monte Carlo simulations method by using FORTRAN f90 program where P represents number of atoms are presented in a ring.

Temperature (Thermal energy)	Average energy (P=2)	Average energy (P=4)	Average energy (P=8)	Average energy (P=16)	Average energy (P=32)	Average energy (P=64)	Average energy (P=128)	Average energy (P=256)	Average energy (P =∞)
0.0000	0.0000	0.0000	0.0000	0.0000	0.0000	0.0000	0.0000	0.0000	0.5000
0.0010	0.0002	0.0009	0.0010	0.0017	0.0089	0.0120	0.1240	0.2278	0.5000
0.0025	0.0009	0.0049	0.0079	0.0098	0.0298	0.0519	0.2695	0.3941	0.5000
0.0050	0.0028	0.0094	0.0099	0.0168	0.0860	0.1532	0.3939	0.4659	0.5000
0.0075	0.0056	0.0198	0.0343	0.0957	0.1568	0.2544	0.4435	0.4834	0.5000
0.0100	0.0099	0.0410	0.0883	0.1998	0.2056	0.3003	0.4661	0.4842	0.5000
0.0200	0.0398	0.0791	0.1524	0.2695	0.3940	0.4656	0.4910	0.4978	0.5000
0.0400	0.0788	0.1523	0.2695	0.3942	0.4661	0.4853	0.4984	0.4979	0.5000
0.0500	0.0910	0.1856	0.3124	0.4238	0.4774	0.4959	0.4988	0.4983	0.5000
0.0750	0.1436	0.2575	0.3842	0.4609	0.4887	0.4983	0.5014	0.5016	0.5000
0.1000	0.1860	0.3126	0.4241	0.4780	0.4957	0.4995	0.5020	0.5097	0.5000
0.2000	0.3220	0.4314	0.4843	0.5022	0.5061	0.5105	0.5030	0.5217	0.5078
0.3000	0.4228	0.5008	0.5292	0.5368	0.5373	0.5619	0.5482	0.5512	0.5370
0.4000	0.5123	0.5679	0.5851	0.5815	0.5902	0.6067	0.5858	0.6022	0.5894
0.5000	0.5975	0.6394	0.6501	0.6434	0.6562	0.6690	0.6643	0.6656	0.6565

According to the data we produced, variation of average interactions energy with temperature at P = 2, 4, 8, 16, 32, 64, 128, 256 and ∞ are shown in Fig. 4.

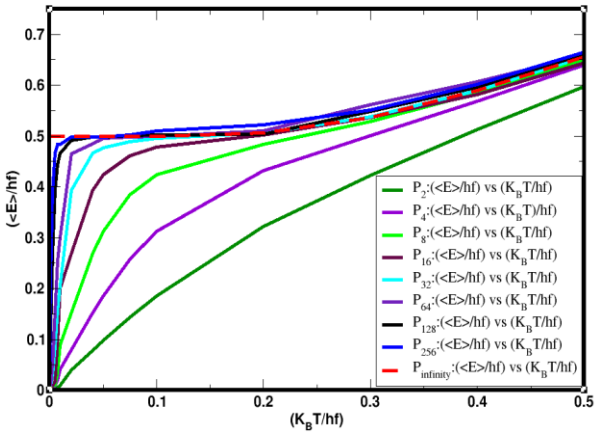

Fig. 4: *Variation of average interaction energy of atoms present in two rings polymer molecule at P = 2, 4, 8, 16, 64, 128, 256 and ∞ as a function of temperature, where values of average interaction energy are plotted along y-axis and thermal energy as a function of temperature are plotted along x-axis.*

In Fig. 4, we can see average interaction energy values of atoms in rings polymer at P = 32 is greater than 16, P = 64 is greater than 32, P = 128 is greater than 64 and P = 256 is greater than 128 at T ≈ 0K temperature. From these observations, we can be more clear that, study of the interaction between more numbers of atoms present in the two rings polymer system, will implies to reach near to exact result reported by quantum mechanics. Here, we have calculated the interaction of each atom in ring 'i' with all atoms in ring 'j' by using Monte Carlo method of simulations. As a result, there will be more chance to get accurate value of average interaction energy from large numbers of data. Hence, value of average interaction energy of atoms in rings at P = 256 is close to 0.5 than other values of P at T ≈ 0K, i.e. the value of P = 256 and P = ∞ can resemble with each other. When the interaction was observed at P = 256, we found that the average interaction energy value of atoms present in rings was 0.5 at T ≈ 0K also shown in Fig. 3(d). Therefore, by using path integral Monte Carlo simulations method based on FORTRAN code, we can reach to the conclusion that more the number of atoms present in the two rings polymer system, there will be more probability to get exact value of interaction energy (0.5) of harmonic oscillator at T = 0K.

4. CONCLUSIONS

In summary, we have studied the interaction of atoms present in two rings polymer molecule by path integral, Monte Carlo simulations method based on FORTRAN code.

We have taken two rings polymer molecule as a system for simulations, in which each ring contains P = 2, 4, 8, 16, 32, 64, 128, 256 and ∞ atoms separately. Firstly, we have taken P = 2, 4, 8, 16 atoms for simulations, and we found that, average interaction energy values of atoms in rings are decreased and reached to zero at T ≈ 0K temperature. It means, if the value of P is less (i.e. P = 2, 4, 8, 16), classical result was obtained at T ≈ 0K temperature. Additionally, we have done the simulations of P = 32, 64, 128 and 256 by using same method mentioned above and found that greater number of atoms present in the system have given nearly exact value i.e. <E> = 0.5 at T ≈ 0K, which was exact zero point energy value of harmonic oscillator problem. That exact energy of harmonic oscillator can be obtained by substituting the value of P ≈ ∞ in the system. However, in this work, the value of P = 256 is exact value near ∞. By taking this value i.e. P = 256 and observing the interaction, we found that the average interaction energy value of atoms present in rings was 0.5 at T ≈ 0K. Therefore, we can be clearer that, more the number of atoms present in the two rings polymer molecule system, the average interaction energy value of atoms in system has exact 0.5 at zero temperature. This value is called zero point energy value of quantum harmonic oscillator.

ACKNOWLEDGEMENTS

We acknowledge the Abdus Salam International Center for Theoretical Physics (ICTP) OEA/NT-14 for partial support.

REFERENCES

[1] Feynman, R. P., & Hibbs, A. R. (1965). *Quantum mechanics and path integrals [by] RP Feynman [and] AR Hibbs*. McGraw-Hill.

[2] Van der Waerden, B. L. (1968). Sources of quantum mechanics. *American Journal of Physics*, *36*(4), 374-375.

[3] Brush, S. G. (1987). Resource letter HP-1: History of physics. *American Journal of Physics*, *55*(8), 683-691.

[4] Dirac, P. A. (2005). The Lagrangian in quantum mechanics. In *Feynman's Thesis—A New Approach To Quantum Theory* (pp. 111-119).

[5] Dirac, P. A. M. (1981). *The principles of quantum mechanics* (No. 27). Oxford university press.

[6] Feynman, R. P. (2005). Space-time approach to non-relativistic quantum mechanics. In *Feynman's Thesis—A New Approach To Quantum Theory* (pp. 71-109).

[7] Huang, K. (2010). *Quantum field theory: From operators to path integrals*. John Wiley & Sons.

[8] Wiegel, F. W. (1975). Path integral methods in statistical mechanics. *Physics Reports*, *16*(2), 57-114.

[9] Feynman, R. P. (1965). Feynman lectures on physics. Volume 3: Quantum mechancis. *flp*.

[10] Amit, D. J., & Martin-Mayor, V. (2005). *Field theory, the renormalization group, and critical phenomena: graphs to computers*. World Scientific Publishing Company.

[11] Creutz, M., & Freedman, B. (1981). A statistical approach to quantum mechanics. *Annals of Physics*, *132*(2), 427-462.

[12] Smit, J. (2002). *Introduction to quantum fields on a lattice*. Cambridge University Press.

[13] Mudhasani, S. (2011). GPU-based Implementation of the Variational Path Integral Method.

[14] Woller, J. (1996). The basics of Monte Carlo simulations. University of Nebraska-Lincoln. *Physical Chemistry Lab. Available at: http://www. chem. unl. edu/zeng/joy/mclab/mcintro. html. Accessed*, *14*, 2008.

[15] Mudhasani, S. (2011). GPU-based Implementation of the Variational Path Integral Method.

[16] Zee, A. (2010). *Quantum field theory in a nutshell* (Vol. 7). Princeton university press.

[17] Metcalf, M. (1999). Fortran 90/95/HPF. *ACM SIGPLAN Notices*, *34*(12), 24-29.

[18] Metcalf, M. (2001, April). Fortran 90/95/HPF information file (part 3, books). In *ACM SIGPLAN Fortran Forum* (Vol. 20, No. 1, pp. 27-30). New York, NY, USA: ACM.

[19] Wigner, E. (1932). Phys. Rev. *On the Quantum Correction for Thermodynamic Equilibrium*, *40*, pp-749.

[20] Kirkwood, J. G. (1933). Quantum statistics of almost classical assemblies. *Physical Review*, *44*(1), 31.

[22] Singer, J. V. L., & Singer, K. (1984). Molecular Dynamics Based on the First Order Quantum Correction in the Wigner-Kirkwood Expansion. *CCP5 Quarterly*, *14*, 24.

[23] Chandler, D., &Wolynes, P. G. (1981). Exploiting the isomorphism between quantum theory and classical statistical mechanics of polyatomic fluids. *The Journal of Chemical Physics*, *74*(7), 4078-4095.

[24] DeRaedt, B., Sprik, M., & Klein, M. L. (1984). Computer simulation of muonium in water. *The Journal of chemical physics*, *80*(11), 5719-5724.

Nepal Physical Society

Ghantaghar, Kathmandu, Nepal

Presenting this certificate to **Hari Krishna Neupane** from

Tribhuvan University , Kathmandu Nepal

for attending the

International Conference on Frontiers of Physics -2022

(ICFP-2022)

held on January 22-24, 2022 via virtual platform.

Prof. Dr. Narayan P. Chapagain

Conference Chair, ICFP-2022

President, Nepal Physical Society

February 1, 2022

Association of Nepali Physicists in America-ANPA

Certificate of Appreciation

THIS CERTIFICATE IS PRESENTED TO

MR. HARI K. NEUPANE

Tribhuvan University, Nepal

FOR YOUR PRESENTATION DURING THE ANPA CONFERENCE 2021

Nmalakar

DR. NABIN MALAKAR
CONVENER, ANPA CONFERENCE 2021

DR. JAGAN DEVKOTA
PRESIDENT, ANPA

Certificate of Appreciation

presented to

Mr. Hari Krishna Neupane

(Amrit Campus, Tribhuvan University)

for your invaluable contribution, as a resource person, to make the workshop on **Experimental and Computational Approach of Metal Oxide Thin Film (ECAMOTF)** held on March 18 - 19, 2021 a grand success. The program was organized by Atmospheric and Material Research Center at the Department of Physics, Amrit Campus with the support of International Science Programme (ISP) Uppsala University, Sweden in collaboration with IEEE/EDS Nepal Chapter.

Prof. Dr. Bimil Aryal
Dean, IoST
Tribhuvan University

Dr. Puspa Lal Homagai
Campus Chief
Amrit Campus

Prof. Dr. Leela Pradhan Joshi
HoD, Department of Physics
Amrit Campus

Organized by

Atmospheric and Material Science Research Center
Department of Physics
Amrit Campus
Tribhuvan University

Supported by

ISP
International Science Programme,
Uppsala University,
Sweden

In Collaboration with

IEEE
NEPAL CHAPTER

Certificate of Attendance

American Physical Society
March Meeting 2021
March 15–19, 2021 | Online

THIS IS TO CERTIFY THAT

Hari Krishna Neupane

attended the American Physical Society's March Meeting.
Pre-meeting tutorials and short courses were held on March 13 and 14.

APS physics MARCH MEETING2021

Don Wise, Senior Meetings Registrar
March 19, 2021

The Abdus Salam
International Centre
for Theoretical Physics

This is to certify that

Hari Krishna NEUPANE

participated in and completed online

20th International Workshop on Computational Physics and Materials Science: Total Energy and Force Methods

23 - 25 Feb 2021

Directors:
Francesco Mauri (University of Rome Sapienza, Italy)
Tanusri Saha Dasgupta (S. N. Bose National Centre for Basic Sciences, India)
Nicola Seriani (ICTP, Italy)

Atish Dabholkar, Director

Nepal Physical Society

Ghantaghar, Kathmandu

Certificate of Participation

This certificate is awarded to

Mr. Hari Krishna Neupane **from**

Department of Physics, Amrit Campus, TU, Nepal, for his presentation entitled

Structure, electronic and magnetic properties of C sites vacancy defects in water adsorbed G/MoS_2 hetero-structures: First-principles study

On Scientific Session of 37th Annual Convention, February 6, 2021.

Prof. Dr. Narayan Prasad Chapagain	**Dr. Sunil Babu Shrestha**	**Prof. Dr. Leela Pradhan Joshi**
President	Chief Guest	Chair, Scientific Committee
Nepal Physical Society	Vice – Chancellor, NAST	37th Annual Convention, NPS

February 6, 2021

Certificate of Appreciation

THIS CERTIFICATE IS PRESENTED TO

MR. HARI K. NEUPANE

Amrit Campus, Nepal

FOR YOUR PRESENTATION DURING THE ANPA CONFERENCE 2020

DR. CHET R. BHATT
CHAIR, ANPA CONFERENCE 2020

DR. SHREE K. BHATTARAI
PRESIDENT, ANPA